



**HAL**  
open science

## Bio-inspired synthetic crystals

Clémentine Colas

► **To cite this version:**

Clémentine Colas. Bio-inspired synthetic crystals. Material chemistry. Université Paris-Saclay, 2022. English. NNT : 2022UPASF044 . tel-03824926

**HAL Id: tel-03824926**

**<https://theses.hal.science/tel-03824926>**

Submitted on 21 Oct 2022

**HAL** is a multi-disciplinary open access archive for the deposit and dissemination of scientific research documents, whether they are published or not. The documents may come from teaching and research institutions in France or abroad, or from public or private research centers.

L'archive ouverte pluridisciplinaire **HAL**, est destinée au dépôt et à la diffusion de documents scientifiques de niveau recherche, publiés ou non, émanant des établissements d'enseignement et de recherche français ou étrangers, des laboratoires publics ou privés.

# Bio-inspired synthetic crystals

*Cristaux synthétiques bio-inspirés*

## Thèse de doctorat de l'université Paris-Saclay

École doctorale n°571 : sciences chimiques :  
molécules, matériaux, instrumentation et  
biosystèmes (2MIB)

Spécialité de doctorat : Chimie  
Graduate School : Chimie. Référent : Faculté des Sciences d'Orsay

Thèse préparée au **NIMBE** (Université Paris-Saclay CEA, CNRS),  
sous la direction de **Corinne CHEVALLARD**, Directrice de recherche,  
la co-direction de **Virginie CHAMARD**, Directrice de recherche

Thèse soutenue à Paris-Saclay, le 28 juin 2022, par

**Clémentine COLAS**

## Composition du Jury

<b>Brigitte PANSU</b> Professeure, Université Paris-Saclay	Présidente
<b>Thierry AZAIS</b> Maître de Conférence, HDR, Sorbonne Université	Rapporteur & Examineur
<b>François GUYOT</b> Professeur, Sorbonne Université	Rapporteur & Examineur
<b>Damien FAIVRE</b> Directeur de Recherche CEA, Université Aix-Marseille	Examineur
<b>Corinne CHEVALLARD</b> Directrice de Recherche CEA, Université Paris-Saclay	Directrice de thèse
<b>Virginie CHAMARD</b> Directrice de Recherche CNRS, Université Aix-Marseille	Directrice de thèse



# Remerciements

Je tiens tout d'abord à remercier les membres du jury de thèse François Guyot, Thierry Azaïs, Damien Faivre et Brigitte Pansu, qui ont accepté de juger mon travail au travers de ce manuscrit et de la soutenance orale, menant à des discussions scientifiques très enrichissantes et fructueuses.

Je remercie les institutions ayant permis à ce travail de voir le jour CEA, CNRS ainsi que le conseil de recherche européen qui a financé ce projet (European Research Council 587- European Union's Horizon H2020 research and innovation program grant agreement No 724881).

Ce travail n'aurait pas pu voir le jour sans l'encadrement de mes deux directrices de thèse, Virginie Chamard et Corinne Chevallard, que je tiens également à remercier, et grâce à qui j'ai pu aborder le monde passionnant de la biominéralisation. À vous deux, je tiens à signifier ma gratitude pour votre bienveillance et la qualité de la formation scientifique que j'ai reçue au cours de ma thèse.

Corinne tout d'abord, que j'ai eu la chance de côtoyer quasiment quotidiennement, merci pour nos nombreuses interactions, tant au niveau scientifique que personnel, qui sont toujours un plaisir et qui m'ont permis de m'affirmer en tant que chercheuse.

Virginie, j'ai pu grâce à toi aborder des techniques passionnantes qui m'ont menée à plusieurs reprises à travailler sur synchrotron, domaine que j'ai alors découvert et particulièrement apprécié. Merci pour ta patience et ta pédagogie !

Je souhaite également à remercier Frédéric Gobeaux, pour sa participation aux différentes campagnes de mesures, ainsi que son apport scientifique au cours de nombreuses réunions et présentations.

À l'institut Fresnel de Marseille, je remercie toute l'équipe pour leur accueil chaleureux et riche en discussions scientifiques. Plus particulièrement, Patrick Ferrand et Arthur Baroni, qui m'ont permis d'aborder la ptychographie vectorielle, et ce sur des échantillons synthétiques pas toujours conciliants. Également, merci à Tilman Grunewald pour les nombreuses interactions, scientifiques ou non, au cours de ma thèse.

Au CEA, je remercie les membres du NIMBE, notamment Delpine Neff pour m'avoir accompagnée dans l'utilisation du Raman, ainsi que Ludovic Torteche pour son aide (et sa bonne humeur) en AFM. Au LIONS, je salue toutes les personnes avec qui j'ai pu échanger au cours ces années de doctorat: Jean-Philippe Renault, David Carrière, Valérie Geertsens, Olivier Tache, Fabienne Testard, Elodie Collard et Pierre Picot particulièrement. Merci pour les différentes discussions scientifiques que nous ayons pu avoir, qui ont toujours été percutantes, mais également pour tous ces bons moments passés ensemble. Merci également à Serge Pin, pour les goûters aux madeleines qui redonnent courage aux thésards fatigués !

Aux membres du thésarium : Marion Schwartz, Florent Saudrais, Estelle Puel, Yanis Levieux-Souid, Karol Rakotozandriny, mais aussi aux plus anciens, Marine Le-goas et Gaël Giraudon ce fut un plaisir

de partager un bureau avec vous, merci pour votre bonne humeur de chaque jour ! Également, je suis ravie d'avoir pu commencer et finir ma thèse aux côtés de Marie-Claire Pignié, Lucie Huart et Maxime Durelle et d'avoir traversé ensemble à la fois expériences (réussies ou non) en laboratoire, confinements, rédaction et soutenances ! Merci d'avoir été là dans ces périodes si particulières.

Merci aux Licornes atomiques de m'avoir fait découvrir dans le Foot, et merci aux membres de la Dream-team d'avoir toujours répondu présent malgré la distance !

Finalement, je remercie chaleureusement ma famille pour leur soutien indéfectible au cours de ces dernières années, riches en travail et en émotion ! Également, merci à toi Mathieu pour ta présence et ton soutien au quotidien dans cette expérience du doctorat, que je suis contente d'avoir pu partager avec toi.

# TABLE OF CONTENT

---

TABLE OF CONTENT.....	5
RESUME DE LA THESE EN FRANÇAIS.....	8
INTRODUCTION: BIOMINERALS, A CHALLENGE FOR MATERIALS CHEMISTRY .....	14
<b>1. STATE OF THE ART .....</b>	<b>18</b>
<b>1.1 Calcareous biominerals: a common underlying formation mechanism .....</b>	<b>18</b>
1.1.1 Inorganic/organic hybrid structure .....	18
1.1.2 Cyclic growth process.....	20
1.1.3 Non-euhedral, iso-oriented crystals.....	20
1.1.4 Amorphous calcium carbonate .....	22
<b>1.2 Amorphous calcium carbonate in model syntheses .....</b>	<b>23</b>
1.2.1 Intermediate states to crystallization: deviation from classical crystal nucleation .....	24
1.2.2 Amorphous calcium carbonate precipitates .....	25
1.2.3 Polyamorphism of calcium carbonate .....	26
1.2.4 ACC stability .....	27
1.2.5 Liquid precursor in ACC syntheses .....	28
<b>1.3 Amorphous to crystalline transformation .....</b>	<b>33</b>
1.3.1 Dissolution-Crystallization.....	33
1.3.2 Solid-state transformation .....	36
<b>1.4 Thesis.....</b>	<b>39</b>
1.4.1 Choice of a synthetic model: PILP synthesis with Ammonia Diffusion Method .....	39
1.4.2 Choice of a biogenic model : the black-lip pearl oyster. ....	40
1.4.3 Methodological approach .....	41
<b>2 MATERIALS AND METHOD .....</b>	<b>42</b>
<b>2.1 Syntheses.....</b>	<b>42</b>
2.1.1 Reproducibility issues .....	42
2.1.2 'Cap' and 'pellet' syntheses .....	43
2.1.3 Sampling : drying and conservation .....	45
2.1.4 Long-term conservation of the collected film samples.....	47
<b>2.2 Crystallization condition.....</b>	<b>48</b>
2.2.1 Interfacial crystallization. ....	48
2.2.2 Thermally induced crystallization, .....	48
2.2.3 Humidity induced crystallization.....	48
<b>2.3 Optical microscopy.....</b>	<b>50</b>
2.3.1 Phase contrast microscopy (PCM) .....	50
2.3.2 Birefringence microscopy (BM) and Wave plate assisted birefringence microscopy (WBM).....	51
2.3.3 Experimental set-up .....	53
2.3.4 Image processing for data extraction and analysis.....	53

## TABLE OF CONTENT

---

<b>2.4</b>	<b>Electronic microscopy</b> .....	<b>55</b>
2.4.1	Transmission Electron Microscopy (TEM) .....	55
2.4.2	Cryogenic Transmission Electron Microscopy (cryo-TEM) .....	58
2.4.3	Scanning electron microscopy (SEM) .....	59
<b>2.5</b>	<b>Lensless microscopy</b> .....	<b>61</b>
2.5.1	Vectorial Ptychography (VP) .....	62
2.5.2	Bragg Ptychography (BP).....	67
2.5.3	Atomic force microscopy (AFM) .....	74
<b>2.6</b>	<b>Spectroscopy</b> .....	<b>75</b>
2.6.1	Raman spectroscopy .....	75
2.6.2	Scanning Transmission X-ray Microscopy (STXM) and X-ray Absorption Spectroscopy (XAS).....	77
<b>2.7</b>	<b>In situ set-ups</b> .....	<b>80</b>
2.7.1	Synthesis reactor for <i>in situ</i> optical microscopy .....	80
2.7.2	Monitoring of environmental parameters .....	81
2.7.3	Humidity-controlled cell for <i>in situ</i> crystallization follow-up.....	82
<b>3</b>	<b>AMORPHOUS CALCIUM CARBONATE FILM SYNTHESIS</b> .....	<b>84</b>
<b>3.1</b>	<b>Interfacial mineralized film synthesis using the Ammonia Diffusion Method</b> .....	<b>84</b>
3.1.1	Production of mineralized amorphous films in biomimetic syntheses .....	84
3.1.2	Characteristic pattern of the mineralized films synthesized at low calcium and polymer concentrations (20 mM, 20 ppm).....	86
3.1.3	Macroscopic morphology tuning with synthesis parameters .....	88
3.1.4	Assessment of film amorphism (local atomic ordering) .....	89
<b>3.2</b>	<b>Structural properties of the interfacial amorphous films</b> .....	<b>93</b>
3.2.1	Structural features at the microscale.....	93
3.2.2	Structure at the nanoscale.....	97
<b>3.3</b>	<b>Investigation of the mechanisms of film formation</b> .....	<b>98</b>
3.3.1	Time scale of interface and bulk mineralization .....	99
3.3.2	Evolution of the interfacial mineralized structures with time .....	100
3.3.3	Environmental parameters variation with time.....	113
3.3.4	Bulk mineralization .....	115
<b>3.4</b>	<b>Discussion</b> .....	<b>118</b>
3.4.1	Environmental condition evolution .....	119
3.4.2	Quench-induced liquid/liquid phase separation.....	121
3.4.3	Thickening by bulk particle aggregation .....	124
3.4.4	New model proposition .....	127
<b>4</b>	<b>CONTROL OF CRYSTALLIZATION: INCIDENCE ON CRYSTALLINE PROPERTIES</b> .....	<b>129</b>
<b>4.1</b>	<b>Heat-induced crystallization</b> .....	<b>129</b>
4.1.1	Microscale crystallinity.....	130
4.1.2	Structure at the nanoscale: surface and edges analysis. ....	131
4.1.3	Polymorph selection .....	133
4.1.4	Calcium environments in the crystallized films.....	134
4.1.5	Crystal orientation: in-plane and thickness distribution.....	136
4.1.6	Crystalline coherence length and defect distribution .....	138
<b>4.2</b>	<b>Humidity-induced crystallization</b> .....	<b>141</b>
4.2.1	Influence of the relative humidity percentage: microscale crystallinity and polymorphism.....	141

## TABLE OF CONTENT

---

4.2.2	High relative humidity: temporality of crystal growth .....	143
4.2.3	High relative humidity: structural features at the micro- and nanoscale. ....	147
4.2.4	Calcium chemical environment within the crystallized film .....	150
4.2.5	Quantitative investigation of crystalline properties .....	151
4.2.6	Crystalline coherence length and defect distribution .....	155
<b>4.3</b>	<b>Interfacial crystallization .....</b>	<b>157</b>
4.3.1	Spectroscopic overview of the remaining crystals.....	158
4.3.2	Orientation of the calcitic domains.....	159
4.3.3	Structure at the nanoscale .....	159
4.3.4	Quantitative investigation of crystalline properties .....	162
4.3.5	Crystalline coherence length and defect distribution .....	164
<b>4.4</b>	<b>Summary of the results .....</b>	<b>167</b>
<b>4.5</b>	<b>Discussion .....</b>	<b>169</b>
4.5.1	Heat-induced amorphous-to-crystalline transition .....	169
4.5.2	Humidity-induced amorphous-to-crystalline transition .....	170
4.5.3	Interfacial amorphous to crystalline transition.....	172
4.5.4	Heterogeneities in the amorphous film: influence on the crystallization.....	174
4.5.5	Comparison to <i>Pinctada margaritifera</i> crystalline properties. ....	174
<b>5</b>	<b>CONCLUSIONS AND PERSPECTIVES .....</b>	<b>178</b>
<b>5.1</b>	<b>Mineralization pathway in the model system: from free ions to crystalline layer. ....</b>	<b>178</b>
<b>5.2</b>	<b>Relevance of the crystal growth model with regard to biomineralization .....</b>	<b>180</b>
<b>5.3</b>	<b>Perspectives on the current model.....</b>	<b>182</b>
<b>6</b>	<b>APPENDIX .....</b>	<b>185</b>
<b>6.1</b>	<b>Chapter II .....</b>	<b>185</b>
<b>6.2</b>	<b>Chapter III .....</b>	<b>188</b>
6.2.1	STXM .....	192
<b>6.3</b>	<b>Chapter IV.....</b>	<b>196</b>
6.3.1	Heat-induced crystallization .....	196
6.3.2	Humidity (98% RH) induced crystallization .....	202
6.3.3	Interfacial crystallization .....	209
<b>7</b>	<b>ILLUSTRATIONS TABLE .....</b>	<b>214</b>
<b>8</b>	<b>BIBLIOGRAPHY .....</b>	<b>232</b>



## RESUME DE LA THESE EN FRANÇAIS

---

La biominéralisation regroupe l'ensemble des phénomènes biologiques à l'œuvre dans la formation des tissus durs (os, dents, coquille d'œuf...) par les êtres vivants.<sup>1</sup> Les cristaux de carbonate de calcium ( $\text{CaCO}_3$ ) biogéniques, par exemple, sont largement produits par la faune aquatique (mollusques, coraux, oursins, etc.) comme outils de protection, de reproduction ou de vision. Ces fonctions vitales dépendantes des biominéraux calcaires peuvent être assurées en raison d'un contrôle biologique pointu. Celui-ci détermine notamment la morphologie, la composition chimique, et la structure des cristaux, en établissant des conditions de synthèse contrôlées (concentrations chimiques, acidité du milieu, localisation de la minéralisation notamment).

Le milieu biologique présente des conditions de synthèses dites « douces ». Les ions impliqués dans la formation du carbonate de calcium ( $\text{Ca}^{2+}$  et  $\text{CO}_3^{2-}$ ) sont présents en quantités modérées, de l'ordre de quelques dizaines de millimoles. Les matériaux sont par ailleurs formés à température et pression ambiantes. Les synthèses de biominéraux requièrent ainsi un coût énergétique, et donc environnemental, faible.

Parallèlement au faible coût énergétique de leur production, les propriétés mécaniques de ces minéraux dépassent celles des cristaux obtenus en laboratoire par mélange de sels. Les cristaux biogéniques présentent par exemple une meilleure résistance à l'impact, à la torsion ou à l'élongation que leur équivalent synthétique.<sup>2-4</sup> Ces propriétés améliorées sont notamment issues de leur structure hybride, consistant en un arrangement tridimensionnel de matériaux organique et inorganique à différentes échelles. Développer des composites biomimétiques, basés sur notre compréhension des phénomènes biologiques, est donc d'un intérêt particulier pour la chimie des matériaux.

L'observation des biominéraux calcaires au cours du siècle passé a permis d'établir certaines caractéristiques de leur formation. Pour de nombreux bivalves, la croissance s'effectue au niveau du liquide extrapalléal par minéralisation épisodique créant des couches de croissance dans le cristal.<sup>5</sup> À l'échelle microscopique, les cristaux sont organisés en couches alternées de carbonate de calcium et de matrice organique. Chaque couche minérale est elle-même nanostructurée (nano-granules de quelques dizaines de nanomètres, organisées en arrangement dense).<sup>6</sup> Les cristaux formés découlent ainsi d'un contrôle en termes de structure (polymorphisme), de morphologie et d'orientation cristalline. Celui-ci permet d'obtenir des cristaux de calcite, vaterite ou aragonite spatialement distincts, sous forme de prismes, de plaquettes ou encore de sphérulites.<sup>7</sup> Des polymorphes non-cristallins du carbonate de calcium ont également été identifiés,<sup>8</sup> leur rôle dans la biominéralisation calcaire restant à préciser. Les biominéraux calcaires croissent donc par couches, tout en subissant un contrôle polymorphique et morphologique aigu.

Malgré de conséquentes avancées dans la compréhension de la formation des cristaux biogéniques, certaines clés manquent encore aujourd'hui pour définir un modèle biologique. La difficulté de compréhension des mécanismes en jeu est notamment liée au fait que les cristaux biogéniques rassemblent des propriétés inhabituelles. Leurs formes extrêmement complexes, sans faces cristallines développées, et leurs structures composées d'un assemblage

compact de grains sphéroïdaux de quelques dizaines de nanomètres, sont autant d'écarts aux processus décrits par la théorie classique de la nucléation cristalline, et sont ainsi révélateurs d'un chemin de cristallisation complexe. Ces grains, malgré la fine enveloppe organique qui les entoure, partagent localement une même orientation cristalline et peuvent être assemblés en monocristaux étendus sur plusieurs millimètres. Ces grains ont été associés à un intermédiaire amorphe précédant la cristallisation.<sup>9</sup> L'existence de ces états intermédiaires rend indispensable le suivi temporel des phénomènes biologiques associés, pour parvenir à une compréhension des étapes menant à la formation du cristal.

Malheureusement, une approche dynamique *in vivo* est extrêmement complexe. Les espaces de minéralisation sont réduits, et l'observation de dépôts minéralisés est difficile, en raison du stress imposé à l'animal durant l'observation et de la difficulté de mener des études non invasives, mais permettant d'accéder aux paramètres pertinents de la biominéralisation. Une alternative aux contraintes imposées par les études *in vivo* consiste à réaliser des synthèses biomimétiques en laboratoire. Il est en effet possible dans ce cadre de suivre les variations de paramètres environnementaux clés (pH, concentrations, nature des espèces formées) de façon dynamique et sans perturber le milieu de synthèse. Ainsi, les modèles synthétiques peuvent apporter des éléments primordiaux dans la compréhension des phénomènes physico-chimiques à l'œuvre dans la biominéralisation.

Le développement des modèles synthétiques ces dernières décennies a souligné la grande diversité des chemins de cristallisation du carbonate de calcium,<sup>10</sup> au-delà du chemin décrit par la théorie classique. Des états intermédiaires amorphes, rappelant le chemin de cristallisation biologique, ont notamment été décrits.<sup>11</sup> Un second intermédiaire, également proposé de manière récurrente, correspond à un liquide dense, enrichi en solutés, et précurseur du carbonate de calcium amorphe.<sup>12</sup> Cet intermédiaire liquide serait le résultat d'une séparation de phase liquide-liquide dans le milieu réactionnel.<sup>13</sup> La présence de cet intermédiaire dans le milieu biologique étant très difficile à démontrer, l'utilisation de synthèses en laboratoire peut permettre d'évaluer si son existence au cours des phénomènes biologiques est une addition réaliste au modèle biologique actuel.

L'approche développée au cours de ce travail de thèse reprend cette analyse et utilise ainsi une synthèse modèle pour améliorer la compréhension des chemins de formations des cristaux biogéniques. En permettant la compréhension de chaque étape de la formation des cristaux synthétiques et de son impact sur les propriétés finales du matériau formé, les synthèses modèles doivent apporter des clés pour mieux appréhender la biominéralisation.

La synthèse choisie est dite « PILP » (Polymer-Induced Liquid Precursor). Ce type de synthèses est basé sur l'ajout au milieu de synthèse de polyélectrolytes portant des fonctions acides, qui stabilisent l'intermédiaire liquide dense. Cet ajout est pertinent du point de vue biomimétique, car la plupart des protéines impliquées dans la biominéralisation comportent de nombreux acides aminés acides dans leur séquence.<sup>14</sup> Plus précisément, la synthèse modèle retenue consiste à exposer une solution de calcium et de polyacrylate de sodium à une atmosphère de dioxyde de carbone (CO<sub>2</sub>) et d'ammoniac (NH<sub>3</sub>) résultant de la sublimation d'une poudre de carbonate d'ammonium. La dissolution combinée de l'ammoniac et du dioxyde de carbone provoquent l'augmentation du pH et de la sursaturation de la solution vis-à-vis de la précipitation du carbonate de calcium, notamment à proximité de l'interface eau-air. Ce type de synthèses permet ainsi de produire des cristaux bidimensionnels de carbonate de calcium,

sous forme de films nanostructurés à la surface de la solution,<sup>15</sup> qui rappellent la cristallisation en couche des biominéraux calcaires.

Les cristaux formés lors de ces synthèses modèles sont ensuite caractérisés du point de vue chimique et structural, puis comparés à des cristaux biogéniques modèles – les prismes calcitiques de bord de coquille de l’huître perlière de Polynésie française, *Pinctada margaritifera* (*Pm*) – afin de valider la pertinence du modèle biomimétique.

La première partie de l’étude (Chapitre 3, *Amorphous calcium carbonate film synthesis*) se concentre sur les mécanismes d’apparition et la caractérisation des films de carbonate de calcium amorphe formés lors de ces synthèses. La variation des paramètres de synthèses (concentrations ionique et polymère) permet de moduler la morphologie du film. On passe ainsi de films discontinus, formés d’un arrangement compact de disques de taille micronique (~5µm) et peu polydisperses aux faibles concentrations en calcium (20 mM) et polymère (20 ppm), à des films continus pour lesquels les disques ne sont plus identifiables pour les plus fortes valeurs de concentrations (100 mM, 100 ppm). Une illustration de la modulation de morphologie du film, obtenue par variation de la quantité de polymère en solution pour un taux de calcium moyen (50 mM) est présenté en Figure 1. Ainsi, à concentration de calcium constante (50 mM), la quantité de polymère définit une morphologie en disques microniques (Figure 1.a, 20 ppm de polymère), un film discontinu au motif partiellement fusionné (Figure 1.b, 50 ppm de polymère), ou un film continu (Figure 1.c, 100 ppm de polymère).

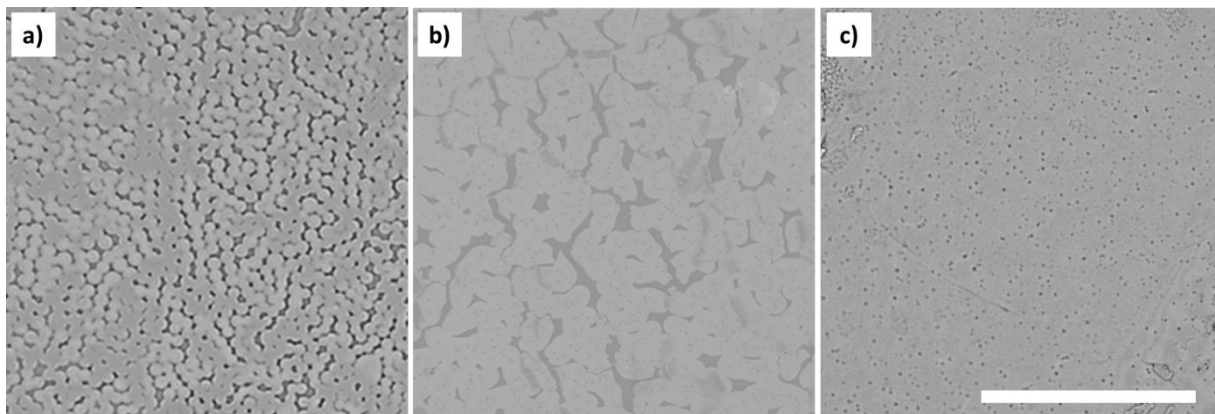
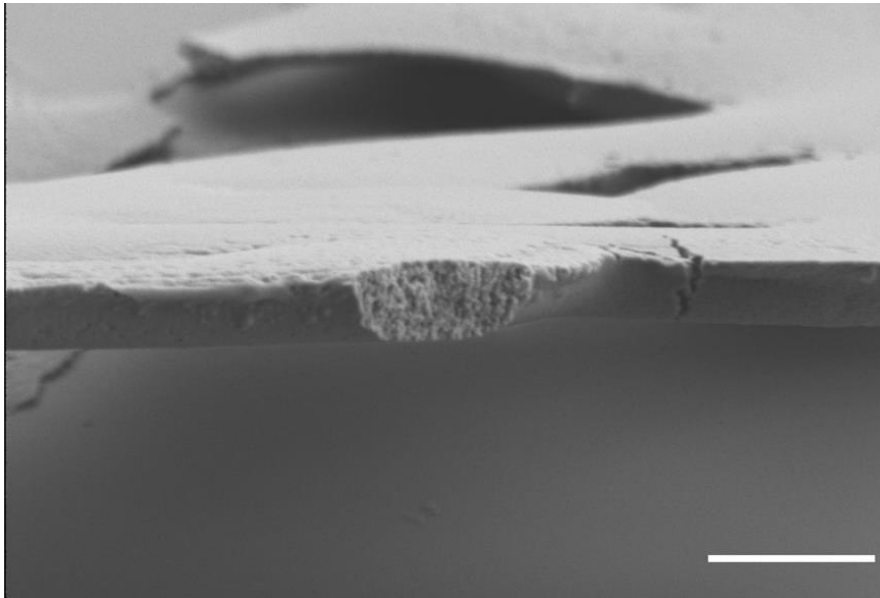


Figure 1 - Micrographies optiques d’absorption de films d’interface extraits à l’état amorphe du milieu réactif par dépôt sur nitrure de silicium. Après séchage sous vide, les films sont observés en microscopie optique. Les solutions réactives ont une concentration en calcium de 50 mM, et de Polyacrylate de sodium de a) 20 ppm, b) 50 ppm, c) 100 ppm. Les films sont extraits du milieu réactif à 18h, 16h et 18h, respectivement. Échelle = 50 µm.

Le film amorphe se construit sur plusieurs heures, avant de se dissoudre au profit de phases cristallines, thermodynamiquement plus stables. Prélevé avant cristallisation, le film peut être caractérisé *ex situ* à l’aide de techniques d’analyse morphologique (SEM, TEM, Cryo-TEM) et chimique (Raman, STXM). Les films produits ont une épaisseur variant entre 500 et 700 nm, comparable à celle des couches présentes chez l’huître perlière *Pm*. Ils sont par ailleurs composés d’un arrangement compact de nanoparticules amorphes (de quelques dizaines de nanomètres, Figure 3), rappelant là encore l’arrangement de grains sphéroïdaux présents chez *Pm*.



*Figure 2 - Micrographie électronique (MEB) d'un film extrait à l'état amorphe après 18h d'exposition d'une solution de concentration en calcium de 20 mM et en polymère de 20 ppm à une poudre de carbonate d'ammonium. Afin de visualiser la nanostructure interne du film, une craquelure dans le film amorphe est observée. Le film est constitué d'un arrangement de nanoparticule dans l'épaisseur. Échelle = 500 nm*

Le suivi temporel de la synthèse des films discontinus permet de proposer un mécanisme de formation. Des observations par microscopie électronique d'échantillons de films amorphes prélevés à temps courts (<1h) suggèrent l'existence d'une séparation de phase liquide/liquide se produisant par décomposition spinodale. Cette décomposition induit la formation d'un motif interfacial (disques) qui sera conservé jusqu'à la cristallisation du film. Par la suite, le film amorphe croit par additions de nanoparticules, formées en solution. Des courants de convection, observables à l'œil nu, provoquent un apport massif de nanoparticules vers la surface qui induisent l'épaississement progressif du film. Ainsi, les films de carbonate de calcium amorphes sont obtenus grâce à un mécanisme de formation en deux étapes, nouvellement décrit (Figure 3): la formation et la croissance radiale de disques émergeant d'une séparation de phase liquide-liquide, et un épaississement progressif dans la direction perpendiculaire à l'interface lié à l'agrégation irréversible de nanoparticules amorphes formées dans la solution.

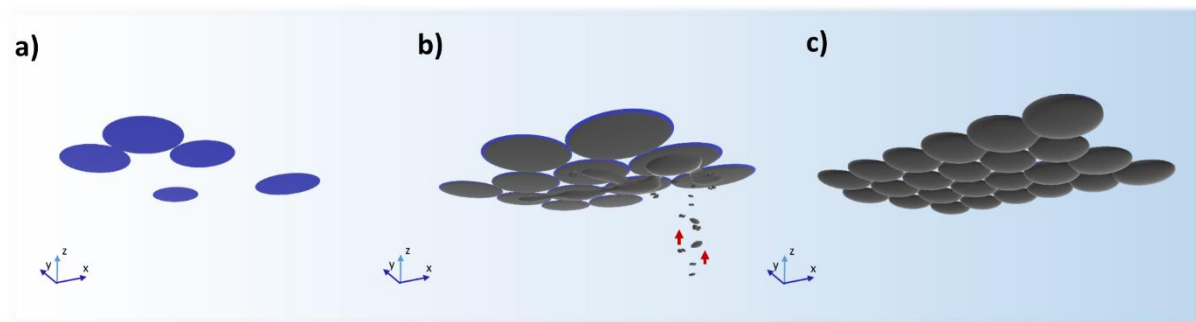


Figure 3 - Représentation schématique du mécanisme de formation par étape du film de carbonate de calcium. a) Séparation de phase liquide-liquide menant à l'émergence de disques fins qui croissent radialement. b) croissance du film en épaisseur, du à l'agrégation de particules du volume de la solution (flèche rouge). c) film amorphe dont l'épaisseur ne varie plus.

La deuxième partie de mon travail de thèse a été consacrée à la cristallisation des films de carbonate de calcium amorphe et à l'évolution de la structure des films, aux différentes échelles spatiales, lors de leur cristallisation. Trois conditions de cristallisation ont été successivement étudiées : la cristallisation induite par chauffage à 300°C (Figure 4.a), censée favoriser une transformation solide-solide du film sans modifications morphologiques (transformation pseudomorphique) ; la cristallisation induite par exposition du film à une atmosphère humide (98% d'humidité relative, Figure 4.b) à température ambiante, associée à des phénomènes de dissolution-reprécipitation ; enfin, la cristallisation spontanée, dans le milieu réactionnel de synthèse (Figure 4.C), obtenue en laissant vieillir le film amorphe à l'interface eau-air. Dans tous les cas, les films transformés présentent de larges domaines de calcite iso-orientés. Le suivi de l'évolution des caractéristiques morphologiques et structurales du film au cours de la cristallisation (modification de la nanostructure et /ou de la morphologie globale) a permis de discuter du type de transformations à l'œuvre, et de suggérer en particulier l'intervention d'un mode de cristallisation hybride associant mécanismes de dissolution/re-précipitation locale et transformation solide/solide lors de la cristallisation induite par chauffage.

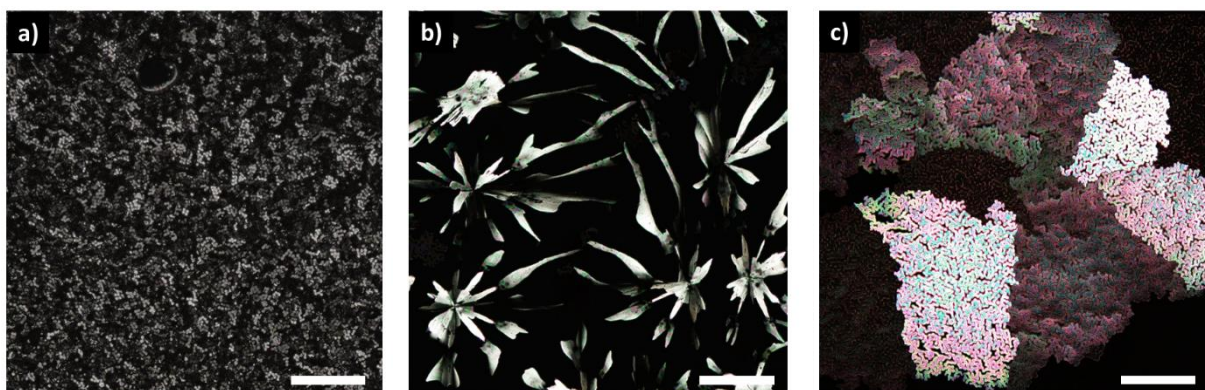


Figure 4 - Micrographies optiques de biréfringence. Le film de départ est un film amorphe constitué d'arrangement de disques microniques ( $[Ca^{2+}] = 20 \text{ mM}$ ,  $[PANa] = 20 \text{ ppm}$ ) a) après chauffage 300°C durant 3 heures, b) après exposition à une humidité élevée (98% HR) durant 14 jours. c) après cristallisation dans le milieu réactif pendant 5 jours. Échelles = 100  $\mu\text{m}$

Les propriétés cristallines résultant des différents modes de transformation ont été étudiées par des techniques spatialement résolutes, telles que la ptychographie optique vectorielle ou

la ptychographie X de Bragg. La ptychographie vectorielle est une technique d'imagerie applicable aux matériaux optiquement anisotropes tels que les matériaux cristallins, permettant d'obtenir des cartographies des propriétés cristallines (biréfringence effective, orientation de l'axe extraordinaire, qualité de l'ordre cristallin dans l'épaisseur de l'échantillon) avec une résolution de microscopie optique. Les caractérisations menées par ptychographie vectorielle confirment la forte influence des conditions de cristallisation sur les propriétés des films calcitiques formés : les films chauffés sont composés de domaines iso-orientés de quelques microns et présentent une légère désorganisation cristalline dans le plan d'observation, tandis que les cristaux d'interface ont une organisation quasi-parfaite sur une échelle de taille dix fois supérieure. Cette technique permet également d'identifier une variation des propriétés cristallines au cours de la croissance des cristaux sous humidité contrôlée (existence de domaines iso-orientés au point de nucléation cristalline, et organisation radiale de l'axe rapide du cristal en bord de structure). La ptychographie vectorielle met donc en lumière que la nature des transitions amorphe-cristal impacte fortement les propriétés finales des cristaux formés, de sorte que la connaissance des propriétés cristallines des biominéraux devrait permettre d'identifier un scénario de croissance réaliste parmi les synthèses modèles disponibles.

La ptychographie de Bragg permet de prolonger ces considérations à l'échelle nanométrique. Cette technique, qui nécessite l'utilisation d'un faisceau X cohérent issu d'une source synchrotron, permet de reconstruire en trois dimensions les propriétés cristallines (déformations, désorientations et cohérence cristalline) présentes dans les cristaux obtenus, à l'échelle de la dizaine de nanomètres. Ainsi, les distorsions des mailles cristallines sont quantifiables, apportant une description sans équivalent des défauts produits par chaque transformation cristalline. Il apparaît que les cristaux de calcite sont composés de domaines cristallins iso-orientés et iso-déformés dont la taille varie entre environ 200 nm et 2 microns. Ces domaines sont eux-mêmes composés de régions de forte cohérence cristalline (cristal sans défaut), de taille et caractéristiques dépendant de la transformation. Les iso-domaines et la cohérence cristalline sont ainsi décrits pour chaque condition de cristallisation. La ptychographie de Bragg permet d'illustrer l'impact des conditions de transition amorphe-cristal sur la structure fine des mono-cristaux de calcite.

La comparaison des propriétés cristallines à l'échelle des iso-domaines cristallins entre les modèles de synthèse et la structure des prismes de *Pm*, met en évidence une similitude remarquable entre le cristal biogénique<sup>16</sup> et le cristal biomimétique produit à l'interface, similitudes qui ne sont pas vérifiées avec les cristaux produits par chauffage ou de façon contrôlée par exposition à une atmosphère humide.

Ce travail de thèse a donc permis de conduire l'analyse fine des propriétés structurales (morphologiques et cristallines) de films de carbonate de calcium issus d'intermédiaires liquide et solide amorphe, et cristallisés sous trois conditions différentes. Les résultats de cette analyse peuvent être mis en parallèle des données obtenues sur les cristaux biogéniques issus de prismes de *Pinctada Margaritifera* : dans les deux cas, les cristaux formés sont organisés en couche de 500 à 700 nm, et ont une nanostructure, caractéristiques partagées avec le biominéral. La similarité constatée entre les structures synthétique et biologique constitue une validation des synthèses modèles choisies et permet de suggérer un mécanisme de biominéralisation faisant intervenir, comme dans les synthèses modèles, une étape de croissance bidimensionnelle associée à une séparation de phase liquide-liquide et une étape de croissance en épaisseur par agrégation de nanoparticules déjà formées.

## INTRODUCTION: BIOMINERALS, A CHALLENGE FOR MATERIALS CHEMISTRY

With their myriad of crystal shapes and sizes, created by finely controlled crystallization pathways, biominerals captivate the materials chemists. Impressive examples of the wide morphological diversity resulting from calcareous biomineralization are highlighted in Figure 5: coccolithophores constituted of specialized body and appendage coccoliths (Figure 5.a), millimetric corals with intricate structures (Figure 5.b) or micronic mineralizing animals like foraminifera (Figure 5.c). This glimpse of the morphology diversity underlines how developed the control of the biomineralization process must be.

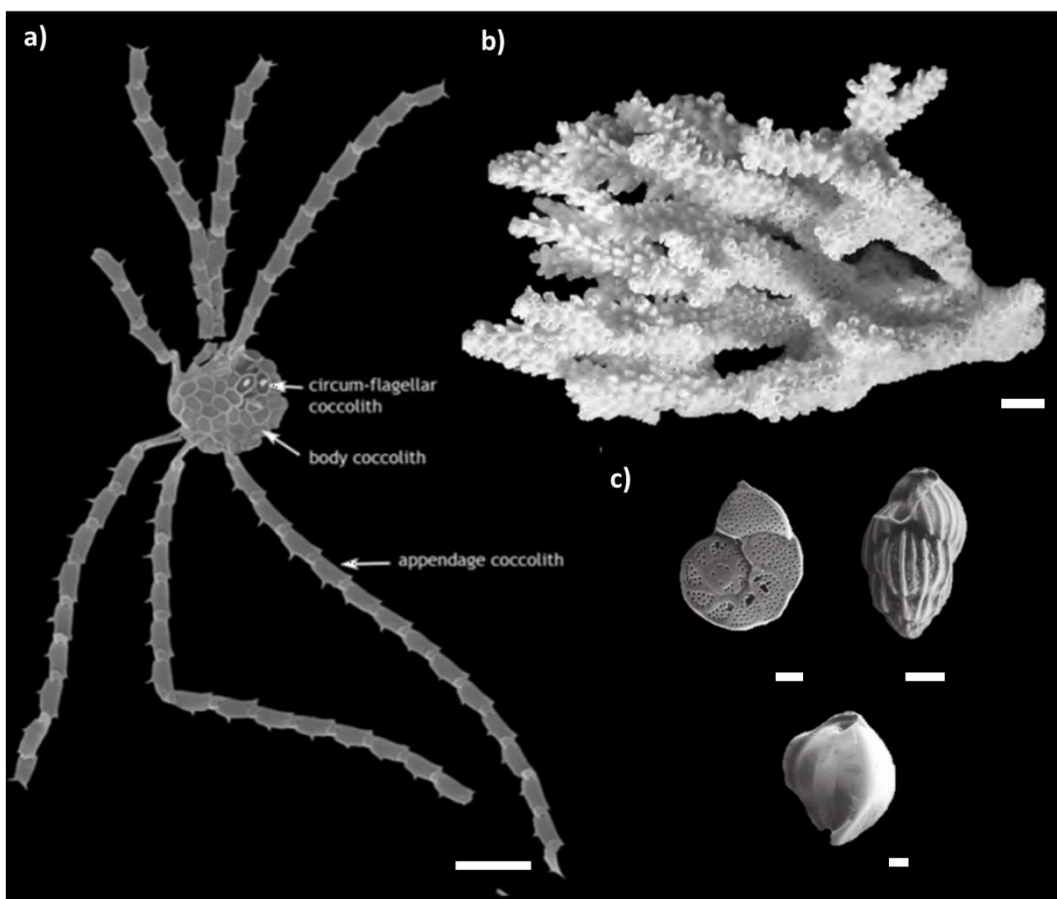


Figure 5 - Electron micrographs (SEM) and photographs showing representative examples of the wide variety of biogenic calcium carbonate crystals. a) Appendage-bearing coccolithophore, *Ophiaster formosus* (SEM). From Young et al.<sup>17</sup> Scale bar = 5  $\mu\text{m}$ . b) Coral, *Acropora solitaryensis* (Photograph). From Bay et al.<sup>18</sup> Scale bar = 10 mm. c) Foraminiferas, *Cibicides refluense*, *Uvigerina* spp., *Quiqueloculina* spp. (SEM). From Pilarczyk et al.<sup>19</sup> Scale bar = 100  $\mu\text{m}$ .

Calcareous biominerals sustain many biological functions. The protection value of a mollusk shell has been known for centuries, but some intricate functions such as the  $\text{CaCO}_3$  photoreceptors of the brittle star were only elucidated recently.<sup>20</sup> Table 1 presents a variety of

functions of calcium carbonate biominerals, as they are used as protective, visual or even reproductive devices. The functions covered by these materials are far from being minor, and the survival of many marine species actually depends on it.

*Table 1 - Adapted from Mann et al. (2001).<sup>1</sup> Variety of calcium carbonate utilities among biominerals, and associated polymorphs.*

Mineral	Organism	Location	Function
<b>Calcite</b>	Trilobite	Eye lens	Optical imaging
	Mollusks	Shell	Exoskeleton
	Crustacean	Crab cuticle	Mechanical strength
	Echinoderms	Shell/spines	Strength/Protection
<b>Aragonite</b>	Cephalopods	Shell	Buoyancy device
	Fish	Head	Gravity receptor
	Gastropods	Love darts	Reproduction
	Mollusks	Shell	Exoskeleton
<b>Vaterite</b>	Ascidians	Spicules	Protection
	Gastropods	Shell	Exoskeleton

The three anhydrous crystalline polymorphs of calcium carbonate can be found in biominerals: calcite, aragonite and vaterite (see Table 1). However, biomineralization clearly involves polymorphic selection: different polymorphs can be synthesized simultaneously, but in a regio-selective way, by a given animal,<sup>21</sup> thanks to a spatially differentiated mineralizing tissue. An illustration of this spatial control is found in various mollusks shells (ex. superfamilies of Pinnacea, Pteriacea, Amnomyacea,...).<sup>7</sup> In these superfamilies, the outer layer is formed of a calcitic layer, while the inner layer is constituted of aragonite. The spatial distribution of these two layers in a bivalve, along with the complex structure of the animal at the mineralization area is shown in Figure 6. In the extrapallial cavity, where mineralization occurs, both aragonite (nacreous layer) and calcite (prismatic layer) are formed next to each other. Ultimately, the spatial differentiation of polymorphs relies on a perfect control of the crystallization event by biological means.



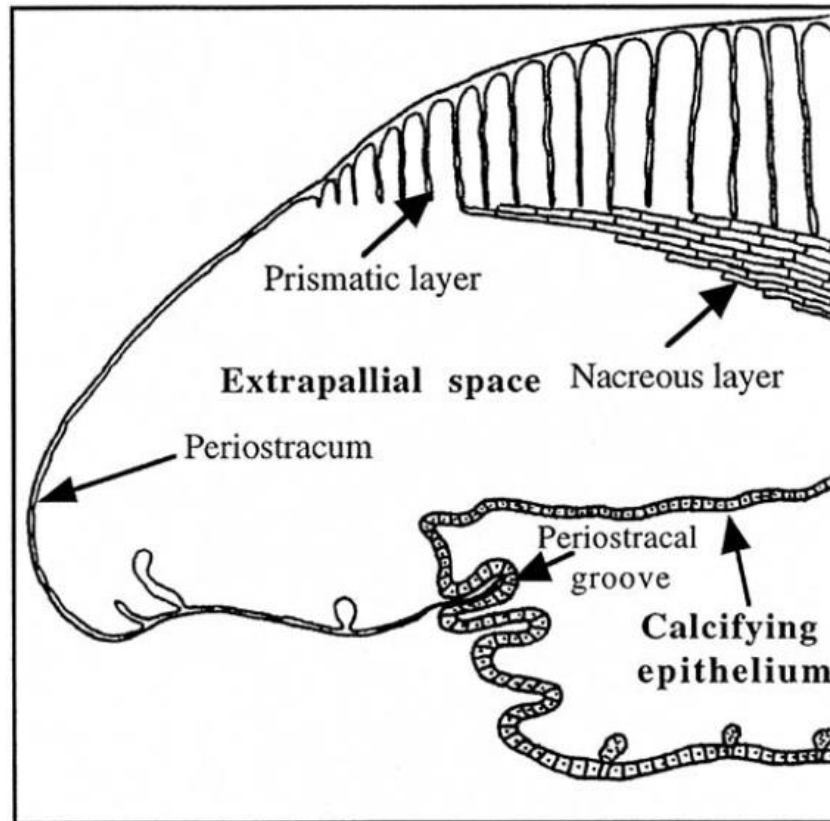


Figure 6 - Schematized morphology of a bivalve constituted of an external prismatic layer, and an internal nacreous layer, at the growing shell edge. From Marin *et al.*<sup>22</sup>

The controlled morphology of these crystals correlates with their enhanced mechanical properties.<sup>23</sup> For example, biogenic calcite in mollusk shells are 50% to 70% harder than geological calcite.<sup>4</sup> Besides, biogenic aragonite has a better resistance against fractures, and a better tensile strength than its synthetic counterpart.<sup>24</sup> These striking observations have motivated materials chemists to produce new materials using a bio-inspired approach, to reach better resistance and strength.<sup>23</sup> However, even though efforts have been made to replicate the calcareous biogenic crystal properties,<sup>25</sup> biomineralization pathways still lead to crystals with better properties than those made in laboratories. To be able to replicate the enhanced mechanical properties of calcareous biominerals, the physico-chemical conditions of their formation must be elucidated.

The biomineralization process takes place under "soft" physico-chemical conditions. Indeed, an additional trait of biomineralization is the capacity of the animals to create properties-enhanced crystals at ambient pressure and temperature. This term of 'soft conditions' could also apply to chemical concentrations, as the medium surrounding the mineralizing animals (sea or fresh water) is a (very) dilute saline solution. In the case of bivalves, the ion concentration in the mineralizing fluid, called the extrapallial fluid,<sup>26</sup> remains in the millimolar range, similar to the one of sea water. It must be stressed that local variations in the ion concentration can happen in the extrapallial space<sup>27</sup>, for a reason that remains a great mystery of the biomineralization process. These soft conditions are of particular interest to materials chemistry, as they represent a prospect to cost-effective and environmentally-friendly syntheses.

In addition, the development of bio-inspired carbonated materials could have a positive environmental impact by playing a role in solving one of the major problems of the 21<sup>st</sup> century: CO<sub>2</sub> storage. Indeed developing alternative ways to sequester CO<sub>2</sub> is of prime importance owing to the impact of CO<sub>2</sub> increase on global warming. Until now, marine life<sup>28</sup> has been a major source of CO<sub>2</sub> intake. Approximately a third of the world's atmospheric carbon dioxide is dissolved in the ocean, as estimated by Gruber *et al.* between 1994 and 2007.<sup>29</sup> But this massive dissolution of continuously increasing amounts of CO<sub>2</sub> has led to ocean acidification, which in turn strongly affects biomineralizing species.<sup>30</sup> Ocean acidification negatively influences calcareous biomineralization by inducing shell dissolution.<sup>31</sup> A pH drop could be catastrophic to biomineralizing species, as calculations predict that carbonate concentration in the ocean could even drop below supersaturation levels of calcite and aragonite<sup>32</sup> (crystalline forms of CaCO<sub>3</sub> widely distributed in biominerals). Bio-inspired calcium carbonate syntheses could therefore be a powerful tool to store CO<sub>2</sub> under the form of high-value materials, this way protecting our source of inspiration, but requires an in-depth understanding of biomineralization, which is still lacking today.

# 1. STATE OF THE ART

---

## 1.1 CALCAREOUS BIOMINERALS: A COMMON UNDERLYING FORMATION MECHANISM

It is still to date difficult to apprehend how, from ions solvated in liquid, crystals with properties close to those of biominerals can emerge. This difficulty derives from a limited knowledge on the conditions of biomineralization, but also from the unusual crystallization pathway, overlooked by classical crystallization theories, encountered during biominerals formation. To understand how they form, one should first look thoroughly at biominerals and identify clues of their formation pathway.

### 1.1.1 Inorganic/organic hybrid structure

The biomineral design includes an organic scaffolding surrounding the calcium carbonate crystals. For example, aragonite tablets of the triangular mussel *Hyriopsis Cumingii* are separated by an organic scaffold, called "biopolymer membrane" in Figure 7.a. *Pinna nobilis* calcitic prisms (birefringence microscopy in Figure 7.c) present a similar scaffold, revealed in Figure 7.d after etching the shell. The scaffold surrounding the prisms is also visible on Figure 7.e, on an elongated cut of a shell. Biominerals are therefore hybrid organic/inorganic materials.

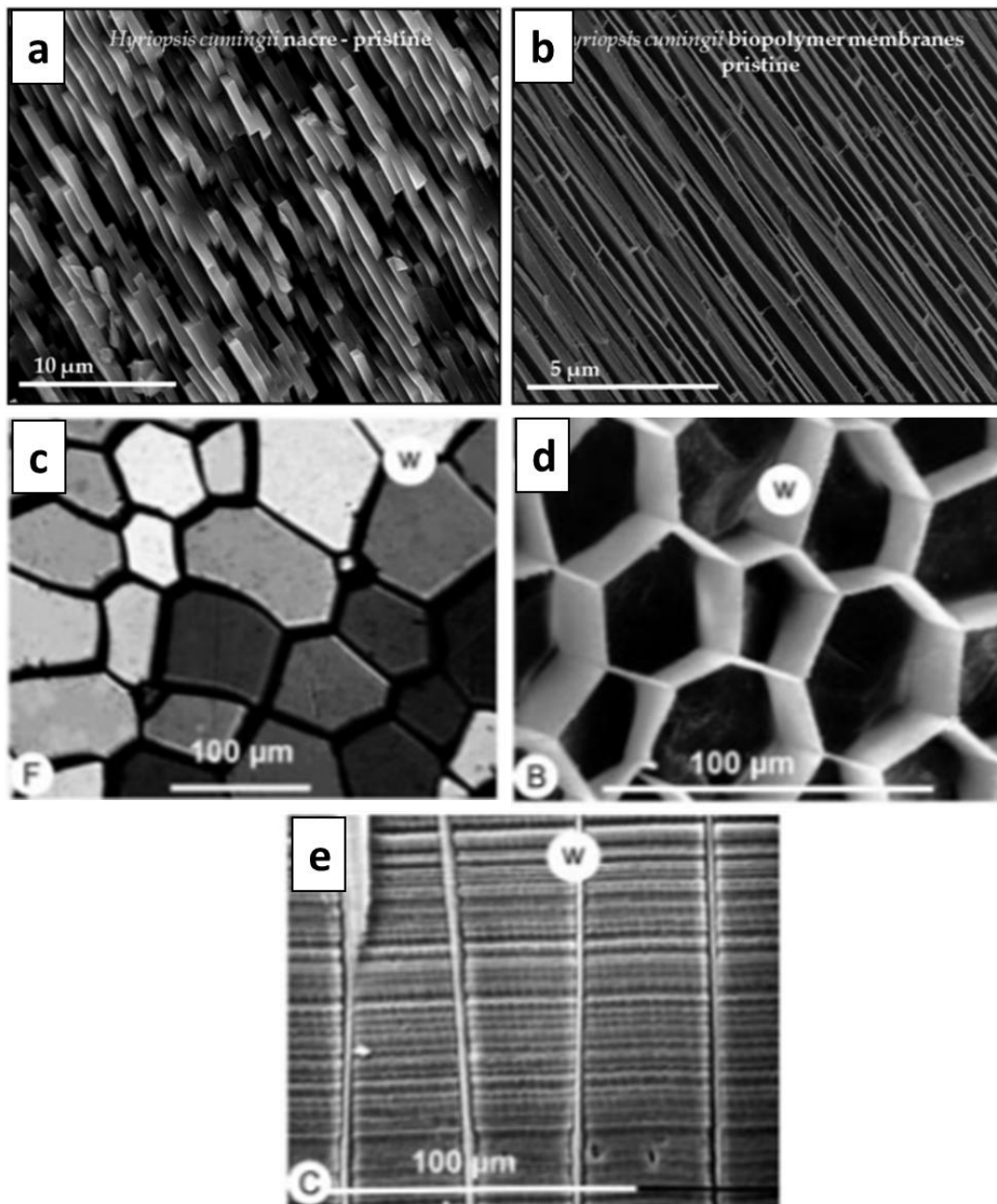


Figure 7 - Electronic micrographs (SEM) and Optical Micrograph (BM) of the organic scaffolding in two biominerals, *Hyriopsis Cumingii* and *Pinna Nobilis*. a) FE-SEM image of pristine nacre tablets in *Hyriopsis Cumingii*. b) FE-SEM image of etched nacre tablets in *Hyriopsis Cumingii*, revealing the organic scaffold. c) *Pinna Nobilis*, section observed under crossed polarizers. The scaffold is marked with a "w" ("walls"). The single crystalline nature of the film is shown by the homogeneous intensity within each prism. d) *Pinna nobilis* etched prisms, transverse cut, revealing the scaffold, marked with "w" ("walls"). e) *Pinna nobilis*, etched prism, vertical section. The scaffold ("w") are visible, along with horizontal growth lines, matching between prisms. a-b) From Greiner et al.<sup>33</sup> c-e) From Dauphin et al.<sup>34</sup>

In addition to the scaffolding that surrounds the inorganic crystals, organic matter is also present in the form of molecules entrapped within the crystalline part of the biominerals (discussed further in part 1.1.3 of this chapter).

The extraction of the shell organic matrix yields between 1 and 5% by mass of the hybrid material (Marin 2004). The matrix is composed of a variety of components: polysaccharides, pigments, lipids and proteins (for more details on the composition, see Marin *et al.*).<sup>35</sup> The diversity of these molecules makes it extremely complex to understand the mechanisms at work in biomineralization. For example, proteins that are involved in biomineralization are composed of specific amino-acid sequences, making them capable of performing several functions. One should note however that domains rich in Asx (Asparagine or Aspartic acid, sensitive to extraction treatment) and Glx (glutamine or glutamic acid, sensitive to extraction treatment) are identified in high amount in the aragonitic and calcitic structures of bivalves.<sup>14,36,37</sup>

### 1.1.2 Cyclic growth process

Striations on the surface of the shells, corresponding to different seasonal growth rates, indicate the cyclical nature of the biomineralization process. Considering a smaller time scale, it has been suggested during the last century that the calcifying organism produces daily growth layers.<sup>38</sup> Today, the existence of mineral growth layers at the micrometer scale is established for some bivalves and echinoderms.<sup>39</sup> As an illustration, the transversely cut and etched prisms in Figure 7.e are composed of mineral layers of micronic thickness. The continuity of a layer is then preserved from one prism to the other. The thin layers between the crystals are sulfated (XANES analysis) and are therefore attributed to an organic deposit.<sup>40</sup> Recently, Duboisset *et al.* proposed that the growth layers of calcitic prisms of *pinctada margaritifera* could be as thin as 500 nm.<sup>41</sup>

### 1.1.3 Non-euhedral, iso-oriented crystals

Single crystalline behavior is a shared characteristic of many biominerals, even when they come in intricate shapes. For example, the calcitic prisms presented in Figure 7.c show a birefringence pattern typical of single crystals (i.e. crystalline iso-oriented domains), with a homogeneous coloration between crossed polarizers. As discussed in the previous section (1.1.2), the cyclic growth process of the shell induces layering in the biomineral. For the prism to be single crystalline, orientation between the growth layers must therefore be preserved.

A striking example of an impeccable morphology and crystallinity control is the sea urchin spine, as depicted by Figure 8.a and .b. The spine has a radial organization, and an intricate pattern of holes in its structure. Despite being very complex, the structure is smooth at the micron scale (Figure 8.b) and behaves like a single crystal (Figure 8.c). This is particularly surprising, since single crystals grown in solution are expected to be faceted. The biomineralization found a way to overcome this issue, and to produce single crystals with complex morphologies.

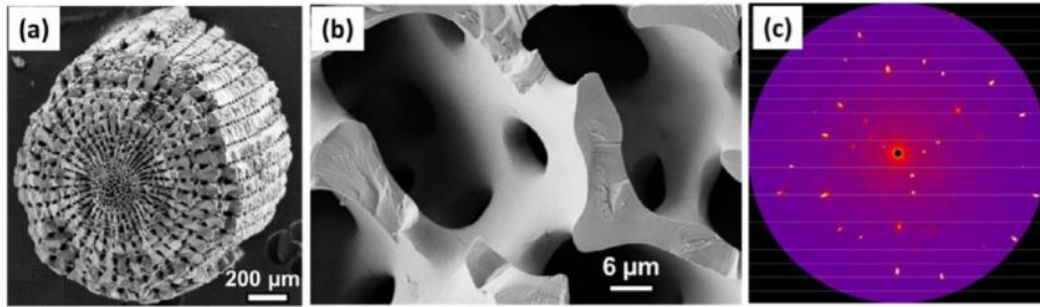


Figure 8 - Single-crystal character of sea urchin spine. a) and b) Electronic micrographs (SEM) of fractured sea urchin spine at two different magnifications. c) X-ray diffraction pattern of the spine. The diffraction pattern is representative of single crystal. From Bergström *et al.*<sup>42</sup>

When a biogenic crystal, behaving like a single crystal, is broken, it does not break by revealing the least energetic crystal planes but a rugged surface<sup>43</sup> (conchoidal fracture), which is unexpected for a single crystal. The exposed surface reveals that the biogenic crystals are constituted of space-filling sub-micronic grains.<sup>39</sup> This particular organization is a reminiscence of the biomineralization process, and is not present when calcium carbonate single crystals are synthesized geologically, or in laboratories. Consequently, the organization and chemical nature at the nanoscale must be further presented.

The presence of sub-micronic grains is a feature shared by most of the calcareous biominerals, and is independent of the polymorphs, crystallinity, or microscopic morphology. Figure 9 presents AFM observations of these granules among several biogenic crystals. In their review dedicated to the prevalence of granular textures in calcareous biomineralization, Wolf *et al.*<sup>6</sup> states that the granule size varies among species but stays in the range of tens to hundreds of nanometers.<sup>6</sup> These objects appear to be the building units of the biogenic crystals. Their prevalence among calcareous biominerals likely reveals the existence of a shared formation mechanism. The space-filling granules are not fused with each other, which would make them undetectable, but rather separated by a narrow region exhibiting a different contrast in AFM (see Figure 9). These darker areas surrounding the grains in phase-lag AFM mappings of Figure 9 are presented as “higher concentrations of organic phases” by Cuif *et al.*,<sup>39</sup> due to their difference in interaction with the AFM tip. Similar arguments are presented by Wolf *et al.*,<sup>44</sup> while Jacob *et al.*<sup>45</sup> observed a higher concentration of carbon in the inter-granular space, agreeing with Cuif’s conclusion on its high organic content. Therefore, from these observations, one could state that the inter-granular space is mostly filled with organic molecules.

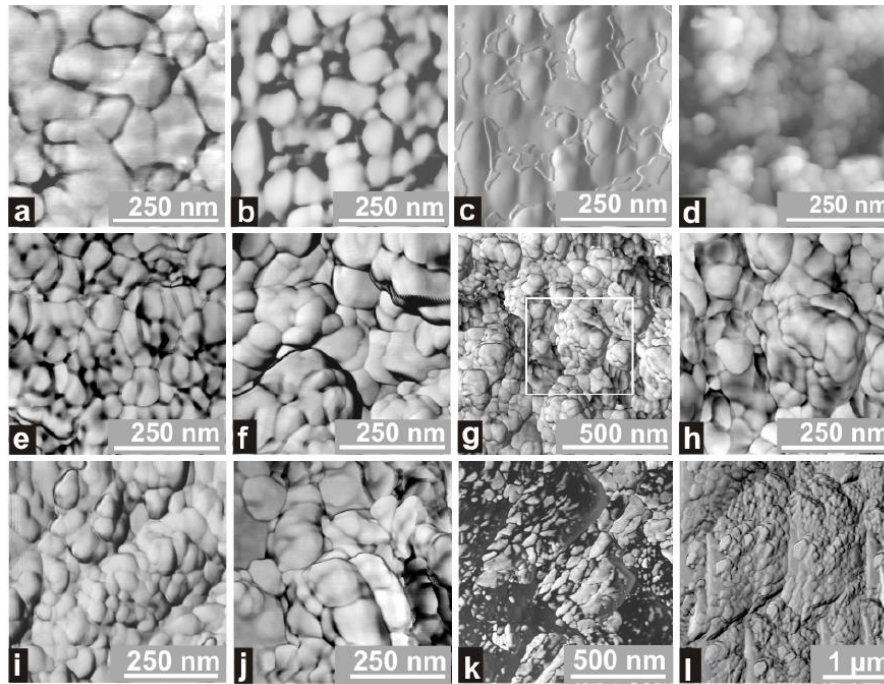


Figure 9 - Uniformity of the pattern in mollusks and coral skeletons as shown by phase-lag AFM mapping (except for (c)) at comparable magnification. (a) Calcite prisms of *Pinctada m.*; (b) Aragonite from the nacreous layer of *Pinctada m.*; (c) same surface viewed in amplitude mode, an AFM tapping mode that emphasizes the changes in surface slopes; (d) nacre of a *Pinctada* pearl. This signal is the direct expression of the surface topography. (e) Aragonite of a *Scleractinia* coral skeleton (*Favia*); (f) Organ-pipe coral (*Tubipora*), a calcitic Alcyonaria; (g,h) The white coral (*Corallium johnsoni*): another calcitic Alcyonaria; (i) The blue coral (*Heliopora coerulea*), the only aragonitic Alcyonaria; (j-l) The red coral (*Corallium rubrum*). From Cuif *et al.*<sup>39</sup>

A mechanism leading to mineral grains surrounded by concentrated organics has been proposed by Seto *et al.*<sup>9</sup> A major difference in their observation is that the inter-granular space is also composed of amorphous calcium carbonate (ACC). The prevalence of this calcium carbonate polymorph will be discussed in the following section.

### 1.1.4 Amorphous calcium carbonate

In the larval stage, of *Merceneria m.* and *Litechinus p.* notably, studies report that the first mineral formed is amorphous calcium carbonate (ACC).<sup>46,47</sup> However, the generality of the observation has been challenged with other species, such as *Crassostreas n.*, for which the larval stage does not seem to involve amorphous calcium carbonate.<sup>48</sup>

In *Mytilus galloprovincialis*, the calcium carbonate formed in the larval stage is assumed to consist of stable ACC.<sup>49</sup> Indeed, ACC can be an integral part of the microstructure established during biomineralization, and remain stable. For example, the spicules of *Pyura pachydermatina* consist of an amorphous calcium carbonate core surrounded by a calcite layer.<sup>50</sup> A physical separation (organic layer) between the crystalline and amorphous phases is then developed during the growth process.<sup>51</sup> A study on the stable ACC of three different species showed that the amorphous phase actually possesses a local order (XAS) and that the

material is hydrated, containing one water molecule per CaCO<sub>3</sub> ion-pair.<sup>52</sup>

In parallel to stable ACC, the existence of transient amorphous calcium carbonate phase has also been proposed in the literature. For example, based on the observation of ACC around the nano-grains in biogenic crystals, Seto *et al.*<sup>9</sup> proposed that crystallization in biominerals goes through an amorphous calcium carbonate phase, and that its crystallization leads to the exclusion of organic molecules. The exclusion of organics would then stop crystallization when the organic concentration becomes too high, leading to an inter-granular space filled with both ACC and organics. A similar model is proposed by Nassif *et al.* where the exclusion of macromolecules during crystallization leads to a thin layer of ACC in aragonite tablets of *Haliotis laevigata*. A most recent study described a similar phenomenon in *Pinctada margaritifera* prisms formation.<sup>41</sup> The transient nature of ACC requires a time-resolved approach to be confirmed.

Transient ACC was indeed detected by monitoring the self repair of a broken spicule,<sup>53</sup> or by looking at the nacre grow front,<sup>54</sup> and inferred from the existence of ACC inclusions in crystalline biogenic aragonite.<sup>55</sup> Different « poly-amorphs » are even described,<sup>8</sup> as having different levels of hydration<sup>55</sup> or organization.<sup>56</sup> Namely, the hypothesis of the dehydration of the ACC prior to crystallization is proposed.<sup>55,57</sup> Demonstrations of ACC as a transient state have been made on some species, but the prevalence of this crystallization pathway must be enlarged.

In summary, calcareous biomineralization results in complex structures of calcium carbonate. If specificities among groups or species exist, global common properties emerge. Thus, the incorporation of organic materials in complex microstructures, the cyclic growth, the nanostructure within iso-oriented domains and finally the presence of amorphous calcium carbonate are properties common to a number of species. These features suggest common underlying mechanisms for the formation of these calcareous biominerals.

Ideally, to understand the biological events happening during biomineralization, one should investigate the mineralization dynamics and answer the following questions: How does the supersaturation evolves? Where does calcium carbonate precipitate? Are there dissolution events? etc. Considerable efforts have been made in this direction, by looking at reconstructing minerals,<sup>55</sup> or aging animals.<sup>58</sup> Nevertheless, these approaches have limitations as they rely on *post-mortem* observations. Even though *post-mortem* analyses have allowed numerous advances in the field, *in vivo* observations would be ideal. Unfortunately, they are very hard to perform, because of spatial constraints (reduced extra-pallial space) or due to the animal stress that disrupts biomineralization during observations. Looking at synthetic bio-inspired models is an effective way to characterize the mineralization dynamics, although not *in vivo*. It can help to gain valuable knowledge on the mineralization pathway, by untangling the complex biological events.

## 1.2 AMORPHOUS CALCIUM CARBONATE IN MODEL SYNTHESSES

Multiple model syntheses have allowed us to reconsider the classical theories of crystal nucleation and to uncover other pathways for crystal formation<sup>10</sup>. Notably, pathways going through amorphous phase formation have been described. These observations resonate with



biogenic calcium carbonates, for which both stable and transient forms of ACC are found (see 1.1.4).

ACC has been transiently stabilized in different model syntheses. It has been detected at high supersaturation values (with respect to calcite) <sup>59–62</sup> or in the presence of additives. <sup>12,15,63,63–66</sup> The conditions of precipitation determine the composition, shape and size of the ACC produced. An overview of the synthetic models producing ACC will be presented in this section, along with the known mechanisms of ACC formation.

### 1.2.1 Intermediate states to crystallization: deviation from classical crystal nucleation

Classical nucleation theories (CNT) rely on the assumption that ion clustering produces the first crystalline aggregates stable against redissolution and that the transient clusters preceding the final crystal already have the symmetry and composition of the bulk crystal. <sup>67</sup> However, non-crystalline transient states have been reported prior to crystallization. For instance, ion clusters, <sup>68</sup> amorphous particles, <sup>60</sup> or reactant-rich liquid droplets <sup>12</sup> that separate from the precursor solution *via* a liquid-liquid phase separation, have been recently identified in calcium carbonate systems. An overview of the so-called “non-classical” crystallization pathways, *via* intermediate states, is presented in Figure 10.

In their description of these alternative routes, De Yoreo *et al.* <sup>10</sup> have in particular described two crystallization pathways that go through an amorphous state (Figure 10). Such routes may need to be considered to explain biogenic crystal formation, as some observations are not accounted for by the classical nucleation theory (smooth intricate designs, conchoidal breakage of single crystal <sup>43</sup> and space-filling nanograins). Model syntheses that produce an amorphous intermediate prior to crystallization must therefore be investigated, as they might actually mimic the mechanisms at play in biocrystallization.

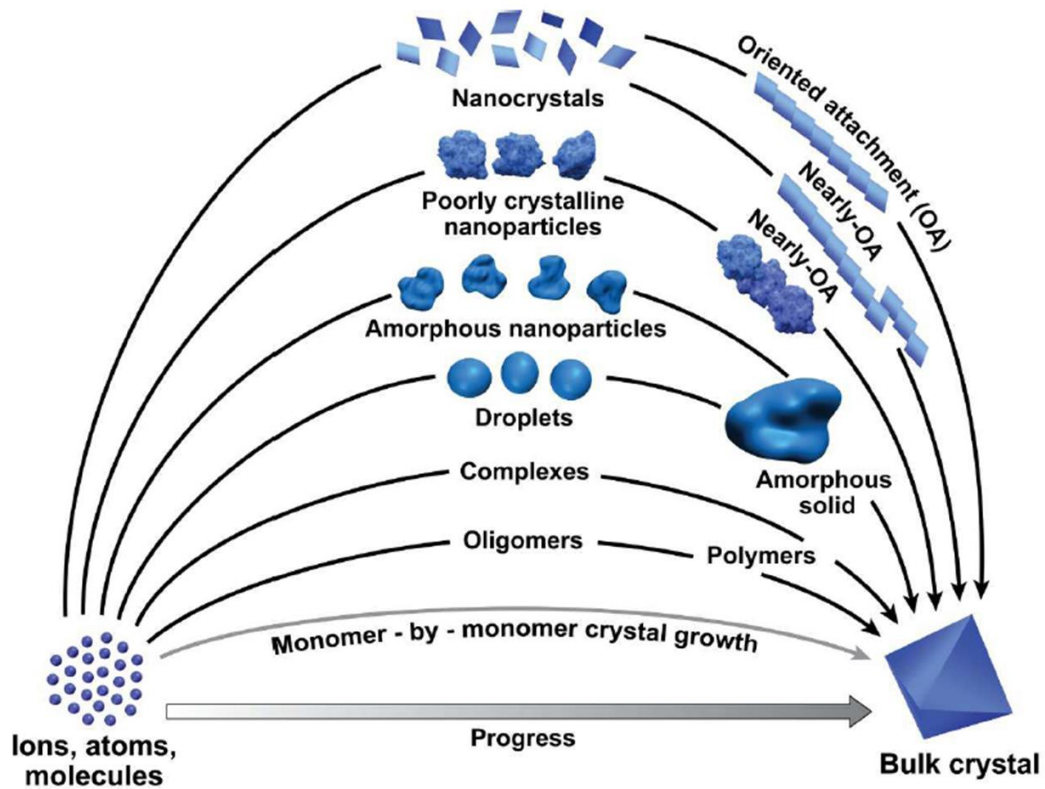


Figure 10 - Crystallization pathways in non-classical nucleation proposed by De Yoreo *et al.*<sup>10</sup> Several transitory states proposed in opposition the ion-by-ion crystal growth. From De Yoreo *et al.*<sup>10</sup>

### 1.2.2 Amorphous calcium carbonate precipitates

A fast and effective method to obtain amorphous calcium carbonate is to use fast mixing.<sup>59–62</sup> In this technique, two reactive solutions are rapidly mixed, leading to the precipitation of submicron-sized ACC particles. Different combinations of solutions can be used: fast addition of a calcium chloride solution into a carbonate solution under stirring,<sup>61,62</sup> direct mixing of ammonium carbonate solution and calcium chloride solution,<sup>59</sup> or sudden addition of a sodium hydroxide solution into a methyl carboxylate and calcium chloride solution.<sup>60</sup> With this latter technique, the composition<sup>62</sup> and size of the particles can be controlled.<sup>60,61</sup> As an example, Albéric *et al.* have used this method to include different amounts of polyaspartic acid or ionic additives in ACC particles by controlling the additive concentration in the carbonate solution before mixing<sup>62</sup>. In addition, modifying the initial supersaturation or synthesis temperature is a way to vary the size of the ACC particles (from 60 nm to 800 nm).<sup>60,61</sup> To be observed, the ACC particles must be extracted so as to avoid its subsequent crystallization. They are therefore separated by filtration, and dried either with ethanol<sup>61,62,69</sup> or acetone.<sup>60</sup>

Titration is an alternative to rapid mixing for producing amorphous calcium carbonate particles. In Gebauer's experiments,<sup>70</sup> the addition of a calcium solution in a carbonate buffer is performed at a injection rate of 10 $\mu$ L/min, i.e., much slower than in the experiments mentioned above. The titration method can produce ACCs of different solubility depending on the solution

pH,<sup>68</sup> which is maintained throughout the titration process, or by adding polymeric additives in the calcium solution.<sup>70</sup>

A third route to produce transient ACC material is to put a calcium solution in contact with a CO<sub>2</sub> gas atmosphere. Thus, atmospheric CO<sub>2</sub> that dissolves in a saturated Ca(OH)<sub>2</sub> solution produces ACC particles, which aggregate at the air-solution interface.<sup>71,72</sup> Alternatively, the decomposition of ammonium carbonate powder into CO<sub>2</sub> and NH<sub>3</sub> gases (ammonia-diffusion method, ADM) close to a calcium solution produces an ACC film at the air-solution interface<sup>73</sup> in the presence of minute amount of polyelectrolyte additive. This last synthesis involves a new intermediate, named PILP, which is a salt-enriched liquid phase, as discussed in more details in section 1.2.5.

### 1.2.3 Polyamorphism of calcium carbonate

The ACC local structure and composition depend on the synthesis conditions. Similarly to the polymorphism characterizing some crystalline compounds, poly-amorphism can be observed among amorphous materials,<sup>8</sup> and in particular with calcium carbonate. More precisely, one should distinguish poly-amorphism and pseudo poly-amorphism.

Poly-amorphism refers to a structural difference: a given chemical compound exhibits different amorphous structures with no difference in composition. When their short-range order is close to the one of the existing crystalline polymorphs, these amorphous structures are said to be 'proto-crystalline'. In the case of calcium carbonate, structural features of aragonite and vaterite have been identified by Tribello *et al.*<sup>74</sup> in calculated amorphous calcium carbonate phases. Using <sup>13</sup>C NMR and FTIR spectroscopies, Gebauer *et al.* have defined three ACC proto-crystalline compounds: proto-vaterite,<sup>75</sup> proto-calcite<sup>75</sup> and proto-aragonite.<sup>76</sup> Experimentally, the selection of a proto-structure is made by controlling the pH and temperature in titration experiments.<sup>75,76</sup> Nevertheless, it must be noted that the proto-order of the transient ACC does not necessarily result in the formation of the crystalline polymorph with the same local order. Indeed, proto-vaterite can lead to pure calcite, and proto-calcite to a mix of calcite and vaterite.

In contrast to polyamorphism, pseudo-polyamorphism refers to a compositional difference. The water content is a major source of pseudo-polyamorphism in ACC. Polymers<sup>64</sup> and inorganic ions, like Mg<sup>2+</sup>,<sup>77</sup> can also be trapped in ACC during synthesis, this way modifying its composition and leading to pseudo-polyamorphism. During synthesis, the amount of polymer in ACC, as well as water content, usually decreases prior to crystallization.<sup>65</sup> Since the variation of composition is gradual, this generates a whole family of amorphous compounds that can show no structural difference. This phenomenon is therefore referred to as pseudo-polyamorphism rather than poly-amorphism, which points to only a few structurally distinct amorphous compounds.

However, at least in the case of water, compositional differences may lead to structural differences. Indeed, in addition to structural water, which shows restricted mobility,<sup>78</sup> particles larger than 30 nm contains a certain amount of mobile water.<sup>79</sup> Goodwin *et al.* have numerically shown that these mobile water molecules evolve in a calcium-poor channel network.<sup>80</sup> Therefore, water might not be homogeneously distributed in large ACC particles, unlike smaller

## 1. STATE OF THE ART

ACC particles which only exhibit structural water with no percolating channel network.

As presented here, polyamorphism and pseudo-polyamorphism are driven by the synthesis conditions (pH, reaction time, etc.). One can wonder how this structural and chemical variation impacts the stability of ACC with respect to crystallization. Stabilization mechanisms resulting from pseudo-polyamorphism (water and molecule inclusions) exist and will be detailed in the next section.

### 1.2.4 ACC stability

The stability of ACC is strongly dependent on both the particle size and the water content. Using molecular dynamics simulations, it has been shown that ACC particles smaller than 4 nm can be more stable than calcite (Figure 11.a), owing to a lower surface energy.<sup>81</sup> However, with increasing particle size, this stability can only be achieved thanks to the incorporation of water molecules which reduce the bulk enthalpy of the particles. Experiments have indeed confirmed the increased amount of mobile water with particle size (Figure 11.b).<sup>79</sup> Thus, during a synthesis, ACC particles will become more and more hydrated up to the point they become unstable with respect to calcite owing to their size. They will then dehydrate<sup>59</sup> (Figure 11.c) and crystallize.

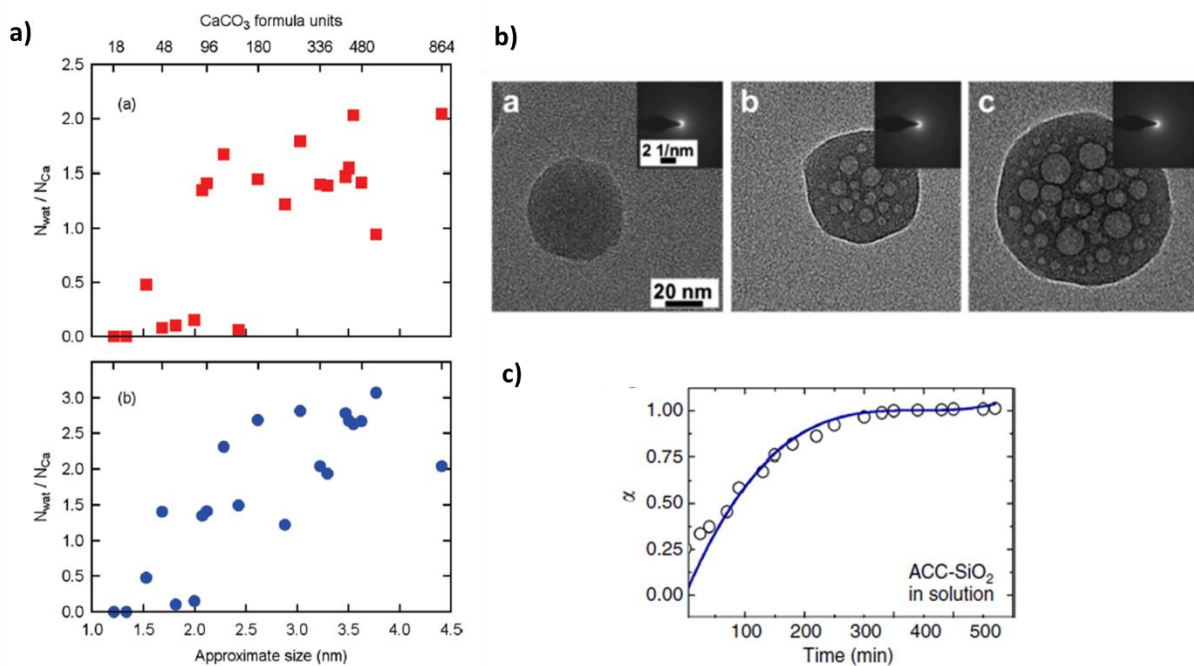


Figure 11 - Hydration evolution in ACC during its formation. a) Thermodynamically favored water-to-calcium ratio as a function of cluster size ( $\text{CaCO}_3$  units). Plot based on theoretical (red) and experimental (blue) entropy corrections. From Raiteri et al.<sup>81</sup> b) Hydration of ACC particle as a function of their growth time. The bigger the particle, the more hydrated, as demonstrated by the beam-induced defects on the particles. From Du et al.<sup>79</sup> c) Dehydration rate  $\alpha$  as a function of ACC-SiO<sub>2</sub> incubation time in pure water. From Ihli et al.<sup>59</sup>

The chemical nature and the amount of added species (water, ions, polymer) in ACC influence the ACC crystallization. For example, magnesium and polyelectrolyte in ACC appear to delay the crystallization process in solution.<sup>63,69,77</sup> Coincidentally, higher crystallization activation

## 1. STATE OF THE ART

energy under heat is observed when ionic species ( $Mg^{2+}$ ) or polyelectrolytes (PAsp) are present within the ACC particles.<sup>62</sup> Similarly, the activation energy of ACC crystallization under heat decreases with increasing hydration level.<sup>59,79</sup> Therefore, both the lack of water<sup>79</sup> and the presence of added molecules inside ACC can act as stabilizers<sup>69</sup> against crystallization, presumably by reducing the ion mobility and therefore ion rearrangements towards crystalline structures.

### 1.2.5 Liquid precursor in ACC syntheses

The idea of a liquid intermediate is developed in different ACC model syntheses.<sup>12,60,73,82–84</sup> The presence of a liquid intermediate for amorphous calcium carbonate was first proposed in a gas diffusion synthesis in which a solution of calcium and polyelectrolyte is exposed to an ammonium carbonate powder (Figure 12). In the setup, the exchange between the gaseous phase, containing ammonia and carbon dioxide, from the sublimation of the powder, and the aqueous phase takes place through a bubble positioned at the top of the solution. A diffusion barrier is placed on the powder (Parafilm, punched three times), enabling a slow introduction of these decomposition products into the solution. A flowing liquid phase (microscopic observations) appears in solution, making it turbid. Some liquid accumulates below the bubble as well. These observations being related to the presence of polyelectrolyte (Polyaspartic acid) the phenomenon is therefore termed "Polymer Induced Liquid Precursor" (PILP).

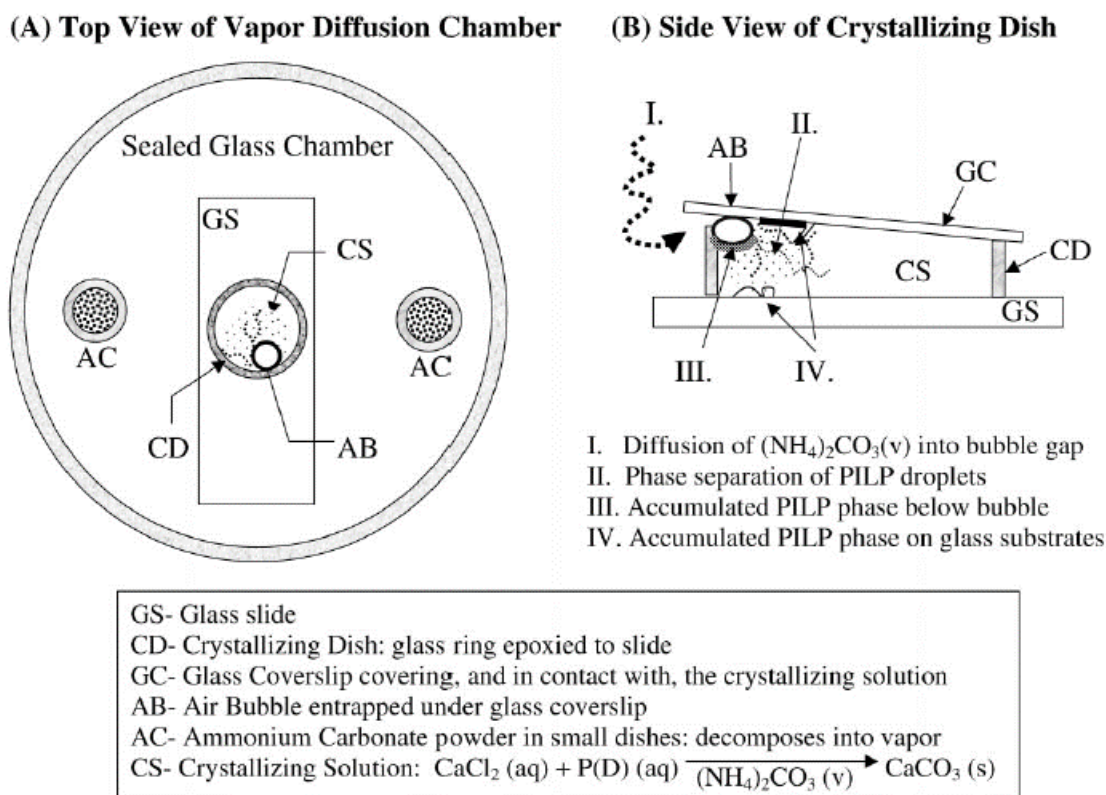


Figure 12 - Schematic representation of the Ammonia Diffusion Method (ADM) as originally presented by Laurie Gower. A dish (CD) filled with calcium carbonate and poly-electrolyte solution (CS). At the surface a bubble is trapped (AB) underneath a glass slide (GS) to create an

## 1. STATE OF THE ART

exchange between the gas phase and the solution. The gas phase is created in a sealed glass chamber by decomposition of ammonium carbonate powder (AC). Diffusion of the decomposition product in the solution (I) leads to a liquid phase separation (II). A dense liquid accumulates at the bottom of the air bubble (III) and falls at the bottom of the dish to form a film (IV). From Gower et al.<sup>12</sup>

At the bottom of the crystallizing dish containing the solution, a film of amorphous calcium carbonate, composed of fused droplets is observed. This film, half a micron thick, finally crystallizes into iso-oriented or spherulitic domains when left in solution. The formation mechanism proposed by Gower and Odom<sup>12</sup> for this film is presented in Figure 13. First, droplets of liquid accumulates at the bottom of the dish and fuse together ("A" in Figure 13). Then, solidification occurs, creating a solid amorphous calcium carbonate film ("B" in Figure 13), where crystallization can take place ("C" in Figure 13). Finally, a calcium carbonate film fully crystallized ("D" in Figure 13) is formed.

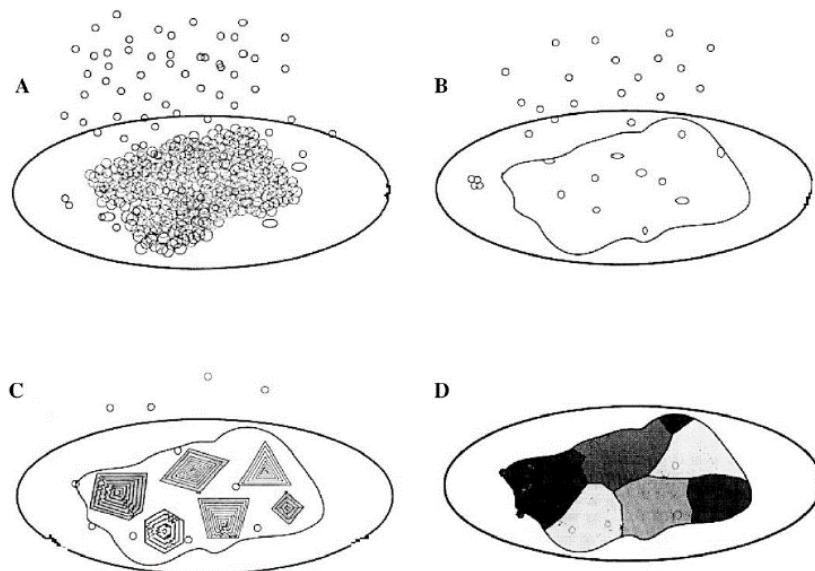


Figure 13 - Film formation at the bottom of the dish. A: fall and coalescence of the dense liquid droplets. B: Film solidification to amorphous calcium carbonate. C: crystallization and growth. D: Crystalline film. From Gower et al.<sup>12</sup>

Following these original observations, liquid precursors have been identified in several systems. First, its detection was based on morphological analysis, such as the presence of spheres<sup>60</sup> in bulk solution (Figure 14.a), hemi-spheres on solid interfaces<sup>73</sup> (Figure 14.b referred to as "liquid-like colloids") or the obtention of fibers resulting from a perfect filling of track etch membranes pores<sup>82</sup> (Figure 14.c). Alongside these *post-mortem* observations, cryo-TEM observations have shown emulsion-like<sup>83</sup> and smooth irregular "droplets" of calcium carbonate (Figure 14.d). Based on these morphological considerations, liquid-liquid phase separations were inferred in fast mixing systems and so-called PILP syntheses.

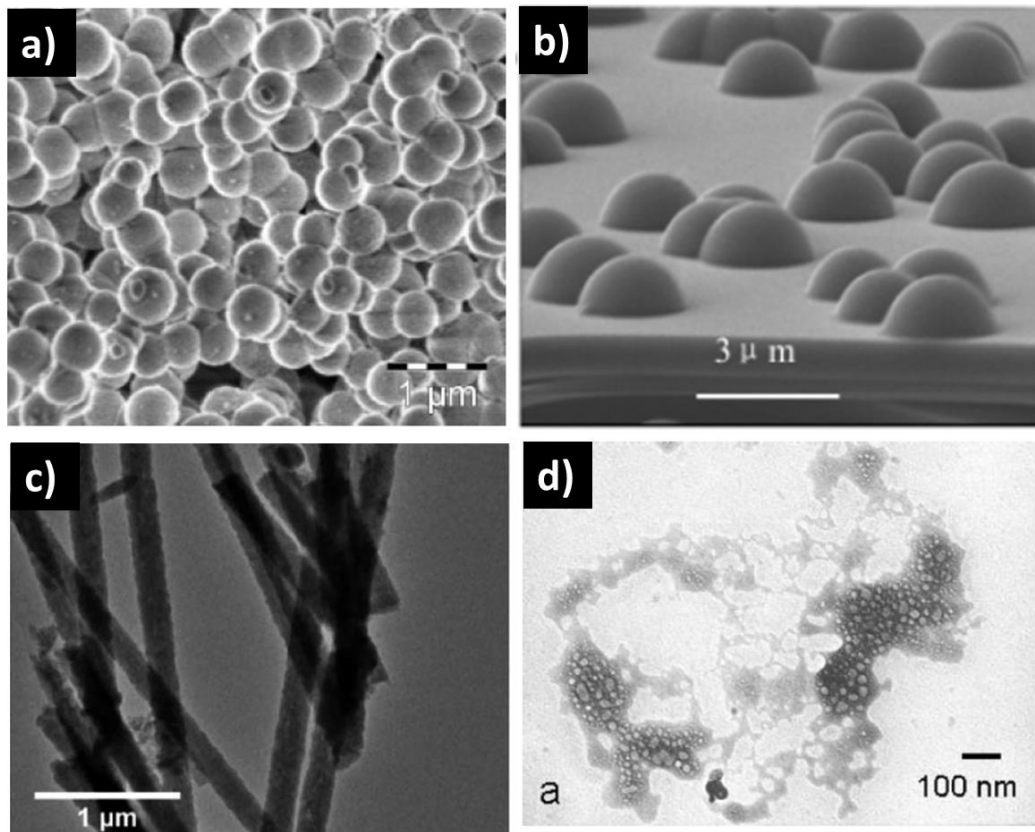


Figure 14 - Evidence of liquid-like behavior in calcium carbonate system. a) ACC spherical particles resulting from a spinodal decomposition after fast mixing (SEM micrograph). From Faatz et al.<sup>60</sup> b) ACC hemispheres deposited on mica before crystallization by gaz diffusion (SEM micrograph). From Xu et al.<sup>73</sup> c) Pilp induced mineralized fibers resulting from mineralization in the vicinity of track-etched membranes. From Schenk et al.<sup>82</sup> Spinodal decomposition pattern 100 ms after fast mixing (cryo-TEM). From Rieger et al.<sup>83</sup>

LLPS is a thermodynamically-driven phenomenon that consists in the demixing of an original solution into two distinct liquid phases, with different solute concentrations. In our systems, such a demixing will result in an "ion-rich" and an "ion-poor" liquid phases. The possibility of an LLPS is determined by the position of the chemical system in the phase diagram (Figure 15.a.) The liquid can phase-separate according to two different mechanisms: either binodal nucleation or spinodal decomposition.

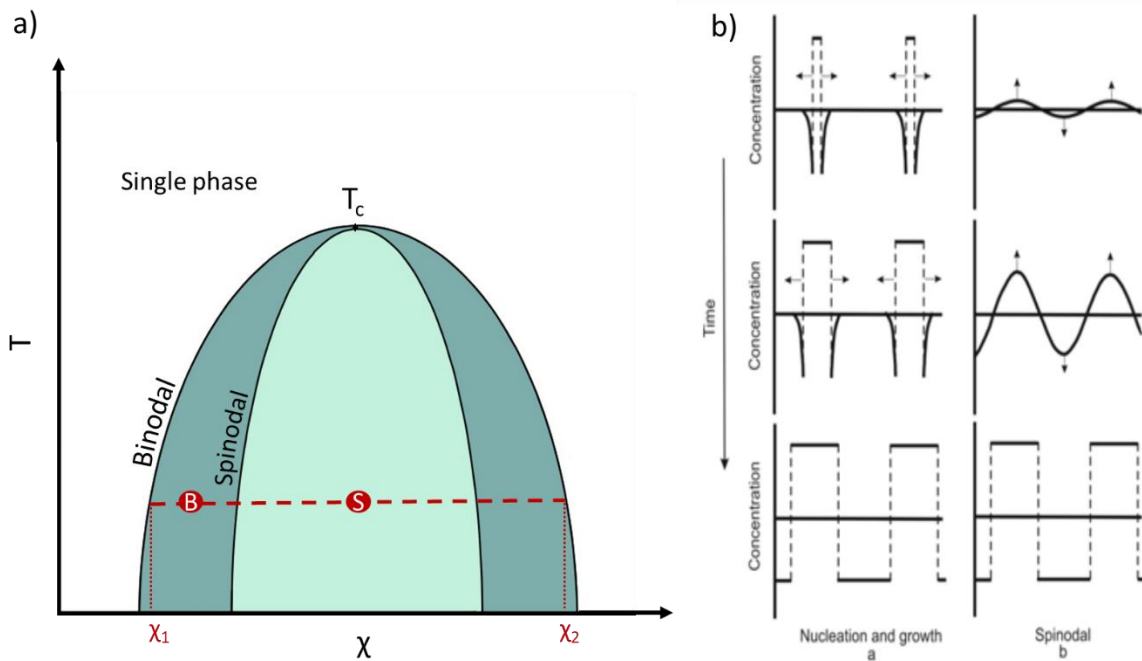


Figure 15 - a) Phase diagram of a liquid system exhibiting a liquid-liquid phase separation. The metastable region, in dark green, is delimited by the binodal and spinodal lines. The unstable region is delimited by the spinodal line.  $T_c$  represents the critical temperature, above which the system remains monophasic. b) Variations of concentration during LLPS. Left part ('Nucleation and growth') shows the concentration variations during phase nucleation in the binodal regime. Right part ('Spinodal') represents the concentration variations during a spinodal decomposition. From Guskov.<sup>85</sup>

When the solute concentration,  $\chi$ , increases, the system crosses the binodal line and becomes metastable with respect to a LLPS. In the metastability domain (exemplified by point B in Figure 15.a), the new phases appear by nucleation and growth process (Figure 15.b). The concentration of the new phases is constant along time (Figure 15.b, "Nucleation and growth"), and equal to  $\chi_1$  and  $\chi_2$  respectively (see Figure 15.a). The number of nucleation events increases as the initial concentration  $\chi$  approaches the spinodal line.

At higher  $\chi$  values, the solution crosses the spinodal line (exemplified by point "S" in Figure 15.a) and becomes unstable with respect to liquid demixing. The concentration fluctuates in all the liquid, this way generating the two new phases. The concentration interface is not sharp (as presented in Figure 15.b, "Spinodal"), and evolves progressively with time until it reaches the ion-poor ( $\chi_1$  in Figure 15.a) and ion-rich ( $\chi_2$  in Figure 15) phase concentration values. Spinodal decomposition is observed when the system crosses the metastability region fast enough to prevent a nucleation-growth process. Therefore a rapid chemical or thermic quench must be made.

We have shown that a LLPS can develop following two different mechanisms, either nucleation and growth, or spinodal decomposition. The type of ongoing LLPS can be inferred from the morphology of the emerging two-phase pattern at short times. Indeed, while binodal nucleation always produces spherical droplets, spinodal decomposition generates a bicontinuous network at short times, which persists at later stages when the two liquid phases are present in the same amount (50:50 binary mixture) (see Figure 16.a). Nevertheless, if the



two phases are in different amounts (off-symmetric mixture), a spherical morphology can later develop during spinodal decomposition (as seen in Figure 16.b). Therefore, the channel-like bicontinuous pattern is the only one that distinguishes spinodal decomposition from binodal nucleation.

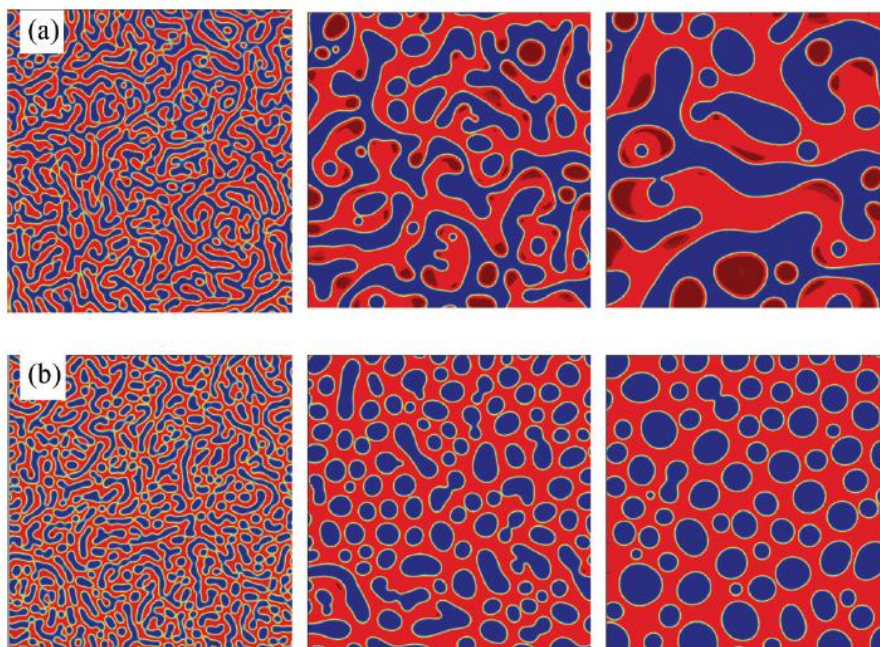


Figure 16 - Morphological evolution of liquid domains resulting from spinodal decomposition. (a) 50:50 binary mixture. (b) 45:55 binary mixture. From Datt *et al.*<sup>86</sup>

Determining the power law that describes the growth of the liquid domain is another way to identify the LLPS scenario. Spinodal decomposition goes through three regimes of domain growth with time<sup>87</sup>: diffusion, viscous and inertial, with a theoretical power law for the domain growth of  $t^{1/3}$ ,  $t$ , and  $t^{2/3}$ , respectively. Each regime has a specific duration, which depends on the region of the phase diagram. Thakre *et al.* demonstrated that depending on the temperature applied during the quench process, the diffusive regime may be observed at a longer time scale, or be too short to be seen.<sup>87</sup> In parallel, binodal nucleation exhibits different power laws for the liquid domain growth, with initially a power law  $t^{1/2}$ , and then  $t^{1/3}$  during coarsening by Ostwald ripening.<sup>88</sup> In principle, the distinction between binodal nucleation and spinodal decomposition can therefore be achieved by determining the power law characterizing the complete dynamics of the liquid domain growth.

However, a direct evidence of the existence of a liquid liquid intermediate in inorganic systems is still scarce to this date. Sebastiani *et al.*<sup>89</sup> proposed that a non-linear behavior in THz absorption (derived from Tera Hertz spectroscopy measurements) prior to  $\text{CaCO}_3$  precipitation events in a titration experiment was due to the co-existence of two liquids. By combining ACC syntheses by titration experiments and  $^{13}\text{C}$  NMR spectroscopy techniques, Bewernitz and coll.<sup>84</sup> revealed the involvement of a liquid precursor in ACC formation, both in the absence and in the presence of a polymer additive. The polymer additive (polyaspartate) was shown to stabilize the liquid phase rather than inducing its formation. Since the liquid precursor exist without the presence of polymer, although short-lived, it will be further referred to as a polymer-stabilized-liquid-precursor (PSLP) instead of PILP as the polymer only stabilizes the liquid precursor long

enough to allow its detection.

This study also evidences the formation of stable pre-nucleation ion clusters prior to the liquid phase appearance. Stable pre-nucleation ion clusters have been first described by Gebauer *et al* in 2008 by titration of calcium into a carbonate solution.<sup>68</sup>

They are described as thermodynamically stable species that are observed in both under- and supersaturated calcium carbonate solutions.<sup>68</sup> In their study, Gebauer *et al.* demonstrated that part of the calcium ions are bound in solution by the carbonate species, prior to any nucleation event. Analytical ultracentrifugation (AUC) measurements revealed the presence of 2 nm structures, present in solution before the precipitation of ACC. Their existence seems to contradict the classical description of crystal nucleation, which considers that pre-nucleation clusters will always redissolve until they reach a critical radius, beyond which point they start to grow, this way initiating the crystal nucleation process.

Theoretical calculations, based on force-field models, have confirmed that stable ion clusters can indeed exist in solution<sup>90,91</sup> and that they can serve as precursors to the formation of a dense liquid phase, and, then, after dehydration, of ACC particles.<sup>92</sup>

In conclusion, both experimental and calculative arguments have been proposed in favor of the existence of stable pre-nucleation ion clusters, that would generate a liquid precursor and ultimately ACC. Still, although the occurrence of a liquid-like precursor in calcium carbonate systems appears now well-established, its molecular nature remains controversial. Xu *and coll.*<sup>93</sup> have indeed proposed that the fluid observed during calcium carbonate synthesis in the presence of polyelectrolyte would be in fact an arrangement of 2 nm diameter ACC nanoparticles, and not a true molecular liquid. Therefore, a better understanding of the structure of the liquid precursor in calcium carbonate crystallization is still needed. Its acknowledged occurrence in synthetic models, however, makes it a serious candidate for explaining the astonishing morphologies observed in calcareous biomineralization.

### 1.3 AMORPHOUS TO CRYSTALLINE TRANSFORMATION

As mention earlier, the tendency of ACC to crystallize strongly depends on its structural properties (its size in particular) and composition, which define its thermodynamic stability. It also depends on the environmental conditions of the crystallization. We will review hereafter the different types of amorphous-to-crystal transformations reported in the literature and detail the conditions that trigger each transformation.

#### 1.3.1 Dissolution-Crystallization

The dissolution-crystallization (D/C) transformation corresponds to the dissolution of the unstable amorphous phase followed by the nucleation of the stable crystalline phase. This kind of transformation occurs systematically when ACC is kept in a liquid environment, and relies on the diffusion of the ion species from the site of dissolution to the site of nucleation and growth of the new crystal.

## 1. STATE OF THE ART

While following the transformation in solution of ACC particles into calcite rhomboedra,<sup>94</sup> Aizenberg *et al.* evidenced the formation of an ACC-depleted area surrounding each crystal, which corresponds to ACC particles that have dissolved to feed the growing crystals (Figure 17 .a). Joint observations of morphology changes and increased concentration of dissolution products (carbon and calcium) in solution have also been made by Rodriguez-Navarro *et al.*<sup>72</sup> (Figure 17 .b), and Zou *et al.*<sup>61</sup> (Figure 17 .c). These results all point to a D/C process for the amorphous-to-crystal transformation in solution.

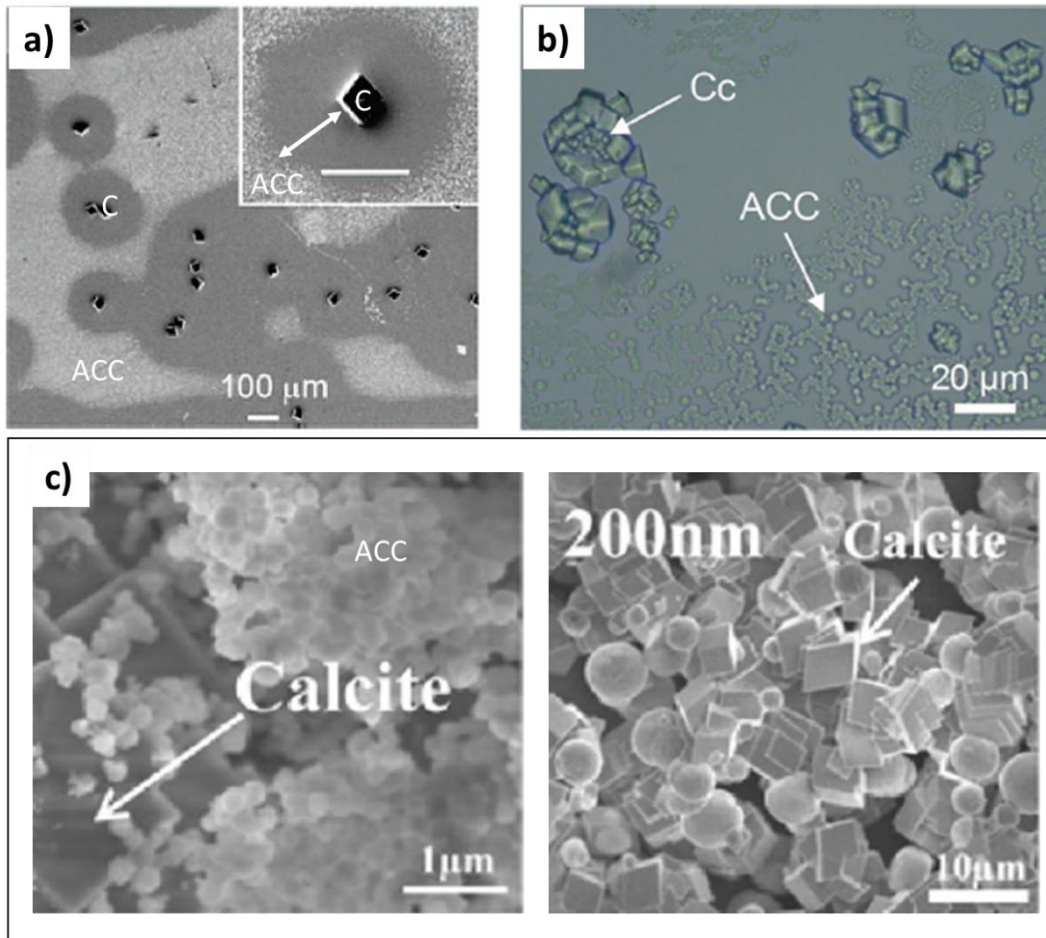


Figure 17 - a) ACC precipitated on gold substrate functionalized with hydroxyl functions. The substrate is left in  $\text{CaCl}_2$  in contact with the gaseous atmosphere resulting from ammonia carbonate decomposition (gas diffusion method). When left in solution amorphous calcium carbonate (marked "ACC") dissolves to the profit of calcite crystals (marked "C"). The depletion zone left by ACC dissolution is highlighted with a double white arrow. From Aizenberg *et al.*<sup>94</sup> b) Interfacial (air-solution) ACC (marked "ACC") and calcite rhomboedras resulting from their dissolution ("Cc"). A saturated  $\text{Ca}(\text{OH})_2$  solution is left 35 min under atmospheric  $\text{CO}_2$  to observe this. From Rodriguez-Navarro *et al.*<sup>72</sup> c) Crystallization of 200 nm ACC particles (produced by fast mixing) that are left in solution. Left : ACC particles coexisting with calcite rhomboedra (~300 s). Right: at 600 s, only calcite (rhomboedra) and vaterite (spheres) crystals are visible. From Zou *et al.*<sup>61</sup>

Atmospheric water can also induce a D/C transformation. Indeed, while studying the stability of ACC exposed to air, Konrad *et al.*<sup>95</sup> determined the critical amount of atmospheric water (0.25 mol per CaCO<sub>3</sub> unit) needed to start the crystallization process of a dry, additive-free ACC. Beyond this amount of water (estimated to four atomic layers), crystallization is induced by a D/C process. Konrad *et al.* nevertheless precise that if the crystallization is triggered by a D/C process, is it not necessarily the only process at play in their system. A similar result was provided by Ihli *et al.*<sup>59</sup> who emphasized that crystallization at ambient temperature is necessarily initiated by a partial D/C process, as the free energy barrier of direct solid/solid transformation is too high to occur in such conditions. Thus, ACC exposed to atmospheric water will begin to crystallize *via* a dissolution-crystallization process.

Since atmospheric water can trigger crystallization, it is interesting to look at the influence of relative humidity (RH) on the crystallization process. Xu *et al.*<sup>96</sup> exposed ACC films to varying RH in the ranges 35% to 90% and, considering the modification of the film nanostructure, suggested that a D/C mechanism was at work in their experiment. Indeed, at all RH values, crystallization resulted in the appearance of pores in the film structure, which was initially a dense arrangement of ACC nanoparticles. The pores became larger at higher RH, with clear fusion between nanoparticles. Such morphological features provide evidence of matter displacement, and therefore of a dissolution process.

Performing *in situ* total X-ray scattering during an amorphous-to-crystal transformation at high relative humidity (85%), Albéric *et al.*<sup>69</sup> could detect both short- and long-range order reorganization during crystallization, consistent with a D/C transformation which involves solute diffusion. By contrast, a solid-solid transformation (see section 1.3.2) would actually only result in short-range rearrangement.

In view of the previous results, the only way to stabilize ACC particles is therefore to take them out of the solution and dry them.<sup>12,69</sup>

When exposed to gas moisture, only a thin layer of liquid is deposited on the particles, so that the growth of 3D crystals, as observed when D/C takes place in solution (see Figure 17.a, .b and .c), is not possible anymore. For example, films removed from the solution before crystallization and exposed to air moisture (Figure 17.a) do not transform into calcite rhombohedra, but keep a flat morphology (Figure 18.a). ACC films exposed to humid air develop 2D spherulitic polycrystalline patterns that depend on the relative humidity (Figure 18 b.c.). The available volume, the ion diffusion coefficient and the supersaturation are actually different when the liquid is an absorbed layer and when it corresponds to the bulk solution, which leads to different morphologies.<sup>97</sup>

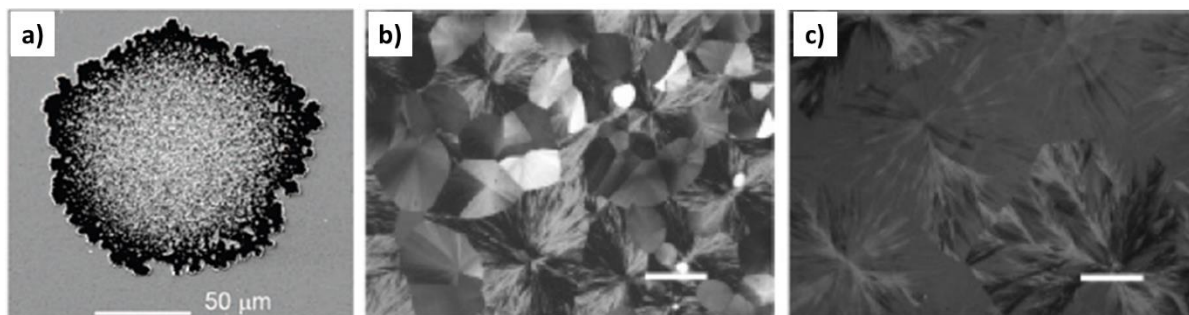


Figure 18 - a) Crystal resulting from the transformation of ACC particles formed on an hydroxylized substrate after exposure to a humid atmosphere (SEM micrograph). ACC particles before transformation are the same as in Figure 17.a (spheres). Illustration from Aizenberg *et al.*<sup>94</sup> b) ACC film (produced by gas diffusion) exposed to 60% RH (birefringence microscopy). c) ACC film (gas diffusion) exposed to 90% RH (birefringence microscopy). b-c : Scale bars = 100 μm. Illustration b-c from Xu *et al.*<sup>96</sup>

### 1.3.2 Solid-state transformation

Solid-state transformation, or solid-solid transition, takes place without the support of an external liquid phase. It is a pseudomorphic transformation as the reorganization of ions leads to the appearance of a new phase without morphological changes. First, the terminology of solid-solid transition will be specified, then its occurrence in calcium carbonate systems as an amorphous-to-crystal transformation will be discussed.

A solid-solid transformation can follow two mechanisms, either “diffusion-less” or “diffusional”.

A diffusionless transformation corresponds to a coordinated movement of atoms. The placement of atoms between parent and daughter phases is related by a mathematical linear transformation. For example, as described by Du *et al.*,<sup>98</sup> diffusionless transformation can be induced by elongation or shear transformation of the crystalline cell. Experimental observations of such a transformation have been made using colloidal particles, so as to make “atomic” displacements visible.<sup>99,100</sup> This type of transformation implies a well-ordered crystalline mother phase, so in the case of ACC it will be left apart.

In contrast, diffusional transformation implies the unrelated displacement of atoms. The diffusion length can be restricted, as in the different movements described by Christian *et al.*<sup>101</sup> where the atoms only run the length of a chemical bond. However, long-range diffusion, associated with the appearance of a liquid intermediate during a solid-solid transition in crystals has also been described in colloidal modeling.<sup>102</sup> Likewise, the presence of a liquid phase during solid-solid transition has been described in metallic glass-to-crystal transformations.<sup>103,104</sup> Such solid-solid transitions thus rely on either short- or long-range diffusive motion and should therefore be classified as diffusional processes. Still, because the range of atomic displacement in a solid-solid transition is reduced, this kind of transition only induces minor morphology modification (although not yet described in the case of a solid-solid transition *via* a liquid intermediate).

Shape-preserving crystallization has been observed in calcium carbonate model syntheses,

## 1. STATE OF THE ART

when ACC is crystallized in solution or by a heat treatment, and referred to as solid-solid, or rather “pseudo-solid-state” transformation as water in ACC may play a role in ion reorganization during crystallization.<sup>64</sup> Thus, it has been shown that an ACC film produced by gas diffusion can preserve its morphology at the microscale when it crystallizes at the air-solution interface.<sup>64,105</sup> In addition, the crystallizing film retains its granular morphology while iso-oriented (Figure 19.a) or polycrystalline (Figure 19.b) domains are formed (Figure 19.c). The conservation of the nanoscale morphology has also been recently observed by De Yoreo *et al.* during the crystallization of ACC particles in solution.<sup>106</sup> Thanks to *in situ* TEM study, De Yoreo and collab. could follow the progressive densification of 100 nm ACC particles without morphology changes. Therefore, in solution, ACC particles can transform into crystalline particles *via* a pseudomorphic transformation, retaining the shape of the amorphous phase at both the micro and nano scales.

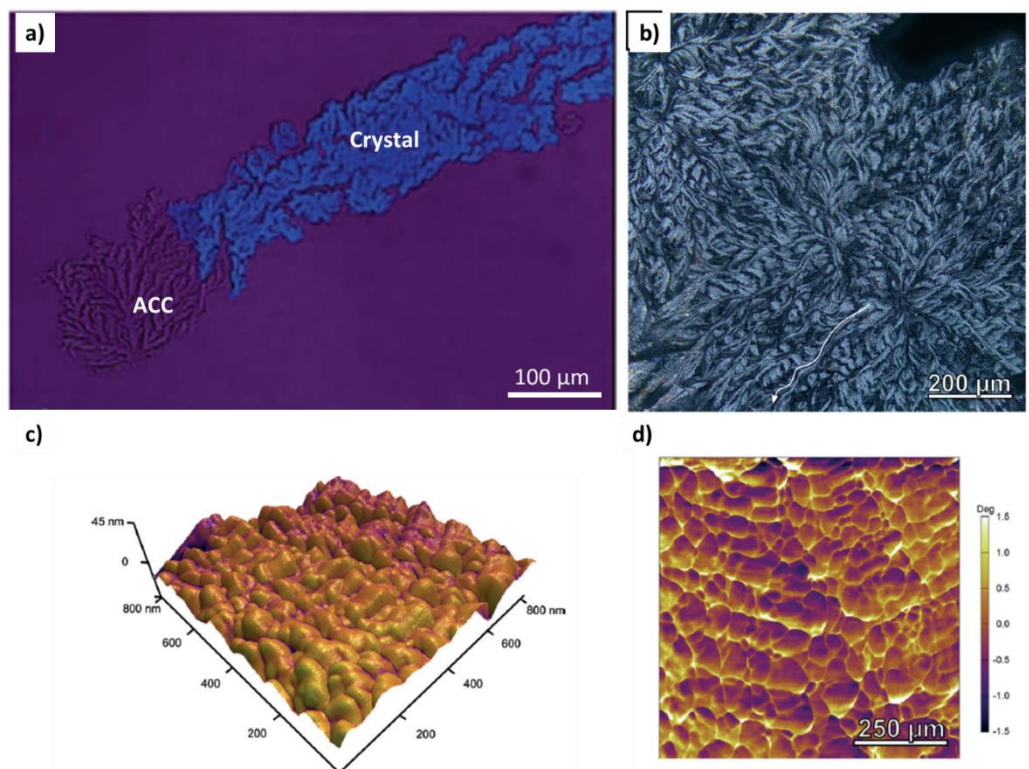


Figure 19 - Pseudomorphic amorphous-to-crystalline transformation at the air-solution interface. a) Partial pseudomorphic transformation at the air-solution interface (Crossed polarizer with lambda-plate micrograph). The purple coloration is representative of an optically isotropic material. The blue coloration is crystalline, and representative of a homogeneously oriented domain. The morphology between the amorphous part of the film (“ACC”) and the crystalline part, (“Crystal”) is kept. From Gower *et al.*<sup>64</sup> b) Crossed polarizer micrograph of interfacial ACC film left to crystallize in solution. The pseudomorphic transformation results into 2D spherulitic calcite crystals. c) Atomic force micrograph of interfacial spherulitic crystal, topological height. d) Atomic force micrograph of interfacial spherulitic crystal, phase image. b-d From Wolf *et al.*<sup>15</sup>

Other environmental conditions allowing shape-preserving amorphous-to-crystalline transition corresponds to thermal activation. Indeed, Xu *et al.*<sup>96</sup> have noticed that the nanogranular structure of an ACC film could be preserved during a heat-induced crystallization at 300°C (Figure 20.a), and Zou *et al.* observed the shape-preserving crystallization of 100 nm

## 1. STATE OF THE ART

particles at 200°C (Figure 20.b).<sup>61</sup> Still, some reorganization is visible in the form of 10 nm to 20 nm pores, which is attributed to internal water loss. Finally, when heating, the water present in ACC is excluded, which triggers a solid-solid transition. As a matter of fact, the energy barrier needed to trigger crystallization by heating is linked to the amount of internal water. When the ACC is previously dried, the energy barrier becomes greater, probably due to reduced molecular mobility,<sup>79</sup> as discussed in section 1.2.4.

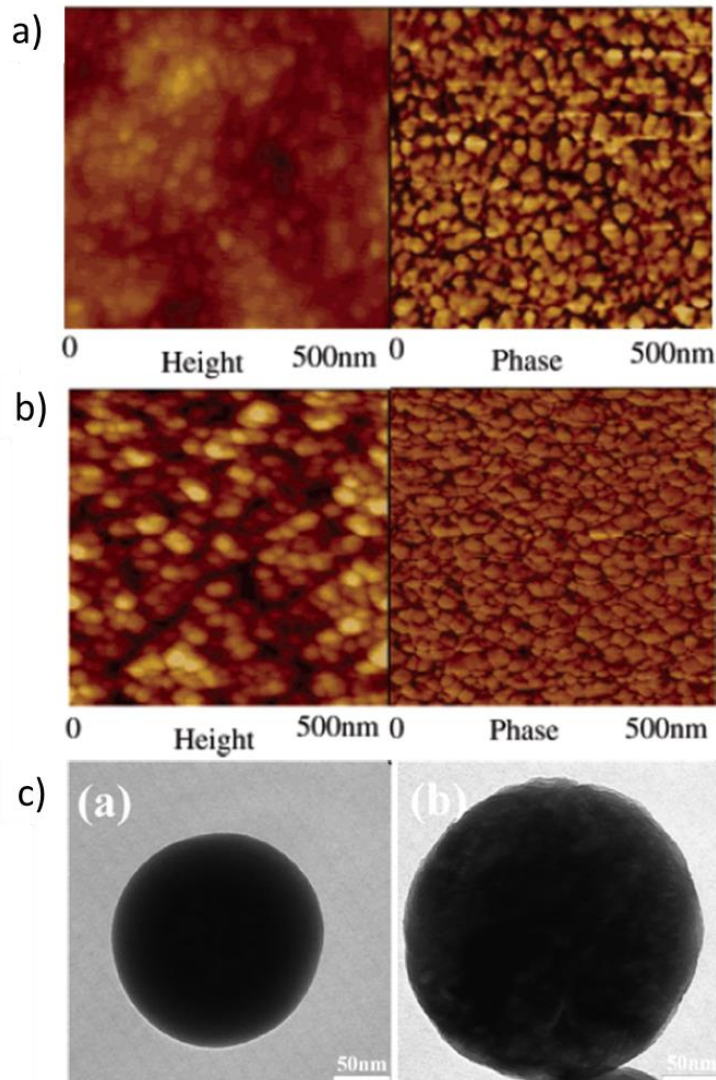


Figure 20 - Pseudomorphic amorphous-to-crystalline transformation under heat. a) AFM-Tapping mode – Nano-metric structure of an ACC film (gas-diffusion) b) AFM-tapping mode, Nano-metric structure of film a) exposed to 300°C, transformed into calcite. Illustrations a) and b) from Xu et al.<sup>96</sup> c) TEM micrograph of a 200nm ACC particle (fast mixing) before (left) and after (right) exposure to 200°C. After exposition to heat, the ACC particle crystallized into calcite, while keeping its round shape. The smoothness on the edge of the ACC particle is disturbed during the crystallization process. After heat, the particle edge becomes rougher. From Zou et al.<sup>61</sup>

In summary, ACC-to-crystalline transformation can rely on different mechanisms. In solution, both dissolution/crystallization and solid-solid (pseudo-morphic) transitions can happen, while heating leads to solid-solid transition. Hybrid mechanism could be, and have been, proposed with a dissolution/crystallization process at the solid surface followed by a solid-solid

transition.<sup>59</sup> Transformation of ACC into crystals is therefore a complex phenomenon, and the pathway leading to crystallization might be influenced by the ACC formed in the first place (pseudo-polymorphism discussed in section 1.2.4).

### 1.4 THESIS

This thesis aims at deepening the understanding of calcareous biomineralization mechanisms by evaluating a hypothetical nucleation pathway formulated on the basis of the knowledge gained from observations of biogenic and synthetic materials. First of all, amorphous intermediates have been observed in the calcareous biominerals nucleation pathway of several genera. Besides, the calcareous biominerals adopt forms unrelated to the idiomorphic forms of the associated polymorph. Their nanostructure consists of a compact arrangement of sub-micronic granules, putting forth some fluidity of the latter during the elaboration of the crystal. Then, the model syntheses enabled to reveal a liquid intermediate in the formation of amorphous calcium carbonate. In parallel, an amorphous to crystal transition allows the conservation of the nanostructure of a calcium carbonate film in liquid medium. All these data allow to formulate the hypothesis that the generic scenario of growth in calcareous biominerals could rely on the formation of a dense liquid intermediate, which would transform into an amorphous solid, and then into the crystal through a pseudo-morphic transformation maintaining the amorphous solid nanogranularity.

In order to test this hypothesis, a model synthesis including a dense liquid intermediate is chosen in order to produce calcium carbonate crystals gathering common properties with the biominerals. A biogenic model is also chosen to assess the agreement between the synthetically produced crystals and the biominerals.

#### 1.4.1 Choice of a synthetic model: PILP synthesis with Ammonia Diffusion Method

To assess the relevance of a liquid intermediate to calcium carbonate biomineralization, a model synthesis going through this route is chosen: PSLP synthesis with the ammonia diffusion method.

This type of ADM results in the formation of a nanostructured ACC films (half-micron thick<sup>12</sup>) *via* a liquid intermediate. Like biominerals, the film includes some organics (polymer, from 30% to 1 wt% in Dai *et al.*<sup>65</sup>) and is therefore a hybrid structure. The concentration and temperature conditions that have been shown to generate a liquid intermediate are in accordance with biomineralization values (see Introduction). Thus, the PSLP synthesis is a good model synthesis to test our hypothesis on the biomineralization pathway. Syntheses have been carried out with sodium polyacrylate, as this polyelectrolyte offers many acidic –COOH functions, similarly to the biomolecules involved in the crystallization of *Pinctada m.*<sup>14</sup>



### 1.4.2 Choice of a biogenic model : the black-lip pearl oyster.

The chosen biological model is the shell of the black lip pearl oyster (*Pinctada margaritifera*), which exhibits two spatially distributed polymorphs, namely aragonitic platelets and calcitic prisms (Figure 21.a) like all shells of the *Pinctada* family. It has been extensively studied and described in the literature,<sup>14,41,107,108</sup> as its structure is rather simple, though displaying features common to many other calcareous biominerals. First, both the aragonitic nacre and the calcitic prisms are composed of space-filling nanoparticles (Figure 21.b). Its growth involves an amorphous calcium carbonate intermediate, as described by Huang *et al.*<sup>107</sup> in aragonitic growth and by Duboisset *et al.* in calcitic growth.<sup>41</sup> The shell grows in a layer-by-layer mode, as shown on the calcitic prism in Figure 21.c. Each layer is about 500 nm thick.<sup>41</sup> At the very border of the shell, the visible early prisms are a few microns wide,<sup>108</sup> and composed of only a few growth layers. In addition, their uniform birefringence indicates that they are cristallographically iso-oriented (Figure 21.d). Finally, the soluble matrix is composed of acidic proteins whose amino-acids are described.<sup>14</sup> Given their numerous properties in common with other calcareous biominerals, the young calcitic prisms of *Pinctada margaritifera* seem to be the perfect biogenic crystals to test the selected model synthesis, and its associated nucleation pathway, by carrying out a structural comparison of synthetic and biogenic crystals.

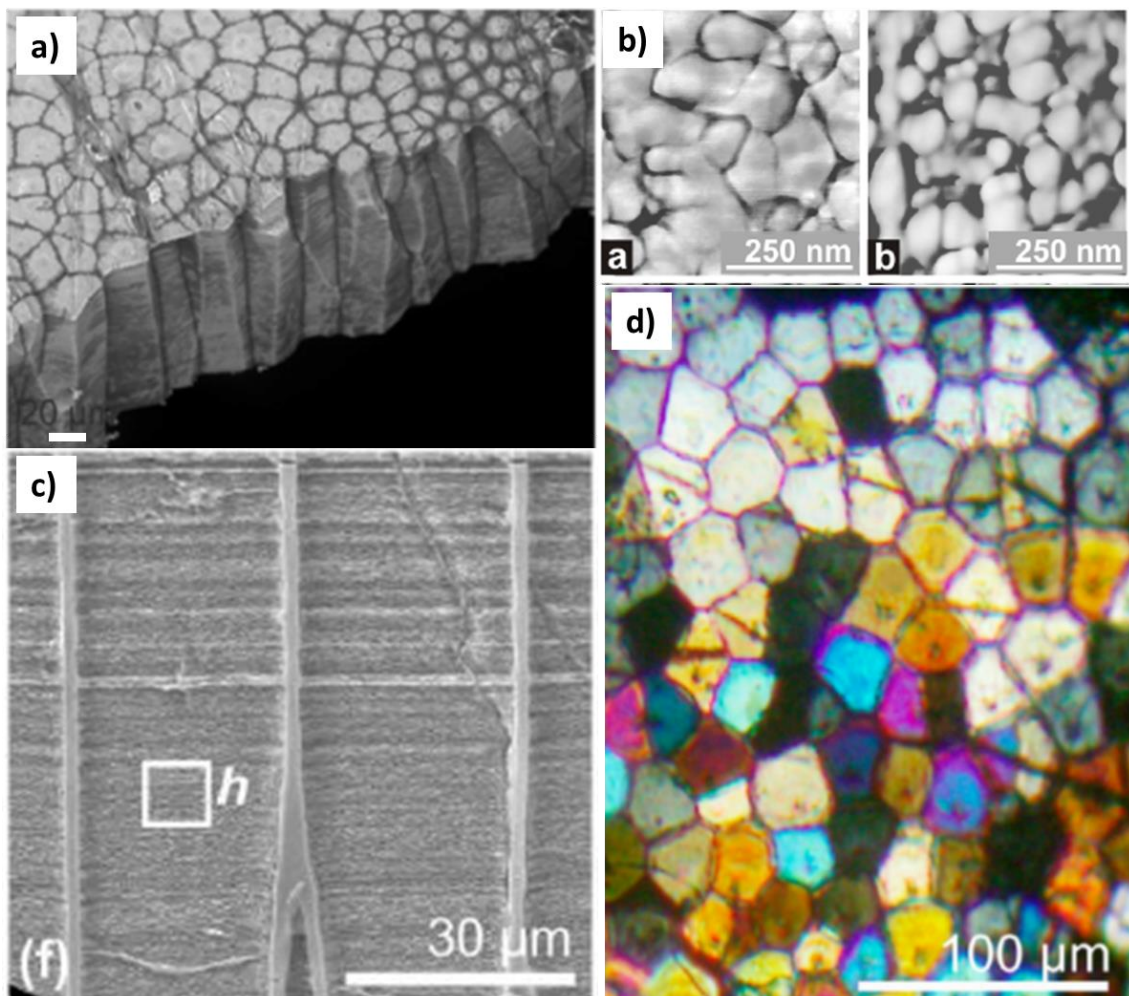


Figure 21 - a) Electronic micrograph (SEM). Calcitic prisms of *Pinctada margaritifera*. The prisms are situated on the external part of the shell. From Dauphin *et al.*<sup>34</sup> b) AFM- micrographs of calcite

from the external part of *Pinctada margaritifera* shell (left) and aragonite from the internal part of the shell. Both polymorphs have the nanogranulated structure shared by many calcareous biominerals. From Cuif et al.<sup>39</sup> c) SEM micrograph. Elongated section of the calcitic prism of *Pinctada margaritifera*. The prisms are separated by an organic scaffold (vertical lines) and shows growth layers shared between prisms (horizontal lines). d) Crossed-polarizers micrograph. Iso-oriented prism of a shell border. The iso-orientation is deduced from the even coloration unity inside a prism. (c-d) From Cuif et al.<sup>108</sup>

### 1.4.3 Methodological approach

The aim of my PhD work was to produce CaCO<sub>3</sub> crystalline films following a nucleation pathway that involves a dense liquid intermediate, and to determine whether such a synthesis can bring structural features close to those of the model biomineral (shell of *Pinctada m.*). First, I have produced an amorphous nanostructured film, using PLSP syntheses, so as to mimic the synthesis of a growth layer in biominerals. A multi-technique characterization of the sample has been carried out to specify the nucleation pathway and make sure it was consistent with the liquid precursor pathway initially selected. Then, I have triggered the crystallization of the ACC film according to different transformation pathways (dissolution/crystallization or solid-solid), either *in situ* or *ex situ*. To characterize the resulting crystals and compare them to *Pinctada m.* prisms, the crystallized samples have been analyzed using state-of-the-art techniques (3D Bragg and Vectorial Ptychography), which revealed their crystalline properties at the nanoscale. The crystalline properties induced by each amorphous-to-crystalline transformation have thus been determined, and their resemblance to the biomineral properties have been assessed.

The data provided by this experimental work will allow me to conclude on the relevance of the 'liquid precursor' assumption to explain the observed biomineral features.

## **2 MATERIALS AND METHOD**

---

### **2.1 SYNTHESSES**

#### 2.1.1 Reproducibility issues

The implementation of the syntheses as presented hereafter is the result of numerous experiments, which allowed me to identify the key environmental factors affecting the reproducibility of the syntheses.

As matter of fact, the reproducibility of the ammonia diffusion method is a well-known concern for experimentalists in the field. This difficulty comes from the multiple equilibria that take place simultaneously: powder sublimation, gas dissolution and precipitation in solution. Extensive studies, made to solve this reproducibility issue, have identified key factors to control this reaction:<sup>11,109</sup> the amount of ammonium carbonate, the extent of the solution free surface, the nature of the gas diffusion barrier and the calcium concentration should strictly remain the same to ensure reproducibility. In addition to those, new parameters have been identified during my PhD thesis, which have been overlooked in the literature until now: the granularity of the ammonium carbonate powder and the relative humidity value of the environment when setting up the synthesis.

The granularity of the powder is of prime importance, as it determines the total area of the powder in contact with the air, and therefore affects the speed of sublimation<sup>110</sup>. As an illustration of this effect, 350 mg of both crushed and uncrushed ammonium carbonate were continuously weighted for 1000 min. The weight loss over time is presented in Figure 22. After 1000 minutes, it was four times superior for the crushed powder than for the uncrushed powder (30 mg of uncrushed carbonate, 126 mg of crushed carbonate after 20 min). This means that a good reproducibility can only be achieved if the granularity of the powder is well controlled and maintained throughout the syntheses.

Powder crushing made manually is a source of irreproducibility, as the resulting grain size distribution is strongly dependent on the experimentalist. Sifting the powder was therefore used in 'pellet' syntheses (see definition below) to reduce this effect.

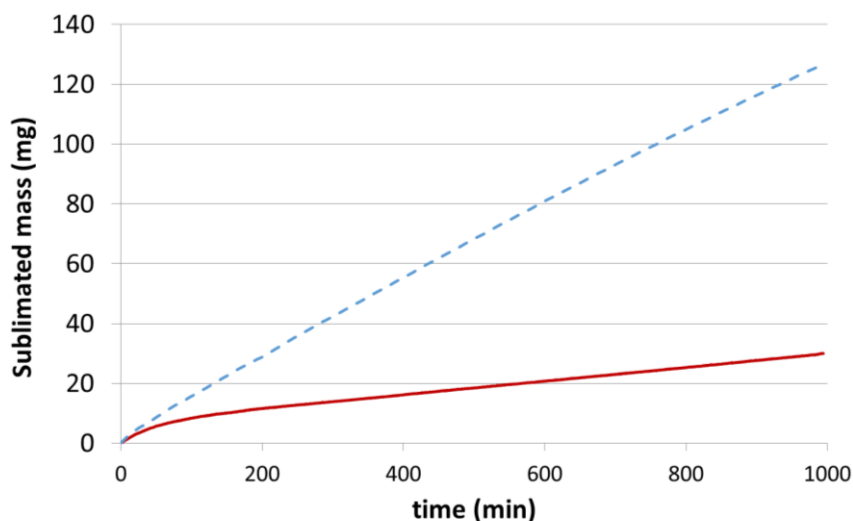


Figure 22 - Weight loss of both uncrushed (red) and crushed ammonium carbonate (blue, dashed) with time.

In addition, the influence of water, which is a product of ammonium carbonate decomposition products, in the atmosphere is often ignored. However, I observed that when setting up a synthesis in a humid environment the reaction kinetics was considerably slowed down. By following the appearance of the film with the naked eye, I could actually estimate that the induction time was 3 times longer when the powder was prepared at 66% relative humidity (RH) than at 45% (3 h instead of 45 min). As a result, to reduce the influence of the relative humidity on the reaction kinetics, grinding, sifting and weighing were all made in a dry environment (~35% RH).

### 2.1.2 'Cap' and 'pellet' syntheses

During this work, two methods were used to perform the syntheses. In the first one, ammonium carbonate is introduced in the reaction chamber as free powder, covered with parafilm to slow down the diffusion of gas vapors. In the second one, ammonium carbonate is dispersed in a KBr pellet, which is introduced as such in the reaction chamber.

#### 'Cap' synthesis:

Ammonium carbonate (Hartshorn salt, >30% NH<sub>3</sub> basis) is crushed in a mortar. Then, 100 mg of the crushed powder is poured in a cap, the surface of which is 0.95 cm<sup>2</sup>, and its free surface is flattened by gentle tapping of the cap. The cap is finally covered with one layer of unpunctured parafilm. Three such caps are placed at 3 cm from the center in a 150 mm diameter Petri dish (VWR) as shown in Figure 23. A 35 mm diameter Petri dish, which contains 3 mL of filtered (0.22 μm Miller PES filter) calcium chloride solution (AVS titrinorm-VWR) mixed with sodium poly-acrylate salt (5.100 kDa, Aldrich) is then positioned at the center of the large Petri dish. Finally, the lid of the reaction chamber (i.e. the 150 mm diam. Petri dish) is put back on, and two layers of parafilm tape are used to close the Petri dish on the side (see Figure 23). The synthesis is performed at 20°C in a temperature-controlled cabinet.

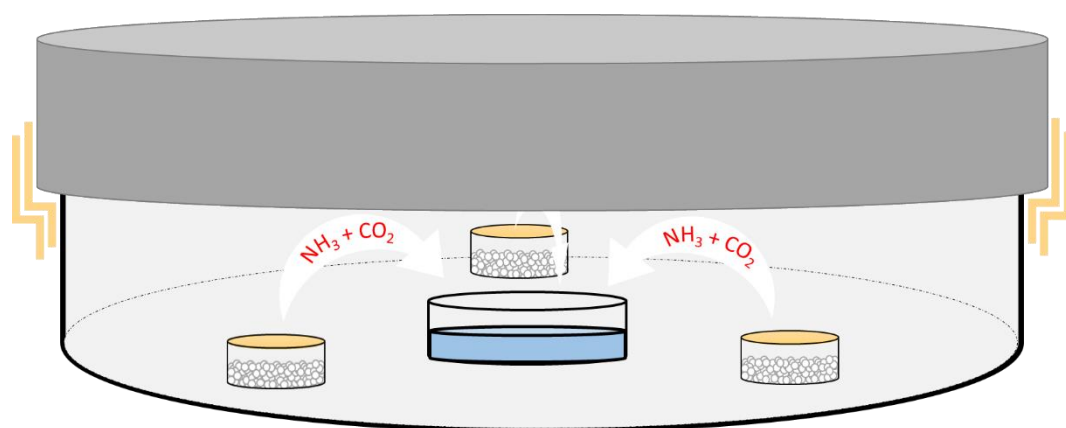


Figure 23 - Schematics of the set-up corresponding to a 'cap' synthesis. A 35 mm diameter Petri dish (reactor) is filled with the reactive solution in blue. Three caps containing the ammonium carbonate powder and covered by a single layer of unpunched parafilm sheet are distributed in the Petri dish. The chamber is a 150 mm Petri dish closed by a double layer of parafilm. The parafilm is schematized in yellow color. The sublimation products dissolving into the solution are schematized with white arrows.

### 'Pellet' synthesis:

Ammonium carbonate (Hartshron salt, >30%  $\text{NH}_3$  basis) is crushed in a mortar and then sifted to only retain the fraction corresponding to sizes in the range from 50 to 150  $\mu\text{m}$ . The powder is mixed with dry potassium bromide to obtain a 10% wt  $(\text{NH}_4)_2\text{CO}_3$ -containing mixture. To do so, 10 mg of  $(\text{NH}_4)_2\text{CO}_3$  and 90 mg of KBr are weighted, mixed and crushed together before being pressed under 10 T for 10 s to create a 1.3  $\text{cm}^2$  pellet. A 35 mm diameter Petri dish, which contains 3 mL of filtered (0.22  $\mu\text{m}$  Miller PES filter) calcium chloride solution (AVS titrinorm-VWR) mixed with sodium poly acrylate salt (5.100 kDa, Aldrich) is then positioned at the center of the large Petri dish. The pellet is added as represented in Figure 24 (at 3 cm from the center of the Petri dish) just before closing the chamber. The lid of the reaction chamber (150 mm diam. Petri dish) is put back on and the air inside the chamber is pressed out to ensure proper closing. The hermeticity is insured by a foam seal fixed to the side of the petri. The synthesis is performed at 20°C in a temperature-controlled cabinet.

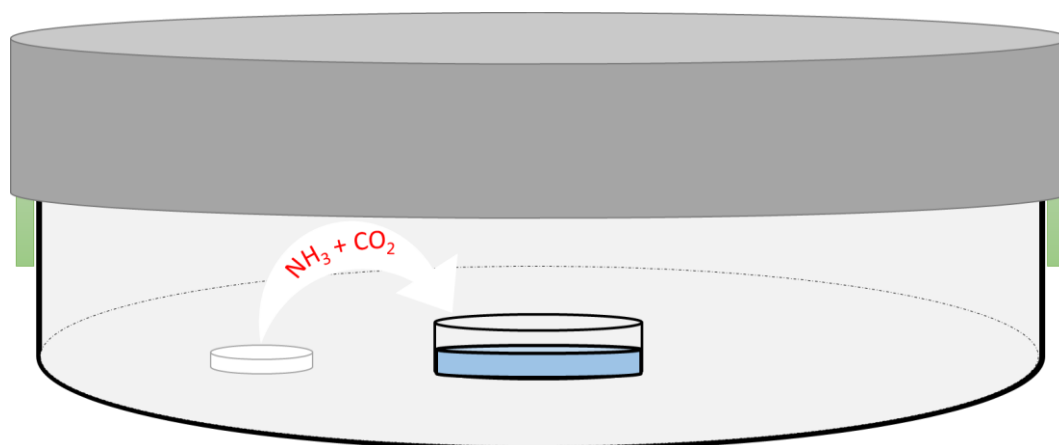


Figure 24 - Schematics of the set-up. A sealed 150 mm Petri dish contains a 35 mm diameter Petri dish filled with the reactive solution in blue. The pellet containing 10%wt of ammonium carbonate is represented in white. The foam seal is represented in green. The sublimation products dissolving into the solution are schematized with the white arrow.

### 2.1.3 Sampling : drying and conservation.

Sampling of the interfacial mineralized structures was made using substrates that have been exposed to an  $O_2$  plasma (0.3 mbar, 5 min) in order to increase their hydrophilicity. Introducing the substrate with an angle in the solution and, then, taking it out slowly allowed to collect one layer of film. The substrate used was either: silicon nitride membrane (0.5x0.5 mm membrane, 200 nm thick), glass substrate, carbon-covered copper TEM grid (30 nm carbon membrane, 200 mesh) or golden TEM grid (uncovered).

The samples were dried after collection by blowing dry gas ( $N_2$  or air) on them, or by exposure to a primary vacuum. In the case of vacuum drying, samples were blotted dried on a Kimtech precision paper then kept 5 min at -0.08 MPa (0.2 bar).

The impact of the drying mode on the film morphology was observed by *in situ* optical microscopy. First, the morphology of a film at low polymer content (20 ppm) of the mineralizing solution was observed (Figure 25). The film is composed of an arrangement of micron-sized discs. Samples produced in the same conditions (three separate syntheses) are collected and dried either under vacuum or under a dry nitrogen flow. The micron-sized disc morphology was observed in all samples, so that both drying techniques (Figure 26.a and .b) appear to preserve the film morphology.

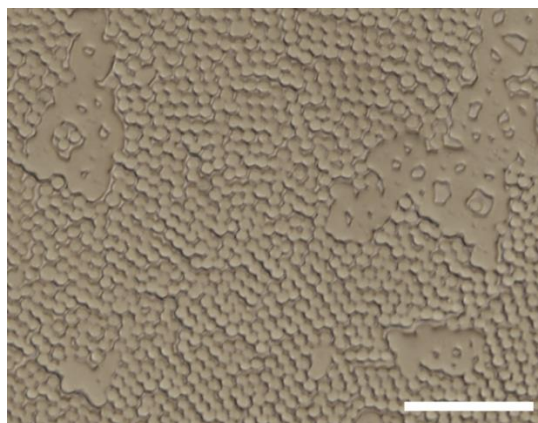


Figure 25 - Optical Micrograph (AM) of a disc patterned interfacial film ( $[Ca^{2+}] = 50 \text{ mM}$ ,  $[PANA] = 20 \text{ ppm}$ ), observed *in situ*. Scal bar =  $50 \mu\text{m}$ .

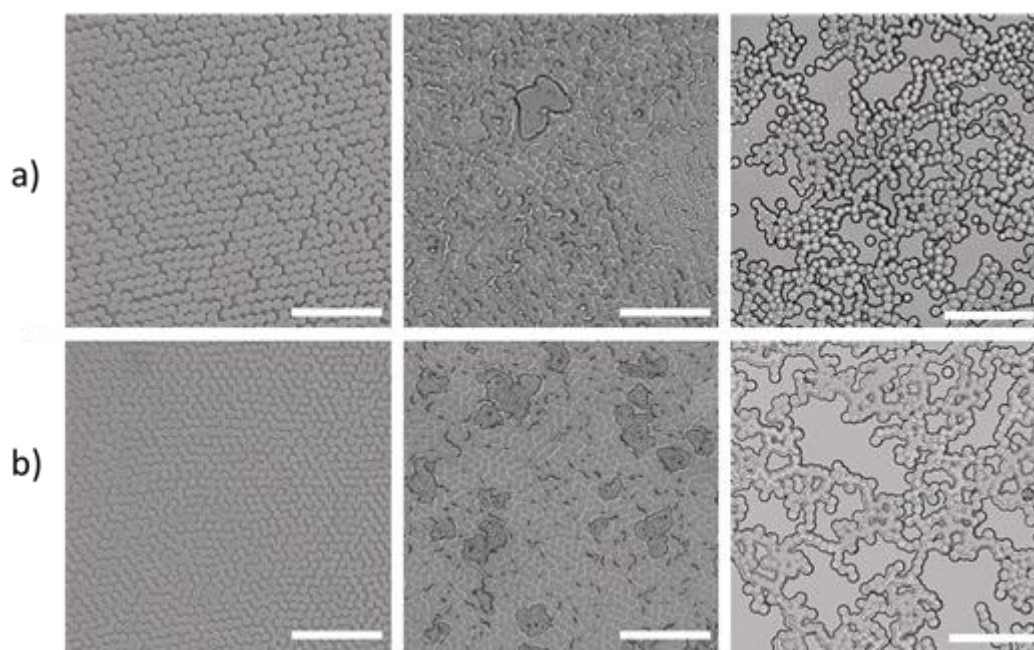


Figure 26 - Optical micrographs (AM) of the morphology of film samples ( $[Ca^{2+}] = 50 \text{ mM}$ ,  $[PANA] = 20 \text{ ppm}$ ). a) The upper line corresponds to samples dried 5 min under vacuum -  $0.08 \text{ MPa}$ . b) the lower line corresponds to samples dried under a dry- $N_2$  flow. Each row represents samples from the same synthesis. Scale=  $50 \mu\text{m}$ . On the synthesis represented by the two images on the right, the density of the micronic disc is reduced, possibly due to heterogeneity of the film at the interface. Scale bar =  $50 \mu\text{m}$ .

However, exposing the sample 5 min at 0.2 bar vacuum allows to dry it more quickly and very homogeneously. In addition, drying under gas flow can induce a partial detachment of the film from the substrate. To achieve a better reproducibility and ensure a homogeneous drying process, drying was therefore performed under vacuum for experiments going beyond large-scale morphology analysis.

In experiments reported in the literature,<sup>96</sup> washing with ethanol is a commonly used method to dry the surface of the ACC film produced by ADM synthesis (see Chapter 1 section 1.3.1).

With the sampling method used in my PhD work, rinsing with ethanol induces severe loss in material, as the film detaches from the substrate. However, the Raman spectra of the ethanol-quenched film, when available, was fully similar to that of a vacuum-dried sample, as shown in the table of figure 5. With both drying methods, a spectrum with a single broad peak at about  $1080\text{ cm}^{-1}$  is obtained, similar to the Raman spectrum (see reference data in this chapter, section 2.6.1.2) of a sample flushed with ethanol shown in Figure 27.

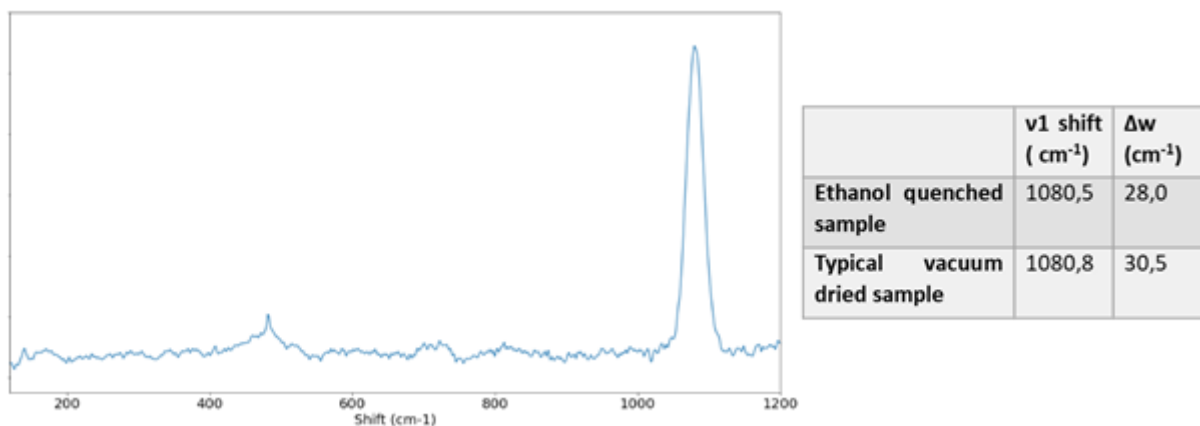


Figure 27 - Raman spectrum of an interfacial ACC film dried with ethanol. The table compares the peak characteristics for the two drying methods (ethanol quench and vacuum drying). Data are extracted by fitting the peak with a Gaussian function.

### 2.1.4 Long-term conservation of the collected film samples

Long-term conservation is ensured by keeping the sample in a low humidity atmosphere, so as to prevent dissolution-crystallisation process due to air humidity (see 1.3.1). A solution of saturated LiBr ( $\geq 99\%$ , Reagent plus) is used to establish a 7% relative humidity<sup>111</sup> in a closed container. The samples are deposited on a 3D-printed support above the LiBr solution, as depicted in Figure 28.a. The kinetics of establishment of the atmosphere has been monitored by a HIH4000-001 Honeywell sensor, and is presented in Figure 28.b. The sensor was fixed to the inside of the chamber lid, and controlled by an Arduino MKR ZERO. After only 10 min, the relative humidity in the chamber reaches 10%, and then slowly goes down to the expected value (Figure 28).



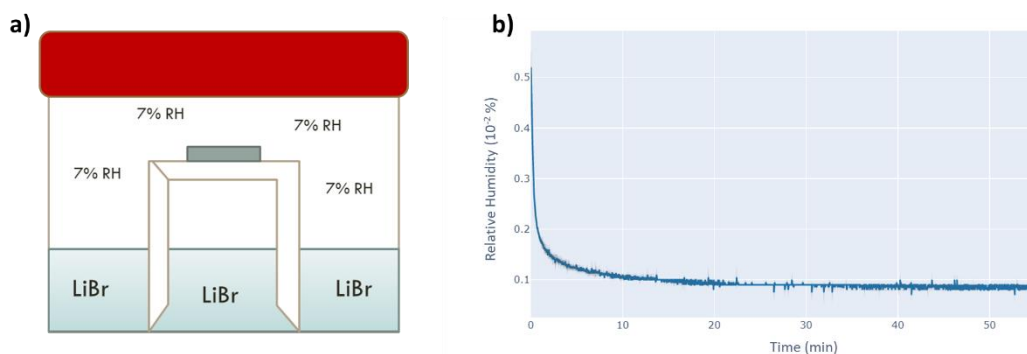


Figure 28 - a) Set-up for long-term conservation of samples. The sample (in grey) is placed on a 3D printed support (in white), above a saturated solution of lithium bromide. b) Relative humidity inside the chamber as a function of time.

## 2.2 CRYSTALLIZATION CONDITION

Three conditions of crystallization are discussed in this work: interfacial crystallization, thermally-induced crystallization and humidity-induced crystallization. Each mode of crystallization corresponds to a specific protocol, which will be presented in this section.

### 2.2.1 Interfacial crystallization.

The film remains at the air/solution interface for several days before collection. Sampling is made using the protocol described in part 2.1.3 of this chapter: the crystalline film is collected at the interface using a hydrophilized substrate and dried for 5 min under  $-0.08$  MPa.

### 2.2.2 Thermally induced crystallization,

Right after collection, as described in part 2.1.3, the optical isotropy of the film sample is verified under crossed polarizers (BM, see 2.3.2.2 of this chapter). The sample is then immediately exposed to a high temperature at  $300^{\circ}\text{C}$ , on a heating plate, to trigger its crystallization. During heating, the temperature compensation of the plate induces  $\pm 6$   $10^{\circ}\text{C}$  oscillations. The standard crystallization protocol is 3 h at  $300^{\circ}\text{C}$  on a heating plate.

### 2.2.3 Humidity induced crystallization

Right after collection, as described in part 2.1.3, the optical isotropy of the film is checked under crossed polarizers (BM, see 2.3.2.2 of this chapter). Crystallization is then initiated by placing the sample in a well-controlled atmosphere. More precisely, the set-up described in section 2.1.4 is used here again, but in combination with other hygroscopic salts in order to vary the relative humidity value. The different chemicals used to control the atmosphere humidity are

## MATERIALS AND METHOD

presented in Table 2. In these conditions, full crystallization of the samples is observed after several days.

Table 2 - Chemicals used to control the atmosphere humidity, and achieved relative humidity.

Salt	Expected RH (20°C)	Product reference
MgCl <sub>2</sub>	33%	≥ 99% Bio Xtra, Sigma-aldrich
NaCl	75.5%	≥ 99.5% Sigma-aldrich
K <sub>2</sub> SO <sub>4</sub>	97,5%	≥ 99% Bio Xtra, Sigma-aldrich

The kinetics of establishment of the relative humidity condition after closing the chamber was monitored (Figure 29) using a humidity sensor (HIH-4000, +/- 3,5% RH) has been hermetically fixed on top of the chamber. The sensor was controlled by an Arduino MEGA 250 connected to a computer for data collection. These measurements have shown that the expected value of relative humidity (Table 3) is reached within 10 min, whatever the targeted relative humidity value.

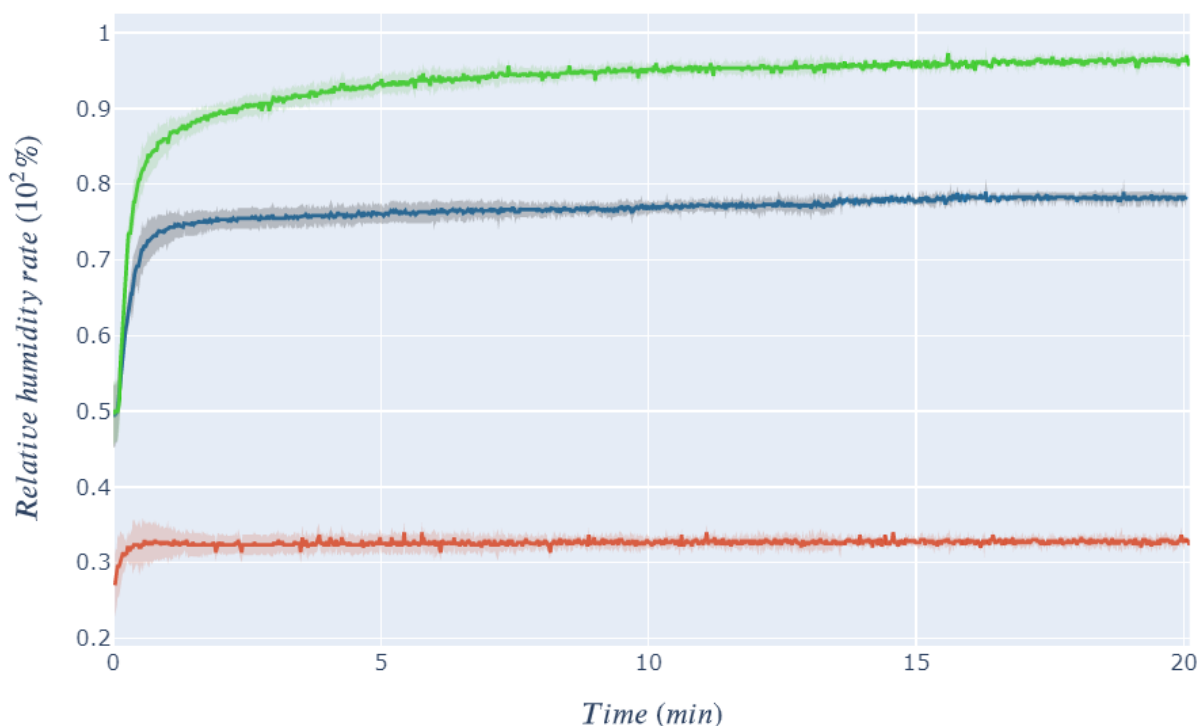


Figure 29 - Kinetics of establishment of the atmosphere. Relative humidity value (% RH) as a function of time, under the influence of K<sub>2</sub>SO<sub>4</sub> (green), NaCl (blue) and MgCl<sub>2</sub> (orange) salt. For each measurement, the experiment was triplicated, and the standard deviation calculated. The standard deviation is plotted then as a mute colored area around each curve.

### 2.3 OPTICAL MICROSCOPY

Absorption microscopy (AM) was used to determine the morphology of our samples. When combined with image processing, it allowed us to evaluate the size of the interfacial objects. Nevertheless, in case of very thin objects (a few tens of nanometers thick), absorption microscopy was insufficient, while phase contrast microscopy enabled the detection of the objects of interest.

In parallel, to evaluate the amorphous nature (2.1.4) and the organization of the crystalline domains, birefringence microscopy was used. Finally, to make birefringence images while observing the morphology of optically isotropic segments, waveplate birefringence microscopy was employed.

#### 2.3.1 Phase contrast microscopy (PCM)

##### 2.3.1.1 *Principle*

Phase contrast microscopy (PCM) is used to image fully transparent specimens (like biological cells) for which light absorption is too weak to allow absorption contrast imaging. On the contrary, such objects can be detected by phase contrast microscopy, as this one makes it possible to detect slight phase shift due to small refractive index variation (like at the cell membrane). The phase shift is translated into an amplitude variation in the observation plane. This conversion is possible by the combined action of a condenser annulus and a phase plate (Figure 30). The annulus selects the direct beam (unmodified by the sample) and focalizes it onto the focal image plane. The beam diffracted by the sample goes through the thicker zone of the phase plate, inducing an important phase shift. The phase shift induces either constructive interferences (negative phase microscopy) or destructive interferences (positive phase microscopy). The interferences modify the amplitude of the wavefield at the image focal plane, which is then directly measurable by the intensity sensitive detector.

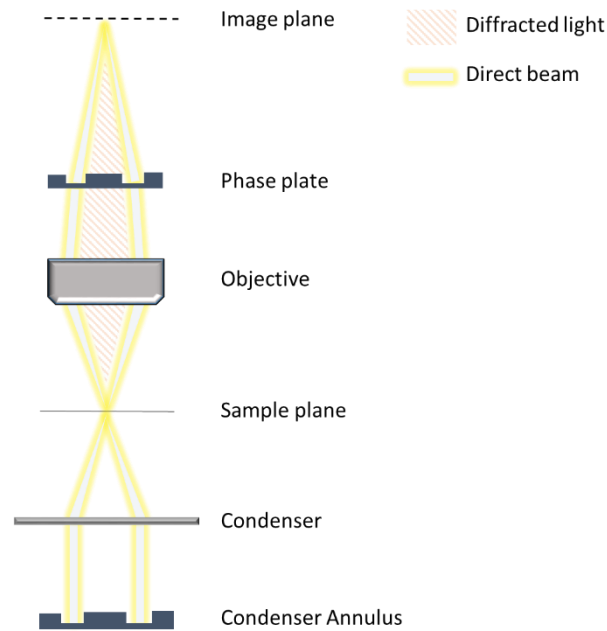


Figure 30 - PCM microscope configuration

The phase shift induced by crossing of a sample of refractive index  $n$  is:

$$\delta = \frac{2\pi (n_0 - n) e}{\lambda}$$

where  $n$  is the refractive index of the object,  $n_0$  the refractive index of the surrounding medium,  $e$  the sample height, and  $\lambda$  the wavelength of the incident beam.

## 2.3.2 Birefringence microscopy (BM) and Wave plate assisted birefringence microscopy (WBM)

### 2.3.2.1 Principle

Birefringent materials are materials that exhibit a refractive index dependent on both the polarization and the direction of the illumination. This is the case of crystals, and in particular of calcium carbonate polymorphs, which are all optically anisotropic.

Any direction along which light propagates in the same way as in an isotropic material (no birefringence effect) is called optical axis of the crystal. Birefringent crystals can have one (uniaxial) or more optical axes. In the case of a uniaxial crystal like  $\text{CaCO}_3$  polymorphs, one should define two refractive indices: the ordinary index  $n_o$  that determines the speed of light that travels along the optical axis (and is therefore polarized perpendicularly to this axis), and the extraordinary index  $n_e$ , which specifies the speed of light that is polarized along the direction of the optical axis. In the case of a positive uniaxial crystal :  $n_e > n_o$ , whereas in the case of a negative uniaxial crystal, one gets  $n_o > n_e$ .

The birefringence of a material can be detected by observation between crossed polarizers. The inlet polarizer is used to deliver a linearly polarized light onto the sample. After crossing the sample, the change in light polarization is analyzed thanks to the outlet polarizer, called

'analyzer', which is oriented at 90° from the polarizer. If the material is isotropic, the polarization of light remains the same, and no light passes through the analyzer. In the case of a birefringent material, if its neutral axes are not parallel or perpendicular to the polarizer axis, the linear incident wave experiences a double refraction, both along the neutral axes of the material, one being perpendicular to the other. Each refracted wave propagates at a different velocity through the sample, which results in an elliptically-polarized light past the sample. In this case, some of the light is transmitted through the polarizer, and the birefringent material appears as bright, gray or colored, areas on the camera.

The Michel-Lévy Diagram<sup>112</sup> (Figure 31) provides the interference colors arising from the superposition of the two propagating waves exiting the sample at the analyzer, assuming that the sample axes are oriented at 45 deg of the polarizer. The diagram presented in Figure 31 highlights the relationship between the sample's thickness, the birefringence and the path difference in nm. We can see that for thin samples, the birefringence effect translates into shades of gray under crossed polarizers. A technique to be visually sensitive to the birefringence effect is to add a retardance wave-plate, which allows to reach the first order color-range (530 nm). In this range, minor shift in the retardance will create a major coloration shift.

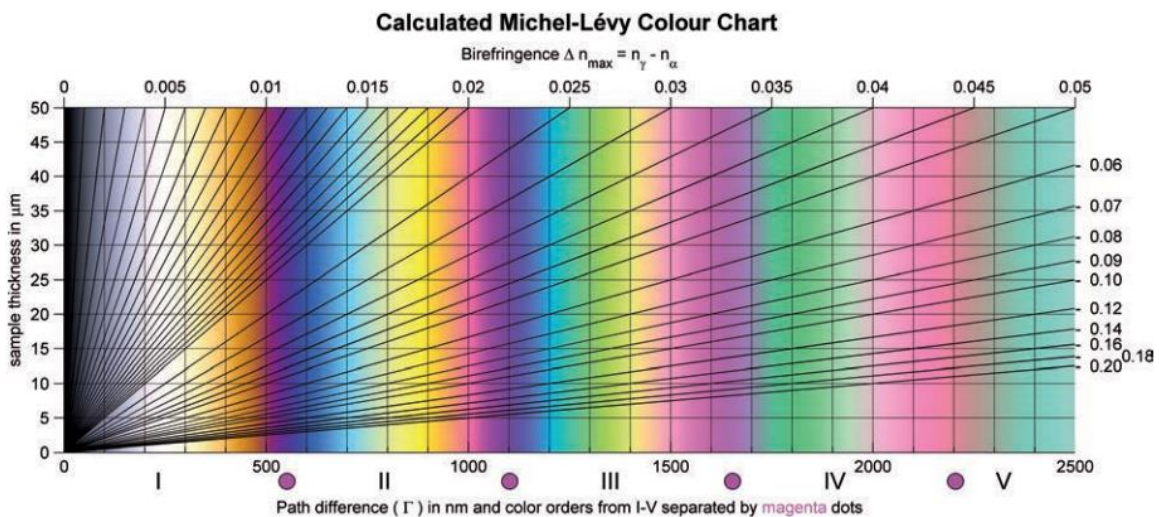


Figure 31 - Michel Levy diagram. The diagram provides the interference color resulting from the crossed-polarized illumination of a sample, depending on the sample birefringence and thickness. From Sørensen et al.<sup>112</sup>

In the case of a sample of homogeneous thickness, the addition of a lambda wave-plate to a birefringence microscope allows highlighting changes of the optical axis orientation, i.e., of crystalline domain orientation.

### 2.3.2.2 Calcium carbonate crystals as birefringent materials

The birefringence properties of the anhydrous polymorphs of calcium carbonate<sup>113</sup> are summarized in the following table, along with the refractive index of amorphous calcium carbonate<sup>114</sup> (ACC):

	Birefringence	Values
<i>Calcite</i>	Uniaxial negative	$n_o = 1.658$ ; $n_e = 1.486$
<i>Vaterite</i>	Uniaxial positive	$n_o = 1.550$ ; $n_e = 1.645$
<i>Aragonite</i>	Biaxial negative	$n_\alpha = 1.531$ $n_\beta = 1.680$ $n_\gamma = 1.686$
ACC	None	$n = 1.51-1.58$

Every crystalline form presented here is a birefringent material. Under crossed polarizers they will therefore be visible (if the optical axis isn't perpendicular to the sample plane). ACC, on the other hand, is optically isotropic, being therefore invisible in this kind of setup. Birefringence is therefore a tool to determine the amorphous nature of calcium carbonate.<sup>12,96,115,116</sup>

### 2.3.3 Experimental set-up

Observations are performed either on an Olympus BX61WI equipped with a DP74 camera or an Olympus BX41 equipped with a DP70 camera. Olympus Analyzer and polarizers are used to perform BM. An Olympus U-TP530 (530 nm) wave plate is added to perform WBM. Olympus UPLFLN-PH objectives are used with their matching annulus in PCM mode.

### 2.3.4 Image processing for data extraction and analysis

The analysis of the disc size distribution was performed using ImageJ software from images acquired in optical absorption microscopy. A protocol was developed to separate the discs from the background in an OM micrograph (Figure 32.a), individualize them and measure their size.

In a first step, the discs are separated from the background. For this, a machine learning module named WEKA<sup>117</sup> is used as a segmentation tool. This tool allows to define "classes" of objects to separate (in this case a "disc" class and a "background" class) from a reference image. The attribution of manually chosen pixels to a class allows the numerical calculation of a segmentation model ("classifier"). This model can then be directly applied to the images of other samples in order to have an automatic separation of the discs from the background. The result of the separation protocol (Figure 32.b) can be used to select the discs only, by thresholding (Figure 32.c). Then, the "Watershed" option is used to separate the discs that have merged (Figure 32.d). Finally the particle analysis gives access to many parameters, including

the Feret diameter, which is used to characterize the size of the discs.

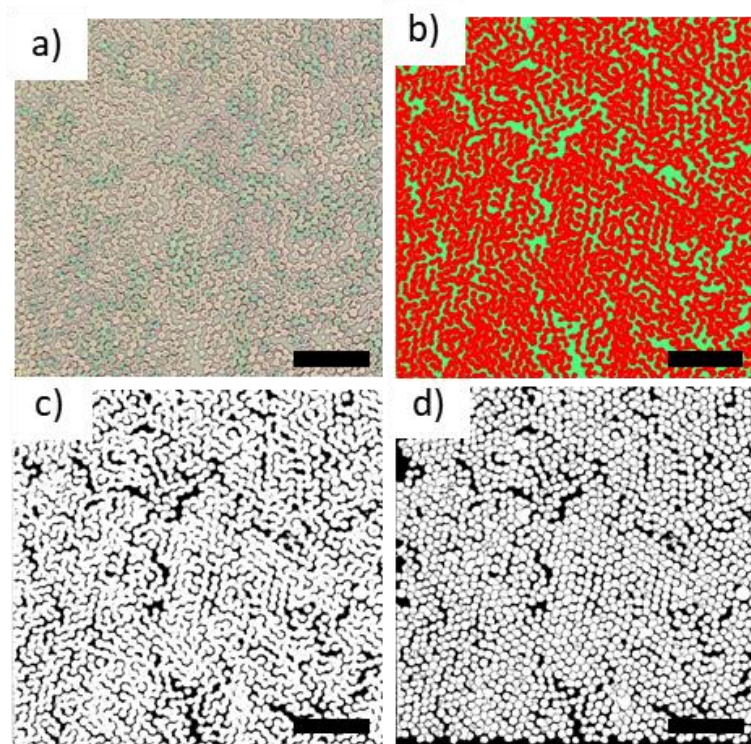


*Figure 32 - Optical micrographs and data treatment. a) Original micrograph of the interfacial mineralized structures. b) Segmentation with Weka machine learning. c) Post thresholding of the segmented image. d) Applied " watershed". Scale bars= 50  $\mu$ m*

The Feret diameter is a measure of the dimension of a single particle. It is the distance between two parallel tangents at the opposite sides of the particle<sup>118</sup>. In the case of circular particles, it is equivalent to the diameter of a particle. The representation of the Feret diameter of a random particle and a sphere are presented in Figure 33.

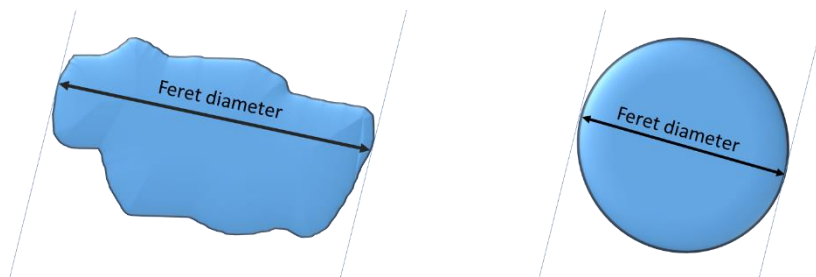


*Figure 33 - Feret diameter in the case of a random particle (left) and in the case of a disc (right).*

## 2.4 ELECTRONIC MICROSCOPY

### 2.4.1 Transmission Electron Microscopy (TEM)

#### 2.4.1.1 Principle

Transmission electron microscopy (TEM) is a technique which is widely used to characterize thin samples (~100 nm, depending on the sample density and constituting elements) and nanoparticles. An electron gun (heated wire, or field emission tip) is used to produce a beam of electrons that are accelerated under a voltage of hundreds of kV, under a high vacuum, inside the microscope chamber. The beam is focused onto the sample thanks to electromagnetic lenses. If a sample placed under the beam is thin enough, electrons will be transmitted, this way allowing imaging of the transmission properties of the sample. Figure 34 shows the various interactions taking place when the beam goes through a sample.

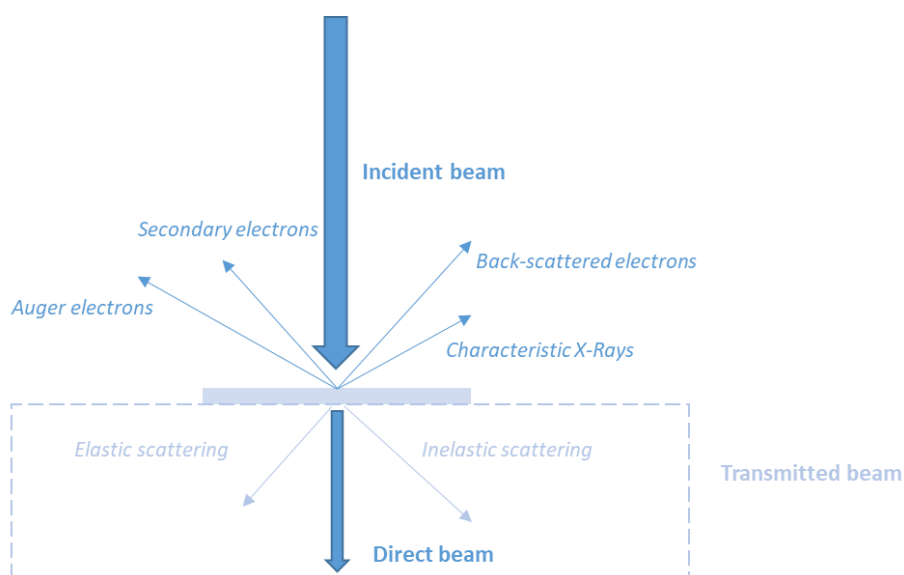


Figure 34 - Schematic representation of the interactions taking place during sample illumination by an electron beam.

Indeed, the interaction of the sample with the electron beam leads to the emission of characteristic X-ray photons, but also Auger electrons, secondary electrons, or backscattered electrons.<sup>119</sup> The transmitted electron beam is composed of inelastically and elastically scattered electrons, as well as electrons that have not been scattered by the sample (direct beam). We used bright-field TEM, meaning the detection area integrates the direct beam and the beam scattered in its surroundings. Depending on the detection angle, contrast can originate either from mass-thickness contrast or from diffraction-contrast.<sup>119</sup>

#### 2.4.1.2 Experimental

A Philips CM12 electron microscope at an operating voltage of 80 kV was used for the investigation. A Gatan camera was used to capture the images. Hydrophilized carbon-coated copper grids were used for sampling. Air/water interface objects were fished directly with the



grid, while bulk species were deposited with a pipette. Samples were immediately blotted on a Kimtech paper then dried under vacuum as described in section 2.1.3.

In order to distinguish the products of syntheses from the artifacts generated by the drying process, samples of reference solutions (calcium chloride solution alone, polymer solution alone, calcium chloride and polymer solution without exposure to ammonium carbonate) were also imaged, following the same drying treatment.

### 2.4.1.3 Image analysis

TEM images were analyzed with ImageJ software. To follow the evolution with time of the statistical size distribution, a series of sample images recorded between 0 min and 25 min of reaction were processed identically. The objects of interest were separated from the background by using local contrast enhancement and thresholding. This generated a binary image on which some particles may appear fused. They were separated using a “watershed” transformation. Then, representative objects were selected according to their circularity, defined as :

$$circularity = 4\pi \frac{Area}{Perimeter^2}$$

Only objects that have a circularity above 0.3 were selected, in order to eliminate background noise (square particles created by the watershed operation).

The edges of the particles were smoothed in order to counterbalance the numerical artifact that increases the perimeter of the particle, and have a proper circularity calculation. Objects that have a circularity above 0.8 were finally analyzed.

When pictures were more contrasted (reaction time of 35 min in chapter 3), they were thresholded by hand following local contrast adjustments and the final circularity test was set to 0.7 (as later discussed in the document, the circularity of the objects is reduced at that time, so the restrictions on circularity have to be loosened to count a proper number of particles). Area, perimeter, Feret diameter and circularity were measured.

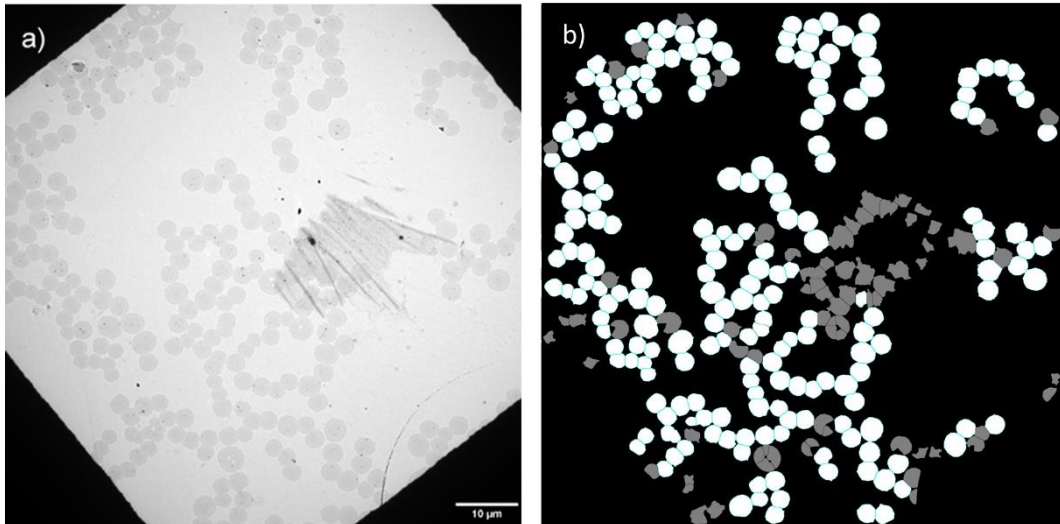


Figure 35 - Numerical treatment of an TEM image. a) Original picture b) Result after treatment. Selected particles in the final analysis are presented in white.

To present the Ferret diameter distribution (or definition see section 2.3.4 of this chapter), violin plots were used. The different statistical data that can be displayed in a single violin diagram are presented in Figure 36. The white dot is the median value, the ends of the box represent the inter-quartile space (i.e., the range of values that covers 25% of the measurements on either side of the median), and the upper and lower points of the black line represent the inter-centile space (i.e., 98% of the measurements). The Kernel density estimation is plotted in a mirror representation on each side of the violin. A kernel density estimation is a calculative method to retrieve the probability density function in a dataset.<sup>120</sup> Violin plot are an alternative to histograms, which more effectively highlights multimodal distributions.

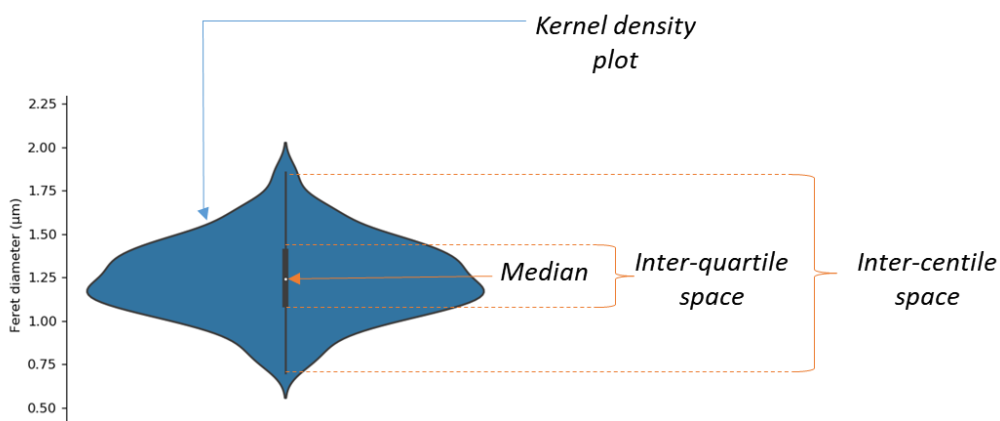


Figure 36 - Violin plot example, with annotated statistical data.

### 2.4.2 Cryogenic Transmission Electron Microscopy (cryo-TEM)

#### 2.4.2.1 Principle

Cryo-TEM imaging relies on the same principle as TEM imaging (see section 2.4.1.1 of this chapter) but is specifically adapted to liquid or highly hydrated samples. Indeed, cryogenic TEM effectively avoids drying artifacts (aggregation, precipitation, etc.) by freezing the sample to be imaged in liquid ethane, so as to preserve its "native" hydrated state. More precisely, the sample is first deposited on a holey-carbon grid, then dry-blotted, and finally plunged in liquid ethane. The whole process takes about 20 s, and results in the formation of a thin film (50 nm to 200 nm) of amorphous ice that surrounds the hydrated objects. The frozen sample is then observed on a TEM microscope equipped with a cryo-holder, which ensures a constant temperature of about 180 °C throughout the measurement.

#### Energy Dispersive Spectroscopy (EDS)

Elemental analysis is possible with TEM microscopy, through the analysis of the emitted X-Rays (Figure 34). During beam-illumination, electron from the inner shells of the sample atoms can be ejected. The energy of the X-rays produced by the de-excitation process (transfer of an electron from an outer shell to the emptied inner shell) is then atom specific. Measuring the emitted X-rays energy is therefore used to deduce which atoms are present in the sample.

#### 2.4.2.2 Experimental

Observations were made on three different cryo-TEM microscopes using the following protocols:

- *JEOL JEM 2100* Film samples were deposited by fishing at the solution/air interface on plasma pre-treated copper grids covered with holey carbon film (Quantifoil R2/2). After the excess liquid on the grid was blotted using a Whatman filter paper, the grid was promptly dipped in liquid ethane to form a thin film of vitreous ice. The cryo-TEM observations were carried out at -180°C using a JEOL JEM 2100 microscope operated at 200 kV. A Gatan Ultra Scan US1000 camera was used to capture the images. EDS was performed using XEDS JEOL (Japan) EX Si(Li) (138 eV resolution) detector. *Experiments were performed at the Institut de Minéralogie, de Physique des Matériaux et de Cosmochimie in Paris.*
- *JEOL 2010 FEG microscope* : Cryo-TEM samples were prepared using the automated Vitrobot System (FEI Company). A 5 µL drop of aqueous sample solution was deposited on plasma pre-treated copper grids covered with a holey carbon film (Quantifoil R2/2). For interfacial objects, the deposition was made by fishing at the solution/air interface. After the excess liquid on the grid was blotted by filter paper, the grid was promptly dipped in liquid ethane to form a thin film of vitreous ice.

The cryo-TEM observations were carried out at  $-180^{\circ}\text{C}$  using a JEOL 2010 FEG microscope operated at 200 kV. A Gatan camera was used to capture the images. *Experiments were performed at the Laboratoire de Physique du Solide in Orsay.*

- *JEOL 2200FS FEG microscope* : Deposition was made on plasma pre-treated copper grids covered with a holey carbon film (Quantifoil R2/2, by fishing at the solution/air interface. After the excess liquid on the grid was blotted by filter paper, the grid was promptly dipped in liquid ethane to form a thin film of vitreous ice. The cryo-TEM observations were carried out at  $-180^{\circ}\text{C}$  using a JEOL 2010 FEG microscope operated at 200 kV. A Gatan camera was used to capture the images. *Experiments were performed at the Institut Curie in Orsay.*

### 2.4.3 Scanning electron microscopy (SEM)

#### 2.4.3.1 Principle

Scanning electron microscopy (SEM) is a technique that is widely used to characterize submicronic objects. An electron gun (heated wire, or field emission tip) produces a flux of electrons. The electrons are accelerated under an electrical voltage of several kV (between 1 and 20 kV) and focused onto the sample thanks to electromagnetic lenses. The equipment is operated under high vacuum. When positioned under the beam, the sample interacts with the electron beam by emitting scattered, secondary or Auger electrons, as already presented earlier (see Figure 34). In this study, the detection of secondary electrons was mainly used, as it provides information on the topography, of major interest for the characterization of our samples.

Elemental detection was performed using EDS (Energy Dispersive Spectroscopy) and crystalline orientation was determined using EBSD (Electron Back-Scatter Diffraction), as detailed below.

#### 2.4.3.2 Secondary electron

Emission of secondary electrons is possible when a sample is illuminated by an electron beam. These electrons are ejected from their original atom and have a low energy. Only secondary electrons close to the surface of the sample manages to exit the sample and reach the detector. The variation of topography is directly linked to the secondary electron emission coefficient, as the minimum escape depth fluctuates as shown in Figure 37.

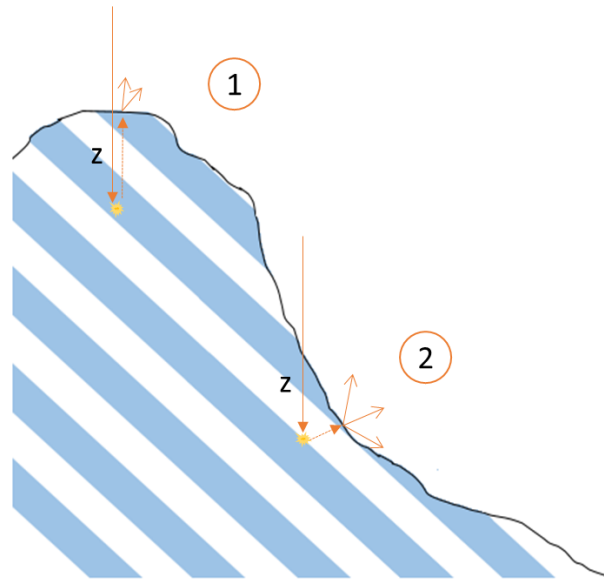


Figure 37 - Minimum escape depth depending on the topography. 1: The incident beam hits a flat surface, the minimum escape depth is maximized. 2: The incident beam hits a tilted surface, the minimum escape depth is reduced. More secondary electrons are emitted in case 2.

### 2.4.3.3 EBSD

Electron back scattered diffraction is based on the collection of the Kikuchi pattern while scanning the sample<sup>121</sup>. This pattern formed on the detector is specific to the crystalline cell parameters and to its orientation, allowing EBSD spectroscopy to produce orientation maps of crystalline samples.

### 2.4.3.4 Experimental

Observations were made on a SEM Gemini Zeiss 500 (FESEM) on unmetallized samples. Two secondary electron detectors were used, namely HE-SE and In-lens. The geometry of these detectors is presented in Figure 38.

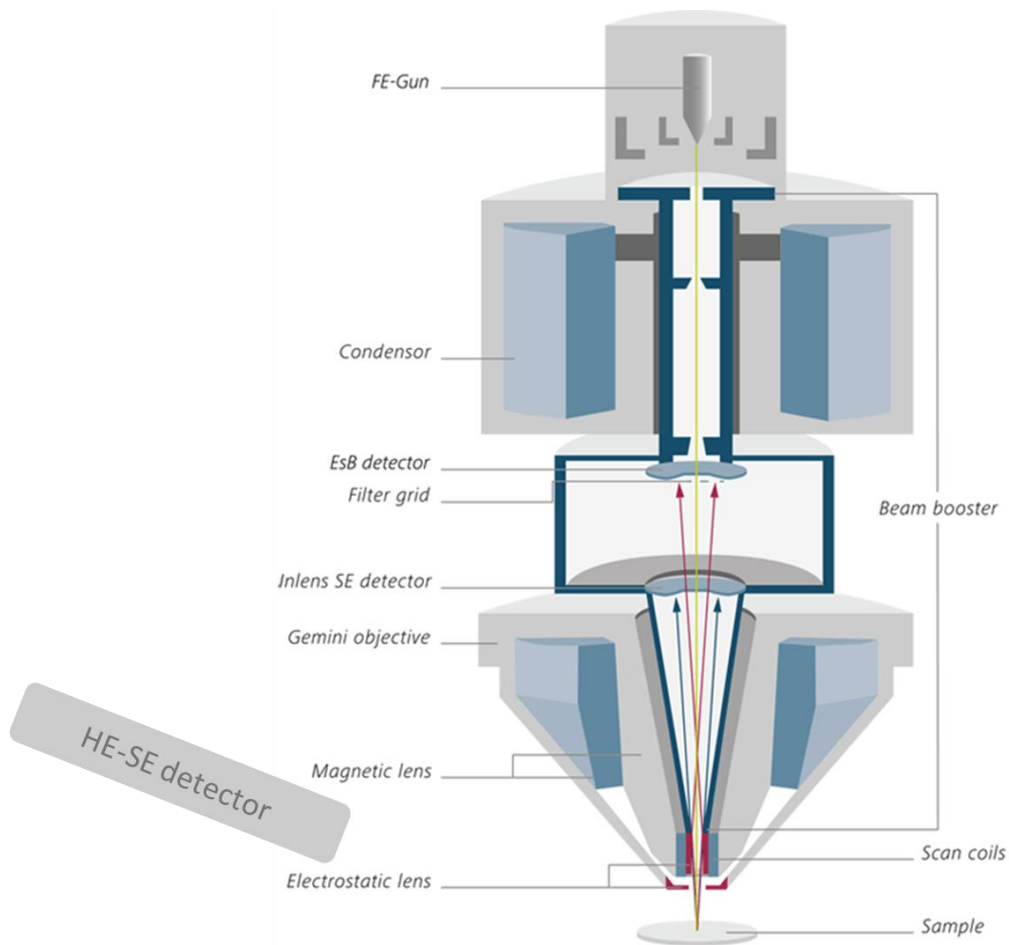


Figure 38 - Configuration of the Gemini 500. The main components are indicated in the figure. In this work, only secondary electron detectors were used, to investigate the topography (Figure 37). Both a detector in the beam axis (in lens) and a detector tilted with regard to the sample (HE-SE detector) were used.

The In-lens detector detects SE electrons directly in the beam path, whereas the side SE detector was used to enhance the topography of the sample (HE-SE). The images were acquired at low electron acceleration voltage in order to obtain high-resolution images of the nanoscopic structure located at the surface of the sample.

To estimate the sample thickness and to perform EBSD measurements, the samples were tilted at 70° angle in the SEM. A EDAX Hikari super detector was used for EBSD measurements.

## 2.5 LENSLESS MICROSCOPY

Two kinds of lensless microscopy are presented in this work. Optical and crystalline properties are investigated by ptychography techniques, while topographical measurements on thin objects resulting from interfacial mineralization are made with atomic force microscopy (AFM).

Ptychography is a microscopy method based on a computational approach<sup>122</sup>. It makes use of a series of diffraction intensity patterns, acquired with a coherent beam (such as the one

produced by a laser in optics). In contrast to a classical microscope, where the image is obtained in the image plane, the measurements are performed in the Fourier space of the sample, which provides access to the intensity distribution of the scattered (or diffracted) field. In order to retrieve the sample image (i.e., propagating this acquired information in the image plane, numerically), one needs to retrieve the phase of the diffracted field, knowing its diffracted intensity which is equal to the squared amplitude of the field. This is achieved numerically, with phase retrieval algorithms, which iteratively retrieve the lost information by propagating back and forth the field between the measurement plane and the sample plane<sup>123</sup>. In order to ensure the convergence of the algorithm, additional information must be added to compensate for the loss of the phase. In ptychography, this information is obtained by scanning the sample with a finite size probe, making sure that the step size between two successive acquisitions is sufficiently small to ensure a strong overlap between the two illuminated areas. This redundancy is key for the convergence of the inversion process. At the end, the full field is retrieved (including phase and amplitude) and can be propagated in any plane of the space, including the sample plane.

### 2.5.1 Vectorial Ptychography (VP)

#### 2.5.1.1 General principle of vectorial ptychography

In this work we have used an implementation in the visible optical regime designed to address specifically microscopic specimens that affect the state of polarization of light.<sup>124</sup> Those are samples which are referred to as optically anisotropic materials. The principle of the so-called vectorial ptychography measurement is illustrated in Figure 39. The specimen is illuminated at several overlapping positions by a finite-size laser beam. Light polarization is controlled by means of a polarizer and an analyzer placed before and after the specimen, respectively. The recorded raw data are the series of diffracted intensity patterns acquired for all scanning positions, for all combinations of orientations of polarizer and analyzer.

These raw data are processed by an iterative algorithm aiming to solve an inverse problem, i.e., finding an optical map of the specimen that gives rise to a set of calculated diffraction patterns as similar as possible to the experimental ones. Under the assumption that

- the specimen behaves as *optically* thin (which excludes volume effects such as multiple scattering),
- the relative illumination positions are known,
- the laser beam is stable during the measurement (intensity, shape, wavefront),
- the measurement geometry is known,

it has been shown that the specimen properties can be reconstructed as so-called Jones maps,<sup>124</sup> which encompass a wide set of optical parameters<sup>125</sup> (see below).

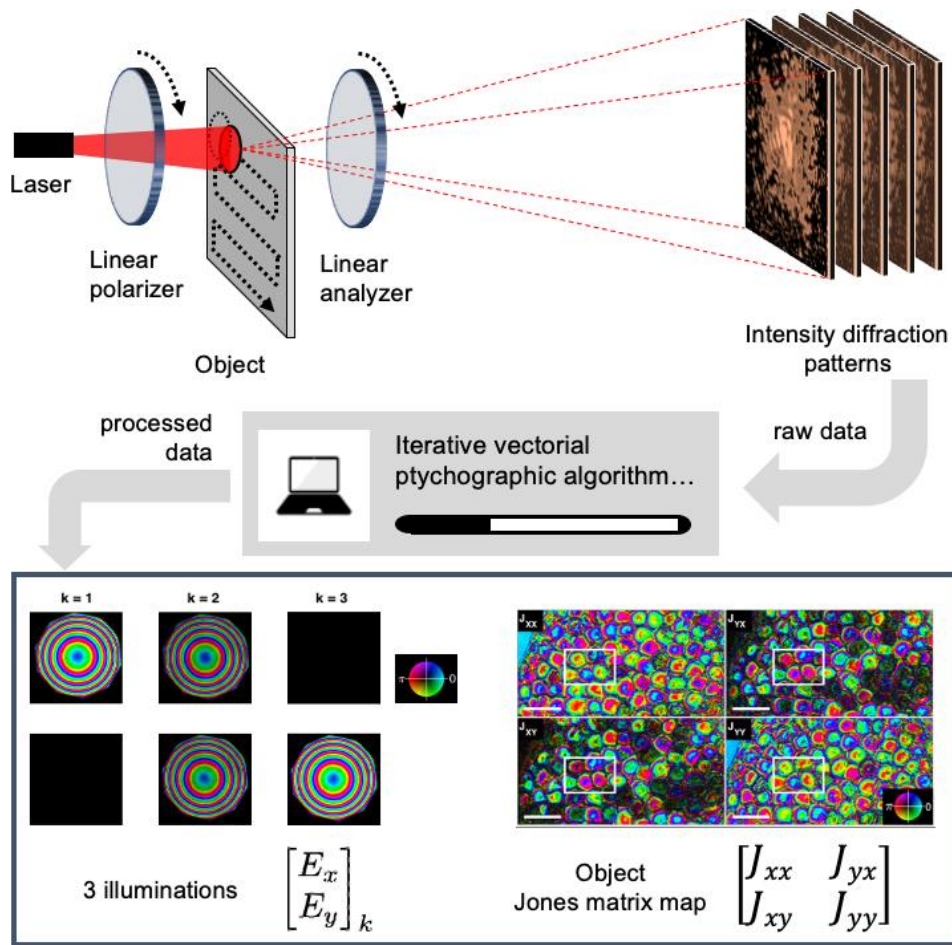


Figure 39 - General principle of vectorial ptychography

### 2.5.1.2 Methods

The optical parameters extracted from the Jones matrix, and presented in Chapter 4, are presented, as well as the material properties they are derived from.

*Unwrapped phase* Given in radian.

Optical definition: The phase refers to the phase shift of the light wave that has travelled through the specimen. A global phase shift  $\phi$  (modulo  $2\pi$ ) is retrieved by the ptychography algorithm. The unwrapped phase  $\phi_u$  is obtained by applying an unwrapping algorithm to the global phase shift  $\phi$ , ensuring that  $\phi_u = 0$  in the region without specimen.

$$\phi = \frac{2\pi}{\lambda} n_o d + C \pmod{2\pi} \quad \rightarrow \quad \phi_u = \frac{2\pi}{\lambda} n_o d$$

*Phase shift*

*Unwrapped phase*

where  $n_o$  is the ordinary index of the material,  $d$  its thickness,  $\lambda$  the wavelength of light and  $C$  a constant.



Material property: If the material has a ordinary index that is constant across its thickness, the unwrapped phase value is directly proportional to a sample effective thickness  $d$  and ordinary index  $n_0$ . Therefore, if  $n_0$  is known, the quantification of the thickness is possible.

Limitations: The algorithmic calculation relies on continuous phase variations to determine the unwrapped phase. If the phase jump between two pixels is too great, a physically impossible height description can result. Sharp edges, inducing strong phase modification in the object plane, are thus problematic for this calculation.

*Retardance* : Given in radian. Values between 0 and  $\pi$ .

Optical definition: Phase retardation between the waves polarized along the fast axis and slow axis of the crystal. The retardance is expressed by the following equation:

$$\Delta\phi = \frac{2\pi}{\lambda} \Delta n_{eff} d$$

Where  $d$  is the thickness of the sample,  $\Delta n_{eff}$  is the effective birefringence, and  $\lambda$  is the incident wavelength.

Material properties: The effective birefringence  $\Delta n_{eff}$  is related to the intrinsic birefringence of the material and accounts for the tilt of the crystal  $c$ -axis with respect to the sample plane, as described by Baroni.<sup>126</sup> The retardance of a known material therefore depends on two parameters: the sample thickness and the orientation of the  $c$ -axis. Unless the thickness is known by another way, the two parameters cannot be separated solely with the retardance value. A material showing strong retardance can have either a significant thickness or a  $c$ -axis close to the sample plane, as shown in Figure 40.

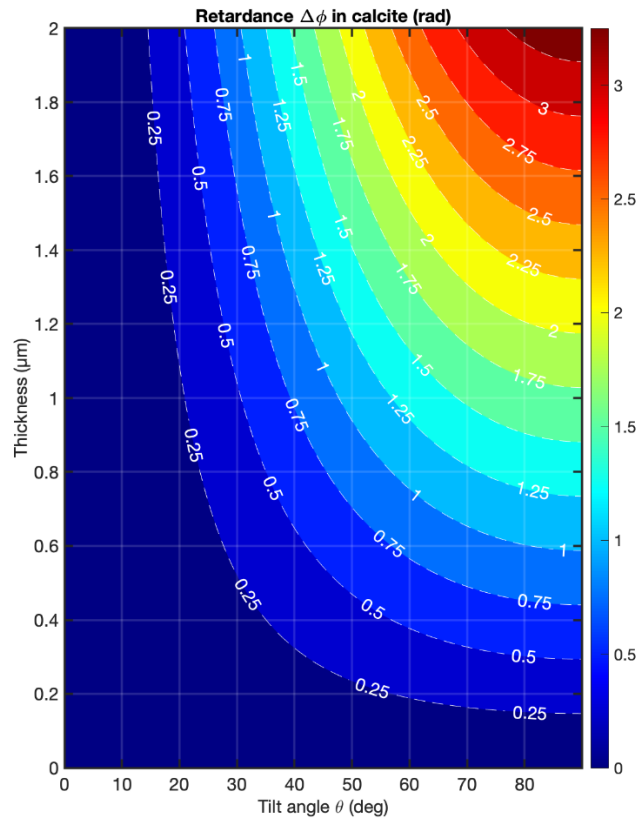


Figure 40 - Retardance in calcite as a function of the crystal thickness and c-axis tilt. The tilt is noted in degrees with respect to the normal to the sample plane.

**Fast-axis orientation** Given in deg, values between 0 and 180 deg (in the object plane).

**Optical definition:** In a birefringent material, light polarized along certain directions in the plane travel in the material without change of polarization. These two directions are referred to as neutral axes of the material. The one corresponding to the fastest propagation is called fast axis.

**Material property:** For a negative uniaxial material such as calcite, one can show that the fast-axis orientation corresponds to the projected direction of the c-axis in the object plane<sup>125</sup>.

Note: random values of fast-axis orientation are returned when an isotropic material is considered.

**Eigenpolarization** : shown as ellipses with major, resp. minor, axis oriented along the fast, resp. slow, axis of the anisotropic material. Becomes a line when the eigenpolarization is linear.

**Optical definition:** Eigenpolarizations refer to states of light polarization that are undisrupted when travelling through the specimen. Mathematically they correspond to the eigenvalues of the Jones matrix. They are plotted as lines or ellipses and their orientations figure out the projection of the fast and slow axis of the crystal in the object plane.

**Material property:** In a uniaxial material, a perfect single crystal has linear orthogonal eigenpolarizations. The misalignment of the crystalline layers parallel to the sample plane

induces elliptical eigenpolarizations.<sup>125</sup>

*Ellipticity* : Eigenpolarization shape quantification. In principle between -1 and 1, although we will be only interested in the absolute value, between 0 and 1.

Optical definition: The ellipticity of the eigen value quantifies its shape in regard to a circle. An ellipticity of 0 is observed when the eigen value is a linear polarization, and +/- 1 when the eigen value is a left/right circular polarization.

*c-axis tilt* : Given in deg, values between 0 and 90 deg.

Definition: Angle between the c-axis of the crystal and the normal to the sample plane. Material property: For a known material,  $n_o$  is known. The simultaneous knowledge of  $\phi_u$  and  $\Delta\phi$  allows to determine independently the effective birefringence  $\Delta n_{eff}$ , since:

$$\Delta n_{eff} = \frac{\Delta\phi}{\phi_u} n_o$$

One can show<sup>125</sup> that the c-axis tilt to the image plane can be directly estimated from  $n_o$  and  $\Delta n_{eff}$ .

Limitations: A problem in the calculation of the unwrapped phase is often observed in our samples, owing to abrupt phase changes, which makes the tilt angle calculation impossible. Nevertheless, the "tit ratio"  $\frac{\Delta\phi}{\phi_u}$  remains a constant if the tilt angle is not modified. This ratio is therefore used to evaluate local tilt variations of the c-axis in the sample.

### 2.5.1.3 Experimental

All measurements were carried out on a custom setup<sup>124</sup> operating at the wavelength of 635 nm, adapted to an inverted microscope body (IX73, Olympus). The specimen was placed on a motorized stage (U-780, Physik Instrumente). Depending on the objective that was used (40x-ACHN-P NA 0.65, resp. 20x-ACHN-P NA 0.4, Olympus), the average scanning step was set to 7  $\mu\text{m}$  (resp. 10  $\mu\text{m}$ ), and the reconstructed Jones maps were spatially sampled at 0.48  $\mu\text{m}$  (resp. 0.8  $\mu\text{m}$ ). At each scanning position, three linear polarizations (at angles 0, 60, 120°) of the incident light and three analyzer polarizations (at angles of 0, 60, 120°) were used, resulting in nine different combinations. Depending on the scanned area, data acquisitions took between 5 and 15 min. Reconstruction of the specimen Jones matrix was performed by means of a conjugate gradient algorithm (typical computing time between 2 and 10 hours)<sup>127</sup>, and further processed to extract all optical parameters<sup>125</sup> (typical computing time 2-5 min).

2.5.2 Bragg Ptychography (BP)

2.5.2.1 Principle

The other approach which is based on the ptychography principles is Bragg ptychography. In Bragg ptychography,<sup>128</sup> the crystalline sample is illuminated by a monochromatic coherent X-ray beam. Owing to the internal atomic periodicity of the crystalline sample (i.e. its crystal lattice), the X-ray beam is diffracted in specific directions of space, leading to strong intensity maxima in space, the so-called Bragg peaks, that are well-separated from the incident illumination. The description of Bragg ptychography measurements requires the introduction of the wavevector transfer  $\mathbf{q}$ , defined as  $\mathbf{q} = \mathbf{k}_f - \mathbf{k}_i$  in the 3D frame ( $\mathbf{q}_1, \mathbf{q}_2, \mathbf{q}_3$ ) displayed in Figure 41 ( $\mathbf{k}_i$  and  $\mathbf{k}_f$  being the incident and exit wave vectors, respectively). The sample is said to be in Bragg condition with respect to the crystalline planes (hkl), when these planes are normal to the wavevector transfer  $\mathbf{q}$ , or, equivalently, when  $\mathbf{q}$  is equal to the Bragg vector  $\mathbf{G}_{hkl}$ , defined as the vector normal to the (hkl) crystalline planes (inset of Figure 41), with  $|\mathbf{G}_{hkl}| = 2\pi/d_{hkl}$  where  $d_{hkl}$  is the inter-reticular distance. In Bragg ptychography experiment, the sample is positioned in Bragg configuration with respect to some crystalline planes (hkl), and the full 3D signal intensity of the Bragg peak (hkl) is measured on a detector as a function of the momentum transfer  $\mathbf{q}$ , as presented in Figure 41.

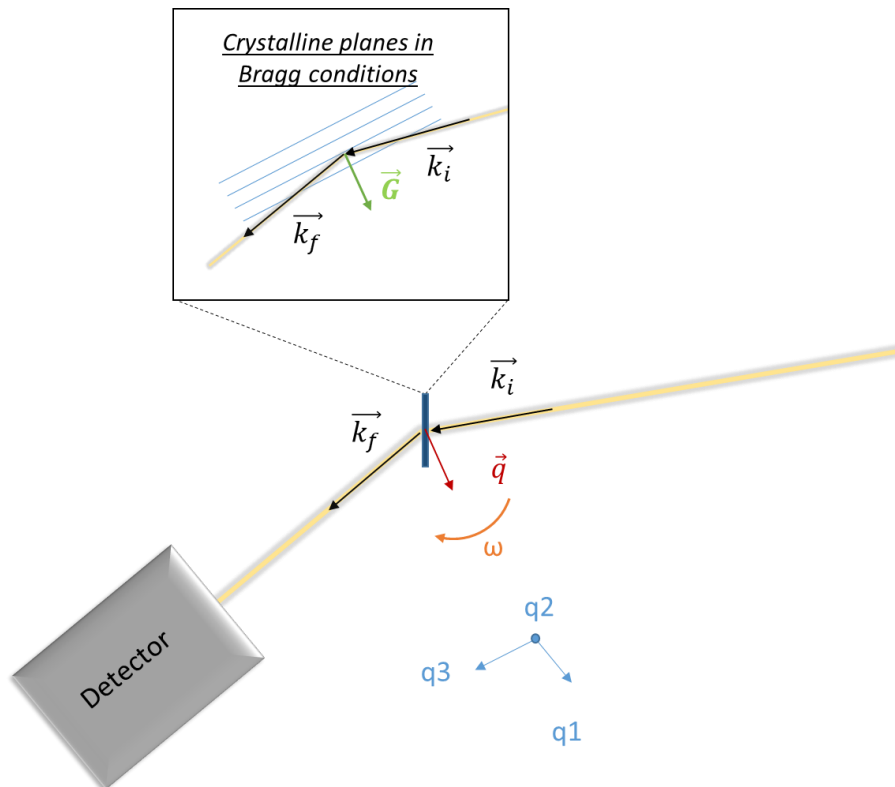


Figure 41 - Configuration of the Bragg ptychography experiment.  $\mathbf{k}_i$  is the incident wave vector and  $\mathbf{k}_f$  the exit wave vector.  $\mathbf{q}$  is the vector transfer resulting from the difference between the incident and exit wave vector. The 3D frame for  $\mathbf{q}$  is depicted by  $(\mathbf{q}_1, \mathbf{q}_2, \mathbf{q}_3)$  in the Figure.  $\mathbf{q}_1$  and  $\mathbf{q}_2$  are along the detector frame,  $\mathbf{q}_3$  is along the rocking curve direction, i.e. it is explored by rotating the sample along the  $\omega$  angle. Inset : when the crystalline planes are oriented in Bragg configuration,  $\mathbf{q}$  is equal to  $\mathbf{G}_{hkl}$ .  $\mathbf{G}_{hkl}$  is normal to the planes and its norm is linked to the inter-reticular space between the (hkl) planes.

In the illuminated volume, small variations of the crystalline lattice (strain and orientational mismatch) induce variations in the norm and orientation of the Bragg vector, as described in Figure 39. In particular, a rotation of an angle  $\alpha$  of the crystalline plane around  $\mathbf{q}_2$  directly translates into a rotation  $\omega$  of the Bragg vector  $\mathbf{G}_{hkl}$  (Figure 42.a). The same rationale is applicable to the rotation of the crystalline planes around  $\mathbf{q}_3$  (Figure 42.b). A variation of the inter-reticular space translates into a variation in the magnitude of  $\mathbf{G}_{hkl}$  (Figure 42.c).

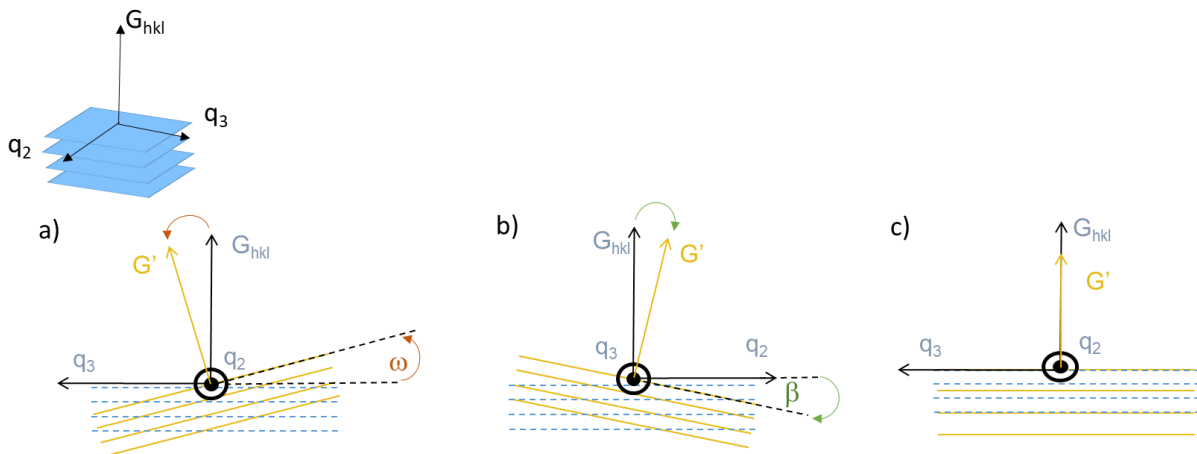


Figure 42 - Representation of 3D the displacement of the  $\mathbf{G}$  (from  $\mathbf{G}_{hkl}$  to  $\mathbf{G}'$ ) vector induced by : a) tilting of the crystalline planes around  $q_2$  b) tilting of the crystalline planes around  $q_3$  c) stretching of the crystalline plane.

By redundantly scanning the probe along the sample and by performing an angular exploration, at each illumination position, along the so-called rocking curve (i.e. along  $\omega$  in Figure 41 and Figure 42), one can access the full 3D intensity distribution in the Fourier space, at each position. These 3D intensity patterns are collected and used in the reconstruction process. In Bragg ptychography, the sample scattering function resulting from the 3D reconstruction process is expressed by:

$$\rho = |\rho| e^{i\phi} \quad (\text{Equation 1})$$

where the phase  $\phi$ , is proportional to the crystalline displacement field  $\mathbf{u}$ , as described by the expression:

$$\phi = \mathbf{G}_{hkl} \cdot \mathbf{u}$$

The crystalline displacement field  $\mathbf{u}$ , which depicts the mismatch between the crystal planes in the sample with respect to an arbitrary perfect crystalline reference, contains information on the 3D crystalline properties. Hence, from the phase,  $\mathbf{u}_{hkl}$ , the projection of the displacement field on the Bragg vector can be extracted and analyzed. As an illustration of the behavior of the displacement with respect to the crystalline properties, a linear increase (or decrease) of  $\mathbf{u}_{hkl}$  with respect to the real space coordinate corresponds to a perfect crystal (no crystalline defect), either homogeneously strained with respect to a chosen crystalline reference or mis-oriented with respect to the chosen reference orientation. Over this distance, where the  $\mathbf{u}_{hkl}$  (or the phase) is evolving linearly with the spatial coordinate, the crystal is perfectly periodic and we refer to this as crystalline coherence in this work. On the opposite, a change in the

gradient of  $\mathbf{u}_{hkl}$  results from local crystalline deformations (strain and orientation) in the crystal.<sup>129</sup>

Therefore, the derivative of  $\mathbf{u}_{hkl}$  is calculated to extract the crystalline defects, the two rotation angles, referred to as Tilt 1 and Tilt 2, and the relative strain, all represented in Figure 43. The frame used is the orthogonal (x, y, z) frame presented in Figure 43: x and y are in the sample plane, and z is along the thickness. The strain quantifies the relative variation of the inter-reticular distance  $d_{hkl}$  to a reference crystal (chosen as geological calcite in this study). It corresponds to the following equation and is unitless:

$$strain = \frac{d_{hkl(ref)} - d_{hkl(sample)}}{d_{hkl(ref)}}$$

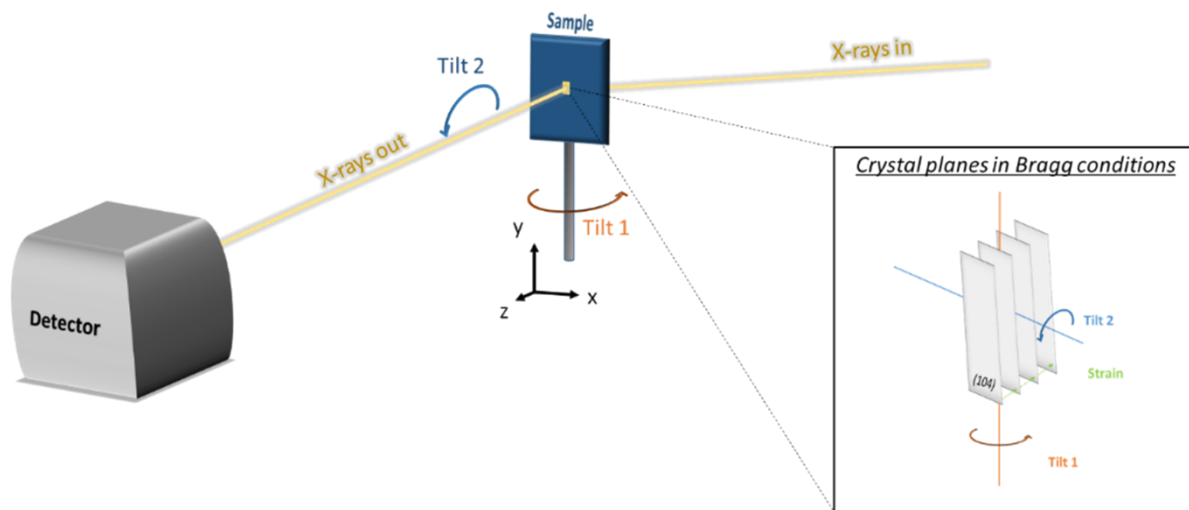


Figure 43 - Representation of the tilts and strain calculated from the displacement field derivatives. (x,y,z) is defined by the sample : x and y correspond to the sample plane, and z to the thickness direction. Tilt 1 and 2 are represented both in the measurement space (the set-up) and at the scale of the crystalline plane in Bragg conditions (in the inset). The strain, ie the relative variation of the inter-reticular distance compared to a reference crystal, is represented along the crystalline planes (inset). Note that Tilt1 and Tilt 2 correspond to  $\omega$  and  $\beta$ , respectively, in Figure 42.

### 2.5.2.2 Experimental

The experiments were carried out at the ID13 nanobranch at ESRF, during two different experimental campaigns, using the extremely brilliant source of the upgraded ESRF. The focused beam was produced with a set of Si nanofocusing lenses, resulting in a beam size of  $\sim 250 \times 300 \text{ nm}^2$  at 15.2 keV with a photon flux of about  $10^{11}$  ph/s. The diffracted signal was recorded with a Maxipix 2D detector (526 x 526 pixels, 55  $\mu\text{m}$  each) placed at about 1.9 m from the sample on a rail, allowing displacement of the detector in the horizontal plane, only. The sample was installed vertically onto a translation stage, itself placed on a rotation device (a hexapod, acting as a pseudo-motor). The transmission diffraction geometry was chosen. For

the Bragg ptychography acquisition, the sample was raster-scanned across the beam in steps of about 50 nm and this 2D map was repeated for a series of angles in the vicinity of the Bragg angle, covering about 3-6°, in steps of about 0.01°. For each of these spatial and angular positions, a 2D diffraction pattern was recorded.

In order to optimize the signal quality, the most intense calcite reflection was chosen (i.e., the (104) Bragg reflection), when it was accessible in the horizontal scattering plane. However, in some cases, this reflection was not accessible and we had to resort to e.g., the (012) and (113) reflections.

The data analysis was done at Institut Fresnel, using an in-house inversion code, developed for the inversion of Bragg ptychography data. The procedure is similar to the one used in Mastropietro<sup>16</sup> and is not detailed here, as it goes beyond the scope of this work. Once the real space information is obtained (description of the sample in the laboratory frame, in 3D), a data treatment is applied to extract the crystalline information.

### 2.5.2.3 Accessible information from the data treatment.

The same data treatment was performed on all studied samples. For the sake of clarity, an example of a dataset processing is shown below. In Chapter 4, only the main results will be presented in the text, the rest of the data being in the Appendix.

The Bragg ptychography reconstruction provides access to the sample scattering function as defined in eq. 1. Our analysis makes use of the retrieved phase in order to extract the tilts and strain, from the calculation of its derivative. The three maps shown in Figure 44 present respectively the distribution of strain and tilts in the sample plane (xy). This representation allows the visual analysis of the crystalline properties distribution. Interestingly, some domains appear, characterized by a homogeneous color, corresponding to a rather homogeneous value of the tilts and strain (150 nm wide). We refer to these domains as iso-domains (or iso-oriented, iso-strained domains). In the whole volume represented, the distribution of strains and tilts can be presented as histograms (Figure 45). In the shown example, we observe that the strain has a typical standard variation of about +/- 0.004, and that the tilt distributions are rather homogeneous in the investigated angular range, indicating that they likely expand beyond a few degrees. When the angular range is sufficient to have all the values of Tilt 1 and Tilt 2, their standard deviation is calculated, then the standard deviation for the global tilt is calculated with the following formula, because the choice of the two axis (q2 and q3) are not specific to

the sample geometry.

$$Tilt = \sqrt{(Tilt\ 1)^2 + (Tilt\ 2)^2}$$

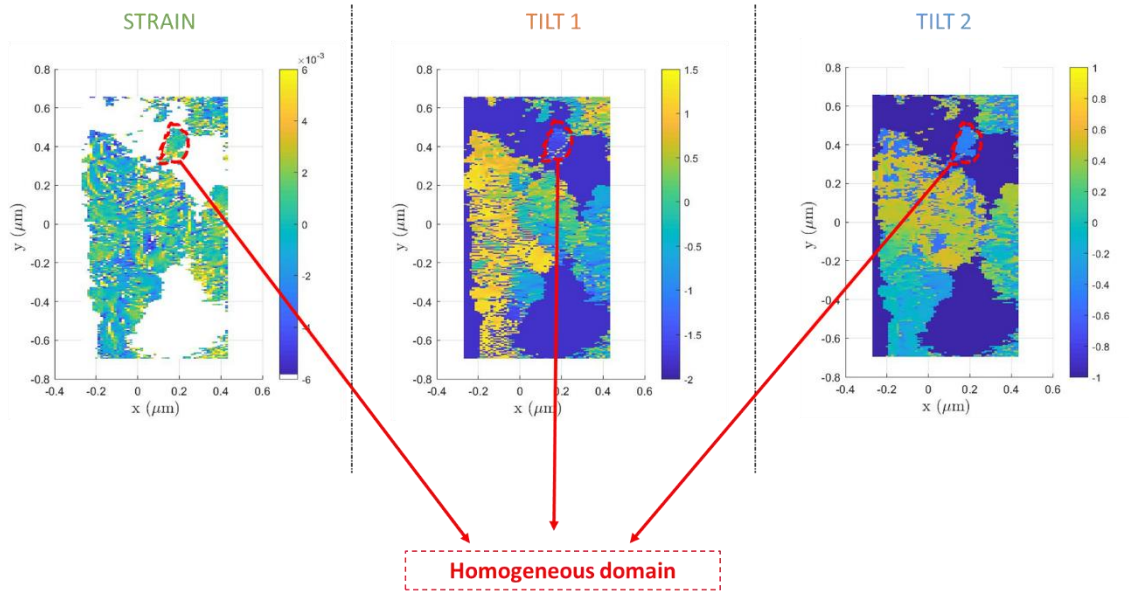


Figure 44 - Maps of the crystalline properties in the (xy) plane. From left to right, Strain, Tilt1 and Tilt 2 values of the same area are shown. An iso-domain, homogeneous in strain and tilts, is surrounded by a red dashed line. The color scales are provided on the plot, for the strain (unitless) and tilts (in degrees).



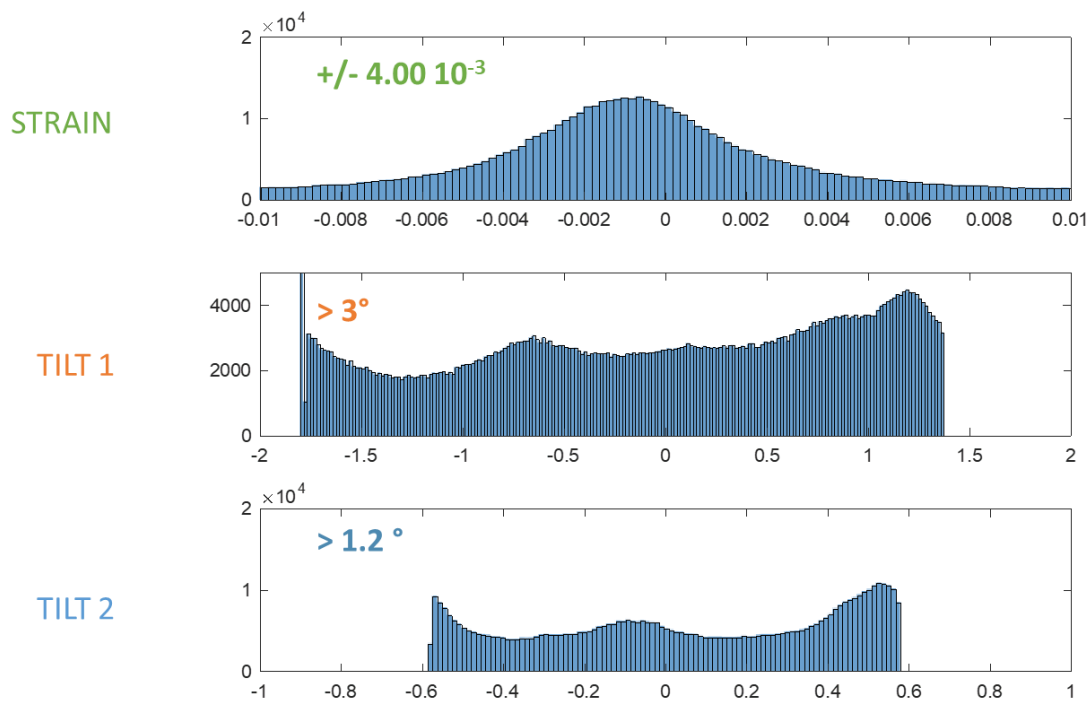


Figure 45 - Histograms of Strain, Tilt 1 and Tilt 2 variations in the volume presented in Figure 43. For the strain, the standard deviation is noted in green. Note that in this case, the distributions of tilts are rather homogeneous and indicate a much larger tilt distribution than the one captured by the angular exploration performed during the Bragg ptychography data acquisition. In consequence, no standard deviation is given and lower bounds of tilt range are instead provided.

To investigate fine variations in the crystalline structure, some domains of iso-strain and iso-orientation along tilt axes are extracted. In Figure 44, the area outlined by a red dotted line is chosen with these considerations for further investigation. The extracted area is presented in Figure 46 within the (xy) and (xz) planes. On these maps, one can see that the strain, Tilt 1 and Tilt 2 are homogeneous in the two planes (by definition).

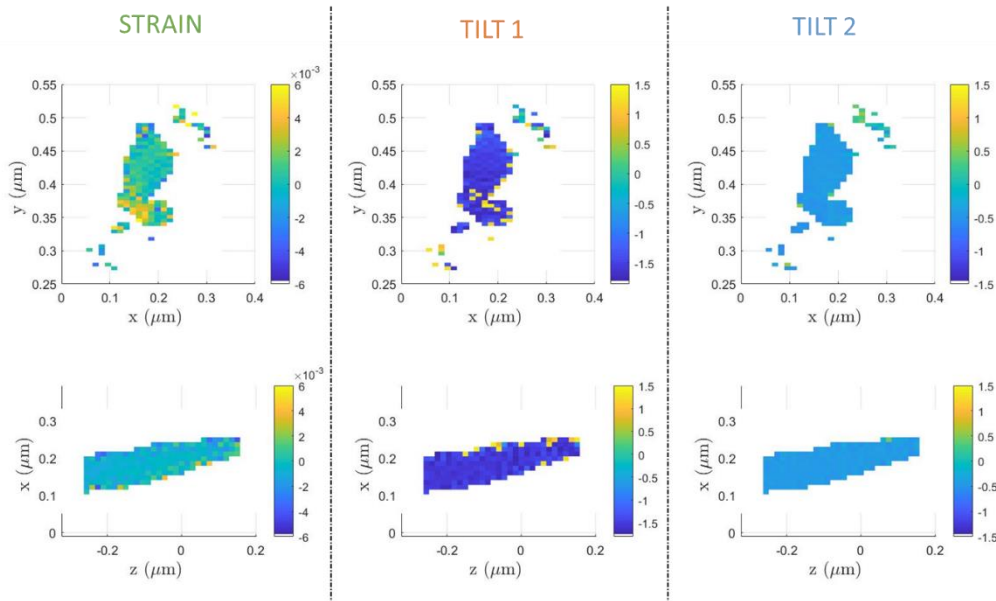


Figure 46 - Crystalline properties of the domains extracted in Figure 44. The spatial distribution of each parameter (from left to right : strain, Tilt 1 and Tilt 2) are shown in (xy) and (xz) planes.

In order to go further, the reconstructed phase map of the chosen domain is shown in Figure 47. The inset shows the phase map in the (xy) plane while the main representation shows the phase in 3D. This representation is useful to evaluate the phase homogeneity, revealing the crystalline coherence. Here, the crystalline coherence length, represented by the bright blue area, is estimated to about 50 nm in the plane, and 200 nm along the sample thickness. The gray volumes superimposed on the 3D image correspond to regions of higher strain values. In the present case, they appear at the edge of the crystalline coherent volume and propagate along the thickness.

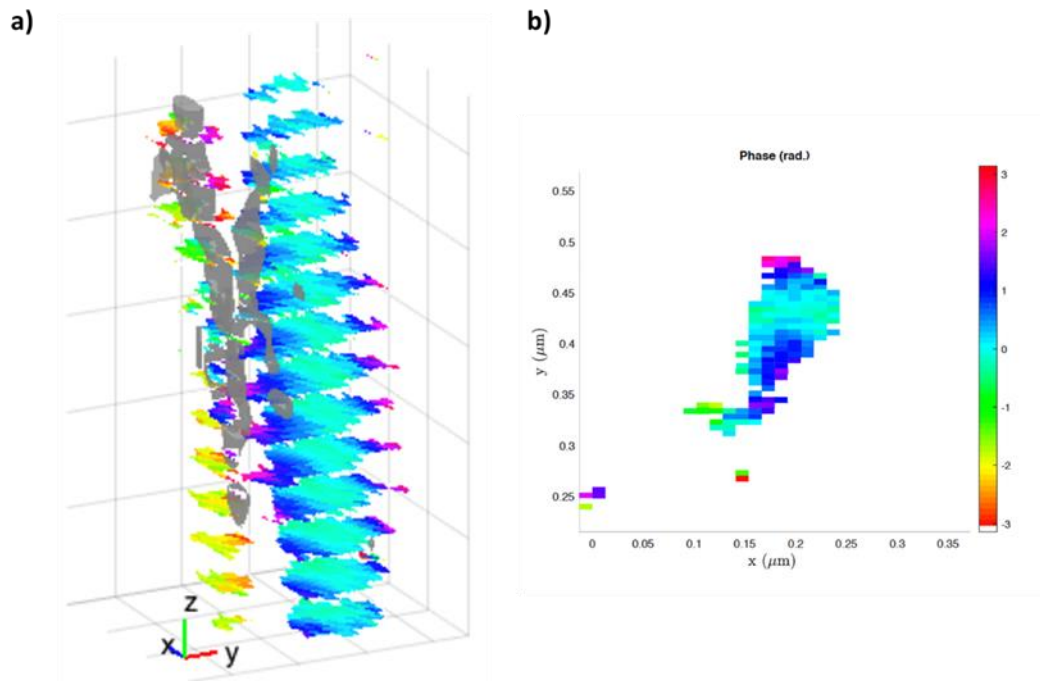


Figure 47 - Plot of the phase variation in the iso-tilt, iso-strain domain. a) 3D phase map of the iso-strain iso-tilt domain presented in Figure 103 with scale (xyz) = 30 nm. b) 2D phase map of the investigated domain.

In summary, in this work, Bragg Ptychography was used to:

- Evaluate the variations in the 3D crystalline properties of the sample : strain and tilts
- Quantify the size of the iso-domains
- Determine the crystalline coherence length

This whole set of information was finally used to compare the crystals produced in supposedly biomimetic syntheses to the reference biogenic crystal<sup>16</sup>.

### 2.5.3 Atomic force microscopy (AFM)

#### 2.5.3.1 Principle

Atomic Force Microscopy is used for topographic measurements of samples, at the nanometer scale. The topographic analyses are based on the measurement of the deflection of a probe (a sharp tip, with a radius of curvature of 5 to 50 nm at the apex, at the end of a cantilever) resulting from its interaction with the sample, when getting in contact with it.

#### 2.5.3.2 Experimental

Atomic Force Microscopy (AFM) imaging was performed on a Nano-Observer microscope (CS Instruments), equipped with a scanner allowing a maximum area of 100 μm × 100 μm. The images were acquired in contact mode, using a 240-AC-PP AFM tip (70 kHz, 2 N/m, tetrahedral

shape, <25 nm radius), in one direction only.

## 2.6 SPECTROSCOPY

### 2.6.1 Raman spectroscopy

#### 2.6.1.1 Principle

Raman spectroscopy relies on the inelastic scattering of light by polarizable molecules. Under the excitation of a monochromatic laser, molecules with polarizable vibrational states will interact with incident photons and release scattered photons with either lower (Stokes effect) or higher energy (anti-Stokes), as shown in Figure 48. The energy difference between the incident and scattered photons is directly related to the energy of the vibrational levels of the molecule, and is thus part of the chemical signature of the molecule. Raman spectra are usually displayed as a function of the wavenumber difference (expressed in  $\text{cm}^{-1}$ ), called the 'Raman shift', between the incident and scattered photons (see Figure Figure 48).

Vibration modes that are visible, or Raman 'active', are those corresponding to excited states of modified polarizability with respect to the initial vibrational state. In calcium carbonate, as in many carbonates,  $^{130}\text{CO}_3^{2-}$  vibrations and lattice modes (Ca-O vibrations) are thus visible.

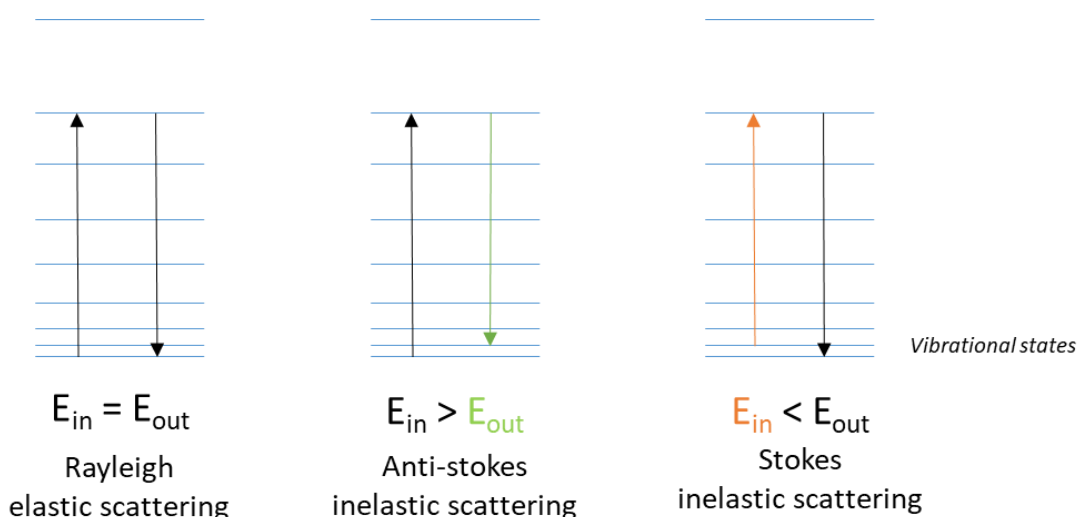


Figure 48 - Representation of Rayleigh, Stokes and anti-Stokes scattering.  $E_{in}$  is the energy of the incident photon, and  $E_{out}$  the energy of the scattered photon.

Lattice vibrational modes are visible at low wavenumbers, that is, under  $700\text{ cm}^{-1}$ . Around  $700\text{ cm}^{-1}$ , one can find the symmetric bending modes ( $\nu_{4a}$  and  $\nu_{4b}$ ). Symmetric stretching ( $\nu_1$ ) and asymmetric stretching ( $\nu_3$ ) are visible at around  $1060\text{ cm}^{-1}$  and  $1400\text{ cm}^{-1}$ , respectively. The asymmetric bending mode is not visible in Raman, but only in infrared spectroscopy.

#### 2.6.1.2 Literature review of calcium carbonate Raman spectra

As thermodynamically stable crystalline polymorphs of calcium carbonate, aragonite and calcite are widely reported among biominerals. However, ionic and organic inclusions in such

biominerals slightly modify the Raman signature of both polymorphs, resulting in a variety of reported spectra for biogenic CaCO<sub>3</sub> crystals. The corresponding Raman shifts, along with those of synthetically produced crystals and amorphous CaCO<sub>3</sub>, are presented in Table 4.

*Table 4 - Reported Raman shifts of several biogenic and synthetic calcium carbonates. Raman shifts extracted from Figure 49. are also displayed .*

<b>Polymorph</b>	<b>v1</b>	<b>v2</b>	<b>v4</b>	<b>Lattice modes</b>	<b>ref</b>
<b>Calcite biogenic</b>	1085	/	711	155, 282	21
<b>Calcite, synth</b>	1085	/	711	154, 280	131
	1085.9	/	712	155, 281.6	This study
<b>Vaterite, biogenic</b>	1074, 1079, 1090	873	680, 748	/	132
<b>Vaterite, synth</b>	1074, 1089	/	738, 750	301, 268, 118	131
	1074, 1080, 1090	874	666, 671, 684, 738, 743, 751	123, 146, 167, 208, 234, 271, 302, 326	133
	1073.8, 1080, 1089.5	/	737.4, 743.4, 750	117.9, 147.1, 177.4, 208.8, 266, 300, 334 .9	This study
<b>Aragonite, biogenic</b>	1083	/	702	149, 178, 189, 204, 246, 256, 270,280	134
<b>Aragonite, synth</b>	1084	/	700, 705	152, 205	131
	1085.5	/	702.3, 706.8	143.8, 154, 180.9, 191.5, 206.7, 215.4	This study
<b>ACC, biogenic</b>	1082	/	/	Broad band	133
	1085	/	/	Broad band	46

Raman spectra of the three anhydrous calcium carbonate polymorphs in their expected habitus (rhombohedral calcite, needle-like aragonite and flower-like vaterite) were acquired. These crystals were produced using the ADM synthesis (2.1.2) without polymer additive. The resulting spectra are reported in Figure 49.

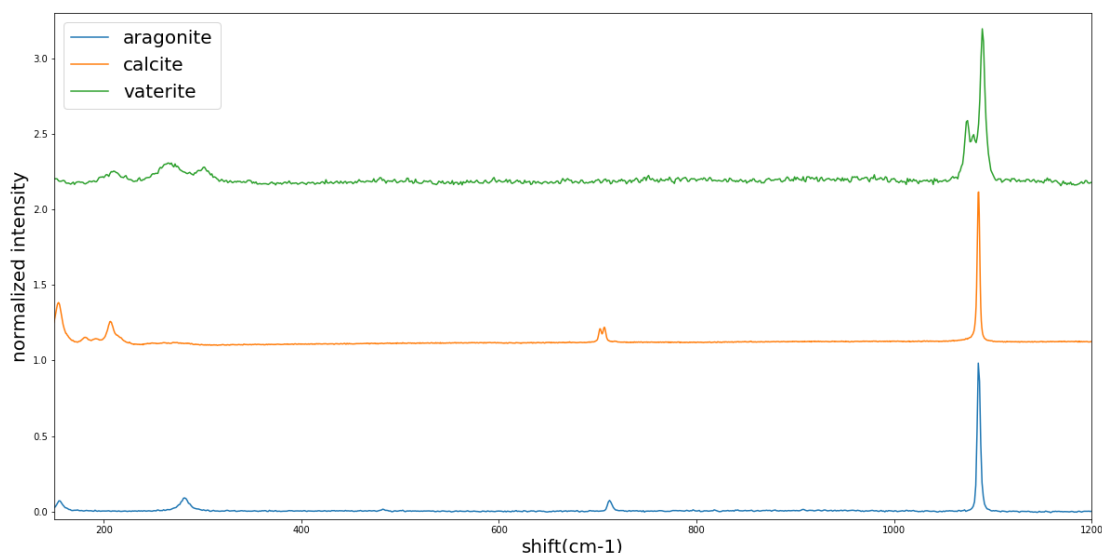


Figure 49 - Raman spectra of the three anhydrous  $\text{CaCO}_3$  polymorphs produced in a ADM synthesis in the absence of polymer additive: calcite (blue), aragonite (orange) and vaterite (green).

### 2.6.1.3 Experimental

The spectrometer used was a Renishaw Invia reflex with a YAG emitting at 532 nm, coupled to Wire software. The detector is a charge-coupled device. To avoid sample alteration, the laser was used to 5% of its full power, and the spectra were accumulated 20 times for 10 seconds.

## 2.6.2 Scanning Transmission X-ray Microscopy (STXM) and X-ray Absorption Spectroscopy (XAS)

### 2.6.2.1 Principle

STXM is a synchrotron-based scanning technique which allows recording absorption-contrast images, with a typical space resolution of 20 to 100 nm, while varying the incident photon energy (soft X-ray energy spans the interval 0.1 – 3 keV). By tuning the photon energy around the absorption edge of specific elements, STXM can provide elemental 2D mappings within the sample plane,<sup>135</sup> and, beyond that, information on the coordination symmetry of the considered element. The shape of the XAS spectrum actually depends on the transitions between core states and empty states, which are strongly sensitive to the local chemical environment. Thus, the electric field produced by the non-spherical distribution of charge (ligands) around the element results in the breaking of electron level degeneracies and in new allowed transitions (crystal field splitting).<sup>136</sup>

In the case of calcium, the 2p to 3d orbital transition results in the so-called  $L_{2,3}$  edges (differentiated by spin-orbit coupling), which are observable in the energetic range between 340 eV and 360 eV. Owing to crystal-field splitting, the  $L_{2,3}$  lines each split into two energy levels, corresponding to  $e_g$  and  $t_{2g}$  molecular orbitals.<sup>137,138</sup> The transition to these orbitals generates two peaks in the XAS spectrum, which energy distance is called the 'peak splitting'

and depends on the symmetry of the coordination polyhedra around the calcium ions and on the strength of the crystal field (see Figure 50). The peak splitting value,  $\Delta_0$ , is equal to the energy gap between the 3d orbitals  $e_g$  and  $t_{2g}$ . In an octahedral configuration,  $e_g$  have a higher energy than  $t_{2g}$ . In this configuration:

$$E_0 = E_{e_g} - 0.6 \times \Delta_0$$

Where  $E_0$  is the energy of the d-orbitals with soherically distributed ligands,  $E_{eg}$  is the  $e_g$  d orbitals energy, and  $\Delta_0$  is the peak splitting.

STXM technique at the calcium L-edge is used to study calcium carbonate samples. The symmetry of carbonate ions around calcium ions differs according to the  $\text{CaCO}_3$  crystalline polymorph. For calcite, it corresponds to the octahedral symmetry. The closer the distribution of the carbonate ligands around the calcium ions is to a spherical distribution, the smaller the peak splitting will be. Thus, measuring the peak splitting for the  $L_2$  and  $L_3$  transitions amounts to studying the level of organization of the  $\text{CO}_3^{2-}$  around the  $\text{Ca}^{2+}$  ions. The literature has indeed used this technique to probe the hydration level of synthetic<sup>139</sup> and biogenic<sup>55</sup> calcium carbonate.

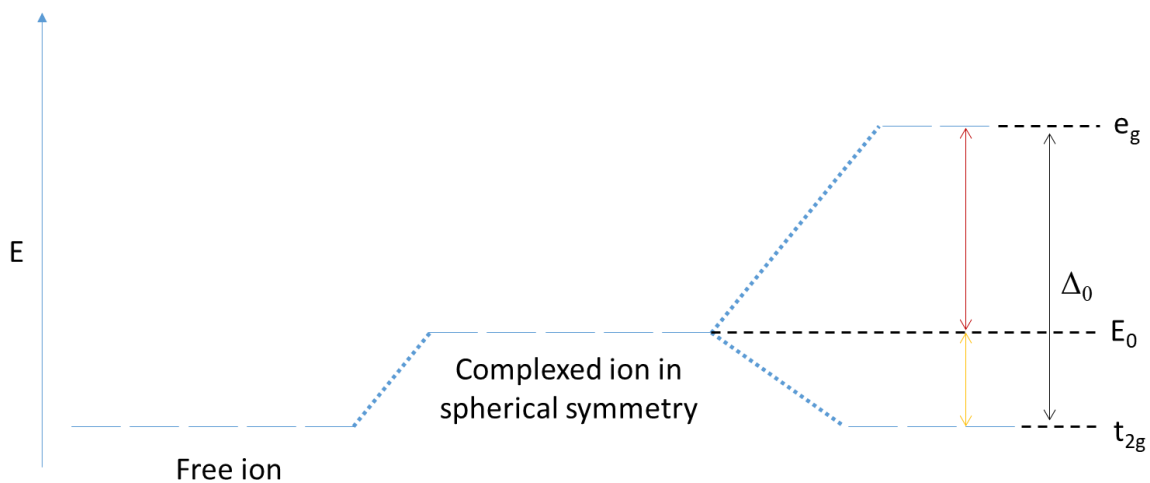


Figure 50 - Energy diagram of 3d orbitals. Left: free ion, all the orbitals have the same energy. Middle: the ion is complexed in a random way (in a spherical symmetry). The orbital energy rises, but in the same way for all orbitals. The energy level is called  $E_0$ , and is specific to the complexing ligand. Right: the ligands are organized in an octahedral symmetry around the central ion. The 3d orbitals of the central ion have 2 energy levels :  $e_g$  and  $t_{2g}$ . The energy difference between the orbitals is noted  $\Delta_0$ .

Little data is available about peak splitting values, but some are proposed by Gong *et al.* from biogenic ACC and calcite in Table 5.

Table 5 - Peak splitting value at  $L_2$  and  $L_3$  resonances extracted from Gong et al.<sup>55</sup>

	$L_3, \Delta_0$ (eV)	$L_2, \Delta_0$ (eV)
Hydrated ACC	<b>1.04</b>	<b>1.03</b>
ACC	<b>1.08</b>	<b>1.14</b>
Calcite	<b>1.22</b>	<b>1.24</b>

### 2.6.2.2 Experimental Set-up

X-ray absorption spectra at both the Ca L-edge and O K-edge were collected on the HERMES beamline of SOLEIL synchrotron. The STXM microscope (Research Instruments GmbH) was equipped with a 50 nm outer ring width Fresnel zone plate (FZP) lens and an order-sorting aperture to focus the monochromated, linearly polarized beam down to a diameter of approximately 60 nm. The TEM grid windows supporting the film samples were fixed on an XYZ scanning stage, Z being the direction collinear with the X-ray beam propagation and used to bring the sample onto the FZP focal plane. STXM images were captured by raster scanning the XY position and recording the transmitted photons using a photomultiplier tube (PMT). Hyperspectral images were also acquired by recording image stacks over the 345 – 360 eV interval with energy steps as low as 0.07 eV.

Energy stacks were recorded using the following parameters:

#### Calcium L-edge :

From 345 to 349 eV, step of 0.5 eV  
 From 349.07 to 356 eV, step of 0.07 eV  
 From 356.5 to 360 eV, step of 0.5 eV

#### Oxygen K-edge :

From 530 to 536 eV, step of 0.5 eV  
 From 536.2 to 555 eV, step of 0.2 eV  
 From 555.5 to 565 eV, step of 0.5 eV

Axis2000 software was used to correct sample drift during acquisition, thanks to Jacobsen's correction. Then, the intensity maps were converted into optical density (OD) maps, where  $OD = I/I_0$ , and  $I_0$  is the background intensity. Unfortunately, owing to the presence of at least residual calcium ions everywhere in our samples,  $I_0$  values could not be satisfactorily extracted from the image background. To overcome this problem, a linear extrapolation of the  $L_3$  pre-edge (in the range 345 to 348.5 eV) was made and used as  $I_0$ . Following this conversion step, a linear regression on the pre-edge part of the  $L_3$  peak (345 - 347.5 eV) was performed and used to zero all OD values in this part of the spectra. Then the spectra were normalized by performing a linear regression on the  $L_2$  post-edge (356.5 - 360 eV), which was used to set all



OD values to 1 over this energy range.

Finally, Lorentzian functions along with two arctangent functions were used to fit the data. The two arctangent functions are defined so that their zero value position coincide with the  $L_{3,2}$  edge position in the absence of peak splitting (as calculated from the calcite reference spectrum – see Figure 51), and their height has a 2:1 ratio. Finally, two Lorentzian functions are used for both  $e_g$  and  $t_{2g}$  deconvolution.

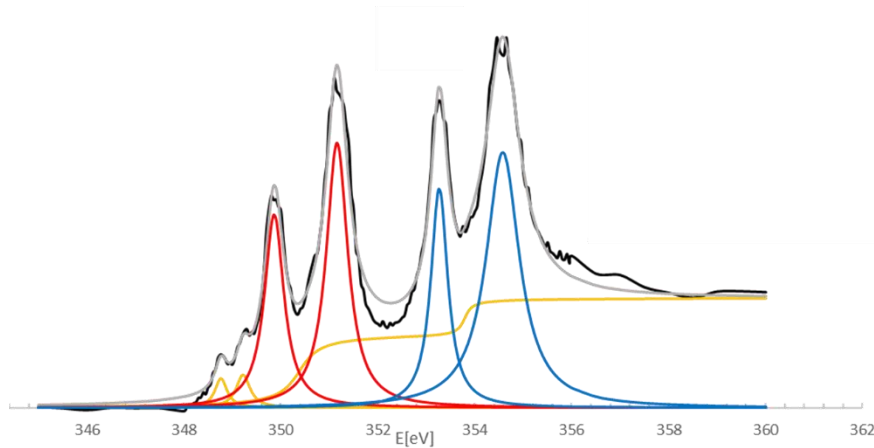


*Figure 51 - X-Ray absorption spectrum of commercial calcite (acquired by STXM). The spectrum deconvolution includes two arctangents (in yellow),  $L_3 t_{2g}$  ( $b'$ ) and  $e_g$  ( $b$ ) absorption peaks in red and  $L_2 t_{2g}$  ( $b'$ ) and  $e_g$  ( $b$ ) absorption peaks in blue. The sum of the deconvolution is in gray, while the experimental data are plotted as a black dashed line.*

The characteristic values, i.e. peak splitting and  $E_0$ , of the X-ray absorption spectrum of the commercial calcite are then extracted and presented in the following table:

	$L_3, \Delta_0$ (eV)	$L_2, \Delta_0$ (eV)	$E_0$ ( $L_2$ ) (eV)
Reference calcite	<b>1.31</b>	<b>1.29</b>	<b>353.78</b>

## 2.7 IN SITU SET-UPS

### 2.7.1 Synthesis reactor for *in situ* optical microscopy

A 150 mm Petri dish was drilled and equipped with an optical glass (Trajan, Serie 1). To allow the phase contrast objective to fit into the system without reducing the gas volume, a 3D printed lid was adapted and equipped with an optical glass window (PLA). The synthesis was carried as described (2.1.2 of this chapter) at 20°C under illumination. The formation and evolution of the interfacial film were followed by phase contrast microscopy with a 10x phase-

contrast objective. Note that due to the height of the solution, the Köhler setting cannot be optimal, so that light is unevenly distributed along the sample. This nevertheless allows a qualitative analysis in phase contrast mode. The reaction was followed with an Olympus DP74 camera, and the data were collected using Cellsens software.

### 2.7.2 Monitoring of environmental parameters

#### 2.7.2.1 pH

The pH of the solution directly controls the supersaturation of the solution with respect to calcium carbonate precipitation. Indeed, as presented in Figure 52, the acid-base equilibria between carbonate and its protonated species are governed by the pH value.

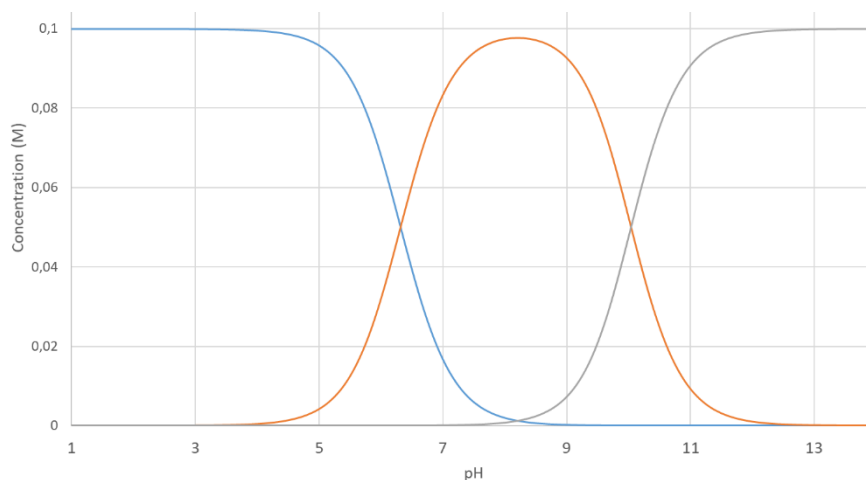


Figure 52 - pH dependence of the carbonate system, calculated from MINTEQ (the species distribution at fixed pH when introducing 100 mM of carbonate in solution are calculated every 0.1 pH unit). Blue curve :  $\text{H}_2\text{CO}_3$  concentration (mM) as a function of pH in 100 mM carbonate solution. Orange curve :  $\text{HCO}_3^-$  concentration (mM) as a function of pH in 100 mM carbonate solution. Gray curve :  $\text{CO}_3^{2-}$  concentration (mM) as a function of pH in 100 mM carbonate solution.

The pH was taken manually using pH strips (Fisher Brand) at the end of each experiment (from 1 min to 7 days). The small volume of solution (3 mL) used in standard syntheses actually did not allow *in situ* pH measurement using a pH electrode. A dedicated set-up including a pH microelectrode was therefore designed with a comparable gas volume (0.157 L) but enough liquid (6 mL) to make a pH measurement using a microelectrode. A  $(\text{NH}_4)_2\text{CO}_3$ -containing pellet, similar to the one used in standard syntheses was placed in the reactor, close to the Petri dish containing 6 mL of chosen solution. A 3D-printed gasket was used to ensure tightness between the reactor and the microelectrode. The pH micro-electrode (Metrohm 6.0234.100) was calibrated before each measurement using triple point calibration. The pH evolution as a function of time was recorded using the Tiamo software. As shown in Figure 53, both kinds of measurements provided fully compatible results.

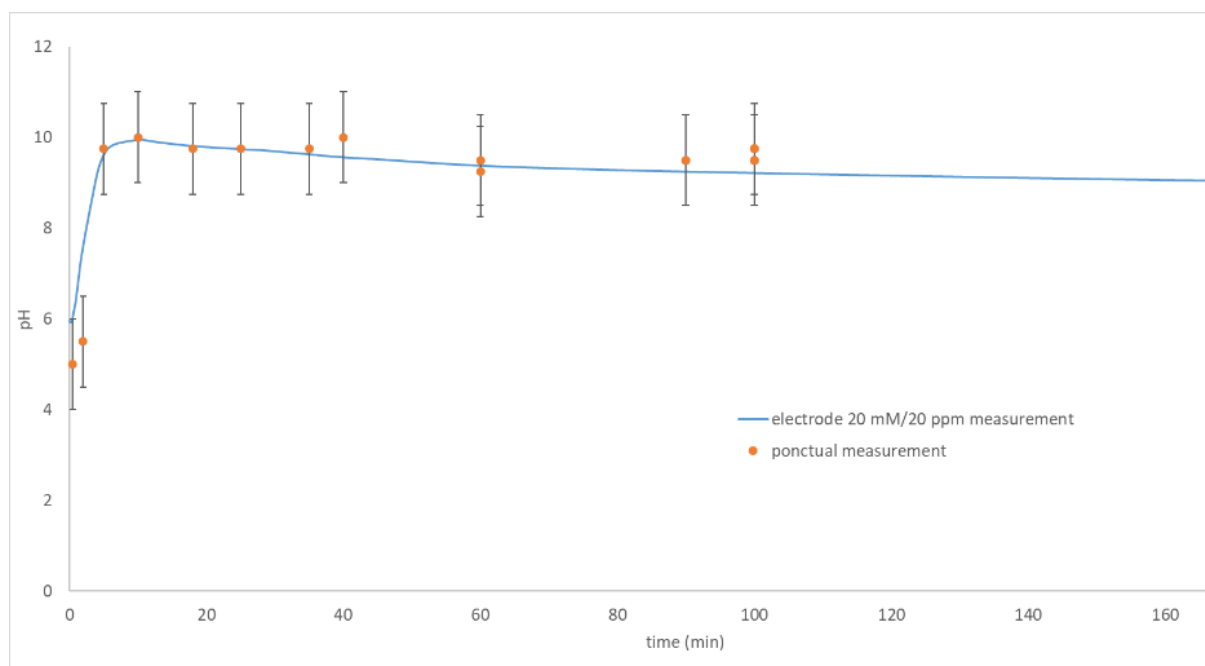


Figure 53 - Discrete pH measurements using pH strips - 3 mL solution (orange dots). The error is estimated to 1 pH unit due to visual pH identification. Continuous pH measurement using a micro-electrode in 6 mL solution. The solution considered here is  $[Ca^{2+}] = 20 \text{ mM}$  and  $[PANA] = 20 \text{ ppm}$ .

### 2.7.2.2 Atmospheric carbon dioxide

The partial pressure of  $CO_2$  in the reactor atmosphere was measured using a IR-based detector sensor (SCD30 from Sensirion). The sensor was exposed at least once a day to atmospheric  $CO_2$  pressure for calibration purposes. Using a laser-cutting device, the sensor was included directly in the reaction chamber and glued. An Arduino MKR Zero in association with an SD card was used to record the data (codes available in the appendix).

### 2.7.3 Humidity-controlled cell for *in situ* crystallization follow-up

In order to follow humidity-induced crystallization by *in situ* optical microscopy, we have designed a microscopy-adapted crystallization cell, which enables the active control of the relative humidity. The relative humidity is determined by a saturated salt solution (see 2.2.3) which is located in the reservoir (Figure 54.a). To achieve a fast establishment of the desired humidity rate, several key parameters are controlled, such as rapid closure, reduced volume of the chamber, homogeneous salt distribution, and airtightness. Two 3D-printed seals are placed in the cell to ensure airtightness, as represented in Figure 54.

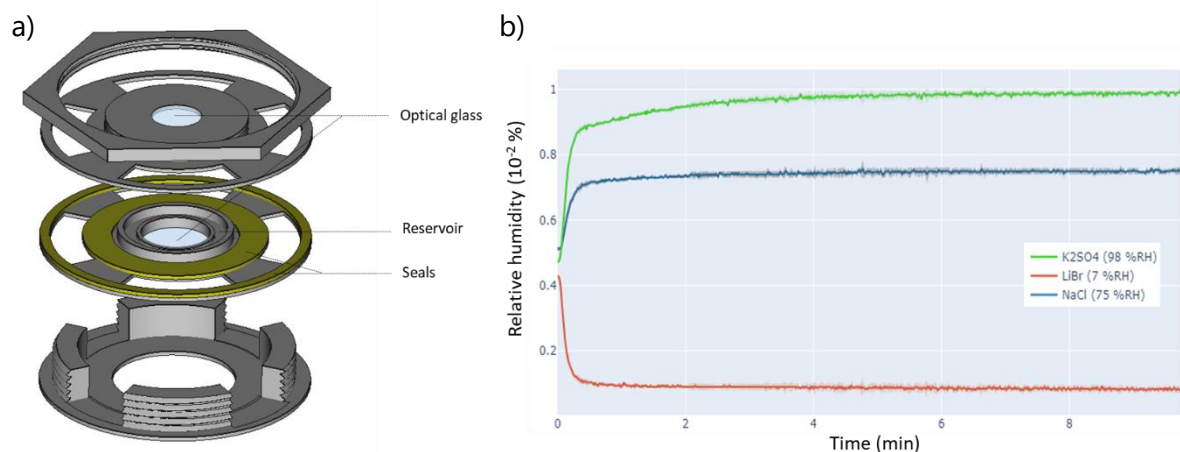


Figure 54 - In situ crystallization cell schematics and performance. a) Schematics of the in situ crystallization cell : seal is represented in yellow, optical glass windows in blue. b) Relative humidity inside the cell ( $t = 0$  min being the closing time) as a function of time.

To assess the reproducibility and speed of establishment of the atmosphere, relative humidity was measured using a HIH-4000 sensor controlled by an ARDUINO MEGA 250. Each measurement was triplicated and standard deviations are visible on each curve. The relative humidity inside the cell is established within a few minutes, as demonstrated in Figure 54.b.

### 3 AMORPHOUS CALCIUM CARBONATE FILM SYNTHESIS

---

In order to determine whether a liquid precursor could be involved in calcareous biomineralization, amorphous calcium carbonate films were produced at the air-solution interface using ammonia diffusion method (ADM) syntheses in the presence of sodium polyacrylate. The structural properties of these films were characterized at all scales (i.e. between the atomic to the mm scale) by using *ex situ* techniques, providing evidence that before crystallization they exhibit a space-filling nanostructure similar to the one of biominerals. In a second step, time-resolved studies were carried out at early reaction times, which highlighted a two-step mechanism of the film formation: first, a spinodal decomposition takes place at the interface, which defines a nanometer-thin smooth mineralized pattern in the form of interconnected micro-sized discs; then, the film thickens by irreversible aggregation of bulk amorphous nanoparticles. This scenario appears to be common to the two fully investigated syntheses ( $[Ca^{2+}] = 20$  mM,  $[PANa] = 20$  ppm and  $[Ca^{2+}] = 100$  mM,  $[PANa] = 50$  ppm) although in the case of a higher polymer content it leads to a fully continuous film with only remnants of discs.

#### 3.1 INTERFACIAL MINERALIZED FILM SYNTHESIS USING THE AMMONIA DIFFUSION METHOD

To ensure the reliability of our study, great care has been taken to set up a reproducible synthesis method. Indeed, as described in the chapter Materials and methods (section 2.1.1), ADM syntheses are extremely sensitive to variations of the environmental parameters, and in particular to variations of the gas atmosphere through time. The use of dry ammonium carbonate powder, sieved for a well-controlled particle size distribution and included in a KBr pellet, has greatly improved the reproducibility of the syntheses.

##### 3.1.1 Production of mineralized amorphous films in biomimetic syntheses

The ammonia-diffusion method was chosen for the syntheses because there is some evidence that it involves a dense liquid precursor. Following our hypothesis, it should be able to mimic some generic aspects of the calcareous biomineralization, especially the one involved in calcifying mollusks. Indeed ADM-produced synthetic minerals have much in common with biominerals (as described in Chapter 1).

Figure 55 recalls the ADM method and the main chemical species involved in the formation of the calcium carbonate film. The set-up (volumes and concentration used) is precisely described in the Materials and methods chapter. In short, a calcium chloride solution is put in contact with an atmosphere composed of  $NH_3$  and  $CO_2$  gases formed by the spontaneous decomposition of ammonium carbonate,  $(NH_4)_2CO_3$ . Ammonia dissolution induces a rapid increase of the solution pH, which in turn promotes  $CO_2$  dissolution, hydration and dissociation into carbonate species. This way, the calcium carbonate supersaturation index rises in the

solution, which soon leads to mineralized structure formation, especially at the interface.

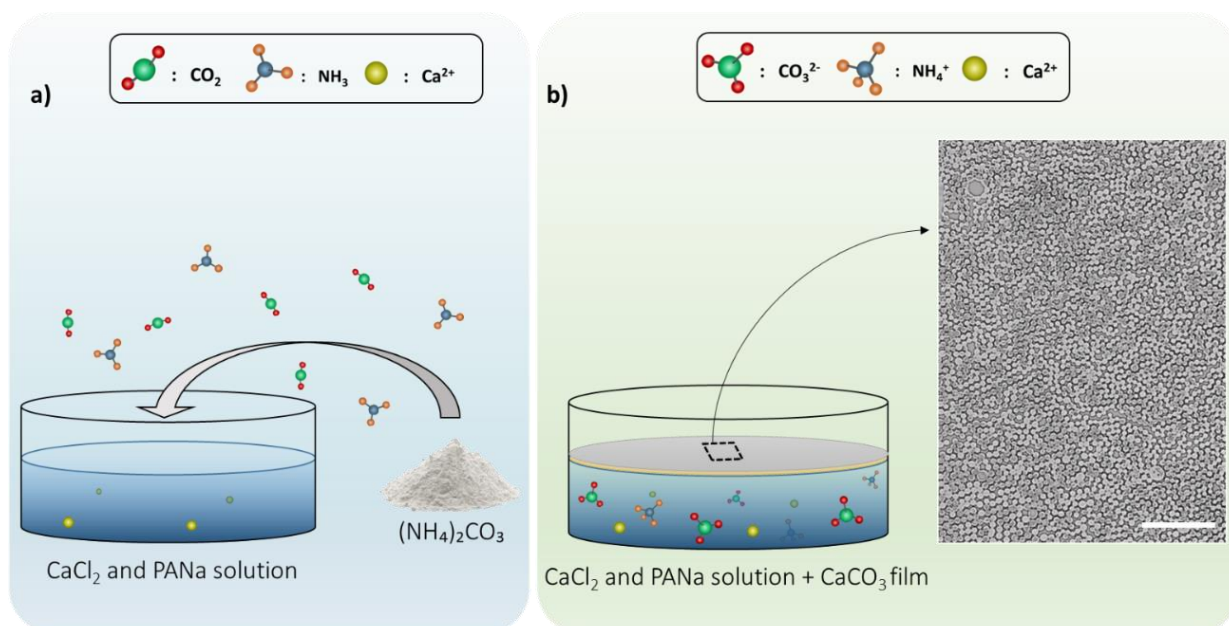


Figure 55 - Ammonia diffusion method (ADM). a) Chemical species during gas diffusion. A solution of calcium chloride is exposed to gaseous carbon dioxide and ammonia. b) The gaseous species dissolve in solution, leading to ammonium and carbonated species in bulk. The film formed at the interface is represented in gray and covers the free surface. The inset presents an optical microscopy transmission image of an interfacial film produced with  $[Ca^{2+}] = 20 \text{ mM}$ ,  $[PANa] = 20 \text{ ppm}$  and deposited on SiN membrane after 18 hours of reaction. Scale bar =  $50 \mu\text{m}$ .

When the synthesis is conducted in the absence of added polymer, crystalline rhombohedra (Figure 56.a) and flower-like crystals (Figure 56.b) are seen both at the gas-solution interface and at the bottom of the dish. A few needle-like crystals are also seen. Raman spectra, presented in the Materials and methods (2.6.1.3), identified these crystals as the anhydrous crystalline polymorphs of  $CaCO_3$ : calcite, vaterite and aragonite, respectively.

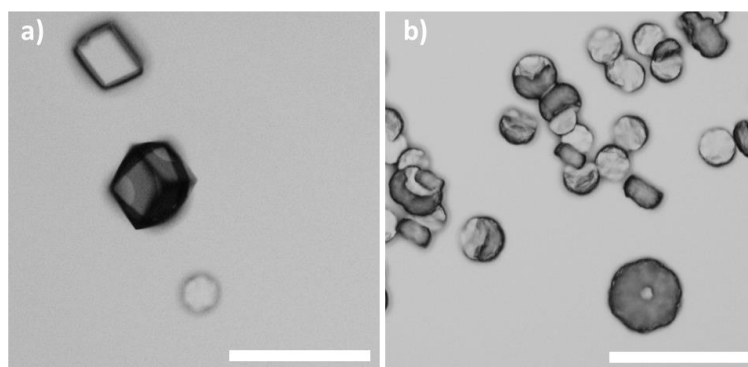


Figure 56 - Optical micrograph (AM) of crystals grown with the ADM method (without added polymer).  $100 \text{ mM}$  calcium chloride solution exposed to ammonium carbonate for 18h. a) Flower-like crystals b) Rhomboedral crystals. Scale bar =  $50 \mu\text{m}$

In order to induce a Polymer Stabilized Liquid precursor (PSLP) mechanism, polymer molecules are added in the solution. As discussed in the previous chapter, sodium polyacrylate has been selected owing to its highly acidic character. Performing biomimetic syntheses additionally requires using millimolar range of calcium concentration (see IntroductionIntroduction), with little polymer amount (1.1.1).

In the presence of added polyelectrolyte, the dissolution of the gaseous species and their chemical reaction with the other species in solution lead to the formation of an interfacial mineralized film. Figure 55.b shows a typical film formed at the interface when the concentrations in solution are 20 mM of calcium chloride and 20 ppm of sodium polyacrylate. These films appear to be made of amorphous calcium carbonate, as further discussed in section 3.1.4.

The previous observations have been made after the collection of the film sample on a solid substrate in order to allow *ex situ* analyses. In this case, a drying step is necessary to stop the reaction and prevent *ex situ* precipitation/crystallization events. The film sample is therefore dried under vacuum (0.2 bar) and then stored in a dry atmosphere before further analysis or use. Dry storage is provided by placing the film in a LiBr-regulated atmosphere, that is, at 6-7% RH (see the set-up presented in 2.1.4).

### 3.1.2 Characteristic pattern of the mineralized films synthesized at low calcium and polymer concentrations (20 mM, 20 ppm)

The films produced at low polymer concentration (20 ppm) present a striking particularity: they exhibit a pattern of interconnected discs. This disc pattern is seen both using *ex situ* and *in situ* imaging (section 2.1.3), so that one can guarantee it is not due to some artifact related to film sampling or drying. In addition, it appears for the two kinds of synthesis described in the Materials and methods, as long as the polymer concentration is 20 ppm, which are:

- the "cap synthesis", for which approximately 18 hours of reaction is needed to obtain a film.
- the "pellet synthesis", for which approximately one hour is needed to obtain a film.

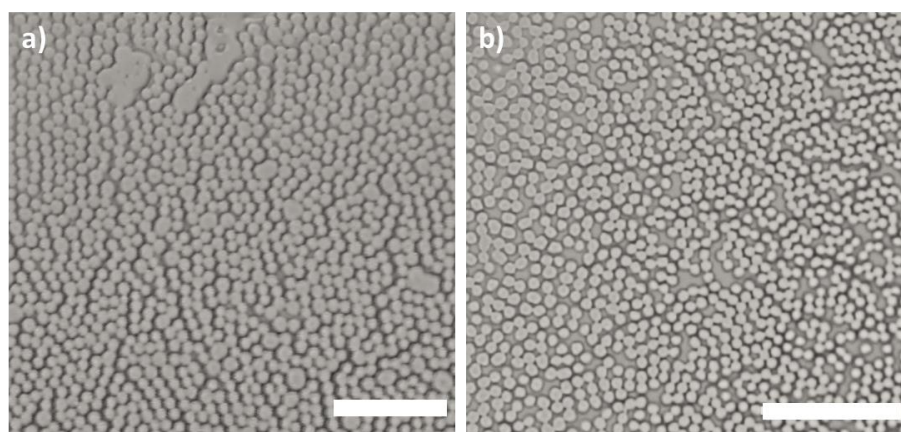


Figure 57 - Optical micrographs (AM) of the interfacial film acquired in situ. The amount of PANa in both syntheses is 20 ppm a) Cap synthesis, with 50 mM of  $\text{CaCl}_2$  b) Pellet synthesis, with 20 mM of  $\text{CaCl}_2$ . Differences in lighting and image sharpness are due to the use of two different microscopes and cameras. Scale bar = 50  $\mu\text{m}$ .

A qualitative analysis of the optical micrographs of the film reveals the presence of a homogeneous disc population. Using machine learning for object detection, statistical size distributions can be obtained (see detailed procedure in Materials and methods). Corresponding histograms are presented in Figure 58. Size distributions are 5.6  $\pm$  1.0  $\mu\text{m}$  for the cap synthesis and 4.1  $\pm$  0.7  $\mu\text{m}$  for the pellet synthesis, which confirm the narrowness of the disc size distribution.

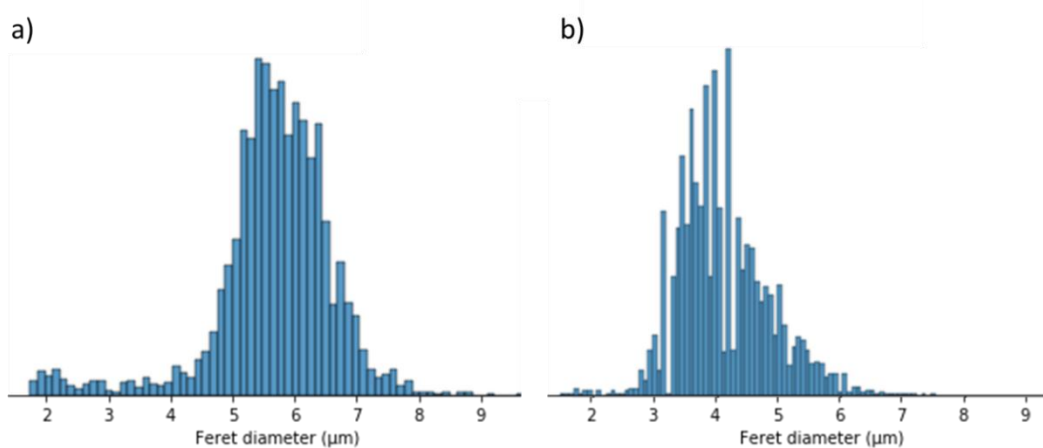


Figure 58 - Feret diameter distribution calculated from image analysis. a)  $[\text{Ca}^{2+}] = 20 \text{ mM}$ ,  $[\text{PANa}] = 20 \text{ ppm}$  cap synthesis. Data from two separated syntheses b)  $[\text{Ca}^{2+}] = 20 \text{ mM}$ ,  $[\text{PANa}] = 20 \text{ ppm}$  pellet synthesis. Data from two separated syntheses. The Feret diameter, as presented in the Materials and methods, is used to retrieve the diameter of a circular object.

The disc pattern (appearance, size distribution), although evidenced during my PhD work in more than sixty syntheses, is very sensitive to any change in the synthesis parameters (relative humidity, ammonium carbonate granularity for instance). Unwanted deviations from the reference conditions can for example produce larger discs, continuous films or even a lack of interfacial film. This is fully in line with the reported difficulty, mentioned by different scientific teams, to replicate ADM syntheses<sup>109</sup> owing to its high sensitivity to environmental parameter changes. However, thanks to the specificity of the disc pattern, it was quite easy to discard



problematic syntheses, thus ensuring the reliability of our results

### 3.1.3 Macroscopic morphology tuning with synthesis parameters

For a given set of synthesis parameters, the film morphology after 18 hours of reaction appears highly reproducible. However, varying the concentrations of calcium and polymer creates a variety of film morphologies. We varied the composition of sodium polyacrylate from 20 ppm to 100 ppm, and the calcium concentration from 20 mM to 100 mM. As a consequence, the observed morphology ranges from discontinuous films (with a disc-like pattern) to continuous films.

At low polymer concentration (20 ppm), the disc morphology is present whatever the amount of calcium in solution (Figure 59.a .b .c). However, at calcium concentration above 20 mM, image analysis cannot effectively separate the discs, as these are very often fused to each other. Still, the disc diameter appears unchanged in Figure 59.a .b and .c. Increasing the calcium amount leads to a denser film, to the point that for 100 mM of calcium the discs are barely visible.

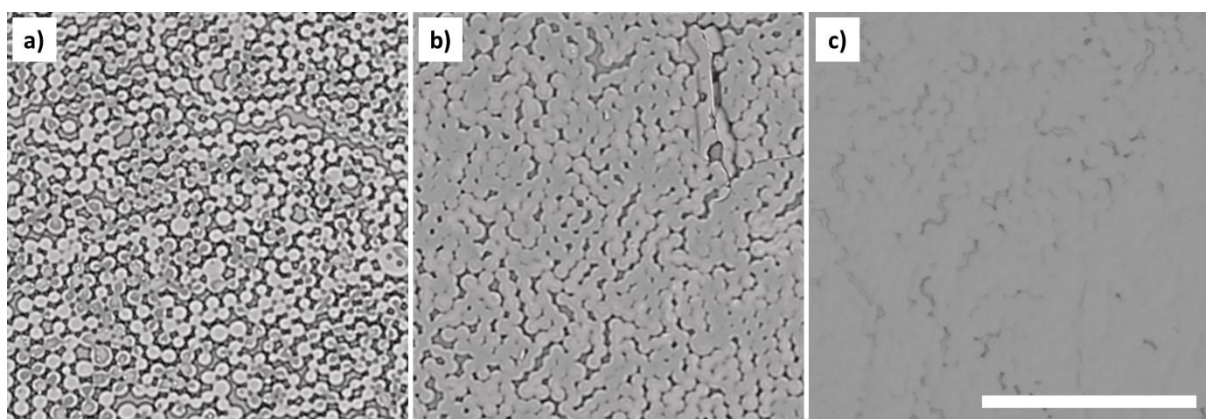


*Figure 59 - Optical Micrographs (AM) of the morphology exhibited by the interfacial film upon variation of the calcium content. The films are taken out after 18 hours of cap synthesis. From left to right, calcium concentration is 20 mM, 50 mM and 100 mM respectively. The polymer concentration is kept at 20 ppm. Scale bar = 50  $\mu$ m.*

Raising the polymer concentration while maintaining the calcium content constant results in the disappearance of the discs. As illustrated by Figure 60, increasing the amount of polymer results in the widening of the discs (see the larger structures in Figure 60.b) and leads to a continuous film at 100 ppm.

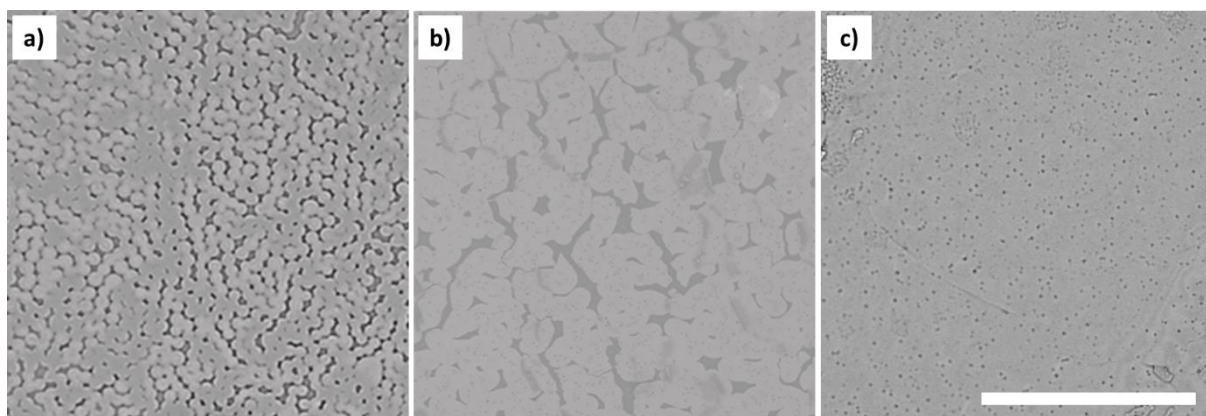


Figure 60 - Optical Micrographs (AM) of the morphology of the interfacial film upon variation of the polymer content. The films are taken out after a) 18, b) 16 and c) 18 hours of cap synthesis. From left to right, polymer concentration is 20 ppm, 50 ppm and 100 ppm respectively. The calcium content is kept at 50 mM. Scale bar = 50  $\mu\text{m}$ .

Thus the morphology of the interfacial mineralized structures at long reaction times ( $\sim 18\text{h}$ ) evolves from discontinuous films, at 20 ppm, to continuous films at polymer concentration above 50 ppm.

At the microscale, the disc pattern, characteristic of discontinuous films (Figure 61.a,  $[\text{Ca}^{2+}] = 20\text{ mM}$ ,  $[\text{PANA}] = 20\text{ ppm}$ ), is visible on continuous films as well (Figure 61.b,  $[\text{Ca}^{2+}] = 100\text{ mM}$ ,  $[\text{PANA}] = 50\text{ ppm}$ ), but as traces only. These remnants of discs are undetectable by optical microscopy, as they are poorly contrasted. Still, they reveal a common mechanism in the formation of all interfacial films.

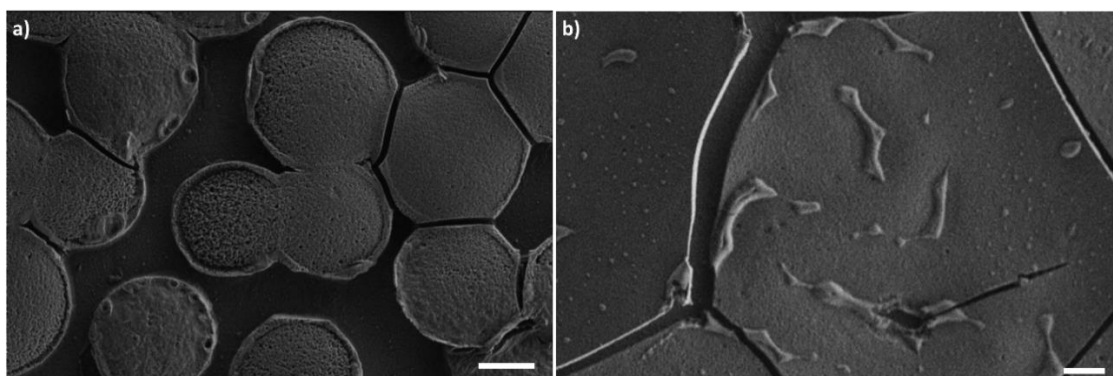


Figure 61 - Electron micrographs (SEM) showing the disc morphology in two synthesis conditions. a)  $[\text{Ca}^{2+}] = 20\text{ mM}$ ,  $[\text{PANA}] = 20\text{ ppm}$ , 18 h of reaction, heated  $300^\circ\text{C}$  3h. HE-SE detector, 1 kV. Scale bar = 2  $\mu\text{m}$ . b)  $[\text{Ca}^{2+}] = 100\text{ mM}$ ,  $[\text{PANA}] = 50\text{ ppm}$ , 18 h of reaction, heated  $300^\circ\text{C}$  3h. Traces of disc morphology are visible on the continuous film. HE-SE detector, 1 kV. Scale bar = 2  $\mu\text{m}$ . Cracks in both a) and b) are induced by the heat treatment. As presented in section 4.1.1, due to the heat treatment, the films are crystalline.

### 3.1.4 Assessment of film amorphism (local atomic ordering)

Right after sampling and drying, the amorphism/crystallinity of the film is probed using birefringence microscopy (BM). As presented in the Materials and methods section (2.3.2),

birefringence imaging is a tool to identify whether our film is crystalline or amorphous, as only crystalline forms of calcium carbonate are birefringent. After 18 hours of reaction (with either cap or pellet synthesis), the film, either continuous or discontinuous depending on the synthesis conditions, is non-birefringent, as exemplified in Figure 62.b, and hence amorphous. The observations are completed by waveplate-assisted birefringence microscopy (WBM) imaging, as it allows both to image the film morphology at the micron scale and to detect any optical anisotropy (Figure 62.c).

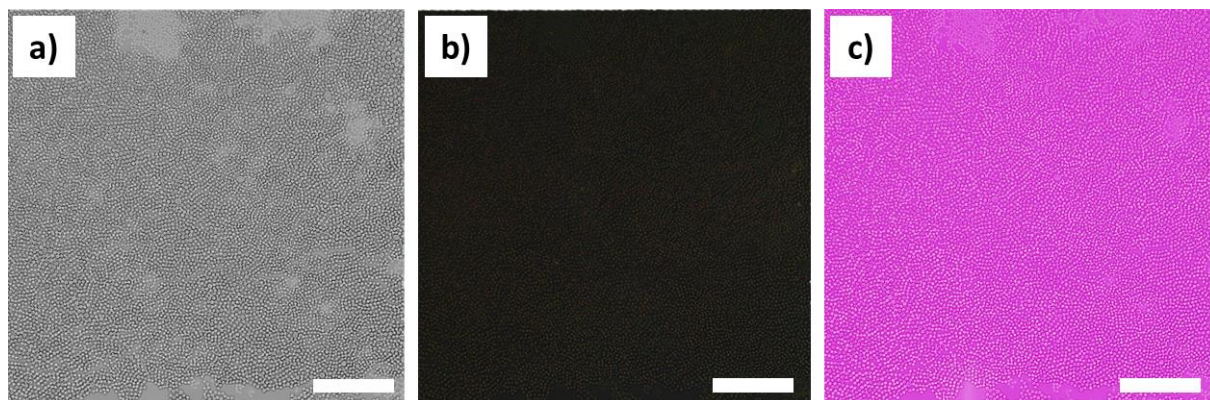


Figure 62 - Optical micrographs of the disc-patterned film ( $[Ca^{2+}] = 20 \text{ ppm}$ ,  $[PANa] = 20 \text{ mM}$ ) sampled after 18h of reaction. Right after sampling, the film is observed in a) OM b) BM. The black coloration indicates that the material observed is optically isotropic. c) WBM. The pink coloration indicates that the material observed is optically isotropic. Scale bar =  $100 \mu\text{m}$ .

In addition, Raman spectroscopy was used to study the differences that may exist between amorphous films collected at different times, or produced from different initial solution compositions. As described in the Materials and methods amorphous calcium carbonate owns a specific signature with a broad band in the  $\nu_1$  region. The Raman spectra of the films synthesized at  $[Ca^{2+}] = 20 \text{ mM}$ ,  $[PANa] = 20 \text{ ppm}$  and  $[Ca^{2+}] = 100 \text{ mM}$ ,  $[PANa] = 100 \text{ ppm}$  respectively, presented in Figure 63, both exhibit a broad  $\nu_1$  band at  $1081 \text{ cm}^{-1}$ . The width of the  $\nu_1$  band is about  $30 \text{ cm}^{-1}$ , larger than its crystalline counterparts, as expected. These features are in full agreement with the Raman spectra of synthetic and biogenic ACC reported in the literature (see section 2.6.1.2).

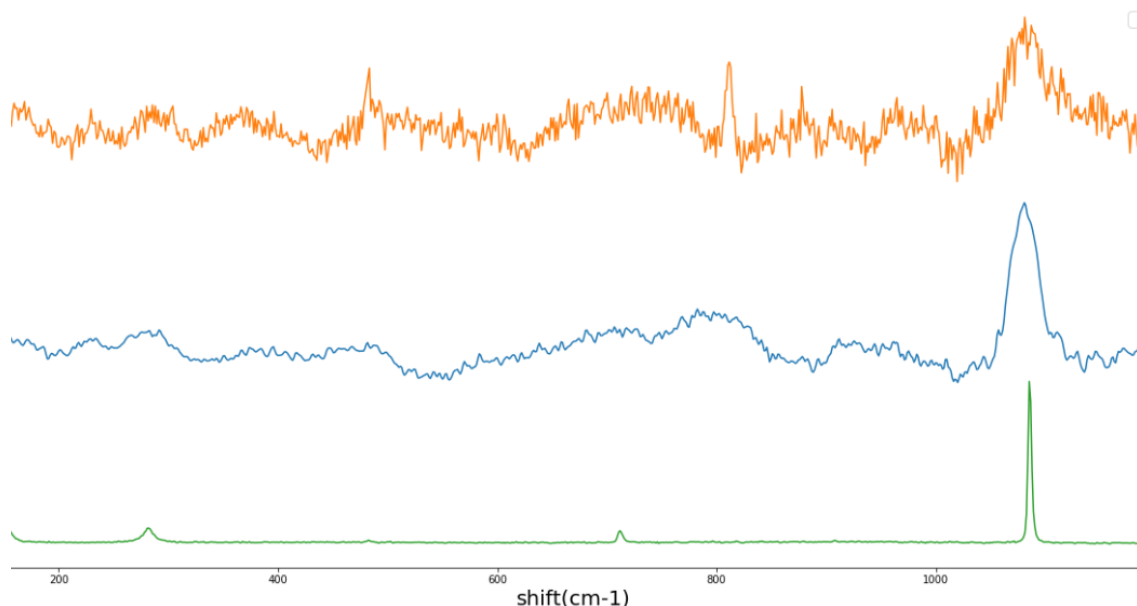


Figure 63 - Typical Raman spectra of film samples produced at  $[Ca^{2+}] = 20 \text{ mM}$ ,  $[PANa] = 20 \text{ ppm}$  (17h sampling) in orange and at  $[Ca^{2+}] = 100 \text{ mM}$ ,  $[PANa] = 100 \text{ ppm}$  (17h sampling) in blue. The spectrum of calcite is shown in green as a reference.

The  $\nu_1$  position is independent of the sampling time (1h to 28h), as demonstrated by the values reported in Table 2. The spectroscopic signature of ACC is similar for all different concentrations investigated (Figure 63) and different sampling times.

Table 6 - Position and width of the ACC  $\nu_1$  band at different sampling times for  $[Ca^{2+}] = 20 \text{ mM}$ ,  $[PANa] = 20 \text{ ppm}$ .

Sampling time	Ammonium carbonate source	Shift ( $\text{cm}^{-1}$ )	Width ( $\text{cm}^{-1}$ )
1h30	Pellet	1080	39
28h	Pellet	1080	27
17h	Cap	1081	40

The protocol for amorphous conservation appears fully effective in preserving the film characteristics for at least three months after sampling. As shown in Figure 4, both the birefringence and spectral properties of the amorphous film sample remained unchanged over this period.

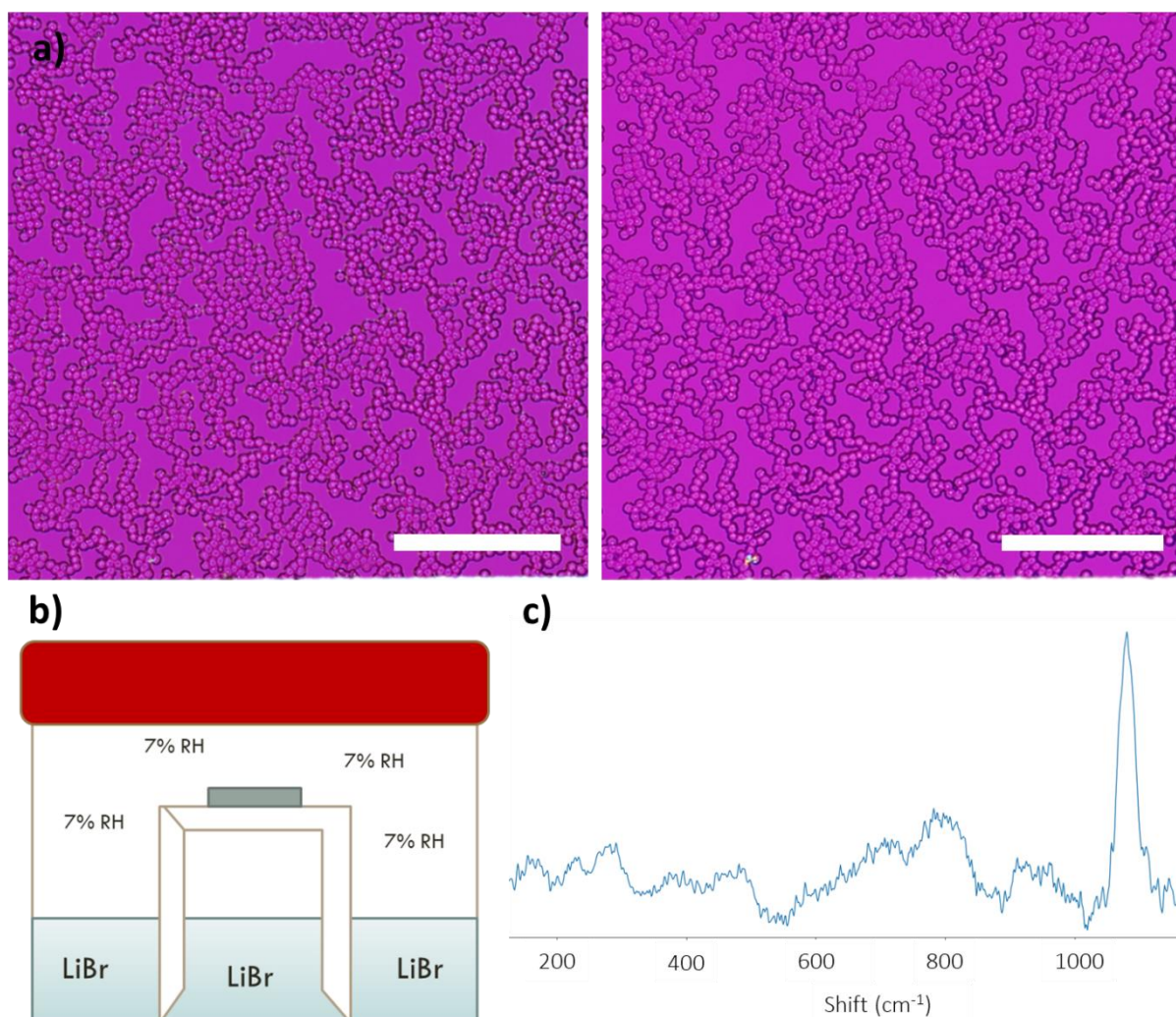


Figure 64 - a) Optical micrograph (WBM). Left image is made right after sampling, right image is made after a three-month storage. b) Schematic of the set-up used for long-term conservation. Saturated LiBr solution controls the relative humidity of the atmosphere. Sample (represented with a gray square) is placed above the solution. c) Raman spectrum of a film sample ( $[Ca^{2+}] = 100 \text{ mM}$ ,  $100 \text{ ppm}$ ), collected after 17 hours of reaction) and kept for 3 months in LiBr. Scale bar =  $100 \mu\text{m}$ .

Amorphous calcium carbonate films could be successfully produced using the ADM method with some added sodium polyacrylate. The syntheses resulted in either discontinuous or continuous films, depending on the salt and polymer concentrations used, all of which exhibit micron-sized discs as, at least transient, microscale structures.

## **3.2 STRUCTURAL PROPERTIES OF THE INTERFACIAL AMORPHOUS FILMS**

Continuous films have a biomimetic aspect, as they resemble the mineral layers deposited in oyster shells. However, the peculiar morphology of the discontinuous films, composed of disc-like units, can be very helpful to understand the film formation and the mechanisms at play during the crystallization process, as they are very easy to follow. For a more thorough investigation, we therefore focused on the two following conditions: the condition  $[\text{Ca}^{2+}] = 20$  mM;  $[\text{PANa}] = 20$  ppm, which produces discontinuous films with a disc pattern, and the condition  $[\text{Ca}^{2+}] = 100$  mM;  $[\text{PANa}] = 50$  ppm, for which continuous films were observed. Further mention of “disc patterned” or “continuous” film will refer to these two conditions.

### **3.2.1 Structural features at the microscale**

The in-plane film morphology was observed using scanning electron microscopy. The observed discontinuous films (Figure 65.a) show fused discs of a few microns ( $\sim 4\mu\text{m}$ , 3.1.2), in agreement with the optical microscopy images. A corona of pores (highlighted in the inset of Figure 65.a) is visible at the disc edges. The discs appear rather smooth, although a poorly defined nanostructure can be visible in some parts of the discs.

The continuous film is mostly homogeneous, but it is speckled by bumps on its surface (white arrow in Figure 65.b). Remnants of discs are present on some parts of the film (left side of Figure 65.b). The edges of the discs are made of a porous layer (red arrow in of Figure 65.b), similar to the one visible in discontinuous films. The film is nanostructured, as presented in the inset of Figure 65.b. Large cracks distributed over the film, resulting from heat treatment (detailed in the next paragraph), create wrinkles in the continuous film.

Due to the limited availability of the equipment, SEM observations could only be performed on amorphous disc patterned films, whereas in the case of the continuous films there were performed on heated films. Still, it is unlikely that the observed nanostructure in the latter case would be due to heating, as heating of ACC film at  $300^\circ\text{C}$  for 3 hours has been shown to rather induce a solid-state shape-preserving transformation.<sup>96</sup>

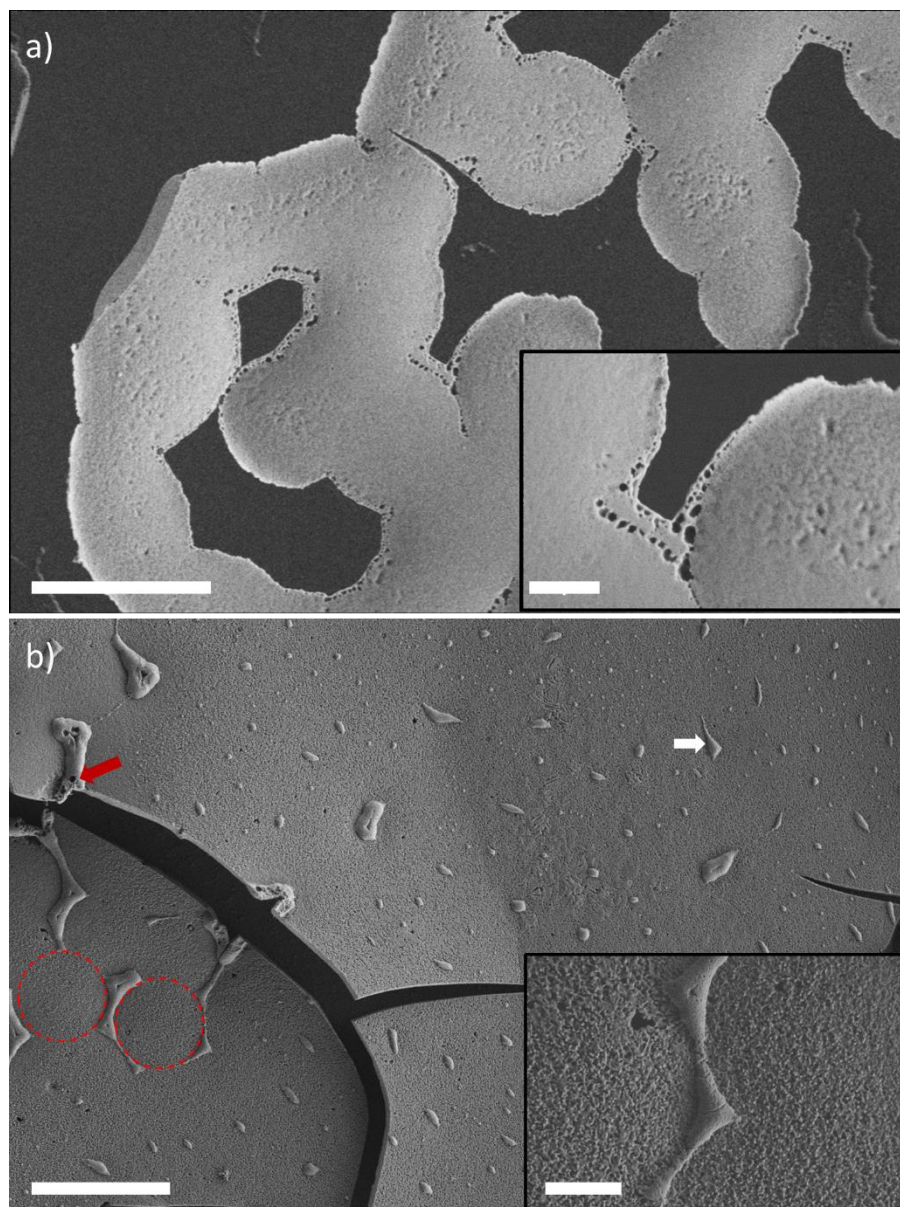


*Figure 65 - Electron micrographs (SEM) of disc patterned and continuous films. a) Amorphous disc patterned Calcium carbonate film ( $[Ca^{2+}] = 20 \text{ mM}$ ,  $[PANa] = 20 \text{ ppm}$ , 18.5 h). Scale bar = 5  $\mu\text{m}$ . Inset, zoom. HE-SE detector, 2 kV. Scale bar = 1  $\mu\text{m}$ . b) Crystallized continuous Calcium carbonate film ( $[Ca^{2+}] = 20 \text{ mM}$ ,  $[PANa] = 20 \text{ ppm}$ , 17 hours). The white arrow points towards the matter scattered on the continuous film. The red arrow highlights the porous matter at the end of remnant discs (highlighted by red dashed circles). HE-SE detector, 1 kV. Scale bar = 5  $\mu\text{m}$ . Inset, zoom. Scale bar = 1  $\mu\text{m}$ .*

Further SEM observations, performed at the film edges, allowed us to provide an estimate of the film thickness. These observations were made on cracks available in the film by tilting the sample by 70° (Figure 66). Observations of disc patterned films reported in Figure 66.a, Figure 65.a and Figure 67.a were carried out on amorphous material. The amorphous nature of the sample, following vacuum and beam exposure, was verified by birefringence microscopy on the imaged area. Partial crystallization was noticed in some regions of the film, not presented here. On these films, the vacuum inside the SEM chamber was sufficient to peel the film off and reveal the film edges through the cracks, allowing for a thickness evaluation of 640 +/- 90

nm.

In the case of continuous amorphous films, cracks were induced by heating the sample very fast (sample deposited on already hot heating plate, at 300°C) resulting in rapid crystallization of the film. As a result of these SEM observations, the film thickness could be estimated to and 530 +/- 40 nm for the continuous film.

A closer look at Figure 66.a shows that in the case of the disc-patterned film the thickness is not actually constant but rather varies along the discs, the thickness being usually maximum at the center of the discs, and much smaller at the periphery. In Figure 66.a the orange dashed lines highlight such a thickness variation: the circular dashed line outlines a thin disc-shaped layer, while the straight dashed line highlights the increase in thickness at the center of the disc. This thickness variation results in areas where the thin layer was torn and did not detach from the substrate under vacuum (orange arrow in Figure 66 a).

On the continuous film, a layer is visible everywhere along the edge, which is illustrated by the plain white arrows in Figure 66 b).



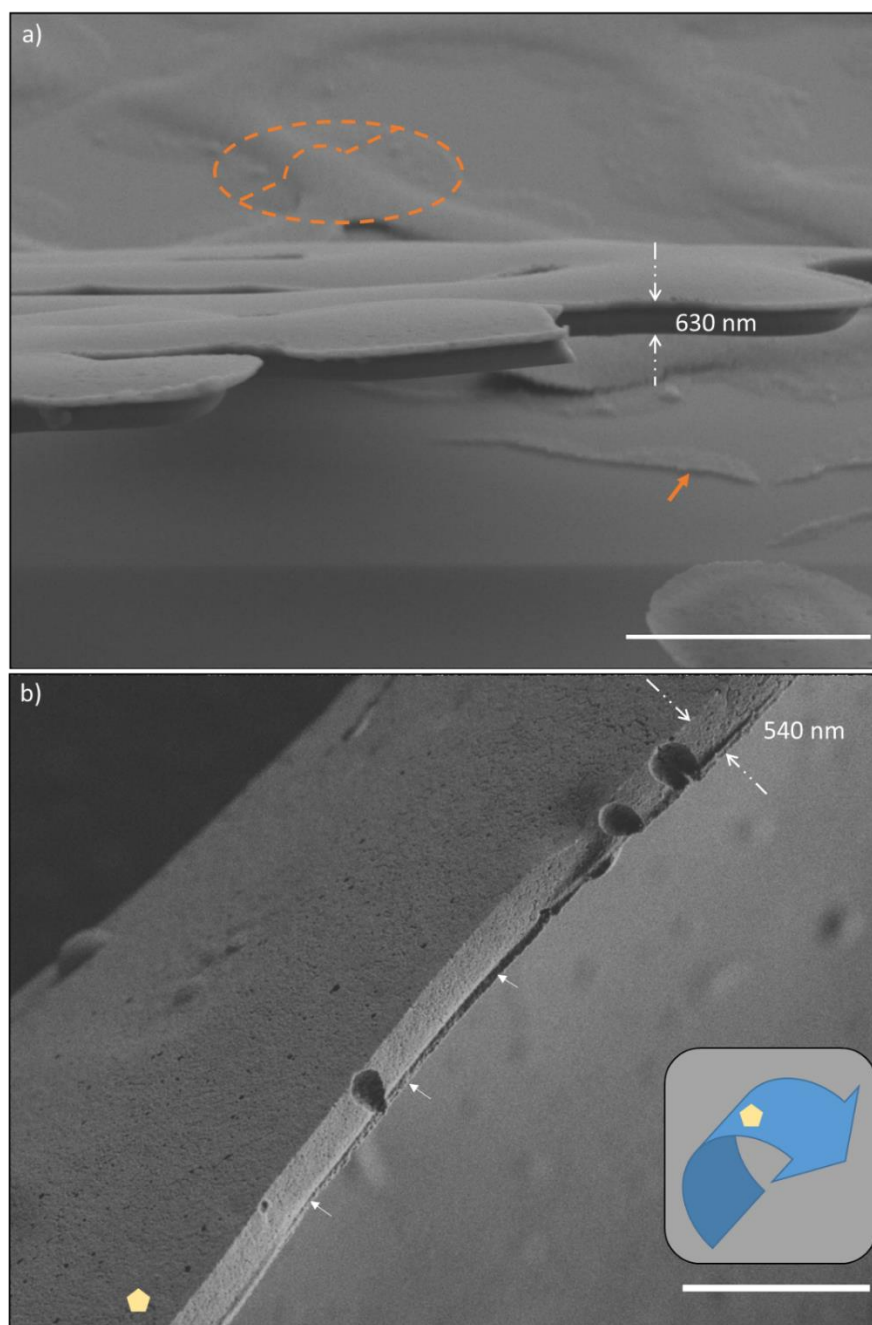


Figure 66 - Electron micrographs (SEM) leading to film thickness estimate. The thickness measured between white dashed arrows is written in both a) and b). a) Disc-pattern film ( $[Ca^{2+}] = 20 \text{ mM}$ ,  $[PANa] = 20 \text{ ppm}$ ). The dashed orange line underlines the thickness variation of a thin disc, the thickness being maximum at the center of the line. The orange arrow highlights some part of the film that did not detach from the substrate under vacuum. On this image, only the side initially in contact with the air-solution interface is visualized. HE-SE detector, 5 kV. Scale bar =  $5 \mu\text{m}$ . b) Continuous film ( $[Ca^{2+}] = 100 \text{ mM}$ ,  $[PANa] = 50 \text{ ppm}$ ) that has detached from the substrate. The side initially in contact with the solution is indicated by a yellow pentagon. For better visualization, a schematic representation (in blue) of the area investigated has been added. HE-SE detector, 1 kV. Scale bar =  $2 \mu\text{m}$ .

### 3.2.2 Structure at the nanoscale

SEM observations on broken edges have revealed the internal structure of the film (Figure 67). Particles of a few tens of nanometers are packed in a space-filling manner (Figure 67 a and b), thus forming a very homogeneous structure.

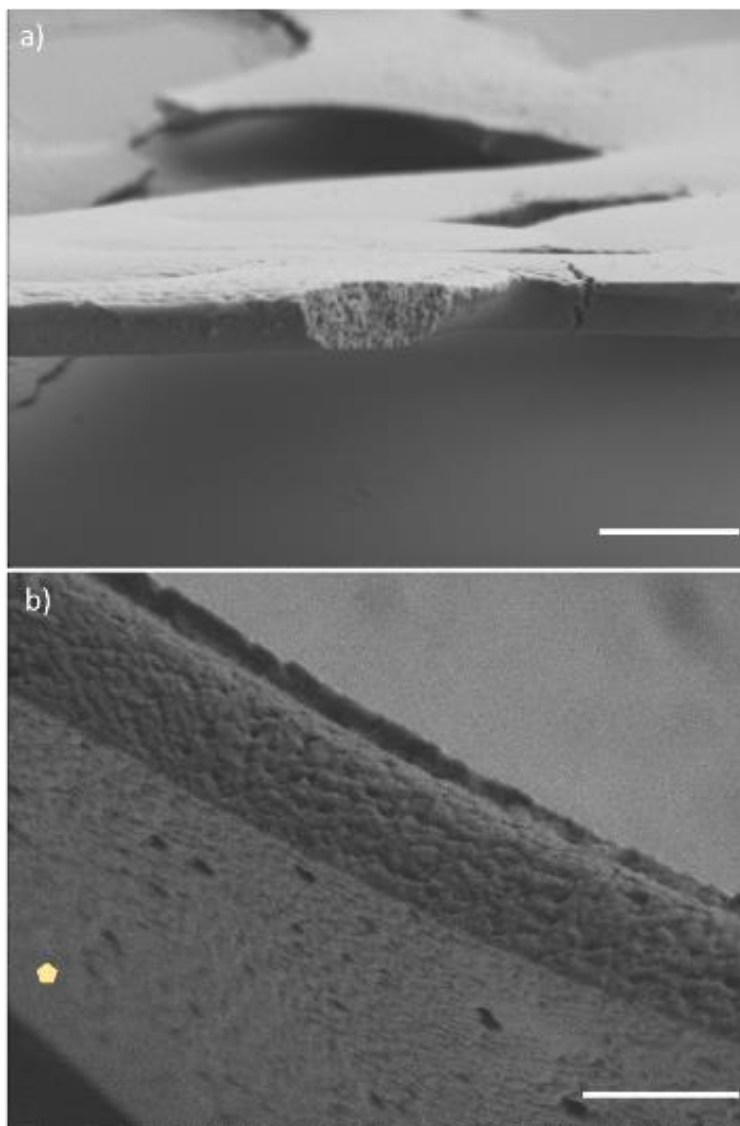


Figure 67 - Electron micrographs (SEM) of the film internal structure. Broken edges are investigated in a) Disc-pattern film ( $[Ca^{2+}] = 20$  mM,  $[PANA] = 20$  ppm) HE-SE detector, 2 kV. Scale bar = 1  $\mu$ m. b) continuous film ( $[Ca^{2+}] = 100$  mM,  $[PANA] = 50$  ppm), heated at 300°C. The face initially in contact with the solution is indicated by a yellow pentagon. HE-SE detector, 1 kV. Scale bar = 500 nm.

The two superimposed layers which compose the continuous film that were visible in Figure 66 b are again visible in the magnified picture of a broken edge shown in Figure 67 b. This picture reveals an upper layer (in blue), a bottom layer (in pink) and a pear-shaped hole that extends through the entire film thickness (Figure 68). The blue and pink areas have a similar nanostructure. The separation between the two layers appears to be a region of accumulation of pores (see the white arrow that points to this region in Figure 68). The pear-shaped holes

are commonly observed at the broken edges of the continuous film (three of them are visible on Figure 66b), likely because they correspond to points of film fragility.

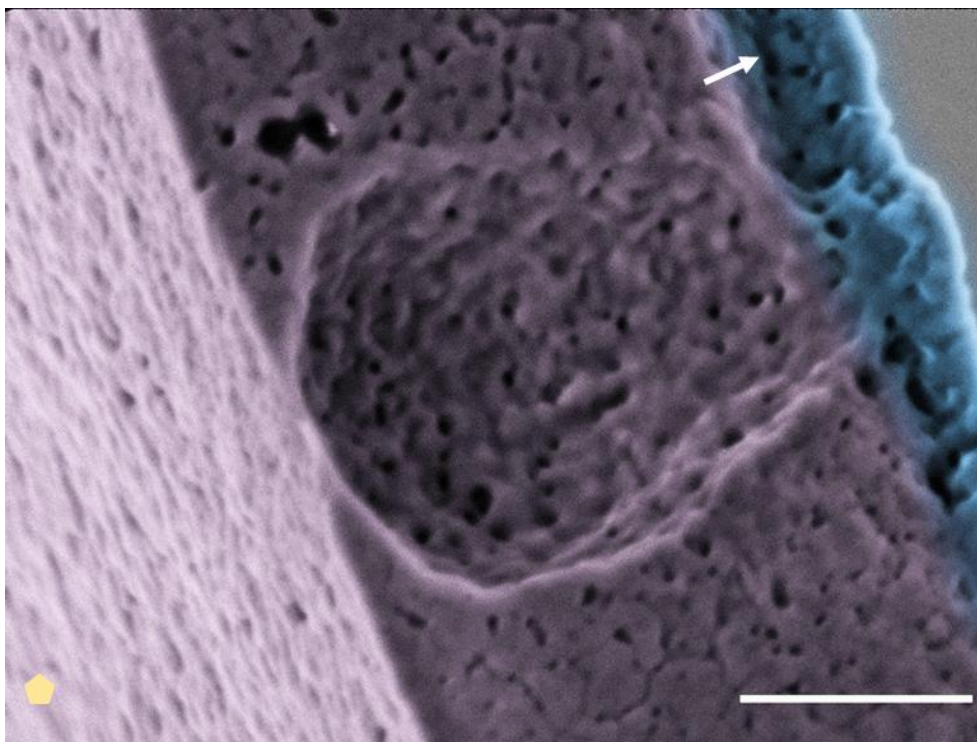


Figure 68 - Electron micrograph (SEM) showing the internal structure of a continuous film. The interface in contact with water is indicated by a yellow pentagon. The upper layer is highlighted in blue while the bottom layer is colored in pink. The white arrow shows the higher density of pores at the junction between the two layers. In lens detector, 1 kV. Scale bar = 200 nm.

---

The amorphous films produced by ADM syntheses exhibit a sub-micron thickness and a space-filling nanostructure whatever the synthesis conditions.

---

### 3.3 INVESTIGATION OF THE MECHANISMS OF FILM FORMATION

In order to get information on the mechanisms of film formation, and more particularly on the putative formation of a liquid precursor phase, we carried out experiments providing a characterization of the temporal evolution of the system. Both the bulk and interface chemical evolution were recorded, either by *in situ* measurements (pH measurement, optical microscopy imaging) or by *ex situ* observations after quenching of the reaction (cryo-TEM, STXM). All the results presented in this section were obtained with pellet synthesis of the reference disc-patterned films at concentrations  $[Ca^{2+}] = 20$  mM and  $[PANa] = 20$  ppm.

### 3.3.1 Time scale of interface and bulk mineralization

Observations with the naked eye indicate that the interface mineralization is already at work after 40 min of reaction. Thin white strands are indeed visible at the interface, which turns into a complete film at the air-solution interface over time (Figure 69a).

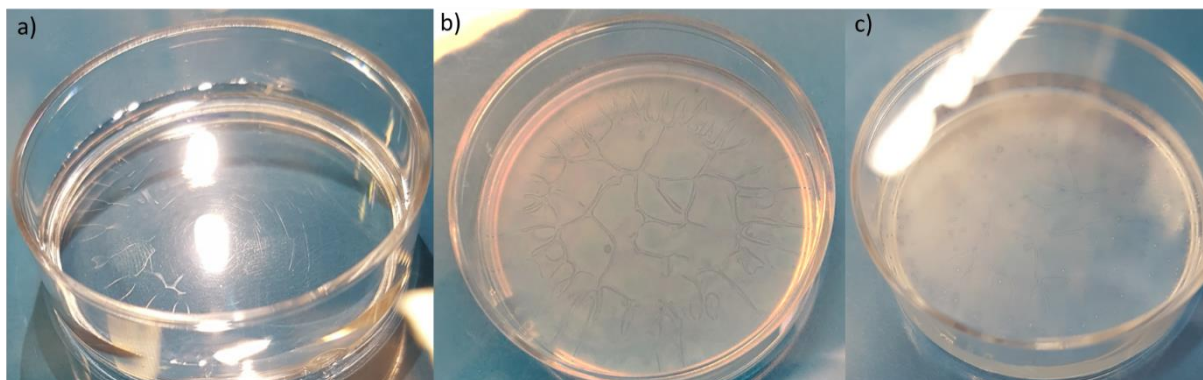


Figure 69 - Photographs showing the film formation as visible to the naked eye. a) Elongated white strands first become visible after 40 min. b) After 60 min, mineralized structures cover the whole interface. c) After 5 hours, a complete film has formed. The KBr pellet is on the left side of the Petri dish.

In parallel, light scattering species become visible in the bulk a few minutes after the first observations of the interfacial mineralized structures. They form large convection rolls that are easily detected also with the naked eye (Figure 70 a, b and c). The rolls are located underneath the elongated white strands. This clearly indicates a coupling between the bulk and interface mineralization.

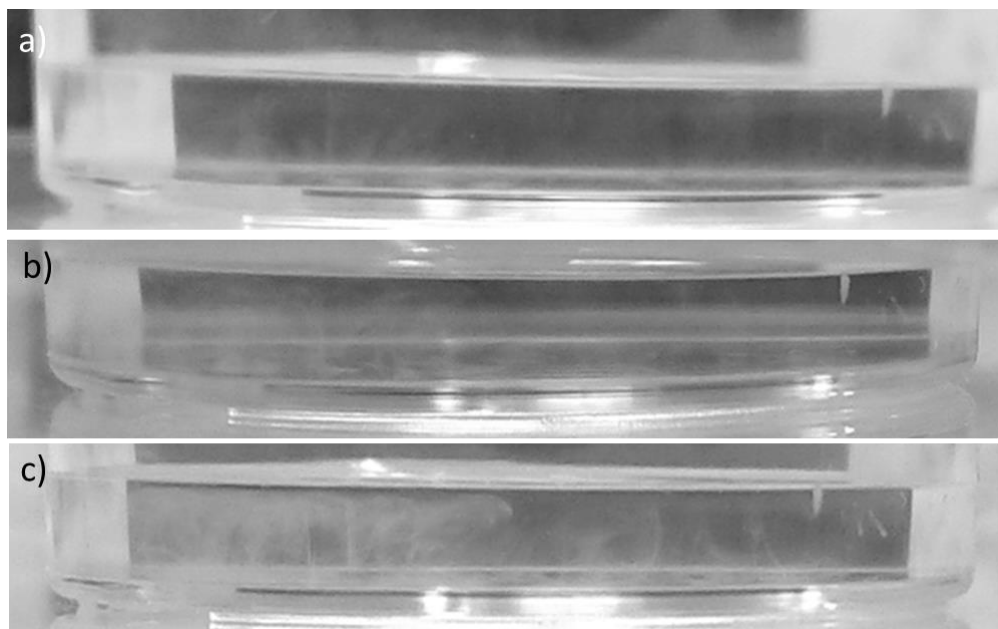


Figure 70 - Photographs showing light scattering species evolution in bulk a) 5 min after film appearance. White vertical lines appear in solution. b) 6 min after film appearance. The lines intensify. c) 7 min after film appearance. The light scattering species expand laterally at the

surface, forming the rolls.

Following the appearance of the convection rolls, the solution becomes completely turbid (~90 min of reaction). It further progressively clarifies until it becomes transparent and the bottom of the Petri is covered with a white deposit (~3 hours of reaction). The presence of scattering species in bulk is thus limited in time.

### 3.3.2 Evolution of the interfacial mineralized structures with time

In order to decipher the mechanisms of film formation, an in-depth study of the evolution of the interfacial structures morphology with time has been performed. Before 18 min of reaction, no interfacial structures could be detected by *in situ* optical microscopy owing to a lack of contrast. Putative structures were therefore sampled out of the reactor and observed *ex situ* by TEM or phase contrast microscopy (PCM). As TEM has a better space resolution than PCM, it was used for the precise characterization of the mineralized interfacial structures.

The resulting TEM images are presented in Figure 71. Most interfacial objects, already present at short reaction time, have a round disc-like shape (Figure 71 a-f). They present an homogeneous contrast and their typical size increases with time. Owing to the used sampling method, the density of collected objects may substantially differ from the interfacial object density. Therefore, density quantification after sampling has not been used in this study.

On the contrary, the size evolution was thoroughly characterized by extracting the distribution of Feret diameter from the images, as described in the Materials and methods. The statistical size distribution for each reaction time is presented in Figure 71.g, using the so-called violin plots. As a reminder, the envelope of the colored area represents the kernel density plot, that is, the probability density function that describes the size statistical distribution. The increase of the interfacial structures diameter with time is further reported in Table 7 where the mean diameters are provided. After one minute, the mean Feret diameter is of  $1.26 \pm 0.23 \mu\text{m}$ . The interfacial objects grow radially until 10 min of reaction (blue dashed line in Figure 71.g), at which time their mean diameter is  $3.32 \pm 0.7 \mu\text{m}$ . Then, the growth stops and the diameter of the objet remains constant (as highlighted by the orange pointed line) until 35 min of reaction. Finally, at 35 min of reaction, the mean diameter is  $5.11 \pm 0.54 \mu\text{m}$ , which is similar to the diameter of the discs observed in the mature ACC film. This means that the interfacial structures stop growing radially after 35 min of reaction (Figure 58.b).

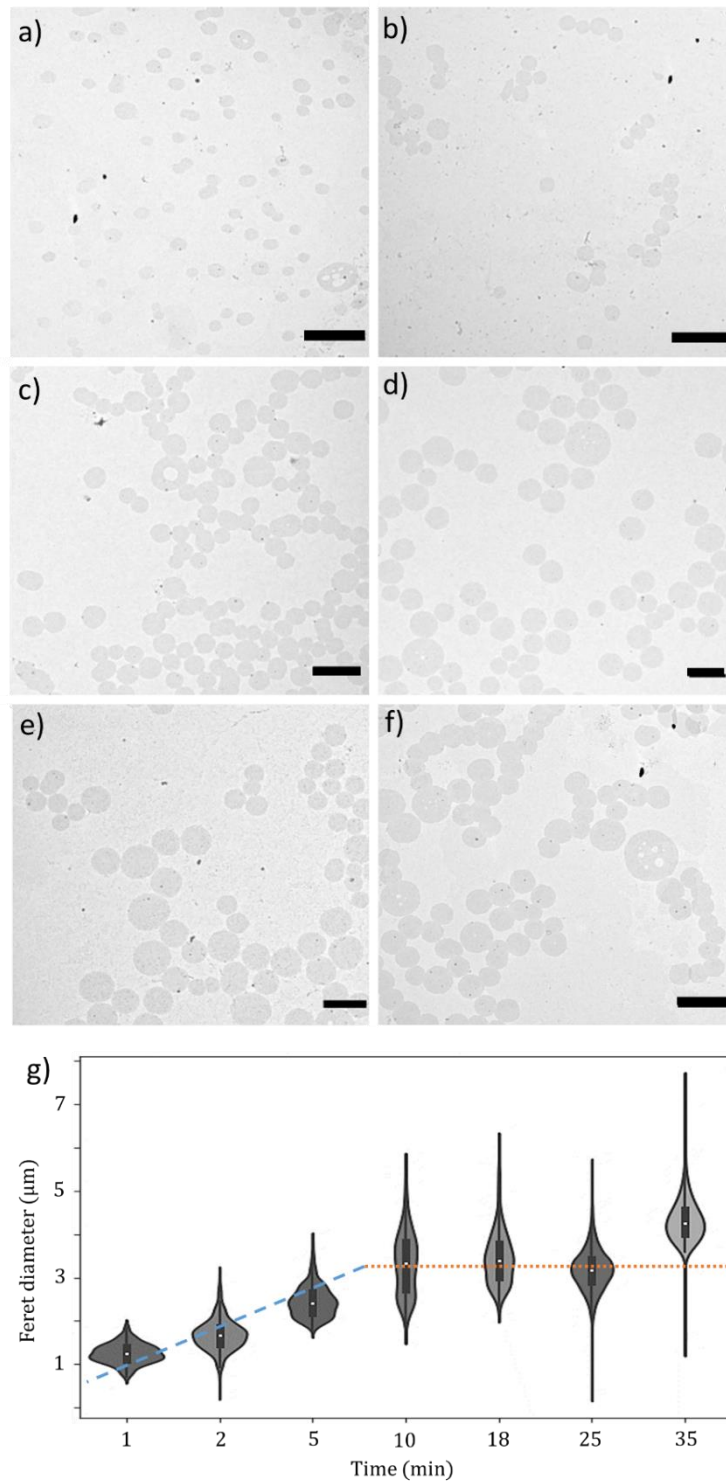
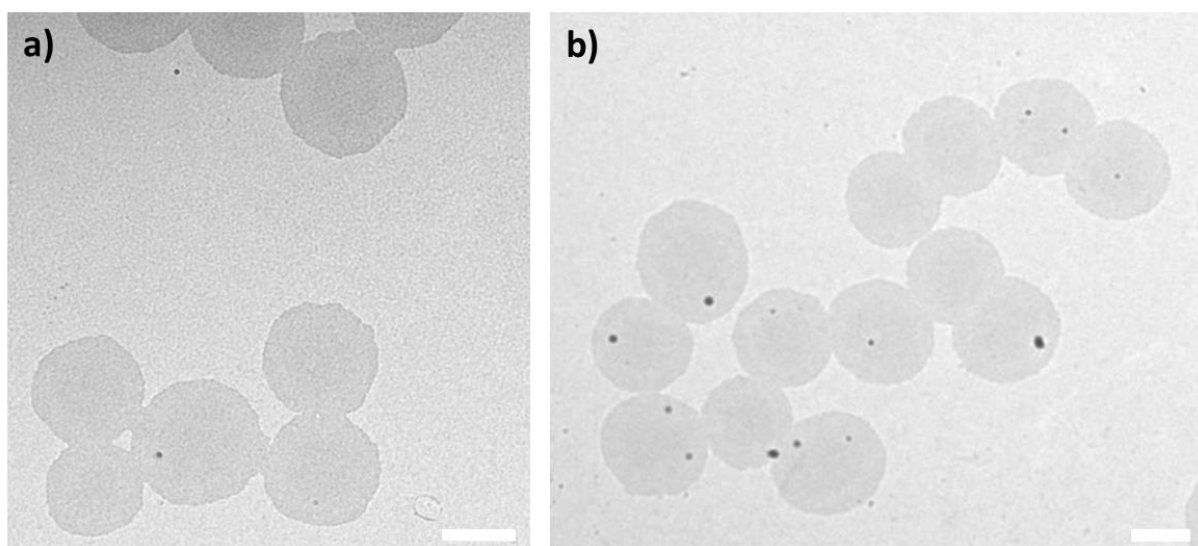


Figure 71 - Electron micrographs (TEM) of the interfacial mineralized structures at early reaction times. a-f) Interfacial mineralized objects at a) 1 min, b) 2 min, c) 5 min, d) 10 min, e) 18 min f) 25 min. Scale bar = 2  $\mu\text{m}$ . g) Violin plots: statistical size distribution of the particle Feret diameter with time. Description of the violin plots is available in the Material and methods, 2.4.1.3. The blue dashed line present the radial growth of the particle up to 10 min. The orange dashed line highlights the steady Feret diameter evolution between 10 and 25 min. At 35 min, the Feret diameter rises again.

*Table 7 - Mean Feret diameter and standard deviation for each sampling time.*

<i>time (min)</i>	<i>1</i>	<i>2</i>	<i>5</i>	<i>10</i>	<i>18</i>	<i>25</i>	<i>35</i>
<i>Feret diameter (<math>\mu\text{m}</math>)</i>	1.26	1.68	2.45	3.32	3.45	3.18	5.11
<i>Standard deviation (<math>\mu\text{m}</math>)</i>	0.23	0.35	0.35	0.7	0.6	0.45	0.54
<i>Number of particles counted</i>	350	650	1060	450	430	2650	265

Between 18 and 25 min of reaction, the center of the discs shows a stronger contrast than the periphery (Figure 72.a and b). This contrast difference was not observed at shorter times (1 to 10 min).



*Figure 72 - Electron Micrographs (TEM) of the discs. A denser region is visible in the disc center. a) 18 min. b) 25 min. Scale bar = 2  $\mu\text{m}$ .*

AFM measurements allow evaluating the thickness of the interface objects. For example, the disc formed after 20 min of reaction shown in Figure 73 is 4 nm thick at its edge, then gradually thickens to 5 nm at the center. As these measurements were performed late in the course of the thesis, the generalization of these observations to different times is lacking, but similar height variations are present on the objects at 10 min and 30 min, as presented in the Appendix

(Figure A. 1).

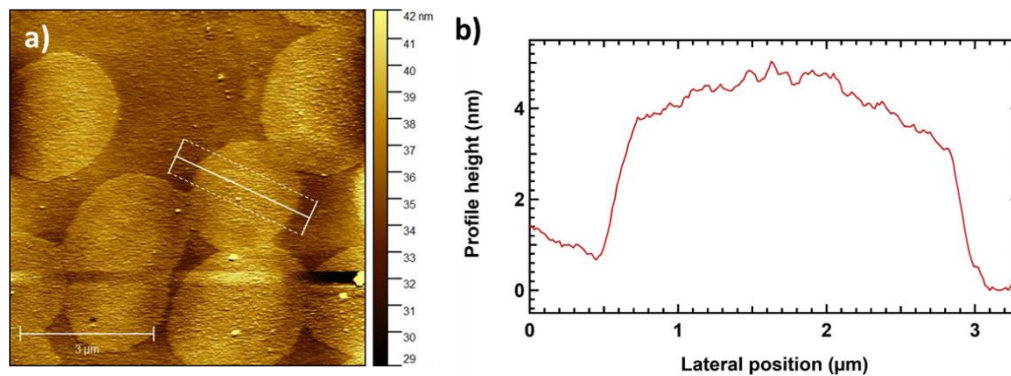
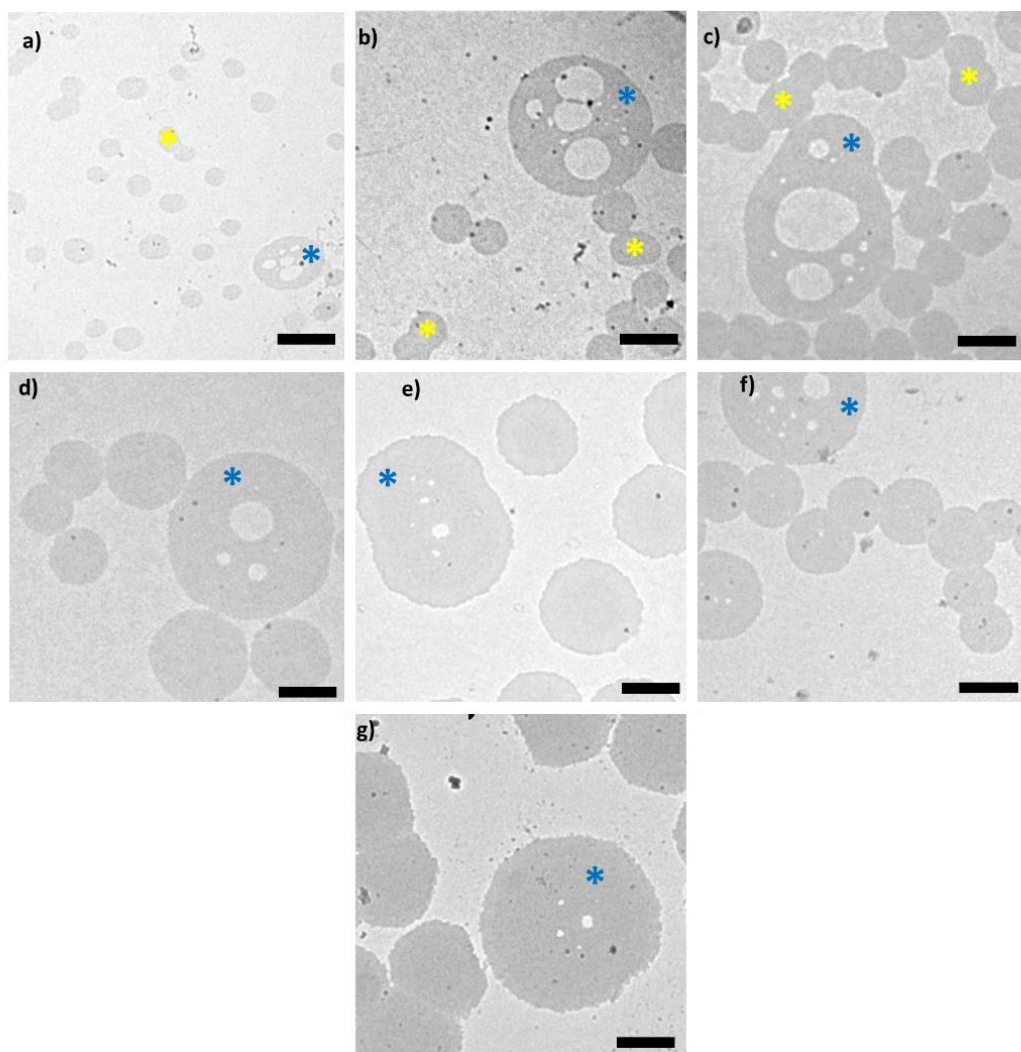


Figure 73 - AFM imaging of discs after 20 min of reaction a) Topography mapping. b) Height profile of the segments traced in a). The height is averaged between the dashed line for a better signal. The measurement is performed following the observation in STXM spectroscopy, presented in Figure 80. Scale bar = 3  $\mu\text{m}$ .

In addition, double-emulsion patterns (indicated by blue asterisks in Figure 74) are identified for reaction times of 1 min and beyond. These patterns correspond to large rounded-shaped domains with void inclusions in Figure 74 b and c). Finally, dumbbell-like fusion patterns and elongated shapes are highlighted in Figure 74 with yellow asterisks. They suggest the existence of coalescence mechanisms between the disc-shaped objects.





*Figure 74 - Electron micrographs (TEM) showing the double-emulsion and fusion patterns at the interface at a) 1 min, b) 2 min, c) 5 min, d) 10 min, e) 18 min, f) 25 min, g) 35 min. Double emulsion patterns are marked with a blue asterisk, and fusion patterns with a yellow one. Scale bar = 2  $\mu$ m.*

In parallel of TEM imaging, cryo-TEM observations were carried out so as to avoid potential artifacts due to sample drying. At 5 min of reaction, the discs and double-emulsion patterns are also visible using this technique, as presented in Figure A. 2. (see Appendix). However, due to a lack of sensitivity and to a poor statistic of observations, this method was not used further in the study.

As mentioned in the section 3.3.1 of this chapter, the film becomes visible to the naked eye after about 40 min. TEM observations confirm that the interfacial structures change drastically around this time of reaction, both at the nano- and microscale. Instead of the homogeneous population of discs observed at earlier times, the mineralized structures now exhibit three different levels of contrast (Figure 75.a) observed for the same reaction time (35 min). These three contrasts are characteristic of three types of structures, named I, II and III and shown in Figure 75.

Structures of type I, marked in yellow in Figure 75.a, correspond to homogeneous discs that

poorly absorb the electron beam (object of highest intensity value, in yellow in Figure 75.b). These discs are fully similar to those observed at earlier times of reaction (see Figure 75.c *18 min* and *Structure I*).

Structures of type II, marked in orange in Figure 75 a, also correspond to discs, but exhibit a higher contrast with respect to the background than structures of type I. As a matter of fact, they appear to be about twice as absorbing as structures of type I (see Figure 75.b). These structures show rapid spatial variations in intensity, which evidences some granularity at the nanoscale (Figure 75.c *Structure II*). Finally, these structures are surrounded by a corona of lower contrast (see Figure 76.b).

Last, structures of type III are characterized by a strong heterogeneity of contrast. Whereas their edge show the same contrast as the discs of type II, their inside absorb much more the electron beam, due to an increased thickness (as attested by SEM images, see Figure 65) and possibly increased density. Like structures of type II, structures of type III exhibit a nanostructure (Figure 75.c *Structure III* and Figure 76.a). And like structures of type II, they are surrounded by a weakly-contrasted layer (Figure 76.a, region between the two arrows). On the color intensity map of a TEM picture displaying the three structures, the intensity of this layer appears to be the same as the intensity of the corona in the structures of type II, or as the mean intensity in the structures of type I (see Figure 76.b, light purple color).

At 35 minutes, the edges of the three kinds of structures have lost the smoothness of early discs edges (observed between 1 and 25 min) and now appear nanostructured (see Figure 75.c).

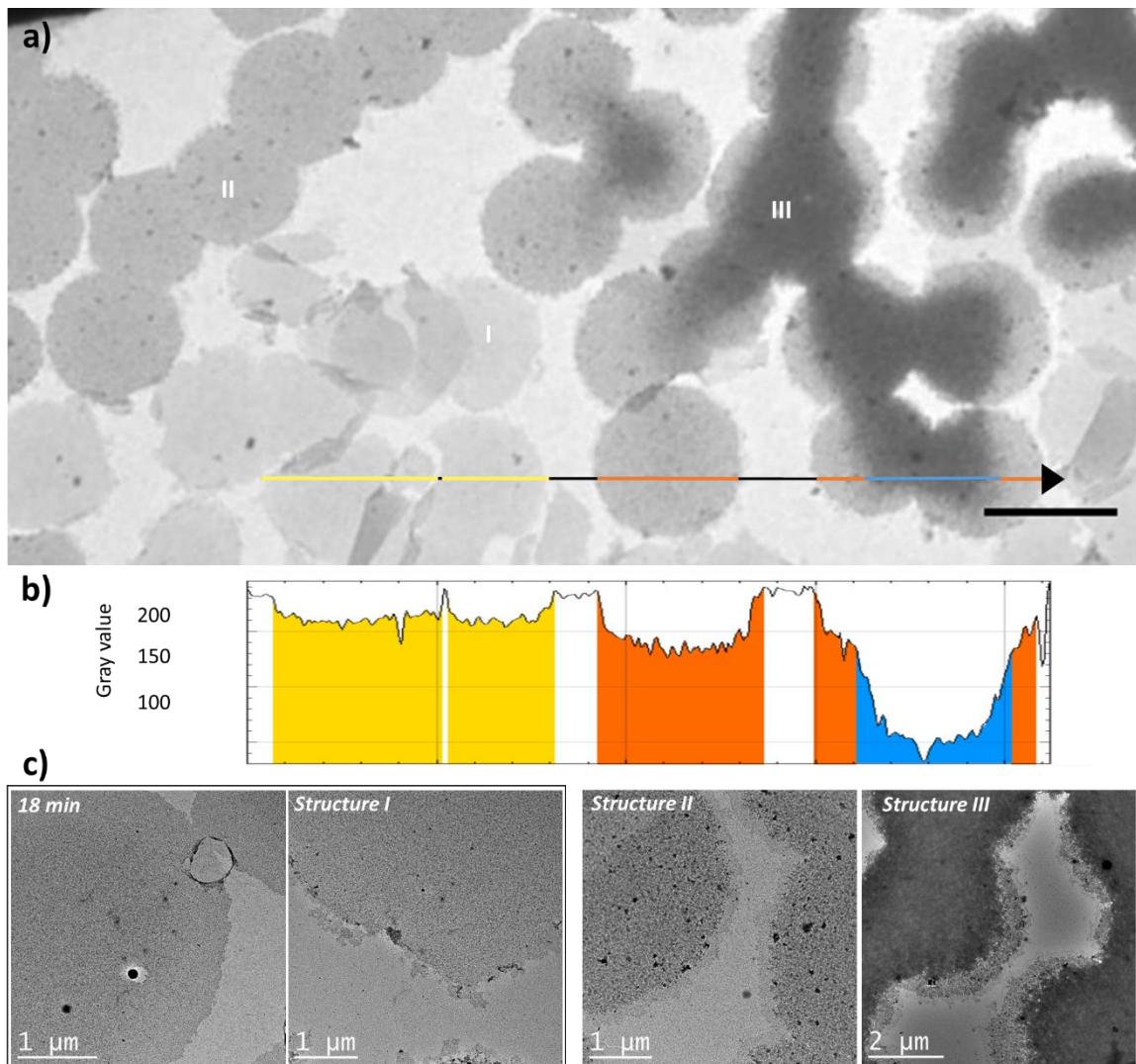
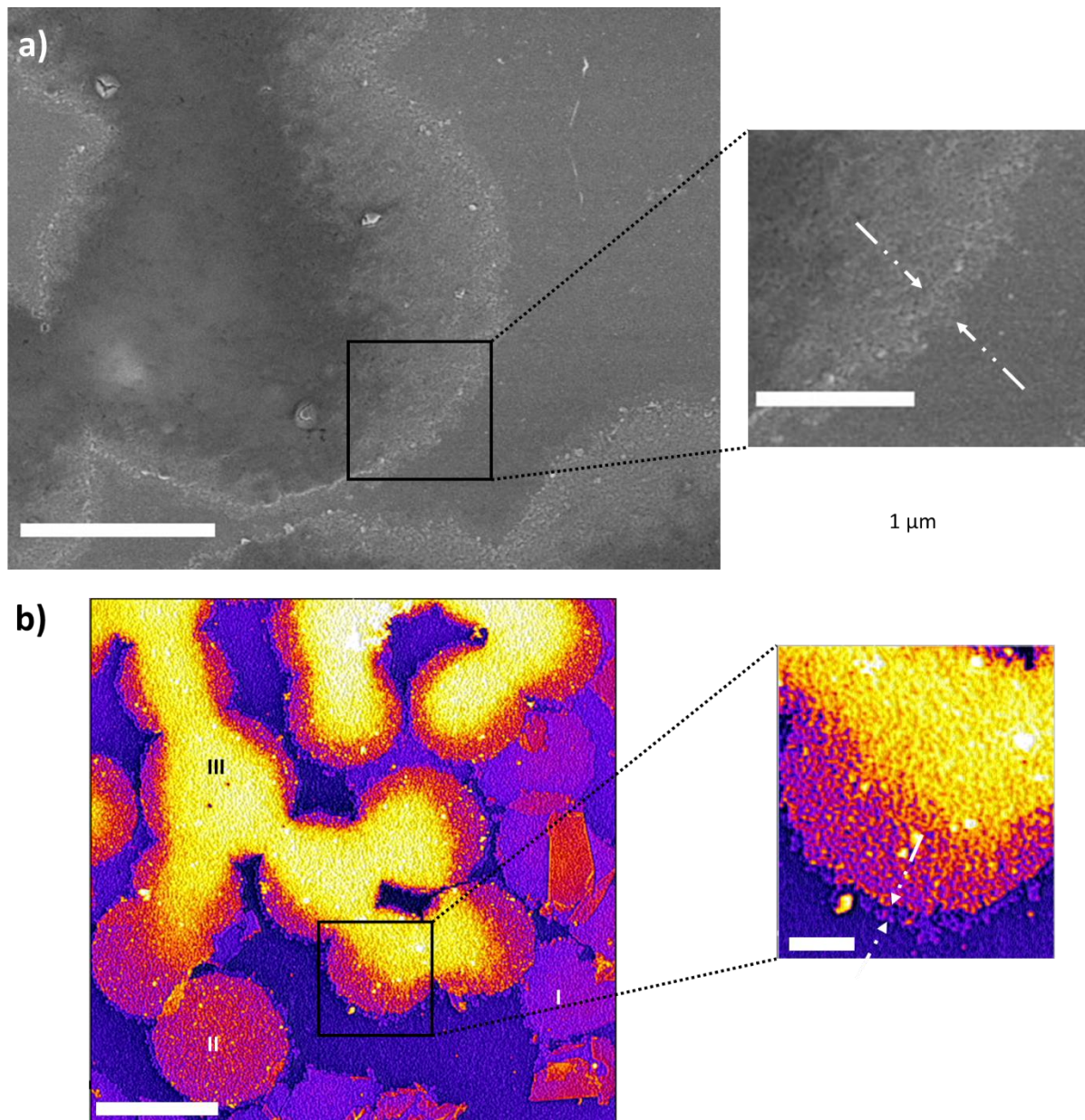


Figure 75 - Electron micrographs (TEM) of a film sampled at 35 min nad 18 min a) TEM micrograph at 35 min. The three types of intensities are marked I, II and III. Scale bar = 5  $\mu\text{m}$ . b) Pixel intensity along the arrow drawn in a). The three intensity plateaus are colored in yellow, orange and blue respectively. They correspond to the regions along the arrow partitioned with the same color in a). c) TEM images of the three structures. From left to right: disc at 18 min, structure I (35 min), structure II (35 min) and structure III (35 min).



*Figure 76 - Electron micrograph (a. SEM, b. TEM). Imaging of an ACC film sampled after 35 min*  
 a) Structure III, Scale bar = 2  $\mu\text{m}$ , the inset highlights the thin layer present on the disc edge with white dashed arrows. In lens detector, 1 kV. Scale bar = 1  $\mu\text{m}$ . b) Colored map of the pixel intensity. The three identified types of structures are labeled I, II and III respectively. The purple color of structures I is visible on the periphery of structures II and III (highlighted by white dashed arrows on a structure III in the inset).

PCM observations on film samples collected on solid substrates at similar reaction times confirm the TEM observations, revealing the coexistence of the three types of structures, with a larger statistic, beyond 35 min (Figure A. 3).

AFM measurements show that the type II structures (at 35 min) are thicker than the objects collected at earlier times, measuring 15 nm in thickness (Figure 77).

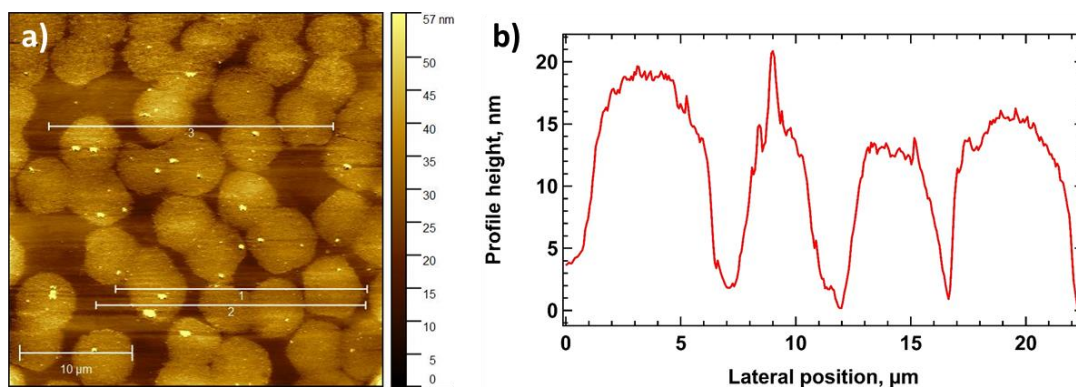


Figure 77 - AFM imaging of type II structure after 35 min of reaction. a) Topography mapping. b) Height profile of the segments traced in a). The height is averaged between the dashed line for a better signal. Scale = 10  $\mu\text{m}$ .

In parallel, to see the evolution of the interfacial structures at a large scale, and without sampling artifacts, a set-up was developed to allow for *in situ* observations with a phase contrast microscope. These observations revealed a large increase in the optical contrast of the film when the structures of type III become visible in TEM (35 min). The intensity varies from a clear gray to a dark-blue coloration surrounded by a white halo (Figure 78.a and .b). The highly contrasted areas develop as elongated domains (Fig. 24 a), resembling the morphology of the white strands visible with the naked eye at the same time (Figure 69). Underneath the film, small bulk species are visible by PCM at 35 min (Figure A. 4).

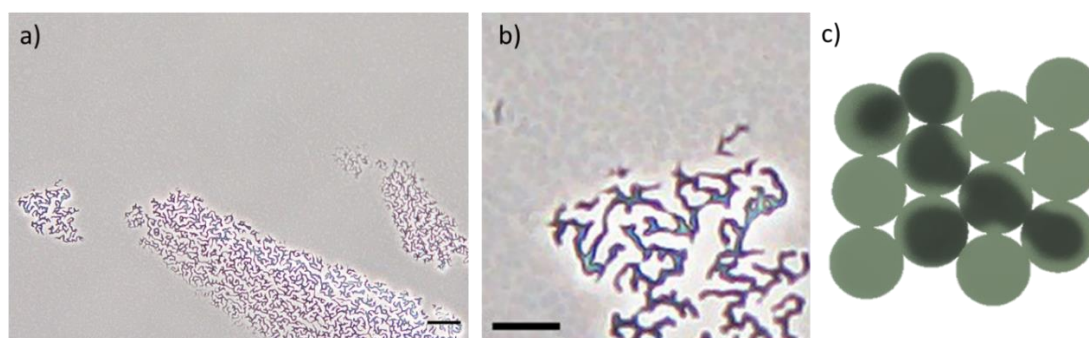


Figure 78— Optical micrograph (PCM *in situ*) of the interfacial film. a) Surface of the solution at 35 min of reaction. Scale bar = 50  $\mu\text{m}$ . b) Close-up of a). Scale bar = 20  $\mu\text{m}$ . c) Schematic representation of the interfacial pattern, providing an explanation on the observed structures in a and b.

Based on previous observations, we propose that this contrast increase is due to the appearance of structures of type III. The fact that these structures are thicker, or denser, than the structures of type I and II (Figure 75 a), could explain that a halo effect is observed in PCM, which hides the disc-like border of the structures, as proposed in Figure 78 c).

The contrast develops in the form of a propagation front (Figure 79 a, b and c). While developing, the contrast intensifies following the pre-existing pattern formed by the discs. Figure 79 illustrates the “filling” of the pre-existing pattern, by matter deposition that creates contrast in PCM (inset of Figure 79 a), then develops to fill (inset of Figure 79 b), and exceed, the pre-existing pattern (inset of Figure 79 c).

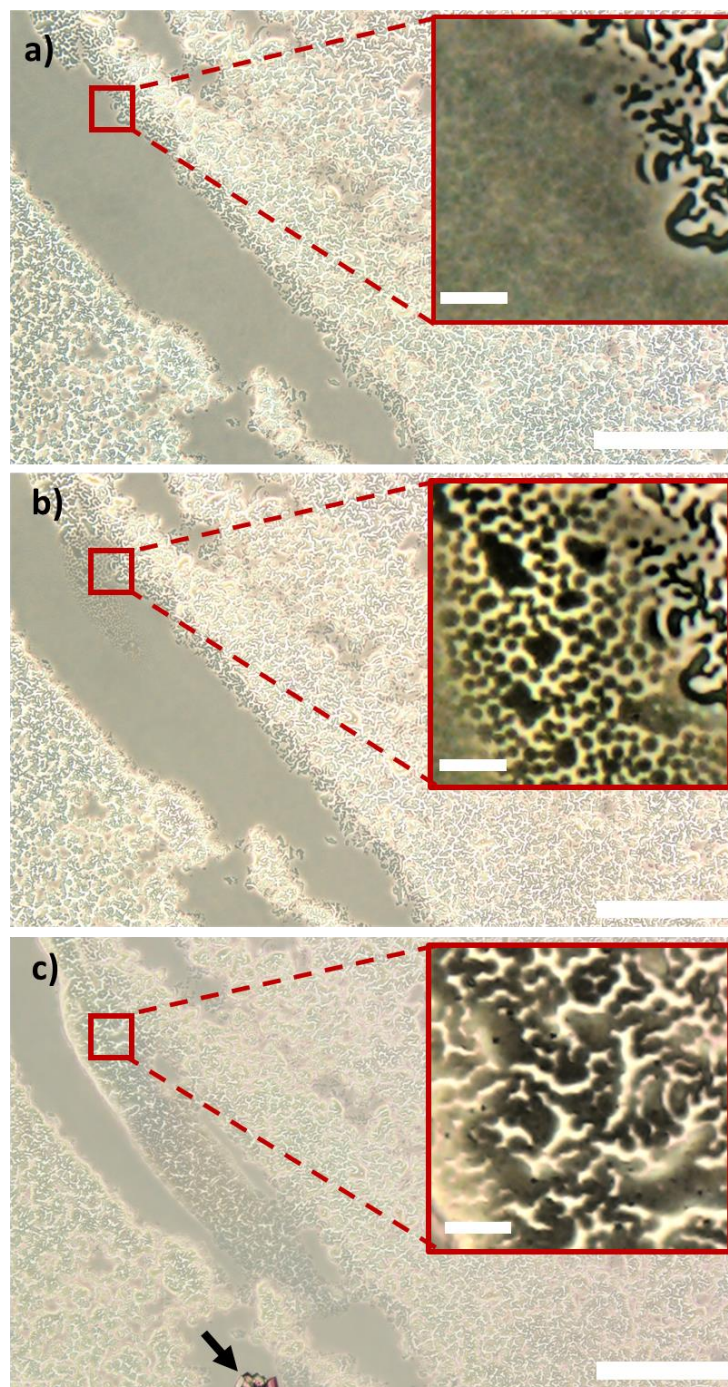


Figure 79 - Optical micrograph (PCM *in situ*). Phase contrast microscopy. Evolution of the phase contrast with time. Insets, all numerically enhanced, provide a zoomed-in view of this evolution. a) Time "t" = 45 min of reaction. b) t + 4.5 min. c) t + 52.5 min. The black arrows point to a 3D rhombohedral crystal grown at the interface. Scale bars = 100  $\mu\text{m}$ ; inset scale bars = 20  $\mu\text{m}$ .

To highlight possible chemical differences among the three structures, STXM microscopy was performed at the calcium L-edge on the HERMES beamline (SOLEIL synchrotron). Images of the different structures acquired at the calcium L<sub>3</sub>-edge (351.2 eV) are in qualitative agreement with the TEM images (Figure 80). Thus, disc and double-emulsion patterns are observed here as well. However, unlike with TEM, probably because of sensitivity issues, a corona of weaker absorption is already visible surrounding the discs after 10 min of reaction (Figure 80.a). This

corona remain visible at longer reaction times, from 20 to 30 min, similar to what was observed in TEM (Figure 80.b .c). At 40 min, STXM images reveal type I, II and III structures, (Figure 80.d highlights an area with type II and III structures) and evidence a stronger absorption in the center of type III structures. Therefore, the structures visible in TEM are equally visible in soft X-ray transmission microscopy at the Ca L-edge.

However, hyperspectral imaging at the Ca L-edge makes it additionally possible to identify changes in the calcium chemical environment, either due to ligand exchange or crystallization (see Materials and methods). Therefore, as described in the Materials and methods, stacks of images were acquired while mapping the  $L_2$  and  $L_3$  resonances. The  $L_2$  and  $L_3$  peak splitting as well as the  $E_0$  energy (i.e., the energy of the  $L_{2,3}$  edges in the case of a spherical charge distribution around the calcium ions – see the Materials and methods) were calculated by deconvolving spectra averaged in selected regions. The deconvolution procedure is available in the Materials and methods, and all the deconvolutions are available in the appendix (6.2.1).

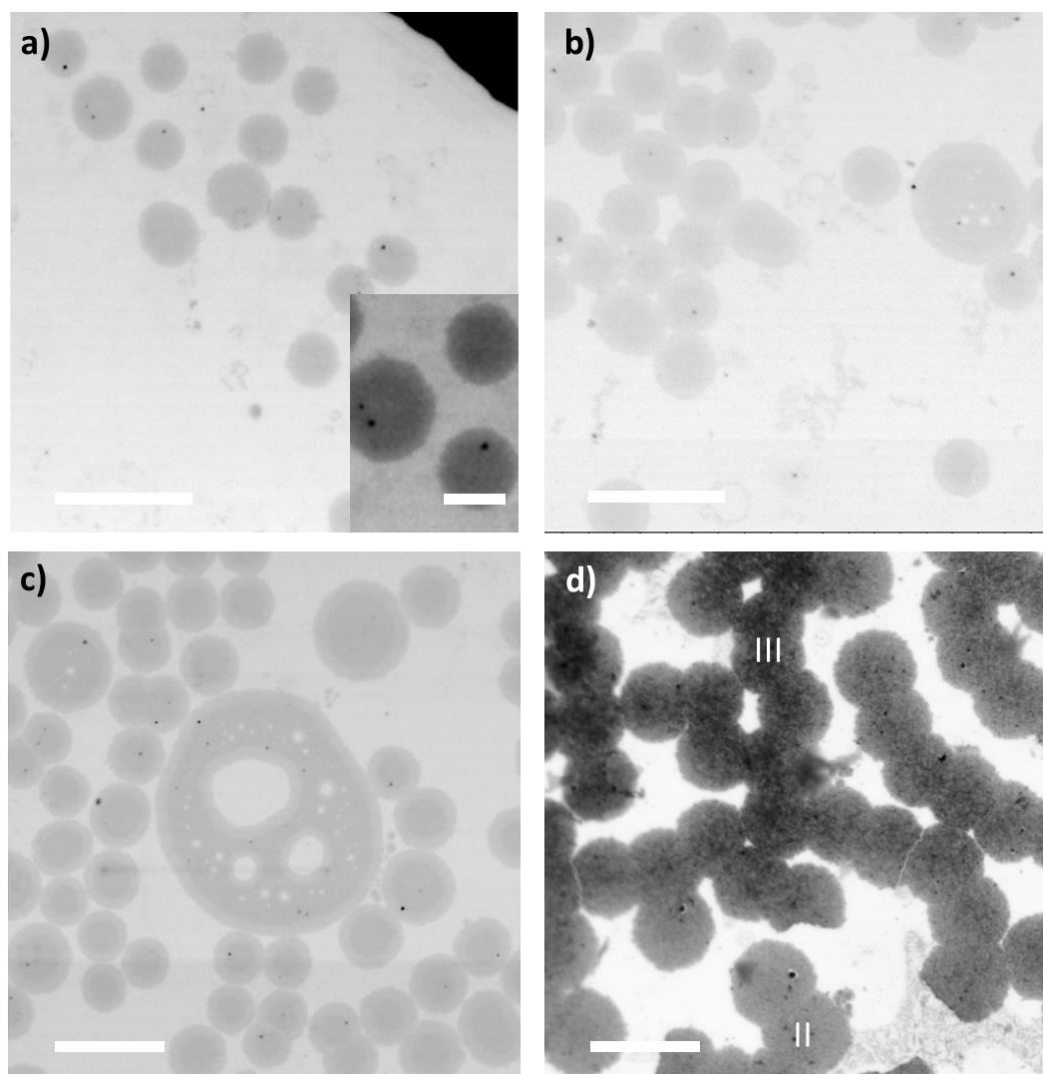


Figure 80 – STXM image at the calcium  $L_3$ -edge (351.2 eV) of a film sampled at a) 10 min of reaction. Inset: enhanced contrast, revealing the corona. b) 20 min c) 30 min d) 40 min. Type II and III structures, as defined earlier in this section, are identified by Roman numbers. Scale bar = 5  $\mu$ m.

The result of such a deconvolution applied to a normalized disc spectrum at 30 min of reaction is shown in Figure 81. As a reminder, peak splitting affects both the  $L_2$  and  $L_3$  transitions. Only samples at short times ( $< 40$  min) could be measured, as the thickness of film sampled at later times is too large to allow for calcium L-edge spectroscopy. Data extracted from spectra deconvolution at early times of reaction are gathered in Table 8. They show that there are no major differences regarding the chemical environment of calcium ions between the analyzed reaction times (Table 8). The peak splitting is always much smaller to that of calcite (1.29, see Materials and methods), pointing to a much more disordered structure than in the crystal, and fitting with ACC data (Materials and methods). It should be noted that a possible cause for the lack of difference between the spectra of the samples at early times could be due to the intense vacuum in the STXM chamber ( $10^{-5}$  mbar). The intense vacuum could dehydrate the sample and erase hydration differences, without inducing crystallization though.

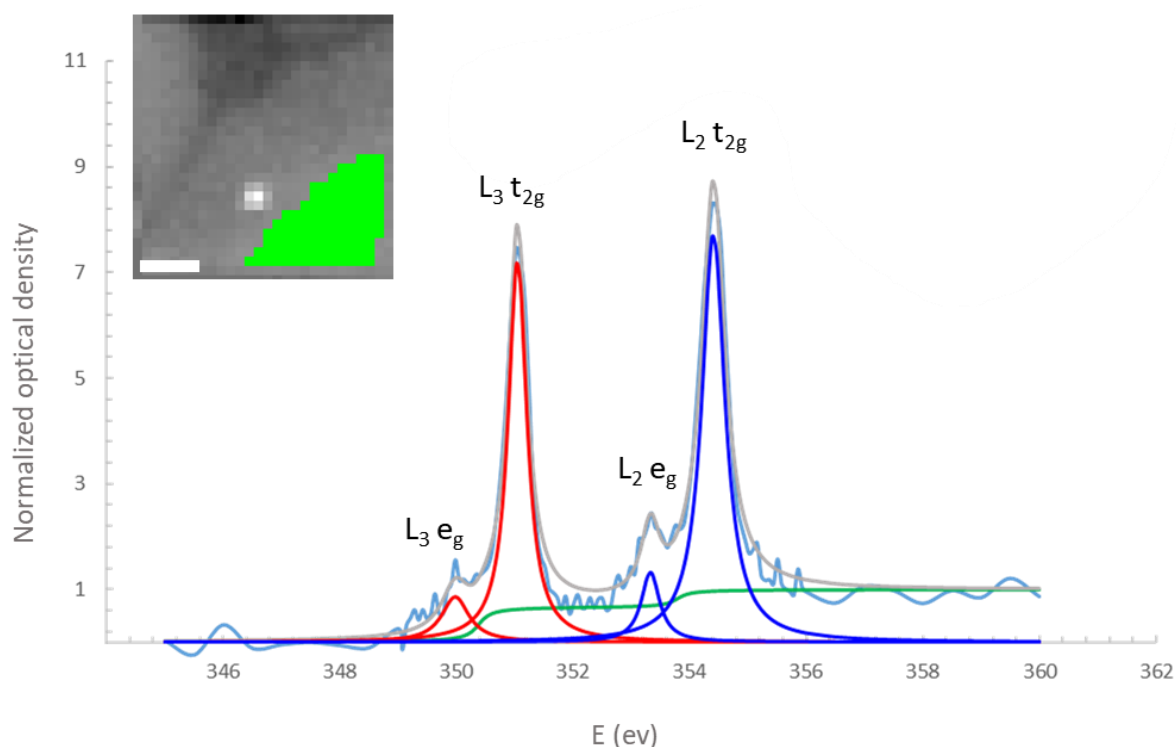


Figure 81 - Normalized X-ray absorption spectrum of the disc formed at 30 min of reaction. Measurements have been performed at the Ca L-edge. Two arctan functions, in green, and four Lorentzian functions (in red for the  $L_3$  resonance and in blue for the  $L_2$ ) have been used for deconvolution. The sum of these functions yields the gray spectrum, while the experimental curve is drawn in light blue. Inset: Optical density map at Ca L-edge. The spectrum is taken from the averaged of the green area. Scale bar =  $0.4 \mu\text{m}$ .



Table 8 - Peak splitting ( $\Delta_0$ ) and energy of the theoretical spherical complexation of the calcium ion ( $E_0$ ) in samples taken at 10 min, 20 min, 30 min and 40 min of reaction. At 40 minutes, structures II and III are measured.

t (min)	10	10 (corona)	30	30 (corona)	40 (structure II)	40 (structure III)
$\Delta_0 (L_3)$	0.98	0.98	1.06	1.08	1.13	1.04
$\Delta_0 (L_2)$	1.10	1.10	1.08	1.06	1.04	1.10
$E_0$	353.74	353.75	353.77	353.78	353.81	353.81

When the reaction is more advanced, at 1 hour, the discs are no more transparent in cryo-TEM. They are surrounded by a corona composed of loosely interconnected particles (Figure 82). Both discs and coronas were investigated with EDS measurements. This analysis is qualitative, as ratios between calcium, carbon and oxygen cannot be precisely determined because of the signal arising from the ice layer and holey carbon support. Still, both the dark disc, corresponding to a type III structure, and the thin corona around it appear to be composed of calcium ( $K_\alpha = 3,692$  keV,  $K_\beta = 4,013$  keV), carbon ( $K_\alpha = 0.277$  keV) and oxygen ( $K_\alpha = 0.525$  keV), fully consistent with calcium carbonate material.

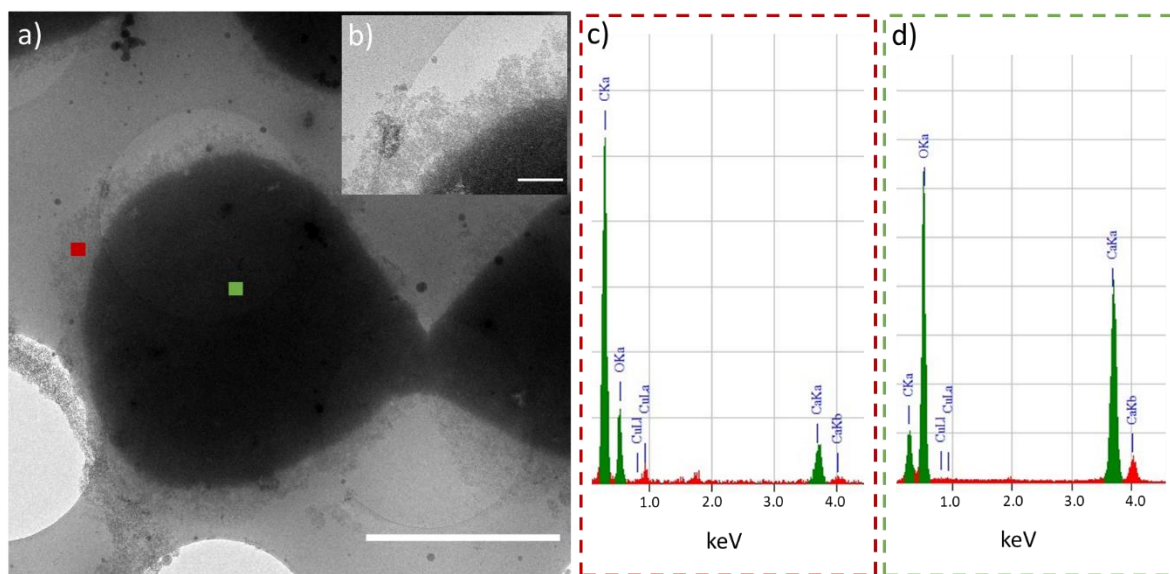


Figure 82 - Electron micrograph (cryo-TEM) and EDS measurements of a film sample collected at a reaction time of 1 hour. a) Cryo-TEM image. Red and green squares correspond to the areas investigated by EDS analysis. Scale bar = 2  $\mu\text{m}$ . b) Zoomed-in view of the upper region of the central disc. Scale bar = 200 nm. c) EDS analysis of the corona (red square in a)). d) EDS analysis of the disc center (green square in a)). The specific signals of the available elements are expected at the following energy values: carbon ( $K_\alpha = 0.277$  keV), calcium ( $K_\alpha = 3.692$  keV,  $K_\beta = 4.013$  keV), and oxygen ( $K_\alpha = 0.525$  keV). A small signal from copper (originating from the grid) is also visible ( $L_\alpha = 0.928$  KeV,  $L_\beta = 0.947$  keV). The slight signal at  $\sim 1.7$  keV is attributed to silicon

*contamination.*

### 3.3.3 Environmental parameters variation with time

---

Interfacial mineralized structures already exist after 1 min of reaction, grow radially with time until 35 min, then thicken by developing a granular nanostructure.

---

The supersaturation of the solution with respect to  $\text{CaCO}_3$  precipitation is dependent on the calcium and carbonate concentrations in solution. The carbonate concentration, in turn, is determined by two control parameters, which are the solution pH and the partial  $\text{CO}_2$  pressure ( $p\text{CO}_2$ ) in the gas atmosphere. Actually, if the solution is in equilibrium with the gas atmosphere, the  $\text{CO}_2$  pressure determines the amount of dissolved carbonated species according to the Henry's law. Finally, the pH value controls the ratio between the different carbonated species (see Materials and methods).

In order to specify the chemical environment of the syntheses, measurements of the pH and  $\text{CO}_2$  atmospheric pressure were performed *in situ*, as a function of time (see the protocol of measurement in the Materials and methods for each) and are presented in Figure 83, Figure 84.

When 6 mL of the reference solution (20 mM/20 ppm) is poured in the reactor chamber in the presence of ammonium carbonate, the pH of the solution rises from 6 to 10 within 10 minutes (Figure 83 b). Then, the pH slowly decreases with time (Figure 83 a), to finally reach 8.6 after 16 hours and keeps this pH value for up to 16 days (not shown here).

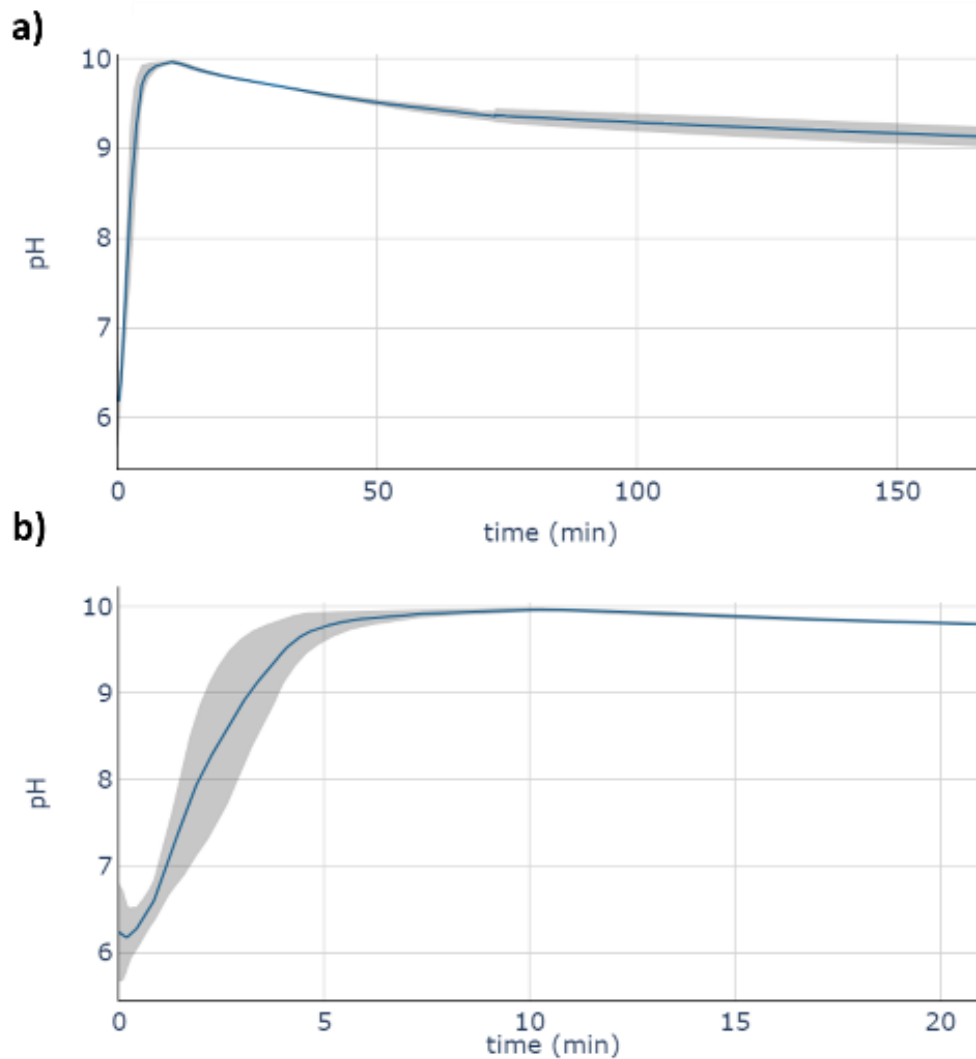


Figure 83 - pH evolution over time in 6 mL of  $[Ca^{2+}] = 20 \text{ mM}$ ,  $[PANa] = 20 \text{ ppm}$ . a) Evolution over 160 min. b) Evolution over the first 20 min. Gray area represents the standard deviation in each point. Measurements have been triplicated until 72 min, and then duplicated.

In parallel, the  $CO_2$  level rises promptly (within 2 min) in the reactor chamber and remains at high values ( $\sim 2000 \text{ ppm}$ ) for 3 to 4 hours (Figure 84 a). It then gradually decreases to the atmospheric value after 10 hours (500 ppm, not shown here).

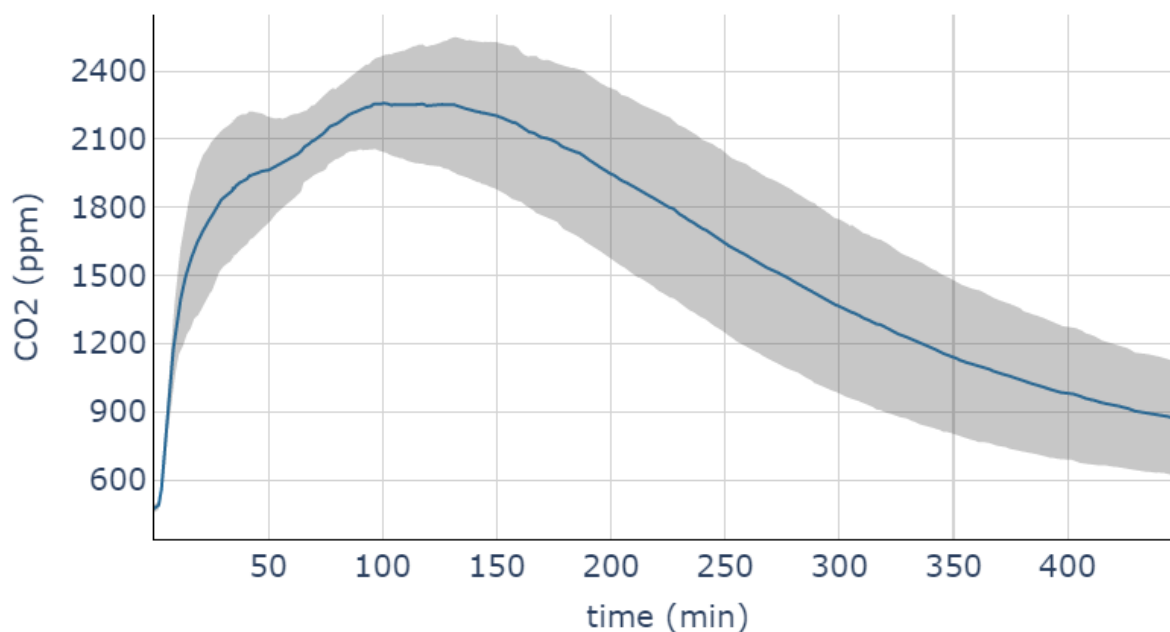


Figure 84 - In situ recording of  $\text{CO}_2$  partial pressure inside the reactor chamber. Long-term (7.5 hours) recording of the atmosphere in contact with a  $[\text{Ca}^{2+}] = 20 \text{ mM}$ ,  $[\text{PANa}] = 20 \text{ ppm}$  solution.

Assuming that the solution is in equilibrium with the gas atmosphere, one could estimate the amount of carbonated species in solution at any time. For example, at 75 min, 2000 ppm of  $\text{CO}_2$  are present in the gas phase (Figure 84), and the pH value in the solution is of 9.5, so that, according to the Henry's law (Henry's constant is  $1.78 \cdot 10^2 \text{ M/atm}$  at this pH), 1.1 mmol of carbonated species should be dissolved in solution. This value is quite too high, since the maximum amount of dissolved  $\text{CO}_2$  in a pellet synthesis is 0.1 mmol. Therefore, the solution is not in equilibrium with the gas phase during the syntheses, making it impossible to calculate the supersaturation index of the solution from the pH and  $\text{pCO}_2$  values.

Nevertheless, evidence of mineralization in the bulk solution, established from visual inspection (convection rolls) and optical microscopy (particles), led us to further analyze the bulk composition through time.

---

Supersaturation values vary strongly during the first hour of reaction as the pH rises from 6 to 10 (within 10 min) and  $\text{CO}_2$  levels from ambient to 2000 ppm.

---

### 3.3.4 Bulk mineralization

To determine the morphology of the scattering species, present in the bulk and that compose the observed convection rolls, a sample was pipetted at 38 min and observed by TEM microscopy (Figure 85). The sample is made of large aggregates (several microns wide) of nanoparticles. The nanoparticles size determination is, however, difficult to estimate using these observations. In addition, sample preparation, which includes drying, may have favored particle aggregation.

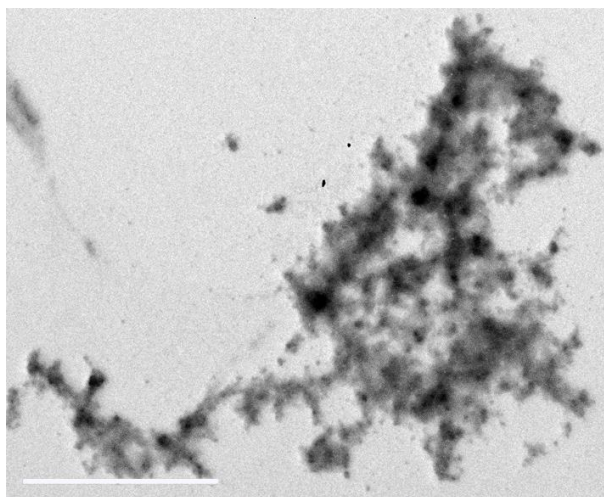


*Figure 85 - Electron micrograph (TEM) of a bulk sample collected at 38 min of reaction (reference conditions 20 mM / 20 ppm). Sampling was made in the light-scattering area of the solution. The sample was dried under primary vacuum (Materials and methods 2.1.3) before TEM imaging. Scale bar = 1  $\mu$ m.*

These aggregates were further analyzed in STXM, resulting in the spectrum presented in Figure 86. The peak splitting  $\Delta_0$  (i.e., the energy difference between  $e_g$  and  $t_{2g}$  d-orbitals) is measured at the  $L_2$  and  $L_3$  edges from the deconvolution (Figure 86). As for  $E_0$ , it is calculated from the  $t_{2g}$  and  $e_g$  energy values, assuming an octahedral configuration of the carbonate ions around the calcium ion (Materials and methods, Figure 18).

We thus find  $\Delta_0(L_2) = 1.06$  eV and  $\Delta_0(L_3) = 1.05$  eV, respectively, while  $E_0 = 353,78$  eV in particles. This is consistent with amorphous calcium carbonate references (See materials and methods, 2.6.2.2). It has a weaker crystalline field than our reference calcite spectra, but the same ligand environment. ( $\Delta_0 = 1.29$  eV,  $E_0 = 353,77$  eV, see materials and method).

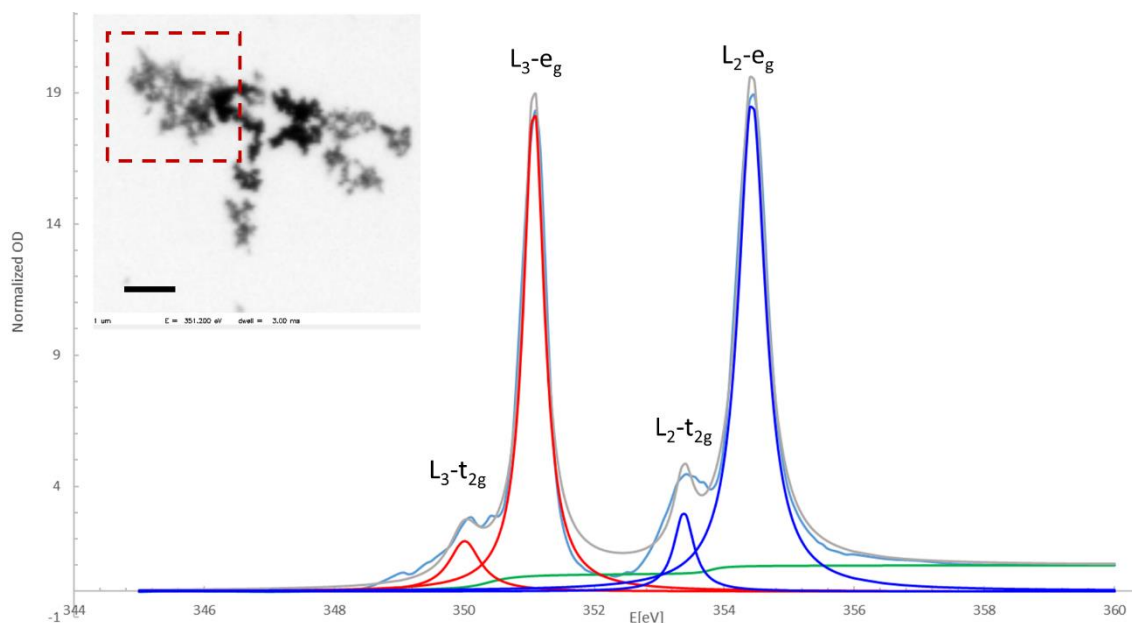


Figure 86 - Normalized X-ray absorption spectrum of bulk particles at 42 min of reaction. Measurements have been performed at the Ca L-edge. Inset: image of the particles acquired at 351.2 eV. Scale bar = 1  $\mu\text{m}$ . The red dashed square shows the area considered for hyperspectral imaging: the spectrum was extracted by averaging the signal over a few particles in this area. For deconvolution, two arctan functions, in green, and four Lorentzian functions (in red for the  $L_3$  resonance and in blue for the  $L_2$ ) have been used. The sum of these functions yields the gray spectrum, while the experimental curve is drawn in light blue.

The same aggregates could also be observed by cryo-TEM, when sampled in the close vicinity of the interface at 1h of reaction (Figure 87.a). Due to the rapid quenching in liquid ethane, which results in an amorphous ice layer, the sample was here conserved in its native state. The size of the particles composing the aggregates can be estimated to 30 nm.

An elemental analysis (Figure 87.b) indicates the presence of carbon ( $K_{\alpha} = 0.277$  keV), calcium ( $K_{\alpha} = 3.692$  keV,  $K_{\beta} = 4.013$  keV) and oxygen ( $K_{\alpha} = 0.525$  keV), confirming that the observed objects are made of calcium carbonate.

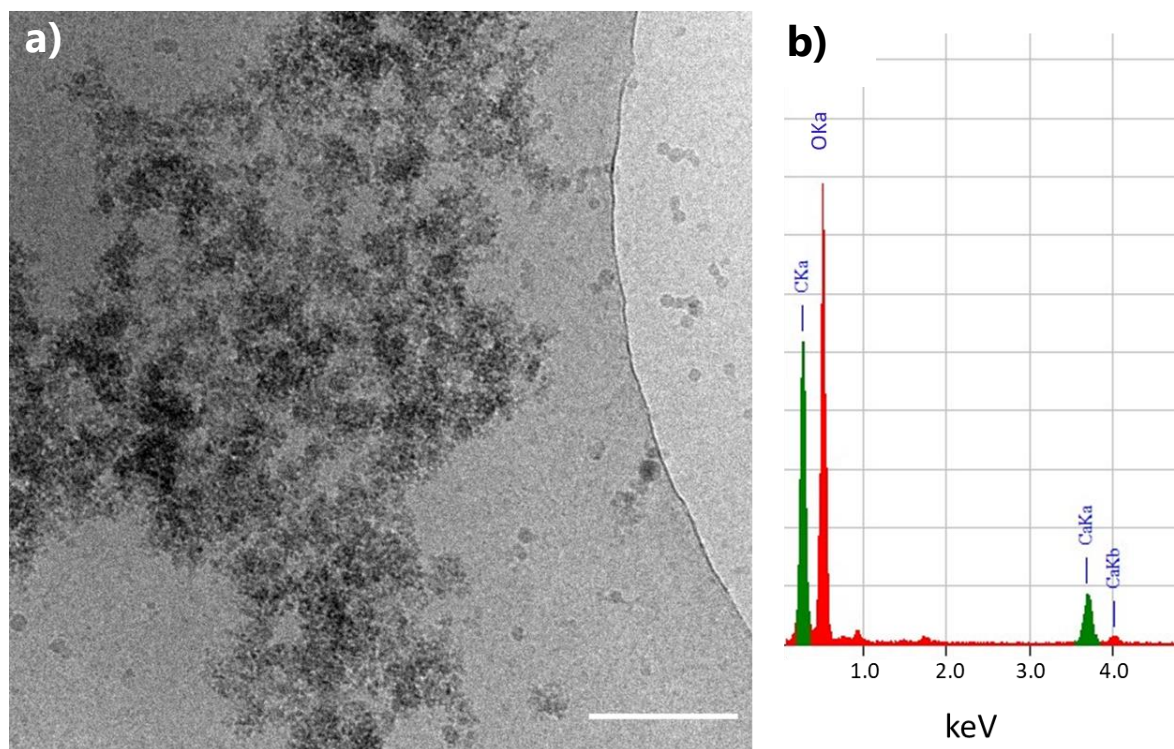


Figure 87 - Electron micrograph (cryo-TEM) and EDS analysis of the bulk particles. a) Observation of the bulk species at 1h reaction time. Scale bar = 200 nm. b) Objects are analyzed in EDS (right). The specific signals of the available elements are expected at the following energy values: carbon ( $K_a= 0.277$  keV), calcium ( $K_a= 3.692$  keV,  $K_b= 4.013$  keV), and oxygen ( $K_a= 0.525$  keV). A small signal from copper (originating from the grid) is also visible ( $L_a= 0.928$  KeV,  $L_b= 0.947$  keV). The slight signal at  $\sim 1.7$  keV is attributed to silicon contamination.

### 3.4 DISCUSSION

By combining *ex situ* and *in situ* measurements throughout the synthesis, from the atomic to the micro scale, the reported study of ACC film formation by ADM syntheses brings new information on the temporal evolution of the mineralized structures, both at the interface and in the bulk of the mineralizing solution. The large dataset collected thus makes it possible to suggest a mechanism of formation, independent of the crystallization mechanisms that follow. It therefore decorrelates the processes of amorphous formation from those of crystallization, as might be the case in biomineralization.

In this discussion, we will first focus on the temporal evolution of the chemical synthesis conditions, based on the available evidence. As a matter of fact, the solution undergoes a significant pH quench at the very beginning of the reaction. Thus, the possibility of a phase separation resulting from these conditions is considered, as well as the potential mechanism of demixing that occurs. Subsequently, the dramatic change in growth mechanism of the interface mineralized structures is discussed in relation with the formation of bulk mineralized species. Finally, a model of interface amorphous film formation is proposed, as well as a consideration of the impact of the polymer quantity in the reactive medium on the film

morphology.

### 3.4.1 Environmental condition evolution

Carbon dioxide and ammonia gases induce opposing effects on the pH of the solution when they dissolve into the calcium mineralizing solution. Indeed, ammonia dissolution leads to the basification of the solution, whereas carbon dioxide acidifies it. The pH value is seen to undergo a rapid increase from 6 to 10 (within 10 min, see Figure 83), before it slowly decreases until it reaches pH 8.6 after 16 h of reaction.

The initial increase of the pH above 10 results from a non-stoichiometric dissolution of the gases. Indeed, the Henry's constant of ammonia, which dictates its solubility, is 62 M/atm,<sup>140</sup> that is, about  $2 \cdot 10^3$  times higher than that of CO<sub>2</sub> (0.034 M/atm<sup>140</sup>), if the dissociation of both species in solution is neglected.<sup>140</sup> At the starting pH (~6), ammonia actually undergoes acid-base dissociation into ammonium ions, whereas CO<sub>2</sub> molecules only undergo a hydration process, furthermore limited by a slow kinetics.<sup>141</sup> As a result, the effective ammonia Henry's constant ( $2.5 \cdot 10^5$  M/atm for a 10 ppm NH<sub>3</sub> pressure, Phreeqc calculation) is about  $5 \cdot 10^6$  times higher than that of CO<sub>2</sub> (0.05 M/atm, Phreeqc calculation - Figure 88.a), and leads to a massive dissolution of ammonia in solution and a pH jump.



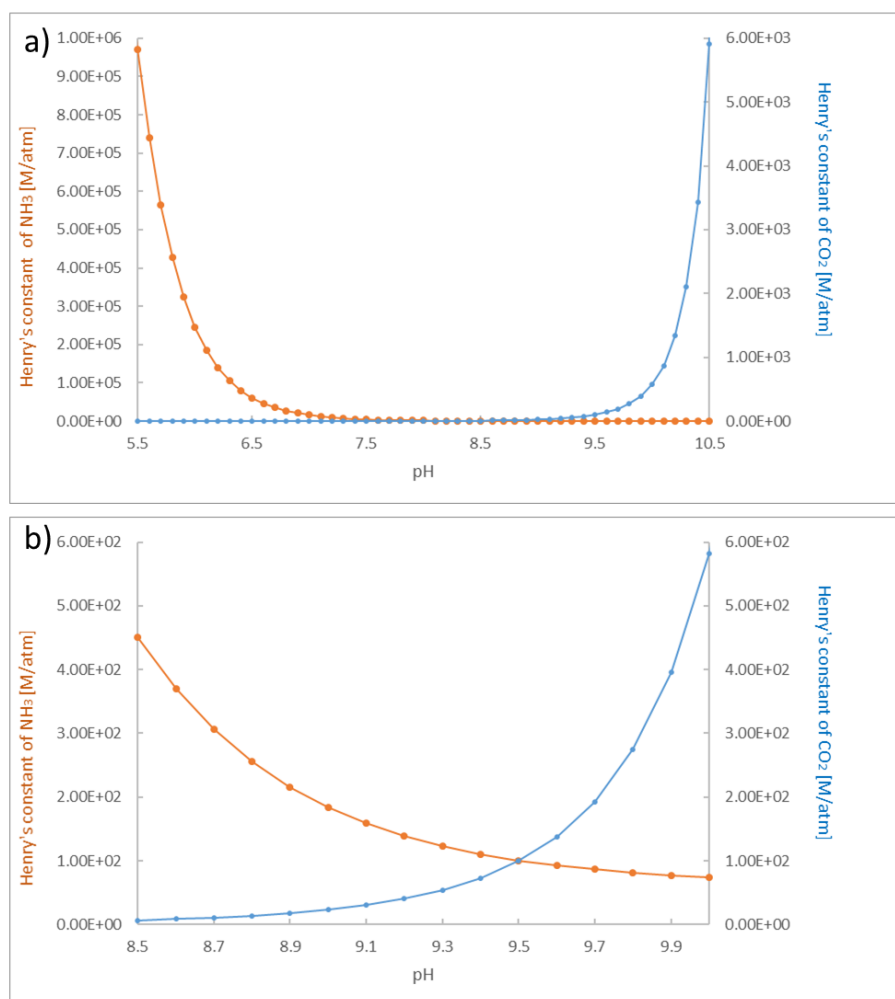


Figure 88 - Henry's constant of  $\text{CO}_2$  and  $\text{NH}_3$  gases as a function of pH. The blue curve corresponds to  $\text{CO}_2$  gas, and the orange curve to  $\text{NH}_3$  gas. The data have been calculated using PHREEQC software (<https://www.usgs.gov/software/phreeqc-version-3>), by considering a partial pressure of 10 ppm only for the two gases in order to ease the calculations.

The ammonia dissolution therefore induces a pH quench of the solution, even faster at the interface than in the bulk of the solution, where the measurements were carried out.

Once a pH above 9 is reached,  $\text{CO}_2$  gas becomes much more soluble as shown by its increased Henry's constant (equal to  $10^2$  M/atm at pH = 9.5, just like that of ammonia, see Figure 88.b). In addition, its hydration is much faster at these higher pH values,<sup>141</sup> therefore allowing its effective dissociation into bicarbonate and carbonate ions. Still, the  $\text{CO}_2$  level remains quite high during the first hours of the synthesis, since the thermodynamic equilibrium is not reached (as discussed in 3.3.3). After 10 hours, the atmospheric  $\text{CO}_2$  level returns to the value of the room atmosphere.

In the literature, pH monitoring in ADM-based calcium carbonate syntheses have already been reported in similar systems,<sup>11,109</sup> although very few include polymer additives.<sup>93,105</sup> In particular, Ihli *et al.*<sup>109</sup> have studied the influence of different chemical and physical parameters – namely the solution volume, concentration, physical barriers to gas diffusion – on syntheses performed in the absence of polymer in the mineralizing solution. The difference between Ihli's syntheses and those reported in this manuscript, apart from the absence of polymer additive in Ihli's

work, lies in two aspects: first, the volume-to-surface ratio of the solution is twice as large in Ihlí's work as compared to the work reported here (1.4 in Ihlí's study instead of 0.7 in this work), which slows down the gas dissolution process and the solution homogenization; second, the amount of ammonium carbonate powder is also larger (31 mmole of  $(\text{NH}_4)_2\text{CO}_3$  for 70 mL of 25 mM  $\text{CaCl}_2$  solution, instead of 0.1 mmole for 6 mL of 20 mM solution in this work), which likely results in a higher supersaturation index at long reaction times in the solution. Still, the curve obtained for the temporal evolution of the pH value is in qualitative agreement with our observations: the pH increases up to a value close to 10, and then decreases and stabilizes at 9.25 from 20 to 50 hours of reaction time. The early plateau at pH lower than 9.5, sometimes observed at the beginning of the reaction in Ihlí's work, is likely due to a longer homogenization time, as it disappears when the solution is stirred or when the height of the solution is decreased, leading to conditions similar to ours (Figure 83). Given the ion diffusion coefficient in water ( $10^{-9} \text{ m}^2/\text{s}$ ) and the solution height in our system (0.62 cm), the diffusion-based homogenization would be too long ( $4 \cdot 10^4 \text{ s}$ ) to explain the observation. Thus, the rapid homogenization in absence of stirring is likely induced by convection movements (solutal<sup>142,143</sup> or evaporation-induced).<sup>144</sup> Harris *et al.*<sup>11,105</sup> have reported a rise in pH with no intermediate plateau as well. In particular, the authors noticed<sup>11</sup> that the rise in pH was even faster when the volume of the reaction chamber is decreased, which is likely due to a faster increase in the gas partial pressures, and fully matches our experimental observations.

To my knowledge, the monitoring of the partial  $\text{CO}_2$  pressure has not been reported yet in the literature. Although such a monitoring does not provide access to the supersaturation index in the bulk, since the solution is not in equilibrium with the gas phase, it does highlight potential variability between syntheses, which can still occur in spite of an increased control of the powder state (% RH and grinding, see Materials and methods 2.1.1).

In conclusion, our measurements evidence an initial pH quench of the mineralizing solution, which strongly favors the dissolution and dissociation of carbon dioxide, especially at the air-solution interface.  $\text{CO}_2$  pressure monitoring further shows that the mineralizing solution is not in thermodynamic equilibrium with the gas phase, at least at short reaction times, when the pH is rather low, so that the  $\text{pCO}_2$  value cannot be used to determine the temporal evolution of the bulk carbonate concentration. Still, the initial pH jump strongly favors the increase of the supersaturation index in the solution, and thus the precipitation of calcium carbonate throughout the solution after some induction time.

### 3.4.2 Quench-induced liquid/liquid phase separation

Between 10 min and 30 min reaction time interfacial mineralized objects appear as thin discs that are a few nanometers thick (Figure 73 and Figure A. 1). Despite their small mean thickness, AFM microscopy evidences that they are thicker in the center than at the edge (variation from 4 nm to 5 nm, Figure 73). This variation in thickness is not associated with any variation in calcium chemical environment, as proven by STXM measurements (Table 8). The bulge in the center is therefore attributed to the initial lens shape resulting from the spreading of a drop at the interface (Figure 89 "In solution"). The existence of a liquid transient state is further confirmed by the fusion and double-emulsion patterns observed in TEM pictures (see Figure 74).

Still, the height of the collected objects does not gradually return to zero at the edge of the discs, as expected in the case of a drop deposited on a solid substrate (Figure 89 “Liquid-like sampling”), but rather quickly jumps to zero, indicating that the drops were already partially or fully solidified prior to sampling in view of AFM measurements (Figure 89 “Solidified sampling”). The collected mineralized objects would therefore be liquid droplets spontaneously solidified at the interface, or solidified in response to the introduction of dry air when the reaction chamber was opened for sample collection. When considering the size evolution reported in Figure 71, one can see that the Feret diameter increases from 1 to 10 min and then stays constant until 35 min, at which time it appears to have increased a bit. A reaction time of 10 min could therefore correspond to a time when the disc assembly has already solidified at the air-solution interface.

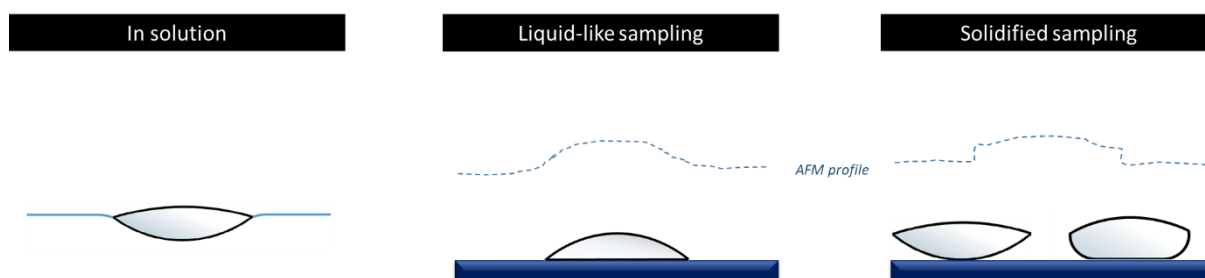


Figure 89 - Morphology of a liquid droplet at the air-solution interface. “In solution”: The surface tension influences the morphology of the wetting liquid. “Liquid-like sampling”: expected morphology and AFM profile of the droplet when taken out of the solution as a liquid. “Solidified sampling”: expected morphology and AFM profile of the droplet when taken out of the solution after solidification (left: fully solidified, right: partially solidified). Not to scale.

The detection of liquid droplets at the interface points to a liquid-liquid phase separation. However, this one might be restricted to the air-solution interface, as no scattering signal from the bulk could be detected during preliminary SAXS measurements over the period of time corresponding to the interfacial discs formation. Two mechanisms could lead to the observed liquid-liquid phase separation at the interface, as described in the introductory chapter (1.2.5), namely, binodal nucleation and spinodal decomposition. Still, a particular feature of our interfacial objects, namely the occurrence of double-emulsion patterns (Figure 74), points to as spinodal decomposition. Indeed, in binary mixtures, the presence of double-emulsion patterns has been associated with spinodal decomposition only, in the case of bicontinuous phase separation resulting from a deep quench.<sup>145</sup> Indeed, when phase separation occurs by spinodal decomposition, the interface between the ion-rich and the ion-poor phases is diffuse in the beginning.<sup>85</sup> Consequently, if the growth of the interface is rapid, the achieved local concentration can lie in the binodal nucleation zone. As a consequence, nucleation of a new phase can occur, and a double-emulsion pattern is observed.

Liquid/liquid phase separation in synthetic calcium carbonate systems has first been proposed in 2000 by L. Gower and D. Odom<sup>12</sup> and then reported in several other CaCO<sub>3</sub> synthesis studies,<sup>146–149</sup> with often limited direct evidence though, owing to the fact that it is very difficult to demonstrate the liquid character of a transient phase (see 1.2.5). In particular, Gower *et al.*<sup>12</sup> have described the accumulation of dense liquid droplets at the water-air interface in ADM syntheses performed in the presence of poly-aspartic acid. Later on, Cantaert *et al.*<sup>146</sup> have described droplets fusion at the air-solution interface, and imaged bulk liquid droplets using

cryo-TEM, in ADM syntheses performed in the presence of a positively charged polyelectrolyte (poly(allylamine hydrochloride)). The authors then attributed the increase in turbidity observed during ADM synthesis to light scattering by phase-separated liquid droplets, which later convert into amorphous particles. In syntheses relying on CO<sub>2</sub> diffusion into Ca(OH)<sub>2</sub> solution droplets, devoid of polymer additive and deposited on Si or glass substrates, Rodriguez-Navarro *et al.*<sup>72</sup> have observed bicontinuous patterns, typical of spinodal decomposition. Interestingly, the latter syntheses have led to the formation of micron-sized ACC hemispheres in compact arrangement at the gas-liquid interface, instead of the flat discs observed in our experiments. Still, in both cases, the spinodal decomposition was enabled by the deep chemical quench induced by the gas diffusion (of CO<sub>2</sub> only in Rodriguez-Navarro's study).

In the ADM syntheses reported here, although a surface-directed liquid-liquid phase separation has been clearly evidenced, no occurrence of a bulk liquid/liquid phase separation could be detected.

No studies until now have explicitly mentioned the formation of interfacial disc-like droplets at the air-solution interface during ADM syntheses. This could be due to the very low thickness of the discs (~5 nm), which makes it difficult to detect them with optical microscopy, and to their transient nature when the polymer additive allows their subsequent fusion by stabilizing long enough the liquid intermediate. As a consequence, these interfacial objects appear to have been fully overlooked. However, in a different kind of syntheses, which relies on the rapid CO<sub>2</sub> outgassing of a CaCO<sub>3</sub> solution,<sup>150</sup> similar structures, not mentioned in the paper though, clearly appear in the pictures acquired using waveplate-assisted birefringence microscopy (see Figure 90).

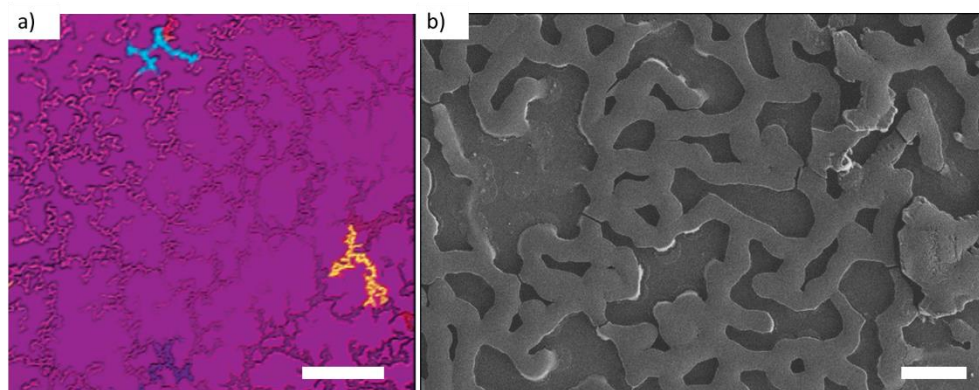


Figure 90 - Similarity of interfacial structure as presented in Amos *et al.*<sup>150</sup> and our experiment. a) Interfacial ACC film (in purple) going through a crystallization process (in blue and yellow), during a PSLP experiment. Scale bar = 100  $\mu\text{m}$ . b) Electronic micrograph (SEM) of an amorphous calcium carbonate film ( $[\text{Ca}^{2+}] = 20 \text{ mM}$ ,  $[\text{PANA}] = 20 \text{ ppm}$ , 18.5 h of reaction) created during this work. The image is taken at 2 kV with HE-SE detector.

In summary, our results clearly indicate that a liquid-liquid phase separation occurs at the interface, leading to an assembly of disc-like droplets, of micron diameter and thickness less than 5 nm. This phase separation is achieved by a spinodal decomposition mechanism, allowed by the rapid quench in pH resulting from the ammonium carbonate decomposition. To my knowledge, this study is the first to identify these discs as a signature of an interface spinodal

decomposition and to report the radial growth of the disc-like droplets at the air-solution interface (see Figure 71). Then, likely after about 10 min of reaction, the spinodal decomposition is arrested by spontaneous dehydration of the liquid phase which leads to its solidification. In this way, liquid-liquid phase separation directs the formation of a mineralized pattern at the air-solution interface.

### 3.4.3 Thickening by bulk particle aggregation

After 35 min of reaction, three kinds of structures are observed (Figure 75). Structures of type I have a similar structure to the objects observed at shorter times (<35 min) and are about 5 nm thick in their center (AFM measurements). Structures of type II have a more pronounced nanostructure and a greater but still homogeneous contrast. AFM measurements (Figure 77) have shown that type II structures are thicker (~20 nm) than type I. Finally, structures of type III are characterized by an increase in absorption due to a nanostructured material (TEM). This higher absorption is attributed to an increase in thickness (SEM observations).

The coexistence of these three types of structures raises the question of their relations to each other, and to the early disc-shaped structures, and finally suggests a sequence of formation. The type II structures being of the same contrast and homogeneity as the edge of the type III structures, it seems that the latter are in fact type II structures modified by a localized aggregation of nanoparticles. In contrast, the aggregation of nanoparticles does not occur on the type I structures, which remain homogeneous and smooth. Type II structures may arise from the homogeneous deposition of particles on structures of type I as they follow exactly the shape of structures of type I and show a constant thickness (Figure 75.a, homogeneous coloration of type II structures). Aggregation may also take place on the periphery of the disc at this stage, as the border of the structures of type II is not smooth (see Figure 75.c), in addition to previously observed objects. Moreover, the diameter of the discs is larger at 35 min, pointing to the addition of material at the border of the disc at this reaction time. Since the structures of type I are similar to the discs at shorter time, it is likely that they exist prior to the formation of type II, and therefore type III structures. Thus, the temporality of the thickening would be: I → II → III. This can be summarized by saying that, after an initial radial growth, the interfacial discs undergo a nanostructured thickening.

This thickening process most likely arises from the irreversible aggregation of bulk nanoparticles. Light-scattering species are indeed detected in solution at the time when the interface objects start to thicken (~40 min). These species correspond to aggregates of amorphous nanoparticles, as shown by TEM and STXM images. When collected close to the interface, they appear as loose aggregates composed of 30 nm particles (cryo-TEM pictures). These aggregates do not exhibit smooth round morphologies, typical of liquid droplets (Figure 87) and therefore appear to be amorphous solid particles. They look very much the same as the loose prenucleation cluster aggregates observed by Dey *et al.*<sup>151</sup>, using cryo-TEM, in calcium phosphate syntheses.

The detection of the light-scattering bulk particles is in line with the reported observations on calcium carbonate ADM syntheses.<sup>93,109,152</sup> Ihli *et al.*<sup>109</sup> have described an increase in the measured turbidity of the solution, associated with the precipitation of calcium carbonate,

without specifying the particle size however. In Ihli's study, the reported induction as measured in turbidimetry time was shorter (15 min) as expected in the absence of added polyelectrolyte. Xu *et al.*<sup>93</sup> determined that in presence of ds-DNA, a precipitation event take place after 150 min of reaction, opacifying the solution. In their seminal paper<sup>152</sup>, Gower and Odom actually mentioned a turbidity increase, detected by visual inspection only, that they associated with the presence of liquid droplets in solution. Still, no experimental demonstration was actually carried out. The results presented here are, to my knowledge, the first actual characterization of the interplay between the interface and bulk mineralization, based on time-resolved measurements of both processes.

The presence of light-scattering bulk particles highlights the formation of large convection rolls in the solution (~45 min Figure 70), until the solution becomes fully turbid (90 min, not shown here). As a matter of fact, the morphology of the film at long reaction time (60 min, Figure 91.a) is similar to Marangoni cells observed in systems subjected to Rayleigh-Bénard-Marangoni convection,<sup>153</sup> and may actually result from a solutal Rayleigh-Bénard-Marangoni instability owing to the concentration gradient at the free surface of the mineralizing solution<sup>154</sup>. In the case of combined thermal and solutal Marangoni convections (Figure 91.b), the patterns at the interface of a binary fluid (water and saline solution) fully resemble our observations. To my knowledge, the existence of convection rolls has never been mentioned in the literature concerning PILP-related ADM syntheses.

Both the observation of convection rolls in solution and the pattern formed at the interface point towards a convection-assisted thickening of the interfacial film. The localized appearance, at the start of the thickening process, of a phase contrast in the film (Figures 66 and Figure 78), and the propagation of a thickening front would hence be triggered by the arrival of an upward flow of nanoparticles, owing to localized ascending currents in convection rolls.

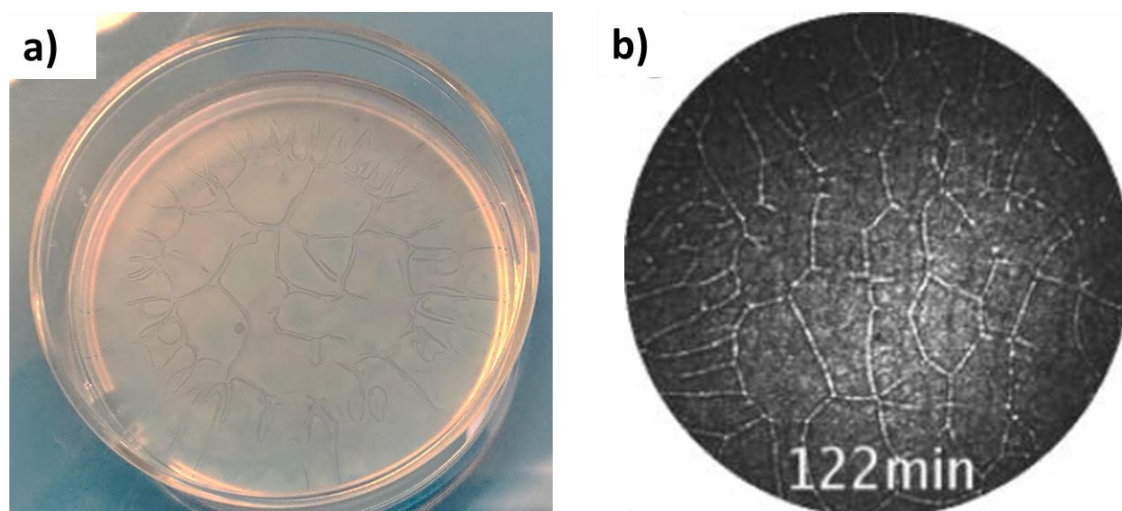


Figure 91 - Interfacial pattern a) formed in our system after 60 min of reaction in a pellet synthesis. (b) formed by convection Shadowgraph taken at the air-water interface of an evaporating binary fluid (Water-NaCl solution). From Zhang *et al.*<sup>155</sup>

Finally, while type III structures clearly result from the reported thickening process, the fact that the structures of type II follow the shape of the early discs, and exhibit constant thickness is confusing. Traces of intermediate states between type I and type II structures have not been

detected, maybe owing to a lack of data at intermediate reaction times, so that the transformation mechanism from type I to II could not be evidenced. One could imagine though that bulk particles diffuse and then homogeneously adsorb on the early discs before convection rolls developed. Alternatively, the structures of type II could result from the spreading of a liquid-like assembly of ACC clusters, similar to the one proposed by Xu *et al.*<sup>93</sup> to explain PILP mechanisms of crystal formation, on the early discs.

During the thickening process, nanoparticles not only aggregate underneath the interface structures, but also likely at the edge of the structures. This assumption is supported by the presence of a porous corona surrounding the interfacial mineralized structures (Figure 65). The V-shaped junction between the core and the corona of the mineralized discs (see Figure 92.a) is reminiscent of the three-phase contact line all around the droplets at the interface (see the red arrow in Figure 92.b). This junction, creating an irregularity at the particles aggregation point could very well be a source of defects during the thickening process (similarly to the pinhole defects observed in PVD processes<sup>156</sup>), therefore creating pores around the edges of the former droplet.

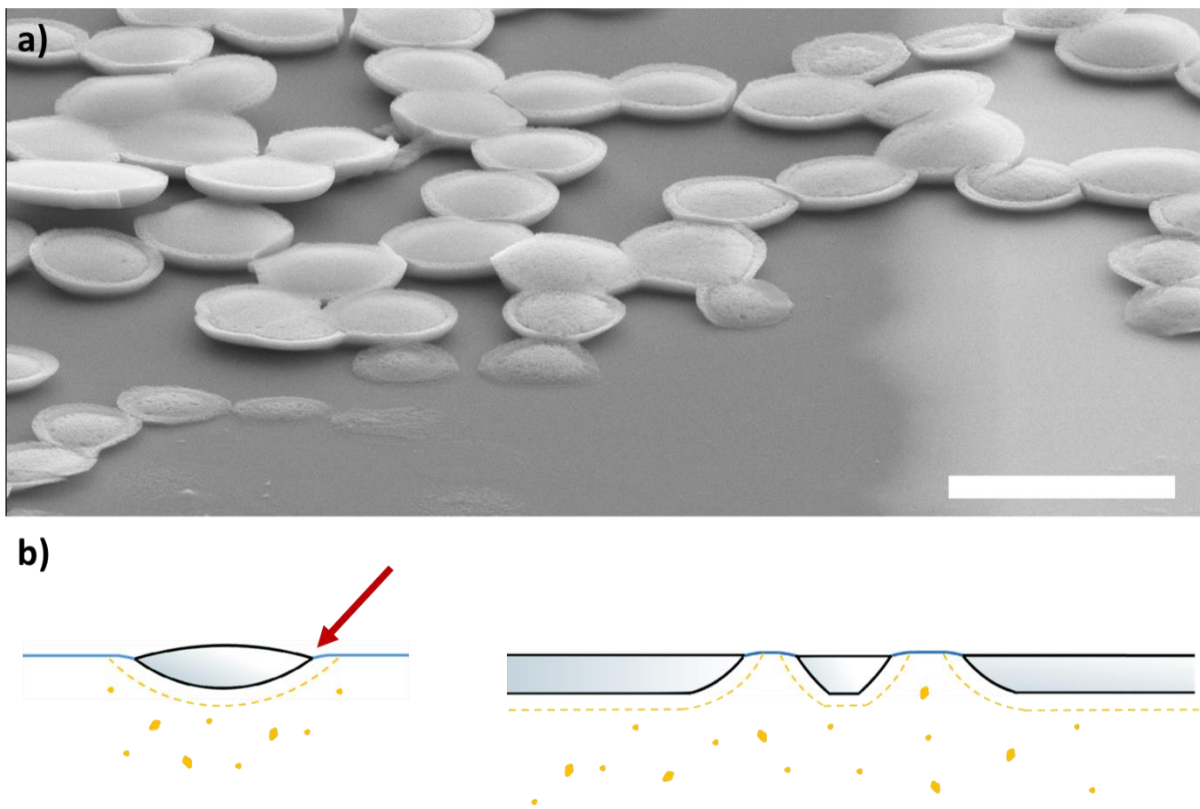


Figure 92 - Morphological traces of the thickening process. a) Electron micrograph (SEM) of a film ( $[Ca^{2+}] = 20 \text{ mM}$ ,  $[PANa] = 20 \text{ ppm}$ , 19 h of reaction) heated at 300 °C directly after sampling. The observations are made with a 70° angle, at 15 kV, with the HE-SE detector. Scale bar = 10  $\mu\text{m}$ . b) Schematic representation of the attachment process of bulk particles (in yellow) in the case of a disc patterned (left) and continuous (right) film. The addition of particles leads to the thickening of the film (yellow dashed line). The red arrow indicates the location of the three-phase contact line surrounding the initially liquid droplet.

In summary, following the initial patterning of the interface by a surface-directed LLPS, the assembly of disc-like droplets solidify and thicken by an irreversible aggregation of bulk amorphous nanoparticles. Over time, this thickening process is strongly enhanced by the development of convection rolls in the bulk, which both homogenize the concentrations throughout the solution and generate upward flows of particles towards the interface. This process ends up when sedimentation, probably due to aggregation of nanoparticles in bulk, finally takes place.

### 3.4.4 New model proposition

The reported findings evidence a two-step mechanism of film formation (Figure 93). First, a chemical quench causes a surface-directed liquid-liquid phase separation by spinodal decomposition at the interface. The denser calcium carbonate liquid phase then wets the interface forming slightly bulging discs of micron size and nanometer thickness (Figure 73). The discs grow radially, without any change in their chemistry, until they reach a size of about  $3.5\ \mu\text{m}$ .

In a second step, a homogeneous layer of nanostructured material is deposited on the interfacial discs, which cover their entire surface, this way initiating a first thickening of the mineralized structures. Bulk nanoparticles, brought to the interface by convection rolls, then adsorb on this second layer (Figure 93), inducing a fast thickening of the mineralized structures, until the sedimentation of the bulk aggregates takes place and the thickening of the film stops.

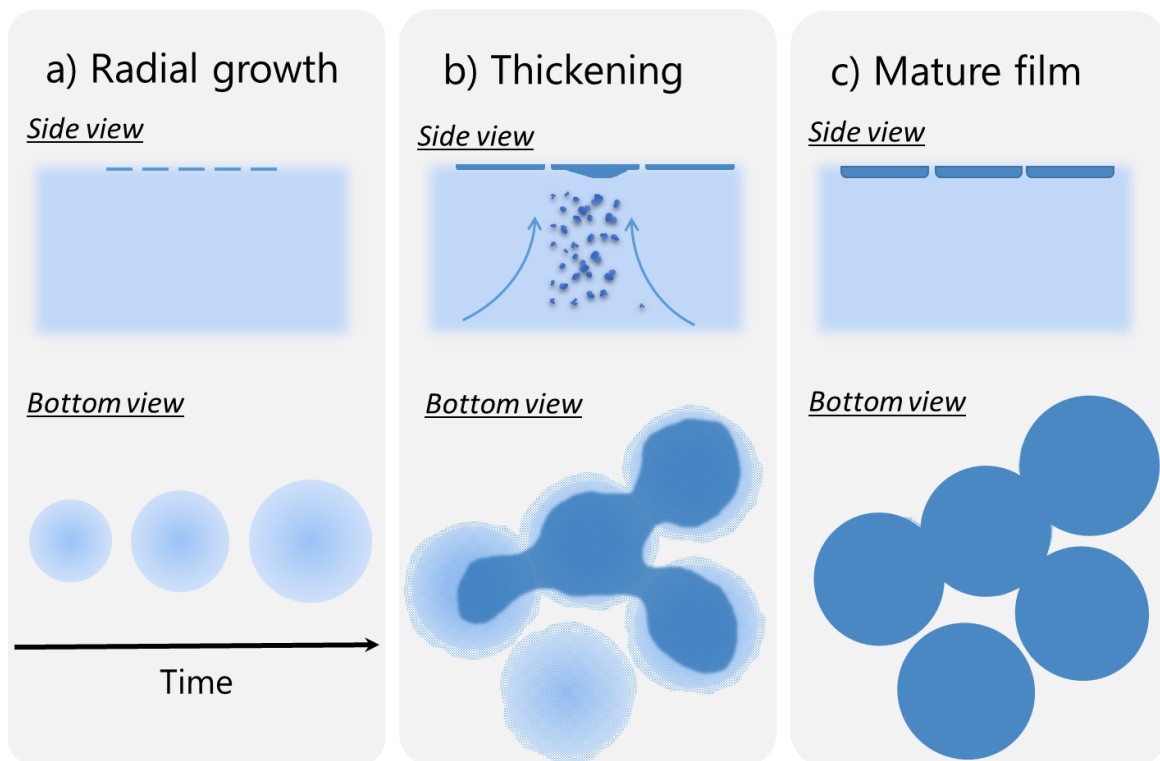


Figure 93 - Schematic representation of the amorphous film formation at the interface. In each panel, a cross-section of the bulk solution and interface objects ("side view") and a bottom view of the interface objects only ("Bottom view") are represented a) Domains of liquid spread at the



*interface grow radially with time. b) A homogeneous layer of particles is added first to the disc pattern. Then, bulk particles, brought to the surface by convection rolls massively aggregate onto the disc pattern, leading to strong thickness heterogeneities. c) Finally, a mature ACC film of constant thickness is formed.*

This two-step mechanism is believed to be common to both discontinuous and continuous films, as the latter exhibit traces of micron-sized discs formed at early reaction times (Figure 65). However, the larger amount of polymer additive in the continuous film syntheses likely provides a longer-term stabilization of the phase-separated liquid, thus allowing the near-complete coalescence of the interfacial liquid droplets before the liquid dehydrates and solidifies.

In conclusion, the mechanism of ACC film formation in ADM syntheses has been deciphered by combining *in situ* and *ex situ* structural analyses, this way evidencing the involvement of both a surface-directed liquid-liquid phase separation and amorphous nanoparticle aggregation in the formation process. Although the generality of this process needs to be investigated further, it appears in line with experimental observations reported in the literature. In particular, the templating effect of the phase-separated liquid is fully consistent with the observations of a "surface membrane on the vaterite crystals"<sup>157</sup> or "membraneous substrate that mediate the growth of CaCO<sub>3</sub> crystals"<sup>158</sup> reported long ago in CaCO<sub>3</sub> syntheses in the presence of poly-aspartic acid polymer. Occasionally, we could actually see patches of the film detaching from the interface and falling down in the solution, along with helicoid crystals, similar to the one reported in references,<sup>157,158</sup> at the bottom of the Petri dish.

## 4 CONTROL OF CRYSTALLIZATION: INCIDENCE ON CRYSTALLINE PROPERTIES

---

In the previous chapter, I have shown that amorphous calcium carbonate films of controlled morphology can be synthesized using ADM syntheses in the presence of sodium poly-acrylate. Amorphous calcium carbonate is a metastable state, and therefore appears as a transient state prior to crystallization. Its consistent observation in biominerals indicates that it plays a key role in the biocrystallization pathway, although not fully understood to date. This observation led me to study the crystallization of the synthesized amorphous films following three distinct crystallization pathways, so as to decipher the influence of the crystallization conditions on the produced crystals. In this chapter, I will therefore present these three crystallization routes, corresponding to thermal heating, exposure to a high humidity atmosphere, and spontaneous crystallization at the air-solution interface, respectively.

These different pathways have indeed produced crystalline films with different morphology, nanostructure and crystalline properties. For each type of transformation, the structural features of the crystallized film have been determined, using both microscopy and spectroscopy techniques, providing informations on the structure at the microscale (WBM, SEM), nanoscale (SEM) and atomic scale (Raman, STXM). Vectorial and Bragg ptychography imaging have provided further insights into the crystalline properties, in terms of distribution of crystalline orientations, crystal coherence length and defects distribution. Although all three crystallization routes lead to iso-oriented calcite crystals, the shape and nanostructure of the latter differ from one to the other.

As a conclusion of this chapter, the impact of the crystallization conditions on the resulting crystals will be highlighted and the mechanisms of the amorphous-to-crystalline transformation will be discussed.

### 4.1 HEAT-INDUCED CRYSTALLIZATION

The amorphous-to-crystalline transformation involves the dehydration of the amorphous phase, which is thermodynamically unfavourable. It is therefore associated with an activation energy barrier that needs to be overcome in order to trigger the crystallization process. In particular, thermal heating can be used as a crystallization trigger. In this section we will present the crystals resulting from the heating, at 300°C, of amorphous calcium carbonate films produced by ADM syntheses. The temperature used was chosen by considering the results of Xu *et al.*,<sup>96</sup> where such a temperature was shown to allow the complete transformation of ACC material into calcite, without any change in the nanostructure. In their work on the dehydration and crystallization of ACC in air,<sup>59</sup> Ihli *et al.* further confirm that this temperature is enough to induce the full dehydration of the amorphous calcium carbonate, whatever its initial hydration level.

In the following, unless otherwise specified, only the results for disc-patterned films will be presented, as this allows a better visualization of the change in morphology during

crystallization. The corresponding analysis for continuous films will be presented in the appendix (6.3.1).

#### 4.1.1 Microscale crystallinity

When heated at 300°C for three hours, the amorphous disc-pattern film becomes birefringent. Under birefringence wave plate-assisted microscopy (BWM), it now exhibits domains about ~1 to a few 10 microns in size, whose color differs from the "sensitive tint", i.e. the pink color that is characteristic of the non-birefringent materials. The film has therefore crystallized, while retaining its microscale morphology. In Figure 94, the preservation of the morphology is evidenced by the presence of the very same disc pattern before (Figure 94.a) and after (Figure 94.b) heating. Large domains of homogeneous color are visible, which encompass several discs but sometimes terminate in the middle of a disc (Figure 94.b, inset). Some parts of the film remain pink, however, after the heating process (see the blue and yellow arrows in Figure 91.b). This could of course mean that they did not crystallize. Yet, other effects could explain the absence of detected birefringence:

- the sample could be too thin to exhibit birefringence; this might explain the absence of birefringence of the low-absorbing discs in the left-hand part of the picture (blue arrows);
- the c-axis of the crystal (extra-ordinary axis) could be perpendicular to the image plane or one of the neutral axes of the crystal could be oriented along the polarizer direction; this undoubtedly explains the pink colour of some discs in the right-hand part of the picture, which are surrounded by discs of colour other than pink.

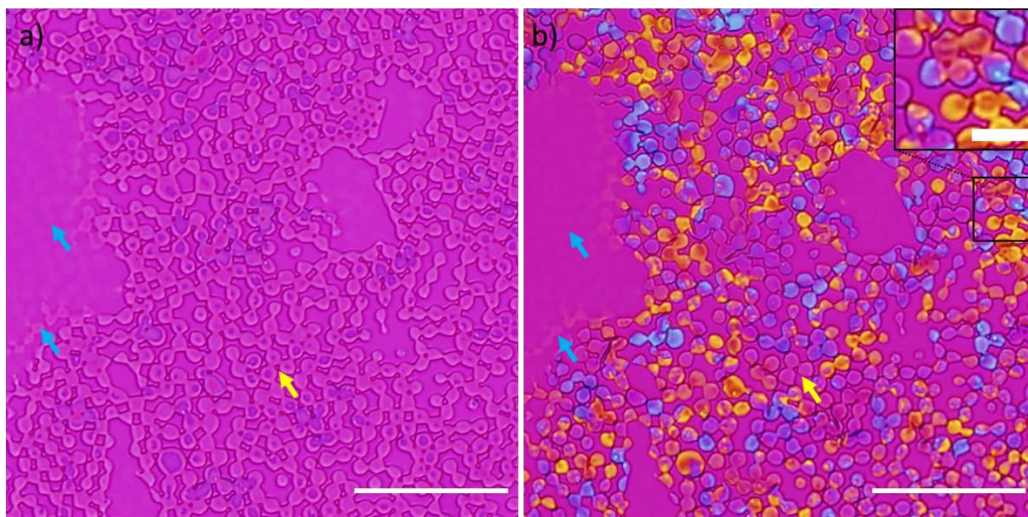


*Figure 94 - Optical micrographs (WBM) of a disc patterned film before and after heat treatment. a) Film immediately after sampling (17h in pellet synthesis,  $[Ca^{2+}] = 20$  mM,  $[PANA] = 20$  ppm). Scale bar = 50  $\mu$ m. b) Same film heated at 300°C for 3h just after initial observation. Scale bar = 50  $\mu$ m. Inset: Zoom showing areas with abrupt changes of coloration within discs. Blue and yellow arrows highlight untransformed coloration areas.*

Therefore, heating at 300°C the disc-pattern films triggers the amorphous-to-crystalline transformation of the discs, almost everywhere in the sample, while preserving the disc pattern.

*Continuous film:* Birefringent domains were less developed in the case of continuous films, unless they were deposited on conductive substrates, like gold or copper TEM grids, prior to heating. In addition, these domains were located mostly along cracks. (Figure A. 21).

### 4.1.2 Structure at the nanoscale: surface and edges analysis.

SEM microscopy was used to investigate the morphological features of the crystallized film at the nanoscale. It evidences once again the preservation of the micron-sized discs during crystallization, and additionally shows that cracks have been induced everywhere in the disc assembly by the heating process. These cracks separate discs from each other, thus revealing the internal structure of the film.

Although all discs exhibit a surface nanostructure, some appear smoother than others owing to a more compact nanostructure (Figure 95a). This surface nanostructure is not even homogeneous within a single disc. Last, the discs are surrounded by a corona approximately 250 nm wide (Figure 95), reminiscent of that of the amorphous discs (Figure 67). However, the core and the corona of the discs do not differ in nanostructure (Figure 96.a and .b). One can sometimes observe a lack of nanogranular material at the junction between the core and corona.

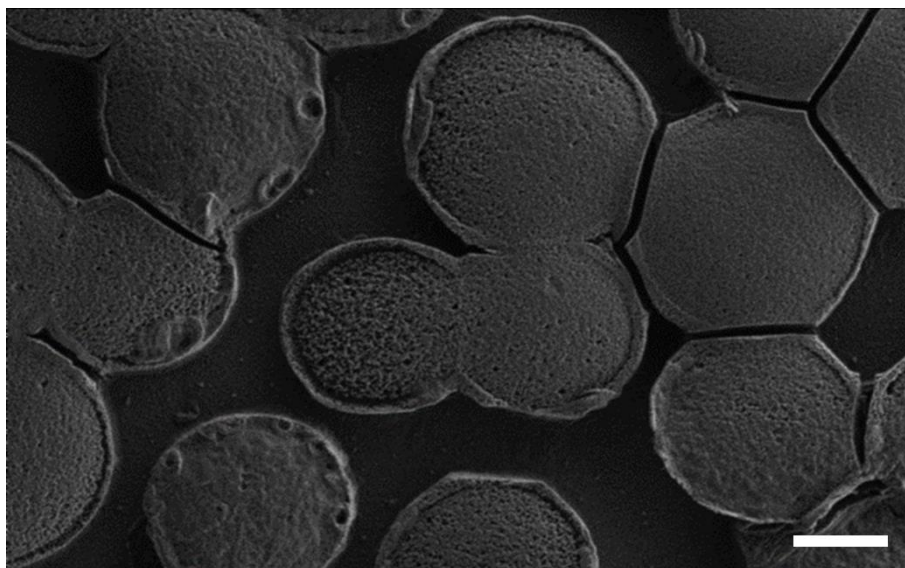


Figure 95 - Electron micrograph (SEM) of a disc-patterned film heated at 300°C for 3h. HE-SE detector, 1 kV. Scale bar = 2  $\mu$ m.

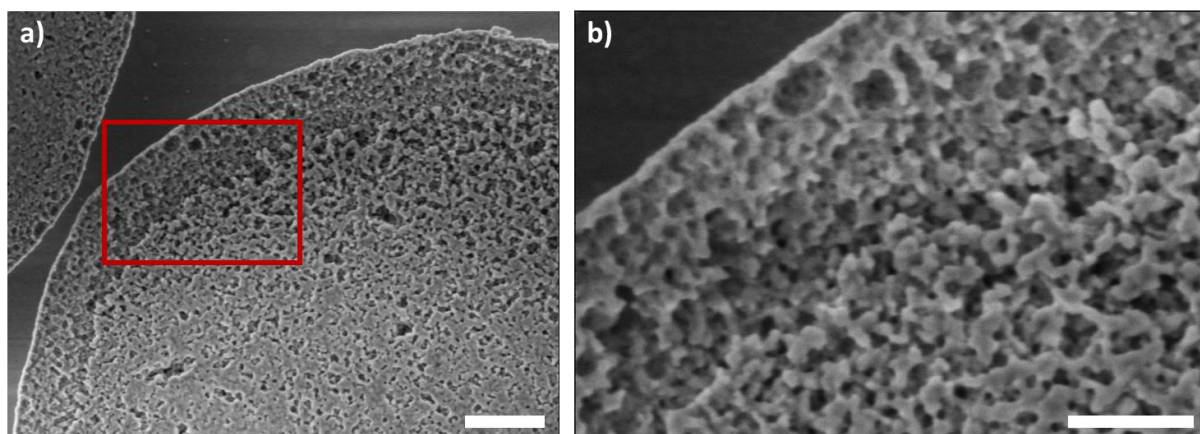


Figure 96 - Electron micrograph (SEM) of the border of a disc with its corona. The red rectangle corresponds to the enlarged image shown in b). In lens detector, 1 kV. Scale bar = 400 nm. b) Zoomed-in view of the corona. In lens detector, 1 kV. Scale bar = 200 nm.

In back-scattered electron mode (sensitive to the atomic number Z in the investigated area), the corona is indistinguishable from the core (Figure 97.a). Elemental analysis based on EDS measurements (Figure 97.b, .c, .d and .e) actually shows that the corona is chemically identical to the core. Calcium, carbon and oxygen distributions are indeed the same everywhere within the discs (Figure 97.b), meaning that in addition to being structurally similar the core and corona are made of the same material.

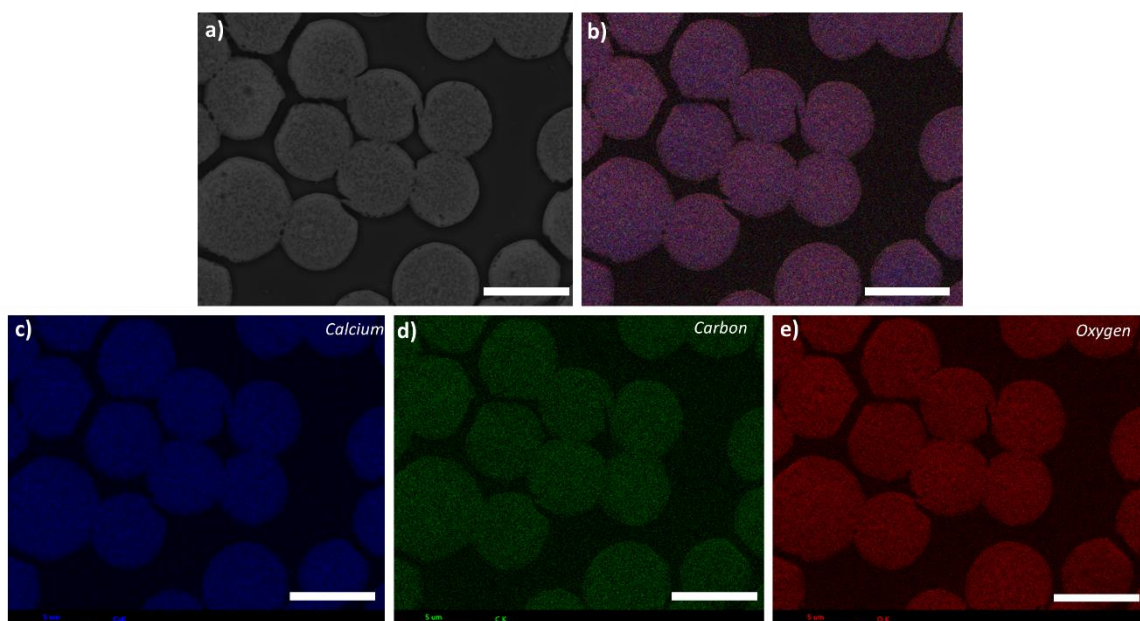


Figure 97 - Elemental maps based on EDS measurements performed on a crystallized disc-patterned film. a) SEM micrograph in back-scattered electron mode. b) Composite image of the elemental maps shown in c, d and e. c) Calcium distribution in the investigated area. d) Carbon distribution. e) Oxygen distribution. The elemental maps are not quantitative, the intensity scale has been selected in each case to optimize the visualization of the distribution. Scale bar = 5  $\mu\text{m}$ .

Heating produces cracks in the sample, thus exposing some edges and revealing the internal structure of the film. On broken edges, the nano-structuring inside the film appears visible by

SEM (Figure 98). The crystallized disc-patterned films are shown to be homogeneously composed of aggregated nanoparticles, like their amorphous counterparts.

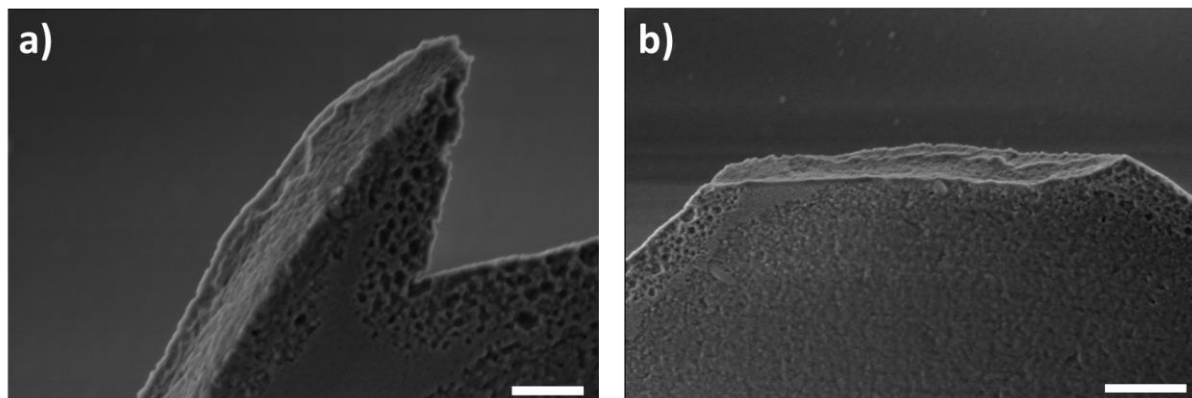


Figure 98 - Electron micrographs (SEM) showing the edges of discs following the heat treatment. a) and b) correspond to different discs and different angle of observation. In lens detector, 1 kV. Scale bars = 200 nm.

*Continuous films:* The morphology of the heated continuous films was already presented in Chapter 2 (Figure 65.b, Figure 67.b and Figure 68) and is in particular characterized by a space-filling nanostructure, very similar to the disc-patterned films presented here.

#### 4.1.3 Polymorph selection

The crystals produced at 300°C are made of calcite, as shown by Raman spectroscopy (Figure 99). The detected vibration bands actually correspond to the vibration bands visible on the reference spectrum of calcite (Materials and methods 2.6.1.2).

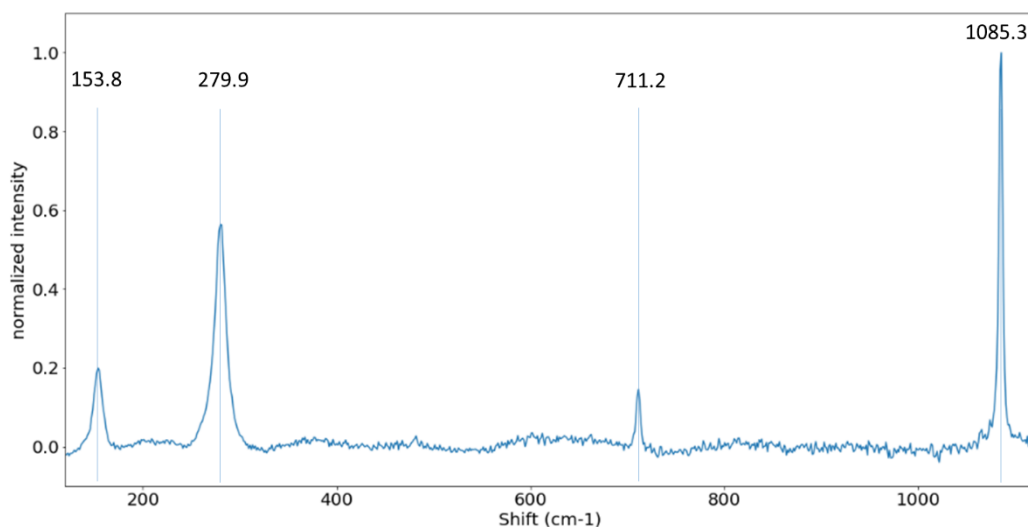


Figure 99 - Raman spectrum of a heated disc-patterned film sample - (cap synthesis, 16h30 of reaction) heated for 3 hours at 300°C. The bands fit the calcite reference spectrum as  $\nu_1$  band is

located at  $1085.3\text{ cm}^{-1}$ ,  $\nu_4$  at  $711.2\text{ cm}^{-1}$ , and lattice bands at  $279.9\text{ cm}^{-1}$  and  $153.8\text{ cm}^{-1}$ .

Calcite signal is systematically detected when the light-absorbing discs in Figure 94 are analyzed by Raman spectromicroscopy. Therefore, the light-absorbing discs that remained pink after heating are actually crystallized, their crystalline orientation making however their detection by birefringence microscopy impossible. On the contrary, the thinner discs, highlighted by blue arrows in Figure 94, do not emit any Raman signal, so that it is not possible to conclude whether they are uncrystallized regions or crystallized regions too thin to be detected.

*Continuous films:* Although non-birefringent, continuous films exhibit a Raman spectrum with a clear calcite signature (Figure A. 21). Therefore, the lack of birefringence is probably due to the orientation of the neutral or extraordinary axes (as mentioned in 4.1.1).

#### 4.1.4 Calcium environments in the crystallized films

In order to investigate the calcium environment, and to obtain a high spatial resolution imaging of the calcite distribution in the sample, I performed STXM spectroscopy at the  $L_2$ ,  $L_3$  edge of calcium (Materials and method, 2.6.2). Owing to the very strong resonance at the Ca L-edge, only samples thinner than a couple of 100 nm can be analyzed by STXM. The usual film thickness produced from the synthesis protocol I have established, is around 500 nm to 700 nm, making it too thick for STXM analysis. We therefore focused on thinner areas of the sample as presented in Figure 100.a, where typical OD at the  $L_2$  edge is under 2 (most absorbing investigated area, in Figure 7.b).

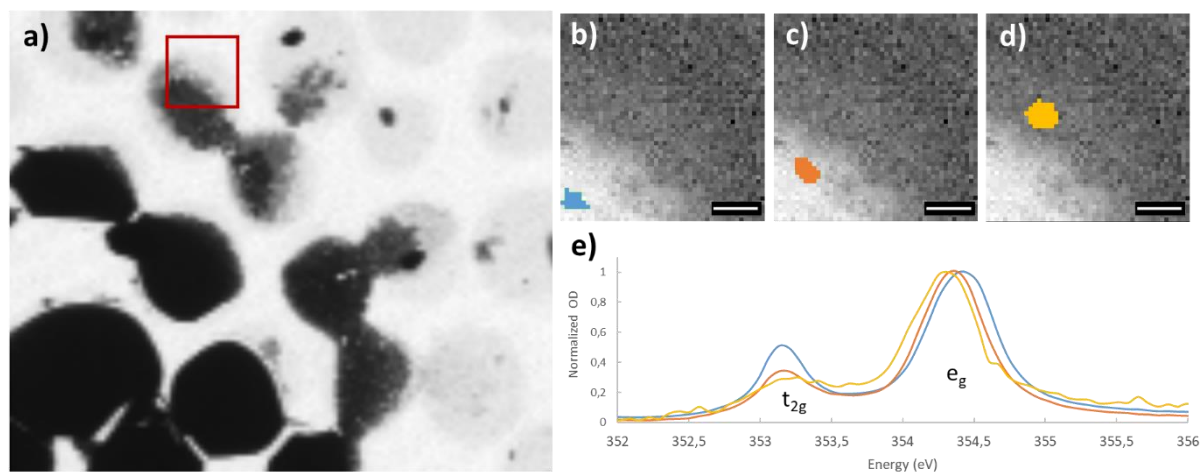


Figure 100 - a) STXM absorption map at 351.2 eV. The area corresponding to the red square was investigated by hyperspectral imaging and analysed in b-e). Scale bar = 5  $\mu\text{m}$ . b-d) Optical density maps at the Ca L-edge showing the three different regions (colored areas) where XAS spectra have been averaged to provide the curves displayed in e). e) X-ray absorption spectra at the calcium  $L_2$  edge in different places of the film sample. The blue spectrum was averaged over the blue area in b), the orange spectrum over the orange area in c) and the yellow spectrum from the yellow area in d).

Different calcium environments are detected in the heated-film sample. These environments are characterized by two parameters: the peak splitting  $\Delta_0$  and the energy level  $E_0$ . As a reminder (see Materials and methods 2.6.2) the peak splitting is the energy difference between the two non-degenerate d-orbitals  $e_g$  and  $t_{2g}$ , resulting from the crystal field effect, that is, from the anions structuring around the calcium ions. The stronger the crystal field effect in the investigated sample, the greater the degeneracy breaking of the d-orbitals and, therefore, the wider the peak splitting. On the other hand,  $E_0$  is the energy of the calcium 3d orbitals when the anions distribution around calcium ions is fully spherical so that the 3d-orbitals are fully degenerated (i.e., the crystal splitting effect vanishes). As explained in the Materials and methods,  $E_0$  was calculated by assuming that the acquired spectrum results from an octahedral configuration of the carbonate ions around the calcium ions, similar to the calcite configuration in which each calcium ions is surrounded by six carbonate ions. For this calculation, only the  $L_2$  resonance is shown, but the full spectra (including the  $L_3$  and  $L_2$  resonances) are available in the Appendix Figure A. 13, Figure A. 14 and Figure A. 15).

The most-absorbing part of the disc (Figure 100.b, blue spectrum) has the same peak splitting as calcite ( $\Delta_{\text{calcite}} = 1.29$  eV,  $E_0 = 353.78$  eV). Therefore, one can state that it has actually crystallized into calcite, although the film thickness in the investigated region is much smaller than the mean thickness of the film (Figure 100.a).

The intermediate absorption area (Figure 100.c, orange spectrum) has a weaker crystal field (weaker  $\Delta_0$ ), but similar  $E_0$  as calcite. This means it has a less organized structure although calcium ions are still surrounded by 6 carbonate ions. This could be the spectral signature of either pure amorphous calcium carbonate with little organization, or of a mixture of both amorphous calcium carbonate and calcite.

Finally, the less-absorbing area (Figure 100.d, yellow spectrum) has the weakest crystal field (weaker  $\Delta_0$ ), but still the same  $E_0$  as calcite. Moreover, the  $L_3$ - $t_{2g}$  peak is almost absent (see Figure 100). The value of the  $L_2$  peak splitting and the decrease of the  $L_3$ - $t_{2g}$  peak is characteristic of a purely amorphous calcium carbonate, in a dehydrated state<sup>55</sup>. Therefore, the thin part of the film, did not crystallize despite the heat treatment. This result suggests that the low-absorbing discs in Figure 91.b, which are not birefringent, may actually be amorphous.

There are therefore at least two coexisting calcium chemical environments in the heated sample, one corresponding to calcite and the other one to an amorphous state.

Table 9 - Peak splitting and  $E_0$  energy values, calculated from Figure 100 spectra.

<b>Component</b>	<b><math>L_3, \Delta_0</math> (eV)</b>	<b><math>L_2, \Delta_0</math> (eV)</b>	<b><math>E_0</math> (eV)</b>
<b>Yellow spectra</b>	1.07	1.08	353.64
<b>Orange spectra</b>	1.17	1.18	353.64
<b>Blue spectra</b>	1.25	1.25	353.66



---

Film crystallized under heat retain their original shape and remain nanostructured. They are made of iso-oriented domains of calcite from a 1  $\mu\text{m}$  to  $\sim 10 \mu\text{m}$ . The thinner parts of the film remains amorphous despite the heat treatment.

---

#### 4.1.5 Crystal orientation: in-plane and thickness distribution

To go beyond the birefringence analysis of the crystalline orientation within the films, vectorial ptychography measurements were carried out on heated film samples at a spatial resolution similar to optical microscopy. The investigation was performed in an area where the thickness of the discs is equal to the mean film thickness ( $\sim 500 - 700 \text{ nm}$ ) (not shown here). Based on previous observations (4.1.3 of this chapter), the discs are made of calcite crystals. They exhibit birefringence (the fast axis observed in the sample plane being a projection of the c-axis of the crystal), so vectorial ptychography can be used to retrieve mappings of their crystalline properties.

Heat-induced crystals exhibit a weak retardance ( $\propto \Delta n_{eff} d$ ), inferior to 1.5 rad in all our measurements (Figure 101.a). When it is inferior to 0.5 rad (dark blue in Figure 101.a), it cannot be distinguished from the background noise anymore. A weak retardance indicates a c-axis close to the normal of the image plane, or a thin sample.

The ratio between the unwrapped phase and the retardance, which amounts to the ratio between  $n_0$  and  $\Delta n_{eff}$  (Materials and methods 2.5.1.2), is not constant in the whole sample ('tilt ratio', Figure 101.b), mostly because the retardance could have significantly different values from one disc to another (Figure 101.a), while the unwrapped phase (Figure 101.e) remains relatively constant. This latter finding indicates that the disc thickness in the investigated area is rather constant (assuming that the materials is homogeneous with a constant  $n_0$  value). The space variations of the unwrapped phase-to-retardance ratio therefore suggest that  $\Delta n_{eff}$ , and consequently the tilt of the c-axis with regard to the image plane, varies across the sample, with nevertheless groups of discs in close contact having the same tilt ratio, represented by constant coloration in Figure 101.b.

As a first summary, on the whole investigated area, the c-axis tilt with respect to the image plane, and hence the fast-axis orientation, varies. Both parameters can be locally constant (Figure 101.b and .c). Domains of shared orientation are distributed over the image.

The eigenpolarizations have an ellipticity of about 0.2 (Figure 101.d, measured for retardance values  $> 0.5 \text{ rad}$ ). As a reminder, ellipticity of the eigenmodes is a consequence of the misalignment of the crystalline layers in the sample thickness (see Materials and methods 2.5.1.2). The shape of the eigenpolarizations can be visualized in Figure 101.e and f. The observed values suggest a reasonable level of crystalline order in the film thickness.

Figure 101.e shows the eigenpolarizations, and highlights the difference in fast axis orientation among the iso-oriented domains. Figure 101.f, which is an enlarged view of Figure 101.e, evidences two neighboring iso-oriented domains composed of several discs. It further shows that the change in orientation occurs in the middle of a disc (red dashed line).

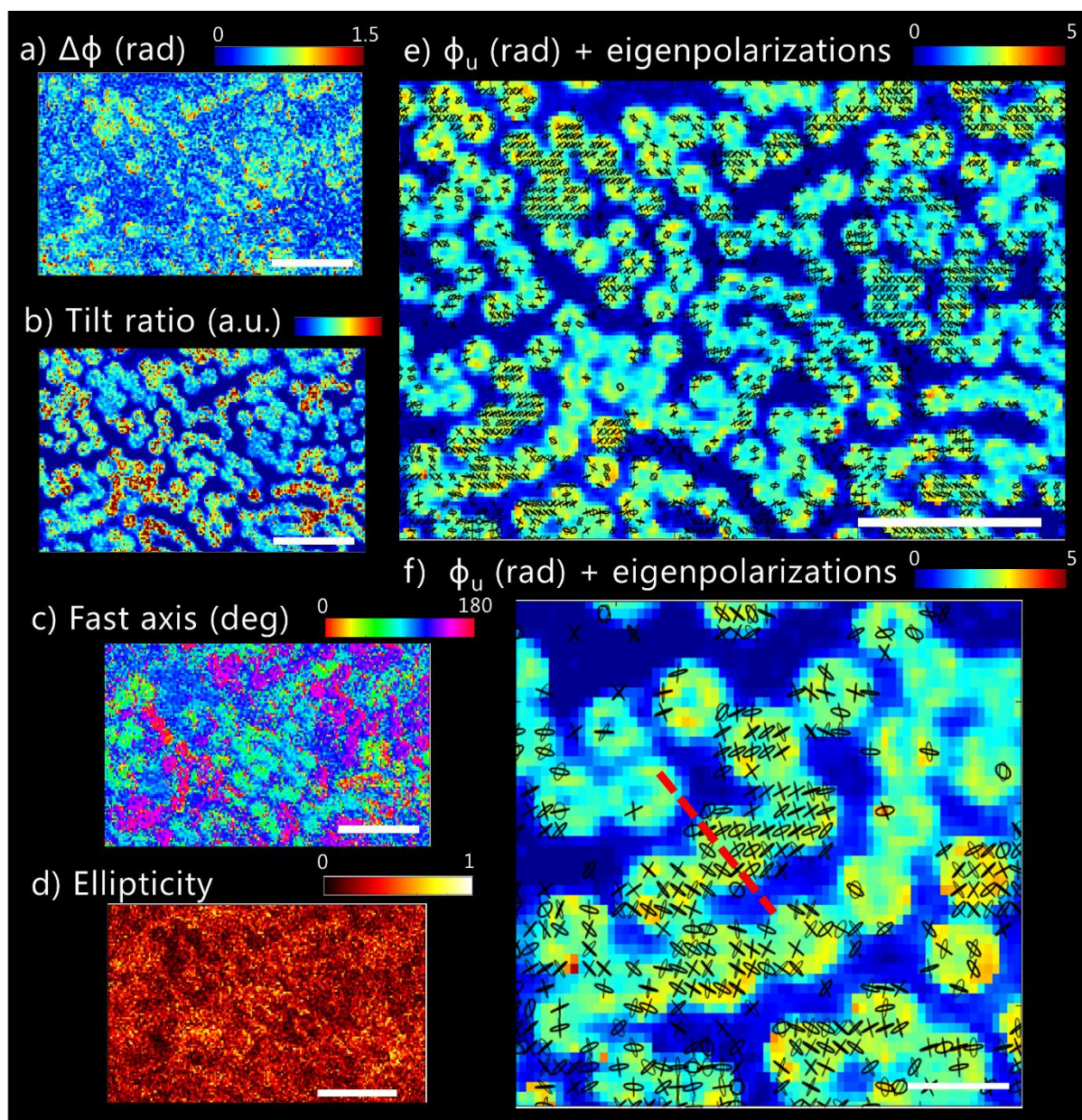


Figure 101 - Vectorial ptychography analysis of a heated film. The film sample has been collected at the surface of a  $[Ca^{2+}] = 20 \text{ mM}$ ,  $[PANa] = 20 \text{ ppm}$  solution after 18h of reaction, and heated at  $300^\circ\text{C}$  for 3h. a) Retardance (in radians, 0 to 1.5). b) c-axis tilt ratio (a.u.). c) Fast-axis orientation (in degrees, from 0 to 180) d) Ellipticity (absolute value, 0 to 1; 0 corresponds to a linear polarization and 1 to a circular one). e) Composite map of unwrapped phase (in radians, 0 to 5) and eigenpolarizations (black). Eigenpolarizations are plotted only between 0.5 and 1 rad of retardance. Owing to the low values of retardance, unwrapped phase is used for the sake of understanding. The unwrapped phase is less intense in the center of some discs in Figure 101.e and f. It is attributed to a slight focus misalignment (also visible on the reconstructed transmission data). f) Zoom from e) for better visualization of the eigenpolarizations. The red dashed line separates two iso-oriented domains. Scale bars: a,b,c,d =  $20 \mu\text{m}$ ; e =  $20 \mu\text{m}$ ; f =  $5 \mu\text{m}$ .

In summary, iso-oriented domains do not identify with discs, but rather encompass several discs, before they abruptly end anywhere within the sample plane, and possibly within a disc. Their typical size, as determined from vectorial ptychography pictures is consistent with the value determined by birefringence, that is 10  $\mu\text{m}$  to 20  $\mu\text{m}$ . Vectorial ptychography additionally reveals some crystal disorder in the film thickness, although rather limited.

*Continuous film:* The birefringence in continuous film being mainly situated along cracks, quantitative vectorial ptychography could not be performed .

### 4.1.6 Crystalline coherence length and defect distribution

Bragg ptychography allows one to go even further in the characterization of the crystalline properties, and to retrieve the distribution of crystalline defects (strain and tilts) with a space resolution of a few tens of nanometers.

The strain, defined as the relative variation of the inter-reticular spacing between the inspected crystal and geological calcite, and the tilts of the crystalline planes around two axes (namely Tilt 1 and Tilt 2) are derived from the measurements. For a complete description of the strain, tilts as well as a complete explanation of the Bragg ptychography data analysis, see the Materials and methods (2.5.2.3). Here again, for the sake of clarity, only the results on the disc-patterned films will be presented, although a comparison of these results with those relative to the continuous films is made at the end of the section. The data related to the continuous films, not presented here, are available in the appendix (Figure A. 24).

In the disc-patterned heated films, the distribution of defects (Figure 102) shows that the sample is composed of domains of rather homogeneous strain and tilts values, refer to as iso-strain, iso-tilt areas. Their shapes are clearly visible on the Tilt 1 and Tilt 2 maps, characterized by homogeneous color on both representations (see for instance the domain circled by a red dashed line in Figure 102). In the investigated area (0.7  $\mu\text{m}$  x 1.35  $\mu\text{m}$ ), the relative strain shows a standard deviation of +/- 0.0040, while the tilt range is greater than about 1.2° for Tilt 1 and than 3.0° for Tilt 2 (Figure A. 16). Areas of iso-strain and iso-tilt can be extracted. Such a domain, about 200 nm wide (xy) and 400 nm long (z), is visible in Figure 103.

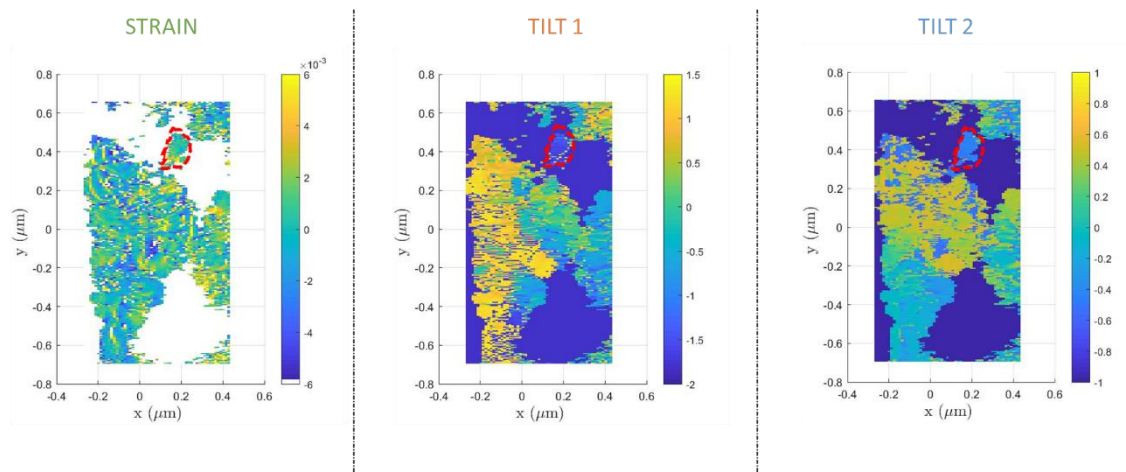


Figure 102 - 2D maps of the crystalline properties (strain, Tilt 1 and Tilt 2) in the sample plane ( $xy$ ), retrieved from the Bragg ptychography data. The film sample was collected at the free surface of a  $[Ca^{2+}] = 20 \text{ mM}$ ,  $[PANa] = 20 \text{ ppm}$  solution after 18.5h of reaction, and heated at  $300 \text{ }^\circ\text{C}$  for 3 h. The red dashed line surrounds the iso-strain et iso-tilt domain shown in Figure 103.

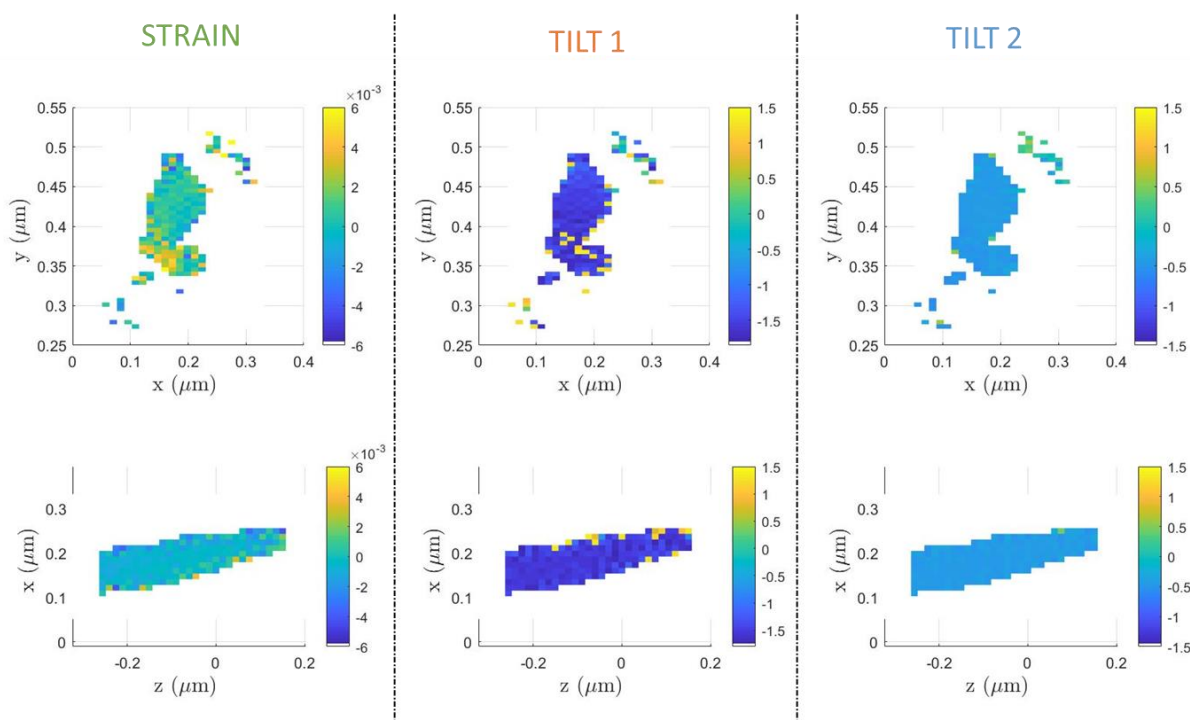
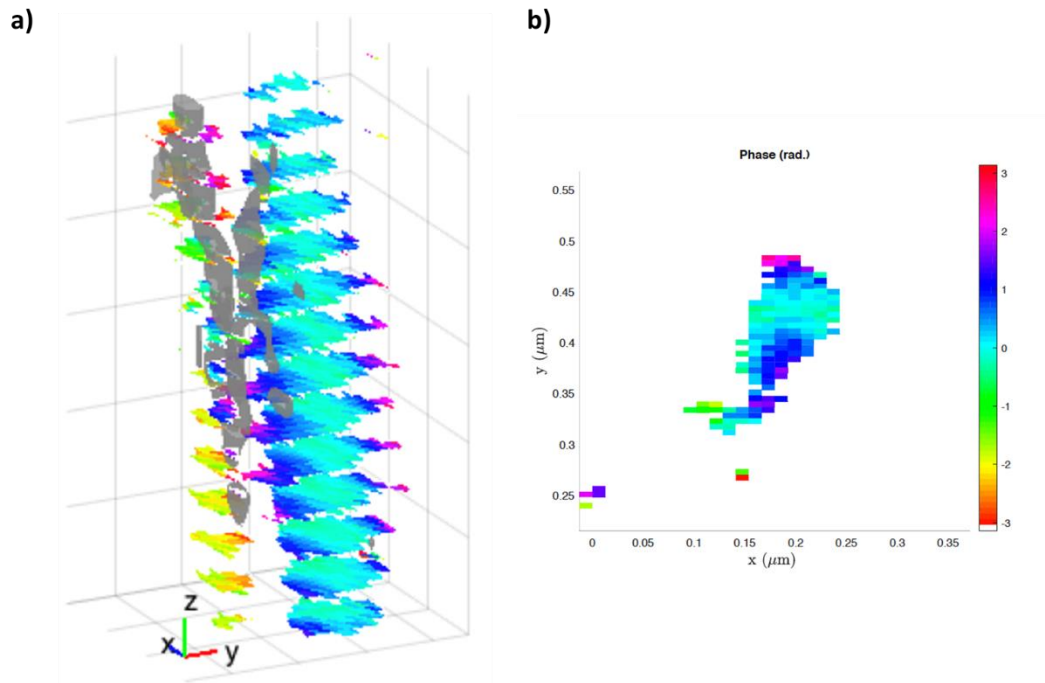


Figure 103 - Iso-strain, iso-tilt domain extracted from Figure 102. The strain, Tilt 1 and Tilt 2 maps are presented in the sample plane ( $xy$ ) and along the sample thickness ( $z$ ). Heated film at  $300 \text{ }^\circ\text{C}$  for three hours ( $[Ca^{2+}] = 20 \text{ mM}$ ,  $[PANa] = 20 \text{ ppm}$ , 18.5 h reaction time).

Inside the chosen domain, the phase variation (Figure 104) can be extracted and plotted in three dimensions. It allows addressing the crystalline coherence length (i.e., the length over

which the crystal is perfect, without any defect). It is represented by the bright blue area in Figure 104.a and .b, and estimated to about 50 nm laterally (xy) and 300 nm along the z direction. The high-strains regions (represented in gray in Figure 104.a) are located in the periphery of the constant phase domain, and extend throughout the whole thickness.



*Figure 104 - Plot of the phase variation in the iso-tilt, iso-strain domain. a) 3D phase map of the iso-strain iso-tilt domain presented in Figure 103 with scale (xyz) = 30 nm. The high strain values (> 0.004) are shown in gray. b) 2D cross section of the phase map.*

The crystals resulting from the heating of the continuous films show defect distribution values (Figure A. 17, Figure A. 18) similar to those presented in Figure 105. Iso-strain and iso-tilt domains of 200 nm (Figure A. 19) can be extracted, and their phase variation and high-strain values can be plotted as well. The domains have a coherence length of 50 nm wide (xy) and 150 nm to 200 nm in z, with high-strains values distributed around the continuous phase. A comparison of the defect distribution resulting from the heating of the disc-patterned and continuous film is summarized in Figure 105. The tilt angle distribution in the continuous film is narrower, with a standard deviation of  $0.66^\circ$  (since the whole Bragg peak is investigated in this case, the global tilt range is calculated, see Materials and method), instead of a tilt variation larger than  $3.0^\circ$  for the disc-patterned film. Nevertheless, the transformation creates crystals with comparable strain values, and same coherence length.

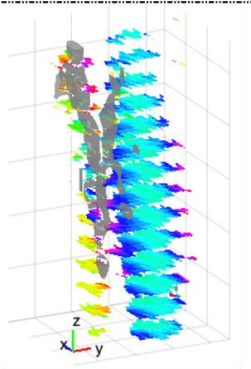
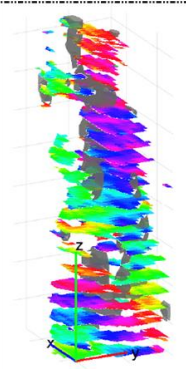
<i>Disc-patterned film</i>		<i>Continuous film</i>	
Domain: 200 nm		Domain: 200 nm	
Strain : +/- 0.0040		Strain : +/- 0.0046	
Tilt 1 > 3° Tilt 2 > 1.2°		Tilt 1 +/- 0.44° Tilt 2 +/- 0.50°	
Coherence length		Coherence length	
50 nm (xy) x 300 nm (z)		50 nm (xy) x 200 nm (z)	

Figure 105 - Comparison of the crystalline properties of a disc-patterned (scale (xyz) = 30 nm) and a continuous (scale (xyz) = 100 nm) heated film retrieved from Bragg ptychography data. The crystalline properties (strain, tilt), the coherence length and 3D phase map, with high-strain represented in gray (> 0.004 in the disc-patterned film, > 0.003 in the continuous film) are shown.

Film crystallized under heat both retain their disc-pattern morphology and their nanostructure. They are made of iso-oriented domains of calcite from a 1 μm to ~20 μm. The thinner part of the film remains amorphous despite the heat treatment. At the nanoscale, the crystal is composed of iso-strain, iso-tilt domains about 200 nm wide and 400 nm long, and exhibit a coherence length of about 50-200 nm, with minor strain values (~0.004) but a significant tilt.

## 4.2 HUMIDITY-INDUCED CRYSTALLIZATION

Alternatively, crystallization could be induced by the presence of water in the atmosphere. Amorphous films were exposed to a controlled humidity rate for 5 days (see Materials and methods 2.2.1), which resulted in the development of crystalline films.

First, the crystallinity and structure at the microscale of films crystallized under three different relative humidity values (33%, 75% and 98%), are presented. Based on these results, the structure and crystalline properties at the nanoscale are described for crystals grown under high relative humidity (98%) only. Finally, the crystal defect distributions and coherence length, probed by Bragg ptychography, are reported. In the following, unless otherwise specified, only results on the disc-patterned films are shown, as it allows better visualization of the change in morphology during crystallization. Still, similar results were obtained on continuous films when investigated (at 98% RH).

### 4.2.1 Influence of the relative humidity percentage: microscale crystallinity and polymorphism

Three different relative humidity rates in the chamber were used to induce crystallization: 33%, 75% and 98%. At the microscale, it translated into different crystalline morphologies. At 33%

RH, the disc morphology is preserved after crystallization, and polycrystals form, encompassing the disc pattern (Figure 106.a and a'). Crystallization might be only partial as the coloration in WBM shows little changes. At 75% RH (Figure 106.b), spherulites grow while keeping the disc pattern in their core only (Figure 106.b'). Elongated flat crystals form at the spherulite border (Figure 106.b'). At high humidity rate (98% RH, (Figure 106.c), 2D spherulites form, with long elongated crystalline domains, named branches hereafter (Figure 106.c'), radiating from a crystalline core (Figure 106.c').

The specific disc pattern, as visible in Figure 106.a' and .b' is not seen under birefringence microscopy at high relative humidity value, but its presence will be further discussed in section 4.2.2. A few discs with a very weak birefringence signal remain visible next to the spherulite (yellow arrow in Figure 106.c''). In this case, the discs appear rather co-oriented with each other and with the branch they are connected to. In the background, light pink discs, probably uncrystallized, are observed (blue arrow in Figure 106.c''). Continuous films exposed to high humidity conditions produce similar elongated crystals (Figure A. 21).

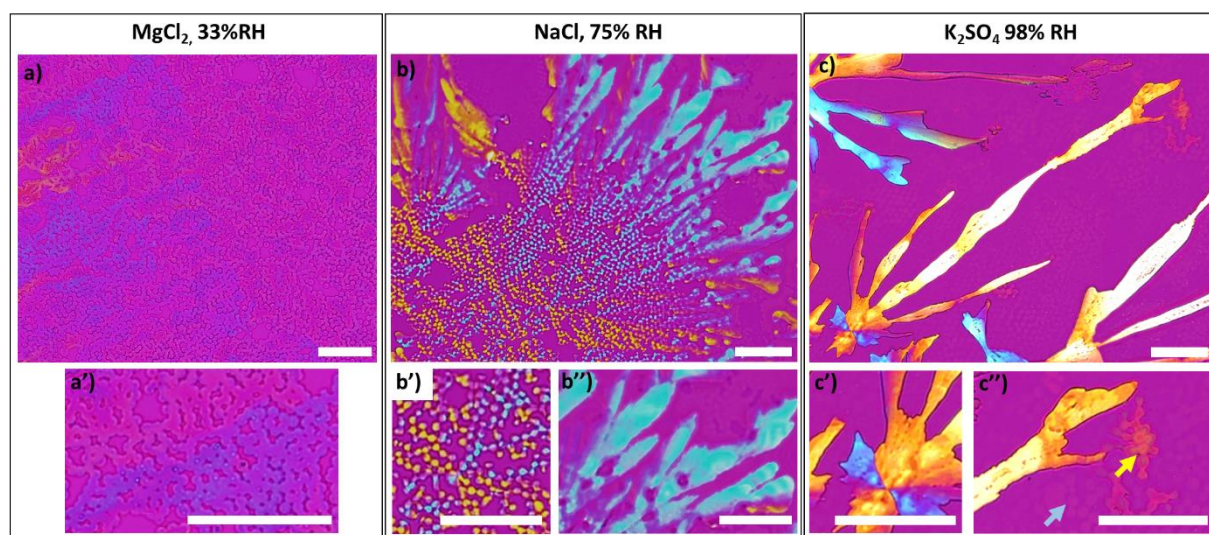


*Figure 106 - Optical micrographs (WBM) of film samples crystallized under controlled relative humidity. The crystalline samples originate from the same film, collected after 18h of reaction at the surface of a  $[Ca^{2+}] = 20$  mM,  $[PANa] = 20$  ppm solution. a) Film kept under a 33% RH atmosphere for 5 days. a') Zoomed-in view of a slightly birefringent polycrystalline area. b) Film kept under a 75% RH atmosphere for 5 days. b') Remaining discs at the spherulite center, zoom-in view from b). b'') Elongated crystals, zoomed-in view from b). c) Film kept under a 98% RH atmosphere for 5 days. c') Radial symmetry around the spherulitic center, zoomed-in view from c). c'') Elongated crystal tip, zoomed-in view from c). The yellow arrow highlights the presence of discs that are co-oriented with the top of the neighboring branch. The blue arrow points to the remaining optically isotropic discs. Scale bars = 50  $\mu$ m*

Furthermore, the change in relative humidity enables the crystallization to be driven towards different polymorphs. Table 10 summarizes the Raman characterization results. It shows that at low relative humidity (33%), vaterite is observed in 100% of the syntheses, against only 30% for calcite. At 75% RH, the trend is reversed (30% vaterite, 100% calcite). Finally, at 98% RH, only calcite is observed. Directing the crystallization to calcite is therefore possible using high

relative humidity rate.

*Table 10 - Polymorphs occurrence in crystallized films when exposed to controlled % RH atmosphere. Based on Raman spectra analysis (three syntheses are investigated for 33% RH and 75% RH datas, five for 98% RH). Film crystallized at 33% and 75% RH showed both calcite and vaterite on the same sample.*

	<b>33% RH</b>	<b>75% RH</b>	<b>98% RH</b>
<i>Vaterite occurrence</i>	100%	60%	0%
<i>Calcite occurrence</i>	60%	100%	100%

*Continuous films:* under high relative humidity (98% RH) branched calcitic spherulites are observed (Figure A. 21).

In conclusion, exposure to a highly humid environment results in long, calcitic spherulites with iso-oriented branches. The observed morphology transformation implies an important displacement of matter during the amorphous-to-crystal phase transition. On the contrary, low humidity atmosphere allows for shape preservation, but results in a poor control over polymorph selection and crystallinity (single *versus* poly-crystallinity). Intermediate relative humidity, like 75%, produces intermediary mechanisms with discs remaining in the crystal core, but gradually disappearing towards the edge, where elongated crystals form. In the context of this study, focused on iso-oriented calcitic domains to allow a comparison with the biogenic prismatic layer of *Pinctada m.*, I have restricted my work to high humidity 98% RH crystallization condition, for which such domains are mostly produced.

#### 4.2.2 High relative humidity: temporality of crystal growth

Using transmission optical microscopy, I could follow the temporal evolution of a film sample exposed to a relative humidity rate of 98%. After 2.5 days of exposure, branched spherulites are already formed, as shown in Figure 107.a, where the spherulites edges provide a strong optical contrast (appearing as black lines in Figure 107) owing to a refraction effect. However, as emphasized below, their evolution is not yet complete.

Discs are still visible around the spherulites (inset of Figure 107.a), as well as in the spherulite branches and around the crystal nucleation point (Figure 107.a, blue arrows), i.e. around the center of the spherulite (see Figure 106.c'). In this latter region, the discs appear embedded within the spherulitic crystals.

The poorly contrasted discs outside the spherulites are not birefringent, as evidenced by observations performed in parallel (not shown here), and appear to fade away with time, as



they become less and less light-absorbing (Figure 107 b, after 7 days of exposure). After 30 days, the discs have almost completely disappeared (Figure 107 c). Still, the shape of the large crystals has not changed from 2.5 days to 30 days of exposure. As for the discs embedded within the spherulites, they remain visible throughout the observation period, although subtle changes may affect them.

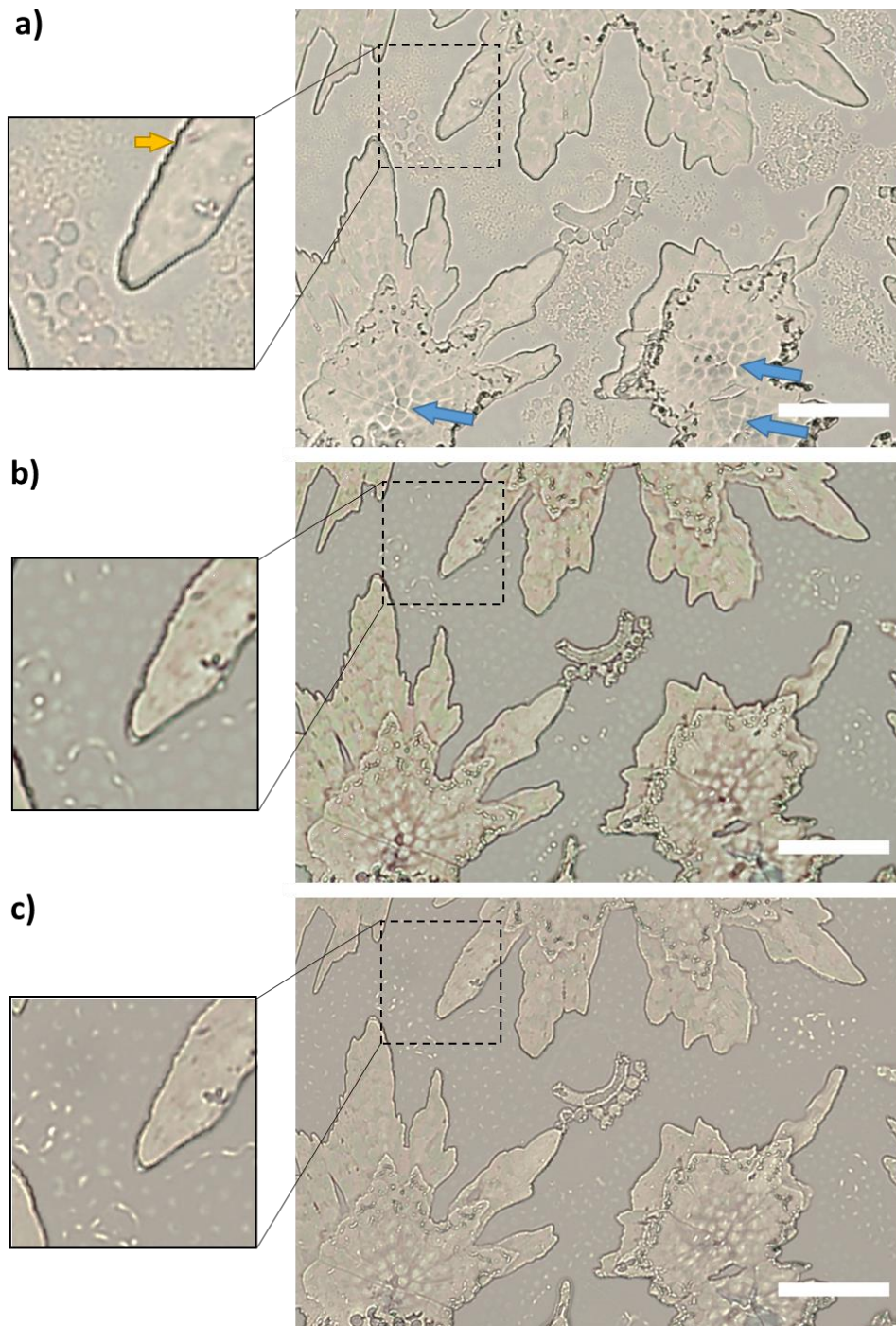


Figure 107 – Optical micrograph (AM) showing the evolution of remnant discs when exposed to high humidity for a long period of time. Sample collected after 18h at the interface of a  $[Ca^{2+}] = 20 \text{ mM}$ ,  $[PANA] = 20 \text{ ppm}$  solution. a) 2.5 days exposure to 98% RH atmosphere. The blue arrows points to the center of the spherulites. The yellow arrow in the inset highlights the border of the crystals (black lines). b) 7 days exposure to 98% RH atmosphere. c) 30 days exposure to 98% RH atmosphere. Scale bar =  $100 \mu\text{m}$ .

The observations reported above were made by taking the sample out of the crystallization chamber. However, in order to avoid possible artefacts produced by the atmosphere change, crystallization under high humidity was further observed using an *in situ* set-up (see Chapter Materials and Methods, 2.7.3). In the crystallization chamber used for *in situ* observations, the relative humidity increases faster, and stabilizes to a slightly higher humidity value (99% RH) than in the pot-crystallization chamber (as described in the Materials and Method, 2.2.3). This likely explains the slightly different morphology of the developed spherulites, which now appear as a dendritic, or 'seaweed', structures see Figure 108).<sup>159</sup>

Figure 108 shows the evolution of a growing branch length over time. The crystal first grows rapidly, with a linear increase of the branch length through time (Figure 108.d), and then more slowly after about 50 min of exposure to humid air (break in the curve of Figure 108.d). At this time, a second crystal starts to grow (blue crystal indicated by the yellow arrow in Figure 108.b, and shown in the inset of Figure 108.b). After 9 hours of crystallization, the growth of the branch stops, as evidenced by the plateau on the curve in Figure 108.d. This corresponds to the time when neighboring spherulites contact each other, so that their growth is inhibited. One can guess that the observed slow down of the growth kinetics at about 50 min was due to first interactions with the neighboring growing crystals, through the depletion of the surrounding medium in ionic species.

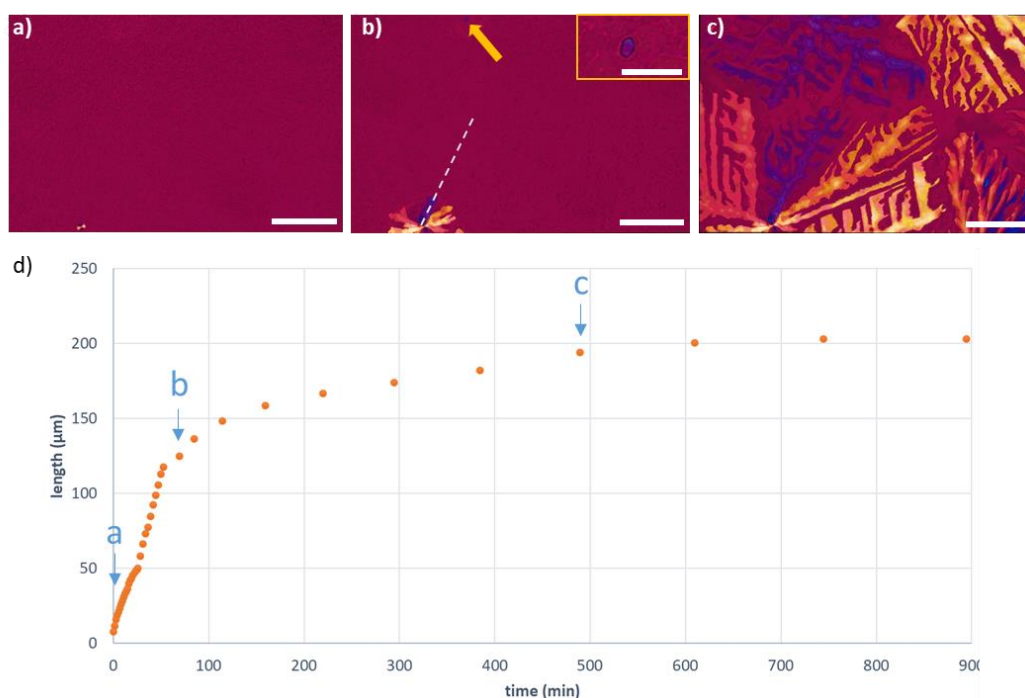
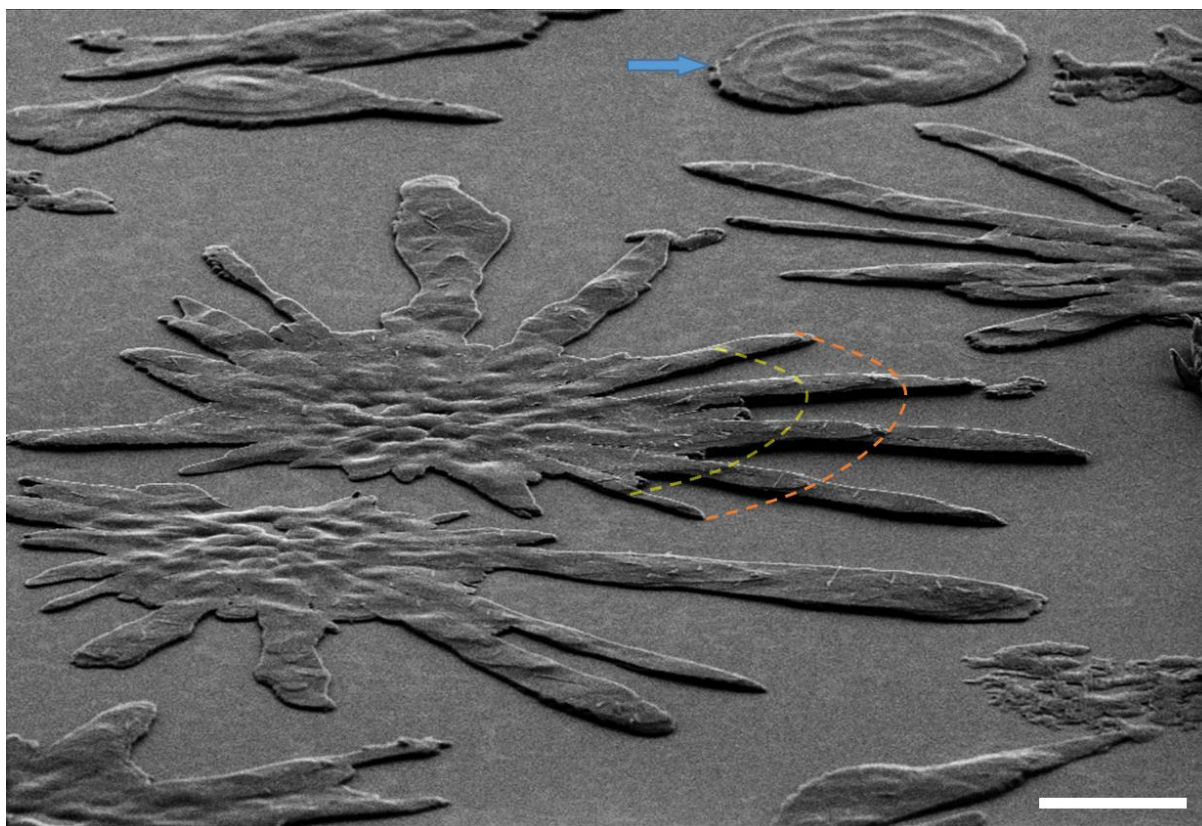


Figure 108 - Optical micrographs (*in situ* WBM) of the crystallization under high humidity (99%RH). Observations were made with the crystallization cell directly under the microscope. The observation time, given as the time elapsed since the cell was closed, is: a) 10s; b) 58 min; and c) 9.5h. The dashed line in b) highlights the branch used for the growth measurement plotted in d) Inset of b): close-up that provides a better view of the crystal indicated by the arrow. Scale bar = 100 μm. d) Branch length evolution as a function of time. The times when pictures a), b) and c) were taken are marked on the plot.

In summary, the temporal follow-up of the crystallization under high humidity thus reveals a dissolution process, which impacts a large number of amorphous discs and feeds the growing spherulitic crystals.

### 4.2.3 High relative humidity: structural features at the micro- and nanoscale.

Spherulites were observed in SEM to get a better understanding of their structural organization and morphology (Figure 109). In Figure 109, two branched spherulites are visible in the center of the image, while a complete spherulite lies in the background, as highlighted by the blue arrow. The branches vary cyclically in thickness, in a step-like manner. The thickness increases with a gentle slope and then drops sharply, creating a step. When visible, the edges of the steps appear located at the same distance from the center for all branches of a given spherulite, as highlighted by the orange and yellow dashed lines in Figure 109. Similarly, the complete spherulite in the background has circular step-like height variation.



*Figure 109 - Electron micrographs (SEM) of spherulites resulting from the crystallization of an amorphous disc-patterned film kept under high humidity (98% RH) for 30 days. Orange and yellow dashed lines highlight the equal distance of the steps from the center on four different branches. Two branched spherulites are observed in the center. The blue arrow points to a space-filling spherulite, exhibiting visible steps arranged circularly. For the observation, the sample was tilted by 70°. HE-SE detector, 5 kV. Scale bar = 20  $\mu\text{m}$ .*

The center of the branched spherulite is not flat (Figure 109), but composed of circular bumps, whose size corresponds to that of the original amorphous discs ( $\sim 5 \mu\text{m}$ ). These bumps are further observed in Figure 110, along with remnants of the amorphous disc pattern everywhere

on the crystal surface (as highlighted by the red dashed ellipses in Figure 110.a). These discs are still nanostructured while the crystalline material between them appears very smooth (Figure 110.b,c). A corona, reminiscent of the one observed in heat-induced crystallization, is visible on the periphery of those discs (Figure 109.c). Finally, the space between spherulites is covered with disc imprints (highlighted by the green dashed lines in Figure 110). Those imprints correspond to ghosts of discs (Figure 110.d) that have likely been dissolved during the crystallization process.

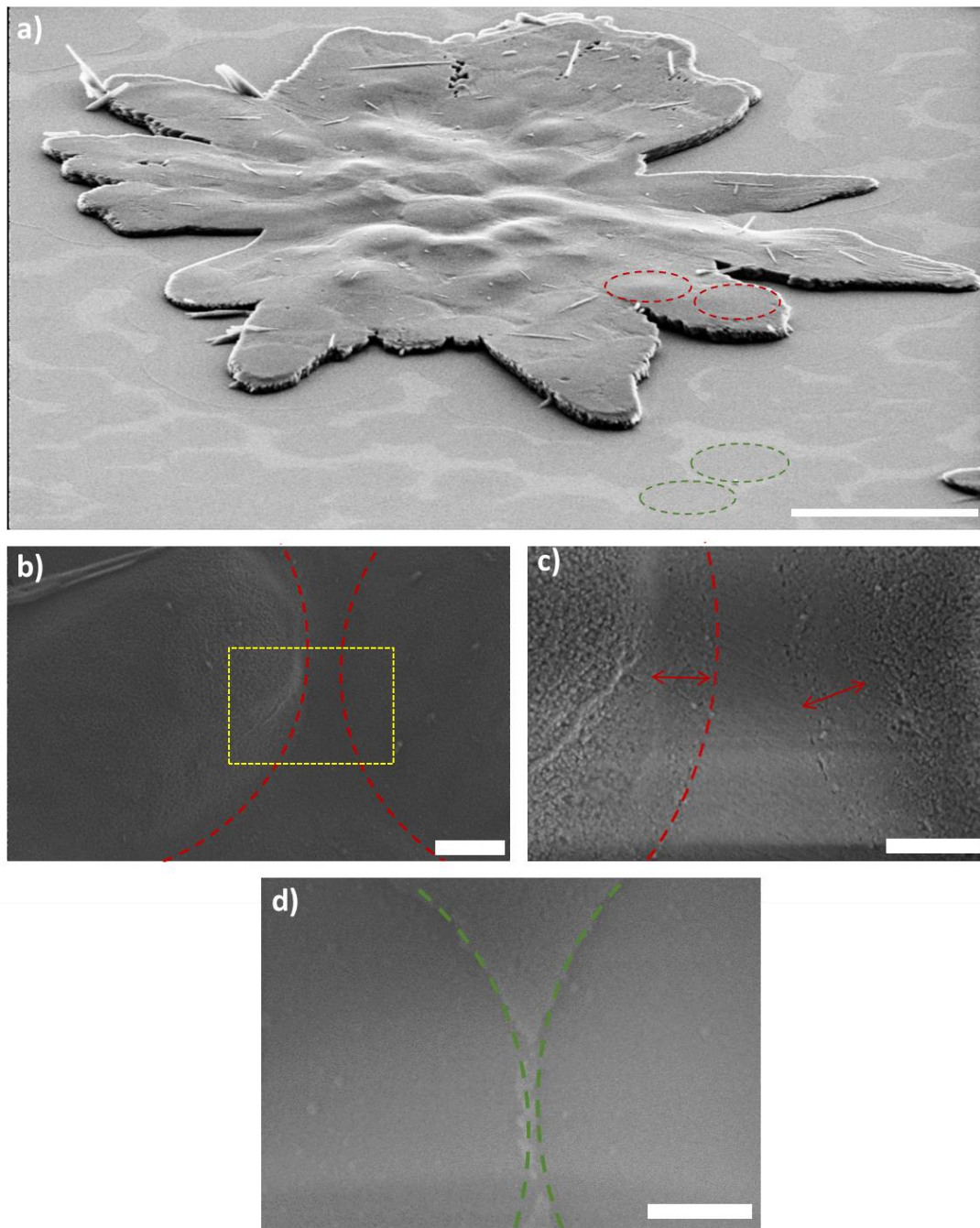


Figure 110 - Electron micrographs (SEM) of a spherulite resulting from the crystallization of an amorphous disc-patterned film kept under high humidity (98% RH) for 30 days. a) Large-scale view of the spherulite. Red dashed ellipses point to traces of discs at the surface of the spherulite. Green dashed ellipses point to disc imprints in between the crystals. HE-SE detector, 5 kV. Scale

bar = 20  $\mu\text{m}$ . b) Disc shapes at the surface of the spherulitic crystal. The red dashed lines outline the discs edges. The nanostructure is different in the discs and in the space between them. HE-SE detector, 1 kV. Scale bar = 1  $\mu\text{m}$ . c) Zoom-in view, corresponding to the yellow dashed rectangle in b). The red double arrow shows the radial extent of the corona that surrounds the discs. In-Lens detector, 1 kV. Scale bar = 400 nm. d) Disc imprints in between the crystals. The disc edge is outlined by a green dashed line. In lens detector, 1 kV. Scale bar = 400 nm.

When seen from the side, the spherulites appear as the superposition of two layers: a thin smooth layer on the top, covering a thick granular underlayer (Figure 111.a), the ensemble being approximately 700 nm thick. During crystallization, the top layer of the amorphous film was in direct contact with the humid atmosphere and was therefore more prone to dissolve. In some places, the tip of the long branches (i.e. longer than a few tens of microns) exhibits even more layers, as shown in Figure 111.b. There, each crystalline layer corresponds to a juxtaposition of platelets arranged radially (relative to the centre of the spherulite), the most distal one being  $\sim 700$  nm thick.

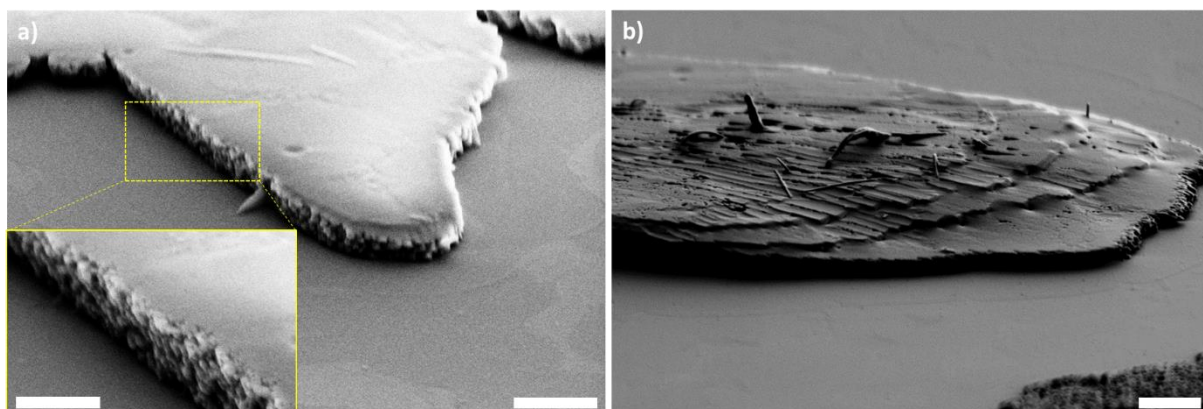


Figure 111 - Electron micrographs (SEM), taken with a tilt of 70°, of spherulitic branch tips. The film was kept at 98% RH for 30 days. a) Short branch ( $\sim 10 \mu\text{m}$ ) HE-SE detector, 5 kV. Scale bar = 2  $\mu\text{m}$ . Inset: close-up of the area in the yellow dashed rectangle. HE-SE detector, 5 kV. Scale bar = 1  $\mu\text{m}$ . b) Long branch ( $\sim 100 \mu\text{m}$ ) with a layered structure on the tip. HE-SE detector, 2 kV. Scale bar = 2  $\mu\text{m}$ .

The crystallized discs at the tip of the spherulite (mentioned in section 4.2.1 of this chapter) were further analysed with respect to their crystalline properties (Figure 112.a). As shown by WBM (Figure 112.a) and EBSD (Figure 112.b), they form large iso-oriented crystalline domains, co-oriented with the closest spherulite branch. The discs exhibit an advanced dissolution process, resulting in a strongly contrasted nano-granular structure (Figure 112.c). The nanostructure of these discs appears fully similar to that of the underlayer of the spherulite branches. As a matter of fact, no separation between the two nanostructures is visible, the former appearing as the continuation of the latter.

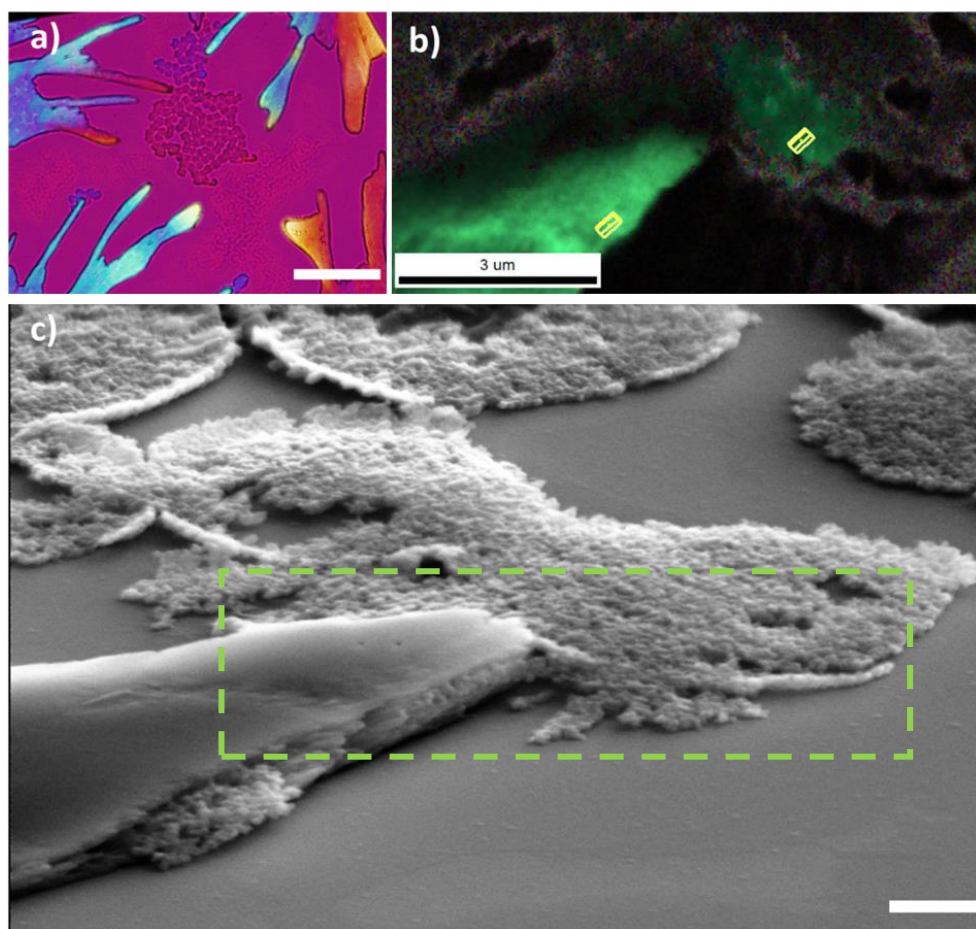


Figure 112 - Optical (WBM) and electron micrographs (SEM at 70°) of a film sample crystallized by exposure to a 98% RH atmosphere for 30 days. Iso-oriented discs crystallized in continuity with a nearby spherulite are visible. a) Large-scale WBM micrograph. Scale bar = 50  $\mu\text{m}$ . b) EBSD image corresponding to the green dashed rectangle shown in c). Oriented calcite crystalline cells (in yellow) have been indicated in two places, namely at the branch tip and in the neighboring crystallized discs (the *c*-axis is the longest side of the hexagonal cell). Scale bar = 3  $\mu\text{m}$ . c) SEM micrograph of the spherulite tip investigated by EBSD. HE-SE detector, 5 kV. Tilt angle 70°, Scale bar = 1  $\mu\text{m}$ .

In summary, the structural analysis of the crystals produced by exposure to a high relative humidity shows that the disc pattern is still very prominent, although a large number of amorphous discs have dissolved away. Discs are in particular embedded within the spherulitic crystals, which actually retain a granular nanostructure, reminiscent of the amorphous discs nanostructure.

#### 4.2.4 Calcium chemical environment within the crystallized film

STXM spectromicroscopy at the Ca L-edge was performed at the border of a spherulite branch. Owing to the crystal thickness ( $\sim 700$  nm), very little signal was received by the detector, often below the detector noise level. Still, areas could be selected that allow  $t_{2g}$  and  $e_g$  identification and peak splitting calculation. In particular, the thinner extremity of a branch (see Figure A. 23)

allowed the extraction of the peak splitting value. The peak splitting values were calculated to be 1.29 eV for the  $L_3$  d-orbitals, and 1.28 eV for the  $L_2$  d-orbitals, confirming the calcitic nature of the crystals (see materials and Methods 2.6.2 for reference values).

### 4.2.5 Quantitative investigation of crystalline properties

Vectorial ptychography was again used to retrieve the crystalline properties of the sample at the microscale, now in the case of high-humidity-induced branched spherulites. Within a given spherulite, two kinds of domains were evidenced, which differ by their behavior regarding to the orientation of their neutral axes. They correspond respectively to the center and the branch tip of the spherulite, successively presented hereafter.

In the very center of the spherulite, the retardance ( $\propto \Delta n_{eff} d$ ) is low ( $< 0.5$  rad), while it increases toward the branches (Figure 113.a). A low retardance can result either from a thin sample or from a  $c$ -axis orientation normal to the image plan. However, analyzing the tilt ratio variation ( $\frac{\Delta\phi}{\phi_u} = \frac{\Delta n_{eff}}{n_o}$  - see Materials and methods 2.5.1.2) in the central region, one observes that this ratio is rather constant, at least in the outermost part (Figure 113.b, red pixels). Therefore, the decrease in retardance observed in this central region is indeed due to a reduction in the sample thickness.

In addition, the analysis of the fast axis orientation (Figure 113.c) shows that the center of the spherulite is made of domains of constant fast-axis orientation, which are angularly distributed around the center. Each domain exhibits a radial crystalline orientation, i.e. one of the neutral axes of the crystal is directed towards the center. The transition between domains can be either gradual (yellow-to-orange transition in Figure 113.c) or abrupt (dark-blue to pink in Figure 113.c). The existence of these domains is further illustrated in the plots of the eigenpolarizations (108.e and .f), which additionally shows that the fast axis is everywhere roughly oriented towards the center.



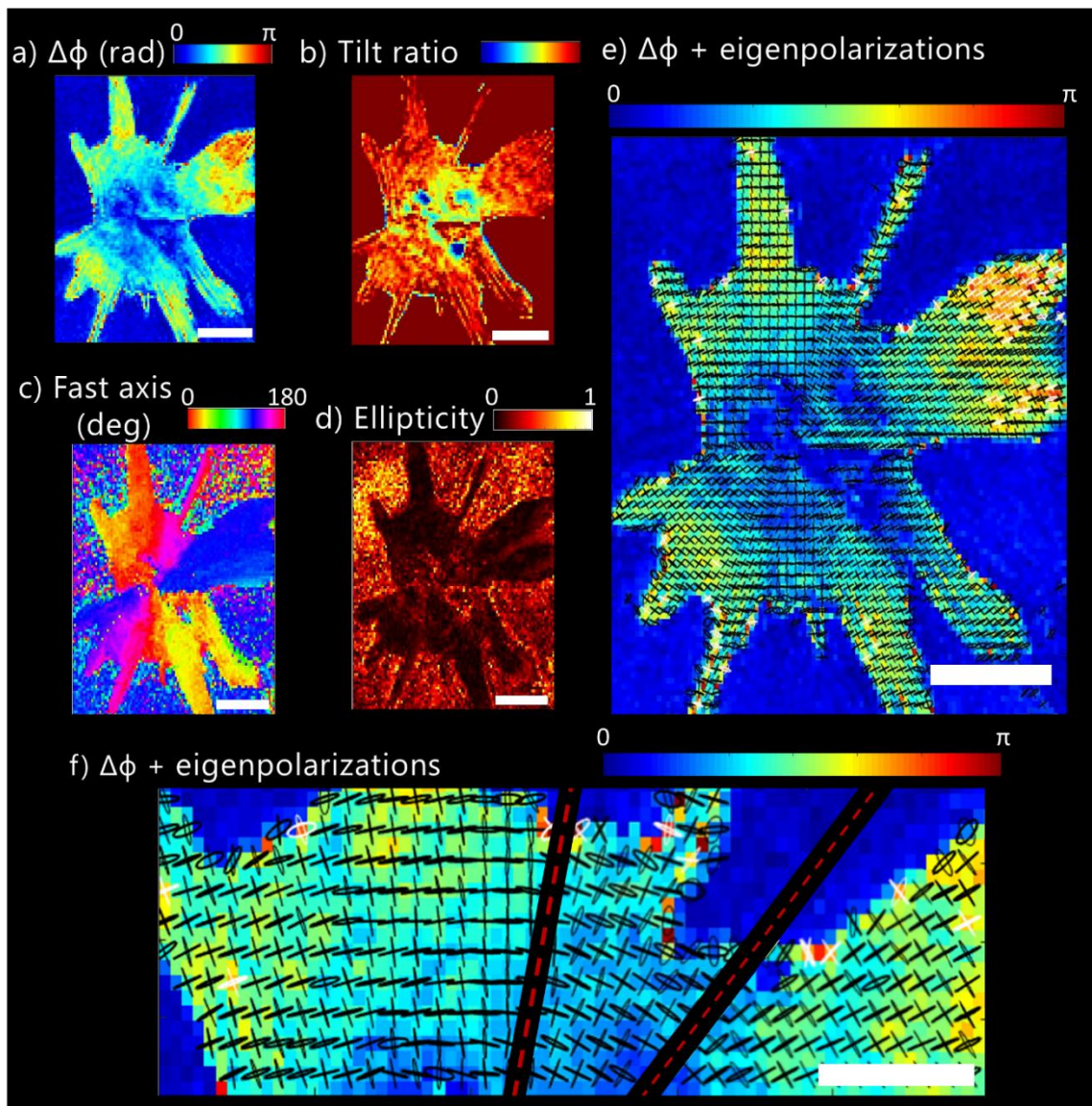


Figure 113 - Vectorial ptychography analysis of the center of a spherulite. The film sample has been collected at the surface of a  $[Ca^{2+}] = 20 \text{ mM}$ ,  $[PANA] = 20 \text{ ppm}$  solution after 18h of reaction, and left 14 days under high relative humidity (98%). a) Retardance (in radians, 0 to  $\pi$ ). b) c-axis tilt ratio (a.u.). c) Fast-axis orientation (in degrees 0 to 180). d) Ellipticity (absolute value, 0 to 1). Note that in the low retardance regions, which appear as optically isotropic, no ellipticity can be measured. e) Composite map of retardance (coloration, in radian, 0 to  $\pi$ ) and eigenpolarizations (black). f) Zoom from e) for better visualization of the eigenpolarizations. The red dashed lines separate iso-oriented domains. Scale bar =  $20 \mu\text{m}$ .

The eigenpolarizations show little ellipticity ( $\sim 0.1$ , see Figure 113.d). The reduced ellipticity of the eigenpolarization is further illustrated in Figure 113.e. In this picture, the identification of the iso-oriented domains paving the center of the spherulite is easily achieved. The rapid change in orientation between iso-oriented domains is highlighted in Figure 113.f, where a dashed red lines indicate the limit between the neighboring domains.

Then, vectorial ptychography analysis was performed on a branch emerging from the spherulite center (Figure 114) and revealed a slightly different crystalline behavior. First, at the

tip of the spherulite, the eigenpolarizations does not show a constant orientation but rather a radial orientation, as highlighted by the white dashed arrows that extend the direction of the eigenpolarizations. Therefore, the branch tip does not form an iso-oriented domain. On the contrary, the *c*-axis tilt ratio exhibits little variations (Figure 114.b), meaning that the tilt to the image plane is constant, like in the spherulite core. The ellipticity remains low ( $\sim 0.1$ ) in this part of the crystal (Figure 114.c), which confirms the crystal is well-ordered in depth.

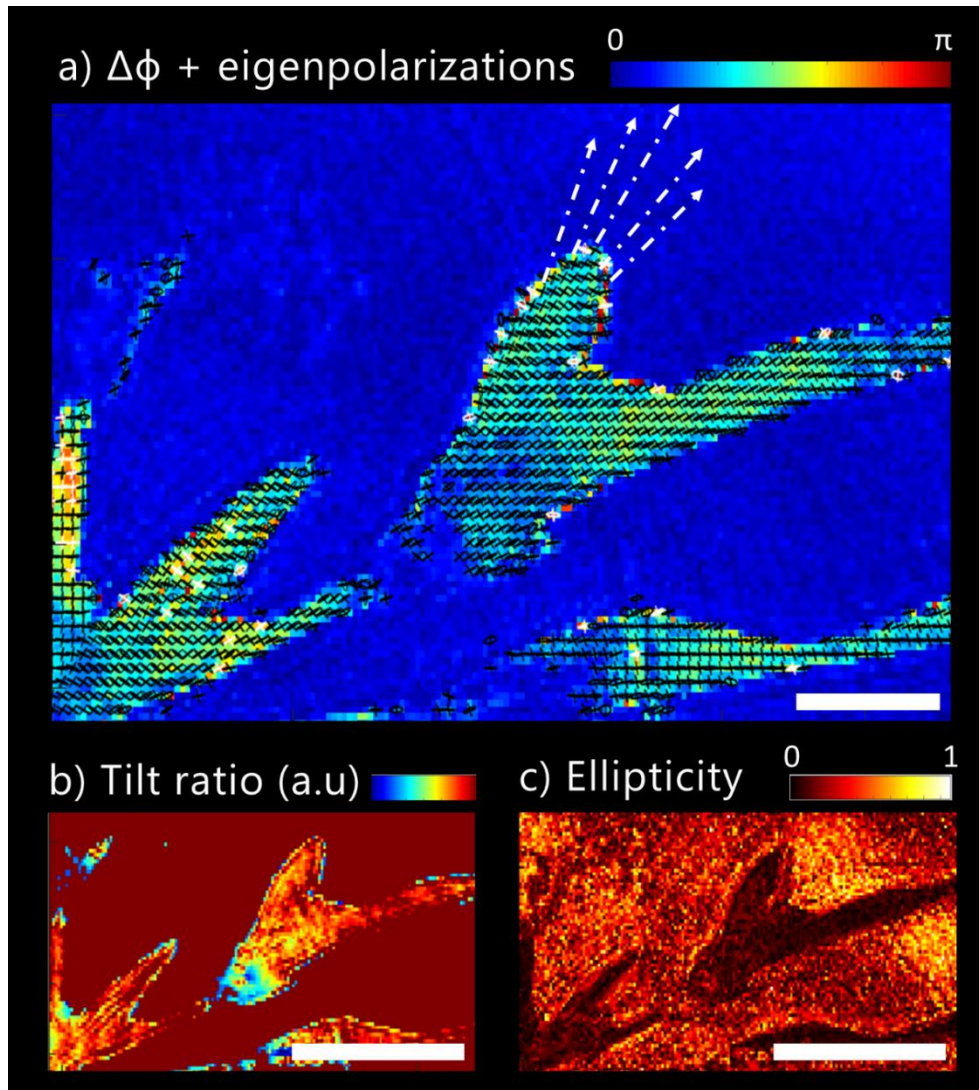
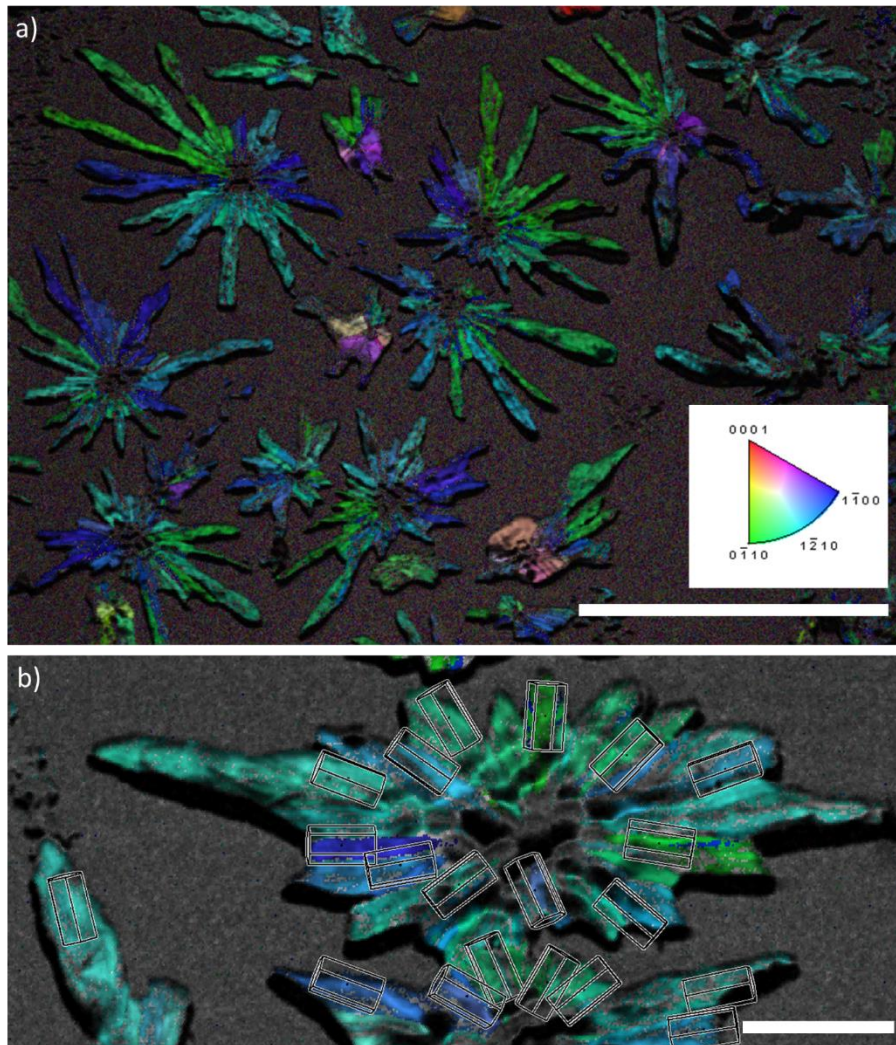


Figure 114 - Vectorial ptychography analysis of a branch emerging from the center of a spherulite. The film sample has been collected at the surface of a  $[Ca^{2+}] = 20$  mM,  $[PANa] = 20$  ppm solution after 18h of reaction, and left 14 days under high relative humidity (98%). a) Composite map of retardance (coloration, in radians) and eigenpolarizations (black). The white dashed arrows show the orientations of the fast-axis at the branch tip. b) *c*-axis tilt ratio (a.u.). c) Ellipticity of the eigenpolarizations. Scale bars: (a) = 20  $\mu$ m. (b,c) = 50  $\mu$ m.

Information on the *c*-axis orientation could also be extracted from EBSD measurements. First, these measurements show a same *c*-axis orientation is shared by most spherulites (Figure 115.a), as the light green to dark blue coloration is mostly present. The center of the spherulites shows no orientation in EBSD, most probably because it is not flat enough (as observed in Figure 109.a and Figure 110.a), making the measurement of the orientation difficult. The

orientation of the crystalline cell for these coloration are shown in Figure 115.b, which shows a spherulite with oriented hexagonal crystalline cells. The c-axis of the calcite crystal is oriented along the longest side of the hexagonal cell. In all branches, the orientation of the c-axis appears almost parallel to the sample plane.



*Figure 115 - EBSD measurement of branched spherulites. The film sample has been collected at the surface of a  $[Ca^{2+}] = 20 \text{ mM}$ ,  $[PANa] = 20 \text{ ppm}$  solution after 18h of reaction, and left 30 days under high relative humidity (98%). a) Large-field view containing several spherulites. The coloration in the inset encodes the crystalline orientation. The orientation in the center could not be estimated owing to a lack of flatness in this region. b) Zoomed-in view, crystalline cells represent the crystalline orientation on a given branched spherulite.*

*Continuous films:* Measurements made on continuous films show similar results. Figure A. 24 illustrates the properties of a spherulite core following its growth under high relative humidity (98% RH). The core of the spherulite contains iso-oriented domains (delimited by the red lines), with a neutral axis oriented radially with respect to the center and a weak ellipticity (linearity of eigenpolarizations).

In summary, the spherulitic crystals grown under humid atmosphere are characterized by a fast axis which is everywhere, at least on average, radially oriented (i.e. towards the center of the spherulite). The central part of the spherulite is made of micron-sized iso-oriented domains that are azimuthally distributed and are separated by regions of rapides changes in the fast-axis direction. Conversely, branch tips exhibit gradual changes of the fast-axis orientation. The tilt of the c-axis appears almost constant both at the center and in the branches, and likely throughout the spherulite. Finally, the spherulitic crystal appears well-ordered in depth as the ellipticity is low everywhere in the structure.

**4.2.6 Crystalline coherence length and defect distribution**

The nanoscale distribution of the crystalline defects in a film exposed to 98% relative humidity was retrieved by Bragg ptychography, in the same way as in sections 4.1.6

The tip of the branch of a spherulite was investigated, resulting in the distribution of strain and tilts (Figure A. 25), which shows that the sample is composed of iso-strain and iso-tilt areas. Overall, the strain distribution has a standard deviation of 0.0049 while the tilt has a standard deviation of 0.44° for Tilt 1, and a range variation larger than 2.1° for Tilt 2 (Figure A. 26). Areas of iso-strains and and iso-tilts can be extracted. An iso-strain, iso-tilt domain, about 400 nm wide in the sample plane (and 800 nm along the thickness), is presented in Figure 116.

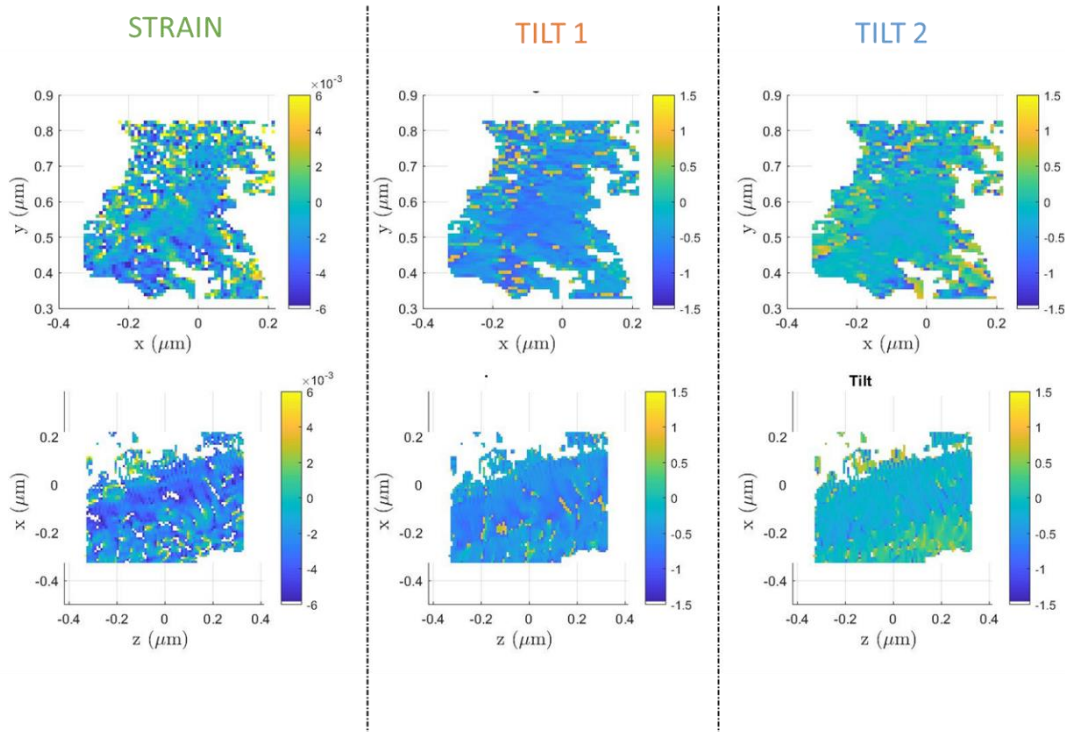
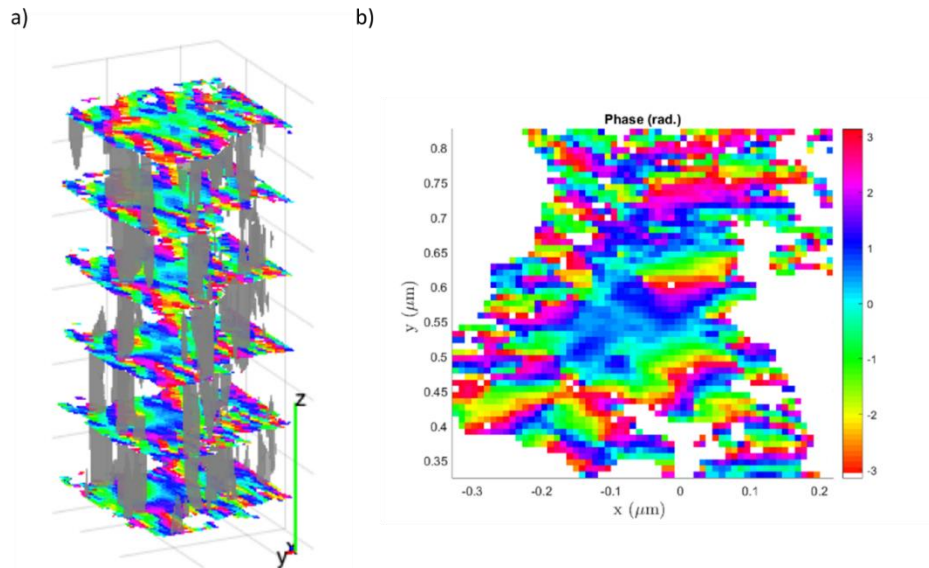


Figure 116 - Iso strain, iso-tilt domain extracted from (Figure A. 12). The strain, Tilt 1 and Tilt 2 maps are presented in the sample plane (xy) and along the sample thickness (z). Film crystallized at 98% RH for 14 days ([Ca<sup>2+</sup>] = 20 mM, [PANa] = 20 ppm, 16.5 h reaction time).

In this domain, the phase varies rapidly as seen on the 3D (Figure 117.a) and 2D (Figure 117.b) representations. The largest measured coherence length is about 100 nm ( $xy$ ) and goes down to 50 nm in depth. In addition, the domain presents a large number of highly strained regions, propagating through the entire thickness (shown in gray in Figure 117.a).



*Figure 117 - Phase maps of the iso-strain iso-tilt domain presented in Figure 116. a) 3D phase map with scale ( $xyz$ )= 30 nm. The gray iso volumes correspond to regions of large strains ( $> 0.005$ ). b) 2D-cross section of the phase map.*

The Bragg ptychography analysis on a continuous film was performed at the center of a spherulite (Figure 118, "Continuous film"). The crystalline properties are different than the one retrieved for the disc-patterned film exposed to 98% RH (Figure 118, "Disc patterned film"). First, the iso-strain, iso-tilt domains are bigger (1.2  $\mu\text{m}$ ). Second, the resulting crystal has smaller strain ( $\pm 0.0011$ ) and tilt ( $\pm 0.066^\circ$ ) standard deviation. The crystalline coherent domains are much larger, up to 600 wide nm, and 400 nm deep (in  $z$ ). Finally, the high strain regions are observed at the periphery of the crystalline domain only (they were rather observed inside the domain in the disc-patterned film).

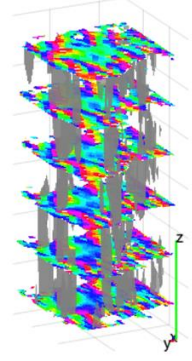
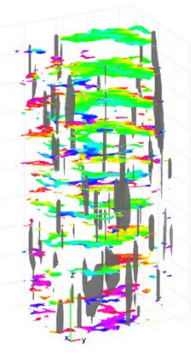
<i>Disc-patterned film (tip of spherulite)</i>		<i>Continuous film (center of spherulite)</i>	
Investigated volume		Investigated volume	
Strain : +/- 0.0049 Tilt 1 +/- 0.44° Tilt 2 > 2.1°		Strain : +/- 0.0011 Tilt : +/- 0.066°	
Coherence length		Coherence length	
100 nm (xy) x 50 nm (z)		600 nm (xy) x 400 nm (z)	

Figure 118 - Comparison of the crystalline properties, extracted from Bragg ptychography data, of a disc-patterned and continuous film crystallized at 98% RH. The crystalline properties (strain, Tilt 1 and Tilt 2), the coherence length (size of constant phase domains) and 3D phase maps with high strain ( $> 0.005$  for the disc-patterned film,  $> 0.002$  for the continuous film) are provided.

Changing the relative humidity to induce crystallization allows controlling the shape and polymorph of the resulting crystals. At high relative humidity (98%), branched spherulites are formed, which are composed of a smooth layer (where the original disc pattern is still visible), and a nanostructured thick layer. The crystalline properties varies between the spherulite core and its branches although the crystalline orientation appears everywhere radial.

### 4.3 INTERFACIAL CRYSTALLIZATION

The monitoring of the film formation has evidenced that when left at the air-solution interface, most of the film dissolves away and that 3D crystals grow at the interface. After 5 days, very little film material remains at the air-solution interface. Still, some iso-oriented or polycrystalline domains are detected (Figure 119). The initially produced disc-like pattern is still observable in these domains. In particular, large patches of iso-oriented crystallized discs are visible, ranging from a few microns to a hundred microns in size. On continuous films, single- or poly-crystalline domains, 500  $\mu\text{m}$  x 500  $\mu\text{m}$  wide, that is, as large as the used silicon nitride membrane itself, could be sampled. The formation of these large iso-oriented domains will be presented below because of the similarity of these domains to biogenic crystals. However, due to time constraints, interfacial crystallisation could not be studied as thoroughly as the two transformation routes presented above, so that the reported observations relate to a small number of samples. Thus, further confirmation will certainly be needed before definitive conclusions can be drawn.

## 4.3.1 Spectroscopic overview of the remaining crystals

Both iso-oriented and polycrystalline patches are collected at the interface for a given synthesis (Figure 119.a and .b) The Raman analysis of the iso-oriented domains (Figure 119.a) reveals four vibration bands between  $100\text{ cm}^{-1}$  and  $1150\text{ cm}^{-1}$ , at  $1086$ ,  $712$ ,  $281$  and  $155\text{ cm}^{-1}$ . These bands match well with the  $\nu_1$ ,  $\nu_2$ , and two lattices bands of calcite, respectively (see Materials and methods 2.6.1.2 for reference values). In contrast, the Raman spectrum of the polycrystalline domain (Figure 119.b) presents the Raman bands of vaterite ( $\nu_1 = 1074\text{ cm}^{-1}$ ,  $1083\text{ cm}^{-1}$  and  $1090\text{ cm}^{-1}$ ; Lattice bands =  $297\text{ cm}^{-1}$  and  $265\text{ cm}^{-1}$ ).

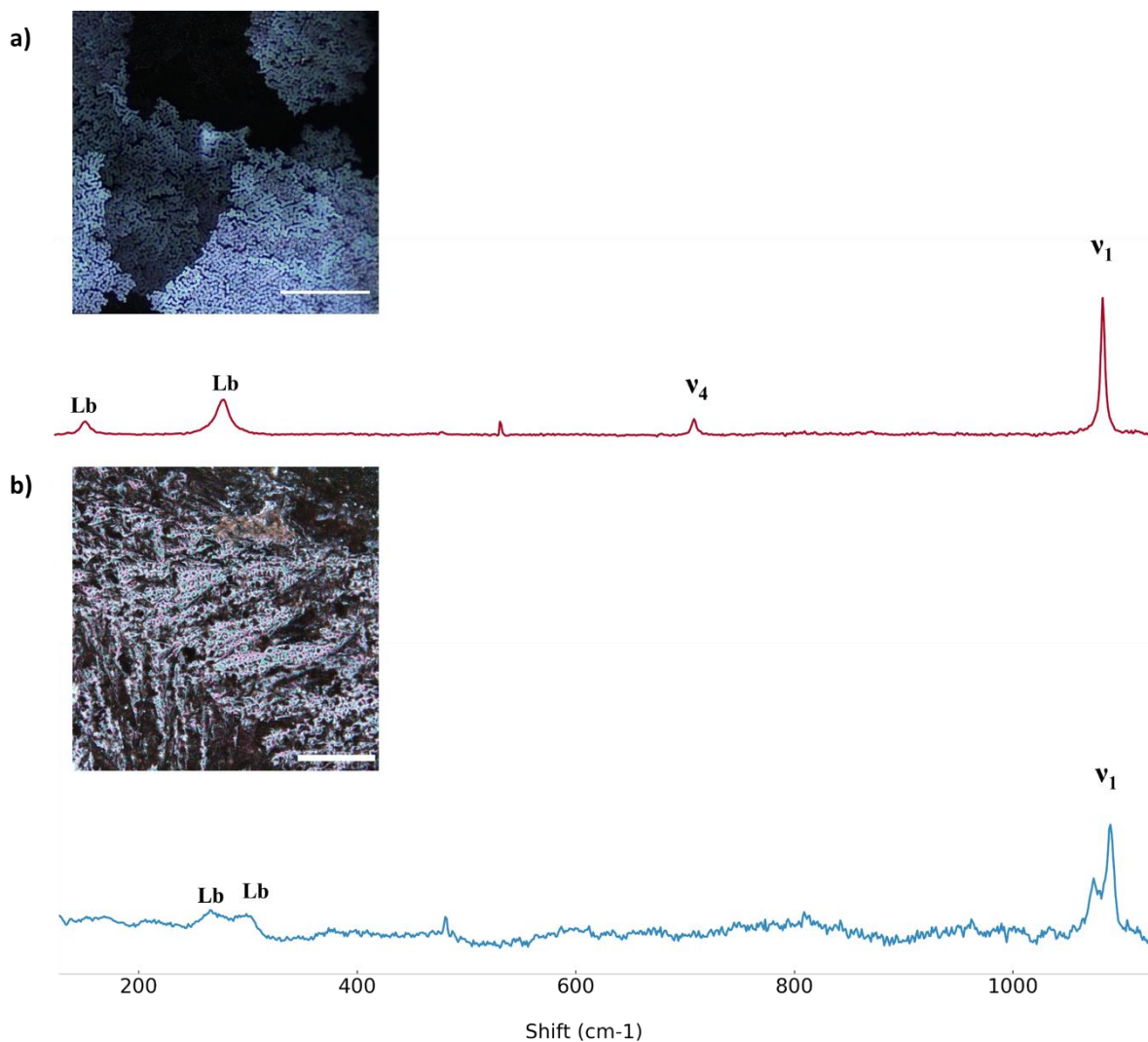


Figure 119 - Optical micrographs (BM) and Raman spectra of both single-crystalline and polycrystalline interfacial 2D crystals. Lb stands for lattice bands. a) Single-crystal resulting from the interfacial crystallization of a film ( $[\text{Ca}^{2+}] = 20\text{ mM}$ ,  $\text{PANA} = 20\text{ ppm}$ ) left at the interface for 5 days. The peak positions, provided by deconvolution, are  $1086\text{ cm}^{-1}$  for  $\nu_1$ ,  $712\text{ cm}^{-1}$  for  $\nu_4$ ,  $281$  and  $155\text{ cm}^{-1}$  for Lb. b) Poly-crystalline structure resulting from the interfacial crystallization of a film ( $[\text{Ca}^{2+}] = 20\text{ mM}$ ,  $\text{PANA} = 20\text{ ppm}$ ) left at the interface for 3 days. The peak positions, provided by deconvolution, are  $1074\text{ cm}^{-1}$ ,  $1083\text{ cm}^{-1}$  and  $1090\text{ cm}^{-1}$  for  $\nu_1$ ;  $297$  and  $265\text{ cm}^{-1}$  for Lb. Due to lack of signal, the  $\nu_4$  band of calcite and the other lattice bands are not visible.

*Continuous film:* The iso-oriented calcitic domains can be as large as the silicon nitride membrane (500  $\mu\text{m}$ , Figure A. 31 and Figure A. 32).

#### 4.3.2 Orientation of the calcitic domains

Rotating a film sample exhibiting iso-oriented domains between crossed polarizers evidences that the crystalline orientation changes randomly from one iso-oriented region to the neighboring one. This is illustrated in Figure 120 where three iso-oriented domains are highlighted in green, and light up at different angles. At  $0^\circ$  (Figure 120.a), the domain in the middle appears fully dark, in contrast with the neighboring domains which transmit some light. At a  $40^\circ$  rotation angle (Figure 120.b), the domain in the middle strongly transmits light, while the neighboring domains are almost totally black. Since the domains have different extinction angles, they have a different orientation of their neutral axis.

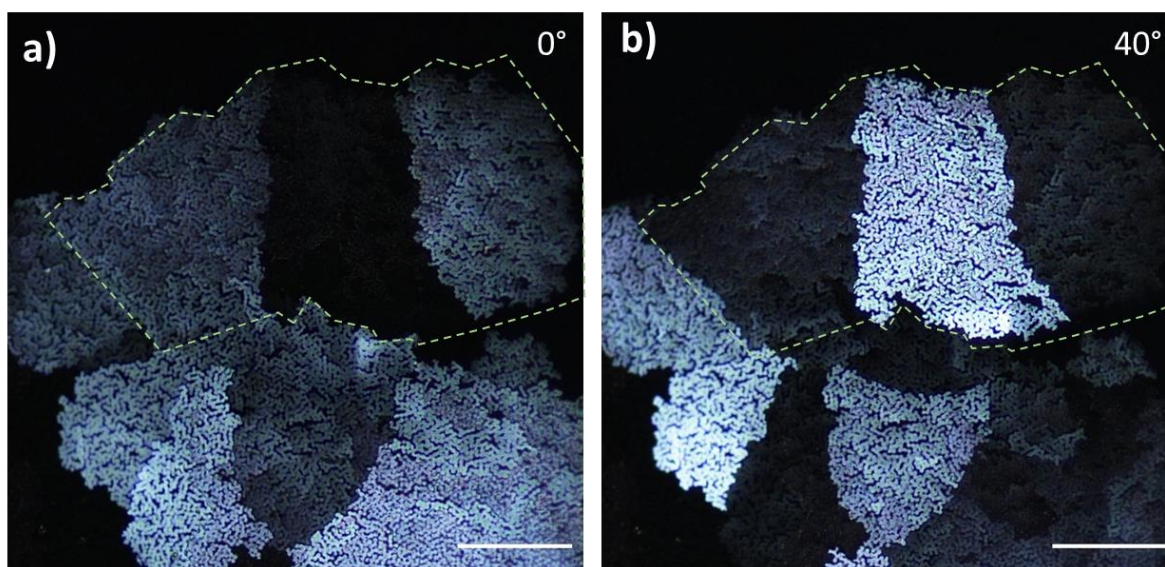


Figure 120 - Optical micrographs (BM) of a film sample crystallized at the air-solution interface. The film was produced by ADM synthesis ( $[\text{Ca}^{2+}] = 20 \text{ mM}$ , PANa = 20 ppm) and left at the interface for 5 days. a) Iso-oriented patches. The green dashed line contours three adjacent patches of different intensities. b) Iso-oriented patches similar to (a) but observed after a  $40^\circ$  rotation of the sample. The green dashed line contours three adjacent patches of different intensities. Scale bar = 100  $\mu\text{m}$ .

#### 4.3.3 Structure at the nanoscale

Using SEM, the usual and distinctive disc morphology is again observed at the microscale (Figure 121.a). At the surface, protrusions composed of oriented pillars are visible in some areas (Figure 121.a). Disc edges also appear to be decorated with pillars of same angular orientation as the surface pillars (as further detailed later in this paragraph in figure Figure 123). These pillars, although not faceted, are likely crystalline overgrowths, which reveal the actual crystalline orientation of the underneath or adjacent discs.



In parallel, at the nanoscale, the structure is loose (Figure 121.b) on the surface that was in contact with air. In some regions, a myriad of small crystals (20 nm in size), resembling rhombohedra, are sometimes visible (not shown here). Therefore, although the microscale morphology is preserved, an unusual surface nanostructure is observed, which was not present in the amorphous film.

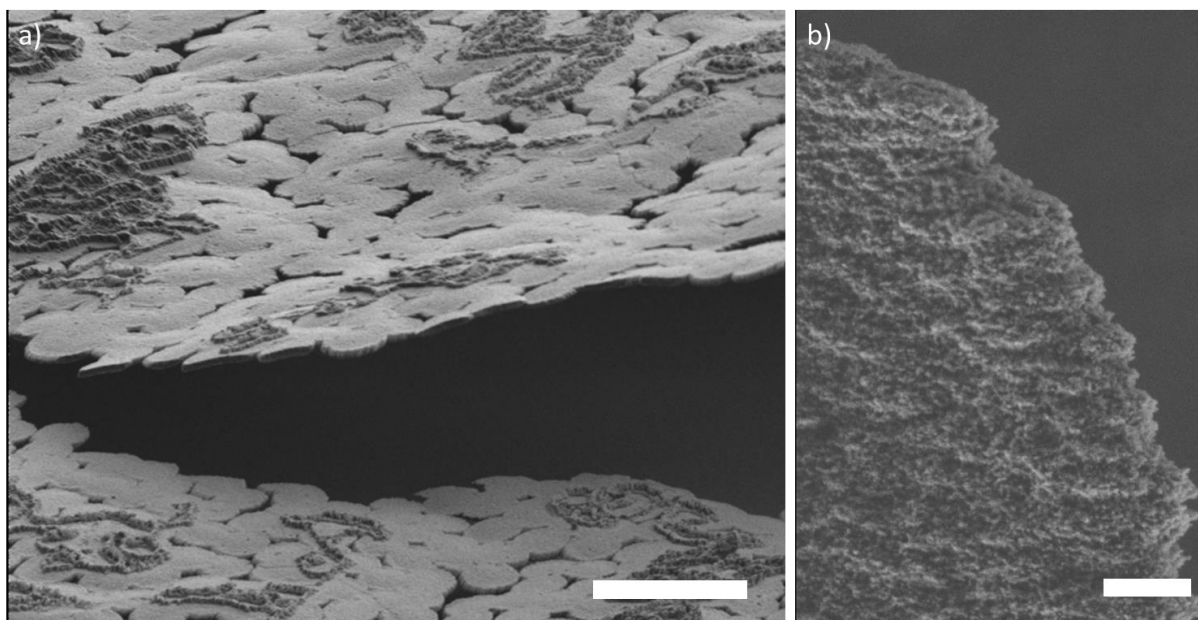


*Figure 121 – SEM micrograph of a film sample. a Side view of the film crystallized at the air-solution interface. The film was produced by ADM synthesis ( $[Ca^{2+}] = 20\text{ mM}$ , PANa = 20 ppm) and left at the interface for 5 days. The visible side of the film was the one in contact with the atmosphere during the synthesis. Oriented pillars are seen on the surface (orange arrows), and between the discs (blue arrow). HE-SE detector, 2 kV. Scale bar = 10  $\mu\text{m}$ . b) Structure of surface of the film. HE-SE detector, 1 kV. Scale bar = 400 nm .*

The investigation of the nanostructure in the film thickness was carried out by observing disc broken edges resulting from the film rupture owing to the vacuum in the SEM chamber. It revealed three layers of different nanostructural properties (Figure 122). A nano-granulated structure is present in both the top and bottom layers (Figure 122. b). The nanostructure of the inner layer in between is hard to identify as, depending on the observations, the inner layer appears to be either very smooth (Figure 122.a) or more nanostructured (Figure 122.c).

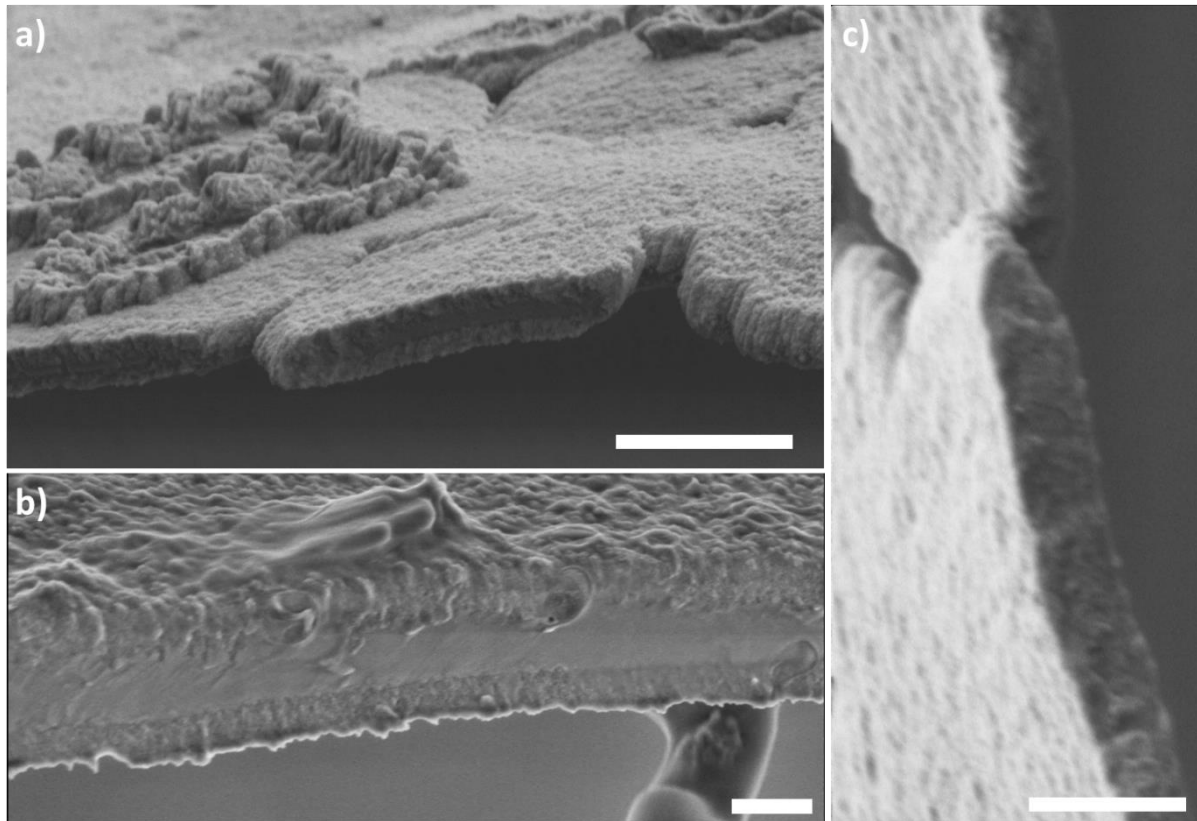


Figure 122 - Electron micrographs (SEM) of films produced by ADM synthesis ( $[Ca^{2+}] = 20 \text{ mM}$ ,  $PANa = 20 \text{ ppm}$ ) and left at the interface for 5 days, observed at  $70^\circ$ . The upper side of the film was the one in contact with the atmosphere during the synthesis. Three different areas are investigated. a) HE-SE detector, 2 kV. Scale bar =  $2 \mu\text{m}$ . b) In-lens detector, 1 kV. Scale bar =  $400 \text{ nm}$  c) HE-SE detector, 2 kV. Scale bar =  $1 \mu\text{m}$ .

The film thickness is not fully constant over the whole film sample, but rather exhibits some variations (from 500 to 600 nm), which seem to be due to a change in the external layer thickness and orientation of the pillar overgrowths. This is illustrated in Figure 123, where two areas of different thicknesses are shown, separated by a red dashed line. In the left part of the picture, the pillars, both on the edge of the disc, and on the surface, are oriented like the blue pillars drawn. The thickness of the granular external layer is about 100 nm. In the right side, no edge pillar can be distinguished on the disc broken edge, but those above on the surface are oriented to the left, and appear more tilted, like the orange drawn pillars. In addition, the granularity of the film on the surface is homogeneous. The interface between the two domains is sharp, as the thickness changes, and the external layer thins in the middle of a disc.

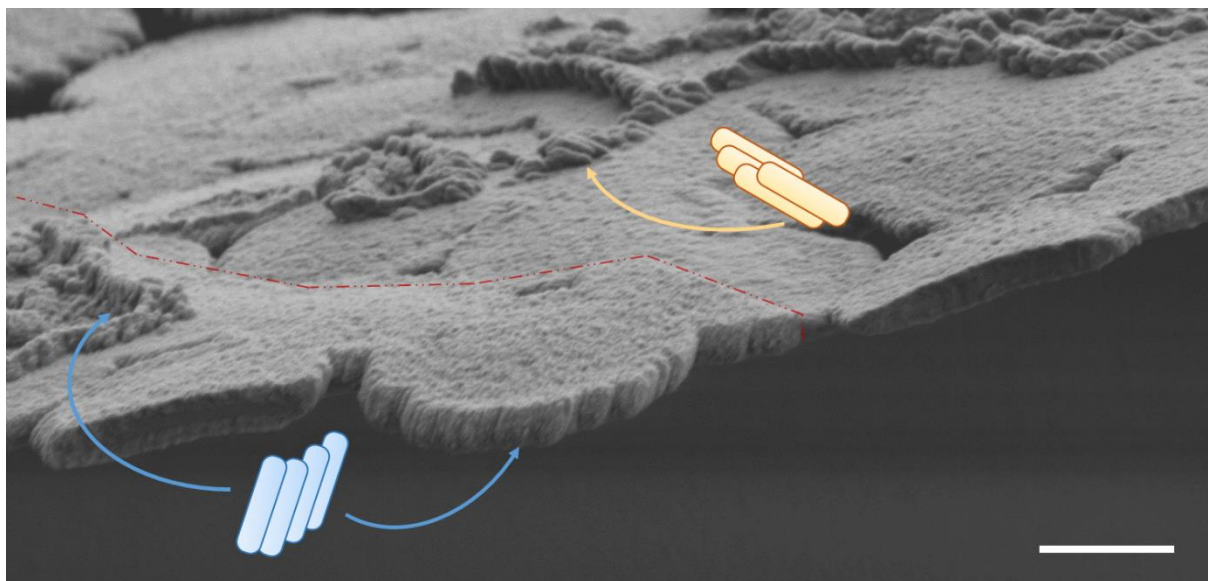


Figure 123 - Electron micrograph (SEM) of a disc-patterned film ( $[Ca^{2+}] = 20 \text{ mM}$ ,  $[PANA] = 20 \text{ ppm}$ ) left at the air-solution interface for five days. The upper side of the film was the one in contact with the atmosphere during the synthesis. The red dashed line highlights the height difference between two domains. On both domains, elongated protusions are visible on the film side in contact with the atmosphere. Blue and yellow sketches highlight the tilt of the pillars for the left and right domains, respectively. Image is taken with the HE-SE detector at a voltage of 2 kV. Scale bar = 2  $\mu\text{m}$ .

In summary, these observations highlight a transformation that appears shape-preserving at the microscale. Dissolution processes could be at the origin of the change in the internal structure of the film, which now appears as a three-layer structure with a very compact inner layer surrounded by nanostructured top and bottom layers. Finally, crystal overgrowths, in the form of pillars, are often visible revealing the crystalline orientation of the adjacent discs.

*Continuous films:* The film surface shows partial presence of a corona (smooth border in Figure A. 33.a, corona in .b). No rhombohedra or pillars are seen on the surface, the nanostructure on the surface is however loose, similarly to Figure 121.b. No cracks are visible on the continuous films crystallized at the interface, therefore, the nanostructure in the film thickness could not be probed.

#### 4.3.4 Quantitative investigation of crystalline properties

After 5 days at the air-solution interface, the crystallized film was not birefringent enough to allow vectorial ptychography (only noisy values of retardance, fast axis orientation and ellipticity could be obtained). On the other hand, ptychographic measurements could be carried out on a film with discs twice as large, and presumably thicker, likely owing to a slight change in the establishment of the gas atmosphere during the amorphous film synthesis. This one will therefore be presented hereafter.

The retardance ( $\propto \Delta n_{eff} d$ ) map shows two distinct main values, revealing a difference in the crystalline orientation and/or thickness (Figure 124.a).

Nevertheless, the fast axis map (Figure 124.b) shows that the orientation of the optical axis in the sample plane is constant in the investigated domain. Moreover, the tilt ratio,  $\frac{\Delta n_{eff}}{n_0}$ , (Figure 124.b) is also constant. Therefore, the crystalline axes have a constant orientation throughout the sample (assuming that  $n_0$  does not change over the sample), which means the sample is fully iso-oriented. The observed retardance variation is therefore likely due to a thickness change.

Finally, the ellipticity of the eigenpolarizations is rather weak in the sample ( $\sim 0.1$ , Figure 124.d), which demonstrates that the crystalline orientation is very homogeneous across the film thickness, and that the whole sample forms a "single-crystal", i.e. it is iso-oriented both in the plane and across the film thickness. Information regarding the fast-axis orientation and the eigenpolarizations ellipticity have been superimposed to the retardance map in Figure 124.e.

To conclude, the investigated crystal is a single-crystal, highly ordered in depth and presenting abrupt thickness jumps.

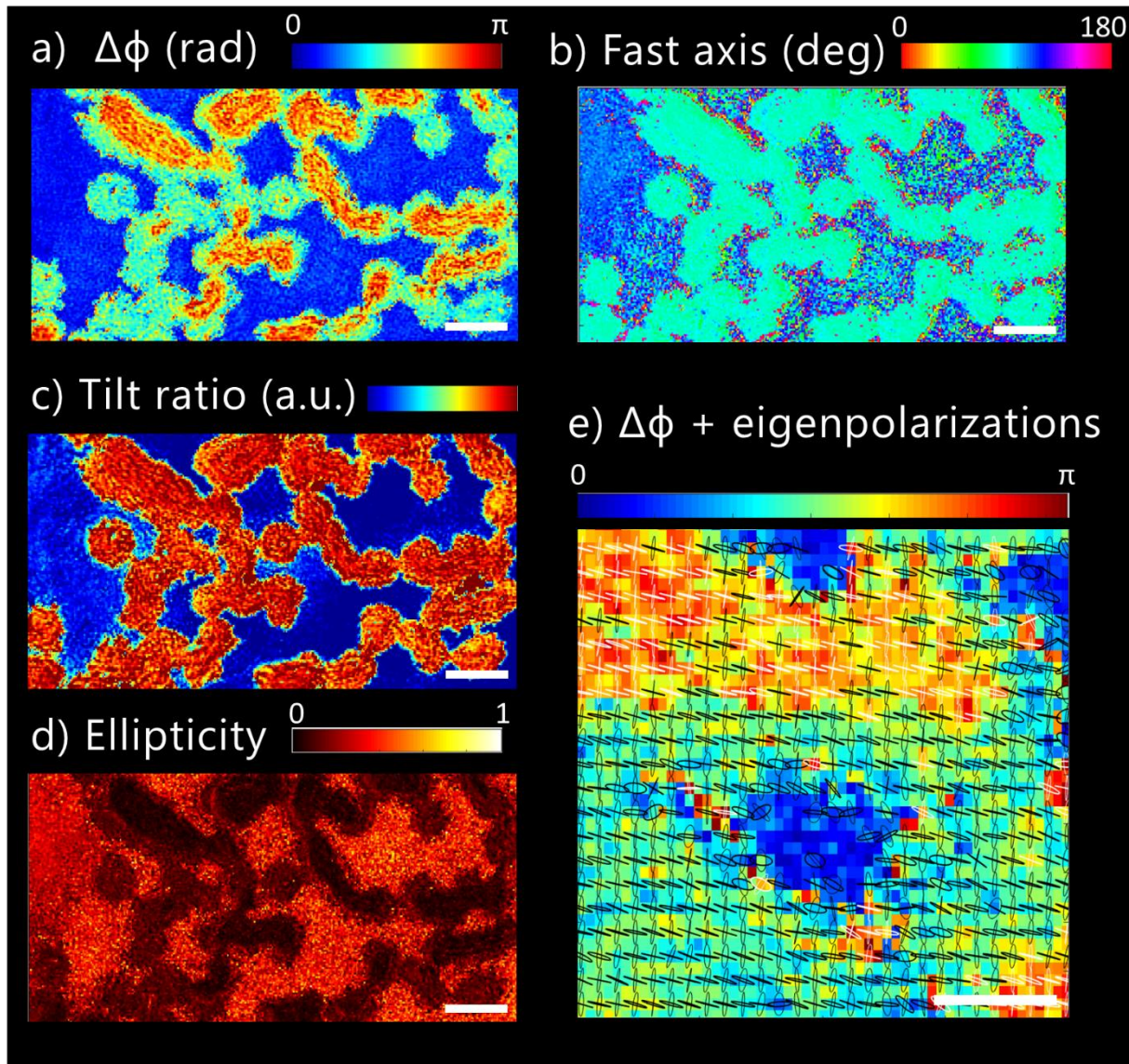


Figure 124 - Vectorial ptychography analysis of a film sample crystallized at the air-solution interface. The film sample has been collected at the surface of a  $[Ca^{2+}] = 20 \text{ mM}$   $[PANa] = 20 \text{ ppm}$  solution, after 28h of reaction. a) Retardance in radians (0 to  $\pi$ ). b) Fast-axis orientation in degrees (0 to 180). c) c-axis tilt ratio (a.u) d) Ellipticity of the eigenpolarizations (0 to 1; 0 corresponds to a linear polarization and 1 to a circular one). e) Composite map of retardance (coloration, in radians, 0 to  $\pi$ ) and eigenpolarizations (black). Eigenpolarizations are plotted only when the retardance is above 0.5 radian. a,b,c,d = 20  $\mu\text{m}$ ; e = b: 5  $\mu\text{m}$

*Continuous films:* the continuous films crystallized at the interface for 5 days show too little retardance for vectorial ptychography analysis to be performed.

#### 4.3.5 Crystalline coherence length and defect distribution

The distribution of the crystalline defects at the nanoscale, was retrieved by Bragg ptychography in the same way as in section 4.1.6.

The maps of strain and tilts, retrieved for the disc patterned film crystallized at the air-solution interface (Figure A. 34), show that the sample is composed of large iso-strain, iso-tilt domains (1.5-2  $\mu\text{m}$  wide). An iso-strain, iso-tilt domain, 2  $\mu\text{m}$  large (xy), and 400 nm deep (z) is shown in Figure 125.

On the whole investigated area, the strain presents a standard variation of  $\pm 0.0010$  and a tilt standard variation of  $\pm 0.092^\circ$  (Figure A. 34). Therefore, the sample crystallized at the interface has the smallest strain and tilt values among all examined samples (see the summary of results for comparison, section 4.4).

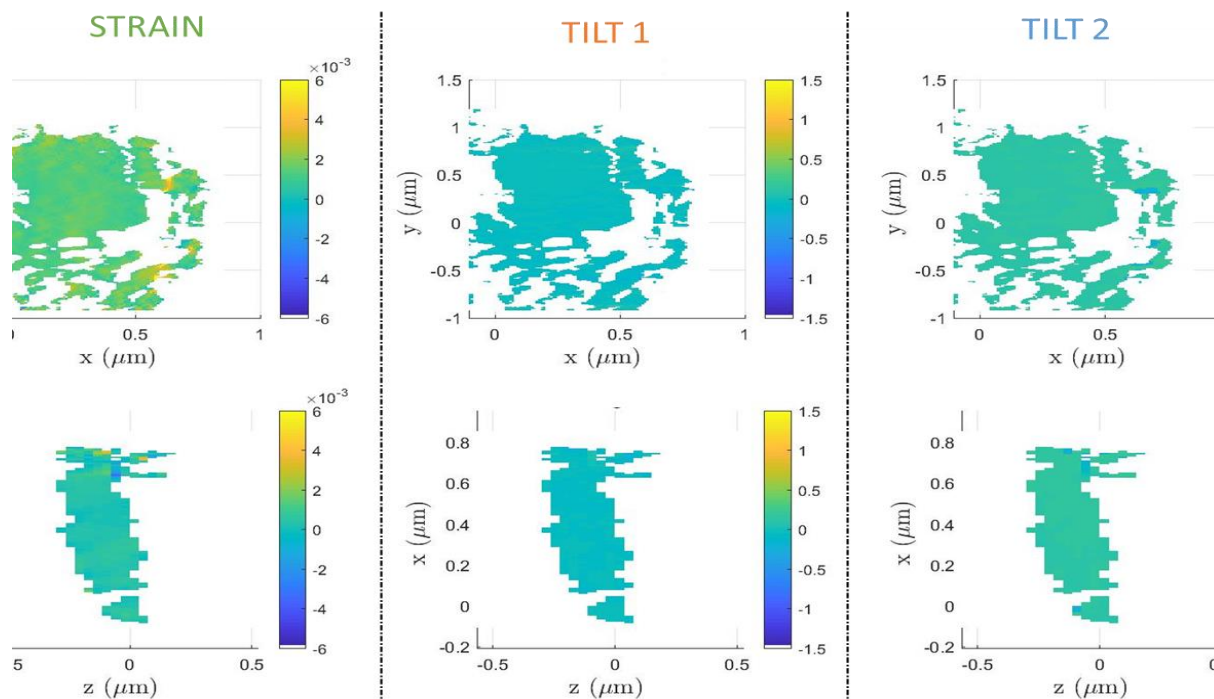


*Figure 125 - An iso-strain iso-tilt domain extracted from Figure A. 12. The strain, Tilt 1 and Tilt 2 maps are presented in the sample plane (xy) and along the sample thickness (z). The film sample was collected at the surface of a  $[\text{Ca}^{2+}] = 20 \text{ mM}$ ,  $[\text{PANA}] = 20 \text{ ppm}$  solution, after 5 days of reaction.*

Once again, the phase in this iso-strain, iso-tilt domain can be investigated. It is plotted in Figure 126, where constant phase values are observed over regions as large as 700 nm (bright green region), and 250 nm in depth. The high strain regions, corresponding to crystalline defects, are shown in gray in Figure 126, and are located at the periphery of the domain.

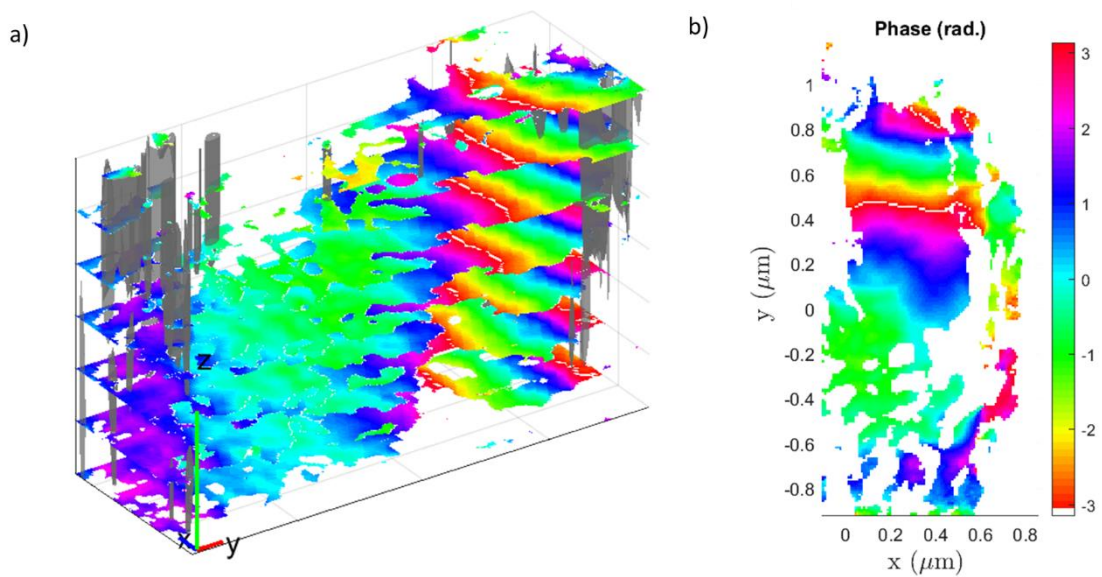


Figure 126 - Phase map of the iso-strain iso-tilt domain presented in Figure 125 a) 3D phase with scale  $(xyz) = 100 \text{ nm}$ . The gray iso volumes correspond to regions of large strains  $(> 0.001)$ . b) 2D cross-section of the phase map.

The analysis of the continuous films grown at the interface shows similar results, as presented in Figure A. 35, Figure A. 37, Figure A. 39 and Figure 127.

<i>Disc-patterned film</i>		<i>Continuous film</i>	
Investigated volume		Investigated volume	
Strain : +/- 0.0010		Strain : +/- 0.0032	
Tilt: +/- 0.092°		Tilt : +/- 0.12°	
Coherence length		Coherence length	
700 nm (xy) x 250 nm (z)		800 nm (xy) x 350 nm (z)	

Figure 127 - Comparison of the crystalline properties, retrieved from Bragg ptychography data, of a disc-patterned (scale  $(xyz) = 100 \text{ nm}$ ) and continuous (scale  $(xyz) = 100 \text{ nm}$ ) film, crystallized at the interface. The crystalline properties (strain, Tilt 1 and Tilt 2), the coherence length (size of the iso-strain iso-tilt domain) and the 3D phase map with high strain regions  $(> 0.001$  for the disc patterned-film,  $> 0.002$  for the continuous film) are shown.

Structures crystallized at the air-solution interface represent a small part of the original amorphous film. Some of them behave like single crystal, up to 500  $\mu\text{m}$  in size, under polarized microscopy. The detailed analysis of their crystalline properties show that they are formed of large iso tilted and iso-strain areas (1.5 to 2  $\mu\text{m}$ ), which exhibit a remarkable coherence length of up to 800 nm.

---

#### 4.4 SUMMARY OF THE RESULTS

Results presented in this chapter are summarized in Table 11, for both disc patterned ( $[\text{Ca}^{2+}] = 20 \text{ mM}$ ;  $[\text{PANA}] = 20 \text{ ppm}$ ) and continuous ( $[\text{Ca}^{2+}] = 100 \text{ mM}$ ;  $[\text{PANA}] = 50 \text{ ppm}$ ) films, with differences between the two highlighted when existing. As crystallization at the interface was investigated later in my thesis, fewer analytical data are available. These results will be discussed in the following section.



Table 11 - Summary of the results presented in this chapter.

	Disc-patterned film	Continuous film
Heat treatment	<b>Shared :</b> Pseudomorph (SEM), Nanostructured (SEM) Iso-oriented domains (max. 20 $\mu\text{m}$ ) WBM, VP	
	Investigated volume	Investigated volume
	Strain : +/- 0.0040 Tilt 1 > 3° Tilt 2 > 1.2°	Strain : +/- 0.0046 Tilt : +/- 0.66°
	Coherence length	Coherence length
	50 nm (xy) x 300 nm (z)	50 nm (xy) x 200 nm (z)
Humidity (98% RH)	<b>Shared :</b> Branched spherulite (SEM) ; Nanostructured (SEM) Varying granularity on the surface. Smoother surface, granulated in depth Iso-oriented domains in spherulite core (VP), Ordered in depth (VP) <b>Disc-patterned:</b> Original pattern still visible in spherulite (OM, SEM)	
	Investigated volume (tip of a branch)	Investigated volume (core)
	Strain : +/- 0.0049 Tilt 1 +/- 0.44° Tilt 2 > 2.1°	Strain : +/- 0.0011 Tilt : +/- 0.066°
	Coherence length	Coherence length
	100 nm (xy) x 50 nm (z)	600 nm (xy) x 400 nm (z)
Interfacial crystallization	<b>Shared:</b> Pseudomorph (OM, WBM) <b>Disc-patterned:</b> Micronic shape preserved, but loss of corona, replaced by pillar on disc periphery (OM,SEM), Iso-oriented domains: 100 $\mu\text{m}$ Nanostructured, with two granularity in depth (SEM), Ordered in depth (VP) <b>Continuous:</b> > 500 $\mu\text{m}$ with continuous (WBM), Corona partially present (SEM)	
	Investigated volume	Investigated volume
	Strain : +/- 0.0010 Tilt range: +/- 0.092°	Strain : +/- 0.0032 Tilt : +/- 0.12°
	Coherence length	Coherence length
	700 nm (xy) x 250 nm (z)	800 nm (xy) x 350 nm (z)

## 4.5 DISCUSSION

The results reported in this chapter allow us to discuss several aspects of the amorphous-to-crystal transformations. First, the physico-chemical mechanisms underlying the different crystallization pathways will be described, based on the study of the micro- and nanometric morphological changes during crystallization. Then, the heterogeneity of the crystallization process within a given amorphous film is analyzed and the reasons leading to this heterogeneity are discussed. Finally, a comparison between the crystals synthetically produced and the biogenic crystals is carried out, considering in particular the crystalline properties as determined by Bragg ptychography.

### 4.5.1 Heat-induced amorphous-to-crystalline transition

The heat-induced transformation retains the morphology of the amorphous film at all scales. At the micro-scale, the discs are preserved in the disc patterned films (Figure 94), still exhibiting a corona, like in the amorphous state. In continuous films, the few discs observed in the amorphous film (Figure 65.b), reminiscent of the liquid-liquid phase separation that initiated the film formation, are still visible after crystallization. At the nanoscale, a dense arrangement of particles is observed in both cases (Figure 98 and Figure 67.b), although the determination of the particle size is difficult using SEM.

Thus, the heat-induced crystallization of the ACC films appears shape-preserving. It is in line with the literature, which depicts the ACC crystallization by heating as a solid-solid transformation characterized by a short-order structural rearrangement,<sup>69</sup> which preserves the nanostructure for temperatures above 160°C.<sup>93</sup> Still, the dehydration process that changes hydrated ACC into calcite, has been shown to induce a small compaction of the nanostructures, this way increasing slightly the surface roughness<sup>61</sup> and generating pores. These observations are in full agreement with our observations of a more visible surface nanostructure after heating and with the appearance of pores Figure 95.

As detected by Bragg ptychography, ACC crystallization at 300°C generates small (200 nm wide) iso-strain iso-tilt domains, meaning that multiple crystal nuclei are formed within the film (Figure 94), in agreement with a fast crystallization process.

The preservation of an ACC layer after heating at 300°C for 3h is more puzzling owing to the reported data characterizing the dehydration and crystallization in air,<sup>59</sup> which show that such a temperature induces the transformation of the ACC regardless of its initial hydration state. However, the thickness of this layer was roughly estimated to 1 to 2 nm, by comparing the  $L_2$  post-edge optical density to the one of a nanometer-thick  $\text{CaCO}_3$  layer (considering the density of calcite, 2.71 g/cm<sup>3</sup>). Such a thin layer could indeed be thermodynamically stable<sup>81</sup> or be stabilized by a high polymer content (degradation of PANa only occurs at about 400°C).<sup>160</sup>

#### 4.5.2 Humidity-induced amorphous-to-crystalline transition

The extent of the morphology changes is much more important in the humidity-induced crystallization, and depends on the relative humidity rate imposed during crystallization. The nascent crystalline phase always takes the form of a spherulite. The crystal propagation then takes place with a more or less important conservation of the original disc pattern. At low relative humidity (33%), the disc pattern is preserved and can be observed by birefringence microscopy (Figure 106.a). At intermediate relative humidity (75%) (Figure 106.b), the crystals first grow while preserving the disc morphology, and then generate elongated branches that encompass the discs. At high relative humidity (98%), the discs appear fully embedded within the spherulitic structure, and cannot be detected by birefringence microscopy anymore, but only by transmission (Figure 107) or electron microscopy (Figure 109). Only a few isolated discs are visible, which show clear signs of a dissolution process (Figure 112), further confirmed by the disc imprints surrounding the spherulites everywhere (Figure 110). Therefore, it is quite clear that crystallization under high humidity (98% RH) relies on a dissolution-crystallization process, which involves species diffusion over large distances, up to several microns, contrarily to heat-induced crystallization.

In our experiments, the physisorbed water layer that forms on top of the ACC film allows the diffusion of ions, albeit in a limited way due to the high viscosity within this layer. These conditions favour the formation of spherulites, which are polycrystalline structures typical of diffusion-limited crystal growth,<sup>161</sup> arising during non-equilibrium crystallization at high supersaturation or in a high viscosity medium (Figure 128). While studying the crystallization of inorganic materials in a gel matrix, Oaki *et al.* demonstrated the influence of the driving force on the crystal morphology<sup>97</sup>. At low ion diffusivity (high medium viscosity), or high supersaturation, spherulites are observed, while at high ion diffusivity (low viscosity), or low supersaturation, single crystals form. Between these two extremes, intermediate morphologies can be observed, such as ordered single-crystalline or poly-crystalline dendrites. These concepts are also relevant to 2D spherulitic growth, for which Tegze *et al.*<sup>162</sup> have shown that supersaturation and diffusivity direct faceted (oriented) or non-faceted (non-oriented) crystallization. In our experiments, one can note that when the relative humidity rate rises faster, and is slightly higher (99% RH) than in the standard conditions, the observed morphology evolves from spherulites to polycrystalline seaweed structures, that indeed are shown to appear at lower viscosity than spherulites.

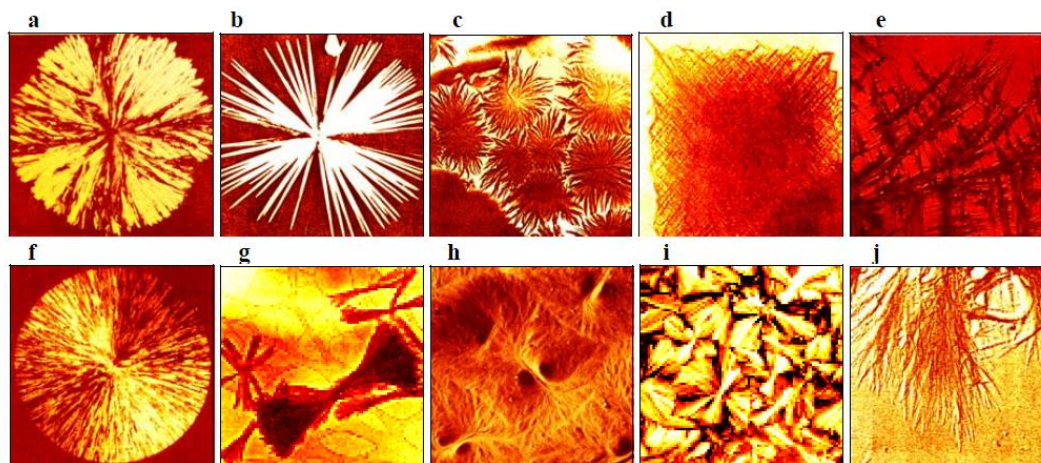


Figure 128 - Variety of spherulites morphologies observed in polymeric systems. From Gránásy *et al.*<sup>163</sup>

The core of the observed  $\text{CaCO}_3$  spherulite, at 98% RH, is divided into iso-oriented domains with a mean radial orientation, which often exhibit abrupt orientational changes between them (Figure 110). At the tip of the branches, the crystalline orientation is still radial but now varies gradually with the azimuthal position, as expected for spherulites. These observations are in agreement with the features of type 1 spherulites, as defined by Gránásy *et al.*,<sup>163</sup> which develop radially from a transient single- or polycrystalline nucleus (as opposed to type 2 spherulites which develop from a thread-like fibre). However, most of the  $\text{CaCO}_3$  spherulites resulting from humidity-induced crystallization do not reach an isotropic shape (yet, fully-developed spherulites can be detected occasionally – see the blue arrow in Figure 109), but rather show a limited number of branches, likely owing to a limited crystallization process. Finally, the size of the spherulite is expected to exhibit a linear growth regime at early times,<sup>164–166</sup> similarly to what was evidenced for the seaweed morphology (Figure 108).

Spherulitic crystallization is a complex phenomenon characterized by multiple secondary nucleation events at the crystallization growth front, owing to static (impurities) or dynamic (quenched orientational defects) heterogeneities. These nucleation events result in non-crystallographic branching of the developing crystal (tip splitting) and finally generate a great diversity of space-filling morphologies.<sup>167</sup> However, in the experiments reported here, the observed spherulites exhibit open morphologies, most of the time with a few branches only emerging from the center, as well as with cyclic variations of the thickness along the branches (reported above as step-like variations). These specific features likely result from a coupling between the dissolution process, essential for the release of ions needed to feed the growing crystal, and the spherulite formation. If this dissolution process is too slow with respect to the kinetics of crystallization, the crystallization front is periodically arrested due to the depletion of free ions in the surrounding medium (this corresponds to the top of the steps, where the branch is thickest and where almost no dissolution had affected the underneath discs), and resumes its propagation after the dissolution has released sufficient ions in the surrounding medium (bottom of the steps, where a significant dissolution has occurred, thus allowing again crystal growth).

While the development of the spherulite final morphology occurs within 2.5 days, a second

crystallization process occurs in parallel which lasts over a much longer period of time: indeed uncrystallized discs, which are still visible between crystals after 2.5 days (Figure 107), completely disappear in the course of the next weeks, while the crystal shape and dimensions remain identical. Thus, the dissolution of the uncrystallized discs feed a re-precipitation process that happens between the discs. This filling process seems to occur at the edge of the spherulite only, and not in the centre, where the discs remain therefore well differentiated and easy to distinguish. Crystallization under high-humidity atmosphere should therefore be explained considering this continuous dissolution process along with the observed preservation of some discs, embedded within the crystals, which retain their nanostructure throughout the crystallization process. Based on these two observations, a hybrid mechanism for crystallization is proposed. As a first step, a dissolution/crystallization process takes place in the physisorbed water layer at the surface of the ACC film, leading to the formation of a 2D spherulite on top of the disc assembly, owing to the low ion diffusivity and high supersaturation index in the medium. This process relies on the dissolution of some nanostructured ACC discs. Simultaneously, the discs underneath the spherulitic 2D crystals start to crystallize in an iso-oriented manner with respect to the spherulite, following a solid-solid, shape-preserving transformation. This leads to the observed nanostructured spherulitic crystals, with disc still visible. The dissolution-crystallization process remains active beyond this solid-solid phase transition. It then affects the still amorphous discs, at the periphery of the spherulite, this way releasing ions which precipitate into a smooth crystalline material, devoid of nanostructure, between the crystallized discs, owing to the now much lower supersaturation in the medium.

In conclusion, crystallization under high-humidity atmosphere implies two related, although spatially-differentiated, crystallization mechanisms, namely dissolution-crystallization and solid-state transformation. Such a hybrid mechanism has already been hypothesized for the crystallization of ACC particles in air,<sup>59,95</sup> but could not be demonstrated in the absence of specific features of the dissolution/precipitation process. The results presented here are therefore fully original as they clearly demonstrate such a hybrid mechanism, which partially preserves the micro- and nanoscale structure of the native ACC film.

### 4.5.3 Interfacial amorphous to crystalline transition

The underlying mechanisms of the interfacial crystallization are more difficult to determine due to a less thorough study of this transformation, which in particular could not include any temporal study of the crystallization process. However, it is reasonable to assume that the interfacial crystallization is, like the humidity-induced crystallization, a surface-driven crystallization. One can actually imagine that crystallization starts with a nucleation event at the bottom surface of the film, in contact with the solution, either as a result of a dissolution-crystallization event or from the attachment of a bulk crystal nucleus. The small number of nucleation events (even more limited in the 100 mM/50 ppm synthesis), leading to the observed large iso-oriented domains, supports this scenario as the supersaturation of the solution at this stage of the synthesis is likely quite low. A crystallization starting from the top side of the film is unlikely, as it would result, like in the humidity-induced crystallization, in spherulitic morphologies. Finally a purely solid-solid crystallization starting from the core of the film and propagating outwards is also improbable as it would require the dehydration of the amorphous state, which is kinetically hindered at room temperature owing to a high

activation energy.<sup>59</sup>

The proposed mechanism is compatible with the observed microscale shape retention during interfacial crystallization. Indeed, the discs are still visible after crystallization. However, they do not show a corona anymore and the film thickness now shows a three-layer structure, the inner layer being much smoother than the original amorphous nanostructure or than the bottom and top layers, which appear quite granular. The difficulty to image by SEM the nanostructure could reveal a much more compact and space-filling nanostructure, or a partial disappearance of the nanostructure due to nanoparticle fusion. The nanostructure of the top and bottom layers is somehow similar to the one of the amorphous layer, although it could not be precisely characterized.

In parallel, the existence of pillars at the edges and on the top surface of the discs, likely points to a dissolution/crystallization phenomenon occurring before film sampling. Parts of the film were seen to sink into the solution, which may favor such a dissolution/crystallization process. It is interesting to note that the tilt, with respect to the film surface, of the pillars (both at the edges of the discs and at the film surface) remains constant over the iso-oriented domains (Figure 123), likely revealing the local crystalline orientation of the underlying film.

The thickness of the of the film changes from one domain to another (Figure 123), meaning that it depends on the local orientation of the film. This supports the hypothesis of a partial dissolution of the discs, of variable amplitude according to the local crystalline orientation, just like what happens for single crystals whose crystallographic faces present different interfacial energies, and thus solubility.<sup>168</sup> Moreover, it has been reported that the unstable crystal faces of calcite undergo dissolution and epitaxial growth when exposed to solution<sup>64</sup> in agreement with our observations. Therefore, a dissolution-recrystallization process likely follows the initial crystallization of the film and modifies its structural features without apparently affecting its crystalline properties. The inner layer of the film would therefore correspond to the unaltered crystalline structure resulting from the first crystallization of the film only. Yet, in the case of disc patterned films, we could show by vectorial ptychography that the crystalline film has a very low ellipticity, meaning that the recrystallization process has not induced disorder in the film thickness.

The crystallized domains at the interface have a high quality of crystal organization over long lateral distances (iso-oriented domains of several tens of  $\mu\text{m}$  in WBM), Pseudomorphic transformation of interfacial ACC films has been reported in the literature in both iso-oriented<sup>64</sup> and spherulitic crystals.<sup>105</sup> In the case of spherulitic crystals, the nanostructure at the surface of the film was shown to be the same as that of the amorphous film. In our case, the analysis of the nanostructure is not relevant on the surface, due to the dissolution process. Unfortunately, the analysis of broken edges did not allow us to determine the nanostructure of the crystalline inner layer, so that although highly probable the hybrid mechanism cannot be proven completely. To prove this scenario, it would be necessary to sample the crystalline film at shorter times, before dissolution occurs, or to characterize the nanostructure of the inner layer in a FIB cut of the crystal.

In summary, crystallization at the interface corresponds to a transformation which is shape-preserving at the microscale only, and produces micron-sized iso-oriented crystalline domains, likely by combining a dissolution/precipitation process on the side of the ACC film in contact

with the solution, and a solid/solid transformation that ensures the homoepitaxial crystallization of the rest of the film. A more detailed characterization of the mechanism would require a temporal follow-up of the film structure evolution.

### 4.5.4 Heterogeneities in the amorphous film: influence on the crystallization

The influence of the environmental conditions has been addressed in the previous section and the mechanisms at work for each type of crystallization have been determined. However, the response of the ACC film to the crystallisation conditions is not homogeneous over the whole film, which likely reveals the heterogeneous nature of the amorphous film itself. For instance, upon exposure to 300°C, part of the film fails to crystallize (Figure 100, STXM), while, upon exposure to air moisture, some of the discs stay optically isotropic up to 7 days, meaning that they have not crystallized. Finally, the interfacial film can be dissolved in favor of 3D crystal growth, or it can retain its microscopic morphology and form either 2D vaterite spherulites or 2D calcite iso-oriented domains. Differences in products obtained when exposing the same film to the same crystallization conditions are likely due to heterogeneity in the original film.

In the case of the heat-induced crystallization, the observed heterogeneities in response may result from the uneven hydration level of the ACC film, or from a heterogeneous polymer distribution within the film. Indeed, the ion mobility is known to influence the activation energy of the crystallization, so that a lower hydration rate<sup>59,79</sup>, or a larger amount of polymer, increases this energy barrier,<sup>69</sup> making more difficult for the film to crystallize. In addition, it has been shown that this activation energy decreases with the size of the ACC particles. Thus, the uneven film thickness, arising from the heterogeneous particle aggregation during the amorphous film formation, could also explain the retention of the amorphous material, despite heating, where the film is thinner (Figure 100).

When crystallization follows a dissolution process, the local supersaturation, resulting from ACC solubilization, influences both the polymorph selection and crystal morphology. The solubility will depend on the local composition (polymer content) of the amorphous calcium carbonate (see 1.2.4). Then, a higher supersaturation will lead to both an increase in polycrystallinity,<sup>97</sup> and to the preferential crystallization of vaterite<sup>169</sup>. Thus, the difference in polymorph selection and morphology observed in humidity-induced crystallization within the film may again originate from a spatially heterogeneous water and polymer content.

### 4.5.5 Comparison to *Pinctada margaritifera* crystalline properties.

As described in the introductory chapter (1.4.2), the biomineral prisms that compose the outer part of the oyster *Pinctada margaritifera* shell are iso-oriented crystals<sup>108</sup> of calcite.<sup>7</sup> They are formed by an assembly of mineral layers (500 nm-thick)<sup>16</sup> made of a compact arrangement of nanometric grains.<sup>170</sup> Similarly, the crystals resulting from the chosen conditions in this work all show iso-oriented calcite domains and whose detailed crystalline properties have been accessed by Bragg ptychography.

The prisms of juvenile *Pinctada margaritifera* shell edges are thin enough<sup>39</sup> to be analyzed with vectorial and Bragg ptychography approaches. First, quantitative analysis of the optical properties of the prisms confirms their iso-orientation.<sup>125</sup> 3D orientation mapping of the fast axis orientation shows that inside a prism (up to 20  $\mu\text{m}$  in diameter) the orientation of the c-axis of the crystal remains constant, both in the sample plane and in depth. Moreover, the ellipticity of the eigenpolarizations is low.<sup>16</sup> Similar observations are made in the case of crystals crystallized at the interface, (Figure 124), by heating (Figure 101, although the ellipticity is slightly larger) and in the humidity-induced spherulites, yet in the core only (Figure 113). Nevertheless, it must be noted that the radial orientation of the iso-oriented domains in the spherulites core is not found in the calcitic prisms.

In parallel, Bragg ptychography characterization of the shell prisms have revealed iso-strain iso-tilt domains in the crystal.<sup>16</sup> Typical iso-strain and iso-tilt domains are 1.4  $\mu\text{m}$  long and correspond to a strain distribution characterized by a standard deviation of  $\pm 0.002$  relative to a reference calcite crystal. The tilt range is around  $1.2^\circ$  (Figure 129) and the coherence length is of 400 nm or more (Figure 130). These typical strain value and coherence length are again similar to those measured in interfacial crystallization (continuous film or not) and in the core of the spherulites (continuous film) (see summary of results). However, the tilt range of the synthetic crystals is inferior to those of the biogenic model. This difference could be explained by the geometrical constraints in the biogenic crystals (resulting from the growth on the flexible periostracum for example), which could enhance the tilt distribution.

Finally, the samples that have crystalline properties (micro and nanoscale) corresponding to the biogenic crystals are those grown at the air-solution interface.



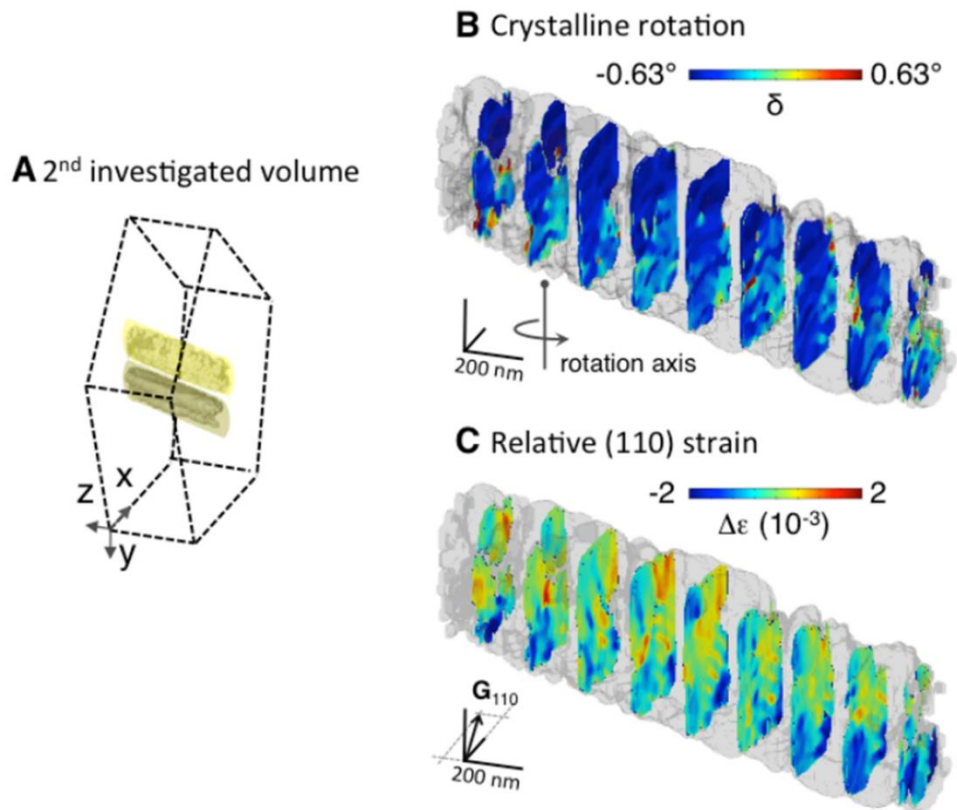


Figure 129 - Bragg ptychography on a *Pinctada margaritifera* calcitic prism. A) Volume investigated in the prism. B) 3D map showing the tilt distribution in the probed volume (in degrees). C) 3D map showing the strain distribution in the probed volume. From Mastropietro et al.<sup>16</sup>

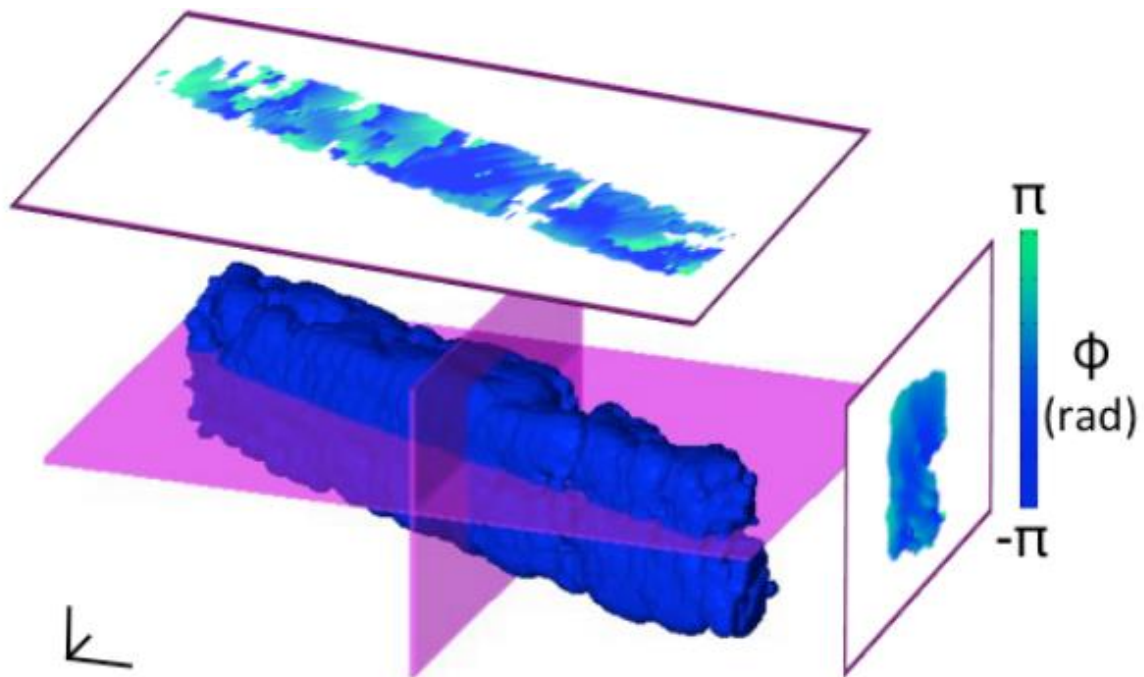


Figure 130 - 3D Bragg ptychography on a *Pinctada margaritifera* calcitic prism. The phase (in rad) is shown in 3D in the investigated volume. Areas of continuous coloration (ex. dark blue) show a coherence length of 400 nm. Scale bar in 3D: 200 nm. From Mastropietro et al.<sup>16</sup>

In conclusion of this chapter, the control of the crystallization conditions of a calcium carbonate film synthesized by the PSLP route effectively allows the control of the polymorph selection, morphology and polycrystallinity. Surprisingly, the micron disc pattern is maintained in all three crystallization pathways considered here, highlighting the robustness of the initial amorphous calcium carbonate morphology during crystallization. The preservation of the microscopic morphology does not prevent the production of crystals with different overall morphology and crystal properties. Interfacial crystallization is the shape-preserving transformation that leads to synthetic crystals closest to biogenic crystals.

## 5 CONCLUSIONS AND PERSPECTIVES

---

In this concluding chapter, the main results will be summarized, and ideas for further development of the model will be proposed. Finally, perspectives for deepening the understanding of the biogenic system using model syntheses will be discussed.

### 5.1 MINERALIZATION PATHWAY IN THE MODEL SYSTEM: FROM FREE IONS TO CRYSTALLINE LAYER.

The gas diffusion synthesis implemented in this study yields two-dimensional calcium carbonate crystals through intermediate liquid and solid amorphous states to crystallization. During the synthesis, an amorphous calcium carbonate film is formed at the air-solution interface before being consumed by crystallization. The crystallization pathway can be interrupted to determine the mechanisms of the amorphous film formation, or drive its crystallization by various *ex situ* mechanisms.

It has been shown that amorphous films with controlled morphologies can be produced in a reproducible manner by removing the film from the air-solution interface prior to crystallization. Depending on the initial composition of the solution, films are obtained as a discontinuous assembly of micron-sized discs (~5  $\mu\text{m}$ ) or as continuous films. Increasing the amount of calcium leads to a densification of the film, while increasing the amount of polymer produces a widening of the interface structures. In order to obtain continuous films, sufficient amounts of calcium (>50mM) and polymer (50 ppm) must be used. However, the presence of residual micron-sized discs embedded in the continuous films suggests that a common mechanism is at work in the formation of the amorphous films. Therefore, the synthesis conditions leading to discontinuous disc-patterned films were chosen as reference conditions to determine the formation mechanisms that lead to the production of amorphous nanostructured films of 500-700nm thickness.

We could follow the evolution of the interfacial discs during the first hour of reaction, and this way show that the discs result from an interface-driven liquid-liquid phase separation occurring *via* spinodal decomposition. The chemical quench induced by ammonia dissolution actually results in a rapid pH increase and creates the conditions for the liquid-liquid phase separation. The shape of the discs, with thinner edges and thicker center (4 nm at the edge, 5 nm in the center) are evocative of liquid droplets that partially wet the surface of the solution. In addition, the observed double emulsion patterns are suggestive of a very low surface tension and unambiguously point to a demixing process that occurs *via* a spinodal decomposition process. The first stage of film formation therefore occurs *via* an LLPS process at the interface. This defines a 2D motif that subsequently thickens by irreversible aggregation of bulk amorphous nanoparticles.

Diffusion, and then convection, enables bulk nanoparticles to aggregate on the pre-established motif. Nanoparticle aggregation is strongly enhanced by the appearance and development of convection rolls in the solution, which lead to a thickening propagation front within the film.

At the end of the formation process a disc-patterned film, made of densely packed nanoparticles, a few hundred nanometers thick, is formed. Such a nanostructured disc-like morphology is ideal for studying the crystallization process of an amorphous calcium carbonate layer whose structure<sup>39</sup> and thickness<sup>41</sup> are similar to those of *Pinctada margaritifera* growth layers. By stopping the reaction before the amorphous film crystallizes spontaneously at the interface, one can trigger the *ex situ* crystallization of the film following two different pathways, namely heat-induced and humidity-induced crystallization pathways. A spontaneous crystallization of the ACC film at the air-solution interface was also considered, as it can lead to the development of large iso-oriented 2D calcite crystals.

The disc pattern is retained after crystallization, at least to some extent, regardless of the trigger used to induce crystallization (heat, high relative humidity, or aging at the interface). In two conditions, namely heat exposure and aging at the interface, the crystals keep the microscale morphology of the ACC film. In contrast, under high humidity, the discs appear embedded in spherulitic structures and therefore do not define the crystal overall morphology like in the two other crystallization processes.

First, under heat, the amorphous-to-crystal transition takes place *via* a solid-solid phase transition. The discs exhibit a compact nanostructure, similar to the one of the original amorphous discs. Iso-oriented domains, independent of the film morphology, up to 20 microns in size, are identified by wave plate-assisted birefringence microscopy. Vectorial ptychography shows that some disorientation exists in the crystal depth. With Bragg ptychography, we have identified that this transition gives rise to the largest relative strain in the crystal ( $\pm 4.0 \times 10^{-3}$ ), and to the smallest coherence length (200 nm). Crystallization by thermal initiation transforms the amorphous films into small calcite domains with significant strain.

Then, under high humidity, crystallization occurs by a dissolution/crystallization mechanism followed by a solid-solid phase transition. Discs are still visible on SEM micrographs of the spherulite. However, different nanostructures are present in the discs and the filling between them. Our observations indicate that the discs crystallize by iso-oriented growth from the already crystallized layer in contact with the humid atmosphere, and a dissolution-crystallization process fills the empty space between the discs. Vectorial ptychography shows that there is no disorientation in the depth of the crystals, and that the distribution of orientation of the fast axis depends on the growth stage of the spherulite. Thus, while the core consists of iso-oriented domains, the branch tip shows a spatially variable crystalline orientation. Bragg ptychography measurements, which were performed on different parts of the spherulite, could highlight some differences in the crystalline properties. However, in the core of the spherulite, where the disc morphology is well preserved, the coherence length is large (1  $\mu\text{m}$ ), and the relative strain is small ( $\pm 1.0 \times 10^{-3}$ ).

Finally, when left at the air-solution interface, the ACC film undergoes a pseudomorphic crystallization at the microscale. The film retain the disc assembly morphology, and iso-oriented domains, several hundred microns long, are visible (WBM). However, at the nanoscale, the corona surrounding the discs has disappeared and the film now has a three-layer structure with the top and bottom layers exhibiting a very different nanostructure than the internal layer. In fact, no nanostructure associated with the inner layer could be clearly evidenced by SEM, which means that if such a nanostructure exists, it must correspond to a very compact assembly of nanoparticles. The surface of the film show signs of dissolution/recrystallization, with

features that apparently depend on the crystalline orientation of the underlying discs. Vectorial ptychography shows no disorientation within the crystal depth, and a constant fast axis orientation of the crystals over distances up to 100  $\mu\text{m}$ . Bragg ptychography measurements show that the crystalline domain coherence length is large (up to 2  $\mu\text{m}$ ), and that the strain is small ( $\pm 1.0 \times 10^{-3}$ ). The interfacial crystallization thus produces large iso-oriented domains hundreds of microns in length, with small crystalline deformations.

As a conclusion, all three crystallization conditions lead to the conservation of the initial disc pattern, at least to some degree. Nevertheless, the resulting crystals have different crystalline properties, which can be compared to those of biogenic crystals like *Pinctada margaritifera* oyster shell. The crystals grown at the interface and the core of the spherulites have crystalline properties closer to those of the biogenic crystals (iso-orientation, coherence length and strain/tilt values). Here, the humid environment favors the ACC film dissolution and the slow crystallization process allows the ACC to dehydrate before crystallization, in contrast to what happens in heat-induced crystallization where crystallization is very rapid (1 min). This slow process is likely a prerequisite to obtain "biogenic-like" crystals. These conclusions regarding the syntheses led us to re-examine the relevance of our model syntheses to reproduce the mechanisms at work in calcareous biomineralization.

## 5.2 RELEVANCE OF THE CRYSTAL GROWTH MODEL WITH REGARD TO BIOMINERALIZATION

In this section, the relevance of the growth scenario (see below), derived from the analysis of the model syntheses, to describe the processes of calcareous biomineralization will be assessed. The biomimetic character of the chosen environmental conditions, the occurrence of a liquid/liquid phase separation, the possibility of convective motions in the biological mineralizing fluid, and finally the impact of an amorphous transient will be successively discussed.

Our results on ADM-based  $\text{CaCO}_3$  syntheses indicate that it is indeed possible to induce calcium carbonate precipitation in a way which is shape-preserving at both the micro- and nanoscale, and delivers crystals with crystalline properties very similar to those of the biomineral. This mineralization pathway involves the build-up of a 2D amorphous pattern and its thickening by bulk nanoparticle aggregation, followed by a crystallization process combining localized dissolution/recrystallization and solid-solid transformation of the nanoparticle assembly, so as to ensure the formation of iso-oriented domains of micrometer size.

The choice of ADM-based syntheses was made because these syntheses, when carried out in the presence of polyelectrolyte, allows the production of crystalline films that share some characteristic features with calcareous biominerals. However, these syntheses are associated with a strong pH increase, up to values of 9.5-10, i.e. much higher than the physiological pH that ensures the preservation of biological proteins in their native state. Accessing the pH and ionic concentration values during the biomineralization process has proved difficult owing to the limited space available and the potential disturbance induced by the measurements. Nevertheless, a recent study on the ocean quahog (a mollusc) has determined the spatial variations of pH, as well as calcium and carbonate concentrations within the extra-pallial fluid

(EPF).<sup>27</sup> These experiments show that the pH remains around 7 most of the time, but that increases in pH occur sporadically. During these events, the pH near the mantle rises to 9.5, while the pH at the shell remains unchanged. Along with the pH increase, the calcium concentration rises. Dissolved inorganic carbon also varies in the EPF, although the dynamics of this change was not as well characterized. Therefore, the conditions used in our study, which trigger a liquid-liquid phase separation, could match with those prevailing during biomineralization.

Liquid/liquid phase separation (LLPS) has already been highlighted in different biological systems as a way to compartmentalize cells and create membraneless organelles (to achieve filtration or concentration buffering for example).<sup>171</sup> In calcium carbonate biomineralization however, there is no direct evidence of an LLPS to date, only the observation that crystals produced in syntheses involving an LLPS have many features in common with biominerals. It has therefore been proposed that the space-filling nanograins that compose calcareous biominerals could originate from an LLPS. However, the origin of the calcium carbonate liquid precursor is not clear. In corals, it was proposed that ionic species concentrate within the cells, which leads to mineralization after excretion of the concentrated liquid.<sup>172</sup> In the case of oysters, it has been suggested, based on model experiments, that a liquid-liquid phase separation, induced by a specialized protein (Pif80) within the mantle cells, would generate a coacervate allowing the formation and stabilization of amorphous CaCO<sub>3</sub> granules, later released in the extra-pallial fluid.<sup>173</sup> In parallel, following observations of the growth of calcitic prisms in the *Pinna nobilis* mussel, Wolf *et al.*<sup>44</sup> also proposed that a liquid mineral precursor is produced in vesicles that they called 'calcosomes', within the mantle cells, before it forms viscous nanoparticles aggregating onto the growing prisms. Thus, although appealing to explain the space-filling character of the biomineral nanostructure, the existence of an LLPS in calcareous biomineralization remains quite elusive.

During the syntheses reported in this manuscript, no liquid-liquid phase separation could be detected in the bulk of the solution, contrarily to what was depicted on similar systems.<sup>12,84,174</sup> However, an interface-driven liquid-liquid phase separation could be evidenced. This LLPS allows the formation of a 2D pattern at the interface, on which specific addition of bulk amorphous nanoparticles takes place (thickening stage). These amorphous nanoparticles do not exhibit a fully liquid character, as assessed by cryo-TEM, but could be similar to the gel-like PILP droplets observed by Wolf *et al.*<sup>175</sup> So far, the involvement of a 2D LLPS in the biomineralization processes has never been considered. For instance, the 2D radial growth of the early prisms (discs) of in the periostracal groove of *Pinctada fucata* oyster has been attributed to the inhibition of the 3D growth by the periostracum surrounding the growing discs<sup>176</sup>. Yet, a liquid precursor could explain the observed flexibility of the early discs during their radial growth.<sup>177</sup> Therefore, the concept of an initially soft 2D pattern formed through a liquid-liquid phase separation could apply to biomineralisation and explain its early stage characteristics.

Whether the mineral precursors are formed inside or outside the cells of the mineralizing epithelium, and how they travel to the growth site is still a matter of debate<sup>178</sup>. It has been observed that mantle cells of *Pinctada fucata* can synthesize calcium carbonate *in vitro*<sup>179</sup>. In addition, vesicles that transport crystalline calcium carbonate to prisms under repair could be identified in *Crassostrea virginica*<sup>180</sup>. Others suggest that the mineralizing mantle is in close contact with the crystalline layers during the episodes of crystallization<sup>27,39</sup> so that a purely

diffusive process could be at play. In our synthetic mineralizing system, the displacement of the amorphous particles occurs by convection. One can thus wonder whether such a convective motion could develop in biomineralization. As a matter of fact, patterns strongly resembling convection-driven patterns have been identified in biominerals.<sup>181</sup> The exothermic character of calcite precipitation would generate a temperature gradient across the extra-pallial fluid, which could induce a Rayleigh-Bénard instability. Therefore, the convection of particles demonstrated in this work could potentially take place during biomineral formation. Still, the convection of nanoparticles to the site of mineralization is not essential to the growth model outlined here, so that another process could take place without modifying the mineralization pathway.

It has been demonstrated in several biological systems that crystallization occurs *via* an amorphous precursor.<sup>8</sup> The transformation to crystal then requires passing through a dehydrated state<sup>6,54,55,57</sup> before crystallising. This crystallization generates micron-sized iso-oriented crystals that behave like single crystals although with a nanostructure.<sup>108</sup> Calcium carbonate films produced with ADM syntheses and crystallized under humid atmosphere (and likely those crystallized at the interface) also result from an amorphous transient, and share the crystalline and morphological characteristics of the biogenic crystals. The growth model extracted from the analysis of these syntheses, thus appears fully relevant to describe biocrystallization, and was actually shown to involve a solid-state amorphous-to-crystal transformation, which is suspected to be at play in biocrystallization.<sup>53–55</sup>

Our findings therefore validate the current views on amorphous-to-crystal transition in biominerals, and fully support the involvement of an LLPS in calcareous biomineralization. However, instead of the usually assumed bulk LLPS, we detected a surface-directed LLPS, which plays a crucial role in defining the mineral morphology. These results shed new light on the early mechanisms of biomineralization and open up new perspectives, presented in the following section.

### 5.3 PERSPECTIVES ON THE CURRENT MODEL

As direct perspectives of this work, one could consider carrying out a more thorough investigation of the bulk LLPS, as well as of the interfacial crystallization of the amorphous film.

We could actually confirm that a liquid-liquid phase separation occurs in our system, but only in the vicinity of the air-solution interface. In contrast with statements of the literature related to similar systems,<sup>152</sup> the occurrence of a bulk liquid-liquid phase separation, prior to bulk nanoparticle formation, could not be demonstrated in our experiments. Preliminary SAXS measurements did evidence an intensity increase at low  $q$  values, meaning that bulk nanoparticles are growing (data not shown), but this increase occurred at reaction times corresponding to the observation of already solidified amorphous particles in bulk (cryo-TEM). Still, SAXS measurements, if sensitive enough, would provide an effective way to highlight such a bulk LLPS and to decipher the actual mechanism involved (nucleation or spinodal decomposition) by characterizing the evolution of the droplet size with time. I therefore believe that performing SAXS studies in combination with time-resolved cryo-TEM imaging could provide a definitive answer on the existence of a bulk LLPS. A bulk LLPS could be part of the biological control over biomineralization, both by allowing the production of a patterned layer

of amorphous material, similar to what occurs in our ADM syntheses, and by carrying the ACC material from the cells to the mineralizing area.<sup>173</sup>

In addition, as clearly stated in this manuscript, the investigation of the interfacial crystallization could not be fully carried out due to time constraints, so that the mechanisms at work in the amorphous-to-crystal transformation remains partly elusive. As the crystalline film resulting from an interfacial crystallization is the most closely related, in terms of crystalline properties, to the biogenic material, a thorough understanding of the mechanisms at play would be very valuable. To gain a complete insight into these mechanisms, both the dehydration of the amorphous film at the interface and its subsequent crystallization should be followed over time. Dehydration could be investigated by ATG measurements or STXM measurements performed in controlled humidity environment. As for crystallization, one could use SEM and possibly Bragg ptychography measurements to characterize the film crystalline structure at earlier times and, in particular, to prove or disprove that the three-layer crystalline structure arises from a dissolution-recrystallization process.

Bragg ptychography proved to be a key technique to determine the crystal defects distribution and the typical crystal coherence length in given crystallization conditions. The acquisition time of such a technique has been considerably reduced by the advent of 4<sup>th</sup> generation synchrotron source,<sup>182</sup> so that it is now conceivable to perform a series of measurements within a single beam time. It could therefore be used to decipher whether the large coherence length values observed for crystals formed at the air-solution interface result directly from the amorphous-to-crystal transformation, or whether subsequent reorganizations after crystallization take place. Performing Bragg ptychography measurements over time would therefore provide hints on the nature of the amorphous to crystal transformation that takes place.

Going further, a chemical modification of the model synthesis could be envisioned. Indeed, the techniques used during my PhD work did not allow the characterization of the polymer distribution both at the micro- and nano-scale. Still, such a distribution would be a very useful information as one expects the polymer to be trapped within the crystal for a solid/solid transformation, but to be released further away during a dissolution/crystallization process. However, owing to the very small quantity of materials available from the interface, the global amount of occluded polymer could not even be determined using ATG technique. To overcome this issue, a different polymer additive, containing for example nitrogen, could be used so as to visualize the polymer distribution by elemental analysis spectroscopy (EDS). Then, the displacement of the polymer additive during crystallization could be visualized by elemental mapping and give information on the transformation processes.

Differently, fluorescently-labeled polyelectrolytes could also be introduced in the synthesis, as minor part of the polymer additive. This would allow following the microscale distribution of polymer by fluorescence microscopy during the whole mineralization process,<sup>183</sup> and possibly help the detection of the bulk LLPS. Densification of the polymer at the interface and in bulk are valuable information to discover its role in the liquid/liquid phase separation. During crystallization, expulsion or occlusion of the polymer in the crystalline phase could provide an indication on the mobility of the macromolecular chain during crystallization and therefore on the viscosity of the surrounding medium.



Besides, my PhD work raises the question of the actual replication of the biological environment to study the formation, and subsequent crystallization, of amorphous calcium carbonate layers in really biomimetic conditions. During the syntheses reported in this manuscript, we observed the build-up of a dense mineral layer by aggregation, onto a predefined patterned layer (following a surface-driven LLPS), of amorphous particles in a high pH environment (pH >9.5). However, these conditions are only met, in the biological environment, in the vicinity of the mantle cells.<sup>27</sup> The pH of the medium surrounding the mineralization site is much lower (~7.5), so that biomineralization takes place under a chemical gradient, which could impact the formation or transport of the amorphous particles. The implementation of a model synthesis that involves a spatial chemical gradient could allow one to reproduce the actual biological conditions and assess whether the nucleation of amorphous or liquid particles can occur in these conditions, specific to the extracellular environment. In their study, Stemmer *et al.*<sup>27</sup> proposed that CaH-ATP ionic pumps regulate simultaneously the pH decrease and the calcium influx in the epithelial mantle. Although reproducing such a process in lab syntheses is unrealistic, one could imagine producing localized pH gradients in the solution by grafting pH-regulating biomolecules on a substrate.<sup>184</sup>

## 6 APPENDIX

---

### 6.1 CHAPTER II

Arduino code to collect Relative Humidity data with HIH 4000 sensor, controlled by an ARDUINO MEGA 2550

```
int sensorPin = A0;

int ledPin = 13;

float sensorValue = 0;

int RH =0;

int RH1=0;

void setup() {

  pinMode(ledPin, OUTPUT);

  Serial.begin(9600);

}

void loop() {

  sensorValue = analogRead(sensorPin)*5.0/1023;

  digitalWrite(ledPin, HIGH);

  delay(sensorValue);

  digitalWrite(ledPin, LOW);

  RH=((sensorValue/5)-0.16)/0.0062;

  Serial.print("T (s):");

  Serial.print(" ");

  Serial.println(millis()/1000);

  Serial.print(" ");

  Serial.print("RH :");

  Serial.print(RH);
```

```
Serial.print("%");Serial.print(" ");  
  
delay(1000);  
  
}
```

Arduino code to collect CO<sub>2</sub> (ppm) data with SCD30 sensor, controlled by an ARDUINO MKRZERO and included data collection on SD card.

```
#include "SCD30.h";  
#include <SD.h>  
#include <RTCZero.h>  
#include <Wire.h>  
  
RTCZero rtc;  
const byte seconds = 0;  
const byte minutes = 0;  
const byte hours = 0;  
  
void setup() {  
  
  Wire.begin();  
  Serial.begin(115200);  
  rtc.begin(); // initialize RTC  
  // Set the date  
  rtc.setHours(hours);  
  rtc.setMinutes(minutes);  
  rtc.setSeconds(seconds);  
  delay(5000);  
  
  // initialize SD card:  
  bool SDAvailable = SD.begin(28);  
  if (SDAvailable) {  
    String logFile = "DATALOG.CSV";  
    String ECH = "Capteur_CO2";  
    File dataFile = SD.open(logFile, FILE_WRITE);  
    if (dataFile) {  
      dataFile.print(rtc.getHours());  
      dataFile.print("/");  
      dataFile.print(rtc.getMinutes());  
      dataFile.print("/");  
      dataFile.print(rtc.getSeconds());  
      dataFile.println();  
      dataFile.println(ECH);  
      dataFile.print("Time: ");  
      dataFile.print("CO2 (ppm): ");  
      dataFile.print("Temperature (°C)= ");  
      dataFile.println("Relative humidity (% RH)= ");  
    }  
  }  
}
```

```
    delay(1000);
    dataFile.println("SCD30 Raw Data");
    dataFile.close();
  }
  delay(1000);
  analogReference(AR_EXTERNAL);

  scd30.initialize();
}
}
void loop() {
  File dataFile = SD.open("DATALOG.CSV", FILE_WRITE);
  float result[3] = {0};
  Serial.print("test");
  if (scd30.isAvailable()) {
    scd30.getCarbonDioxideConcentration(result);
    dataFile.print(rtc.getHours());
    dataFile.print(":");
    dataFile.print(rtc.getMinutes());
    dataFile.print(":");
    dataFile.print(rtc.getSeconds());
    dataFile.print(" ");
    dataFile.print(result[0]);
    dataFile.print(" ppm ");
    dataFile.print(result[1]);
    dataFile.print(" celcius ");
    dataFile.print(result[2]);
    dataFile.println("% ");
  }
  dataFile.close();
  delay(2000);
}
```

## 6.2 CHAPTER III

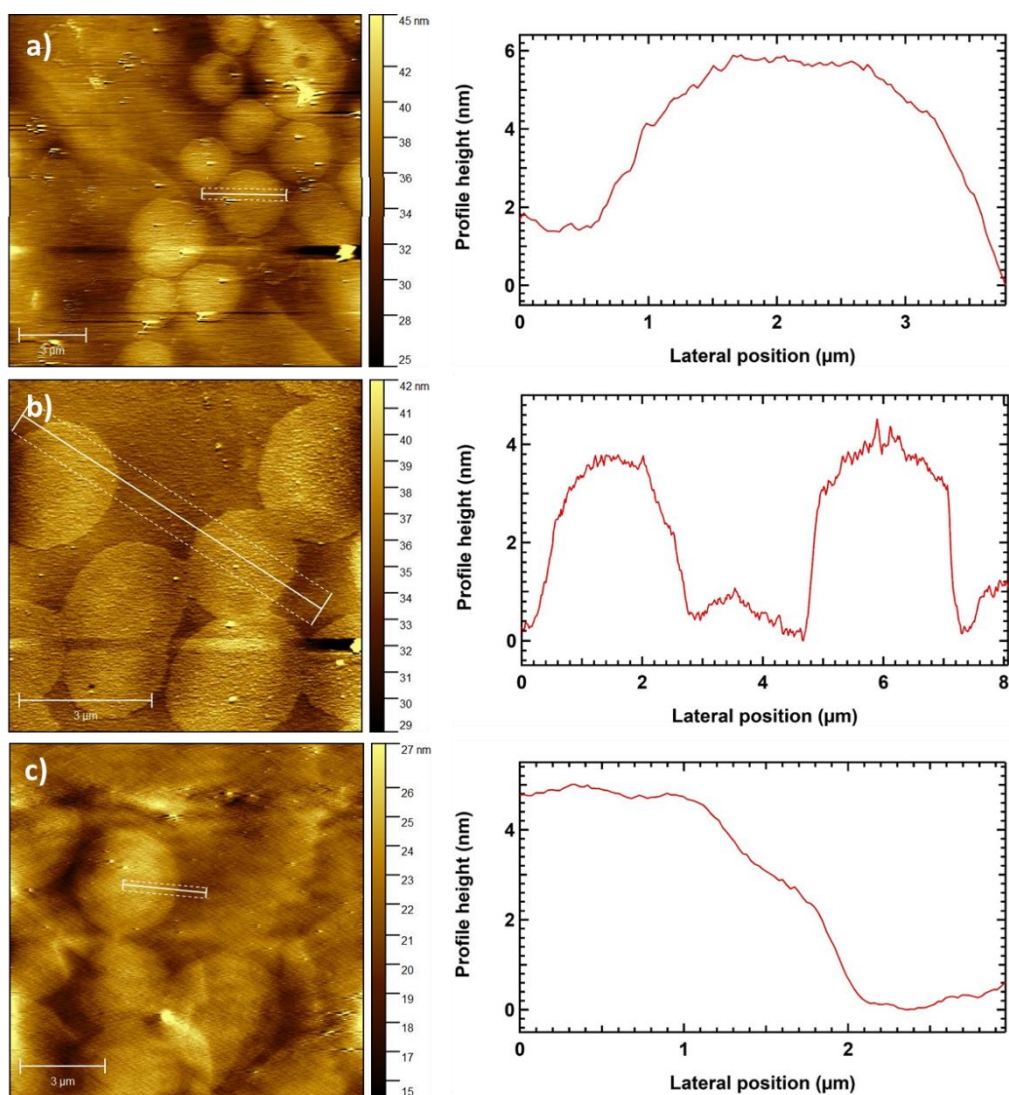


Figure A. 1 - AFM topography mapping and height profiles of interfacial discs, following the observation in STXM spectroscopy. The height profiles have been measured along the segments traced in the topography mapping. The height is averaged over between the two dashed line for a better signal. a) 10 min of reaction. Scale bar = 3 μm. b) 20 min of reaction. Scale bar = 3 μm. c) 30 min of reaction. Scale bar = 3 μm.

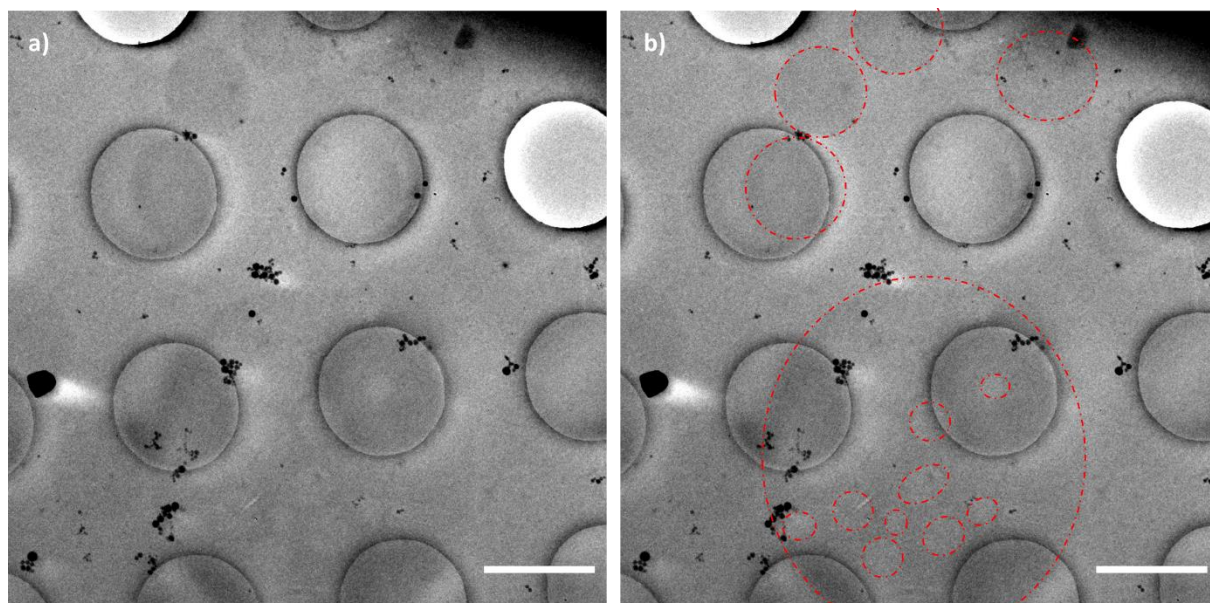


Figure A. 2 - Electron micrographs (Cryo- TEM) of a film sample extracted at 5 min of reaction.  $[Ca^{2+}] = 20$  mM,  $[PANa] = 20$  ppm. a) Raw image. b) Same image with visual aid (red dotted lines) to discern the discs shapes in the upper part of the image and double emulsion pattern at the bottom of the image. Scale bar =  $2\mu\text{m}$ .

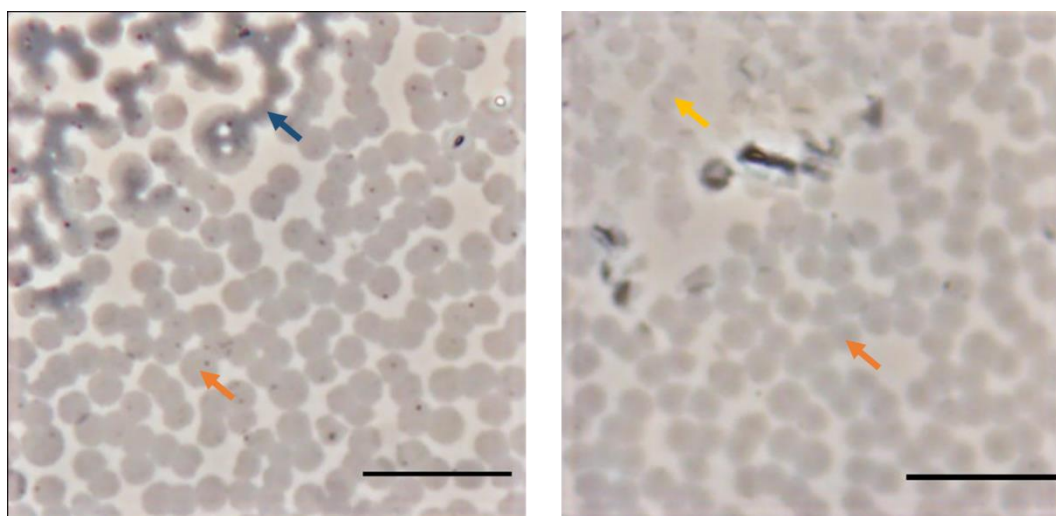


Figure A. 3 - Optical micrographs (PCM) of a film sample ( $[Ca^{2+}] = 20$  mM,  $[PANa] = 20$  ppm) collected after 35 min of reaction. The yellow, orange and blue arrows point to structures I, II and III respectively. These images were taken on adjacent holes of the TEM grid, is the same lighting conditions.



*Figure A. 4 - Optical micrograph (AM) of bulk species underneath the film at 35 min of reaction. The dark dots, highlighted by orange dashed circles, are distributed in the depth of the solution.*

Annex A.5. To investigate the influence of the solute species (calcium and polymer) on the pH variations resulting from ammonium carbonate decomposition, pH monitoring through time was carried out in a calcium/polymer (20 mM/20 ppm), then calcium (20 mM) solution and, finally, pure water solution, in the ADM reaction chamber (Petri dish). The global shape of the curve is similar in the three cases, with a fast rise at early times and then a slow decrease leading to a plateau (see Figure A. 5.a). However, in the case of a calcium solution, the rise in pH is delayed and the pH reaches its highest value after 20 min (Figure A. 5.b) instead of about 10 min in the two other cases. In addition, the two curves related to calcium/polymer and water solutions are undistinguishable before 10 min. They clearly separate after 37 min of reaction (separation of their respective standard deviation), as indicated by the dashed black line in Figure A. 5.b, the decrease in the calcium/polymer solution being then faster than the one of pure water. At longer reaction time (> 75 min) finally, the pH of the calcium/polymer and calcium solution overlap.

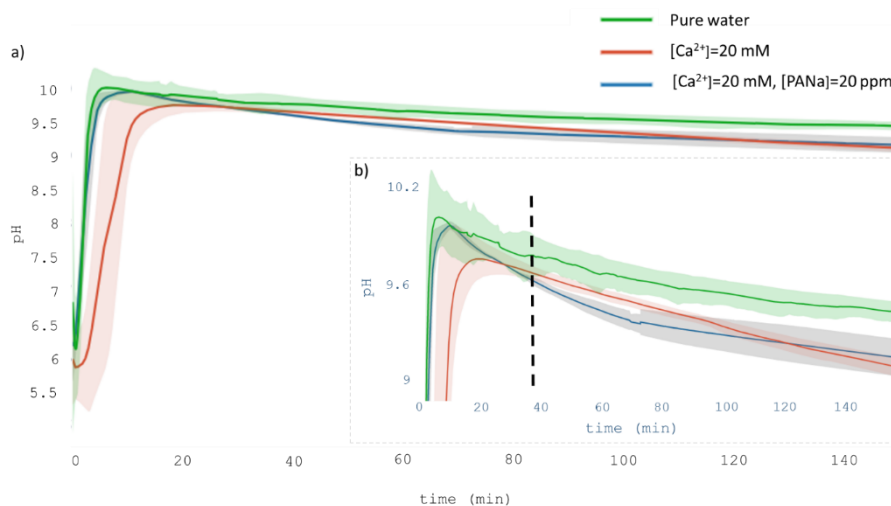


Figure A. 5 - pH evolution over time in a 6 mL solution. Blue, red and green curves represent the pH evolution in calcium solution with added polymer, pure calcium solution, and pure water, respectively. Concentrations are specified in the legend. Light gray, green and red areas represent the standard deviations of the blue, red and green curves, respectively. a) Measurements over 150 min. b) Zoom-in of the pH evolution with time. Black dashed lines highlight the point where the blue and green curves start to differ. For both a) and b), the curve presented here are the average of: blue/ 3 measurements up to 74 min, then 2 measurements; red/ 5 measurements; green/ 3 measurements.

Similarly, to assess the influence of the salt solution on the development of the gas atmosphere, CO<sub>2</sub> measurements have been repeated with pure water, and then without any solution in the reactor chamber, which resulted in the curves presented in Figure 84 b. The evolution of the CO<sub>2</sub> pressure in the presence of the reference solution and in the presence of pure water are similar, as the standard deviation of both curves overlap, although partially, during most of measurement time in Figure 84 b. In contrast, the CO<sub>2</sub> pressure in the absence of solution rises more slowly. The standard deviation is also significantly reduced, as it is 89 ppm, while it went up to 402 ppm and 470 ppm maximum with the reference solution, and pure water respectively. The presence of a solution therefore leads to a stronger (NH<sub>4</sub>)<sub>2</sub>CO<sub>3</sub> sublimation.



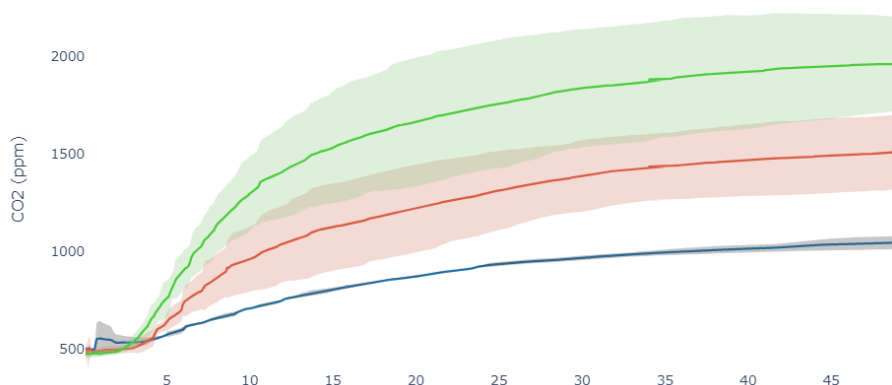


Figure A. 6 - In situ recording of  $\text{CO}_2$  partial pressure inside the reactor chamber. Recording of the early times ( $> 50$  min) of the establishment of the gaseous atmosphere in contact with: - polymer-containing calcium solution ( $[\text{Ca}^{2+}] = 20$  mM;  $[\text{PANa}] = 20$  ppm, green curve) -pure water (red curve) -no water (blue curve). The standard deviations are represented for each curve in their respective color but lightened. Each measurement was triplicated.

### 6.2.1 STXM

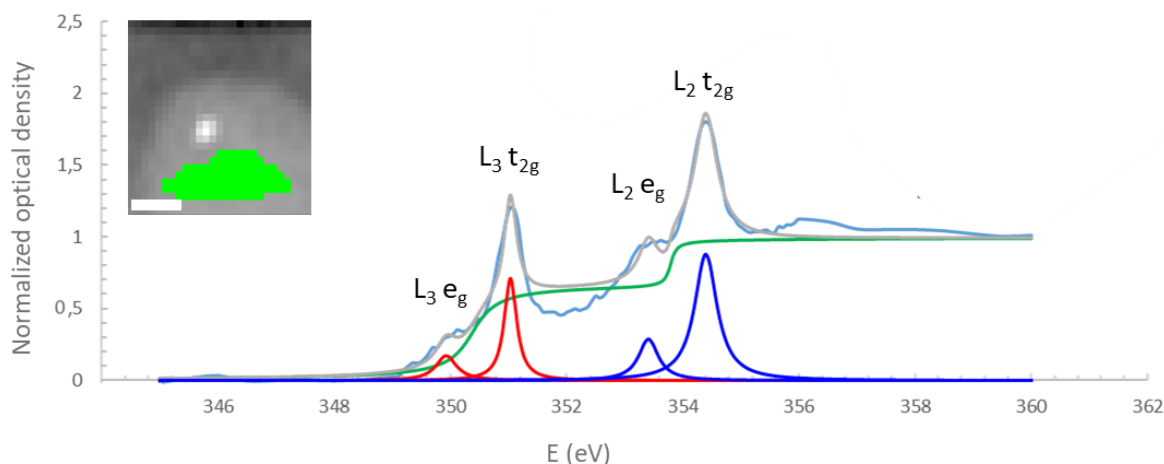


Figure A. 7 - Normalized X-ray absorption spectrum of the core of the disc formed at 10 min of reaction. Measurements have been performed at the Ca L-edge. Two arctan functions, in green, and four Lorentzian functions (in red for the  $L_3$  resonance and in blue for the  $L_2$ ) have been used for deconvolution. The sum of these functions yields the gray spectrum, while the experimental curve is drawn in light blue. Inset: Optical density map at the Ca L-edge. The spectrum was averaged over from the green area. Scale bar =  $0.5 \mu\text{m}$

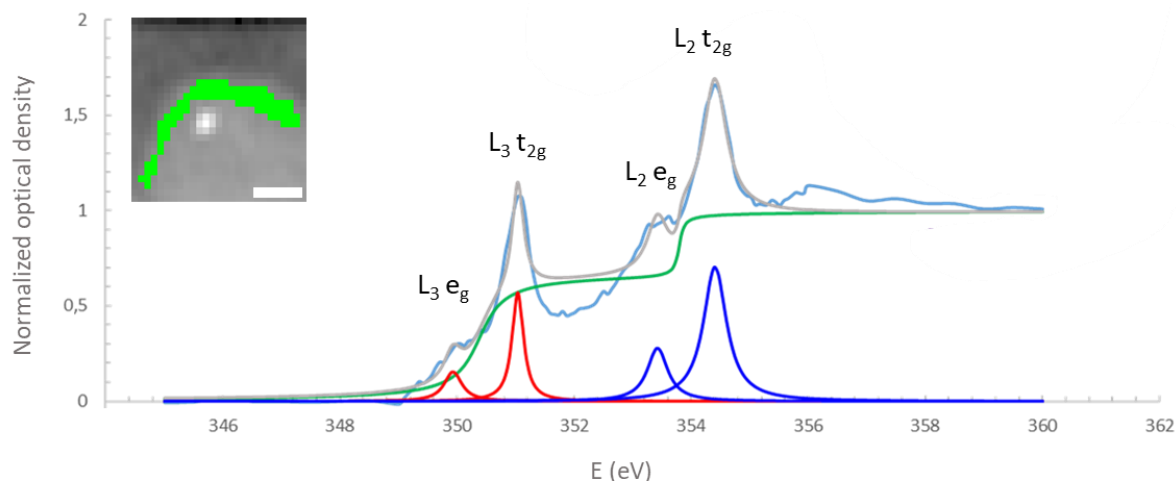


Figure A. 8 - Normalized X-ray absorption spectrum of the corona of the disc formed at 10 min of reaction. Measurements have been performed at the Ca L-edge. Two arctan functions, in green, and four Lorentzian functions (in red for the  $L_3$  resonance and in blue for the  $L_2$ ) have been used for deconvolution. The sum of these functions yields the gray spectrum, while the experimental curve is drawn in light blue. Inset: Optical density map at the Ca L-edge. The spectrum was averaged over from the green area. Scale bar =  $0.5 \mu\text{m}$

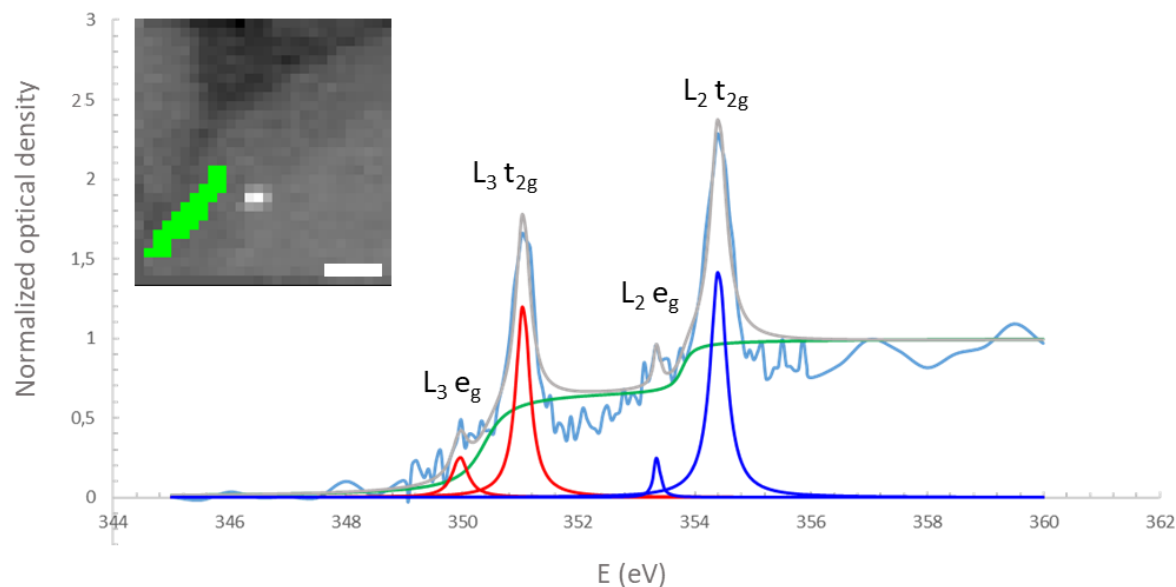


Figure A. 9 - Normalized X-ray absorption spectrum of the corona of the disc formed at 30 min of reaction. Measurements have been performed at the Ca L-edge. Two arctan functions, in green, and four Lorentzian functions (in red for the  $L_3$  resonance and in blue for the  $L_2$ ) have been used for deconvolution. The sum of these functions yields the gray spectrum, while the experimental curve is drawn in light blue. Inset: Optical density map at the Ca L-edge. The spectrum was averaged over from the green area. Scale bar =  $0.3 \mu\text{m}$

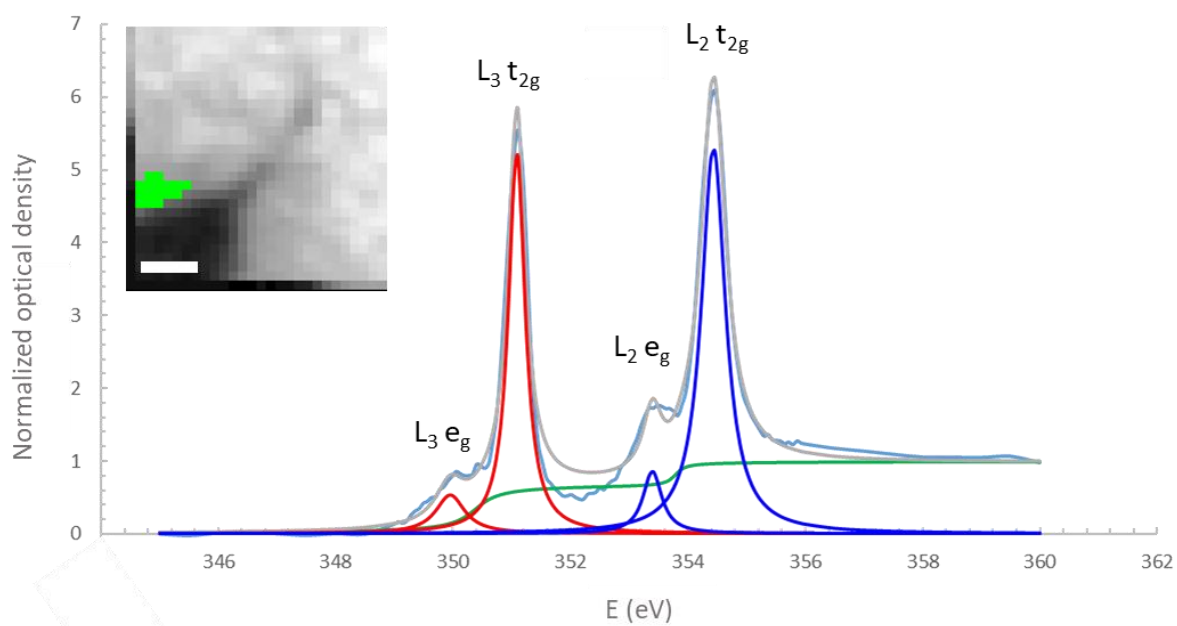


Figure A. 10 - Normalized X-ray absorption spectrum of the edge of a type II structure at 40 min of reaction. Measurements have been performed at the Ca L-edge. Two arctan functions, in green, and four Lorentzian functions (in red for the  $L_3$  resonance and in blue for the  $L_2$ ) have been used for deconvolution. The sum of these functions yields the gray spectrum, while the experimental curve is drawn in light blue. Inset: Optical density map at the Ca L-edge. The spectrum was averaged over from the green area. Scale bar = 0.4  $\mu\text{m}$

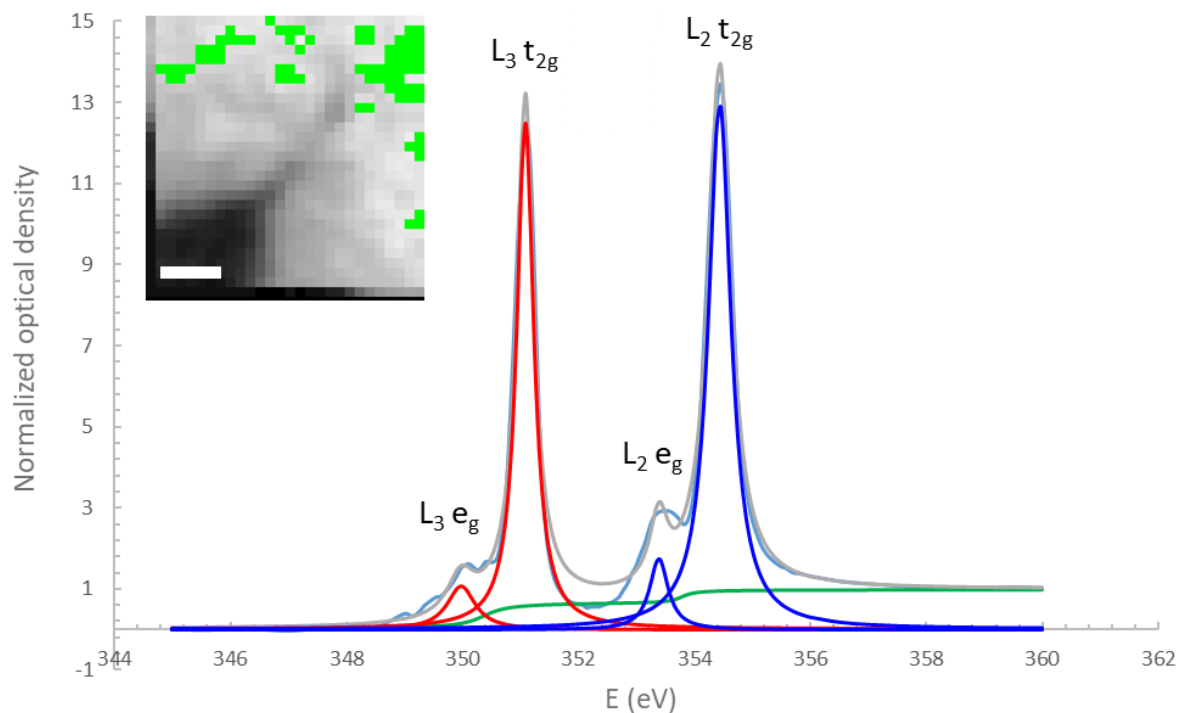


Figure A. 11 - Normalized X-ray absorption spectrum high optical density region of a type III structure at 40 min of reaction. Measurements have been performed at the Ca L-edge. Two arctan functions, in green, and four Lorentzian functions (in red for the  $L_3$  resonance and in blue for the  $L_2$ ) have been used for deconvolution. The sum of these functions yields the gray spectrum, while the experimental curve is drawn in light blue. Inset: Optical density map at the Ca L-edge. The spectrum was averaged over from the green area.

## CHAPTER IV

## 6.3.1 Heat-induced crystallization

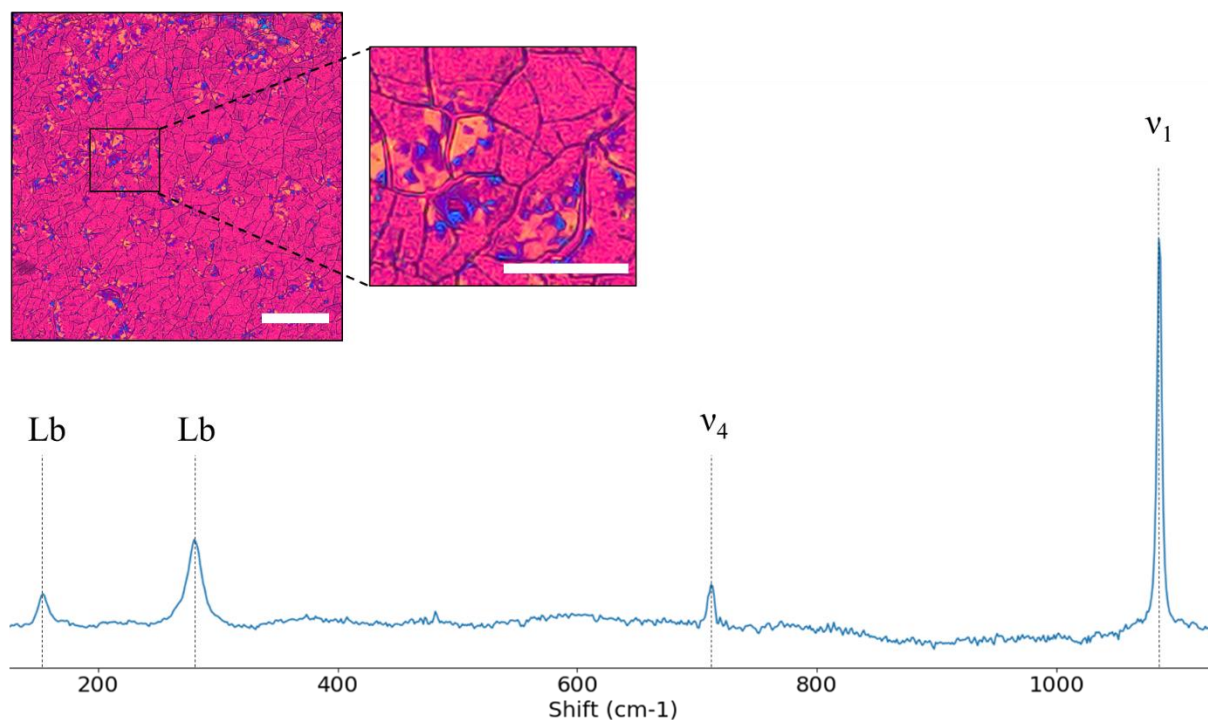


Figure A. 12 - Optical micrograph (WBM) and Raman spectrum of a continuous film sample collected after 17h of reaction, at the surface of a  $[Ca^{2+}] = 100 \text{ mM}$ ,  $[PANa] = 50 \text{ ppm}$  solution, and heated at  $300^{\circ}\text{C}$  for 3h. Scale bar =  $100 \mu\text{m}$ . The zoomed-in area highlights cracks in the film, with surrounding iso-oriented areas (scale bar =  $50 \mu\text{m}$ ). Raman spectrum was taken on the very same film as shown in WBM. The  $\nu_1$  ( $1086 \text{ cm}^{-1}$ ),  $\nu_4$  ( $712 \text{ cm}^{-1}$ ) and lattices bands (Lb,  $281 \text{ cm}^{-1}$  and  $155 \text{ cm}^{-1}$ ) fully match the reference spectrum of calcite (see Materials and methods IV.1).

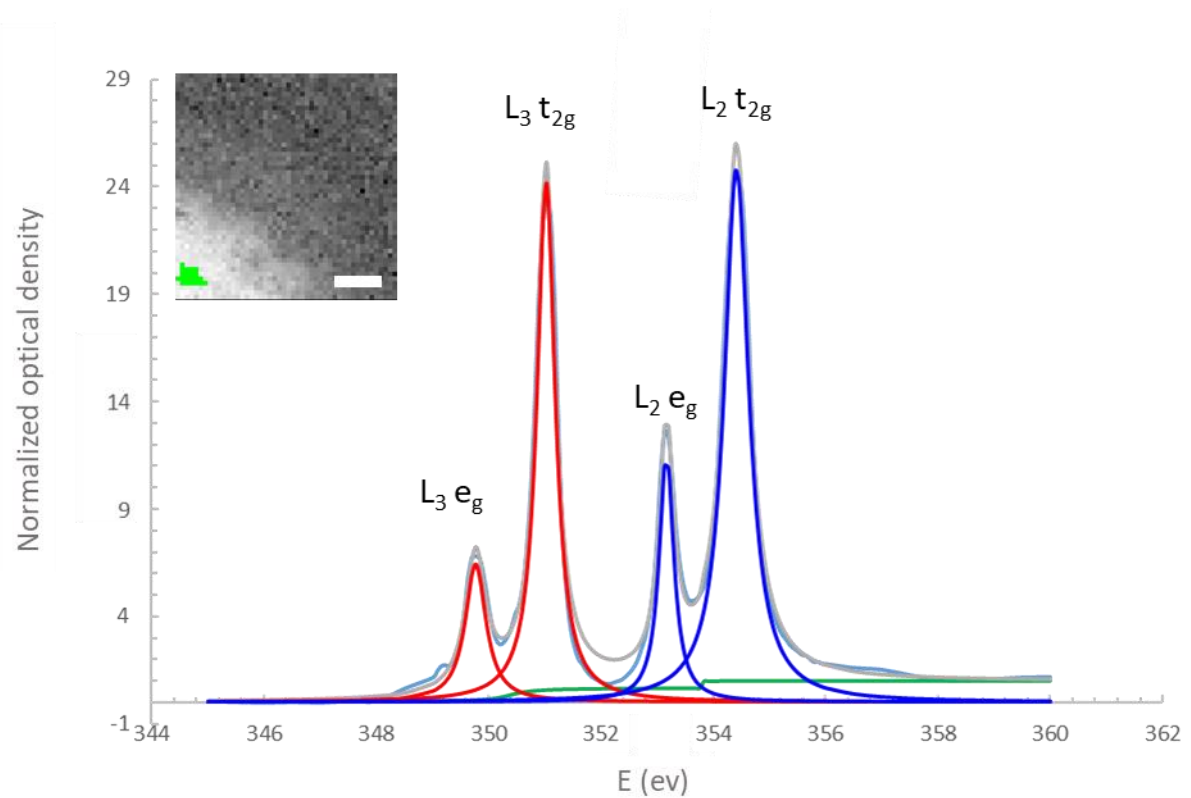


Figure A. 13 - Normalized X-ray absorption spectrum of a disc in a disc patterned film heated at 300°C for 3h. Measurements have been performed at the Ca L-edge. Two arctan functions, not visible due to their reduced little intensity, and four Lorentzian functions (in red for the  $L_3$  resonance and in blue for the  $L_2$ ) have been used for deconvolution. The sum of these functions yields the gray spectrum, while the experimental curve is drawn in light blue. Inset: Optical density map at the Ca L-edge. The spectrum was averaged over from the green area. Scale bar = 0.6  $\mu\text{m}$

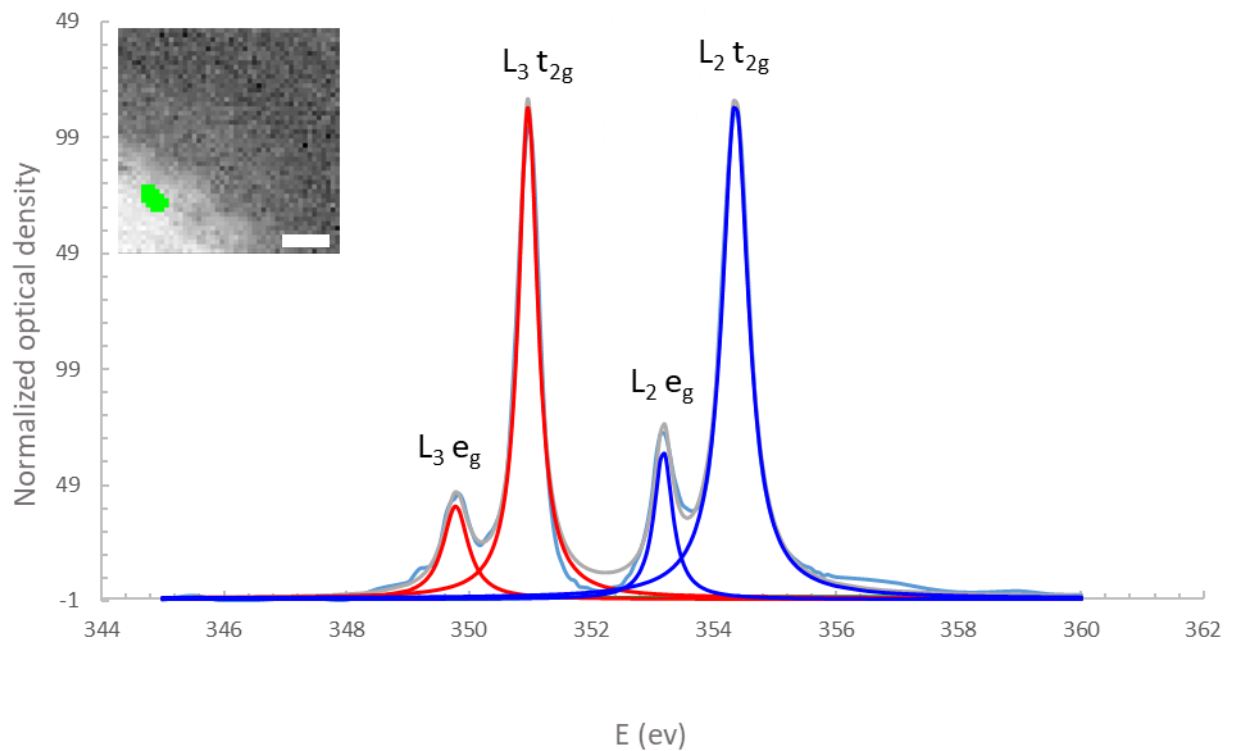


Figure A. 14 - Normalized X-ray absorption spectrum of a disc in a disc patterned film heated at  $300^\circ\text{C}$  for 3h. Measurements have been performed at the Ca L-edge. Two arctan functions, not visible due to their reduced little intensity, and four Lorentzian functions (in red for the  $L_3$  resonance and in blue for the  $L_2$ ) have been used for deconvolution. The sum of these functions yields the gray spectrum, while the experimental curve is drawn in light blue. Inset: Optical density map at the Ca L-edge. The spectrum was averaged over from the green area. Scale bar =  $0.6 \mu\text{m}$

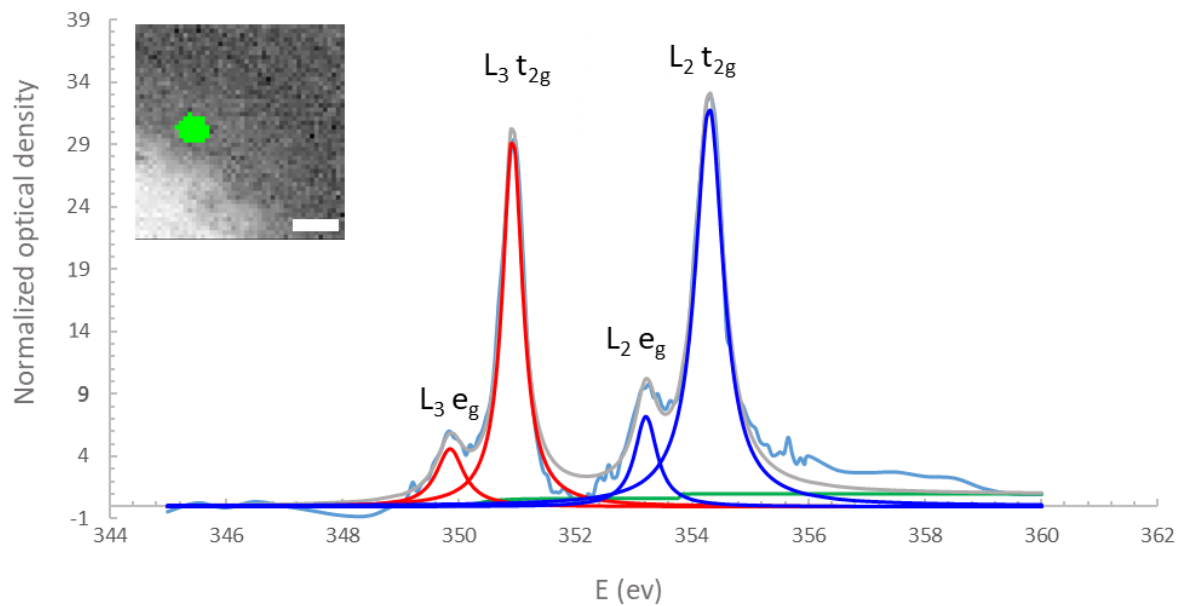


Figure A. 15 - Normalized X-ray absorption spectrum of a disc in a disc patterned film heated at 300°C for 3h. Measurements have been performed at the Ca L-edge. Two arctan functions, not visible due to their reduced little intensity, and four Lorentzian functions (in red for the  $L_3$  resonance and in blue for the  $L_2$ ) have been used for deconvolution. The sum of these functions yields the gray spectrum, while the experimental curve is drawn in light blue Inset: Optical density map at the Ca L-edge. The spectrum was averaged over from the green area. Scale bar = 0.6  $\mu\text{m}$

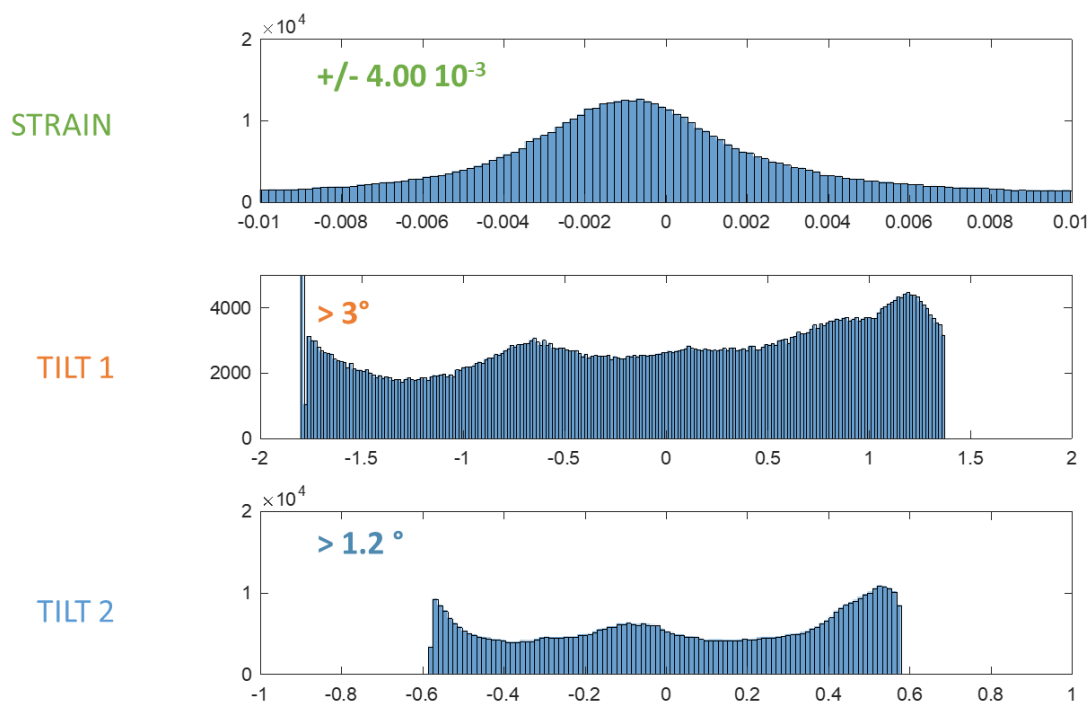




Figure A. 16 - Histograms of the strain, Tilt 1 and Tilt 2 distributions corresponding to the 2D maps presented in Figure 102. The strain standard deviation is noted in green, while the angular range of the Tilt 1 and Tilt 2 distribution are written in orange and blue, respectively.

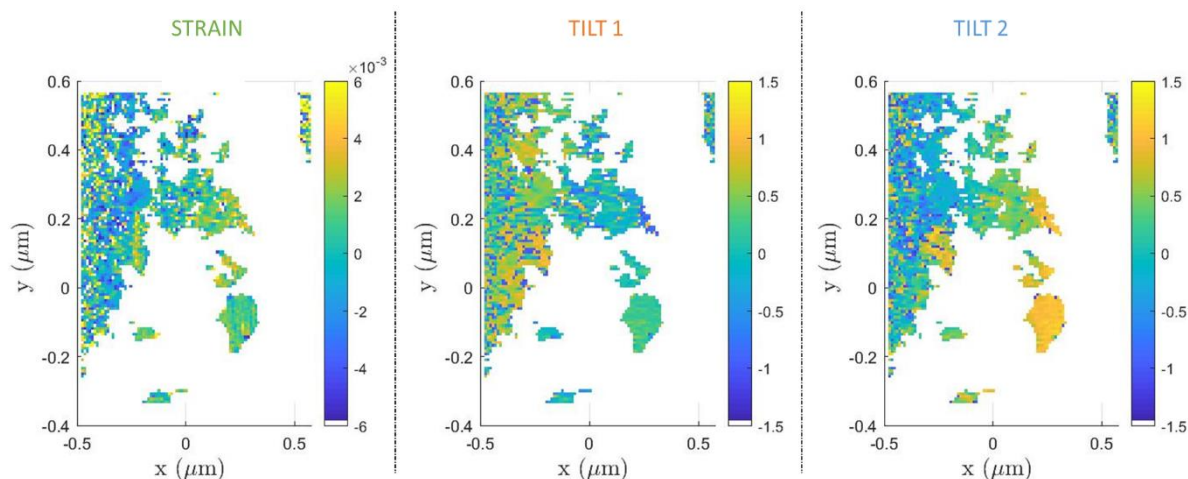


Figure A. 17 - 2D maps of the crystalline properties (strain, Tilt 1 and Tilt 2) in the sample plane ( $xy$ ), retrieved from the Bragg ptychography measurements. The film sample was collected at the free surface of a  $[Ca^{2+}] = 100 \text{ mM}$ ,  $[PANA] = 50 \text{ ppm}$  solution after 18h of reaction, and heated at  $300 \text{ }^\circ\text{C}$  for 1 h.

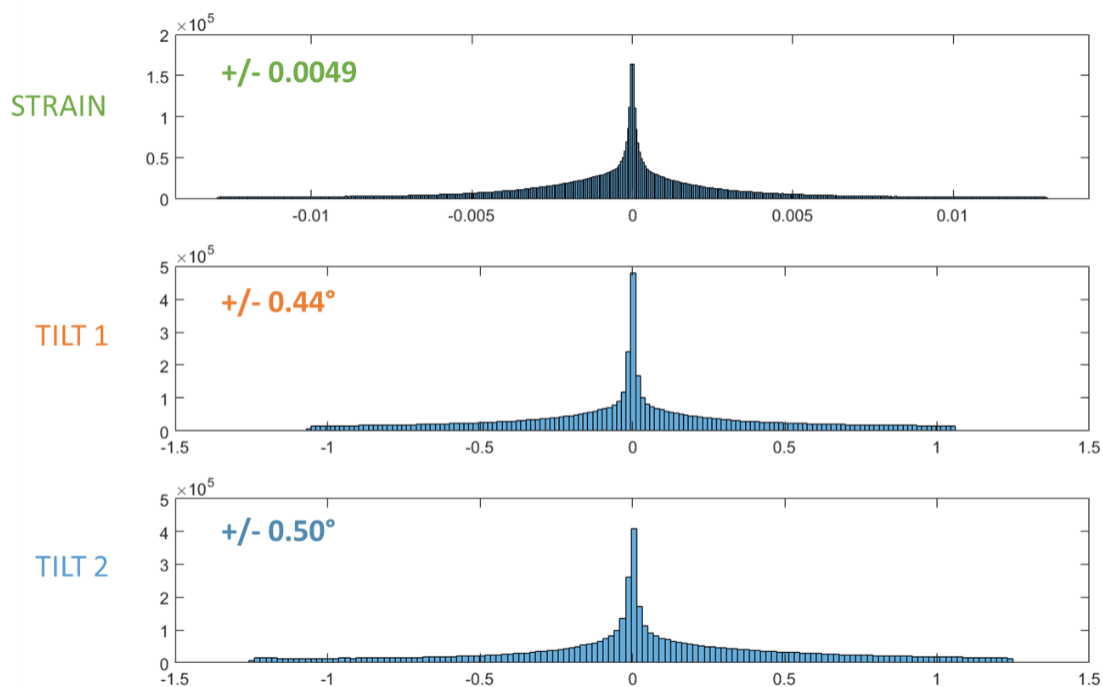


Figure A. 18 - Histograms of the strain, Tilt 1 and Tilt 2 distributions corresponding to the 2D maps presented in Figure A. 17. The standard deviation is noted in green for the strain, orange for Tilt 1 and blue for Tilt 2.

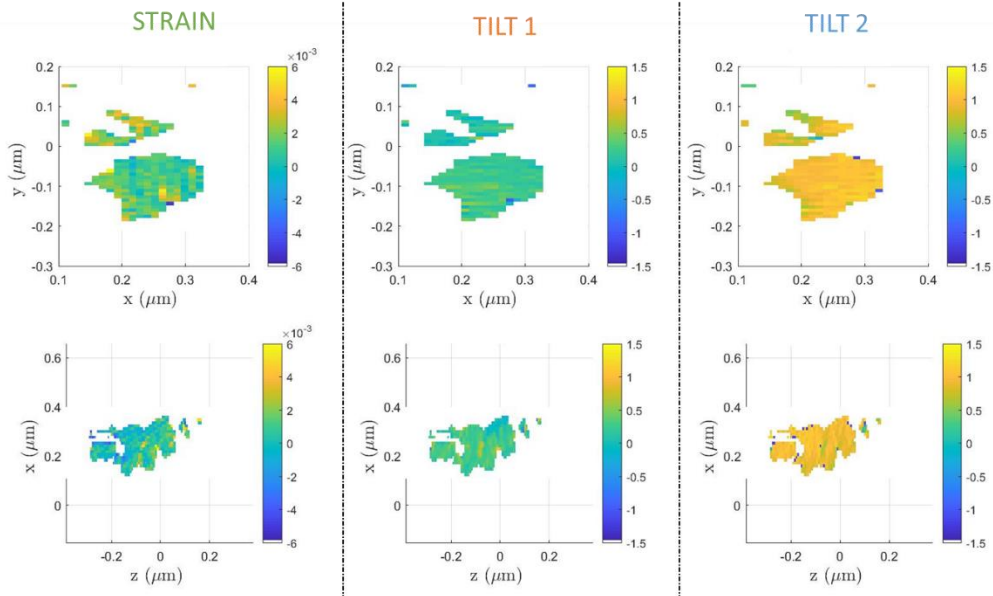


Figure A. 19 - Iso strain, iso-tilt domain extracted from Figure A. 17. The strain, Tilt 1 and Tilt 2 maps are presented in the sample plane ( $xy$ ) and along the sample thickness ( $z$ ).

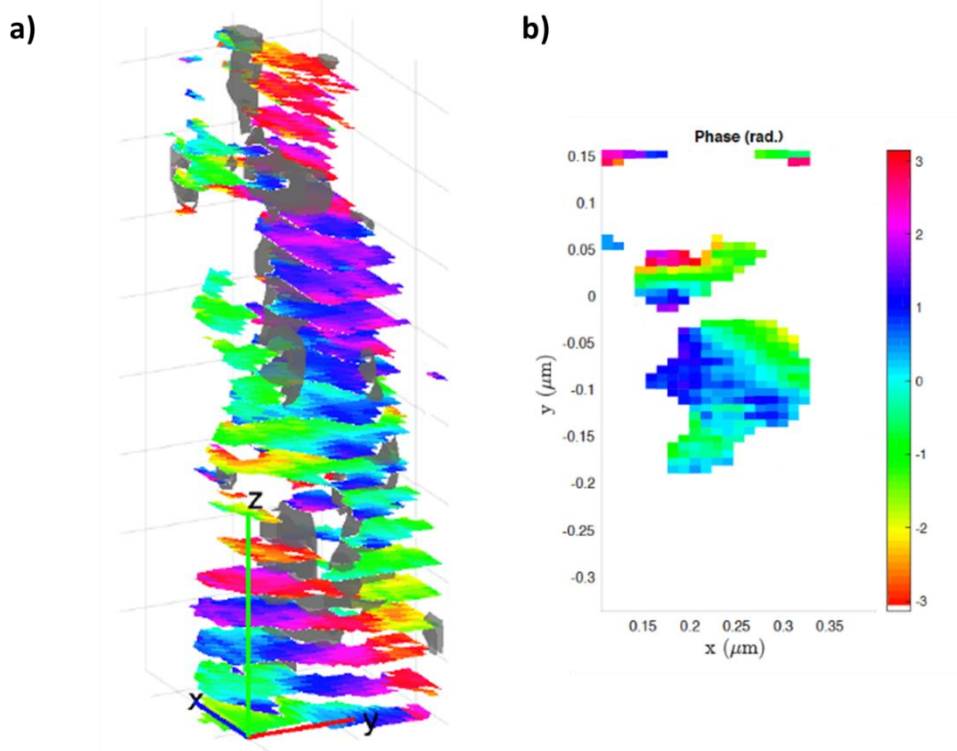


Figure A. 20. Phase map of the sub-region of the iso-strain iso-tilt domain shown in Figure A. 19 a) 3D phase map. Scale ( $xyz$ ) = 100 nm. The gray iso volumes correspond to regions of large strains ( $> 0.003$ ). b) 2D cross section of the phase map.

## 6.3.2 Humidity (98% RH) induced crystallization

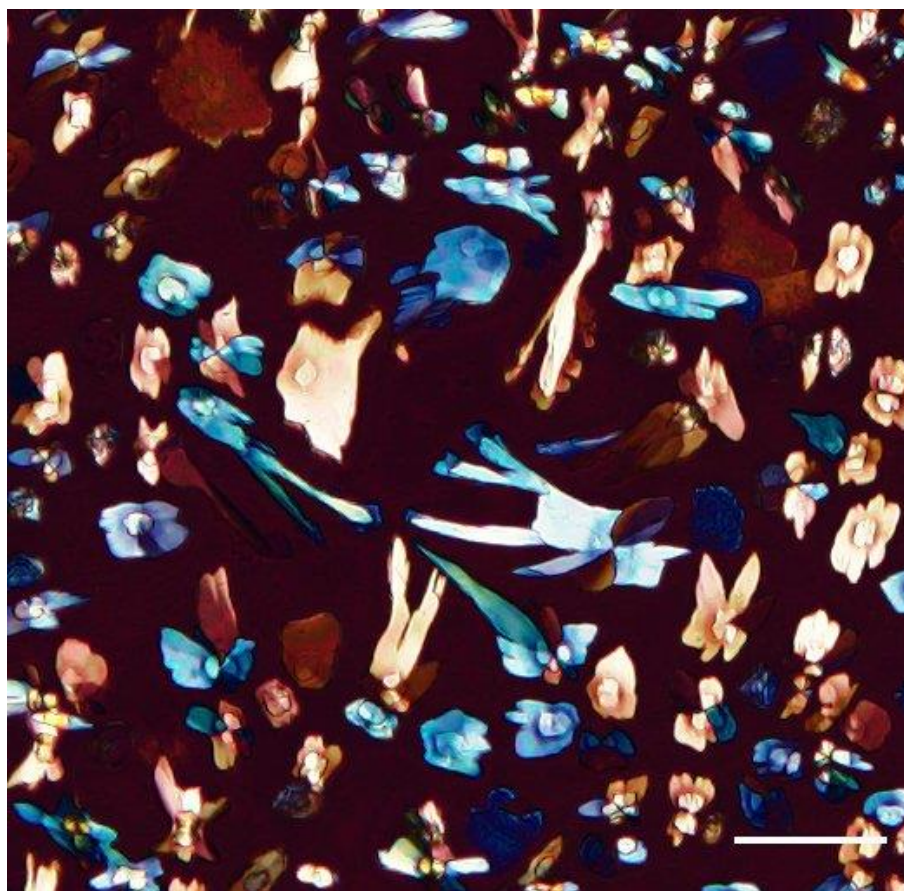


Figure A. 21 - Optical micrograph (WBM) of a continuous film sample collected after 18.5h at the surface of a  $[Ca^{2+}] = 100 \text{ mM}$ ,  $[PANa] = 50 \text{ ppm}$  solution, and kept under 98% RH for 3h. Scale bar = 100  $\mu\text{m}$ .

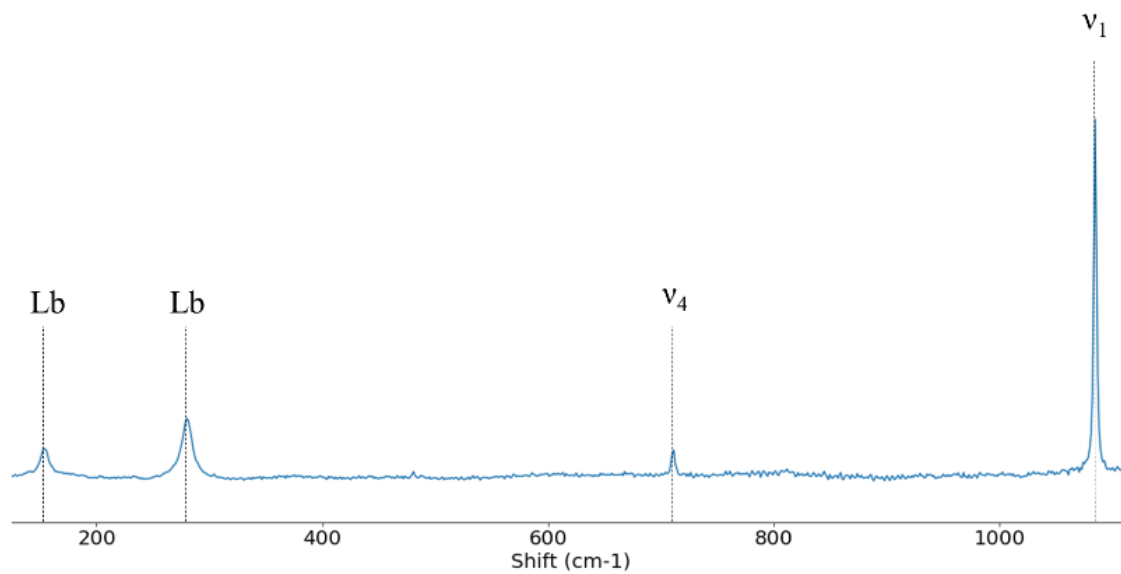


Figure A. 22 - Raman spectrum measured on the film shown in Figure A. 21. The  $\nu_1$  ( $1085\text{ cm}^{-1}$ ),  $\nu_4$  ( $712\text{ cm}^{-1}$ ) and lattices bands (Lb,  $280\text{ cm}^{-1}$  and  $154\text{ cm}^{-1}$ ) fully match the reference spectrum of calcite (see Materials and methods IV.1)

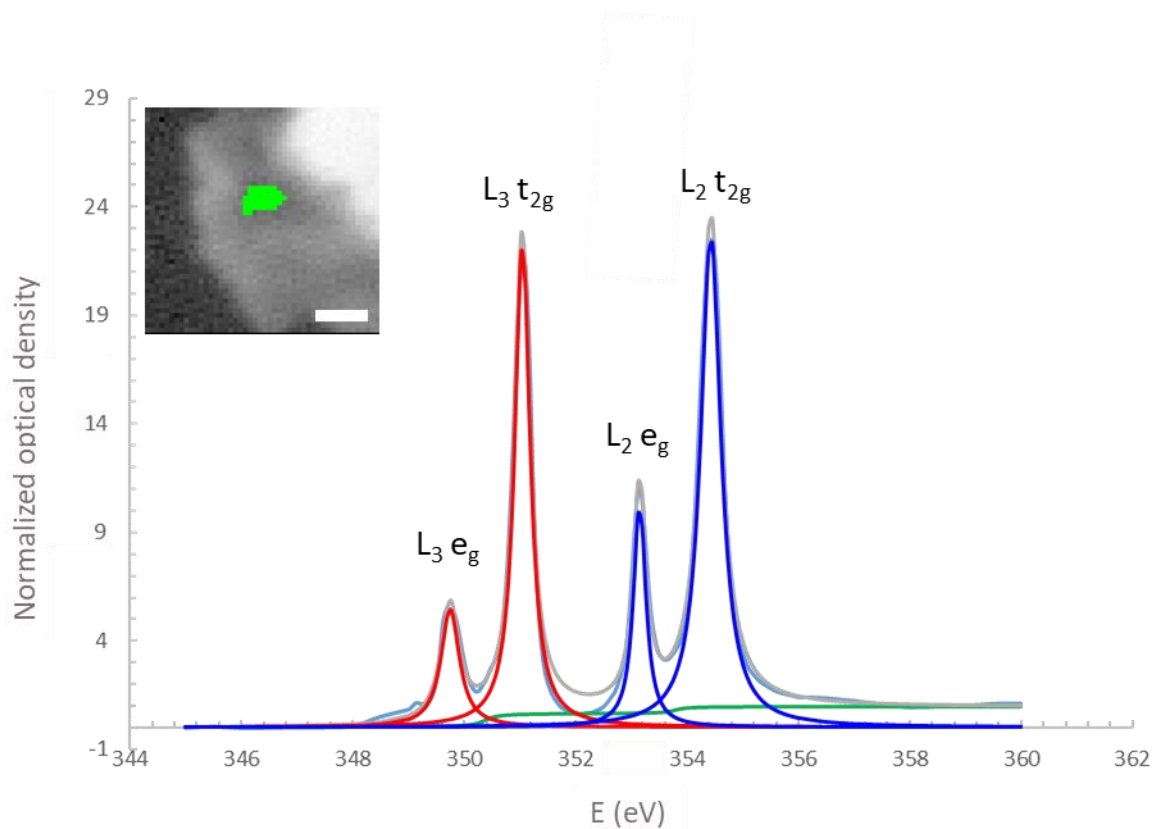


Figure A. 23 - Deconvolution of the X-ray absorption spectrum corresponding to a submicronic area in the spherulite branch tip. Four Lorentzian and two arctan functions were used for the deconvolution. Experimental curve is in light blue, Lorentzian functions fitting the  $L_3$ -edge is in red, Lorentzian functions fitting the  $L_2$ -edge in dark blue, the arctan in green and the sum of the fitting function in gray. Inset: Optical density map at the Ca L-edge. The spectrum was averaged over from the green area. Scale bar =  $0.4 \mu\text{m}$ .

## $\Delta\phi$ + eigenpolarizations

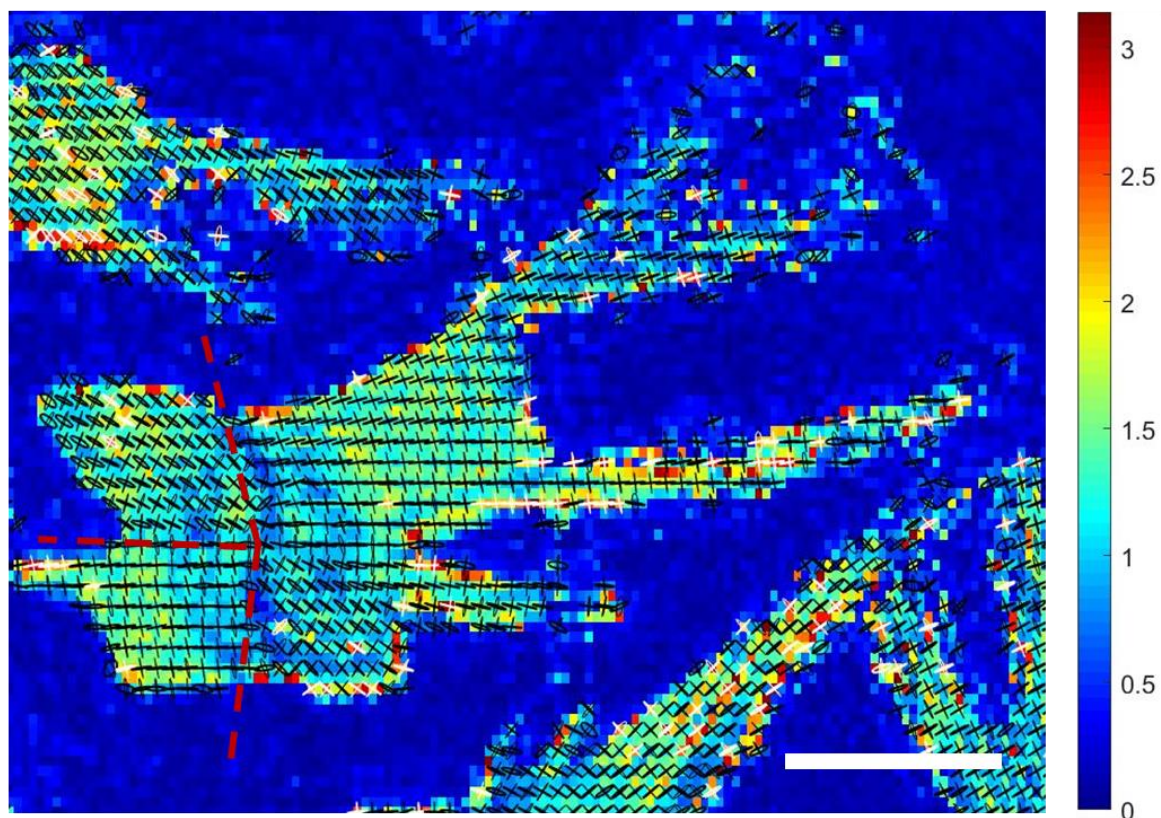


Figure A. 24 - Vectorial ptychography analysis of the center of a spherulite. The film sample has been collected at the surface of a  $[Ca^{2+}] = 100$  mM,  $[PANA] = 50$  ppm solution after 18h of reaction, and left 6 days under high relative humidity (98%). Composite map of retardance (coloration, in radian, 0 to  $\pi$ ) and eigenpolarizations (black). The red dashed lines separate iso-oriented domains. Scale bar = 20  $\mu$ m.

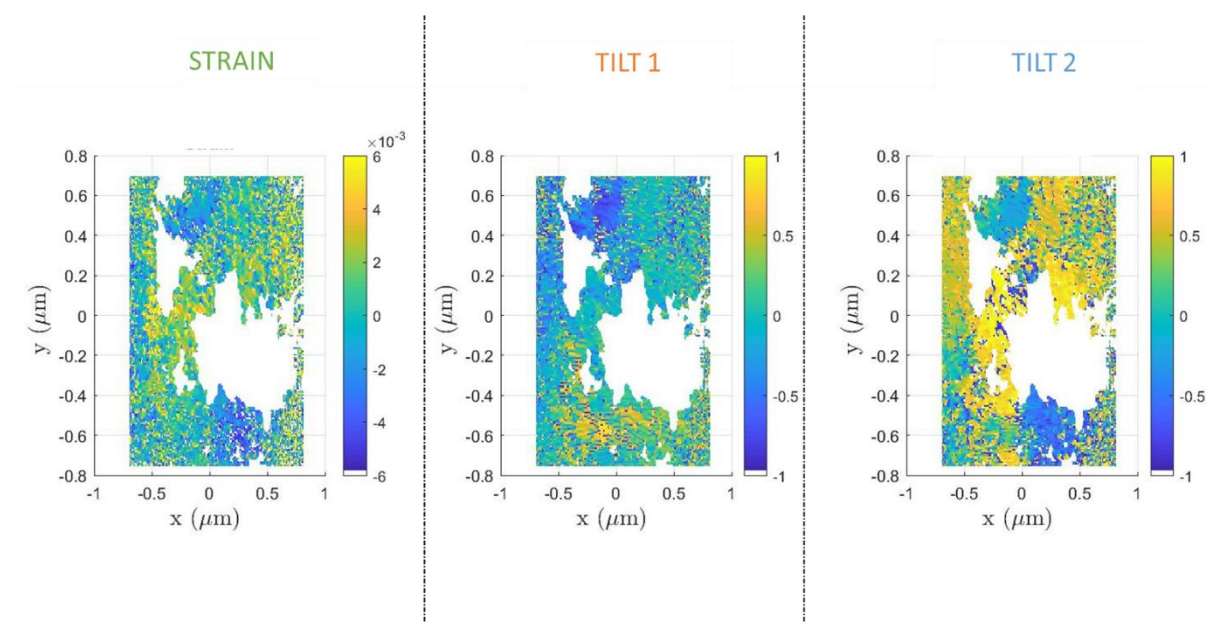


Figure A. 25 - 2D maps of the crystalline properties (strain, Tilt 1 and Tilt 2) in the sample plane ( $xy$ ), calculated from the Bragg ptychography data. The film sample was collected at the free surface of a  $[Ca^{2+}] = 20 \text{ mM}$ ,  $[PANa] = 20 \text{ ppm}$  solution after 16.5h of reaction, and kept under humidity (98% RH) for 14 days.

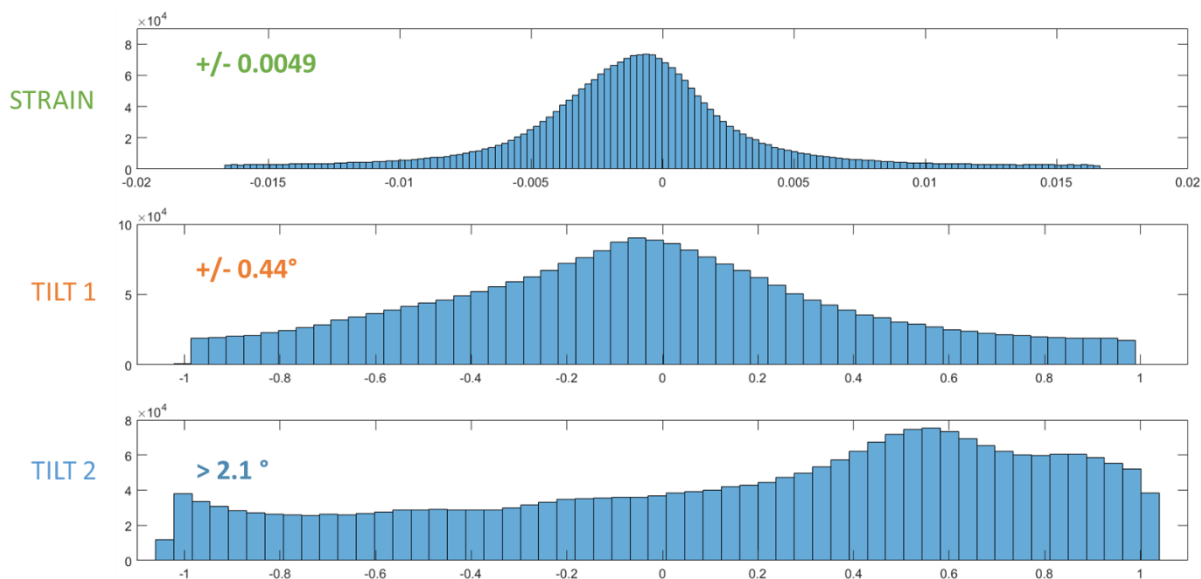


Figure A. 26 - Histograms of the strain, Tilt 1 and Tilt 2 distributions corresponding to the 2D maps presented in Figure A. 25. The strain standard deviation is noted in green, the Tilt 1 standard deviation is noted in orange and the angular range of the Tilt 2 distribution is written in blue.

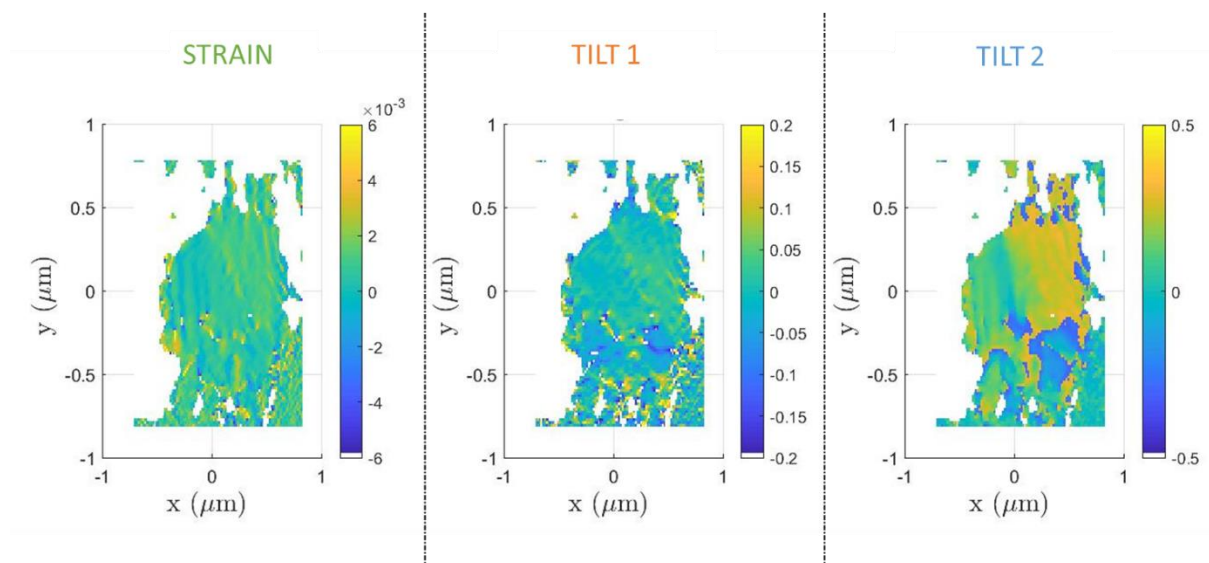


Figure A. 27 - 2D maps of the crystalline properties (strain, Tilt 1 and Tilt 2) in the sample plane ( $xy$ ), retrieved from Bragg ptychography measurements. The film sample was collected at the free surface of a  $[\text{Ca}^{2+}] = 100 \text{ mM}$ ,  $[\text{PANa}] = 50 \text{ ppm}$  solution after 18.5h of reaction, and kept under humidity (98% RH) for 6 days.

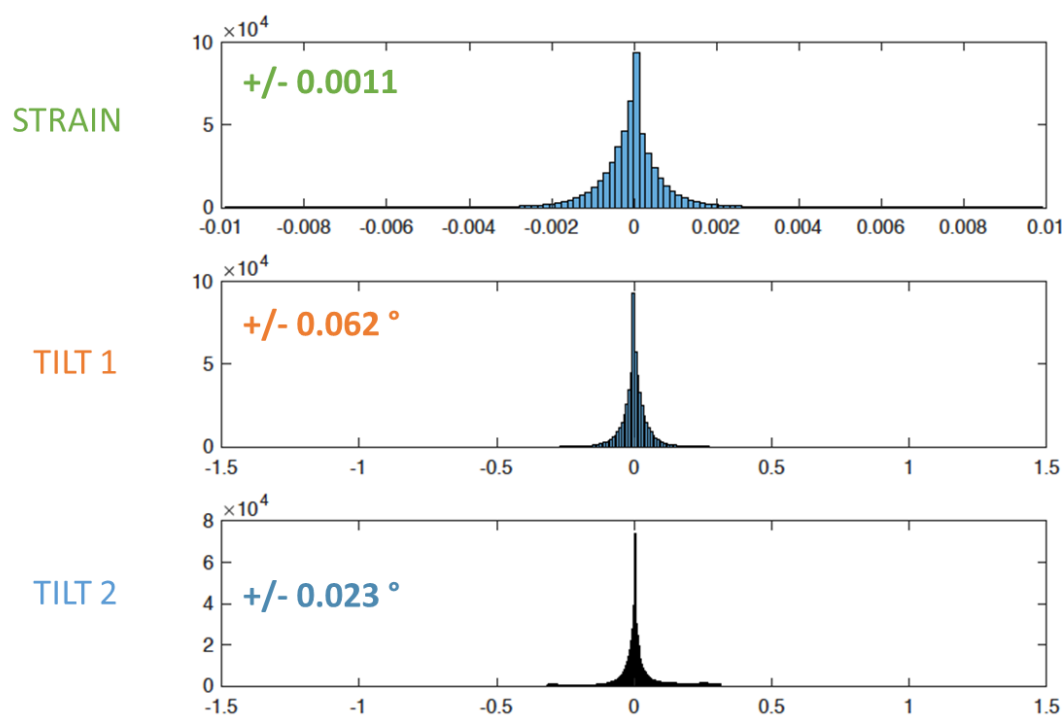


Figure A. 28 - Histograms of the strain, Tilt 1 and Tilt 2 distributions corresponding to the 2D maps presented in Figure A. 27. The strain standard deviation is noted in green, while the standard variation of Tilt 1 and Tilt 2 are written in orange and blue, respectively.



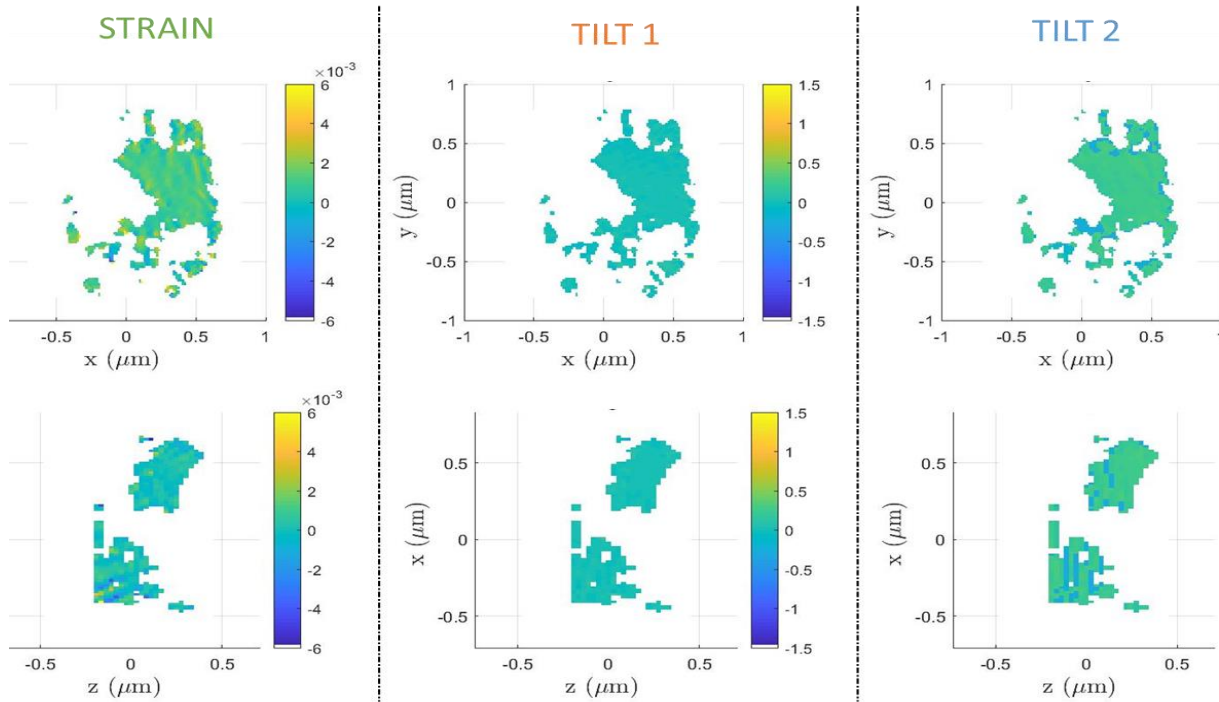


Figure A. 29 - Iso strain and iso-tilted domain extracted from Figure A. 27. The strain, Tilt 1 and Tilt 2 distributions are presented in the sample plane ( $xy$ ) and along the sample thickness ( $z$ ).

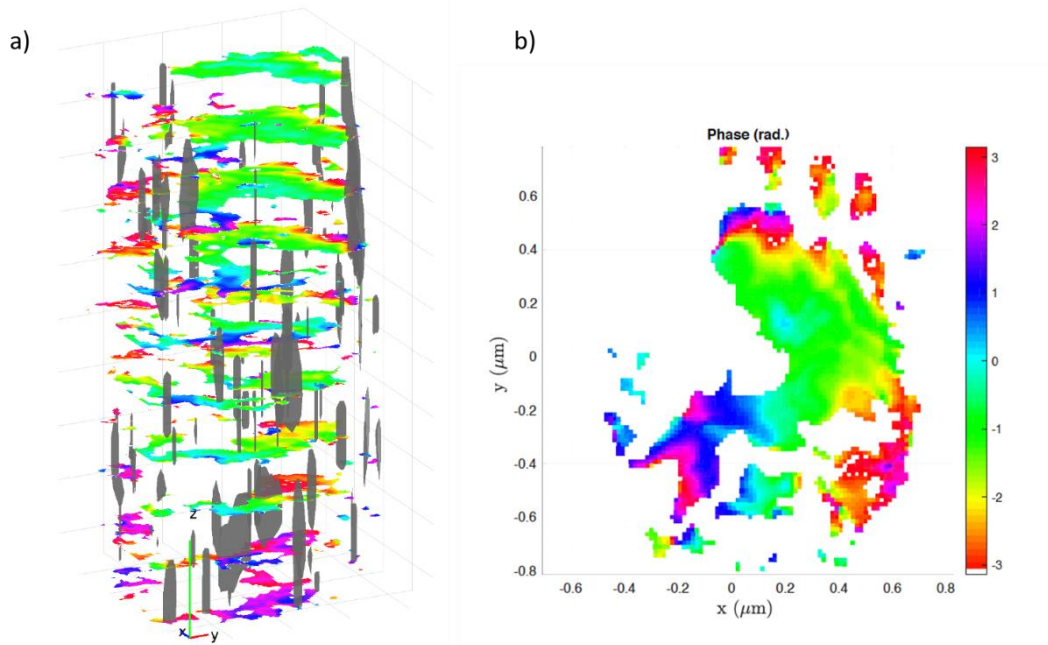


Figure A. 30 - Phase map of the iso-strain iso-tilt domain presented in Figure A. 29 a) 3D phase map with scale ( $xyz$ ) = 100 nm. The gray iso volumes correspond to regions of large strains (> 0.002). b) 2D cross section of the phase map.

## 6.3.3 Interfacial crystallization

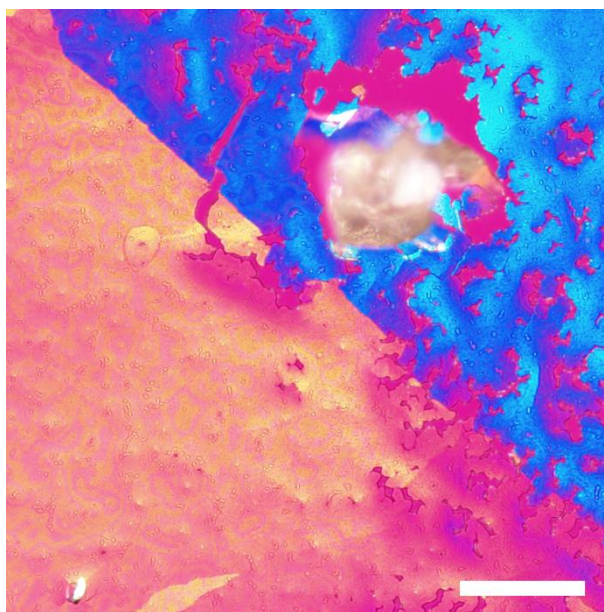


Figure A. 31 - Optical micrograph (WBM) of a continuous film sample collected at the surface of a  $[Ca^{2+}] = 100$  mM,  $[PANa] = 50$  ppm solution and after 5 days of reaction. Scale bar = 100  $\mu$ m.

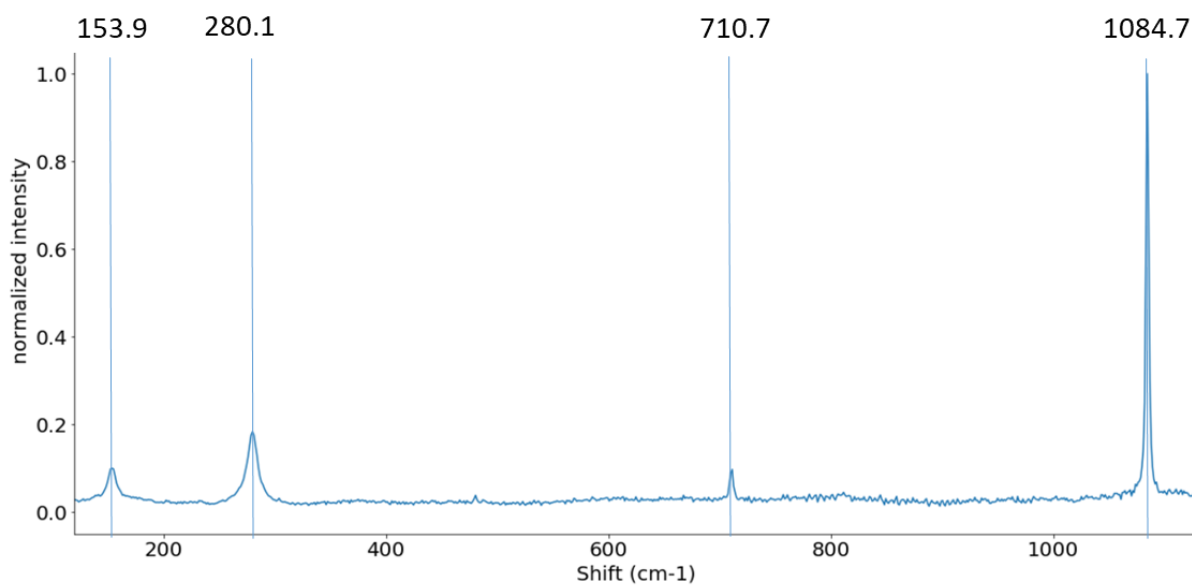


Figure A. 32 - Raman spectrum of an iso-oriented domain of an interfacial continuous film (5 days at the interface). The bands fit the calcite reference spectrum as  $\nu_1$  band is located at 1084.7  $cm^{-1}$ ,  $\nu_4$  at 710.7  $cm^{-1}$ , and lattice bands at 280.1  $cm^{-1}$  and 153.9  $cm^{-1}$ .

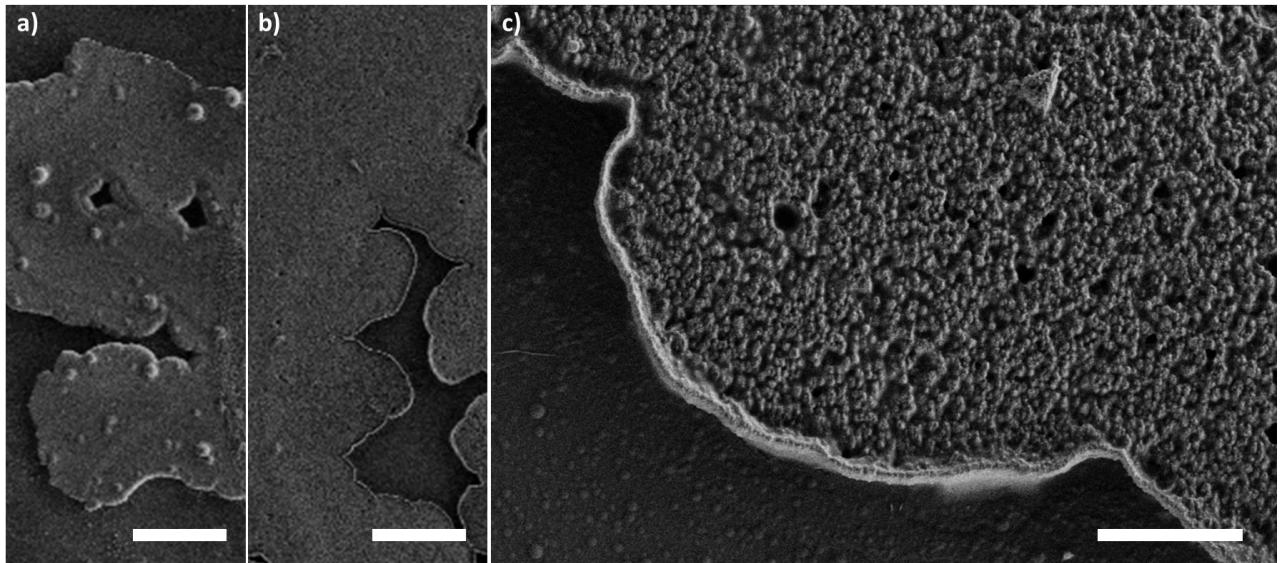


Figure A. 33 - Electron micrograph (SEM) of a continuous film sample collected at the surface of a  $[Ca^{2+}] = 100 \text{ mM}$ ,  $[PANa] = 50 \text{ ppm}$  solution after 5 days of reaction. Scale bars : a,b =  $10 \mu\text{m}$ ; c =  $1 \mu\text{m}$ .

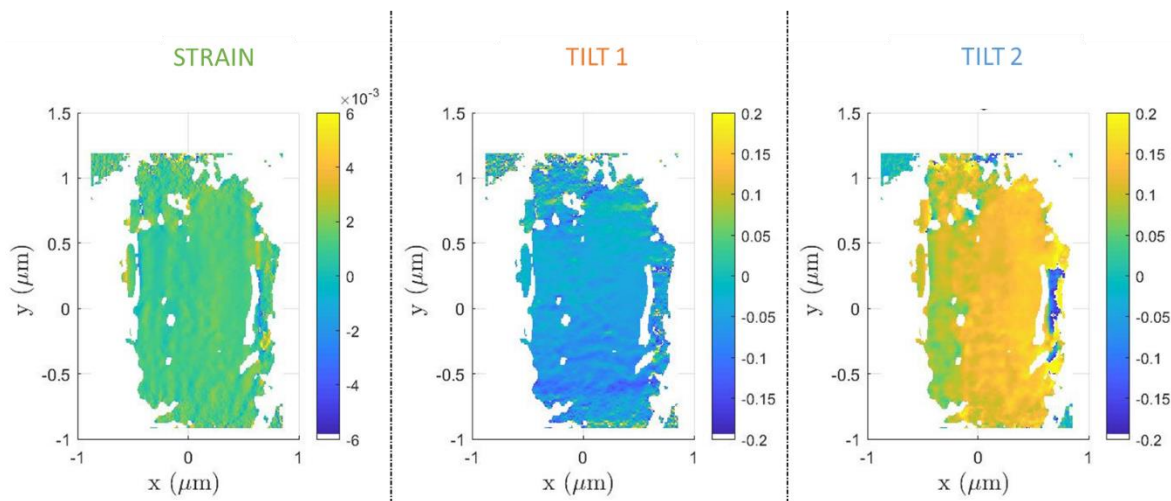


Figure A. 34 - 2D maps of the crystalline properties (strain, Tilt 1 and Tilt 2) in the sample plane ( $xy$ ), retrieved from the Bragg ptychography measurements. The film sample was collected at the free surface of a  $[Ca^{2+}] = 20 \text{ mM}$ ,  $[PANa] = 20 \text{ ppm}$  solution after 5 days of reaction.

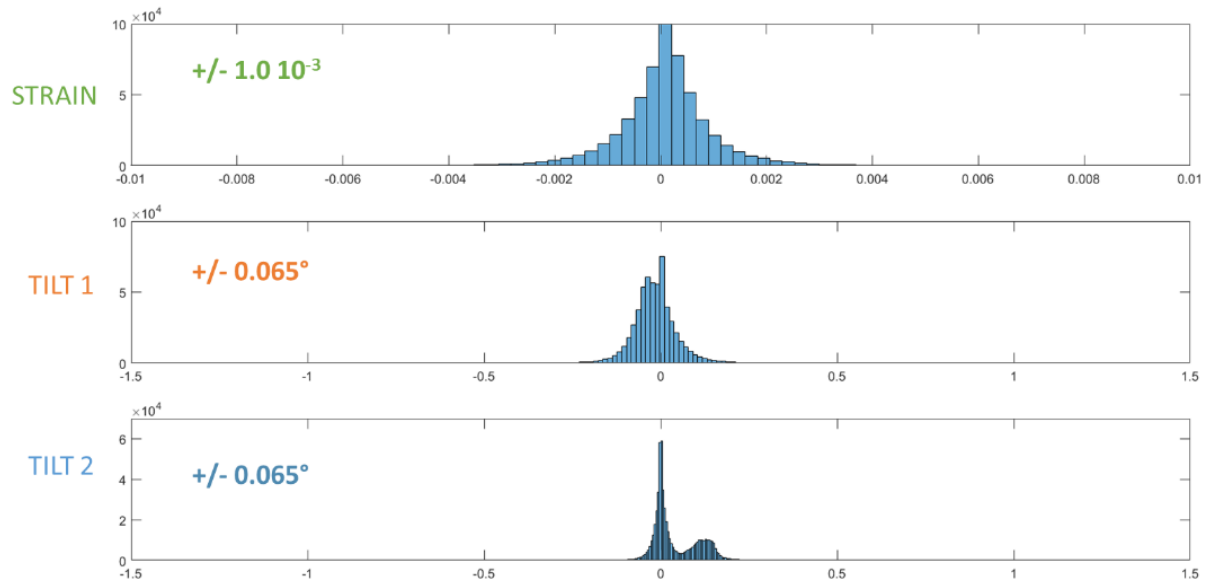


Figure A. 35 - Histogram of the strain, Tilt 1 and Tilt 2 distributions corresponding to the 2D maps presented in Figure A. 34. The strain standard deviation is noted in green, while the standard deviation of Tilt 1 and Tilt 2 are written in orange and blue, respectively.

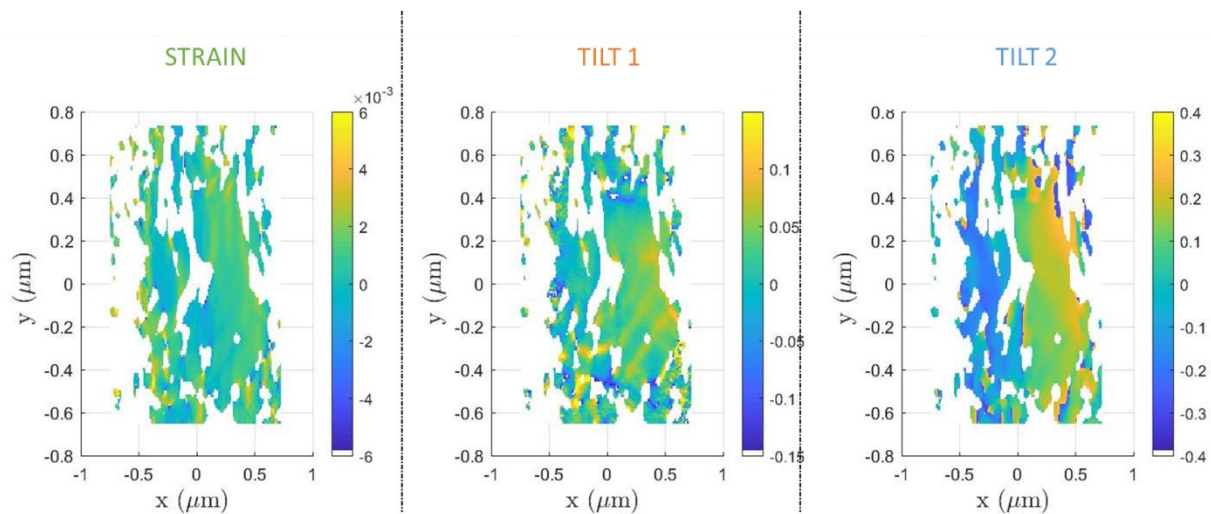


Figure A. 36 - 2D maps of the crystalline properties (strain, Tilt 1 and Tilt 2) in the sample plane (xy), retrieved from the Bragg ptychography measurements. The film sample was collected at the free surface of a  $[Ca^{2+}] = 100 \text{ mM}$ ,  $[PANa] = 50 \text{ ppm}$  solution after 5 days of reaction.

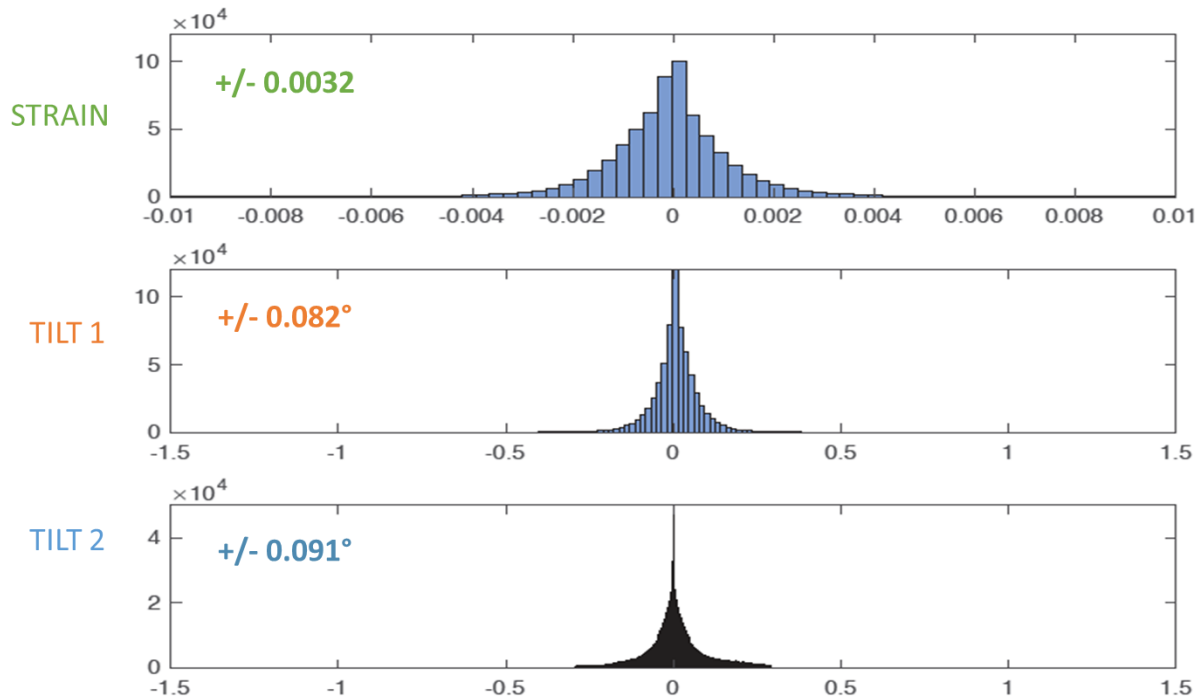


Figure A. 37 - Histograms of the strain, Tilt 1 and Tilt 2 distributions corresponding to the 2D maps presented in Figure A. 36. The strain standard deviation is noted in green, while the standard variation of Tilt 1 and Tilt 2 are written in orange and blue, respectively.

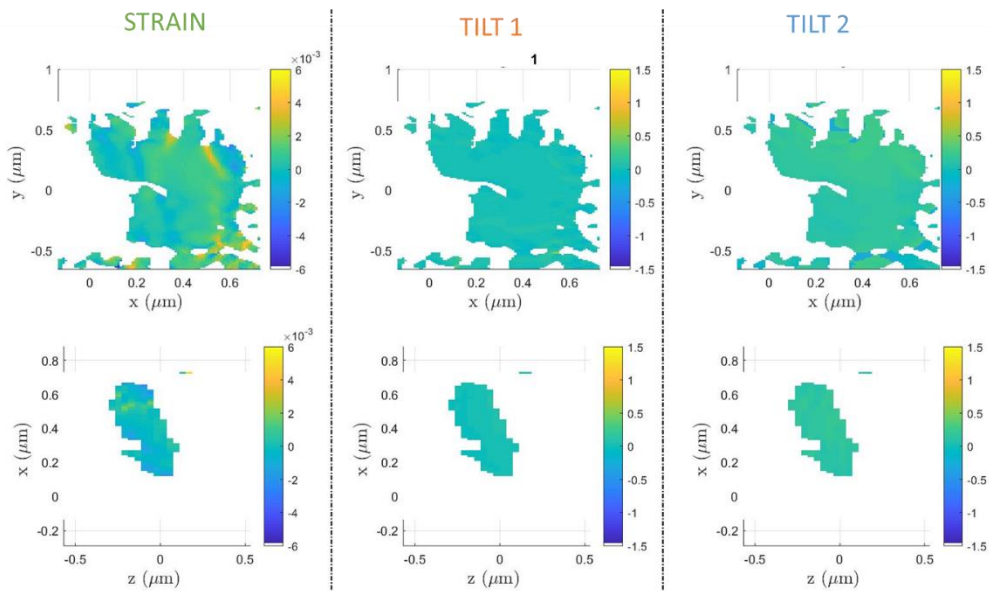
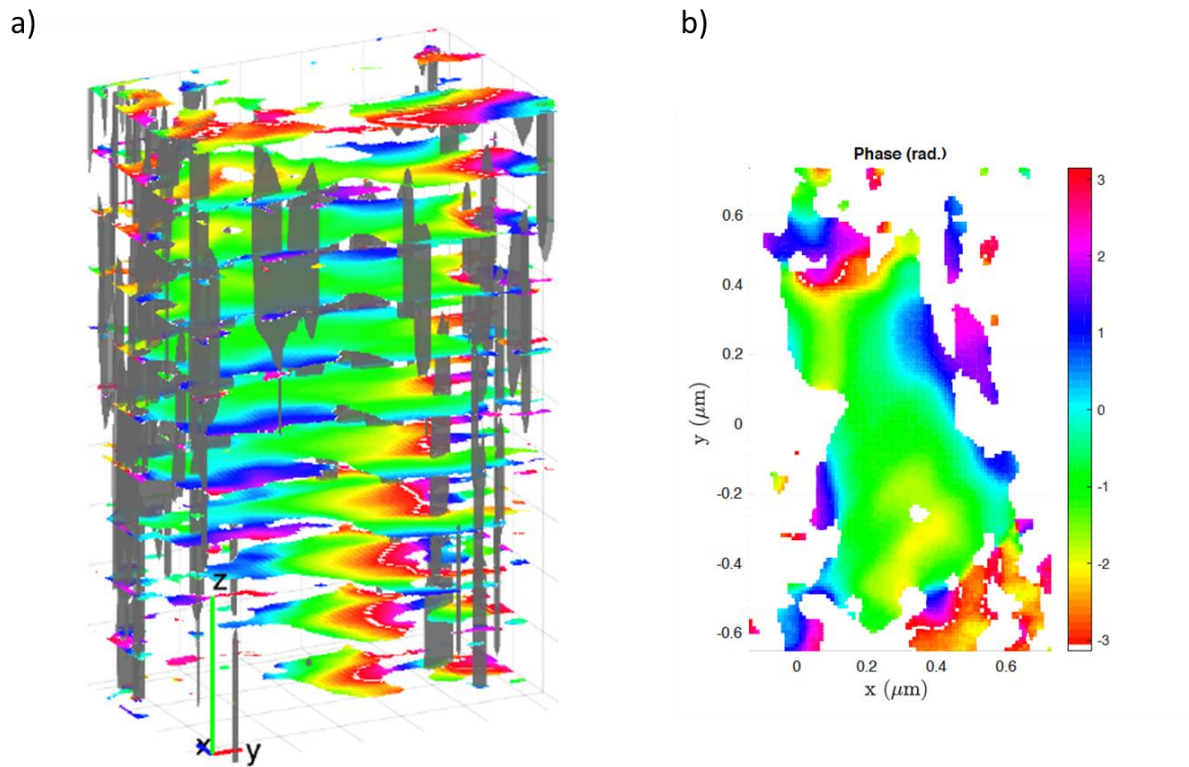


Figure A. 38 - Iso train and iso-tilt domain extracted from Figure A. 36. The strain, Tilt 1 and Tilt 2 maps are presented in the sample plane (xy) and along the sample thickness (z).



## 7 ILLUSTRATIONS TABLE

FIGURE 1 - MICROGRAPHIES OPTIQUES D'ABSORPTION DE FILMS D'INTERFACE EXTRAITS A L'ETAT AMORPHE DU MILIEU REACTIF PAR DEPOT SUR NITRURE DE SILICIUM. APRES SECHAGE SOUS VIDE, LES FILMS SONT OBSERVES EN MICROSCOPIE OPTIQUE. LES SOLUTIONS REACTIVES ONT UNE CONCENTRATION EN CALCIUM DE 50 MM, ET DE POLYACRYLATE DE SODIUM DE A) 20 PPM, B) 50 PPM, C) 100 PPM. LES FILMS SONT EXTRAITS DU MILIEU REACTIF A 18H, 16H ET 18H, RESPECTIVEMENT. ÉCHELLE = 50  $\mu$ M.....10

FIGURE 2 - MICROGRAPHIE ELECTRONIQUE (MEB) D'UN FILM EXTRAIT A L'ETAT AMORPHE APRES 18H D'EXPOSITION D'UNE SOLUTION DE CONCENTRATION EN CALCIUM DE 20 MM ET EN POLYMERE DE 20 PPM A UNE POUDRE DE CARBONATE D'AMMONIUM. AFIN DE VISUALISER LA NANOSTRUCTURE INTERNE DU FILM, UNE CRAQUELURE DANS LE FILM AMORPHE EST OBSERVEE. LE FILM EST CONSTITUE D'UN ARRANGEMENT DE NANOPARTICULE DANS L'ÉPAISSEUR. ÉCHELLE = 500 NM .....11

FIGURE 3 - REPRESENTATION SCHEMATIQUE DU MECANISME DE FORMATION PAR ETAPE DU FILM DE CARBONATE DE CALCIUM. A) SEPARATION DE PHASE LIQUIDE-LIQUIDE MENANT A L'ÉMERGENCE DE DISQUES FINS QUI CROIENT RADIALEMENT. B) CROISSANCE DU FILM EN ÉPAISSEUR, DU A L'AGREGATION DE PARTICULES DU VOLUME DE LA SOLUTION (FLECHE ROUGE). C) FILM AMORPHE DONT L'ÉPAISSEUR NE VARIE PLUS. ....12

FIGURE 4 - MICROGRAPHIES OPTIQUES DE BIREFRINGENCE. LE FILM DE DEPART EST UN FILM AMORPHE CONSTITUE D'ARRANGEMENT DE DISQUES MICRONIQUES ( $[Ca^{2+}] = 20$  MM,  $[PANA] = 20$  PPM) A) APRES CHAUFFAGE 300°C DURANT 3 HEURES, B) APRES EXPOSITION A UNE HUMIDITE ELEVEE (98% HR) DURANT 14 JOURS. C) APRES CRISTALLISATION DANS LE MILIEU REACTIF PENDANT 5 JOURS. ÉCHELLES = 100  $\mu$ M ..12

FIGURE 5 - ELECTRON MICROGRAPHS (SEM) AND PHOTOGRAPHS SHOWING REPRESENTATIVE EXAMPLES OF THE WIDE VARIETY OF BIOGENIC CALCIUM CARBONATE CRYSTALS. A) APPENDAGE-BEARING COCCOLITHOPHORE, OPHIASTER FORMOSUS (SEM). FROM YOUNG AT AL.<sup>17</sup> SCALE BAR = 5  $\mu$ M. B) CORAL, ACROPORA SOLITARYENSIS (PHOTOGRAPH). FROM BAY ET AL.<sup>18</sup> SCALE BAR = 10 MM. C) FORAMINIFERAS, CIBICIDES REFLUGENSE, UVIGERINA SPP., QUIQUELOCULINA SPP. (SEM). FROM PILARCZYK ET AL.<sup>19</sup> SCALE BAR = 100  $\mu$ M. ....14

FIGURE 6 - SCHEMATIZED MORPHOLOGY OF A BIVALVE CONSTITUTED OF AN EXTERNAL PRISMATIC LAYER, AND AN INTERNAL NACREOUS LAYER, AT THE GROWING SHELL EDGE. FROM MARIN *ET AL.*<sup>22</sup> .....16

FIGURE 7 - ELECTRONIC MICROGRAPHS (SEM) AND OPTICAL MICROGRAPH (BM) OF THE ORGANIC SCAFFOLDING IN TWO BIOMINERALS, HYRIOPSIS CUMINGII AND PINNA NOBILIS. A) FE-SEM IMAGE OF PRISTINE NACRE TABLETS IN HYRIOPSIS CUMINGII. B) FE-SEM IMAGE OF ETCHED NACRE TABLETS IN HYRIOPSIS CUMINGII, REVEALING THE ORGANIC SCAFFOLD. C) PINNA NOBILIS, SECTION OBSERVED UNDER CROSSED POLARIZERS. THE SCAFFOLD IS MARKED WITH A "W" ("WALLS"). THE SINGLE CRYSTALLINE NATURE OF THE FILM IS SHOWN BY THE HOMOGENEOUS INTENSITY WITHIN EACH PRISM. D) PINNA NOBILIS ETCHED PRISMS, TRANSVERSE CUT, REVEALING THE SCAFFOLD, MARKED WITH "W" ("WALLS"). E) PINNA NOBILIS, ETCHED PRISM, VERTICAL SECTION. THE SCAFFOLD ("W") ARE VISIBLE, ALONG WITH HORIZONTAL GROWTH LINES, MATCHING BETWEEN PRISMS. A-B) FROM GREINER ET AL.<sup>33</sup> C-E) FROM DAUPHIN ET AL.<sup>34</sup> .....19

## ILLUSTRATIONS TABLE

---

- FIGURE 8 - SINGLE-CRYSTAL CHARACTER OF SEA URCHIN SPINE. A) AND B) ELECTRONIC MICROGRAPHS (SEM) OF FRACTURED SEA URCHIN SPINE AT TWO DIFFERENT MAGNIFICATIONS. C) X-RAY DIFFRACTION PATTERN OF THE SPINE. THE DIFFRACTION PATTERN IS REPRESENTATIVE OF SINGLE CRYSTAL. FROM BERGSTRÖM ET AL.<sup>42</sup> .....21
- FIGURE 9 - UNIFORMITY OF THE PATTERN IN MOLLUSKS AND CORAL SKELETONS AS SHOWN BY PHASE-LAG AFM MAPPING (EXCEPT FOR (C)) AT COMPARABLE MAGNIFICATION. (A) CALCITE PRISMS OF PINCTADA M.; (B) ARAGONITE FROM THE NACREOUS LAYER OF PINCTADA M; (C) SAME SURFACE VIEWED IN AMPLITUDE MODE, AN AFM TAPPING MODE THAT EMPHASIZES THE CHANGES IN SURFACE SLOPES; (D) NACRE OF A PINCTADA PEARL. THIS SIGNAL IS THE DIRECT EXPRESSION OF THE SURFACE TOPOGRAPHY. (E) ARAGONITE OF A SCLERACTINIA CORAL SKELETON (FAVIA); (F) ORGAN-PIPE CORAL (TUBIPORA), A CALCITIC ALCYONARIA; (G,H) THE WHITE CORAL (CORALLIUM JOHNSONI); ANOTHER CALCITIC ALCYONARIA; (I) THE BLUE CORAL (HELIOPIORA COERULEA), THE ONLY ARAGONITIC ALCYONARIA; (J-L) THE RED CORAL (CORALLIUM RUBRUM). FROM CUIF ET AL.<sup>39</sup> .....22
- FIGURE 10 - CRYSTALLIZATION PATHWAYS IN NON-CLASSICAL NUCLEATION PROPOSED BY DE YOREO ET AL.<sup>10</sup> SEVERAL TRANSITORY STATES PROPOSED IN OPPOSITION THE ION-BY-ION CRYSTAL GROWTH. FROM DE YOREO ET AL.<sup>10</sup> .....25
- FIGURE 11 - HYDRATION EVOLUTION IN ACC DURING ITS FORMATION. A) THERMODYNAMICALLY FAVORED WATER-TO-CALCIUM RATIO AS A FUNCTION OF CLUSTER SIZE ( $\text{CaCO}_3$  UNITS). PLOT BASED ON THEORETICAL (RED) AND EXPERIMENTAL (BLUE) ENTROPY CORRECTIONS. FROM RAITERI ET AL.<sup>81</sup> B) HYDRATION OF ACC PARTICLE AS A FUNCTION OF THEIR GROWTH TIME. THE BIGGER THE PARTICLE, THE MORE HYDRATED, AS DEMONSTRATED BY THE BEAM-INDUCED DEFECTS ON THE PARTICLES. FROM DU ET AL.<sup>79</sup> C) DEHYDRATION RATE AS A FUNCTION OF ACC-SIO<sub>2</sub> INCUBATION TIME IN PURE WATER. FROM IHLI ET AL.<sup>59</sup> .....27
- FIGURE 12 - SCHEMATIC REPRESENTATION OF THE AMMONIA DIFFUSION METHOD (ADM) AS ORIGINALLY PRESENTED BY LAURIE GOWER. A DISH (CD) FILLED WITH CALCIUM CARBONATE AND POLY-ELECTROLYTE SOLUTION (CS). AT THE SURFACE A BUBBLE IS TRAPPED (AB) UNDERNEATH A GLASS SLIDE (GS) TO CREATE AN EXCHANGE BETWEEN THE GAS PHASE AND THE SOLUTION. THE GAS PHASE IS CREATED IN A SEALED GLASS CHAMBER BY DECOMPOSITION OF AMMONIUM CARBONATE POWDER (AC). DIFFUSION OF THE DECOMPOSITION PRODUCT IN THE SOLUTION (I) LEADS TO A LIQUID PHASE SEPARATION (II). A DENSE LIQUID ACCUMULATES AT THE BOTTOM OF THE AIR BUBBLE (III) AND FALLS AT THE BOTTOM OF THE DISH TO FORM A FILM (IV). FROM GOWER ET AL.<sup>12</sup> .....28
- FIGURE 13 - FILM FORMATION AT THE BOTTOM OF THE DISH. A: FALL AND COALESCENCE OF THE DENSE LIQUID DROPLETS. B: FILM SOLIDIFICATION TO AMORPHOUS CALCIUM CARBONATE. C: CRYSTALLIZATION AND GROWTH. D: CRYSTALLINE FILM. FROM GOWER ET AL.<sup>12</sup> .....29
- FIGURE 14 - EVIDENCE OF LIQUID-LIKE BEHAVIOR IN CALCIUM CARBONATE SYSTEM. A) ACC SPHERICAL PARTICLES RESULTING FROM A SPINODAL DECOMPOSITION AFTER FAST MIXING (SEM MICROGRAPH). FROM FAATZ ET AL.<sup>60</sup> B) ACC HEMISPHERES DEPOSITED ON MICA BEFORE CRYSTALLIZATION BY GAZ DIFFUSION (SEM MICROGRAPH). FROM XU ET AL.<sup>73</sup> C) PILP INDUCED MINERALIZED FIBERS RESULTING FROM MINERALIZATION IN THE VICINITY OF TRACK-ETCHED MEMBRANES. FROM SCHENK ET AL.<sup>82</sup> SPINODAL DECOMPOSITION PATTERN 100 MS AFTER FAST MIXING (CRYO-TEM). FROM RIEGER ET AL.<sup>83</sup> .....30



FIGURE 15 - A) PHASE DIAGRAM OF A LIQUID SYSTEM EXHIBITING A LIQUID-LIQUID PHASE SEPARATION. THE METASTABLE REGION, IN DARK GREEN, IS DELIMITED BY THE BINODAL AND SPINODAL LINES. THE UNSTABLE REGION IS DELIMITED BY THE SPINODAL LINE.  $T_c$  REPRESENTS THE CRITICAL TEMPERATURE, ABOVE WHICH THE SYSTEM REMAINS MONOPHASIC. B) VARIATIONS OF CONCENTRATION DURING LLPS. LEFT PART ('NUCLEATION AND GROWTH') SHOWS THE CONCENTRATION VARIATIONS DURING PHASE NUCLEATION IN THE BINODAL REGIME. RIGHT PART ('SPINODAL') REPRESENTS THE CONCENTRATION VARIATIONS DURING A SPINODAL DECOMPOSITION. FROM GUSKOV.<sup>85</sup> .....31

FIGURE 16 - MORPHOLOGICAL EVOLUTION OF LIQUID DOMAINS RESULTING FROM SPINODAL DECOMPOSITION. (A) 50:50 BINARY MIXTURE. (B) 45:55 BINARY MIXTURE. FROM DATT ET AL.<sup>86</sup> .....32

FIGURE 17 - A) ACC PRECIPITATED ON GOLD SUBSTRATE FUNCTIONALIZED WITH HYDROXYL FUNCTIONS. THE SUBSTRATE IS LEFT IN  $CaCl_2$  IN CONTACT WITH THE GASEOUS ATMOSPHERE RESULTING FROM AMMONIA CARBONATE DECOMPOSITION (GAS DIFFUSION METHOD). WHEN LEFT IN SOLUTION AMORPHOUS CALCIUM CARBONATE (MARKED "ACC") DISSOLVES TO THE PROFIT OF CALCITE CRYSTALS (MARKED "C"). THE DEPLETION ZONE LEFT BY ACC DISSOLUTION IS HIGHLIGHTED WITH A DOUBLE WHITE ARROW. FROM AIZENBERG ET HAN.<sup>94</sup> B) INTERFACIAL (AIR-SOLUTION) ACC (MARKED "ACC") AND CALCITE RHOMBOEDRAS RESULTING FROM THEIR DISSOLUTION ("CC"). A SATURATED  $Ca(OH)_2$  SOLUTION IS LEFT 35 MIN UNDER ATMOSPHERIC  $CO_2$  TO OBSERVE THIS. FROM RODRIGUEZ-NAVARRO ET AL.<sup>72</sup> C) CRYSTALLIZATION OF 200 NM ACC PARTICLES (PRODUCED BY FAST MIXING) THAT ARE LEFT IN SOLUTION. LEFT : ACC PARTICLES COEXISTING WITH CALCITE RHOMBOEDRA (~300 S). RIGHT: AT 600 S, ONLY CALCITE (RHOMBOEDRA) AND VATERITE (SPHERES) CRYSTALS ARE VISIBLE. FROM ZOU ET AL.<sup>61</sup> .....34

FIGURE 18 - A) CRYSTAL RESULTING FROM THE TRANSFORMATION OF ACC PARTICLES FORMED ON AN HYDROXYLIZED SUBSTRATE AFTER EXPOSURE TO A HUMID ATMOSPHERE (SEM MICROGRAPH). ACC PARTICLES BEFORE TRANSFORMATION ARE THE SAME AS IN FIGURE 17.A (SPHERES). ILLUSTRATION FROM AIZENBERG ET HAN.<sup>94</sup> B) ACC FILM (PRODUCED BY GAS DIFFUSION) EXPOSED TO 60% RH (BIREFRINGENCE MICROSCOPY). C) ACC FILM (GAS DIFFUSION) EXPOSED TO 90% RH (BIREFRINGENCE MICROSCOPY). B-C : SCALE BARS = 100  $\mu$ M. ILLUSTRATION B-C FROM XU ET AL.<sup>96</sup> .....36

FIGURE 19 - PSEUDOMORPHIC AMORPHOUS-TO-CRYSTALLINE TRANSFORMATION AT THE AIR-SOLUTION INTERFACE. A) PARTIAL PSEUDOMORPHIC TRANSFORMATION AT THE AIR-SOLUTION INTERFACE (CROSSED POLARIZER WITH LAMBDA-PLATE MICROGRAPH). THE PURPLE COLORATION IS REPRESENTATIVE OF AN OPTICALLY ISOTROPIC MATERIAL. THE BLUE COLORATION IS CRYSTALLINE, AND REPRESENTATIVE OF A HOMOGENEOUSLY ORIENTED DOMAIN. THE MORPHOLOGY BETWEEN THE AMORPHOUS PART OF THE FILM ("ACC") AND THE CRYSTALLINE PART, ("CRYSTAL") IS KEPT. FROM GOWER ET AL.<sup>64</sup> B) CROSSED POLARIZER MICROGRAPH OF INTERFACIAL ACC FILM LEFT TO CRYSTALLIZE IN SOLUTION. THE PSEUDOMORPHIC TRANSFORMATION RESULTS INTO 2D SPHERULITIC CALCITE CRYSTALS. C) ATOMIC FORCE MICROGRAPH OF INTERFACIAL SPHERULITIC CRYSTAL, TOPOLOGICAL HEIGHT. D) ATOMIC FORCE MICROGRAPH OF INTERFACIAL SPHERULITIC CRYSTAL, PHASE IMAGE. B-D FROM WOLF ET AL.<sup>15</sup> .....37

FIGURE 20 - PSEUDOMORPHIC AMORPHOUS-TO-CRYSTALLINE TRANSFORMATION UNDER HEAT. A) AFM-TAPPING MODE – NANO-METRIC STRUCTURE OF AN ACC FILM (GAS-DIFFUSION) B) AFM- TAPPING MODE, NANOMETRIC STRUCTURE OF FILM A) EXPOSED TO 300°C, TRANSFORMED INTO CALCITE. ILLUSTRATIONS A) AND B) FROM XU ET AL.<sup>96</sup> C) TEM MICROGRAPH OF A 200NM ACC PARTICLE (FAST MIXING) BEFORE (LEFT) AND AFTER (RIGHT) EXPOSURE TO 200°C. AFTER EXPOSITION TO HEAT, THE ACC PARTICLE CRYSTALLIZED INTO CALCITE, WHILE KEEPING ITS ROUND SHAPE. THE SMOOTHNESS ON THE EDGE OF THE ACC PARTICLE IS DISTURBED DURING THE CRYSTALLIZATION PROCESS. AFTER HEAT, THE PARTICLE EDGE BECOMES ROUGHER. FROM ZOU ET AL.<sup>61</sup> .....38

## ILLUSTRATIONS TABLE

---

FIGURE 21 - A) ELECTRONIC MICROGRAPH (SEM). CALCITIC PRISMS OF PINCTADA MARGARITIFERA. THE PRISMS ARE SITUATED ON THE EXTERNAL PART OF THE SHELL. FROM DAUPHIN ET AL.<sup>34</sup> B) AFM- MICROGRAPHS OF CALCITE FROM THE EXTERNAL PART OF PINCTADA MARGARITIFERA SHELL (LEFT) AND ARAGONITE FROM THE INTERNAL PART OF THE SHELL. BOTH POLYMORPHS HAVE THE NANOGRANULATED STRUCTURE SHARED BY MANY CALCAREOUS BIOMINERALS. FROM CUIF ET AL.<sup>39</sup> C) SEM MICROGRAPH. ELONGATED SECTION OF THE CALCITIC PRISM OF PINCTADA MARGARITIFERA. THE PRISMS ARE SEPARATED BY AN ORGANIC SCAFFOLD (VERTICAL LINES) AND SHOWS GROWTH LAYERS SHARED BETWEEN PRISMS (HORIZONTAL LINES). D) CROSSED-POLARIZERS MICROGRAPH. ISO-ORIENTED PRISM OF A SHELL BORDER. THE ISO-ORIENTATION IS DEDUCED FROM THE EVEN COLORATION UNITY INSIDE A PRISM. (C-D) FROM CUIF ET AL.<sup>108</sup> .....40

FIGURE 22 - WEIGHT LOSS OF BOTH UNCRUSHED (RED) AND CRUSHED AMMONIUM CARBONATE (BLUE, DASHED) WITH TIME. ....43

FIGURE 23 - SCHEMATICS OF THE SET-UP CORRESPONDING TO A 'CAP' SYNTHESIS. A 35 MM DIAMETER PETRI DISH (REACTOR) IS FILLED WITH THE REACTIVE SOLUTION IN BLUE. THREE CAPS CONTAINING THE AMMONIUM CARBONATE POWDER AND COVERED BY A SINGLE LAYER OF UNPUNCHED PARAFILM SHEET ARE DISTRIBUTED IN THE PETRI DISH. THE CHAMBER IS A 150 MM PETRI DISH CLOSED BY A DOUBLE LAYER OF PARAFILM. THE PARAFILM IS SCHEMATIZED IN YELLOW COLOR. THE SUBLIMATION PRODUCTS DISSOLVING INTO THE SOLUTION ARE SCHEMATIZED WITH WHITE ARROWS. ....44

FIGURE 24 - SCHEMATICS OF THE SET-UP. A SEALED 150 MM PETRI DISH CONTAINS A 35 MM DIAMETER PETRI DISH FILLED WITH THE REACTIVE SOLUTION IN BLUE. THE PELLET CONTAINING 10%WT OF AMMONIUM CARBONATE IS REPRESENTED IN WHITE. THE FOAM SEAL IS REPRESENTED IN GREEN. THE SUBLIMATION PRODUCTS DISSOLVING INTO THE SOLUTION ARE SCHEMATIZED WITH THE WHITE ARROW. ....45

FIGURE 25 - OPTICAL MICROGRAPH (AM) OF A DISC PATTERNED INTERFACIAL FILM ( $[Ca^{2+}] = 50$  MM,  $[PANA] = 20$  PPM), OBSERVED IN SITU. SCALE: 50  $\mu$ M.....46

FIGURE 26 - OPTICAL MICROGRAPHS (AM) OF THE MORPHOLOGY OF FILM SAMPLES ( $[Ca^{2+}] = 50$  MM,  $[PANA] = 20$  PPM) A) THE UPPER LINE CORRESPONDS TO SAMPLES DRIED 5 MIN UNDER VACUUM - 0.08 MPA. B) THE LOWER LINE CORRESPONDS TO SAMPLES DRIED UNDER A DRY- $N_2$  FLOW. EACH ROW REPRESENTS SAMPLES FROM THE SAME SYNTHESIS. SCALE= 50  $\mu$ M. ON THE SYNTHESIS REPRESENTED BY THE TWO IMAGES ON THE RIGHT, THE DENSITY OF THE MICRONIC DISC IS REDUCED, POSSIBLY DUE TO HETEROGENEITY OF THE FILM AT THE INTERFACE. SCALE BAR = 50  $\mu$ M.....46

FIGURE 27 - RAMAN SPECTRUM OF AN INTERFACIAL ACC FILM DRIED WITH ETHANOL. THE TABLE COMPARES THE PEAK CHARACTERISTICS FOR THE TWO DRYING METHODS (ETHANOL QUENCH AND VACUUM DRYING). DATA ARE EXTRACTED BY FITTING THE PEAK WITH A GAUSSIAN FUNCTION.....47

FIGURE 28 - A) SET-UP FOR LONG-TERM CONSERVATION OF SAMPLES. THE SAMPLE (IN GREY) IS PLACED ON A 3D PRINTED SUPPORT (IN WHITE), ABOVE A SATURATED SOLUTION OF LITHIUM BROMIDE. B) RELATIVE HUMIDITY INSIDE THE CHAMBER AS A FUNCTION OF TIME. ....48

FIGURE 29 - KINETICS OF ESTABLISHMENT OF THE ATMOSPHERE. RELATIVE HUMIDITY VALUE (% RH) AS A FUNCTION OF TIME, UNDER THE INFLUENCE OF  $K_2SO_4$  (GREEN),  $NaCl$  (BLUE) AND  $MgCl_2$  (ORANGE) SALT.

## ILLUSTRATIONS TABLE

---

FOR EACH MEASUREMENT, THE EXPERIMENT WAS TRIPPLICATED, AND THE STANDARD DEVIATION CALCULATED. THE STANDARD DEVIATION IS PLOTTED THEN AS A MUTE COLORED AREA AROUND EACH CURVE. ....	49
FIGURE 30 - PCM MICROSCOPE CONFIGURATION .....	51
FIGURE 31 - MICHEL LEVY DIAGRAM. THE DIAGRAM PROVIDES THE INTERFERENCE COLOR RESULTING FROM THE CROSSED-POLARIZED ILLUMINATION OF A SAMPLE, DEPENDING ON THE SAMPLE BIREFRINGENCE AND THICKNESS. FROM SØRENSEN ET AL. <sup>112</sup> .....	52
FIGURE 32 - OPTICAL MICROGRAPHS AND DATA TREATMENT. A) ORIGINAL MICROGRAPH OF THE INTERFACIAL MINERALIZED STRUCTURES. B) SEGMENTATION WITH WEKA MACHINE LEARNING. C) POST THRESHOLDING OF THE SEGMENTED IMAGE. D) APPLIED "WATERSHED". SCALE BARS= 50 µM .....	54
FIGURE 33 - FERET DIAMETER IN THE CASE OF A RANDOM PARTICLE (LEFT) AND IN THE CASE OF A DISC (RIGHT). .....	54
FIGURE 34 - SCHEMATIC REPRESENTATION OF THE INTERACTIONS TAKING PLACE DURING SAMPLE ILLUMINATION BY AN ELECTRON BEAM. ....	55
FIGURE 35 - NUMERICAL TREATMENT OF AN TEM IMAGE. A) ORIGINAL PICTURE B) RESULT AFTER TREATMENT. SELECTED PARTICLES IN THE FINAL ANALYSIS PRESENTED IN WHITE.....	57
FIGURE 36 - VIOLIN PLOT EXAMPLE, WITH ANNOTED STATISTICAL DATA.....	57
FIGURE 37 - MINIMUM ESCAPE DEPTH DEPENDING ON THE TOPOLOGRAOHY. 1: THE INCIDENT BEAM HITS A FLAT SURFACE, THE MINIMUM ESCAPE DEPTH IS MAXIMIZED. 2: THE INCIDENT BEAM HITS A TILTED SURFACE, THE MINIMUM ESCAPE DEPTH IS REDUCED. MORE SECONDARY ELECTRONS ARE EMITTED IN CASE 2. ....	60
FIGURE 38 - CONFIGURATION OF THE GEMINI 500. THE MAIN COMPONENTS ARE INDICATED IN THE FIGURE. IN THIS WORK, ONLY SECONDARY ELECTRON DETECTORS WERE USED, TO INVESTIGATE THE TOPOGRAPHY (FIGURE 37). BOTH A DETECTOR IN THE BEAM AXIS (IN LENS) AND A DETECTOR TILTED WITH REGARD TO THE SAMPLE (HE-SE DETECTOR) WERE USED.....	61
FIGURE 39 - GENERAL PRINCIPLE OF VECTORIAL PTYCHOGRAPHY .....	63
FIGURE 40 - RETARDANCE IN CALCITE AS A FUNCTION OF THE CRYSTAL THICKNESS AND C-AXIS TILT. THE TILT IS NOTED IN DEGREES WITH RESPECT TO THE NORMAL TO THE SAMPLE PLANE. ....	65

## ILLUSTRATIONS TABLE

- FIGURE 41 - CONFIGURATION OF THE BRAGG PTYCHOGRAPHY EXPERIMENT.  $\mathbf{K}_i$  IS THE INCIDENT WAVE VECTOR AND  $\mathbf{K}_f$  THE EXIT WAVE VECTOR.  $\mathbf{Q}$  IS THE VECTOR TRANSFER RESULTING FROM THE DIFFERENCE BETWEEN THE INCIDENT AND EXIT WAVE VECTOR. THE 3D FRAME FOR  $\mathbf{Q}$  IS DEPICTED BY  $(\mathbf{Q}_1, \mathbf{Q}_2, \mathbf{Q}_3)$  IN THE FIGURE.  $\mathbf{Q}_1$  AND  $\mathbf{Q}_2$  ARE ALONG THE DETECTOR FRAME,  $\mathbf{Q}_3$  IS ALONG THE ROCKING CURVE DIRECTION, I.E. IT IS EXPLORED BY ROTATING THE SAMPLE ALONG THE  $\Omega$  ANGLE. INSET : WHEN THE CRYSTALLINE PLANES ARE ORIENTED IN BRAGG CONFIGURATION,  $\mathbf{Q}$  IS EQUAL TO  $\mathbf{G}_{\text{HKL}}$ .  $\mathbf{G}_{\text{HKL}}$  IS NORMAL TO THE PLANES AND ITS NORM IS LINKED TO THE INTER-RETICULAR SPACE BETWEEN THE (HKL) PLANES.....67
- FIGURE 42 - REPRESENTATION OF 3D THE DISPLACEMENT OF THE  $\mathbf{G}$  (FROM  $\mathbf{G}_{\text{HKL}}$  TO  $\mathbf{G}'$ ) VECTOR INDUCED BY : A) TILTING OF THE CRYSTALLINE PLANES AROUND  $\mathbf{Q}_2$  B) TILTING OF THE CRYSTALLINE PLANES AROUND  $\mathbf{Q}_3$  C) STRETCHING OF THE CRYSTALLINE PLANE.....68
- FIGURE 43 - REPRESENTATION OF THE TILTS AND STRAIN CALCULATED FROM THE DISPLACEMENT FIELD DERIVATIVES.  $(X, Y, Z)$  IS DEFINED BY THE SAMPLE : X AND Y CORRESPOND TO THE SAMPLE PLANE, AND Z TO THE THICKNESS DIRECTION. TILT 1 AND 2 ARE REPRESENTED BOTH IN THE MEASUREMENT SPACE (THE SET-UP) AND AT THE SCALE OF THE CRYSTALLINE PLANE IN BRAGG CONDITIONS (IN THE INSET). THE STRAIN, IE THE RELATIVE VARIATION OF THE INTER-RETICULAR DISTANCE COMPARED TO A REFERENCE CRYSTAL, IS REPRESENTED ALONG THE CRYSTALLINE PLANES (INSET). NOTE THAT TILT1 AND TILT 2 CORRESPOND TO  $\omega$  AND  $\beta$ , RESPECTIVELY, IN FIGURE 42. ....69
- FIGURE 44 - MAPS OF THE CRYSTALLINE PROPERTIES IN THE  $(XY)$  PLANE. FROM LEFT TO RIGHT, STRAIN, TILT1 AND TILT 2 VALUES OF THE SAME AREA ARE SHOWN. AN ISO-DOMAIN, HOMOGENEOUS IN STRAIN AND TILTS, IS SURROUNDED BY A RED DASHED LINE. THE COLOR SCALES ARE PROVIDED ON THE PLOT, FOR THE STRAIN (UNITLESS) AND TILTS (IN DEGREES).....71
- FIGURE 45 - HISTOGRAMS OF STRAIN, TILT 1 AND TILT 2 VARIATIONS IN THE VOLUME PRESENTED IN FIGURE 43. FOR THE STRAIN, THE STANDARD DEVIATION IS NOTED IN GREEN. NOTE THAT IN THIS CASE, THE DISTRIBUTIONS OF TILTS ARE RATHER HOMOGENEOUS AND INDICATE A MUCH LARGER TILT DISTRIBUTION THAN THE ONE CAPTURED BY THE ANGULAR EXPLORATION PERFORMED DURING THE BRAGG PTYCHOGRAPHY DATA ACQUISITION. IN CONSEQUENCE, NO STANDARD DEVIATION IS GIVEN AND LOWER BOUNDS OF TILT RANGE ARE INSTEAD PROVIDED.....72
- FIGURE 46 - CRYSTALLINE PROPERTIES OF THE DOMAINS EXTRACTED IN FIGURE 44. THE SPATIAL DISTRIBUTION OF EACH PARAMETER (FROM LEFT TO RIGHT : STRAIN, TILT 1 AND TILT 2) ARE SHOWN IN  $(XY)$  AND  $(XZ)$  PLANES. ....73
- FIGURE 47 - PLOT OF THE PHASE VARIATION IN THE ISO-TILT, ISO-STRAIN DOMAIN. A) 3D PHASE MAP OF THE ISO-STRAIN ISO-TILT DOMAIN PRESENTED IN FIGURE 103 WITH SCALE  $(XYZ) = 30 \text{ NM}$ . B) 2D PHASE MAP OF THE INVESTIGATED DOMAIN.....74
- FIGURE 48 - REPRESENTATION OF RAYLEIGH, STOKES AND ANTI-STOKES SCATTERING.  $E_{\text{IN}}$  IS THE ENERGY OF THE INCIDENT PHOTON, AND  $E_{\text{OUT}}$  THE ENERGY OF THE SCATTERED PHOTON. ....75

FIGURE 49 - RAMAN SPECTRA OF THE THREE ANHYDROUS  $\text{CaCO}_3$  POLYMORPHS PRODUCED IN A ADM SYNTHESIS IN THE ABSENCE OF POLYMER ADDITIVE: CALCITE (BLUE), ARAGONITE (ORANGE) AND VATERITE (GREEN).  
 .....77

FIGURE 50 - ENERGY DIAGRAM OF 3D ORBITALS. LEFT: FREE ION, ALL THE ORBITALS HAVE THE SAME ENERGY. MIDDLE: THE ION IS COMPLEXED IN A RANDOM WAY (IN A SPHERICAL SYMMETRY). THE ORBITAL ENERGY RISES, BUT IN THE SAME WAY FOR ALL ORBITALS. THE ENERGY LEVEL IS CALLED  $E_0$ , AND IS SPECIFIC TO THE COMPLEXING LIGAND. RIGHT: THE LIGANDS ARE ORGANIZED IN AN OCTAHEDRAL SYMMETRY AROUND THE CENTRAL ION. THE 3D ORBITALS OF THE CENTRAL ION HAVE 2 ENERGY LEVELS :  $E_G$  AND  $T_{2G}$ . THE ENERGY DIFFERENCE BETWEEN THE ORBITALS IS NOTED  $\Delta_0$ .....78

FIGURE 51 - X-RAY ABSORPTION SPECTRA OF COMMERCIAL CALCITE (ACQUIRED BY STXM). THE SPECTRUM DECONVOLUTION INCLUDES TWO ARCTANGENTS (IN YELLOW),  $L_3 T_{2G}$  (B') AND  $E_G$  (B) ABSORPTION PEAKS IN RED AND  $L_2 T_{2G}$  (B') AND  $E_G$  (B) ABSORPTION PEAKS IN BLUE. THE SUM OF THE DECONVOLUTION IS IN GRAY, WHILE THE EXPERIMENTAL DATA ARE PLOTTED AS A BLACK DASHED LINE. ....80

FIGURE 52 - PH DEPENDENCE OF THE CARBONATE SYSTEM, CALCULATED FROM MINTEQA2 (THE SPECIES DISTRIBUTION AT FIXED PH WHEN INTRODUCING 100 MM OF CARBONATE IN SOLUTION ARE CALCULATED EVERY 0.1 PH UNIT). BLUE CURVE :  $\text{H}_2\text{CO}_3$  CONCENTRATION (MM) AS A FUNCTION OF PH IN 100 MM CARBONATE SOLUTION. ORANGE CURVE :  $\text{HCO}_3^-$  CONCENTRATION (MM) AS A FUNCTION OF PH IN 100 MM CARBONATE SOLUTION. GRAY CURVE :  $\text{CO}_3^{2-}$  CONCENTRATION (MM) AS A FUNCTION OF PH IN 100 MM CARBONATE SOLUTION.....81

FIGURE 53 - DISCRETE PH MEASUREMENTS USING PH STRIPS - 3 ML SOLUTION (ORANGE DOTS). THE ERROR IS ESTIMATED TO 1 PH UNIT DUE TO VISUAL PH IDENTIFICATION. CONTINUOUS PH MEASUREMENT USING A MICRO-ELECTRODE IN 6 ML SOLUTION. THE SOLUTION CONSIDERED HERE IS  $[\text{Ca}^{2+}] = 20 \text{ MM}$  AND  $[\text{PANA}] = 20 \text{ PPM}$ . ....82

FIGURE 54 - IN SITU CRYSTALLIZATION CELL SCHEMATICS AND PERFORMANCE. A) SCHEMATICS OF THE IN SITU CRYSTALLIZATION CELL : SEAL IS REPRESENTED IN YELLOW, OPTICAL GLASS WINDOWS IN BLUE. B) RELATIVE HUMIDITY INSIDE THE CELL (T = 0 MIN BEING THE CLOSING TIME) AS A FUNCTION OF TIME.....83

FIGURE 55 - AMMONIA DIFFUSION METHOD (ADM). A) CHEMICAL SPECIES DURING GAS DIFFUSION. A SOLUTION OF CALCIUM CHLORIDE IS EXPOSED TO GASEOUS CARBON DIOXIDE AND AMMONIA. B) THE GASEOUS SPECIES DISSOLVE IN SOLUTION, LEADING TO AMMONIUM AND CARBONATED SPECIES IN BULK. THE FILM FORMED AT THE INTERFACE IS REPRESENTED IN GRAY AND COVERS THE FREE SURFACE. THE INSET PRESENTS AN OPTICAL MICROSCOPY TRANSMISSION IMAGE OF AN INTERFACIAL FILM PRODUCED WITH  $[\text{Ca}^{2+}] = 20 \text{ MM}$ ,  $[\text{PANA}] = 20 \text{ PPM}$  AND DEPOSITED ON SIN MEMBRANE AFTER 18 HOURS OF REACTION. SCALE BAR =  $50 \mu\text{M}$ . ....85

FIGURE 56 - OPTICAL MICROGRAPH (AM) OF CRYSTALS GROWN WITH THE ADM METHOD (WITHOUT ADDED POLYMER). 100 MM CALCIUM CHLORIDE SOLUTION EXPOSED TO AMMONIUM CARBONATE FOR 18H. A) FLOWER-LIKE CRYSTALS B) RHOMBOEDRAL CRYSTALS. SCALE BAR =  $50 \mu\text{M}$ .....85

FIGURE 57 - OPTICAL MICROGRAPHS (AM) OF THE INTERFACIAL FILM ACQUIRED IN SITU. THE AMOUNT OF PANA IN BOTH SYNTHESSES IS 20 PPM A) CAP SYNTHESIS, WITH 50 MM OF  $\text{CaCl}_2$  B) PELLET SYNTHESIS, WITH 20 MM OF  $\text{CaCl}_2$ . DIFFERENCES IN LIGHTING AND IMAGE SHARPNESS ARE DUE TO THE USE OF TWO DIFFERENT MICROSCOPES AND CAMERAS. SCALE BAR = 50  $\mu\text{M}$ . .....87

FIGURE 58 - FERET DIAMETER DISTRIBUTION CALCULATED FROM IMAGE ANALYSIS. A)  $[\text{Ca}^{2+}] = 20 \text{ MM}$ ,  $[\text{PANA}] = 20 \text{ PPM}$  CAP SYNTHESIS. DATA FROM TWO SEPARATED SYNTHESSES B)  $[\text{Ca}^{2+}] = 20 \text{ MM}$   $[\text{PANA}] = 20 \text{ PPM}$  PELLET SYNTHESIS. DATA FROM TWO SEPARATED SYNTHESSES. THE FERET DIAMETER, AS PRESENTED IN THE MATERIALS AND METHODS, IS USED TO RETRIEVE THE DIAMETER OF A CIRCULAR OBJECT. ....87

FIGURE 59 - OPTICAL MICROGRAPHS (AM) OF THE MORPHOLOGY EXHIBITED BY THE INTERFACIAL FILM UPON VARIATION OF THE CALCIUM CONTENT. THE FILMS ARE TAKEN OUT AFTER 18 HOURS OF CAP SYNTHESIS. FROM LEFT TO RIGHT, CALCIUM CONCENTRATION IS 20 MM, 50 MM AND 100 MM RESPECTIVELY. THE POLYMER CONCENTRATION IS KEPT AT 20 PPM. SCALE BAR = 50  $\mu\text{M}$ . .....88

FIGURE 60 - OPTICAL MICROGRAPHS (AM) OF THE MORPHOLOGY OF THE INTERFACIAL FILM UPON VARIATION OF THE POLYMER CONTENT. THE FILMS ARE TAKEN OUT AFTER A) 18, B) 16 AND C) 18 HOURS OF CAP SYNTHESIS. FROM LEFT TO RIGHT, POLYMER CONCENTRATION IS 20 PPM, 50 PPM AND 100 PPM RESPECTIVELY. THE CALCIUM CONTENT IS KEPT AT 50 MM. SCALE BAR = 50  $\mu\text{M}$ . .....89

FIGURE 61 - ELECTRON MICROGRAPHS (SEM) SHOWING THE DISC MORPHOLOGY IN TWO SYNTHESIS CONDITIONS. A)  $[\text{Ca}^{2+}] = 20 \text{ MM}$ ,  $[\text{PANA}] = 20 \text{ PPM}$ , 18 H OF REACTION, HEATED  $300^\circ\text{C}$  3H. HE-SE DETECTOR, 1 KV. SCALE BAR = 2  $\mu\text{M}$ . B)  $[\text{Ca}^{2+}] = 100 \text{ MM}$ ,  $[\text{PANA}] = 50 \text{ PPM}$ , 18 H OF REACTION, HEATED  $300^\circ\text{C}$  3H. TRACES OF DISC MORPHOLOGY ARE VISIBLE ON THE CONTINUOUS FILM. HE-SE DETECTOR, 1 KV. SCALE BAR = 2  $\mu\text{M}$ . CRACKS IN BOTH A) AND B) ARE INDUCED BY THE HEAT TREATMENT. AS PRESENTED IN SECTION 4.1.1, DUE TO THE HEAT TREATMENT, THE FILMS ARE CRYSTALLINE. ....89

FIGURE 62 - OPTICAL MICROGRAPHS OF THE DISC-PATTERNED FILM ( $[\text{Ca}^{2+}] = 20 \text{ PPM}$ ,  $[\text{PANA}] = 20 \text{ MM}$ ) SAMPLED AFTER 18H OF REACTION. RIGHT AFTER SAMPLING, THE FILM IS OBSERVED IN A) OM B) BM. THE BLACK COLORATION INDICATES THAT THE MATERIAL OBSERVED IS OPTICALLY ISOTROPIC. C) WBM. THE PINK COLORATION INDICATES THAT THE MATERIAL OBSERVED IS OPTICALLY ISOTROPIC. SCALE BAR = 100  $\mu\text{M}$ .90

FIGURE 63 - TYPICAL RAMAN SPECTRA OF FILM SAMPLES PRODUCED AT  $[\text{Ca}^{2+}] = 20 \text{ MM}$ ,  $[\text{PANA}] = 20 \text{ PPM}$  (17H SAMPLING) IN ORANGE AND AT  $[\text{Ca}^{2+}] = 100 \text{ MM}$ ,  $[\text{PANA}] = 100 \text{ PPM}$  (17H SAMPLING) IN BLUE. THE SPECTRUM OF CALCITE IS SHOWN IN GREEN AS A REFERENCE. ....91

FIGURE 64 - A) OPTICAL MICROGRAPH (WBM). LEFT IMAGE IS MADE RIGHT AFTER SAMPLING, RIGHT IMAGE IS MADE AFTER A THREE-MONTH STORAGE. B) SCHEMATIC OF THE SET-UP USED FOR LONG-TERM CONSERVATION. SATURATED LIBR SOLUTION CONTROLS THE RELATIVE HUMIDITY OF THE ATMOSPHERE. SAMPLE (REPRESENTED WITH A GRAY SQUARE) IS PLACED ABOVE THE SOLUTION. C) RAMAN SPECTRUM OF A FILM SAMPLE ( $[\text{Ca}^{2+}] = 100 \text{ MM}$ , 100 PPM), COLLECTED AFTER 17 HOURS OF REACTION) AND KEPT FOR 3 MONTHS IN LIBR. SCALE BAR = 100  $\mu\text{M}$ . ....92

FIGURE 65 - ELECTRON MICROGRAPHS (SEM) OF DISC PATTERNED AND CONTINUOUS FILMS. A) AMORPHOUS DISC PATTERNED CALCIUM CARBONATE FILM ( $[\text{Ca}^{2+}] = 20 \text{ MM}$ ,  $[\text{PANA}] = 20 \text{ PPM}$ , 16 HOURS). SCALE BAR =

5  $\mu\text{M}$ . INSET, ZOOM. HE-SE DETECTOR, 2 KV. SCALE BAR = 1  $\mu\text{M}$ . B) CRYSTALLIZED CONTINUOUS CALCIUM CARBONATE FILM ( $[\text{Ca}^{2+}] = 20 \text{ MM}$ ,  $[\text{PANA}] = 20 \text{ PPM}$ , 17 HOURS). THE WHITE ARROW POINTS TOWARDS THE MATTER SCATTERED ON THE CONTINUOUS FILM. THE RED ARROW HIGHLIGHTS THE POROUS MATTER AT THE END OF REMNENT DISCS (HIGHLIGHTED BY RED DASHED CIRCLES). HE-SE DETECTOR, 1 KV. SCALE BAR = 5  $\mu\text{M}$ . INSET, ZOOM. SCALE BAR = 1  $\mu\text{M}$ . .....94

FIGURE 66 - ELECTRON MICROGRAPHS (SEM) LEADING TO FILM THICKNESS ESTIMATE. THE THICKNESS MEASURED BETWEEN WHITE DASHED ARROWS IS WRITTEN IN BOTH A) AND B). A) DISC-PATTERN FILM ( $[\text{Ca}^{2+}] = 20 \text{ MM}$ ,  $[\text{PANA}] = 20 \text{ PPM}$ ). THE DASHED ORANGE LINE UNDERLINES THE THICKNESS VARIATION OF A THIN DISC, THE THICKNESS BEING MAXIMUM AT THE CENTER OF THE LINE. THE ORANGE ARROW HIGHLIGHTS SOME PART OF THE FILM THAT DID NOT DETACH FROM THE SUBSTRATE UNDER VACUUM. ON THIS IMAGE, ONLY THE SIDE INITIALLY IN CONTACT WITH THE AIR-SOLUTION INTERFACE IS VISUALIZED. HE-SE DETECTOR, 5 KV. SCALE BAR = 5  $\mu\text{M}$ . B) CONTINUOUS FILM ( $[\text{Ca}^{2+}] = 100 \text{ MM}$ ,  $[\text{PANA}] = 50 \text{ PPM}$ ) THAT HAS DETACHED FROM THE SUBSTRATE. THE SIDE INITIALLY IN CONTACT WITH THE SOLUTION IS INDICATED BY A YELLOW PENTAGON. FOR BETTER VISUALIZATION, A SCHEMATIC REPRESENTATION (IN BLUE) OF THE AREA INVESTIGATED HAS BEEN ADDED. HE-SE DETECTOR, 1 KV. SCALE BAR = 2  $\mu\text{M}$ . .....96

FIGURE 67 - ELECTRON MICROGRAPHS (SEM) OF THE FILM INTERNAL STRUCTURE. BROKEN EDGES ARE INVESTIGATED IN A) DISC-PATTERN FILM ( $[\text{Ca}^{2+}] = 20 \text{ MM}$ ,  $[\text{PANA}] = 20 \text{ PPM}$ ) HE-SE DETECTOR, 2 KV, AND B) CONTINUOUS FILM ( $[\text{Ca}^{2+}] = 100 \text{ MM}$ ,  $[\text{PANA}] = 50 \text{ PPM}$ ), HEATED AT 300°C. THE FACE INITIALLY IN CONTACT WITH THE SOLUTION IS INDICATED BY A YELLOW PENTAGON. HE-SE DETECTOR, 1 KV. SCALE BAR = 500 NM. ....97

FIGURE 68 - ELECTRON MICROGRAPH (SEM) SHOWING THE INTERNAL STRUCTURE OF A CONTINUOUS FILM. THE INTERFACE IN CONTACT WITH WATER IS INDICATED BY A YELLOW PENTAGON. THE UPPER LAYER IS HIGHLIGHTED IN BLUE WHILE THE BOTTOM LAYER IS COLORED IN PINK. THE WHITE ARROW SHOWS THE HIGHER DENSITY OF PORES AT THE JUNCTION BETWEEN THE TWO LAYERS. IN LENS DETECTOR, 1 KV. SCALE BAR = 200 NM.....98

FIGURE 69 - PHOTOGRAPHS SHOWING THE FILM FORMATION AS VISIBLE TO THE NAKED EYE. A) ELONGATED WHITE STRANDS FIRST BECOME VISIBLE AFTER 40 MIN. B) AFTER 60 MIN, MINERALIZED STRUCTURES COVER THE WHOLE INTERFACE. C) AFTER 5 HOURS, A COMPLETE FILM HAS FORMED. THE KBR PELLETT IS ON THE LEFT SIDE OF THE PETRI DISH. ....99

FIGURE 70 - PHOTOGRAPHS SHOWING LIGHT SCATTERING SPECIES EVOLUTION IN BULK A) 5 MIN AFTER FILM APPEARANCE. WHITE VERTICAL LINES APPEAR IN SOLUTION. B) 6 MIN AFTER FILM APPEARANCE. THE LINES INTENSIFY. C) 7 MIN AFTER FILM APPEARANCE. THE LIGHT SCATTERING SPECIES EXPAND Laterally AT THE SURFACE, FORMING THE ROLLS. ....99

FIGURE 71 - ELECTRON MICROGRAPHS (TEM) OF THE INTERFACIAL MINERALIZED STRUCTURES AT EARLY REACTION TIMES. A-F) INTERFACIAL MINERALIZED OBJECTS AT A) 1 MIN, B) 2 MIN, C) 5 MIN, D) 10 MIN, E) 18 MIN F) 25 MIN. SCALE BAR = 2  $\mu\text{M}$ . G) VIOLIN PLOTS: STATISTICAL SIZE DISTRIBUTION OF THE PARTICLE FERET DIAMETER WITH TIME. DESCRIPTION OF THE VIOLIN PLOTS IS AVAILABLE IN THE MATERIAL AND METHODS, 2.4.1.3. THE BLUE DASHED LINE PRESENT THE RADIAL GROWTH OF THE PARTICLE UP TO 10 MIN. THE ORANGE DASHED LINE HIGHLIGHTS THE STEADY FERET DIAMETER EVOLUTION BETWEEN 10 AND 25 MIN. AT 35 MIN, THE FERET DIAMETER RISES AGAIN..... 101

## ILLUSTRATIONS TABLE

---

- FIGURE 72 - ELECTRON MICROGRAPHS (TEM) OF THE DISCS. A DENSER REGION IS VISIBLE IN THE DISC CENTER. A) 18 MIN. B) 25 MIN. SCALE BAR = 2  $\mu\text{M}$ . ..... 102
- FIGURE 73 - AFM IMAGING OF DISCS AFTER 20 MIN OF REACTION (FOLLOWING THE OBSERVATION IN STXM SPECTROSCOPY). A) TOPOGRAPHY MAPPING. B) HEIGHT PROFILE OF THE SEGMENTS TRACED IN A). THE HEIGHT IS AVERAGED BETWEEN THE DASHED LINE FOR A BETTER SIGNAL. SCALE BAR = 3  $\mu\text{M}$ . ..... 103
- FIGURE 74 - ELECTRON MICROGRAPHS (TEM) SHOWING THE DOUBLE-EMULSION AND FUSION PATTERNS AT THE INTERFACE AT A) 1 MIN, B) 2 MIN, C) 5 MIN, D) 10 MIN, E) 18 MIN, F) 25 MIN, G) 35 MIN. DOUBLE EMULSION PATTERNS ARE MARKED WITH A BLUE ASTERISK, AND FUSION PATTERNS WITH A YELLOW ONE. SCALE BAR = 2  $\mu\text{M}$ . ..... 104
- FIGURE 75 - ELECTRON MICROGRAPHS (TEM) OF A FILM SAMPLED AT 35 MIN NAD 18 MIN A) TEM MICROGRAPH AT 35 MIN. THE THREE TYPES OF INTENSITIES ARE MARKED I, II AND III. SCALE BAR = 5  $\mu\text{M}$ . B) PIXEL INTENSITY ALONG THE ARROW DRAWN IN A). THE THREE INTENSITY PLATEAUS ARE COLORED IN YELLOW, ORANGE AND BLUE RESPECTIVELY. THEY CORRESPOND TO THE REGIONS ALONG THE ARROW PARTITIONED WITH THE SAME COLOR IN A). C) TEM IMAGES OF THE THREE STRUCTURES. FROM LEFT TO RIGHT: DISC AT 18 MIN, STRUCTURE I (35 MIN), STRUCTURE II (35 MIN) AND STRUCTURE III (35 MIN). ..... 106
- FIGURE 76 - ELECTRON MICROGRAPH (A. SEM, B. TEM). IMAGING OF AN ACC FILM SAMPLED AFTER 35 MIN A) STRUCTURE III, SCALE BAR = 2  $\mu\text{M}$ , THE INSET HIGHLIGHTS THE THIN LAYER PRESENT ON THE DISC EDGE WITH WHITE DASHED ARROWS. IN LENS DETECTOR, 1 KV. SCALE BAR = 1 $\mu\text{M}$ . B) COLORED MAP OF THE PIXEL INTENSITY. THE THREE IDENTIFIED TYPES OF STRUCTURES ARE LABELED I,II AND III RESPECTIVELY. THE PURPLE COLOR OF STRUCTURES I IS VISIBLE ON THE PERIPHERY OF STRUCTURES II AND III (HIGHLIGHTED BY WHITE DASHED ARROWS ON A STRUCTURE III IN THE INSET). ..... 107
- FIGURE 77 - AFM IMAGING OF TYPE II STRUCTURE AFTER 35 MIN OF REACTION. A) TOPOGRAPHY MAPPING. B) HEIGHT PROFILE OF THE SEGMENTS TRACED IN A). THE HEIGHT IS AVERAGED BETWEEN THE DASHED LINE FOR A BETTER SIGNAL. SCALE = 10  $\mu\text{M}$ . ..... 108
- FIGURE 78— OPTICAL MICROGRAPH (PCM IN SITU) OF THE INTERFACIAL FILM. A) SURFACE OF THE SOLUTION AT 35 MIN OF REACTION. SCALE BAR = 50  $\mu\text{M}$ . B) CLOSE-UP OF A). SCALE BAR = 20  $\mu\text{M}$ . C) SCHEMATIC REPRESENTATION OF THE INTERFACIAL PATTERN, PROVIDIND AN EXPLANATION ON THE OBSERVED STRUCTURES IN A AND B. ..... 108
- FIGURE 79—OPTICAL MICROGRAPH (PCM IN SITU). PHASE CONTRAST MICROSCOPY. EVOLUTION OF THE PHASE CONTRAST WITH TIME. INSETS, ALL NUMERICALLY ENHANCED, PROVIDE A ZOOMED-IN VIEW OF THIS EVOLUTION. A) TIME "T" = 45 MIN OF REACTION. B) T + 4.5 MIN. C) T + 52.5 MIN. THE BLACK ARROWS POINT TO A 3D RHOMBOHEDRAL CRYSTAL GROWN AT THE INTERFACE. SCALE BARS = 100  $\mu\text{M}$ ; INSET SCALE BARS = 20  $\mu\text{M}$ . ..... 109
- FIGURE 80 – STXM IMAGE AT THE CALCIUM L<sub>3</sub>-EDGE (351.2 EV) OF A FILM SAMPLED AT A) 10 MIN OF REACTION. INSET: ENHANCED CONTRAST, REVEALING THE CORONA. B) 20 MIN C) 30 MIN D) 40 MIN. TYPE II AND III STRUCTURES, AS DEFINED EARLIER IN THIS SECTION, ARE IDENTIFIED BY ROMAN NUMBERS. SCALE BAR = 5  $\mu\text{M}$  ..... 110



## ILLUSTRATIONS TABLE

---

- FIGURE 81 - NORMALIZED X-RAY ABSORPTION SPECTRUM OF THE DISC FORMED AT 30 MIN OF REACTION. MEASUREMENTS HAVE BEEN PERFORMED AT THE CA L-EDGE. TWO ARCTAN FUNCTIONS, IN GREEN, AND FOUR LORENTZIAN FUNCTIONS (IN RED FOR THE  $L_3$  RESONANCE AND IN BLUE FOR THE  $L_2$ ) HAVE BEEN USED FOR DECONVOLUTION. THE SUM OF THESE FUNCTIONS YIELDS THE GRAY SPECTRUM, WHILE THE EXPERIMENTAL CURVE IS DRAWN IN LIGHT BLUE. INSET: OPTICAL DENSITY MAP AT CA L-EDGE . THE SPECTRUM IS TAKEN FROM THE AVERAGED OF THE GREEN AREA. SCALE BAR = 0.4  $\mu\text{M}$ ..... 111
- FIGURE 82 - ELECTRON MICROGRAPH (CRYO-TEM) AND EDS MEASUREMENTS OF A FILM SAMPLE COLLECTED AT A REACTION TIME OF 1 HOUR. A) CRYO-TEM IMAGE. RED AND GREEN SQUARES CORRESPOND TO THE AREAS INVESTIGATED BY EDS ANALYSIS. SCALE BAR = 2  $\mu\text{M}$ . B) ZOOMED-IN VIEW OF THE UPPER REGION OF THE CENTRAL DISC. SCALE BAR = 200 NM. C) EDS ANALYSIS OF THE CORONA (RED SQUARE IN A)). D) EDS ANALYSIS OF THE DISC CENTER (GREEN SQUARE IN A)). THE SPECIFIC SIGNALS OF THE AVAILABLE ELEMENTS ARE EXPECTED AT THE FOLLOWING ENERGY VALUES: CARBON ( $K_A = 0.277$  KEV), CALCIUM ( $K_A = 3.692$  KEV,  $K_B = 4.013$  KEV), AND OXYGEN ( $K_A = 0.525$  KEV). A SMALL SIGNAL FROM COPPER (ORIGINATING FROM THE GRID) IS ALSO VISIBLE ( $L_A = 0.928$  KEV,  $L_B = 0.947$  KEV). THE SLIGHT SIGNAL AT  $\sim 1.7$  KEV IS ATTRIBUTED TO SILICON CONTAMINATION..... 112
- FIGURE 83 - PH EVOLUTION OVER TIME IN 6 ML OF  $[\text{CA}^{2+}] = 20$  MM,  $[\text{PANA}] = 20$  PPM. A) EVOLUTION OVER 160 MIN. B) EVOLUTION OVER THE FIRST 20 MIN. GRAY AREA REPRESENTS THE STANDARD DEVIATION IN EACH POINT. MEASUREMENTS HAVE BEEN TRIPPLICATED UNTIL 72 MIN, AND THEN DUPLICATED. .... 114
- FIGURE 84 - IN SITU RECORDING OF  $\text{CO}_2$  PARTIAL PRESSURE INSIDE THE REACTOR CHAMBER. LONG-TERM (7.5 HOURS) RECORDING OF THE ATMOSPHERE IN CONTACT WITH A  $[\text{CA}^{2+}] = 20$  MM,  $[\text{PANA}] = 20$  PPM SOLUTION. .... 115
- FIGURE 85 - ELECTRON MICROGRAPH (TEM) OF A BULK SAMPLE COLLECTED AT 38 MIN OF REACTION (REFERENCE CONDITIONS 20 MM / 20 PPM). SAMPLING WAS MADE IN THE LIGHT-SCATTERING AREA OF THE SOLUTION. THE SAMPLE WAS DRIED UNDER PRIMARY VACUUM (MATERIALS AND METHODS 2.1.3) BEFORE TEM IMAGING. SCALE BAR = 1  $\mu\text{M}$  ..... 116
- FIGURE 86 - NORMALIZED X-RAY ABSORPTION SPECTRUM OF BULK PARTICLES AT 42 MIN OF REACTION. MEASUREMENTS HAVE BEEN PERFORMED AT THE CA L-EDGE. INSET: IMAGE OF THE PARTICLES ACQUIRED AT 351.2 EV. SCALE BAR = 1  $\mu\text{M}$ . THE RED DASHED SQUARE SHOWS THE AREA CONSIDERED FOR HYPERSPECTRAL IMAGING: THE SPECTRUM WAS EXTRACTED BY AVERAGING THE SIGNAL OVER A FEW PARTICLES IN THIS AREA. FOR DECONVOLUTION, TWO ARCTAN FUNCTIONS, IN GREEN, AND FOUR LORENTZIAN FUNCTIONS (IN RED FOR THE  $L_3$  RESONANCE AND IN BLUE FOR THE  $L_2$ ) HAVE BEEN USED. THE SUM OF THESE FUNCTIONS YIELDS THE GRAY SPECTRUM, WHILE THE EXPERIMENTAL CURVE IS DRAWN IN LIGHT BLUE. .... 117
- FIGURE 87 - ELECTRON MICROGRAPH (CRYO-TEM) AND EDS ANALYSIS OF THE BULK PARTICLES. A) OBSERVATION OF THE BULK SPECIES AT 1H REACTION TIME. SCALE BAR = 200 NM. B) OBJECTS ARE ANALYZED IN EDS (RIGHT). THE SPECIFIC SIGNALS OF THE AVAILABLE ELEMENTS ARE EXPECTED AT THE FOLLOWING ENERGY VALUES: CARBON ( $K_A = 0.277$  KEV), CALCIUM ( $K_A = 3.692$  KEV,  $K_B = 4.013$  KEV), AND OXYGEN ( $K_A = 0.525$  KEV). A SMALL SIGNAL FROM COPPER (ORIGINATING FROM THE GRID) IS ALSO VISIBLE ( $L_A = 0.928$  KEV,  $L_B = 0.947$  KEV). THE SLIGHT SIGNAL AT  $\sim 1.7$  KEV IS ATTRIBUTED TO SILICON CONTAMINATION..... 118

FIGURE 88 - HENRY’S CONSTANT OF CO<sub>2</sub> AND NH<sub>3</sub> GASES AS A FUNCTION OF PH. THE BLUE CURVE CORRESPONDS TO CO<sub>2</sub> GAS, AND THE ORANGE CURVE TO NH<sub>3</sub> GAS. THE DATA HAVE BEEN CALCULATED USING PHREEQC SOFTWARE (HTTPS://WWW.USGS.GOV/SOFTWARE/PHREEQC-VERSION-3), BY CONSIDERING A PARTIAL PRESSURE OF 10 PPM ONLY FOR THE TWO GASES IN ORDER TO EASE THE CALCULATIONS..... 120

FIGURE 89 - MORPHOLOGY OF A LIQUID DROPLET AT THE AIR-SOLUTION INTERFACE. “IN SOLUTION”: THE SURFACE TENSION INFLUENCES THE MORPHOLOGY OF THE WETTING LIQUID. “LIQUID-LIKE SAMPLING”: EXPECTED MORPHOLOGY AND AFM PROFILE OF THE DROPLET WHEN TAKEN OUT OF THE SOLUTION AS A LIQUID. “SOLIDIFIED SAMPLING”: EXPECTED MORPHOLOGY AND AFM PROFILE OF THE DROPLET WHEN TAKEN OUT OF THE SOLUTION AFTER SOLIDIFICATION (LEFT: FULLY SOLIDIFIED, RIGHT: PARTIALLY SOLIDIFIED). NOT TO SCALE..... 122

FIGURE 90 - SIMILARITY OF INTERFACIAL STRUCTURE AS PRESENTED IN AMOS ET AL.<sup>150</sup> AND OUR EXPERIMENT. A) INTERFACIAL ACC FILM (IN PURPLE) GOING THROUGH A CRYSTALLIZATION PROCESS (IN BLUE AND YELLOW), DURING A PSLP EXPERIMENT. SCALE BAR = 100 μM. B) ELECTRONIC MICROGRAPH (SEM) OF AN AMORPHOUS CALCIUM CARBONATE FILM ([CA<sup>2+</sup>] = 20 MM, [PANA] = 20 PPM, 18.5 H OF REACTION) CREATED DURING THIS WORK. THE IMAGE IS TAKEN AT 2 KV WITH HE-SE DETECTOR..... 123

FIGURE 91 - INTERFACIAL PATTERN A) FORMED IN OUR SYSTEM AFTER 60 MIN OF REACTION IN A PELLET SYNTHESIS. (B) FORMED BY CONVECTION SHADOWGRAPH TAKEN AT THE AIR-WATER INTERFACE OF AN EVAPORATING BINARY FLUID (WATER-NACL SOLUTION). FROM ZHANG ET AL.<sup>155</sup> ..... 125

FIGURE 92 - MORPHOLOGICAL TRACES OF THE THICKENING PROCESS. A) ELECTRON MICROGRAPH (SEM) OF A FILM ([CA<sup>2+</sup>] = 20 MM, [PANA] = 20 PPM, 19 H OF REACTION) HEATED AT 300 °C DIRECTLY AFTER SAMPLING. THE OBSERVATIONS ARE MADE WITH A 70° ANGLE, AT 15 KV, WITH THE HE-SE DETECTOR. SCALE BAR = 10 μM. B) SCHEMATIC REPRESENTATION OF THE ATTACHMENT PROCESS OF BULK PARTICLES (IN YELLOW) IN THE CASE OF A DISC PATTERNED (LEFT) AND CONTINUOUS (RIGHT) FILM. THE ADDITION OF PARTICLES LEADS TO THE THICKENING OF THE FILM (YELLOW DASHED LINE). THE RED ARROW INDICATES THE LOCATION OF THE THREE-PHASE CONTACT LINE SURROUNDING THE INITIALLY LIQUID DROPLET. .... 126

FIGURE 93 - SCHEMATIC REPRESENTATION OF THE AMORPHOUS FILM FORMATION AT THE INTERFACE. IN EACH PANEL, A CROSS-SECTION OF THE BULK SOLUTION AND INTERFACE OBJECTS (“SIDE VIEW”) AND A BOTTOM VIEW OF THE INTERFACE OBJECTS ONLY (“BOTTOM VIEW”) ARE REPRESENTED A) DOMAINS OF LIQUID SPREAD AT THE INTERFACE GROW RADIALLY WITH TIME. B) A HOMOGENEOUS LAYER OF PARTICLES IS ADDED FIRST TO THE DISC PATTERN. THEN, BULK PARTICLES, BROUGHT TO THE SURFACE BY CONVECTION ROLLS MASSIVELY AGGREGATE ONTO THE DISC PATTERN, LEADING TO STRONG THICKNESS HETEROGENEITIES. C) FINALLY, A MATURE ACC FILM OF CONSTANT THICKNESS IS FORMED. .... 127

FIGURE 94 - OPTICAL MICROGRAPHS (WBM) OF A DISC PATTERNED FILM BEFORE AND AFTER HEAT TREATMENT. A) FILM IMMEDIATELY AFTER SAMPLING (17H IN PELLET SYNTHESIS, [CA<sup>2+</sup>] = 20 MM, [PANA] = 20 PPM). SCALE BAR = 50 μM. B) SAME FILM HEATED AT 300°C FOR 3H JUST AFTER INITIAL OBSERVATION. SCALE BAR = 50 μM. INSET: ZOOM SHOWING AREAS WITH ABRUPT CHANGES OF COLORATION WITHIN DISCS. BLUE AND YELLOW ARROWS HIGHLIGHT UNTRANSFORMED COLORATION AREAS. .... 130

FIGURE 95 - ELECTRON MICROGRAPH (SEM) OF A DISC-PATTERNED FILM HEATED AT 300°C FOR 3H. HE-SE DETECTOR, 1 KV. SCALE BAR = 2 μM. .... 131

FIGURE 96 - ELECTRON MICROGRAPH (SEM) OF THE BORDER OF A DISC WITH ITS CORONA. THE RED RECTANGLE CORRESPONDS TO THE ENLARGED IMAGE SHOWN IN B). IN LENS DETECTOR, 1 KV. SCALE BAR = 400 NM. B) ZOOMED-IN VIEW OF THE CORONA. IN LENS DETECTOR, 1 KV. SCALE BAR = 200 NM. .... 132

FIGURE 97 - ELEMENTAL MAPS BASED ON EDS MEASUREMENTS PERFORMED ON A CRYSTALLIZED DISC-PATTERNED FILM. A) SEM MICROGRAPH IN BACK-SCATTERED ELECTRON MODE. B) COMPOSITE IMAGE OF THE ELEMENTAL MAPS SHOWN IN C, D AND E. C) CALCIUM DISTRIBUTION IN THE INVESTIGATED AREA. D) CARBON DISTRIBUTION. E) OXYGEN DISTRIBUTION. THE ELEMENTAL MAPS ARE NOT QUANTITATIVE, THE INTENSITY SCALE HAS BEEN SELECTED IN EACH CASE TO OPTIMIZE THE VISUALIZATION OF THE DISTRIBUTION. SCALE BAR = 5  $\mu$ M. .... 132

FIGURE 98 - ELECTRON MICROGRAPHS (SEM) SHOWING THE EDGES OF DISCS FOLLOWING THE HEAT TREATMENT. A) AND B) CORRESPOND TO DIFFERENT DISCS AND DIFFERENT ANGLE OF OBSERVATION. IN LENS DETECTOR, 1 KV. SCALE BARS = 200 NM. .... 133

FIGURE 99 - RAMAN SPECTRUM OF A HEATED DISC-PATTERNED FILM SAMPLE - (CAP SYNTHESIS, 16H30 OF REACTION) HEATED FOR 3 HOURS AT 300°C. THE BANDS FIT THE CALCITE REFERENCE SPECTRUM AS  $\nu_1$  BAND IS LOCATED AT 1085.3  $\text{CM}^{-1}$ ,  $\nu_4$  AT 711.2  $\text{CM}^{-1}$ , AND LATTICE BANDS AT 279.9  $\text{CM}^{-1}$  AND 153.8  $\text{CM}^{-1}$ . .... 133

FIGURE 100 - A) STXM ABSORPTION MAP AT 351.2 EV. THE AREA CORRESPONDING TO THE RED SQUARE WAS INVESTIGATED BY HYPERSPECTRAL IMAGING AND ANALYSED IN B-E). SCALE BAR = 5  $\mu$ M. B-D) OPTICAL DENSITY MAPS AT THE CA L-EDGE SHOWING THE THREE DIFFERENT REGIONS (COLORED AREAS) WHERE XAS SPECTRA HAVE BEEN AVERAGED TO PROVIDE THE CURVES DISPLAYED IN E). E) X-RAY ABSORPTION SPECTRA AT THE CALCIUM  $L_2$  EDGE IN DIFFERENT PLACES OF THE FILM SAMPLE. THE BLUE SPECTRUM WAS AVERAGED OVER THE BLUE AREA IN B), THE ORANGE SPECTRUM OVER THE ORANGE AREA IN C) AND THE YELLOW SPECTRUM FROM THE YELLOW AREA IN D). .... 134

FIGURE 101 - VECTORIAL PTYCHOGRAPHY ANALYSIS OF A HEATED FILM. THE FILM SAMPLE HAS BEEN COLLECTED AT THE SURFACE OF A  $[\text{CA}^{2+}] = 20 \text{ MM}$ ,  $[\text{PANA}] = 20 \text{ PPM}$  SOLUTION AFTER 18H OF REACTION, AND HEATED AT 300°C FOR 3H. A) RETARDANCE (IN RADIANS, 0 TO 1.5). B) C-AXIS TILT RATIO (A.U.). C) FAST-AXIS ORIENTATION (IN DEGREES, FROM 0 TO 180) D) ELLIPTICITY (ABSOLUTE VALUE, 0 TO 1; 0 CORRESPONDS TO A LINEAR POLARIZATION AND 1 TO A CIRCULAR ONE. E) COMPOSITE MAP OF UNWRAPPED PHASE (IN RADIANS, 0 TO 5) AND EIGENPOLARIZATIONS (BLACK). EIGENPOLARIZATIONS ARE PLOTTED ONLY BETWEEN 0.5 AND 1 RAD OF RETARDANCE. OWING TO THE LOW VALUES OF RETARDANCE, UNWRAPPED PHASE IS USED FOR THE SAKE OF UNDERSTANDING. THE UNWRAPPED PHASE IS LESS INTENSE IN THE CENTER OF SOME DISCS IN FIGURE 101.E AND F. IT IS ATTRIBUTED TO A SLIGHT FOCUS MISALIGNMENT (ALSO VISIBLE ON THE RECONSTRUCTED TRANSMISSION DATA). F) ZOOM FROM E) FOR BETTER VISUALIZATION OF THE EIGENPOLARIZATIONS. THE RED DASHED LINE SEPARATES TWO ISO-ORIENTED DOMAINS. SCALE BARS: A,B,C,D = 20  $\mu$ M; E = 20  $\mu$ M; F = 5  $\mu$ M. .... 137

FIGURE 102 - 2D MAPS OF THE CRYSTALLINE PROPERTIES (STRAIN, TILT 1 AND TILT 2) IN THE SAMPLE PLANE (XY), RETRIEVED FROM THE BRAGG PTYCHOGRAPHY DATA. THE FILM SAMPLE WAS COLLECTED AT THE FREE SURFACE OF A  $[\text{CA}^{2+}] = 20 \text{ MM}$ ,  $[\text{PANA}] = 20 \text{ PPM}$  SOLUTION AFTER 18.5H OF REACTION, AND HEATED AT 300 °C FOR 3 H. THE RED DASHED LINE SURROUNDS THE ISO-STRAIN ET ISO-TILT DOMAIN SHOWN IN FIGURE 103. .... 139

FIGURE 103 - ISO-STRAIN, ISO-TILT DOMAIN EXTRACTED FROM FIGURE 102. THE STRAIN, TILT 1 AND TILT 2 MAPS ARE PRESENTED IN THE SAMPLE PLANE (XY) AND ALONG THE SAMPLE THICKNESS (Z). HEATED FILM AT 300 °C FOR THREE HOURS ( $[Ca^{2+}] = 20$  MM,  $[PANA] = 20$  PPM, 18.5 H REACTION TIME). ..... 139

FIGURE 104 - PLOT OF THE PHASE VARIATION IN THE ISO-TILT, ISO-STRAIN DOMAIN. A) 3D PHASE MAP OF THE ISO-STRAIN ISO-TILT DOMAIN PRESENTED IN FIGURE 103 WITH SCALE (XYZ) = 30 NM. THE HIGH STRAIN VALUES ( $> 0.004$ ) ARE SHOWN IN GRAY. B) 2D CROSS SECTION OF THE PHASE MAP. .... 140

FIGURE 105 - COMPARISON OF THE CRYSTALLINE PROPERTIES OF A DISC-PATTERNED (SCALE (XYZ) = 30 NM) AND A CONTINUOUS (SCALE (XYZ) = 100 NM) HEATED FILM RETRIEVED FROM BRAGG PTYCHOGRAPHY DATA. THE CRYSTALLINE PROPERTIES (STRAIN, TILT), THE COHERENCE LENGTH AND 3D PHASE MAP, WITH HIGH-STRAIN REPRESENTED IN GRAY ( $> 0.004$  IN THE DISC-PATTERNED FILM,  $> 0.003$  IN THE CONTINUOUS FILM) ARE SHOWN. .... 141

FIGURE 106 - OPTICAL MICROGRAPHS (WBM) OF FILM SAMPLES CRYSTALLIZED UNDER CONTROLLED RELATIVE HUMIDITY. THE CRYSTALLINE SAMPLES ORIGINATE FROM THE SAME FILM, COLLECTED AFTER 18H OF REACTION AT THE SURFACE OF A  $[Ca^{2+}] = 20$  MM,  $[PANA] = 20$  PPM SOLUTION. A) FILM KEPT UNDER A 33% RH ATMOSPHERE FOR 5 DAYS. A') ZOOMED-IN VIEW OF A SLIGHTLY BIREFRINGENT POLYCRYSTALLINE AREA. B) FILM KEPT UNDER A 75% RH ATMOSPHERE FOR 5 DAYS. B') REMAINING DISCS AT THE SPHERULITE CENTER, ZOOM-IN VIEW FROM B). B'') ELONGATED CRYSTALS, ZOOMED-IN VIEW FROM B). C) FILM KEPT UNDER A 98% RH ATMOSPHERE FOR 5 DAYS. C') RADIAL SYMMETRY AROUND THE SPHERULITIC CENTER, ZOOMED-IN VIEW FROM C). C'') ELONGATED CRYSTAL TIP, ZOOMED-IN VIEW FROM C). THE YELLOW ARROW HIGHLIGHTS THE PRESENCE OF DISCS THAT ARE CO-ORIENTED WITH THE TOP OF THE NEIGHBORING BRANCH. THE BLUE ARROW POINTS TO THE REMAINING OPTICALLY ISOTROPIC DISCS. SCALE BARS = 50  $\mu$ M ..... 142

FIGURE 107 – OPTICAL MICROGRAPH (AM) SHOWING THE EVOLUTION OF REMNANT DISCS WHEN EXPOSED TO HIGH HUMIDITY FOR A LONG PERIOD OF TIME. SAMPLE COLLECTED AFTER 18H AT THE INTERFACE OF A  $[Ca^{2+}] = 20$  MM,  $[PANA] = 20$  PPM SOLUTION. A) 2.5 DAYS EXPOSURE TO 98% RH ATMOSPHERE. THE BLUE ARROWS POINTS TO THE CENTER OF THE SPHERULITES. THE YELLOW ARROW IN THE INSET HIGHLIGHTS THE BORDER OF THE CRYSTALS (BLACK LINES). B) 7 DAYS EXPOSURE TO 98% RH ATMOSPHERE. C) 30 DAYS EXPOSURE TO 98% RH ATMOSPHERE. SCALE BAR = 100  $\mu$ M. .... 145

FIGURE 108 - OPTICAL MICROGRAPHS (IN SITU WBM) OF THE CRYSTALLIZATION UNDER HIGH HUMIDITY (99%RH). OBSERVATIONS WERE MADE WITH THE CRYSTALLIZATION CELL DIRECTLY UNDER THE MICROSCOPE. THE OBSERVATION TIME, GIVEN AS THE TIME ELAPSED SINCE THE CELL WAS CLOSED, IS: A) 10S; B) 58 MIN; AND C) 9.5H. THE DASHED LINE IN B) HIGHLIGHTS THE BRANCH USED FOR THE GROWTH MEASUREMENT PLOTTED IN D) INSET OF B): CLOSE-UP THAT PROVIDES A BETTER VIEW OF THE CRYSTAL INDICATED BY THE ARROW. SCALE BAR = 100  $\mu$ M. D) BRANCH LENGTH EVOLUTION AS A FUNCTION OF TIME. THE TIMES WHEN PICTURES A), B) AND C) WERE TAKEN ARE MARKED ON THE PLOT. .... 146

FIGURE 109 - ELECTRON MICROGRAPHS (SEM) OF SPHERULITES RESULTING FROM THE CRYSTALLIZATION OF AN AMORPHOUS DISC-PATTERNED FILM KEPT UNDER HIGH HUMIDITY (98% RH) FOR 30 DAYS. ORANGE AND YELLOW DASHED LINES HIGHLIGHT THE EQUAL DISTANCE OF THE STEPS FROM THE CENTER ON FOUR DIFFERENT BRANCHES. TWO BRANCHED SPHERULITES ARE OBSERVED IN THE CENTER. THE BLUE ARROW POINTS TO A SPACE-FILLING SPHERULITE, EXHIBITING VISIBLE STEPS ARRANGED CIRCULARLY. FOR THE OBSERVATION, THE SAMPLE WAS TILTED BY 70°. HE-SE DETECTOR, 5 KV. SCALE BAR = 20  $\mu$ M. .... 147

FIGURE 110 - ELECTRON MICROGRAPHS (SEM) OF A SPHERULITE RESULTING FROM THE CRYSTALLIZATION OF AN AMORPHOUS DISC-PATTERNED FILM KEPT UNDER HIGH HUMIDITY (98% RH) FOR 30 DAYS. A) LARGE-SCALE VIEW OF THE SPHERULITE. RED DASHED ELLIPSES POINT TO TRACES OF DISCS AT THE SURFACE OF THE SPHERULITE. GREEN DASHED ELLIPSES POINT TO DISC IMPRINTS IN BETWEEN THE CRYSTALS. HE-SE DETECTOR, 5 KV. SCALE BAR = 20  $\mu$ M. B) DISC SHAPES AT THE SURFACE OF THE SPHERULITIC CRYSTAL. THE RED DASHED LINES OUTLINE THE DISCS EDGES. THE NANOSTRUCTURE IS DIFFERENT IN THE DISCS AND IN THE SPACE BETWEEN THEM. HE-SE DETECTOR, 1 KV. SCALE BAR = 1  $\mu$ M. C) ZOOM-IN VIEW, CORRESPONDING TO THE YELLOW DASHED RECTANGLE IN B). THE RED DOUBLE ARROW SHOWS THE RADIAL EXTENT OF THE CORONA THAT SURROUNDS THE DISCS. IN-LENS DETECTOR, 1 KV. SCALE BAR = 400 NM. D) DISC IMPRINTS IN BETWEEN THE CRYSTALS. THE DISC EDGE IS OUTLINED BY A GREEN DASHED LINE. IN LENS DETECTOR, 1 KV. SCALE BAR = 400 NM. .... 148

FIGURE 111 - ELECTRON MICROGRAPHS (SEM), TAKEN WITH A TILT OF 70°, OF SPHERULITIC BRANCH TIPS. THE FILM WAS KEPT AT 98% RH FOR 30 DAYS. A) SHORT BRANCH (~10  $\mu$ M) HE-SE DETECTOR, 5 KV. SCALE BAR = 2  $\mu$ M. INSET: CLOSE-UP OF THE AREA IN THE YELLOW DASHED RECTANGLE. HE-SE DETECTOR, 5 KV. SCALE BAR = 1  $\mu$ M. B) LONG BRANCH (~100  $\mu$ M) WITH A LAYERED STRUCTURE ON THE TIP. HE-SE DETECTOR, 2 KV. SCALE BAR = 2  $\mu$ M. .... 149

FIGURE 112 - OPTICAL (WBM) AND ELECTRON MICROGRAPHS (SEM AT 70°) OF A FILM SAMPLE CRYSTALLIZED BY EXPOSURE TO A 98% RH ATMOSPHERE FOR 30 DAYS. ISO-ORIENTED DISCS CRYSTALLIZED IN CONTINUITY WITH A NEARBY SPHERULITE ARE VISIBLE. A) LARGE-SCALE WBM MICROGRAPH. SCALE BAR = 50  $\mu$ M. B) EBSD IMAGE CORRESPONDING TO THE GREEN DASHED RECTANGLE SHOWN IN C). ORIENTED CALCITE CRYSTALLINE CELLS (IN YELLOW) HAVE BEEN INDICATED IN TWO PLACES, NAMELY AT THE BRANCH TIP AND IN THE NEIGHBORING CRYSTALLIZED DISCS (THE C-AXIS IS THE LONGEST SIDE OF THE HEXAGONAL CELL). SCALE BAR = 3  $\mu$ M. C) SEM MICROGRAPH OF THE SPHERULITE TIP INVESTIGATED BY EBSD. HE-SE DETECTOR, 5 KV. TILT ANGLE 70°, SCALE BAR = 1  $\mu$ M. .... 150

FIGURE 113 - VECTORIAL PTYCHOGRAPHY ANALYSIS OF THE CENTER OF A SPHERULITE. THE FILM SAMPLE HAS BEEN COLLECTED AT THE SURFACE OF A  $[Ca^{2+}] = 20$  MM,  $[PANA] = 20$  PPM SOLUTION AFTER 18H OF REACTION, AND LEFT 14 DAYS UNDER HIGH RELATIVE HUMIDITY (98%). A) RETARDANCE (IN RADIANS, 0 TO  $\pi$ ). B) C-AXIS TILT RATIO (A.U.). C) FAST-AXIS ORIENTATION (IN DEGREES 0 TO 180). D) ELLIPTICITY (ABSOLUTE VALUE, 0 TO 1). NOTE THAT IN THE LOW RETARDANCE REGIONS, WHICH APPEAR AS OPTICALLY ISOTROPIC, NO ELLIPTICITY CAN BE MEASURED. E) COMPOSITE MAP OF RETARDANCE (COLORATION, IN RADIAN, 0 TO  $\pi$ ) AND EIGENPOLARIZATIONS (BLACK). F) ZOOM FROM E) FOR BETTER VISUALIZATION OF THE EIGENPOLARIZATIONS. THE RED DASHED LINES SEPARATE ISO-ORIENTED DOMAINS. SCALE BAR = 20  $\mu$ M. .... 152

FIGURE 114 - VECTORIAL PTYCHOGRAPHY ANALYSIS OF A BRANCH EMERGING FROM THE CENTER OF A SPHERULITE. THE FILM SAMPLE HAS BEEN COLLECTED AT THE SURFACE OF A  $[Ca^{2+}] = 20$  MM,  $[PANA] = 20$  PPM SOLUTION AFTER 18H OF REACTION, AND LEFT 14 DAYS UNDER HIGH RELATIVE HUMIDITY (98%). A) COMPOSITE MAP OF RETARDANCE (COLORATION, IN RADIANS) AND EIGENPOLARIZATIONS (BLACK). THE WHITE DASHED ARROWS SHOW THE ORIENTATIONS OF THE FAST-AXIS AT THE BRANCH TIP. B) C-AXIS TILT RATIO (A.U.). C) ELLIPTICITY OF THE EIGENPOLARIZATIONS. SCALE BARS: (A) = 20  $\mu$ M. (B,C) = 50  $\mu$ M. .... 153

FIGURE 115 - EBSD MEASUREMENT OF BRANCHED SPHERULITES. THE FILM SAMPLE HAS BEEN COLLECTED AT THE SURFACE OF A  $[Ca^{2+}] = 20$  MM,  $[PANA] = 20$  PPM SOLUTION AFTER 18H OF REACTION, AND LEFT 30 DAYS UNDER HIGH RELATIVE HUMIDITY (98%). A) LARGE-FIELD VIEW CONTAINING SEVERAL SPHERULITES. THE COLORATION IN THE INSET ENCODES THE CRYSTALLINE ORIENTATION. THE ORIENTATION IN THE CENTER COULD NOT BE ESTIMATED OWING TO OF A LACK OF FLATNESS IN THIS REGION. B) ZOOMED-IN VIEW, CRYSTALLINE CELLS REPRESENT THE CRYSTALLINE ORIENTATION ON A GIVEN BRANCHED SPHERULITE. . 154

FIGURE 116 - ISO STRAIN, ISO-TILT DOMAIN EXTRACTED FROM (FIGURE A. 12). THE STRAIN, TILT 1 AND TILT 2 MAPS ARE PRESENTED IN THE SAMPLE PLANE (XY) AND ALONG THE SAMPLE THICKNESS (Z). FILM CRYSTALLIZED AT 98% RH FOR 14 DAYS ( $[Ca^{2+}] = 20$  MM,  $[PANA] = 20$  PPM, 16.5 H REACTION TIME)..... 155

FIGURE 117 - PHASE MAPS OF THE ISO-STRAIN ISO-TILT DOMAIN PRESENTED IN FIGURE 116. A) 3D PHASE MAP WITH SCALE (XYZ)= 30 NM. THE GRAY ISO VOLUMES CORRESPOND TO REGIONS OF LARGE STRAINS ( $> 0.005$ ). B) 2D-CROSS SECTION OF THE PHASE MAP. .... 156

FIGURE 118 - COMPARISON OF THE CRYSTALLINE PROPERTIES, EXTRACTED FROM BRAGG PTYCHOGRAPHY DATA, OF A DISC-PATTERNED AND CONTINUOUS FILM CRYSTALLIZED AT 98% RH. THE CRYSTALLINE PROPERTIES (STRAIN, TILT 1 AND TILT 2), THE COHERENCE LENGTH (SIZE OF CONSTANT PHASE DOMAINS) AND 3D PHASE MAPS WITH HIGH STRAIN ( $> 0.005$  FOR THE DISC-PATTERNED FILM,  $> 0.002$  FOR THE CONTINUOUS FILM) ARE PROVIDED..... 157

FIGURE 119 - OPTICAL MICROGRAPHS (BM) AND RAMAN SPECTRA OF BOTH SINGLE-CRYSTALLINE AND POLYCRYSTALLINE INTERFACIAL 2D CRYSTALS. LB STANDS FOR LATTICE BANDS. A) SINGLE-CRYSTAL RESULTING FROM THE INTERFACIAL CRYSTALLIZATION OF A FILM ( $[Ca^{2+}] = 20$  MM, PANA = 20 PPM) LEFT AT THE INTERFACE FOR 5 DAYS. THE PEAK POSITIONS, PROVIDED BY DECONVOLUTION, ARE  $1086\text{ cm}^{-1}$  FOR  $\nu_1$ ,  $712\text{ cm}^{-1}$  FOR  $\nu_4$ , 281 AND  $155\text{ cm}^{-1}$  FOR LB. B) POLY-CRYSTALLINE STRUCTURE RESULTING FROM THE INTERFACIAL CRYSTALLIZATION OF A FILM ( $[Ca^{2+}] = 20$  MM, PANA = 20 PPM) LEFT AT THE INTERFACE FOR 3 DAYS. THE PEAK POSITIONS, PROVIDED BY DECONVOLUTION, ARE  $1074\text{ cm}^{-1}$ ,  $1083\text{ cm}^{-1}$  AND  $1090\text{ cm}^{-1}$  FOR  $\nu_1$ ; 297 AND  $265\text{ cm}^{-1}$  FOR LB. DUE TO LACK OF SIGNAL, THE  $\nu_4$  BAND OF CALCITE AND THE OTHER LATTICE BANDS ARE NOT VISIBLE. .... 158

FIGURE 120 - OPTICAL MICROGRAPHS (BM) OF A FILM SAMPLE CRYSTALLIZED AT THE AIR-SOLUTION INTERFACE. THE FILM WAS PRODUCED BY ADM SYNTHESIS ( $[Ca^{2+}] = 20$  MM, PANA = 20 PPM) AND LEFT AT THE INTERFACE FOR 5 DAYS. A) ISO-ORIENTED PATCHES. THE GREEN DASHED LINE CONTOURS THREE ADJACENT PATCHES OF DIFFERENT INTENSITIES. B) ISO-ORIENTED PATCHES SIMILAR TO (A) BUT OBSERVED AFTER A  $40^\circ$  ROTATION OF THE SAMPLE. THE GREEN DASHED LINE CONTOURS THREE ADJACENT PATCHES OF DIFFERENT INTENSITIES. SCALE BAR =  $100\text{ }\mu\text{m}$ . .... 159

FIGURE 121 – SEM MICROGRAPH OF A FILM SAMPLE. A SIDE VIEW OF THE FILM CRYSTALLIZED AT THE AIR-SOLUTION INTERFACE. THE FILM WAS PRODUCED BY ADM SYNTHESIS ( $[Ca^{2+}] = 20$  MM, PANA = 20 PPM) AND LEFT AT THE INTERFACE FOR 5 DAYS. THE VISIBLE SIDE OF THE FILM WAS THE ONE IN CONTACT WITH THE ATMOSPHERE DURING THE SYNTHESIS. ORIENTED PILLARS ARE SEEN ON THE SURFACE (ORANGE ARROWS), AND BETWEEN THE DISCS (BLUE ARROW). HE-SE DETECTOR, 2 KV. SCALE BAR =  $10\text{ }\mu\text{m}$ . B) STRUCTURE OF SURFACE OF THE FILM. HE-SE DETECTOR, 1 KV. SCALE BAR =  $400\text{ nm}$  ..... 160

FIGURE 122 - ELECTRON MICROGRAPHS (SEM) OF FILMS PRODUCED BY ADM SYNTHESIS ( $[Ca^{2+}] = 20$  MM, PANA = 20 PPM) AND LEFT AT THE INTERFACE FOR 5 DAYS, OBSERVED AT  $70^\circ$ . THE UPPER SIDE OF THE FILM WAS THE ONE IN CONTACT WITH THE ATMOSPHERE DURING THE SYNTHESIS. THREE DIFFERENT AREAS ARE INVESTIGATED. A) HE-SE DETECTOR, 2 KV. SCALE BAR =  $2 \mu\text{M}$ . B) IN-LENS DETECTOR, 1 KV. SCALE BAR = 400 NM C) HE-SE DETECTOR, 2 KV. SCALE BAR =  $1 \mu\text{M}$ ..... 161

FIGURE 123 - ELECTRON MICROGRAPH (SEM) OF A DISC-PATTERNED FILM ( $[Ca^{2+}] = 20$  MM, PANA = 20 PPM) LEFT AT THE AIR-SOLUTION INTERFACE FOR FIVE DAYS. THE UPPER SIDE OF THE FILM WAS THE ONE IN CONTACT WITH THE ATMOSPHERE DURING THE SYNTHESIS. THE RED DASHED LINE HIGHLIGHTS THE HEIGHT DIFFERENCE BETWEEN TWO DOMAINS. ON BOTH DOMAINS, ELONGATED PROTUSIONS ARE VISIBLE ON THE FILM SIDE IN CONTACT WITH THE ATMOSPHERE. BLUE AND YELLOW SKETCHES HIGHLIGHT THE TILT OF THE PILLARS FOR THE LEFT AND RIGHT DOMAINS, RESPECTIVELY. IMAGE IS TAKEN WITH THE HE-SE DETECTOR AT A VOLTAGE OF 2 KV. SCALE BAR =  $2 \mu\text{M}$ ..... 162

FIGURE 124 - VECTORIAL PTYCHOGRAPHY ANALYSIS OF A FILM SAMPLE CRYSTALLIZED AT THE AIR-SOLUTION INTERFACE. THE FILM SAMPLE HAS BEEN COLLECTED AT THE SURFACE OF A  $[Ca^{2+}] = 20$  MM [PANA] = 20 PPM SOLUTION, AFTER 28H OF REACTION. A) RETARDANCE IN RADIAN (0 TO  $\pi$ ). B) FAST-AXIS ORIENTATION IN DEGREES (0 TO 180). C) C-AXIS TILT RATIO (A.U) D) ELLIPTICITY OF THE EIGENPOLARIZATIONS (0 TO 1; 0 CORRESPONDS TO A LINEAR POLARIZATION AND 1 TO A CIRCULAR ONE). E) COMPOSITE MAP OF RETARDANCE (COLORATION, IN RADIAN, 0 TO  $\pi$ ) AND EIGENPOLARIZATIONS (BLACK). EIGENPOLARIZATIONS ARE PLOTTED ONLY WHEN THE RETARDANCE IS ABOVE 0.5 RADIAN. A,B,C,D =  $20 \mu\text{M}$ ; E =  $5 \mu\text{M}$ ..... 164

FIGURE 125 - AN ISO-STRAIN ISO-TILT DOMAIN EXTRACTED FROM FIGURE A. 12. THE STRAIN, TILT 1 AND TILT 2 MAPS ARE PRESENTED IN THE SAMPLE PLANE (XY) AND ALONG THE SAMPLE THICKNESS (Z). THE FILM SAMPLE WAS COLLECTED AT THE SURFACE OF A  $[Ca^{2+}] = 20$  MM, [PANA] = 20 PPM SOLUTION, AFTER 5 DAYS OF REACTION. .... 165

FIGURE 126 - PHASE MAP OF THE ISO-STRAIN ISO-TILT DOMAIN PRESENTED IN FIGURE 125 A) 3D PHASE WITH SCALE (XYZ) = 100 NM. THE GRAY ISO VOLUMES CORRESPOND TO REGIONS OF LARGE STRAINS ( $> 0.001$ ). B) 2D CROSS-SECTION OF THE PHASE MAP..... 166

FIGURE 127 - COMPARISON OF THE CRYSTALLINE PROPERTIES, RETRIEVED FROM BRAGG PTYCHOGRAPHY DATA, OF A DISC-PATTERNED (SCALE (XYZ) = 100 NM) AND CONTINUOUS (SCALE (XYZ) = 100 NM) FILM, CRYSTALLIZED AT THE INTERFACE. THE CRYSTALLINE PROPERTIES (STRAIN, TILT 1 AND TILT 2), THE COHERENCE LENGTH (SIZE OF THE ISO-STRAIN ISO-TILT DOMAIN) AND THE 3D PHASE MAP WITH HIGH STRAIN REGIONS ( $> 0.001$  FOR THE DISC PATTERNED-FILM,  $> 0.002$  FOR THE CONTINUOUS FILM) ARE SHOWN. .... 166

FIGURE 128 - VARIETY OF SPHERULITES MORPHOLOGIES OBSERVED IN POLYMERIC SYSTEMS. FROM GRÁNÁSY ET AL.<sup>163</sup> ..... 171

FIGURE 129 - BRAGG PTYCHOGRAPHY ON A PINCTADA MARGARITIFERA CALCTIC PRISM. A) VOLUME INVESTIGATED IN THE PRISM. B) 3D MAP SHOWING THE TILT DISTRIBUTION IN THE PROBED VOLUME (IN DEGREES). C) 3D MAP SHOWING THE STRAIN DISTRIBUTION IN THE PROBED VOLUME. FROM MASTROPIETRO ET AL.<sup>16</sup> ..... 176

## ILLUSTRATIONS TABLE

---

FIGURE 130 - 3D BRAGG PTYCHOGRAPHY ON A PINCTADA MARGARITIFERA CALCTIC PRISM. THE PHASE (IN RAD) IS SHOWN IN 3D IN THE INVESTIGATED VOLUME. AREAS OF CONTINUOUS COLORATION (EX. DARK BLUE) SHOW A COHERENCE LENGTH OF 400 NM. SCALE BAR IN 3D: 200 NM. FROM MASTROPIETRO ET AL.<sup>16</sup>.. 177



## 8 BIBLIOGRAPHY

- (1) Mann, S. *Biomineralization: Principles and Concepts in Bioinorganic Materials Chemistry*; Oxford University Press, 2001.
- (2) Gu, G. X.; Takaffoli, M.; Buehler, M. J. Hierarchically Enhanced Impact Resistance of Bioinspired Composites. *Advanced Materials* **2017**, *29* (28), 1700060. <https://doi.org/10.1002/adma.201700060>.
- (3) Melaibari, A.; Wagih, A.; Basha, M.; Kabeel, A. M.; Lubineau, G.; Eltaher, M. A. Bio-Inspired Composite Laminate Design with Improved out-of-Plane Strength and Ductility. *Composites Part A: Applied Science and Manufacturing* **2021**, *144*, 106362. <https://doi.org/10.1016/j.compositesa.2021.106362>.
- (4) Kunitake, M. E.; Mangano, L. M.; Peloquin, J. M.; Baker, S. P.; Estroff, L. A. Evaluation of Strengthening Mechanisms in Calcite Single Crystals from Mollusk Shells. *Acta Biomaterialia* **2013**, *9* (2), 5353–5359. <https://doi.org/10.1016/j.actbio.2012.09.030>.
- (5) Chave, K. E. Physics and Chemistry of Biomineralization. 13.
- (6) Wolf, S. E.; Böhm, C. F.; Harris, J.; Demmert, B.; Jacob, D. E.; Mondeshki, M.; Ruiz-Agudo, E.; Rodríguez-Navarro, C. Nonclassical Crystallization in Vivo et in Vitro (I): Process-Structure-Property Relationships of Nanogranular Biominerals. *Journal of Structural Biology* **2016**, *196* (2), 244–259. <https://doi.org/10.1016/j.jsb.2016.07.016>.
- (7) Kennedy, W. J.; Taylor, J. D.; Hall, A. Environmental and Biological Controls on Bivalve Shell Mineralogy. *Biological Reviews* **1969**, *44* (4), 499–530. <https://doi.org/10.1111/j.1469-185X.1969.tb00610.x>.
- (8) Cartwright, J. H. E.; Checa, A. G.; Gale, J. D.; Gebauer, D.; Sainz-Díaz, C. I. Calcium Carbonate Polyamorphism and Its Role in Biomineralization: How Many Amorphous Calcium Carbonates Are There? *Angewandte Chemie International Edition* **2012**, *51* (48), 11960–11970. <https://doi.org/10.1002/anie.201203125>.
- (9) Seto, J.; Ma, Y.; Davis, S. A.; Meldrum, F.; Gourrier, A.; Kim, Y.-Y.; Schilde, U.; Sztucki, M.; Burghammer, M.; Maltsev, S.; Jäger, C.; Cölfen, H. Structure-Property Relationships of a Biological Mesocrystal in the Adult Sea Urchin Spine. *PNAS* **2012**, *109* (10), 3699–3704. <https://doi.org/10.1073/pnas.1109243109>.
- (10) Yoreo, J. J. D.; Gilbert, P. U. P. A.; Sommerdijk, N. A. J. M.; Penn, R. L.; Whitelam, S.; Joester, D.; Zhang, H.; Rimer, J. D.; Navrotsky, A.; Banfield, J. F.; Wallace, A. F.; Michel, F. M.; Meldrum, F. C.; Cölfen, H.; Dove, P. M. Crystallization by Particle Attachment in Synthetic, Biogenic, and Geologic Environments. *Science* **2015**. <https://doi.org/10.1126/science.aaa6760>.
- (11) Harris, J.; Wolf, S. Desiccator Volume: A Vital Yet Ignored Parameter in CaCO<sub>3</sub> Crystallization by the Ammonium Carbonate Diffusion Method. *Minerals* **2017**, *7*, 122. <https://doi.org/10.3390/min7070122>.
- (12) Gower, L. B.; Odom, D. J. Deposition of Calcium Carbonate films by a Polymer-Induced Liquid-Precursor (PILP) Process. *Journal of Crystal Growth* **2000**, *16*.
- (13) Wolf, S. L. P. Liquid Precursors in Non-Classical Crystallization. 114.
- (14) Farre, B.; Brunelle, A.; Laprèvote, O.; Cuif, J.-P.; Williams, C. T.; Dauphin, Y. Shell Layers of the Black-Lip Pearl Oyster *Pinctada Margaritifera*: Matching Microstructure and Composition. *Comparative Biochemistry and Physiology Part B: Biochemistry and Molecular Biology* **2011**, *159* (3), 131–139. <https://doi.org/10.1016/j.cbpb.2011.03.001>.
- (15) Wolf, S. L. P.; Jähme, K.; Gebauer, D. Synergy of Mg<sup>2+</sup> and Poly(Aspartic Acid) in Additive-Controlled Calcium Carbonate Precipitation. *CrystEngComm* **2015**, *17* (36), 6857–6862. <https://doi.org/10.1039/C5CE00452G>.
- (16) Mastropietro, F.; Godard, P.; Burghammer, M.; Chevillard, C.; Daillant, J.; Duboisset, J.; Allain, M.; Guenoun, P.; Nouet, J.; Chamard, V. Revealing Crystalline Domains in a Mollusc Shell

- Single-Crystalline Prism. *Nature Materials* **2017**, *16*, 946–952.  
<https://doi.org/10.1038/nmat4937>.
- (17) Young, J. R.; Andruleit, H.; Probert, I. Coccolith Function and Morphogenesis: Insights from Appendage-Bearing Coccolithophores of the Family Syracosphaeraceae (Haptophyta)1. *Journal of Phycology* **2009**, *45* (1), 213–226. <https://doi.org/10.1111/j.1529-8817.2008.00643.x>.
- (18) Bay, M. Proceedings of the 13th International Marine Biological Workshop. **2009**, 124.
- (19) Pilarczyk, J. E.; Sawai, Y.; Matsumoto, D.; Namegaya, Y.; Nishida, N.; Ikehara, K.; Fujiwara, O.; Gouramanis, C.; Dura, T.; Horton, B. P. Constraining Sediment Provenance for Tsunami Deposits Using Distributions of Grain Size and Foraminifera from the Kujukuri Coastline and Shelf, Japan. *Sedimentology* **2020**, *67* (3), 1373–1392. <https://doi.org/10.1111/sed.12591>.
- (20) Aizenberg, J.; Tkachenko, A.; Weiner, S.; Addadi, L.; Hendler, G. Calcitic Microlenses as Part of the Photoreceptor System in Brittlestars. *Nature* **2001**, *412* (6849), 819–822.  
<https://doi.org/10.1038/35090573>.
- (21) Nehrke, G.; Poigner, H.; Wilhelms-Dick, D.; Brey, T.; Abele, D. Coexistence of Three Calcium Carbonate Polymorphs in the Shell of the Antarctic Clam *Laternula Elliptica*. *Geochemistry Geophysics Geosystems* **2012**, *13*. <https://doi.org/10.1029/2011GC003996>.
- (22) Marin, F.; Luquet, G. Molluscan Shell Proteins. *Comptes Rendus Palevol* **2004**, *3* (6–7), 469–492. <https://doi.org/10.1016/j.crpv.2004.07.009>.
- (23) Taylor, J.; Layman, M. The Mechanical Properties of Bivalve (Mollusca) Shell Structures. *Palaeontology* **1972**, *15*, 73–87.
- (24) Sun, J.; Bhushan, B. Hierarchical Structure and Mechanical Properties of Nacre: A Review. *RSC Adv.* **2012**, *2* (20), 7617. <https://doi.org/10.1039/c2ra20218b>.
- (25) Clegg, W. J. The Fabrication and Failure of Laminar Ceramic Composites. *Acta Metallurgica et Materialia* **1992**, *40* (11), 3085–3093. [https://doi.org/10.1016/0956-7151\(92\)90471-P](https://doi.org/10.1016/0956-7151(92)90471-P).
- (26) Crenshaw, M. A. The Inorganic Composition of Molluscan Extrapallial Fluid. *Biol Bull* **1972**, *143* (3), 506–512. <https://doi.org/10.2307/1540180>.
- (27) Stemmer, K.; Brey, T.; Gutbrod, M. S. In Situ Measurements of PH, Ca<sup>2+</sup>, and DIC Dynamics within the Extrapallial Fluid of the Ocean Quahog *Arctica Islandica*. *Journal of Shellfish Research* **2019**, *38* (1), 71. <https://doi.org/10.2983/035.038.0107>.
- (28) Lee, S.-W.; Park, S.-B.; Jeong, S.-K.; Lim, K.-S.; Lee, S.-H.; Trachtenberg, M. C. On Carbon Dioxide Storage Based on Biomineralization Strategies. *Micron* **2010**, *41* (4), 273–282.  
<https://doi.org/10.1016/j.micron.2009.11.012>.
- (29) Gruber, N.; Clement, D.; Carter, B. R.; Feely, R. A.; van Heuven, S.; Hoppema, M.; Ishii, M.; Key, R. M.; Kozyr, A.; Lauvset, S. K.; Lo Monaco, C.; Mathis, J. T.; Murata, A.; Olsen, A.; Perez, F. F.; Sabine, C. L.; Tanhua, T.; Wanninkhof, R. The Oceanic Sink for Anthropogenic CO<sub>2</sub> from 1994 to 2007. *Science* **2019**, *363* (6432), 1193–1199. <https://doi.org/10.1126/science.aau5153>.
- (30) Guinotte, J. M.; Fabry, V. J. Ocean Acidification and Its Potential Effects on Marine Ecosystems. *Annals of the New York Academy of Sciences* **2008**, *1134* (1), 320–342.  
<https://doi.org/10.1196/annals.1439.013>.
- (31) Bednaršek, N.; Tarling, G. A.; Bakker, D. C.; Fielding, S.; Cohen, A.; Kuzirian, A.; McCorkle, D.; Lézé, B.; Montagna, R. Description and Quantification of Pteropod Shell Dissolution: A Sensitive Bioindicator of Ocean Acidification. *Glob Change Biol* **2012**, *18* (7), 2378–2388.  
<https://doi.org/10.1111/j.1365-2486.2012.02668.x>.
- (32) Caldeira, K.; Wickett, M. E. Ocean Model Predictions of Chemistry Changes from Carbon Dioxide Emissions to the Atmosphere and Ocean. *Journal of Geophysical Research: Oceans* **2005**, *110* (C9). <https://doi.org/10.1029/2004JC002671>.
- (33) Greiner, M.; Fernández-Díaz, L.; Griesshaber, E.; Zenkert, M. N.; Yin, X.; Ziegler, A.; Veintemillas-Verdaguer, S.; Schmahl, W. W. Biomineral Reactivity: The Kinetics of the Replacement Reaction of Biological Aragonite to Apatite. *Minerals* **2018**, *8* (8), 315.  
<https://doi.org/10.3390/min8080315>.

- (34) Dauphin, Y. Soluble Organic Matrices of the Calcitic Prismatic Shell Layers of Two Pteriomorphid Bivalves. *Journal of Biological Chemistry* **2003**, *278* (17), 15168–15177. <https://doi.org/10.1074/jbc.M204375200>.
- (35) Marin, F. The Formation and Mineralization of Mollusk Shell. *Frontiers in Bioscience* **2012**, *S4* (3), 1099–1125. <https://doi.org/10.2741/s321>.
- (36) Weiner, S. Aspartic Acid-Rich Proteins: Major Components of the Soluble Organic Matrix of Mollusk Shells. *Calcif Tissue Int* **1979**, *29* (1), 163–167. <https://doi.org/10.1007/BF02408072>.
- (37) Gotliv, B.-A.; Addadi, L.; Weiner, S. Mollusk Shell Acidic Proteins: In Search of Individual Functions. *ChemBioChem* **2003**, *4* (6), 522–529. <https://doi.org/10.1002/cbic.200200548>.
- (38) Clark, G. R. Growth Lines in Invertebrate Skeletons. *Annual Review of Earth and Planetary Sciences* **1974**, *2* (1), 77–99. <https://doi.org/10.1146/annurev.ea.02.050174.000453>.
- (39) Cuif, J.-P.; Dauphin, Y.; Nehrke, G.; Nouet, J.; Perez-Huerta, A. Layered Growth and Crystallization in Calcareous Biominerals: Impact of Structural and Chemical Evidence on Two Major Concepts in Invertebrate Biomineralization Studies. *Minerals* **2012**, *2* (1), 11–39. <https://doi.org/10.3390/min2010011>.
- (40) Dauphin, Y.; Cuif, J.; Doucet, J.; Salomé, M.; Susini, J.; Williams, C. In Situ Mapping of Growth Lines in the Calcitic Prismatic Layers of Mollusc Shells Using X-Ray Absorption near-Edge Structure (XANES) Spectroscopy at the Sulphur K-Edge. *Marine Biology* **2003**, *142* (2), 299–304. <https://doi.org/10.1007/s00227-002-0950-2>.
- (41) Duboisset, J.; Ferrand, P.; Baroni, A.; Grünewald, T. A.; Dicko, H.; Grauby, O.; Vidal-Dupiol, J.; Saulnier, D.; Gilles, L. M.; Rosenthal, M.; Burghammer, M.; Nouet, J.; Chevillard, C.; Baronnet, A.; Chamard, V. Amorphous-to-Crystal Transition in the Layer-by-Layer Growth of Bivalve Shell Prisms. *Acta Biomaterialia* **2022**. <https://doi.org/10.1016/j.actbio.2022.01.024>.
- (42) Bergström, L.; Sturm (née Rosseeva), E. V.; Salazar-Alvarez, G.; Cölfen, H. Mesocrystals in Biominerals and Colloidal Arrays. *Acc. Chem. Res.* **2015**, *48* (5), 1391–1402. <https://doi.org/10.1021/ar500440b>.
- (43) O’neill, P. L. Polycrystalline Echinoderm Calcite and Its Fracture Mechanics. *Science* **1981**, *213* (4508), 646–648. <https://doi.org/10.1126/science.213.4508.646>.
- (44) Wolf, S. E.; Lieberwirth, I.; Natalio, F.; Bardeau, J.-F.; Delorme, N.; Emmerling, F.; Barrea, R.; Kappl, M.; Marin, F. Merging Models of Biomineralisation with Concepts of Nonclassical Crystallisation: Is a Liquid Amorphous Precursor Involved in the Formation of the Prismatic Layer of the Mediterranean Fan Mussel *Pinna Nobilis*? *Faraday Discussions* **2012**, *159*, 433. <https://doi.org/10.1039/c2fd20045g>.
- (45) Jacob, D. E.; Soldati, A. L.; Wirth, R.; Huth, J.; Wehrmeister, U.; Hofmeister, W. Nanostructure, Composition and Mechanisms of Bivalve Shell Growth. *Geochimica et Cosmochimica Acta* **2008**, *72* (22), 5401–5415. <https://doi.org/10.1016/j.gca.2008.08.019>.
- (46) Addadi, L.; Raz, S.; Weiner, S. Taking Advantage of Disorder: Amorphous Calcium Carbonate and Its Roles in Biomineralization. *Advanced Materials* **2003**, *15* (12), 959–970. <https://doi.org/10.1002/adma.200300381>.
- (47) Weiss, I. M.; Tuross, N.; Addadi, L.; Weiner, S. Mollusc Larval Shell Formation: Amorphous Calcium Carbonate Is a Precursor Phase for Aragonite. *Journal of Experimental Zoology* **2002**, *293* (5), 478–491. <https://doi.org/10.1002/jez.90004>.
- (48) Microtexture of larval shell of oyster, *Crassostrea nippona*: A FIB-TEM study | Elsevier Enhanced Reader <https://reader.elsevier.com/reader/sd/pii/S1047847709001853?token=FB47C2CF4C1D9A9B668DA8D35A26A24CECF25BC62B1483824B2AD772CA16C0882D0446790CB2DCE6DAE32F33FE0FE2F2&originRegion=eu-west-1&originCreation=20220428140459> (accessed 2022 -04 -28). <https://doi.org/10.1016/j.jsb.2009.07.014>.
- (49) Schönitzer, V.; Weiss, I. M. The Structure of Mollusc Larval Shells Formed in the Presence of the Chitin Synthase Inhibitor Nikkomycin Z. *BMC Struct Biol* **2007**, *7* (1), 71. <https://doi.org/10.1186/1472-6807-7-71>.

- (50) Aizenberg, J.; Weiner, S.; Addadi, L. Coexistence of Amorphous and Crystalline Calcium Carbonate in Skeletal Tissues. *Connective Tissue Research* **2003**, *44* (1), 20–25. <https://doi.org/10.1080/03008200390152034>.
- (51) Aizenberg, J.; Lambert, G.; Weiner, S.; Addadi, L. Factors Involved in the Formation of Amorphous and Crystalline Calcium Carbonate: A Study of an Ascidian Skeleton. *J. Am. Chem. Soc.* **2002**, *124* (1), 32–39. <https://doi.org/10.1021/ja016990l>.
- (52) Levi-Kalisman, Y.; Raz, S.; Weiner, S.; Addadi, L.; Sagi, I. Structural Differences Between Biogenic Amorphous Calcium Carbonate Phases Using X-Ray Absorption Spectroscopy. *Advanced Functional Materials* **2002**, *12* (1), 43–48. [https://doi.org/10.1002/1616-3028\(20020101\)12:1<43::AID-ADFM43>3.0.CO;2-C](https://doi.org/10.1002/1616-3028(20020101)12:1<43::AID-ADFM43>3.0.CO;2-C).
- (53) Politi, Y. Sea Urchin Spine Calcite Forms via a Transient Amorphous Calcium Carbonate Phase. *Science* **2004**, *306* (5699), 1161–1164. <https://doi.org/10.1126/science.1102289>.
- (54) DeVol, R. T.; Sun, C.-Y.; Marcus, M. A.; Coppersmith, S. N.; Myneni, S. C. B.; Gilbert, P. U. P. A. Nanoscale Transforming Mineral Phases in Fresh Nacre. *J. Am. Chem. Soc.* **2015**, *137* (41), 13325–13333. <https://doi.org/10.1021/jacs.5b07931>.
- (55) Gong, Y. U. T.; Killian, C. E.; Olson, I. C.; Appathurai, N. P.; Amasino, A. L.; Martin, M. C.; Holt, L. J.; Wilt, F. H.; Gilbert, P. U. P. A. Phase Transitions in Biogenic Amorphous Calcium Carbonate. *PNAS* **2012**, *109* (16), 6088–6093. <https://doi.org/10.1073/pnas.1118085109>.
- (56) Radha, A. V.; Forbes, T. Z.; Killian, C. E.; Gilbert, P. U. P. A.; Navrotsky, A. Transformation and Crystallization Energetics of Synthetic and Biogenic Amorphous Calcium Carbonate. *PNAS* **2010**, *107* (38), 16438–16443. <https://doi.org/10.1073/pnas.1009959107>.
- (57) Politi, Y.; Metzler, R. A.; Abrecht, M.; Gilbert, B.; Wilt, F. H.; Sagi, I.; Addadi, L.; Weiner, S.; Gilbert, P. U. P. A. Transformation Mechanism of Amorphous Calcium Carbonate into Calcite in the Sea Urchin Larval Spicule. *PNAS* **2008**, *105* (45), 17362–17366. <https://doi.org/10.1073/pnas.0806604105>.
- (58) Beniash, E.; Aizenberg, J.; Addadi, L.; Weiner, S. Amorphous Calcium Carbonate Transforms into Calcite during Sea Urchin Larval Spicule Growth. *Proc Biol Sci* **1997**, *264* (1380), 461–465. <https://doi.org/10.1098/rspb.1997.0066>.
- (59) Ihli, J.; Wong, W. C.; Noel, E. H.; Kim, Y.-Y.; Kulak, A. N.; Christenson, H. K.; Duer, M. J.; Meldrum, F. C. Dehydration and Crystallization of Amorphous Calcium Carbonate in Solution and in Air. *Nature Communications* **2014**, *5*, 3169. <https://doi.org/10.1038/ncomms4169>.
- (60) Faatz, M.; Gröhn, F.; Wegner, G. Amorphous Calcium Carbonate: Synthesis and Potential Intermediate in Biomineralization. *Advanced Materials* **2004**, *16* (12), 996–1000. <https://doi.org/10.1002/adma.200306565>.
- (61) Zou, Z.; Bertinetti, L.; Politi, Y.; Jensen, A. C. S.; Weiner, S.; Addadi, L.; Fratzl, P.; Habraken, W. J. E. M. Opposite Particle Size Effect on Amorphous Calcium Carbonate Crystallization in Water and during Heating in Air. *Chemistry of Materials* **2015**, *27* (12), 4237–4246. <https://doi.org/10.1021/acs.chemmater.5b00145>.
- (62) Zou, Z.; Yang, X.; Albéric, M.; Heil, T.; Wang, Q.; Pokroy, B.; Politi, Y.; Bertinetti, L. Additives Control the Stability of Amorphous Calcium Carbonate via Two Different Mechanisms: Surface Adsorption versus Bulk Incorporation. *Advanced Functional Materials* *n/a* (n/a), 2000003. <https://doi.org/10.1002/adfm.202000003>.
- (63) Rodriguez-Blanco, J. D.; Shaw, S.; Bots, P.; Roncal-Herrero, T.; Benning, L. G. The Role of PH and Mg on the Stability and Crystallization of Amorphous Calcium Carbonate. *Journal of Alloys and Compounds* **2012**, *536*, S477–S479. <https://doi.org/10.1016/j.jallcom.2011.11.057>.
- (64) Gower, L. B. Biomimetic Model Systems for Investigating the Amorphous Precursor Pathway and Its Role in Biomineralization. *Chem. Rev.* **2008**, *108* (11), 4551–4627. <https://doi.org/10.1021/cr800443h>.
- (65) Dai, L.; Douglas, E. P.; Gower, L. B. Compositional Analysis of a Polymer-Induced Liquid-Precursor (PILP) Amorphous CaCO<sub>3</sub> Phase. *Journal of Non-Crystalline Solids* **2008**, *354* (17), 1845–1854. <https://doi.org/10.1016/j.jnoncrysol.2007.10.022>.

- (66) Wolf, S. E.; Leiterer, J.; Pipich, V.; Barrea, R.; Emmerling, F.; Tremel, W. Strong Stabilization of Amorphous Calcium Carbonate Emulsion by Ovalbumin: Gaining Insight into the Mechanism of 'Polymer-Induced Liquid Precursor' Processes. *Journal of the American Chemical Society* **2011**, *133* (32), 12642–12649. <https://doi.org/10.1021/ja202622g>.
- (67) Kelton, K. F.; Greer, A. L. *Nucleation in Condensed Matter: Applications in Materials and Biology*; Elsevier, 2010.
- (68) Gebauer, D.; Völkel, A.; Cölfen, H. Stable Prenucleation Calcium Carbonate Clusters. *Science* **2008**, *322* (5909), 1819–1822. <https://doi.org/10.1126/science.1164271>.
- (69) Albéric, M.; Bertinetti, L.; Zou, Z.; Fratzl, P.; Habraken, W.; Politi, Y. The Crystallization of Amorphous Calcium Carbonate Is Kinetically Governed by Ion Impurities and Water. *Advanced Science* **2018**, *5* (5), 1701000. <https://doi.org/10.1002/adv.201701000>.
- (70) Gebauer, D.; Cölfen, H.; Verch, A.; Antonietti, M. The Multiple Roles of Additives in CaCO<sub>3</sub> Crystallization: A Quantitative Case Study. *Advanced Materials* **2009**, *21* (4), 435–439. <https://doi.org/10.1002/adma.200801614>.
- (71) Lee, S.-W.; Kim, Y.-J.; Lee, Y.-H.; Guim, H.; Han, S. M. Behavior and Characteristics of Amorphous Calcium Carbonate and Calcite Using CaCO<sub>3</sub> Film Synthesis. *Materials & Design* **2016**, *112*, 367–373. <https://doi.org/10.1016/j.matdes.2016.09.099>.
- (72) Rodriguez-Navarro, C.; Kudłacz, K.; Cizer, Ö.; Ruiz-Agudo, E. Formation of Amorphous Calcium Carbonate and Its Transformation into Mesosstructured Calcite. *CrystEngComm* **2015**, *17* (1), 58–72. <https://doi.org/10.1039/C4CE01562B>.
- (73) Xu, X.; Han, J. T.; Cho, K. Deposition of Amorphous Calcium Carbonate Hemispheres on Substrates. *Langmuir* **2005**, *21* (11), 4801–4804. <https://doi.org/10.1021/la047069v>.
- (74) Tribello, G. A.; Bruneval, F.; Liew, C.; Parrinello, M. A Molecular Dynamics Study of the Early Stages of Calcium Carbonate Growth. *J. Phys. Chem. B* **2009**, *113* (34), 11680–11687. <https://doi.org/10.1021/jp902606x>.
- (75) Gebauer, D.; Gunawidjaja, P. N.; Ko, J. Y. P.; Bacsik, Z.; Aziz, B.; Liu, L.; Hu, Y.; Bergström, L.; Tai, C.-W.; Sham, T.-K.; Edén, M.; Hedin, N. Proto-Calcite and Proto-Vaterite in Amorphous Calcium Carbonates. *Angewandte Chemie International Edition* **2010**, *49* (47), 8889–8891. <https://doi.org/10.1002/anie.201003220>.
- (76) Farhadi-Khouzani, M.; Chevrier, D. M.; Zhang, P.; Hedin, N.; Gebauer, D. Water as the Key to Proto-Aragonite Amorphous CaCO<sub>3</sub>. *Angewandte Chemie International Edition* **2016**, *55* (28), 8117–8120. <https://doi.org/10.1002/anie.201603176>.
- (77) Lose, E.; Wilson, R. M.; Seshadri, R.; Meldrum, F. C. The Role of Magnesium in Stabilising Amorphous Calcium Carbonate and Controlling Calcite Morphologies. *Journal of Crystal Growth* **2003**, *254* (1), 206–218. [https://doi.org/10.1016/S0022-0248\(03\)01153-9](https://doi.org/10.1016/S0022-0248(03)01153-9).
- (78) Michel, F. M.; MacDonald, J.; Feng, J.; Phillips, B. L.; Ehm, L.; Tarabrella, C.; Parise, J. B.; Reeder, R. J. Structural Characteristics of Synthetic Amorphous Calcium Carbonate. *Chem. Mater.* **2008**, *20* (14), 4720–4728. <https://doi.org/10.1021/cm800324v>.
- (79) Du, H.; Steinacher, M.; Borca, C.; Huthwelker, T.; Murello, A.; Stellacci, F.; Amstad, E. Amorphous CaCO<sub>3</sub>: Influence of the Formation Time on Its Degree of Hydration and Stability. *J. Am. Chem. Soc.* **2018**, *140* (43), 14289–14299. <https://doi.org/10.1021/jacs.8b08298>.
- (80) Goodwin, A. L.; Michel, F. M.; Phillips, B. L.; Keen, D. A.; Dove, M. T.; Reeder, R. J. Nanoporous Structure and Medium-Range Order in Synthetic Amorphous Calcium Carbonate. *Chemistry of Materials* **2010**, *22* (10), 3197–3205. <https://doi.org/10.1021/cm100294d>.
- (81) Raiteri, P.; Gale, J. D. Water Is the Key to Nonclassical Nucleation of Amorphous Calcium Carbonate. *J. Am. Chem. Soc.* **2010**, *132* (49), 17623–17634. <https://doi.org/10.1021/ja108508k>.
- (82) Schenk, A. S.; Zope, H.; Kim, Y.-Y.; Kros, A.; Sommerdijk, N. A. J. M.; Meldrum, F. C. Polymer-Induced Liquid Precursor (PILP) Phases of Calcium Carbonate Formed in the Presence of Synthetic Acidic Polypeptides—Relevance to Biomineralization. *Faraday Discussions* **2012**, *159*, 327. <https://doi.org/10.1039/c2fd20063e>.

- (83) Rieger, J.; Frechen, T.; Cox, G.; Heckmann, W.; Schmidt, C.; Thieme, J. Precursor Structures in the Crystallization/Precipitation Processes of CaCO<sub>3</sub> and Control of Particle Formation by Polyelectrolytes. *Faraday Discussions* **2007**, *136* (0), 265–277. <https://doi.org/10.1039/B701450C>.
- (84) Bewernitz, M. A.; Gebauer, D.; Long, J.; Cölfen, H.; Gower, L. B. A Metastable Liquid Precursor Phase of Calcium Carbonate and Its Interactions with Polyaspartate. *Faraday Discussions* **2012**, *159*, 291. <https://doi.org/10.1039/c2fd20080e>.
- (85) Guskov, A. The Formation of Two-Phase Periodic Structures. *AMMS* **2018**, *1* (1). <https://doi.org/10.31031/AMMS.2018.01.000505>.
- (86) Datt, C.; Thampi, S. P.; Govindarajan, R. Morphological Evolution of Domains in Spinodal Decomposition. *Phys. Rev. E* **2015**, *91* (1), 010101. <https://doi.org/10.1103/PhysRevE.91.010101>.
- (87) Thakre, A. K.; den Otter, W. K.; Briels, W. J. Domain Formation and Growth in Spinodal Decomposition of a Binary Fluid by Molecular Dynamics Simulations. *Phys. Rev. E* **2008**, *77* (1), 011503. <https://doi.org/10.1103/PhysRevE.77.011503>.
- (88) Zhang, L.; Peng, Y.; Zhang, L.; Lei, X.; Yao, W.; Wang, N. Temperature and Initial Composition Dependence of Pattern Formation and Dynamic Behavior in Phase Separation under Deep-Quenched Conditions. *RSC Adv.* **2019**, *9* (19), 10670–10678. <https://doi.org/10.1039/C9RA01118H>.
- (89) Sebastiani, F.; Wolf, S. L. P.; Born, B.; Luong, T. Q.; Cölfen, H.; Gebauer, D.; Havenith, M. Water Dynamics from THz Spectroscopy Reveal the Locus of a Liquid–Liquid Binodal Limit in Aqueous CaCO<sub>3</sub> Solutions. *Angewandte Chemie International Edition* **2017**, *56* (2), 490–495. <https://doi.org/10.1002/anie.201610554>.
- (90) Myerson, A. S.; Trout, B. L. Nucleation from Solution. *Science* **2013**, *341* (6148), 855–856. <https://doi.org/10.1126/science.1243022>.
- (91) Demichelis, R.; Raiteri, P.; Gale, J. D.; Quigley, D.; Gebauer, D. Stable Prenucleation Mineral Clusters Are Liquid-like Ionic Polymers. *Nature Communications* **2011**, *2* (1), 1–8. <https://doi.org/10.1038/ncomms1604>.
- (92) Wallace, A. F.; Hedges, L. O.; Fernandez-Martinez, A.; Raiteri, P.; Gale, J. D.; Waychunas, G. A.; Whitlam, S.; Banfield, J. F.; Yoreo, J. J. D. Microscopic Evidence for Liquid–Liquid Separation in Supersaturated CaCO<sub>3</sub> Solutions. *Science* **2013**, *341* (6148), 885–889. <https://doi.org/10.1126/science.1230915>.
- (93) Xu, Y.; Tijssen, K. C. H.; Bomans, P. H. H.; Akiva, A.; Friedrich, H.; Kentgens, A. P. M.; Sommerdijk, N. A. J. M. Microscopic Structure of the Polymer-Induced Liquid Precursor for Calcium Carbonate. *Nature Communications* **2018**, *9* (1). <https://doi.org/10.1038/s41467-018-05006-w>.
- (94) Han, T. Y.-J.; Aizenberg, J. Calcium Carbonate Storage in Amorphous Form and Its Template-Induced Crystallization. *Chem. Mater.* **2008**, *20* (3), 1064–1068. <https://doi.org/10.1021/cm702032v>.
- (95) Konrad, F.; Gallien, F.; Gerard, D. E.; Dietzel, M. Transformation of Amorphous Calcium Carbonate in Air. *Crystal Growth & Design* **2016**, *16* (11), 6310–6317. <https://doi.org/10.1021/acs.cgd.6b00906>.
- (96) Xu, X.; Han, J. T.; Kim, D. H.; Cho, K. Two Modes of Transformation of Amorphous Calcium Carbonate Films in Air. *J Phys Chem B* **2006**, *110* (6), 2764–2770. <https://doi.org/10.1021/jp055712w>.
- (97) Oaki, Y.; Imai, H. Experimental Demonstration for the Morphological Evolution of Crystals Grown in Gel Media. *Crystal Growth and Design* **2003**, *3* (5), 711–716. <https://doi.org/10.1021/cg034053e>.
- (98) Du, C. X.; Anders, G. van; Newman, R. S.; Glotzer, S. C. Shape-Driven Solid–Solid Transitions in Colloids. *PNAS* **2017**, *114* (20), E3892–E3899. <https://doi.org/10.1073/pnas.1621348114>.

- (99) Casey, M. T.; Scarlett, R. T.; Benjamin Rogers, W.; Jenkins, I.; Sinno, T.; Crocker, J. C. Driving Diffusionless Transformations in Colloidal Crystals Using DNA Handshaking. *Nat Commun* **2012**, *3* (1), 1209. <https://doi.org/10.1038/ncomms2206>.
- (100) Fang, H.; Hagan, M. F.; Rogers, W. B. Two-Step Crystallization and Solid–Solid Transitions in Binary Colloidal Mixtures. *Proc Natl Acad Sci USA* **2020**, *117* (45), 27927–27933. <https://doi.org/10.1073/pnas.2008561117>.
- (101) Christian, J. W. CHAPTER 9 - Diffusion in the Solid State. In *The Theory of Transformations in Metals and Alloys*; Christian, J. W., Ed.; Pergamon: Oxford, 2002; pp 378–421. <https://doi.org/10.1016/B978-008044019-4/50013-1>.
- (102) Peng, Y.; Wang, F.; Wang, Z.; Alsayed, A. M.; Zhang, Z.; Yodh, A. G.; Han, Y. Two-Step Nucleation Mechanism in Solid–Solid Phase Transitions. *Nature Materials* **2015**, *14* (1), 101–108. <https://doi.org/10.1038/nmat4083>.
- (103) Pogatscher, S.; Leutenegger, D.; Schawe, J. E. K.; Uggowitzer, P. J.; Löffler, J. F. Solid–Solid Phase Transitions via Melting in Metals. *Nat Commun* **2016**, *7* (1), 11113. <https://doi.org/10.1038/ncomms11113>.
- (104) Su, Y.; Wang, X.-D.; Su, Q.; Du, G.; Ren, Y.; Ståhl, K.; Cao, Q.; Zhang, D.; Jiang, J.-Z. Solid-Solid Phase Transition via the Liquid in a Pd<sub>43</sub>Cu<sub>27</sub>Ni<sub>10</sub>P<sub>20</sub> Bulk Metallic Glass under Conventional Conditions. *Journal of Alloys and Compounds* **2021**, *859*, 157802. <https://doi.org/10.1016/j.jallcom.2020.157802>.
- (105) Harris, J.; Mey, I.; Hajir, M.; Mondeshki, M.; Wolf, S. E. Pseudomorphic Transformation of Amorphous Calcium Carbonate Films Follows Spherulitic Growth Mechanisms and Can Give Rise to Crystal Lattice Tilting. *CrystEngComm* **2015**, *17* (36), 6831–6837. <https://doi.org/10.1039/C5CE00441A>.
- (106) Liu, Z.; Zhang, Z.; Wang, Z.; Jin, B.; Li, D.; Tao, J.; Tang, R.; Yoreo, J. J. D. Shape-Preserving Amorphous-to-Crystalline Transformation of CaCO<sub>3</sub> Revealed by in Situ TEM. *PNAS* **2020**. <https://doi.org/10.1073/pnas.1914813117>.
- (107) Huang, J.; Liu, C.; Xie, L.; Zhang, R. Amorphous Calcium Carbonate: A Precursor Phase for Aragonite in Shell Disease of the Pearl Oyster. *Biochemical and Biophysical Research Communications* **2018**, *497* (1), 102–107. <https://doi.org/10.1016/j.bbrc.2018.02.031>.
- (108) Cuif, J.-P.; Dauphin, Y.; Luquet, G.; Medjoubi, K.; Somogyi, A.; Perez-Huerta, A. Revisiting the Organic Template Model through the Microstructural Study of Shell Development in *Pinctada Margaritifera*, the Polynesian Pearl Oyster. *Minerals* **2018**, *8* (9), 370. <https://doi.org/10.3390/min8090370>.
- (109) Ihli, J.; Bots, P.; Kulak, A.; Benning, L. G.; Meldrum, F. C. Elucidating Mechanisms of Diffusion-Based Calcium Carbonate Synthesis Leads to Controlled Mesocrystal Formation. *Advanced Functional Materials* **2013**, *23* (15), 1965–1973. <https://doi.org/10.1002/adfm.201201742>.
- (110) A theory of the rate of sublimation - Transactions of the Faraday Society (RSC Publishing) <https://pubs.rsc.org/en/content/articlelanding/1933/TF/TF9332900794> (accessed 2022 -03 -28).
- (111) Greenspan, L. Humidity Fixed Points of Binary Saturated Aqueous Solutions. *Journal of Research of the National Bureau of Standards Section A: Physics and Chemistry* **1977**, *81A* (1), 89. <https://doi.org/10.6028/jres.081A.011>.
- (112) Sørensen, B. E. A Revised Michel-Lévy Interference Colour Chart Based on First-Principles Calculations. *European Journal of Mineralogy* **2013**, *25* (1), 5–10. <https://doi.org/10.1127/0935-1221/2013/0025-2252>.
- (113) Lide, D. R.; Baysinger, G.; Chemistry, S.; Berger, L. I.; Goldberg, R. N.; Kehiaian, H. V. CRC Handbook of Chemistry and Physics. 2661.
- (114) Merten, H. L. 54 STABILIZED AMORPHOUS CALCIUM CARBONATE. 18.
- (115) Xu, X.; Han, J. T.; Cho, K. Formation of Amorphous Calcium Carbonate Thin Films and Their Role in Biomineralization. *Chemistry of Materials* **2004**, *16* (9), 1740–1746. <https://doi.org/10.1021/cm035183d>.

- (116) Rivera-Perez, C.; Flores-Sánchez, I. A.; Ojeda Ramírez de Areyano, J. J.; Rojas Posadas, D. I.; Hernández-Saavedra, N. Y. A Shell Matrix Protein of *Pinctada Mazatlanica* Produces Nacre Platelets in Vitro. *Sci Rep* **2020**, *10* (1), 20201. <https://doi.org/10.1038/s41598-020-77320-7>.
- (117) Eibe Frank, Mark A. Hall, and Ian H. Witten. Witten\_et\_al\_2016\_appendix.pdf [https://www.cs.waikato.ac.nz/ml/weka/Witten\\_et\\_al\\_2016\\_appendix.pdf](https://www.cs.waikato.ac.nz/ml/weka/Witten_et_al_2016_appendix.pdf) (accessed 2022 - 03 -28).
- (118) Behaviour of a Particle of Very Small Mass in a Magnetic Field. *Nature* **1948**, *162* (4113), 329–329. <https://doi.org/10.1038/162329a0>.
- (119) Williams, D. B.; Carter, C. B. *Transmission Electron Microscopy: A Textbook for Materials Science*, 2nd ed.; Springer: New York, 2008.
- (120) Chen, Y.-C. A Tutorial on Kernel Density Estimation and Recent Advances. *Biostatistics & Epidemiology* **2017**, *1* (1), 161–187. <https://doi.org/10.1080/24709360.2017.1396742>.
- (121) Baba-Kishi, K. Z.; Dingley, D. J. Backscatter Kikuchi Diffraction in the SEM for Identification of Crystallographic Point Groups. *Scanning* **1989**, *11* (6), 305–312. <https://doi.org/10.1002/sca.4950110605>.
- (122) Rodenburg, J.; Maiden, A. Ptychography. In *Springer Handbook of Microscopy*; Hawkes, P. W., Spence, J. C. H., Eds.; Springer Handbooks; Springer International Publishing: Cham, 2019; pp 819–904. [https://doi.org/10.1007/978-3-030-00069-1\\_17](https://doi.org/10.1007/978-3-030-00069-1_17).
- (123) Rodenburg, J. M.; Faulkner, H. M. L. A Phase Retrieval Algorithm for Shifting Illumination. *Appl. Phys. Lett.* **2004**, *85* (20), 4795–4797. <https://doi.org/10.1063/1.1823034>.
- (124) Ferrand, P.; Baroni, A.; Allain, M.; Chamard, V. Quantitative Imaging of Anisotropic Material Properties with Vectorial Ptychography. *Optics Letters* **2018**, *43* (4), 763. <https://doi.org/10.1364/OL.43.000763>.
- (125) Baroni, A.; Chamard, V.; Ferrand, P. Extending Quantitative Phase Imaging to Polarization-Sensitive Materials. *Physical Review Applied* **2020**, *13*. <https://doi.org/10.1103/PhysRevApplied.13.054028>.
- (126) Baroni, A. Développement de la ptychographie vectorielle pour la microscopie quantitative de matériaux anisotropes. 219.
- (127) Baroni, A.; Allain, M.; Li, P.; Chamard, V.; Ferrand, P. Joint Estimation of Object and Probes in Vectorial Ptychography. *Opt. Express* **2019**, *27* (6), 8143. <https://doi.org/10.1364/OE.27.008143>.
- (128) Godard, P.; Carbone, G.; Allain, M.; Mastropietro, F.; Chen, G.; Capello, L.; Diaz, A.; Metzger, T. H.; Stangl, J.; Chamard, V. Three-Dimensional High-Resolution Quantitative Microscopy of Extended Crystals. *Nat Commun* **2011**, *2* (1), 568. <https://doi.org/10.1038/ncomms1569>.
- (129) Pateras, A. I.; Allain, M.; Godard, P.; Largeau, L.; Patriarche, G.; Talneau, A.; Pantzas, K.; Burghammer, M.; Minkevich, A. A.; Chamard, V. Nondestructive Three-Dimensional Imaging of Crystal Strain and Rotations in an Extended Bonded Semiconductor Heterostructure. *Phys. Rev. B* **2015**, *92* (20), 205305. <https://doi.org/10.1103/PhysRevB.92.205305>.
- (130) Buzgar, N. Apopei, A. The Raman Study of Certain Carbonates. *Geologie. Tomul LV, nr.2*, **2009**
- (131) Kontoyannis, C. G.; Vagenas, N. V. Calcium Carbonate Phase Analysis Using XRD and FT-Raman Spectroscopy. *Analyst* **2000**, *125* (2), 251–255. <https://doi.org/10.1039/A908609I>.
- (132) Wehrmeister, U.; Soldati, A. L.; Jacob, D. E.; Häger, T.; Hofmeister, W. Raman Spectroscopy of Synthetic, Geological and Biological Vaterite: A Raman Spectroscopic Study. *Journal of Raman Spectroscopy* **2009**, n/a-n/a. <https://doi.org/10.1002/jrs.2438>.
- (133) Wehrmeister, U.; Jacob, D. E.; Soldati, A. L.; Loges, N.; Häger, T.; Hofmeister, W. Amorphous, Nanocrystalline and Crystalline Calcium Carbonates in Biological Materials. *Journal of Raman Spectroscopy* **2011**, *42* (5), 926–935. <https://doi.org/10.1002/jrs.2835>.
- (134) Zakaria, F. Z.; Mihály, J.; Sajó, I.; Katona, R.; Hajba, L.; Aziz, F. A.; Mink, J. FT-Raman and FTIR Spectroscopic Characterization of Biogenic Carbonates from Philippine Venus Seashell and



- Porites Sp. Coral. *Journal of Raman Spectroscopy* **2008**, *39* (9), 1204–1209. <https://doi.org/10.1002/jrs.1964>.
- (135) de Groot, F. M. F.; de Smit, E.; van Schooneveld, M. M.; Aramburo, L. R.; Weckhuysen, B. M. In-Situ Scanning Transmission X-Ray Microscopy of Catalytic Solids and Related Nanomaterials. *ChemPhysChem* **2010**, *11* (5), 951–962. <https://doi.org/10.1002/cphc.200901023>.
- (136) De Groot, F. M. F.; Elnaggar, H.; Frati, F.; Wang, R.-P.; Delgado-Jaime, M. U.; Van Veenendaal, M.; Fernandez-Rodriguez, J.; Haverkort, M. W.; Green, R. J.; Van Der Laan, G.; Kvashnin, Y.; Hariki, A.; Ikeno, H.; Ramanantoanina, H.; Daul, C.; Delley, B.; Odelius, M.; Lundberg, M.; Kuhn, O.; Bokarev, S. I.; Shirley, E.; Vinson, J.; Gilmore, K.; Stener, M.; Fronzoni, G.; Decleva, P.; Kruger, P.; Retegan, M.; Joly, Y.; Vorwerk, C.; Draxl, C.; Rehr, J.; Tanaka, A. 2p X-Ray Absorption Spectroscopy of 3d Transition Metal Systems. *Journal of Electron Spectroscopy and Related Phenomena* **2021**, *249*, 147061. <https://doi.org/10.1016/j.elspec.2021.147061>.
- (137) Rez, P.; Blackwell, A. Ca L23 Spectrum in Amorphous and Crystalline Phases of Calcium Carbonate. *J. Phys. Chem. B* **2011**, *115* (38), 11193–11198. <https://doi.org/10.1021/jp203057y>.
- (138) Miedema, P. S.; Ikeno, H.; de Groot, F. M. F. First Principles Multiplet Calculations of the Calcium L<sub>2,3</sub> x-Ray Absorption Spectra of CaO and CaF<sub>2</sub>. *J. Phys.: Condens. Matter* **2011**, *23* (14), 145501. <https://doi.org/10.1088/0953-8984/23/14/145501>.
- (139) Tsao, C.; Yu, P.-T.; Lo, C.-H.; Chang, C.-K.; Wang, C.-H.; Yang, Y.-W.; Chan, J. C. C. Anhydrous Amorphous Calcium Carbonate (ACC) Is Structurally Different from the Transient Phase of Biogenic ACC. *Chemical Communications* **2019**, *55* (48), 6946–6949. <https://doi.org/10.1039/C9CC00518H>.
- (140) Sander, R. Compilation of Henry's Law Constants (Version 4.0) for Water as Solvent. *Atmospheric Chemistry and Physics* **2015**, *15* (8), 4399–4981. <https://doi.org/10.5194/acp-15-4399-2015>.
- (141) Kern, D. M. The Hydration of Carbon Dioxide. *Journal of Chemical Education* **1960**, *37* (1), 14. <https://doi.org/10.1021/ed037p14>.
- (142) Berhanu, M.; Philippi, J.; Courrech du Pont, S.; Derr, J. Solutal Convection Instability Caused by Dissolution. *Physics of Fluids* **2021**, *33* (7), 076604. <https://doi.org/10.1063/5.0052305>.
- (143) Philippi, J.; Berhanu, M.; Derr, J.; Courrech du Pont, S. Solutal Convection Induced by Dissolution. *Physical Review Fluids* **2019**, *4* (10). <https://doi.org/10.1103/PhysRevFluids.4.103801>.
- (144) Song, X.; Nobes, D. S. Experimental Investigation of Evaporation-Induced Convection in Water Using Laser Based Measurement Techniques. *Experimental Thermal and Fluid Science* **2011**, *35* (6), 910–919. <https://doi.org/10.1016/j.expthermflusci.2011.01.010>.
- (145) Tanaka, H. Hydrodynamic Interface Quench Effects on Spinodal Decomposition for Symmetric Binary Fluid Mixtures. *Physical Review E* **1995**, *51* (2), 1313–1329. <https://doi.org/10.1103/PhysRevE.51.1313>.
- (146) Cantaert, B.; Kim, Y.-Y.; Ludwig, H.; Nudelman, F.; Sommerdijk, N. A. J. M.; Meldrum, F. C. Think Positive: Phase Separation Enables a Positively Charged Additive to Induce Dramatic Changes in Calcium Carbonate Morphology. *Advanced Functional Materials* **2012**, *22* (5), 907–915. <https://doi.org/10.1002/adfm.201102385>.
- (147) Bewernitz, M. A.; Gebauer, D.; Long, J.; Cölfen, H.; Gower, L. B. A Metastable Liquid Precursor Phase of Calcium Carbonate and Its Interactions with Polyaspartate. *Faraday Discuss.* **2013**, *159* (0), 291–312. <https://doi.org/10.1039/C2FD20080E>.
- (148) Avaro, J. T.; Wolf, S. L. P.; Hauser, K.; Gebauer, D. Stable Pre-Nucleation Calcium Carbonate Clusters Define Liquid-Liquid Phase Separation. *Angewandte Chemie n/a* (n/a). <https://doi.org/10.1002/ange.201915350>.
- (149) Wolf, S. E.; Leiterer, J.; Pipich, V.; Barrea, R.; Emmerling, F. Strong Stabilization of Liquid Amorphous Calcium Carbonate by Ovalbumin: Gaining Insight into the Mechanism of 'Polymer-Induced Liquid Precursor' Processes. *7*.

- (150) Amos, F. F.; Sharbaugh, D. M.; Talham, D. R.; Gower, L. B.; Fricke, M.; Volkmer, D. Formation of Single-Crystalline Aragonite Tablets/Films via an Amorphous Precursor. *Langmuir* **2007**, *23* (4), 1988–1994. <https://doi.org/10.1021/la061960n>.
- (151) Dey, A.; Bomans, P. H. H.; Müller, F. A.; Will, J.; Frederik, P. M.; de With, G.; Sommerdijk, N. A. J. M. The Role of Prenucleation Clusters in Surface-Induced Calcium Phosphate Crystallization. *Nature Materials* **2010**, *9* (12), 1010–1014. <https://doi.org/10.1038/nmat2900>.
- (152) Gower, L. B.; Odom, D. J. Deposition of Calcium Carbonate Films by a Polymer-Induced Liquid-Precursor (PILP) Process. *Journal of Crystal Growth* **2000**, *16*.
- (153) Medale, M. Cerisier, P. Numerical simulation of Bénard-Marangoni convection in small aspect ratio containers: Numerical Heat Transfer, Part A: Applications: Vol 42, No 1-2 **2010** <https://www.tandfonline.com/doi/abs/10.1080/10407780290059422>
- (154) Trouette, B.; Chénier, E.; Doumenc, F.; Delcarte, C.; Guerrier, B. Transient Rayleigh-Bénard-Marangoni Solutal Convection. *Physics of Fluids* **2012**, *24* (7), 074108. <https://doi.org/10.1063/1.4733439>.
- (155) Zhang, J.; Behringer, R. P.; Oron, A. Marangoni Convection in Binary Mixtures. *Phys. Rev. E* **2007**, *76* (1), 016306. <https://doi.org/10.1103/PhysRevE.76.016306>.
- (156) Panjan, P.; Drnovšek, A.; Gselman, P.; Čekada, M.; Panjan, M. Review of Growth Defects in Thin Films Prepared by PVD Techniques. *Coatings* **2020**, *10* (5), 447. <https://doi.org/10.3390/coatings10050447>.
- (157) Sims, S. D.; Didymus, J. M.; Mann, S. Habit Modification in Synthetic Crystals of Aragonite and Vaterite. *Journal of the Chemical Society, Chemical Communications* **1995**, No. 10, 1031. <https://doi.org/10.1039/c39950001031>.
- (158) Gower, L. A.; Tirrell, D. A. Calcium Carbonate Films and Helices Grown in Solutions of Poly(Aspartate). *Journal of Crystal Growth* **1998**, *191* (1–2), 153–160.
- (159) Gránásy, L.; Pusztai, T.; Börzsönyi, T.; Warren, J. A.; Douglas, J. F. A General Mechanism of Polycrystalline Growth. *Nature Mater* **2004**, *3* (9), 645–650. <https://doi.org/10.1038/nmat1190>.
- (160) McNeill, I. C.; Sadeghi, S. M. T. Thermal Stability and Degradation Mechanisms of Poly(Acrylic Acid) and Its Salts: Part 2—Sodium and Potassium Salts. *Polymer Degradation and Stability* **1990**, *30* (2), 213–230. [https://doi.org/10.1016/0141-3910\(90\)90077-K](https://doi.org/10.1016/0141-3910(90)90077-K).
- (161) Keith, H. D.; Padden, F. J. Spherulitic Crystallization from the Melt. II. Influence of Fractionation and Impurity Segregation on the Kinetics of Crystallization. *Journal of Applied Physics* **1964**, *35* (4), 1286–1296. <https://doi.org/10.1063/1.1713607>.
- (162) Tegze, G.; Tóth, G. I.; Gránásy, L. Faceting and Branching in 2D Crystal Growth. *Phys. Rev. Lett.* **2011**, *106* (19), 195502. <https://doi.org/10.1103/PhysRevLett.106.195502>.
- (163) Gránásy, L.; Pusztai, T.; Tegze, G.; Warren, J. A.; Douglas, J. F. Growth and Form of Spherulites. *Physical review. E, Statistical, nonlinear, and soft matter physics* **2005**, *72* (1), 011605. <https://doi.org/10.1103/PhysRevE.72.011605>.
- (164) Ulčinas, A.; Butler, M. F.; Heppenstall-Butler, M.; Singleton, S.; Miles, M. J. Direct Observation of Spherulitic Growth Stages of CaCO<sub>3</sub> in a Poly(Acrylic Acid)–Chitosan System: In Situ SPM Study. *Journal of Crystal Growth* **2007**, *307* (2), 378–385. <https://doi.org/10.1016/j.jcryspro.2007.06.023>.
- (165) Goldenfeld, N. Theory of Spherulitic Crystallization. *Journal of Crystal Growth* **1987**, *84* (4), 601–608. [https://doi.org/10.1016/0022-0248\(87\)90051-0](https://doi.org/10.1016/0022-0248(87)90051-0).
- (166) Huang, J.; Prasad, A.; Marand, H. Study of the Temperature Dependence of Isothermal Spherulitic Growth Rate Data for Poly(Pivalolactone) in Blends with Poly(Vinylidene Fluoride): A Link between Coherent Secondary Nucleation Theory and Mixing Thermodynamics. *Polymer* **1994**, *35* (9), 1896–1908. [https://doi.org/10.1016/0032-3861\(94\)90979-2](https://doi.org/10.1016/0032-3861(94)90979-2).
- (167) Gránásy, L.; Rátkai, L.; Szállás, A.; Korbuly, B.; Tóth, G. I.; Környei, L.; Pusztai, T. Phase-Field Modeling of Polycrystalline Solidification: From Needle Crystals to Spherulites—A Review.

- Metall and Mat Trans A* **2014**, *45* (4), 1694–1719. <https://doi.org/10.1007/s11661-013-1988-0>.
- (168) Smith, M. E.; Knauss, K. G.; Higgins, S. R. Effects of Crystal Orientation on the Dissolution of Calcite by Chemical and Microscopic Analysis. *Chemical Geology* **2013**, *360–361*, 10–21. <https://doi.org/10.1016/j.chemgeo.2013.09.015>.
- (169) Njegić-Džakula, B.; Falini, G.; Brečević, L.; Skoko, Ž.; Kralj, D. Effects of Initial Supersaturation on Spontaneous Precipitation of Calcium Carbonate in the Presence of Charged Poly-l-Amino Acids. *Journal of Colloid and Interface Science* **2010**, *343* (2), 553–563. <https://doi.org/10.1016/j.jcis.2009.12.010>.
- (170) Dauphin, Y.; Zolotoyabko, E.; Berner, A.; Lakin, E.; Rollion-Bard, C.; Cuif, J. P.; Fratzl, P. Breaking the Long-Standing Morphological Paradigm: Individual Prisms in the Pearl Oyster Shell Grow Perpendicular to the c-Axis of Calcite. *Journal of Structural Biology* **2019**, *205* (2), 121–132. <https://doi.org/10.1016/j.jsb.2019.01.004>.
- (171) Alberti, S.; Gladfelter, A.; Mittag, T. Considerations and Challenges in Studying Liquid-Liquid Phase Separation and Biomolecular Condensates. *Cell* **2019**, *176* (3), 419–434. <https://doi.org/10.1016/j.cell.2018.12.035>.
- (172) Mass, T.; Drake, J. L.; Heddleston, J. M.; Falkowski, P. G. Nanoscale Visualization of Bio-mineral Formation in Coral Proto-Polyps. *Current Biology* **2017**, *27* (20), 3191–3196.e3. <https://doi.org/10.1016/j.cub.2017.09.012>.
- (173) Bahn, S. Y.; Jo, B. H.; Choi, Y. S.; Cha, H. J. Control of Nacre Biomineralization by Pif80 in Pearl Oyster. *Science Advances* **2017**, *3* (8), e1700765. <https://doi.org/10.1126/sciadv.1700765>.
- (174) Gindele, M. B.; Steingrube, L. V.; Gebauer, D. Generality of Liquid Precursor Phases in Gas Diffusion-Based Calcium Carbonate Synthesis. *CrystEngComm* **2021**, *23* (45), 7938–7943. <https://doi.org/10.1039/D1CE00225B>.
- (175) Wolf, S. L. P.; Caballero, L.; Melo, F.; Cölfen, H. Gel-Like Calcium Carbonate Precursors Observed by *in Situ* AFM. *Langmuir* **2017**, *33* (1), 158–163. <https://doi.org/10.1021/acs.langmuir.6b03974>.
- (176) Huang, J.; Jiang, T.; Liu, C.; Liu, Y.; Zheng, G.; Wang, H.; Zhang, G.; Xie, L.; Zhang, R. Transition from Horizontal Expansion to Vertical Growth in the Oyster Prismatic Layer. *Biochemical and Biophysical Research Communications* **2021**, *563*, 47–53. <https://doi.org/10.1016/j.bbrc.2021.05.067>.
- (177) Suzuki, M.; Nakayama, S.; Nagasawa, H.; Kogure, T. Initial formation of calcite crystals in the thin prismatic layer with the periostracum of *Pinctada fucata*. *Micron* **2013**, *45*, 136–139. <https://doi.org/10.1016/j.micron.2012.10.010>.
- (178) Sillanpää, J. K.; Sundh, H.; Sundell, K. S. Calcium Transfer across the Outer Mantle Epithelium in the Pacific Oyster, *Crassostrea Gigas*. *Proc. R. Soc. B.* **2018**, *285* (1891), 20181676. <https://doi.org/10.1098/rspb.2018.1676>.
- (179) Xiang, L.; Kong, W.; Su, J.; Liang, J.; Zhang, G.; Xie, L.; Zhang, R. Amorphous Calcium Carbonate Precipitation by Cellular Biomineralization in Mantle Cell Cultures of *Pinctada Fucata*. *PLoS ONE* **2014**, *9* (11), e113150. <https://doi.org/10.1371/journal.pone.0113150>.
- (180) Mount, A. S.; Wheeler, A. P.; Paradkar, R. P.; Snider, D. Hemocyte-Mediated Shell Mineralization in the Eastern Oyster. *Science* **2004**, *304* (5668), 297–300. <https://doi.org/10.1126/science.1090506>.
- (181) Goswami, A. Structural and Mechanical Studies on Sea Shells, 2014. <https://doi.org/10.13140/RG.2.2.17045.47846>.
- (182) Li, P.; Allain, M.; Grünwald, T. A.; Rommel, M.; Campos, A.; Carbone, D.; Chamard, V. 4th Generation Synchrotron Source Boosts Crystalline Imaging at the Nanoscale. *Light: Science & Applications* **2022**, *11* (1). <https://doi.org/10.1038/s41377-022-00758-z>.
- (183) Pecher, J.; Guenoun, P.; Chevillard, C. Crystalline Calcium Carbonate Thin Film Formation through Interfacial Growth and Crystallization of Amorphous Microdomains. *Crystal Growth & Design* **2009**, *9* (3), 1306–1311. <https://doi.org/10.1021/cg800251t>.

## BIBLIOGRAPHY

---

- (184) Hansen, S. H.; Andersen, M. L.; Cornett, C.; Gradinaru, R.; Grunnet, N. A Role for Taurine in Mitochondrial Function. *Journal of Biomedical Science* **2010**, *17* (1), S23.  
<https://doi.org/10.1186/1423-0127-17-S1-S23>.

**Titre :** Cristaux synthétiques bio-inspirés

**Mots clés :** Biominéralisation, nucléation cristalline, état amorphe, séparation de phase liquide-liquide

**Résumé :** Les biominéraux calcaires présentent une grande variété de formes et de fonctions biologiques, mais également un certain nombre de traits structuraux communs. En particulier, ils apparaissent, dans leur grande majorité, comme formés d'un assemblage de nanoparticules cristallines sphéroïdales, tout en ayant des propriétés cristallines voisines de celles d'un monocristal. La compacité de cette nanostructure suggère l'existence d'un transitoire liquide précédant la formation d'un état amorphe, quant à lui démontré dans un certain nombre de cas. Le chemin de cristallisation, qui mettrait ainsi en jeu des états intermédiaires typiques des processus de cristallisation dits non-classiques, n'est pas entièrement établi à ce jour. En particulier, l'existence d'une phase liquide enrichie en ions reste complexe à démontrer *in vivo*. Afin d'évaluer la pertinence d'une telle hypothèse, une approche basée sur un modèle synthétique incluant une phase liquide dense a été utilisée.

Des films de carbonate de calcium amorphes d'épaisseur sub-micronique ont été produits par diffusion de CO<sub>2</sub> gazeux dans une solution calcique en présence de polyelectrolyte anionique. Le mécanisme de formation des films, associant le développement d'un motif 2D par séparation de phase liquide-liquide et l'agrégation irréversible de nanoparticules amorphes formées en solution, a été démontré. Les films amorphes ont été cristallisés par chauffage, exposition à une humidité relative contrôlée, ou vieillissement dans le milieu réactionnel. La caractérisation de ces cristaux 2D, notamment par ptychographie de Bragg, a permis de décrire les mécanismes de transition amorphe-cristal et préciser les propriétés cristallines pour chaque condition de cristallisation. Certains cristaux présentent des propriétés très semblables aux cristaux biogéniques, appuyant ainsi l'hypothèse d'un intermédiaire liquide dans la biominéralisation calcaire.

**Title :** Bio-inspired synthetic crystals

**Keywords :** Biomineralization, crystal nucleation, amorphous state, liquid-liquid phase separation

**Abstract:** Calcareous biominerals present a great variety of forms and biological functions, but also a number of common structural features. In particular, they appear, in their great majority, to be formed by an assembly of spheroidal crystalline nanoparticles, while having crystalline properties close to those of a single crystal. The compactness of this nanostructure suggests the existence of a liquid transient prior to the formation of an amorphous state, which has been evidenced in a number of cases. The crystallization pathway, which would involve intermediate states typical of so-called non-classical crystallization processes, is not yet fully established. In particular, the existence of an ion-enriched liquid phase remains complex to demonstrate *in vivo*. In order to assess the relevance of such a hypothesis, an approach based on a synthetic model including a dense liquid phase was used.

Amorphous calcium carbonate films of sub-micron thickness were produced by CO<sub>2</sub> gas diffusion in a calcium solution in the presence of anionic polyelectrolyte. The mechanism of film formation, combining the development of a 2D pattern by liquid-liquid phase separation and the irreversible aggregation of amorphous nanoparticles formed in solution, was demonstrated. The amorphous films were crystallized by heating, exposure to controlled relative humidity, or aging in the reaction medium. The characterization of these 2D crystals, in particular by Bragg ptychography, has made it possible to describe the amorphous-crystal transition mechanisms and to specify the crystalline properties for each crystallization condition. Some crystals show properties very similar to biogenic crystals, thus supporting the hypothesis of a liquid intermediate in calcareous biomineralization.